

Doctoral theses at NTNU, 2023:238

Eirik Holm Fyhn

Green's Function Approach to Quantum Phenomena in Heterostructures with Spin- Polarization and Coherence

Doctoral thesis

NTNU
Norwegian University of Science and Technology
Thesis for the Degree of
Philosophiae Doctor
Faculty of Natural Sciences
Department of Physics



NTNU

Norwegian University of
Science and Technology

Eirik Holm Fyhn

Green's Function Approach to Quantum Phenomena in Heterostructures with Spin- Polarization and Coherence

Thesis for the Degree of Philosophiae Doctor

Trondheim, August 2023

Norwegian University of Science and Technology
Faculty of Natural Sciences
Department of Physics

NTNU

Norwegian University of Science and Technology

Thesis for the Degree of Philosophiae Doctor

Faculty of Natural Sciences

Department of Physics

© Eirik Holm Fyhn

ISBN 978-82-326-7176-2 (printed ver.)

ISBN 978-82-326-7175-5 (electronic ver.)

ISSN 1503-8181 (printed ver.)

ISSN 2703-8084 (online ver.)

Doctoral theses at NTNU, 2023:238

Printed by NTNU Grafisk senter

Abstract

Green's functions are powerful tools in theoretical condensed matter physics. They can be used to model a wide range of physical systems, including complicated heterostructures consisting of multiple materials with different types of quantum order, such as magnetism and superconductivity, and with various geometries in arbitrary external electromagnetic fields. Such systems are of special interest because when two different materials are combined in a mesoscopic structure, new physics can arise that was not present in either material separately. For example, putting a spin-singlet superconductor next to a spin-polarized ferromagnet can spawn a spin-triplet superconducting condensate that can carry spin-polarized currents with no resistance. Although quasiclassical Green's function theory can effectively model a wide range of realistic heterostructures and reproduce experimental measurements with high accuracy, there are still systems outside the scope of the theory. For instance, the equations become difficult or even unsolvable in time-dependent systems, and while ferromagnetic systems can easily be incorporated into the quasiclassical theory for normal metals, the same is not true for antiferromagnets.

In this thesis I give a thorough introduction to quasiclassical Green's function theory, starting from the very foundations of quantum mechanics. The main body of work consists of the 10 enclosed research papers. These papers apply Green's functions to study heterostructures, with an emphasis on systems with spin-polarization and coherent superconducting condensates. The work is focused on, but not limited to, quasiclassical theory, and includes the development of new theory, such as quasiclassical theory for antiferromagnetic systems and approaches to studying time-dependent phenomena using quasiclassical Green's functions.

Preface

This thesis is submitted in partial fulfillment of the requirements for the degree of philosophiae doctor at the Norwegian University of Science and Technology (NTNU). The research presented herein was conducted as part of a four-year graduate program in physics. The graduate program also included coursework corresponding to 30 ECTS and one year of teaching duties. My research has been supervised by Professor Jacob Linder, and Professor Justin Wells was my co-supervisor. I have used the template by Jabir Ali Ouassou, which is available at gitlab.com/jabiro/babathesis, as a basis when preparing my thesis. This template is in turn based on the KOMA-Script book class, and is compiled using LuaLatex.

It has been my intention to write the thesis as self-contained as possible, starting from the mathematical foundations of quantum mechanics. It has been satisfying to construct a narrative connecting the state-of-the-art quasiclassical Green's function techniques to the very foundations of quantum mechanics. My hope is that this can prove useful to others trying to enter the field, or simply wanting to learn quantum mechanics. While I have tried to include everything necessary to give a self-contained picture, I have also placed special emphasis on topics that I believe not to be widely known or discussed, such as the subtle distinction between Hermitian (symmetric) and self-adjoint operators, and the geometric connection between spin and rotation. In this way, I hope that both experts and newcomers can find something interesting to learn, or possibly relearn, within these pages.

In addition to the enclosed papers, I have also authored two other publications [1, 2] during my time as a graduate student. However, these are thematically unrelated and not part of this thesis.

Acknowledgements

First and foremost, I am forever grateful to my supervisor Jacob Linder, without whom this thesis would not have been possible. I have been extraordinarily lucky to have such an enthusiastic, helpful, and knowledgeable supervisor. It has been a joy discussing physics with you, and your enthusiasm, kindness, and passion for physics continue to be great sources of inspiration. I will always look back on these years with fondness, and that is in no small part thanks to you.

Next, I want to thank Karl Yngve Lervåg, Åsmund Ervik and Øivind Wilhelmsen. Before my graduate studies, you took the time and effort to patiently guide me as an inexperienced, young student in my very first meeting with publishing in scientific journals. It was an educational and exciting experience that I will never forget. Thank you very much.

Another beacon of guidance for me has been Morten Amundsen. I am thankful for having shared an office with you during the first year of my studies. Working on closely related theories, and sometimes on the same project, you never hesitated to share your insight and experience. Thank you.

I also wish to extend my gratitude to everyone at QuSpin for four enjoyable years, with special thanks to John Ove Fjærestad, Henning Goa Hugdal, Jabir Ali Ouassou, Asle Sudbø, Alireza Qaiumzadeh, Arne Brataas, Haakon Thømt Simensen, Håvard H. Haugen, Even Thingstad, Sol H. Jacobsen, Anna Cecilie Åsland, Jeroen Danon, Jonas Lidal, Niels Henrik Aase, Christian Svingen Johnsen, Vemund Falch, Lina Johnsen Kamra, Bjørnulf Brekke, and of course Karen-Elisabeth Sødahl. Thank you for all the enjoyable and enlightening conversations.

I have also had the great pleasure of collaborating with many talented people outside of QuSpin. I have learned a lot through many emails and Zoom calls, in particular with Ayelet Zalic and Werner M. J. van Weerdenburg, but also with Tom Dvir, Hadar Steinberg, Anand Kamlapure, and Alexander Ako Khajetoorians. I also wish to thank Niels P. E. van Mullekom, Manuel Steinbrecher, Peter Krogstrup, Takashi Taniguchi, and Kenji Watanabe.

Finally, I wish to thank my family for all the unwavering support over the years, and in particular I want to give the most heartfelt of

thanks to my wife, Hursanay. You are not only my wife, but also my partner, best friend, and jinim. In addition to giving me constant guidance and support, you have also made sure that life has been enjoyable along the way. Thank you for everything.

Contents

Publications	ix
1 Introduction	1
1.1 History of computers	1
1.2 Spintronics	4
1.3 Superconducting spintronics	6
1.4 Outline	8
2 Quantum Mechanics	11
2.1 The Mathematics of Quantum Mechanics	11
2.2 Time Evolution in Quantum Mechanics	15
2.3 Many Particle Physics	19
2.4 Non-Interacting Particles	22
2.5 Spin and Conservation Laws	25
2.6 The Electron Magnetic Moment and Spin-Orbit Coupling	32
2.7 Quantum Electrodynamics	44
3 Quantum Theory of Solids	51
3.1 Lattice Models	51
3.2 Magnetism	57
3.3 Superconductivity	69
3.4 External Fields	85
3.4.1 Electrostatic Potential and the Zeeman Effect	86
3.4.2 Peierls Substitution	88
3.4.3 Rashba Spin-Orbit Coupling	92
4 Green's functions	95
4.1 Definition of Green's functions	95
4.2 Equilibrium Green's functions	100

4.3	Example: Non-interacting systems	102
4.3.1	Magnets	104
4.3.2	Superconductors	108
5	Green's Function Perturbation Theory	113
5.1	Quadratic Hamiltonians	113
5.1.1	Example: Impurity scattering	118
5.2	Interaction Picture and Time Ordering	123
5.2.1	Example: Dissipation	135
6	Quasiclassical Keldysh Theory	139
6.1	Green's functions in Wigner coordinates	140
6.2	The Quasiclassical Green's Function and the Eilenberger Equation	151
6.3	Normalization Condition	160
6.4	The Dirty Limit	167
6.5	Boundary conditions	180
6.6	Observables in quasiclassical theory	185
7	Numerics	189
7.1	Parametrization	190
7.2	Discretization	193
7.2.1	The Finite Element Method	193
7.2.2	Collocation Methods	199
7.3	Solving Nonlinear equations	202
7.4	Forward-Mode Automatic Differentiation	205
7.5	Fixed-Point Acceleration	206
8	Research Highlights	211
9	Conclusion and Outlook	219
	Bibliography	221
	Enclosed Publications	259

Publications

- I **Eirik Holm Fyhn and Jacob Linder,** 259
Superconducting vortices in half-metals.
Physical Review B **100**, 224508 (2019)
DOI: 10.1103/physrevb.100.224508
- II **Eirik Holm Fyhn and Jacob Linder,** 271
Controllable vortex loops in superconducting proximity systems.
Physical Review B **100**, 214503 (2019)
DOI: 10.1103/physrevb.100.214503
- III **Eirik Holm Fyhn, Morten Amundsen, Ayelet Zalic, Tom Dvir,** 281
Hadar Steinberg, and Jacob Linder,
Combined Zeeman and orbital effect on the Josephson effect in rippled graphene.
Physical Review B **102**, 024510 (2020)
DOI: 10.1103/physrevb.102.024510
- IV **Tom Dvir, Ayelet Zalic, Eirik Holm Fyhn, Morten Amundsen,** 293
Takashi Taniguchi, Kenji Watanabe, Jacob Linder, and Hadar Steinberg,
Planar graphene-NbSe₂ Josephson junctions in a parallel magnetic field.
Physical Review B **103**, 115401 (2021)
DOI: 10.1103/physrevb.103.115401

- V **Eirik Holm Fyhn and Jacob Linder,** 309
Temporarily enhanced superconductivity from magnetic fields.
 Physical Review B **103**, L100502 (2021)
 doi: 10.1103/physrevb.103.l100502
- VI **Eirik Holm Fyhn and Jacob Linder,** 321
Spin pumping in superconductor-antiferromagnetic insulator bi-layers.
 Physical Review B **103**, 134508 (2021)
 doi: 10.1103/physrevb.103.134508
- VII **Eirik Holm Fyhn and Jacob Linder,** 333
Spin-orbit pumping.
 Physical Review B **105**, L020409 (2022)
 doi: 10.1103/physrevb.105.l020409
- VIII **Werner M. J. van Weerdenburg, Anand Kamlapure, Eirik Holm Fyhn, Xiaochun Huang, Niels P. E. van Mullekom, Manuel Steinbrecher, Peter Krogstrup, Jacob Linder, and Alexander Ako Khajetoorians,** 347
Extreme enhancement of superconductivity in epitaxial aluminum near the monolayer limit.
 Science Advances **9**, eadf5500 (2023)
 doi: 10.1126/sciadv.adf5500
- IX **Eirik Holm Fyhn, Arne Brataas, Alireza Qaiumzadeh, and Jacob Linder,** 379
Quasiclassical theory for antiferromagnetic metals.
 Physical Review B **107**, 174503 (2023)
 doi: 10.1103/physrevb.107.174503
- X **Eirik Holm Fyhn, Arne Brataas, Alireza Qaiumzadeh, and Jacob Linder,** 407
Superconducting proximity effect and long-ranged triplets in dirty metallic antiferromagnets.
 arXiv:2210.09325
 doi: 10.48550/arxiv.2210.09325

Introduction

1

1.1 History of computers

A modern computer does essentially three things. It reads data, manipulates data, and performs calculations. We have had machines that do the latter for a long time. From the simple abacus, dating back to Mesopotamia more than 4000 years ago [3], to the much more complicated difference engine [4]. The difference engine, a mechanical machine named after the method of divided differences and conceived in the 1820s by Charles Babbage, was designed to tabulate polynomial functions.¹ At a time when the way to multiply large numbers was to look up tables of logarithms, it was naturally desirable to be able to compute logarithms and other functions that can be approximated as polynomials through Taylor series.

While mechanical calculators are useful, the true utility of computers is unlocked when the computer can read and manipulate data. A system for data manipulation, such as the instruction set of a computer, is said to be Turing-complete [5, 6] if it fulfills certain conditions, such as the ability to perform conditional branching.² Unlike a mechanical calculator, a Turing-complete machine is a *general purpose machine* capable of executing an infinite number of different algorithms. It can not only perform a predetermined algorithm using the input data, but the input data can itself define the algorithm. This means that a Turing-complete machine can be *programmed* to do more or less any task, given enough time and memory. It would not be an overstatement to say that this feature of computers has had a major impact on modern society.

The first design for a Turing-complete machine was created before Alan Turing was born. It was Charles Babbage's successor to the

-
1. Despite much funding from the British government at the time, the difference engine was not made until much later.
 2. More precisely, a machine is Turing complete if it is computationally equivalent to the *automatic machine* defined by Turing [5]. The automatic machine is a simple theoretical machine that manipulates symbols on a strip of tape. Despite its simplicity, it can implement any computer algorithm.

difference engine, the analytical engine [4]. Although never built, it would have been able to run computer programs written on punched cards. In fact, such programs were written, making them the first computer programs in history. A famous example is the program by Ada Lovelace [7], which would have computed Bernoulli numbers on the analytical engine.³ Punched cards were also used to input data in the early computers, such as the EDSAC [8] produced by the University of Cambridge in 1949.

The first generation of digital computers used vacuum tubes for logic circuitry [9]. However, everything changed when computer manufacturers instead began using MOSFET transistors. This was because of what is known as Dennard scaling, which is the phenomenon that the power use of MOSFET transistors is proportional to their area [10]. Dennard scaling means that even if you double the number of transistors, the required power stays the same as long as the area of each transistor is halved. As transistors became smaller, the power reduction from Dennard scaling allowed manufacturers to turn the transistors on and off faster, thereby drastically increasing clock frequencies. Not only have clock frequencies increased, but the number of transistors in integrated circuits has since essentially doubled every two years, in accordance with the so-called *Moore's law* [11, 12]. As a result, we have seen a vast improvement in both compactness and computational power ever since the first commercial microprocessor was released in 1971. This was the Intel 4004 [13]. It had 2300 transistors running at 740 kHz. In comparison, Apple's M1 Ultra chip from 2021 has 114 billion transistors running at 3.2 GHz [14].

Unfortunately, this way of improving computers by making the transistors smaller and faster cannot last forever. In fact, the method of increasing clock speed stopped working around 2005. Intel's Pentium D 840 processor, released in 2005, had clock speeds up to 3.2 GHz [15]. Although the M1 Ultra chip has about five hundred times more transistors, the clock frequency has not improved compared to the 16 years older Pentium D 840. The primary reason for this boils down to Joule heating [16]. When electrons move they generally produce heat, ex-

3. Ada Lovelace is often considered to be the world's first programmer because of her idea that numbers in a computer could represent more than just numbers. It is also argued that the first programmer was instead Charles Babbage since he wrote the first programs for the analytical engine.

cept if the medium happens to be a superconductor. Depending on the temperature, transistors can become unstable. In some temperature regimes, MOSFETs can enter so-called thermal runaways [17]. A thermal runaway is a positive feedback loop in which the amount of Joule heating increases with temperature. For example, the on-resistance of MOSFETs increases with temperature. Therefore, a constant current through a MOSFET in the on-state will produce more Joule heating when the temperature is higher. This positive feedback loop limits how fast the transistor can operate.

While Moore's law has proven more resilient, this too cannot last forever. With transistors currently on the order of nanometers in size, we might be nearing the limit of what is physically, or at least practically, possible. As a result, the cost for producers to fulfill Moore's law is ever-increasing. Moreover, even if Moore's law could last forever, or even if we are happy with the speed of computers today, we should still seek alternative ways to manufacture computers. The reason for this is that computers consume an unnecessarily large amount of energy. This is not only because of the energy wasted through Joule heating but also the additional energy needed to cool the computers down in order to avoid the above-mentioned thermal runaway. The recommended power supply for a personal computer with the latest graphics cards and CPUs is currently as much as 1300 W [18]. This is more than many heaters. A state-of-the-art personal computer can therefore produce enough heat to heat up an entire room.

It is perhaps not surprising then, that a sizable amount of the world's energy demand comes from information and communication technologies, and that this is only expected to increase [19]. This is not only because there are small computers in almost literally everything today, but also because of the growth of big data centers, not to mention the use of computer graphic cards to mine cryptocurrency [20] or to train large artificial neural networks such as in the currently ongoing explosion of large language models like generative pre-trained transformers (GPT). In a sense, the computers of today are like incandescent light bulbs. The purpose of these light bulbs is to produce light, but they waste around 95 % of the applied energy to heat. Just as incandescent light bulbs have been replaced by much more efficient LED light bulbs, the inefficient way computers work today should be replaced by more

energy-efficient technologies. There are a few contenders in the race to find alternative ways to build computers. The most relevant to the work presented here is called spintronics.

1.2 Spintronics

The idea behind spintronics is to utilize not just the electric charge of electrons, like in conventional electronics, but also the electron spin [21–24]. Every electron carries an intrinsic angular momentum called spin, which origin is explained in section 2.5. Because total angular momentum can be a conserved quantity (see section 2.5), it is possible to use spin to store and manipulate information. Historically, spintronics has most successfully been used to store information, but in theory it could also be used to manipulate data in an energy-efficient way, making spintronics a contender for next-generation energy-efficient computer technology.

What makes spintronics possible is that electrons effectively have magnetic moments which are parallel to their spin [25]. This means that one can rotate electron spin through applied magnetic fields. Alternatively, since the theory of relativity implies that the electric field observed by a static observer is equivalent to a magnetic field observed by a moving observer (see section 2.6), the spin of moving electrons can be influenced by electric fields. This effect is known as the spin-orbit effect because it couples spin and orbital motion inside potentials.

The most prominent example of spintronics in modern computers is possibly in hard disk drives [26]. Hard disk drives are a type of non-volatile memory, meaning that they can hold information without being actively powered. This is done by encoding information using magnetic domains. By sandwiching a nonmagnetic material between two ferromagnets, the electrical resistance will depend on the relative angle between the magnetization directions of the ferromagnets [27–29]. This spintronics effect is called either giant magnetoresistance [30, 31] or tunnel magnetoresistance [32, 33], depending on whether the nonmagnetic material is conducting.⁴ Using this effect, the magnetization orientation of ferromagnets can encode information [34]. The

4. The 2007 Nobel prize in physics was awarded to Albert Fert and Peter Grünberg for the discovery of giant magnetoresistance [29].

information can be read by measuring the resistance, and it can be changed by applying an external magnetic field.

Being made of permanent magnets, the information is kept even when the computer is turned off. This is in contrast to volatile memory, such as dynamic random-access memory (DRAM) [35], in which information is stored through the electric charge. To store information using electric charge, one can for instance use capacitors. If the capacitor is charged, it may represent a 1, and if it is discharged it may represent a 0. When power is turned off, the charge quickly disperses and all information is lost. Equal charges repel, and for this reason, long-term memory has often been stored either by physically altering an object, like optical disks [36] or punched cards [37], or by using magnetic materials, such as magnetic tape [38], floppy disks [39] or hard disk drives [26]. That being said, hard disk drives are currently being superseded by solid-state drives (SSDs) [40], which work using electric charge. The reason why the information does not need to be actively sustained in solid-state drives is that the charge is surrounded by an electrically insulating material in so-called *floating gate MOSFETs* [41].

There are also other examples of spintronics applications, such as in spin organic light-emitting diodes (spin-OLED) [42], magnetoresistive random-access memory (MRAM) [43] and the Datta-Das transistor [44]. However, common for all of these examples is that they rely on charge transport. As a result, they produce waste heat in a similar way to electronics-based computer components. The question therefore remains: How can one store and manipulate information by utilizing spin in a way that does not produce as much waste heat? Insight into possible answers to this question can be found by considering the main mechanism for heat production in computers, which is Joule heating.

As mentioned above, Joule heating refers to the heat produced by electrons passing through a conductor with resistance. Therefore, there are in essence two ways to eliminate this process. One can either remove the passing of electrons, or one can remove the resistance of the conductor. Two promising research directions within the field of spintronics pursue these two different methods for eliminating Joule heating. *Spin insulatronics* removes the passing of electrons by utilizing spin waves in ferromagnetic and antiferromagnetic insulators, thereby separating the charge and spin degrees of freedom. The resistance,

on the other hand, can be removed by using superconductors. To use superconductors within the field of spintronics is the aspiration in the field of *superconducting spintronics*, which is the main motivation of most of the work presented in this thesis.

1.3 Superconducting spintronics

The term *superconducting spintronics* can sound like an oxymoron to readers with some degree of familiarity with superconductors. Superconductors [45], discovered in 1911 [46], are primarily associated with two important effects. First is that electric currents can pass through superconductors with zero resistance, which is what makes superconductors especially useful when the aim is energy efficiency. The second effect, which is often said to be more fundamental to superconductivity, is the so-called *Meissner effect* [45, 47]. This is the effect that superconductors expel magnetic fields from their interiors. That is, superconductors are materials with perfect diamagnetism. Superconductivity and magnetism are therefore competing types of quantum order. In order to penetrate a conventional superconductor with magnetic fields you have to destroy the superconductivity, either completely or partially, by introducing so-called superconducting vortices [45, 48].

On the other hand, spintronics is about manipulating the magnetic properties of electrons. This would seem difficult in materials with perfect diamagnetism. Nevertheless, Keizer *et al.* [49] showed experimentally that a complete synergy between superconductivity and magnetism is possible when they observed resistance-free current through a half-metallic ferromagnet. Half-metals are strongly polarized ferromagnets where all itinerant electrons have their spins aligned in the same direction [50]. Therefore, the only way a resistance-free current, or supercurrent, can pass through half-metals is through so-called *spin-triplet superconductivity* [51].

Conventional superconductivity, meaning superconductivity described by BCS-theory [52], occurs in materials with an effective attraction between electrons (see section 3.3). This can result in the formation of *Cooper pairs*, named after Leon Cooper who, together with John Bardeen and John Schrieffer, developed the above-mentioned BCS theory [52], the first microscopic theory for superconductivity.

Being formed by two electrons, Cooper pairs are bosons, and this allows them to condense into the same quantum state (see section 2.3). This breaks the $U(1)$ symmetry of quantum electrodynamics, which through the Higgs-mechanism makes the photon field massive inside superconductors, resulting in the Meissner effect [53, 54].⁵

The Cooper pairs in conventional superconductors are spin-singlets, meaning that they have zero net spin. Spin-singlet supercurrents therefore carry no spin, making such currents impractical in the context of spintronics. However, as the experiments by Keizer *et al.* [49] prove, it is possible to create supercurrent carried by spin-triplet superconductivity. Using such superconductors, it is possible to transfer spin without any generation of waste heat. While there are examples of materials that are both superconducting and ferromagnetic in certain temperature regimes [55–62], a possibly more promising way to produce spin-triplet superconductivity with regards to future application is through the proximity effect [63, 64]. The *proximity effect* refers to how materials in close proximity to superconductors also show superconducting properties.

By combining common ferromagnets with conventional superconductors, it is possible to create spin-carrying spin-triplet superconductivity [65]. This is also how Keizer *et al.* [49] produced spin-triplet superconductivity inside half-metallic ferromagnets. Depending on the mean free path, the spin-triplet superconductivity created in this way is often odd-frequency [66]. While conventional even-frequency superconductors are condensates of Cooper pairs, resulting in a non-zero expectation value of the Cooper pair annihilation operator (see section 2.3), this is not generally true for odd-frequency superconductors. In purely odd-frequency superconductors there is by definition no standard Cooper pair annihilation operator⁶ with a non-zero expectation value. Hence, these are not condensates of normal Cooper pairs

5. While the Higgs-mechanism is most famous for its role in the standard model, it was first discovered in the context of superconductivity by Anderson [53]. It is therefore also referred to as the Anderson-Higgs-mechanism.

6. By *standard Cooper pair annihilation operator* I mean operators like $c_\lambda c_\mu$, where $c_{\lambda/\mu}$ are electron annihilation operators. One could broaden this definition by going to the Heisenberg picture and evaluate the electron operators at arbitrary times, $c_\lambda(t_1)c_\mu(t_2)$. In this definition, both even-frequency and odd-frequency superconductors will have non-zero Cooper pair expectation values, depending on t_1 and t_2 .

in the same way as conventional superconductors. Instead, they can in some cases be characterized as condensates of composite bosons [67].

The creation of spin-triplet superconductivity, for instance in mesoscopic heterostructures combining conventional spin-singlet superconductivity with either inhomogeneous ferromagnets [49, 65, 68–72] or spin-orbit coupling [73–80] opens the possibility for using superconductivity to transport spin without any dissipation of energy. Currently known superconductors require either very low temperatures, below 39 K for conventional superconductors conforming to BCS theory [81, 82] or below 138 K for unconventional high-temperature superconductors [82–84], or very high pressures of more than 100 GPa [85–88]. These are not ideal conditions for everyday electronics such as personal computers. Nevertheless, they could be overcome in big data centres [89, 90], which represent a substantial portion of the energy consumption from information and communication technologies [19]. Hence, significant energy savings can be obtained from cryogenic computers [89, 90], even if a satisfying solution to the hundred-year-old problem of room-temperature superconductivity [91] is never found.

The field of superconducting spintronics has already spawned proposals for practical applications [92], such as memory cells based on heterostructures involving superconductors and ferromagnets [93–96], which could work together with single-flux-quantum superconducting logic devices [97–99]. Nevertheless, there is still much to explore in terms of fundamental physics related to superconducting spintronics. This is the focus of the work presented here. By expanding our understanding of the physics of mesoscopic systems, we can hopefully facilitate the development of novel energy-efficient information and communication technologies.

1.4 Outline

This thesis starts with a review of the mathematics of quantum mechanics in chapter 2. Starting from the definition of Hilbert spaces and the subtleties between Hermitian and self-adjoint operators, I introduce time-evolution, the quantum theory of many-particle systems, the origin of spin, the electron magnetic moment and spin-orbit coupling, before I end the chapter with a discussion on quantum electrodynamics. Having introduced the fundamental building blocks of

the electron and photon quantum fields, I discuss the quantum theory of solids in chapter 3. First, I show how the periodic potentials in crystalline materials can be captured by lattice models, which is the starting point for much of the theoretical modeling in the remainder of the thesis. Then, I show how electric interactions combined with fermionic statistics give rise to magnetism, and how the motion of the crystal lattice can give rise to superconductivity. Finally, I complete the description of crystalline materials by showing how to include the effect of external electromagnetic fields.

Having shown how to model mesoscopic structures, the next three chapters describe how to use these models to set up differential equations and compute observables. Chapter 4 introduces the concept of Green's functions, both in the mathematical sense and in how the term is used in condensed matter physics. Chapter 5 shows how perturbation techniques can be used to approximate Green's functions when a full solution is difficult to compute. This includes a derivation of the Dyson equation based on the concepts introduced in chapter 4 and a thorough derivation of perturbation theory based on time-ordered Green's functions, including an example from my work. I conclude the chapter with examples of how these concepts can be used to include dissipation and elastic impurity scattering, which are later used in the next chapter as well as in my work more broadly.

Chapter 6 takes the theoretical foundations of Green's functions presented in chapters 4 and 5 and derives quasiclassical Green's function theory, which is capable of modeling complex heterostructures with impurities and a wide array of inhomogeneous effects, both in and out of equilibrium. Quasiclassical theory has been an effective tool in my work, and the derivation I present in chapter 6 is the most general derivation I have seen to this date. It includes an arbitrary number of energy-bands, which can describe a wide range of physical systems, such as antiferromagnets, ferromagnets, Rashba-superconductors or multi-orbital superconductors. I also allow the different energy bands to cross the Fermi surface at different points, and with different gradients, meaning that their densities of states are different, something which is normally not included in quasiclassical theory. I also derive a generalized normalization condition which is valid for this theory, and show how the equations simplify in the diffusive limit. Finally, I

derive boundary conditions for diffusive systems and how to compute observables from quasiclassical Green's functions.

Having shown how to set up differential equations to heterostructures, methods for solving these equations numerically are discussed in chapter 7. This includes how to parametrize the quasiclassical Green's functions, different methods for discretizing the equations, how to solve the resulting set of non-linear equations, and how to ensure that the solution is self-consistent. Finally, chapter 8 reviews some research highlights, and concluding remarks are given in chapter 9.

Quantum Mechanics

Quantum mechanics is arguably the most successful theory in the history of physics. Many of its predictions have been verified to very high accuracy, and most systems seem to be fundamentally described by quantum mechanics. The only exception is possibly general relativity, although there are fascinating efforts to obtain spacetime from a bare-bones version of quantum mechanics [100–103]. In certain situations, for example when considering macroscopic systems, the quantum theory can be well approximated by a classical theory. However, this is often not the case for mesoscopic heterostructures, so to properly model nanophysics one must start from a quantum mechanical description.

In this chapter, I review the important underlying concepts of quantum mechanics that are necessary to model the physics of electrons in crystalline solids. I start from the mathematical foundations of quantum mechanics before I introduce time evolution and the quantum theory of many particles. Next, I explain the physics of non-interacting particles, which must still effectively interact through the rules of quantum mechanics. Thereafter, I show how conservation laws originate from symmetries, which introduces both the origin of spin and the principle of least action. From the principle of least action, I start from the fully relativistic Dirac Lagrangian and derive a non-relativistic effective theory. This explains both the Zeeman effect and spin-orbit coupling, both serving pivotal roles in spintronics. Again using the principle of least action, I conclude the chapter by introducing the electromagnetic field in quantum electrodynamics and deriving an effective theory of interacting electrons which serves as the foundation for the quantum theory of solids in the next chapter.

2.1 The Mathematics of Quantum Mechanics

In quantum mechanics, the current state of a system is encoded in its *state vector*, $|\psi\rangle$ [104]. The state vector is assumed to be the element of a Hilbert space \mathcal{H} , which means that the space is equipped with an inner product and that the space is complete with respect to this inner product [105]. In bracket-notation, the inner product of $|\psi\rangle$ and $|\varphi\rangle$ is $\langle\varphi|\psi\rangle = \langle\psi|\varphi\rangle^*$ and is a complex scalar. The inner product is conjugate

linear in the left argument and linear in the right argument, meaning that if $|\psi\rangle = a|\psi_1\rangle + b|\psi_2\rangle$, then

$$\langle\phi|\psi\rangle = a\langle\phi|\psi_1\rangle + b\langle\phi|\psi_2\rangle, \quad (2.1a)$$

$$\langle\psi|\phi\rangle = a^*\langle\psi_1|\phi\rangle + b^*\langle\psi_2|\phi\rangle. \quad (2.1b)$$

Also, the inner product of a vector with itself is always real and non-negative, meaning that $\langle\psi|\psi\rangle \geq 0$. State vectors are often normalized such that $\langle\psi|\psi\rangle = 1$. The completeness of Hilbert spaces comes from the fact that every Cauchy sequence converges with respect to the norm defined by the inner product [105]. However, for physicists, a more important reason for why the space is assumed complete is that it ensures the existence of an orthonormal basis. That is, there exists a set of vectors, B , such that all $|\psi\rangle \in \mathcal{V}$ can be written

$$|\psi\rangle = \sum_{|b\rangle \in B} |b\rangle \langle b|\psi\rangle. \quad (2.2)$$

The convergence of this series follows from the completeness of \mathcal{V} because of the convergence of Cauchy sequences [105]. The dimensionality of the Hilbert space might be infinite, meaning that the cardinality of B can be infinite and even possibly uncountable. The basis B is said to be complete when it spans the whole space, and one can often see equation (2.2) written in terms of the identity operator 1,

$$1 = \sum_{|b\rangle \in B} |b\rangle \langle b|. \quad (2.3)$$

This is often referred to as a completeness relation and $\langle b|$ must be understood as an operator mapping vectors $|\psi\rangle$ to scalars $\langle b|\psi\rangle$.

Observables are typically assumed to be represented by symmetric, or Hermitian, operators.¹ This is partly because symmetric operators can only have real expectation values [106]. However, the reverse is not true. That is, operators can have real spectra without being Hermitian. For example, in an important paper, Bender and Boettcher [107] showed that the Hermiticity requirement could be replaced by symmetry under the combined operator of parity (P) and time reversal (T). Operators

1. The word *Hermitian* is sometimes used to mean symmetric and sometimes used to mean self-adjoint. Here, I use Hermitian to mean symmetric. The concepts of self-adjoint and symmetric operators are related, as I discuss below.

which are PT-symmetric are also interesting for other physical [108, 109] and mathematical [110, 111] reasons. Nevertheless, in this work, I assume that operators representing observables are Hermitian.

The adjoint, A^\dagger , of an operator, A , is defined such that

$$\langle \varphi | (A|\psi\rangle) = (\langle \varphi | A^\dagger) |\psi\rangle \quad (2.4)$$

for all $|\psi\rangle$ in the domain of A , and the domain of A^\dagger is the set of all $|\varphi\rangle$ for which equation (2.4) holds. The operator A^\dagger acts to the left on the right-hand side of equation (2.4). An operator is called symmetric, or Hermitian, if $A|\psi\rangle = A^\dagger|\psi\rangle$ for all $|\psi\rangle$ in the domain of A . One can see that this leads to real expectation values, $\langle \psi | A | \psi \rangle$, since

$$\langle \psi | A | \psi \rangle^* = \langle \psi | A^\dagger | \psi \rangle = \langle \psi | A | \psi \rangle. \quad (2.5)$$

To determine whether or not an operator is symmetric is not always trivial. For instance, consider a single scalar particle in a one-dimensional system, such that the Hilbert space is $L^2(\mathbb{R})$, consisting of all square-integrable functions on the real line. The operators $K = -\partial^2/\partial x^2$ and $V = -x^4$ are both symmetric, but their sum, $-\partial^2/\partial x^2 - x^4$, is not. In fact, $K + V$ has purely imaginary eigenvalues [104, 106]. This shows that a sum of Hermitian operators need not be Hermitian. However, note that the operator $K + V$ is the Hamiltonian operator corresponding to an unphysical situation with a potential that is unbounded from below. In practice one often assumes that operators corresponding to observables are Hermitian as long as they reflect physically realizable systems.

A more strict operator requirement is that of self-adjoint operators. In order for an operator A to be self-adjoint, it must be symmetric and, in addition, the domains of A and A^\dagger must be the same. As an example of a symmetric but not self-adjoint operator, take the momentum operator $P = -i\partial/\partial x$ acting on particles in an infinitely deep, one-dimensional quantum well, meaning all square-integrable functions on the domain $[0, 1]$ with $\psi(0) = \psi(1) = 0$. This operator is symmetric, but not self-adjoint. This is reflected in the fact that P has no eigenfunctions. While the expectation value, $\langle \psi | P | \psi \rangle = \int_0^1 dx \psi^*(x) P \psi(x)$, is always real for a symmetric operator, the existence of eigenfunctions is only guaranteed for self-adjoint operators. For example, the momentum operator $P = -i\partial/\partial x$ acting on particles in a thin ring is

self-adjoint. The space of particles in a thin ring is the set of all square-integrable functions on $[0, 1]$ with $\psi(0) = \psi(1)$, and the eigenfunctions are $\exp(2\pi ikx)$, where k is in the set of integers.

In practice, it is sufficient for operators to be essentially self-adjoint, meaning that their closures are self-adjoint [106]. Self-adjoint operators are of special interest because of the spectral theorem. In simple terms, the spectral theorem essentially states that self-adjoint operators can be diagonalized [106]. That is, self-adjoint operators have complete sets of eigenstates. However, this is only a simplification and not strictly true. Because we are dealing with infinite-dimensional Hilbert spaces, it is often not possible to properly diagonalize operators in the conventional sense. That is, it is often not possible to find a basis B for which a self-adjoint operator, \mathcal{H} can be written

$$\mathcal{H}|\psi\rangle = \sum_{|b\rangle \in B} \mathcal{H}|b\rangle \langle b|\psi\rangle = \sum_{|b\rangle \in B} |b\rangle h(b) \langle b|\psi\rangle, \quad (2.6)$$

for all $|\psi\rangle$, where $h(b)$ is a scalar.

Take for instance the position operator X . Taking again $L^2(\mathbb{R})$ as the Hilbert space and applying X to a function $\psi \in L^2(\mathbb{R})$ gives $(X\psi)(x) = x\psi(x)$, meaning that X is a so-called *multiplication operator* [105]. This operator is self-adjoint, but it has no eigenvectors, or eigenfunctions, in $L^2(\mathbb{R})$. Instead, it has eigenvectors in a larger space, namely the space of distributions. The δ -distributions are eigenvectors since $x\delta(x - \lambda) = \lambda\delta(x - \lambda)$. However, the space of distributions is *not* a Hilbert space. As a result, we may diagonalize X , but not in terms of proper eigenvectors. We may diagonalize it in terms of *generalized* eigenvectors, so that

$$(X\psi)(x) = \int_{\mathbb{R}} dy \delta(x - y)y \int_{\mathbb{R}} dz \delta(y - z)\psi(z) \quad (2.7)$$

If we identify $|y\rangle = \delta(x - y)$, we can write

$$X|\psi\rangle = \int_{\mathbb{R}} dy |y\rangle y \langle y|\psi\rangle, \quad (2.8)$$

which is on the same form as equation (2.6). This notation is purely formal, however, because $\langle y|\psi\rangle$ is not an inner product in the sense of the Hilbert space, it is a distribution acting on $|\psi\rangle$, and $|y\rangle$ is not a member of the Hilbert space. The generalized eigenvectors are normalized in the sense that $\langle x|y\rangle = \delta(x - y)$.

The spectral theorem states that any self-adjoint operator is unitarily equivalent to a multiplication operator [106]. This means that the operator can be diagonalized in the sense of generalized eigenvectors, even if the operator does not have any proper eigenvectors. Although the generalized eigenvectors are not in the Hilbert space, they span the space in the sense that any element of the Hilbert space can be written in terms of generalized eigenvectors, as in equation (2.8). That is, one can also refer to completeness relations for generalized eigenvectors, which may be written in a formal notation as

$$1 = \int_{\mathbb{R}} dx |x\rangle\langle x|. \quad (2.9)$$

For example, all square-integrable functions can be written as a linear combination of plane waves, the generalized eigenvectors of the momentum operator, even though plane waves themselves are not square-integrable.

In physics literature, the word Hermitian is sometimes also used to refer to self-adjoint operators. However, since the Hilbert space under consideration typically is infinite-dimensional, symmetric operators need not be self-adjoint. This distinction is especially important for the Hamiltonian, which is the total energy operator. The special connection between the Hamiltonian and time-evolution in quantum mechanics, discussed in section 2.2, requires the spectral theorem, which is valid for self-adjoint operators but not symmetric operators. The technical reason is that Stone's theorem [106, 112], which relies on the spectral theorem, establishes a one-to-one correspondence between one-parameter families of strongly continuous unitary operators and self-adjoint operators. It is important that the time-evolution operators are unitary since this preserves the normalization of state vectors, and that they are continuous in one parameter, namely time. Self-adjointness is also important when considering functions of operators, such as the potential energy in the Hamiltonian being a function of the position operator.

2.2 Time Evolution in Quantum Mechanics

In quantum mechanics, one is typically first introduced to the Schrödinger picture, in which the state vectors evolve in time according to the

Schrödinger equation [25],

$$i\frac{\partial}{\partial t}|\psi_S(t)\rangle = \mathcal{H}_S(t)|\psi_S(t)\rangle, \quad (2.10)$$

where t is time, $\mathcal{H}_S(t)$ is the Hamiltonian at time t and the subscript S reminds us that these objects are defined in the Schrödinger picture. One can also define the time-evolution operator $U(t, t_0)$ as being the operator which takes a state vector from time t_0 to t , meaning that

$$|\psi_S(t)\rangle = U(t, t_0)|\psi_S(t_0)\rangle. \quad (2.11)$$

Since equation (2.10) must hold regardless of the choice of $|\psi_S(t_0)\rangle$, one can see that

$$i\frac{\partial}{\partial t}U(t, t_0) = \mathcal{H}_S(t)U(t, t_0). \quad (2.12)$$

From $U(t_0, t)U(t, t_0) = 1$, one also gets

$$-i\frac{\partial}{\partial t}U(t_0, t) = U(t_0, t)\mathcal{H}_S(t). \quad (2.13)$$

In quantum mechanics, quantities define operators which act on state vectors. The expectation value of an operator $A_S(t)$ for a system in state $|\psi_S(t)\rangle$ is defined as [25]

$$\langle A \rangle_{\psi}(t) = \langle \psi_S(t) | A_S(t) | \psi_S(t) \rangle. \quad (2.14)$$

However, one typically only has statistical knowledge of the state of a system. If the probability of the system to be in state $|\psi_S\rangle$ is p_{ψ} , then the expectation value is

$$\langle A \rangle(t) = \sum_{\psi} \langle A \rangle_{\psi}(t) p_{\psi}, \quad (2.15)$$

where the sum goes over a complete set of state vectors. For example, in the grand canonical ensemble [113], which will be assumed here unless otherwise specified, the probability for an eigenstate of the Hamiltonian with eigenvalue $E - \mu N$ is

$$p_{\psi} = \frac{1}{Z} e^{-(E - \mu N)\beta}, \quad (2.16)$$

where Z is the partition function and β is inverse temperature. Note that I have defined the Hamiltonian to include the chemical potential μ

multiplied by the number of particles N . The partition function ensures that the probability distribution is normalized.

The Heisenberg picture is equivalent to the Schrödinger picture, but the time-evolution is attached to the operators instead of the state vectors [114]. This is done in such a way that all expectation values are unchanged, meaning that

$$\langle A \rangle_{\psi}(t) = \langle \psi_S(t) | A_S(t) | \psi_S(t) \rangle = \langle \psi_H | A_H(t) | \psi_H \rangle, \quad (2.17)$$

where the subscripts H indicate that objects are defined in the Heisenberg picture. If $|\psi_H\rangle = |\psi_S(t_0)\rangle$, one can see from

$$\begin{aligned} \langle A \rangle_{\psi}(t) &= \langle \psi_S(t_0) | U^\dagger(t, t_0) A_S(t) U(t, t_0) | \psi_S(t_0) \rangle \\ &= \langle \psi_H | U(t_0, t) A_S(t) U(t, t_0) | \psi_H \rangle \end{aligned} \quad (2.18)$$

that

$$A_H(t) = U(t_0, t) A_S(t) U(t, t_0). \quad (2.19)$$

Taking the derivative of this with respect to t and using equations (2.12) and (2.13), I get that operators in the Heisenberg picture must solve

$$i \frac{\partial A_H}{\partial t} = - [\mathcal{H}_H(t), A_H(t)]_- + U(t_0, t) i \frac{\partial A_S}{\partial t} U(t, t_0), \quad (2.20)$$

which is known as the Heisenberg equation.

The correlation function of two operators, $B(t)$ and $A(t')$, can in the Schrödinger picture be computed through

$$\langle B(t) A(t') \rangle = \sum_{\psi} \langle \psi_S(t) | B_S(t) U(t, t') A_S(t') | \psi_S(t') \rangle p_{\psi}. \quad (2.21)$$

In the Heisenberg picture, this is simply

$$\langle B(t) A(t') \rangle = \sum_{\psi} \langle \psi_H | B_H(t) A_H(t') | \psi_H \rangle p_{\psi}. \quad (2.22)$$

Correlation functions of more than two operators are defined in the same way.

The fact that the Hamiltonian is the operator that generates time evolution in quantum mechanics gives rise to a specific commutation relation between position operators and their corresponding canonical

momentum operators. From Hamiltonian mechanics [115], we know that the time evolution of position \mathbf{r} and the corresponding canonical momentum \mathbf{p} follows Hamilton's equations,

$$\frac{\partial \mathbf{r}}{\partial t} = \nabla_{\mathbf{p}} \mathcal{H}, \quad (2.23a)$$

$$\frac{\partial \mathbf{p}}{\partial t} = -\nabla_{\mathbf{r}} \mathcal{H}, \quad (2.23b)$$

where $\nabla_{\mathbf{p}} \mathcal{H} = (\partial \mathcal{H} / \partial p_x, \partial \mathcal{H} / \partial p_y, \partial \mathcal{H} / \partial p_z)$, and similarly for $\nabla_{\mathbf{r}} \mathcal{H}$. Hamilton's equations can be derived from the principle of least action, which is further discussed in section 2.5, and must therefore also hold as operator identities. But because the Hamiltonian \mathcal{H} generates time evolution, we know from the Heisenberg equation that

$$\frac{\partial \mathbf{r}}{\partial t} = i[\mathcal{H}, \mathbf{r}]_-, \quad (2.24a)$$

$$\frac{\partial \mathbf{p}}{\partial t} = i[\mathcal{H}, \mathbf{p}]_-, \quad (2.24b)$$

where the Hamiltonian must be understood to be in the Heisenberg picture of quantum mechanics. This means that $[\mathcal{H}, \mathbf{r}]_- = -i\nabla_{\mathbf{p}} \mathcal{H}$ and $[\mathcal{H}, \mathbf{p}]_- = i\nabla_{\mathbf{r}} \mathcal{H}$, which is the case when $[r^\alpha, p^\beta]_- = i\delta_{\alpha\beta}$, where $\alpha, \beta \in \{x, y, z\}$ and $\delta_{\alpha\beta}$ is the Kronecker delta. To see why, note that one can prove that $[r^\alpha, p^\beta]_- = i\delta_{\alpha\beta}$ implies $[(r^\alpha)^n, p^\beta]_- = in(r^\alpha)^{n-1}\delta_{\alpha\beta}$ by induction. It holds for $n = 1$ by construction, and if it holds for $n - 1$, such that $[(r^\alpha)^{n-1}, p^\beta]_- = i(n-1)(r^\alpha)^{n-2}\delta_{\alpha\beta}$, then

$$[(r^\alpha)^n, p^\beta]_- = r^\alpha[(r^\alpha)^{n-1}, p^\beta] + [r^\alpha, p^\beta](r^\alpha)^{n-1} = in(r^\alpha)^{n-1}\delta_{\alpha\beta}, \quad (2.25)$$

which concludes the proof.

From $[(r^\alpha)^n, p^\beta]_- = in(r^\alpha)^{n-1}\delta_{\alpha\beta}$ it follows that any operator, A , which can be written in a power series of r^α , meaning that

$$A = \sum_{n=0}^{\infty} a_n (r^\alpha)^n, \quad (2.26)$$

where a_n is any operators such that $[a_n, p^\alpha]_- = 0$, satisfies

$$[A, p^\alpha]_- = i \frac{\partial A}{\partial r^\alpha}. \quad (2.27)$$

Assuming that p^β commutes with p^α for all α and r^α for all $\alpha \neq \beta$, all operators should be possible to write as a series expansion with $[a_n, p^\alpha]_- = 0$. As a result, setting $A = \mathcal{H}$ gives

$$[\mathcal{H}, \mathbf{p}]_- = i\nabla_r \mathcal{H}, \quad (2.28)$$

as required. The same argument, but switching \mathbf{r} and \mathbf{p} shows that

$$[\mathcal{H}, \mathbf{r}]_- = -i\nabla_p \mathcal{H}. \quad (2.29)$$

Hence, $[r^\alpha, p^\beta]_- = i\delta_{\alpha\beta}$ gives the consistency between the Heisenberg equation and Hamilton's equations.

2.3 Many Particle Physics

The Hilbert space of a system of N identical particles can be composed of the tensor product of N single-particle Hilbert spaces. However, for a proper relativistic quantum field theory, interchanging two particles is equivalent to rotating one particle by 2π [116]. In terms of the annihilation operators to be defined below, $vu = uR(2\pi)v$, where $R(2\pi)$ rotates v by 2π . This means that for so-called integer spin fields, such as scalar fields and vector fields, where $R(2\pi)v = v$, the fields must commute. On the other hand, spinor-fields, which satisfy $R(2\pi)\psi = -\psi$, must anticommute. As a result, fields with integer spins are bosons and fields with half-integer spins are fermions [116]. This is the famous spin-statistics theorem [117]. To take this theorem into account, the tensor product is made either symmetric or antisymmetric. The connection between spin and statistics is further discussed in section 2.5.

When considering the most general case with an indefinite number of identical particles, the Hilbert space of interest is called a *Fock space* [114]. A Fock space is a direct sum of N -particle spaces for all N , meaning that

$$\mathcal{V} = \bigoplus_{n=0}^{\infty} S_{\pm} \mathcal{V}_1^{\otimes n} = \mathbb{C} \oplus \mathcal{V}_1 \oplus S_{\pm}(\mathcal{V}_1 \otimes \mathcal{V}_1) \dots, \quad (2.30)$$

where S_+ and S_- symmetrize and antisymmetrize, respectively, \mathcal{V}_1 is the single particle Hilbert space and \mathbb{C} is the set of complex numbers.

A convenient basis for the Fock space, which is used throughout this thesis, is known as the occupancy number representation [114].

Given a basis $\{|\psi_i\rangle\}_i$ for \mathcal{V}_1 , a basis for \mathcal{V} can be written

$$B = \{|n_1, n_2, \dots\rangle\}_{n_1, n_2, \dots}. \quad (2.31)$$

Here, n_1 is the number of particles in the $|\psi_1\rangle$ state, n_2 is the number of particles in the $|\psi_2\rangle$ state, and so on. For fermions, $n_i \in \{0, 1\}$ while for bosons $n_i \in \mathbb{N}^0$. In other words, for fermions,

$$|0, 0, 0, \dots\rangle = |0\rangle \otimes 0 \otimes 0 \otimes \dots, \quad (2.32a)$$

$$|0, 1, 0, \dots\rangle = 0 \otimes |\psi_2\rangle \otimes 0 \otimes 0 \otimes \dots, \quad (2.32b)$$

$$|1, 1, 0, \dots\rangle = 0 \otimes 0 \otimes \frac{1}{\sqrt{2}} (|\psi_1\rangle \otimes |\psi_2\rangle - |\psi_2\rangle \otimes |\psi_1\rangle) \otimes 0 \otimes 0 \otimes \dots, \quad (2.32c)$$

and so on. Here, the zeros on the right-hand sides are the zero elements of their respective vector spaces, and $|0\rangle$ is a state of norm 1 known as the vacuum state. The basis vectors in the occupancy number basis have a definitive number of particles, but a general vector in the Fock space is a superposition of these basis vectors and may therefore have an indefinite number of particles.

The occupancy number representation is especially useful when working with annihilation and creation operators [114]. These are operators which either remove or add a particle of a given state. If we again assume a single-particle basis $\{|\psi_i\rangle\}_i$, then b_i^\dagger will add a particle with state $|\psi_i\rangle$ while b_i will remove a particle with state $|\psi_i\rangle$. For instance, if we are considering a bosonic system, then

$$b_i^\dagger |\dots, n_i, \dots\rangle = \sqrt{n_i + 1} |\dots, n_i + 1, \dots\rangle, \quad (2.33a)$$

$$b_i |\dots, n_i, \dots\rangle = \sqrt{n_i} |\dots, n_i - 1, \dots\rangle. \quad (2.33b)$$

Note that $b_i |\dots, n_i, \dots\rangle = 0$, when $n_i = 0$, and that n_j is not changed for $j \neq i$. Note also that the creation operator is the adjoint of the annihilation operator, which justifies the notation b_i^\dagger . Moreover, it follows from equation (2.33) that one can identify $b_i^\dagger b_i$ as the number operator, giving the number of particles in state n_i , since $b_i^\dagger b_i |\dots, n_i, \dots\rangle = n_i |\dots, n_i, \dots\rangle$. Finally, the commutation relations

$$[b_i, b_j]_- = [b_i^\dagger, b_j^\dagger]_- = 0, \quad (2.34a)$$

$$[b_i, b_j^\dagger]_- = \delta_{ij}, \quad (2.34b)$$

also follow from equation (2.33).

For a fermionic system, one must take into consideration the anti-symmetry, so if $\{c_i\}$ is the set of annihilation operators and $\{c_i^\dagger\}$ is the set of creation operators, then

$$c_i^\dagger |\dots, n_i, \dots\rangle = \begin{cases} (-1)^{\sum_{j<i} n_j} \sqrt{n_i + 1} |\dots, n_i + 1, \dots\rangle & \text{if } n_i = 0, \\ 0 & \text{if } n_i = 1, \end{cases} \quad (2.35a)$$

$$c_i |\dots, n_i, \dots\rangle = \begin{cases} 0 & \text{if } n_i = 0, \\ (-1)^{\sum_{j<i} n_j} \sqrt{n_i} |\dots, n_i - 1, \dots\rangle & \text{if } n_i = 1. \end{cases} \quad (2.35b)$$

Again, we can identify $c_i^\dagger c_i$ as the number operators. In this case, one can deduce the following anticommutation relations

$$[c_i, c_j]_+ = [c_i^\dagger, c_j^\dagger]_+ = 0, \quad (2.36a)$$

$$[c_i, c_j^\dagger]_+ = \delta_{ij}. \quad (2.36b)$$

Creation and annihilation operators are sometimes also defined in terms of the *generalized* eigenvectors discussed above. That is, instead of creating states in a proper basis, they create and annihilate generalized eigenvectors such as $|x\rangle$. For such operators, the Kronecker δ in equations (2.34b) and (2.36b) is changed to Dirac δ -distributions. The creation and annihilation operators corresponding to the generalized eigenvectors of the position operators are called *field operators* [114]. Using the formal notation introduced above, one can write the field operators in terms of a normal basis B and its creation and annihilation operators, c_i^\dagger and c_i , as

$$\psi(\mathbf{r}) = \sum_{b \in B} \langle r|b\rangle c_b, \quad (2.37a)$$

$$\psi^\dagger(\mathbf{r}) = \sum_{b \in B} \langle b|r\rangle c_b^\dagger. \quad (2.37b)$$

There can be multiple field operators corresponding to a single point in space when there are multiple degrees of freedom in addition to the spatial degrees. For instance, a spinor-valued field will have two degrees of freedom per position, so there are two field operators per position.

2.4 Non-Interacting Particles

Identical particles, such as electrons, effectively interact in two ways. First, by the nature of them being identical, they must obey the correct fermionic or bosonic anticommutation or commutation rules. Second, the quantum field interacts with other quantum fields, giving rise to effective interactions between identical particles. For instance, the electron field interacts with the photon field, giving rise to Coloumb interactions between electrons. When referring to non-interacting particles in the context of many-particle quantum mechanics, it means that the Hamiltonian can be written as a sum of identical single-particle Hamiltonians. This means that non-interacting particles, as I define them, can still interact with other fields as long as the other fields are not treated quantum mechanically, and they still interact effectively through the commutation or anticommutation rules.

The Hamiltonian for a single fermion with mass m can typically be written

$$\mathcal{H}_1 = \frac{\mathbf{p}^2}{2m} + U(\mathbf{r}, \mathbf{p}), \quad (2.38)$$

where \mathbf{r} is the position operator, \mathbf{p} is the momentum operator and U may include the electric potential as well as other terms to be discussed later. Hence, the Hamiltonian for N identical, non-interacting particles can be written

$$\mathcal{H}_N = \sum_{i=1}^N \mathcal{H}_1(\mathbf{r}_i, \mathbf{p}_i) = \sum_{i=1}^N \left[\frac{\mathbf{p}_i^2}{2m} + U(\mathbf{r}_i, \mathbf{p}_i) \right], \quad (2.39)$$

where the subscript i means that the operator acts on particle i . For instance, $\mathbf{p}_2|\psi_1\rangle \otimes |\psi_2\rangle \otimes \dots = |\psi_1\rangle \otimes \mathbf{p}|\psi_2\rangle \otimes \dots$.

Equation (2.39) is more conveniently expressed by using the number occupancy representation with the eigenstates of the single-particle Hamiltonian \mathcal{H}_1 . Assuming \mathcal{H}_1 is self-adjoint, these states, which may be generalized eigenstates, span the whole space, as discussed above. That is, any $|\psi\rangle \in \mathcal{V}_1$ can be written $|\psi\rangle = \sum_i^\infty |b_i\rangle \langle b_i|\psi\rangle$, where $\mathcal{H}_1|b_i\rangle = \varepsilon_i|b_i\rangle$, with real ε_i and where the sum might be an integral. The space of N -particle states is a subspace of Fock-space, so one may write any state vector using the occupancy number representation with the eigenstates of \mathcal{H}_1 . Using this basis, the occupancy number

representation states are eigenstates of \mathcal{H}_N , with eigenvalues equal to the sum of the energies of the occupied states,

$$\mathcal{H}_N |n_1, n_2, \dots\rangle = \left(\sum_{i=1}^{\infty} \varepsilon_i n_i \right) |n_1, n_2, \dots\rangle. \quad (2.40)$$

A general state will be a superposition of occupancy number states, but we can write the Hamiltonian in the general case by switching the occupancy number n_i with the number operator $c_i^\dagger c_i$, so

$$\mathcal{H}_N = \sum_{i=1}^{\infty} \varepsilon_i c_i^\dagger c_i. \quad (2.41)$$

It is often also of interest to study systems with an indefinite number of particles, meaning that state vectors can live in the whole Fock space. In this case, one often considers the grand canonical ensemble and the expectation value for the number of particles is determined by the chemical potential, μ . The chemical potential multiplied by the number operator for the total number of particles is added to the Hamiltonian, meaning that

$$\mathcal{H} = \sum_{i=1}^{\infty} (\varepsilon_i - \mu) c_i^\dagger c_i. \quad (2.42)$$

One can also express \mathcal{H} in terms of a basis that is not the set of eigenstates of \mathcal{H}_1 . Generally, the creation and annihilation operators, $\{c_a\}$, for a basis $A = \{|a\rangle\}$ and the annihilation operators, $\{d_b\}$, for another basis, $B = \{|b\rangle\}$, are related through

$$d_b = \sum_{a \in A} \langle b|a\rangle c_a, \quad (2.43a)$$

$$d_b^\dagger = \sum_{a \in A} \langle a|b\rangle c_a^\dagger. \quad (2.43b)$$

Hence,

$$\mathcal{H} = \sum_{m \in A} \sum_{n \in A} c_m^\dagger \sum_{i=1}^{\infty} \langle m|b_i\rangle (\varepsilon_i - \mu) \langle b_i|n\rangle c_n = \sum_{m \in A} \sum_{n \in A} c_m^\dagger M_{mn} c_n, \quad (2.44)$$

where

$$M_{mn} = \sum_{i=1}^{\infty} \langle m|b_i\rangle (\varepsilon_i - \mu) \langle b_i|n\rangle. \quad (2.45)$$

If we use that $\langle a|c_m^\dagger c_n|b\rangle = \delta_{am}\delta_{bn}$ when $|a\rangle$ and $|b\rangle$ are single particle states, we can also express M_{mn} as

$$M_{mn} = \langle m|\mathcal{H}|n\rangle. \quad (2.46)$$

The choice of what basis to use depends on the problem at hand. Often, it is desirable to work with the basis in which the Hamiltonian is diagonal, meaning that it can be written in the form of equation (2.42). However, often either the eigenvalues or the eigenstates of the Hamiltonian are not known, and it is more convenient to use a basis in which one can express the Hamiltonian exactly. For instance, one may use the generalized eigenstates of the position operator, such that the Hamiltonian is expressed in terms of field operators. In this case, the Hamiltonian takes a form more reminiscent of equation (2.39),

$$\mathcal{H} = \int d^3r \psi^\dagger(\mathbf{r}) \left[\frac{-\nabla^2}{2m} + U(\mathbf{r}, -i\nabla) - \mu \right] \psi(\mathbf{r}), \quad (2.47)$$

where the differential operators act on the field operator, ψ . The presence of the differential operators follows from the commutation relation $[r^\alpha, p^\beta] = i\delta_{\alpha\beta}$ derived in section 2.2. To see why, note that

$$\langle \mathbf{r}_1|r^\alpha p^\alpha|\mathbf{r}_2\rangle - \langle \mathbf{r}_1|p^\alpha r^\alpha|\mathbf{r}_2\rangle = (r_1^\alpha - r_2^\alpha)\langle \mathbf{r}_1|p^\alpha|\mathbf{r}_2\rangle = i\langle \mathbf{r}_1|\mathbf{r}_2\rangle, \quad (2.48)$$

where $[r^\alpha, p^\beta] = i\delta_{\alpha\beta}$ was used in the last equality. Since $\langle \mathbf{r}_1|\mathbf{r}_2\rangle = \delta^3(\mathbf{r}_1 - \mathbf{r}_2)$ and $\delta^3(\mathbf{r}_1 - \mathbf{r}_2) = (\mathbf{r}_1 - \mathbf{r}_2) \cdot \nabla \delta^3(\mathbf{r}_1 - \mathbf{r}_2)$ in the sense of distributional derivatives, this means that $\langle \mathbf{r}_1|\mathbf{p}|\mathbf{r}_2\rangle = i[\nabla \delta^3(\mathbf{r}_1 - \mathbf{r}_2)]$ in the sense of distributions. Therefore, for any single particle state $|\varphi\rangle$,

$$\begin{aligned} \langle \mathbf{r}|\mathbf{p}|\varphi\rangle &= \int_{\mathbb{R}^3} d^3x \langle \mathbf{r}|\mathbf{p}|x\rangle \langle x|\varphi\rangle = \int_{\mathbb{R}^3} d^3x i[\nabla \delta^3(\mathbf{r} - \mathbf{x})] \langle x|\varphi\rangle \\ &= -i\nabla_{\mathbf{r}} \langle \mathbf{r}|\varphi\rangle. \end{aligned} \quad (2.49)$$

Setting $|\varphi\rangle = |\mathbf{p}\rangle$ equal to a generalized eigenstate of the momentum operator, I get

$$\mathbf{p}\langle \mathbf{r}|\mathbf{p}\rangle = -i\nabla_{\mathbf{r}} \langle \mathbf{r}|\mathbf{p}\rangle, \quad (2.50)$$

where \mathbf{p} on the left-hand side is a vector and not an operator, so

$$\langle \mathbf{r} | \mathbf{p} \rangle = C e^{-i\mathbf{r} \cdot \mathbf{p}} \quad (2.51)$$

for some constant C . The amplitude of C can be determined to be $|C| = 1/\sqrt{2\pi}$ from the normalization condition $\langle \mathbf{p} | \mathbf{q} \rangle = \delta^3(\mathbf{p} - \mathbf{q})$. Inserting into the expression for the kinetic energy $\mathbf{p}^2/2m$, using equation (2.45), I finally get

$$\begin{aligned} K &= \int_{\mathbb{R}^3} d^3 r_1 d^3 r_2 \psi^\dagger(\mathbf{r}_1) \int_{\mathbb{R}^3} d^3 p \langle \mathbf{r}_1 | \mathbf{p} \rangle \frac{\mathbf{p}^2}{2m} \langle \mathbf{p} | \mathbf{r}_2 \rangle \psi(\mathbf{r}_2) \\ &= \int_{\mathbb{R}^3} d^3 r_1 d^3 r_2 \psi^\dagger(\mathbf{r}_1) \frac{-\nabla_{r_1}^2}{2m} \int_{\mathbb{R}^3} d^3 p \frac{1}{2\pi} e^{-i\mathbf{p}(\mathbf{r}_1 - \mathbf{r}_2)} \psi(\mathbf{r}_2) \\ &= \int_{\mathbb{R}^3} d^3 r \psi^\dagger(\mathbf{r}) \frac{-\nabla_r^2}{2m} \psi(\mathbf{r}). \end{aligned} \quad (2.52)$$

A multitude of physical effects in solids, such as magnetism and superconductivity, comes about because electrons are interacting. They interact with the quantum mechanical electromagnetic field, and this interaction gives rise to various effective interactions between electrons, as will be clear in the next chapter. Nevertheless, systems with magnetic or superconducting properties can often be treated as effective systems of non-interacting quasiparticles. That is, they can often be modeled with quadratic Hamiltonians in the form of equation (2.44).

2.5 Spin and Conservation Laws

Quantum fields, like classical fields, are generally not symmetric under rotation in space. This is the origin of spin and can be understood by considering that there are two ways to rotate fields. Take for instance a vector field, $\mathbf{v} : \mathbf{x} \mapsto \mathbf{v}(\mathbf{x})$. You can rotate by moving all the spatial positions around an axis, $\mathbf{v}(\mathbf{x}) \mapsto \mathbf{v}(R_1 \mathbf{x})$, where R_1 is a rotation operator which can be represented using rotation matrices. On the other hand, you can also rotate the vectors themselves, meaning that $\mathbf{v}(\mathbf{x}) \mapsto R_2 \mathbf{v}(\mathbf{x})$. Generally, the Lagrangian of a closed system is only invariant under the combined transformation of both rotating spatial positions and rotating the field values themselves, $\mathbf{v}(\mathbf{x}) \mapsto R_2 \mathbf{v}(R_1 \mathbf{x})$, for some combination of R_1 and R_2 . This symmetry gives rise to a conserved quantity \mathbf{J} , through Noethers theorem [116, 118], as I show

below. The symmetry is the combination of two transformations, and each gives rise to its own term in the conserved quantity, $\mathbf{J} = \mathbf{L} + \mathbf{S}$. The term \mathbf{L} comes from the rotation of spatial positions, $\mathbf{x} \mapsto R\mathbf{x}$, and is called orbital angular momentum, while the term \mathbf{S} comes from the rotation of the vector values of the field, $\mathbf{v} \mapsto R\mathbf{v}$, and is called spin angular momentum.

The term “spin” is also used to classify fields according to their rotation properties. Different fields rotate according to different irreducible representations of the three-dimensional rotation group, $SO(3)$ [116, 119]. A spin- n field rotates under the $(2n + 1)$ -dimensional representation of $SO(3)$, where n can be integer, $(1, 2, \dots)$, or half-integer, $(1/2, 3/2, \dots)$. How the field transforms under a full rotation is what determines whether they are fermions or bosons, as explained in section 2.3.

The electron field is a spinor field, which is a spin- $1/2$ field. This means that the rotation of spinors can be represented by 2-dimensional matrices. Accordingly, spinors can be represented using 2-tuples. If ψ is a spinor, one can write

$$\psi = \begin{pmatrix} \psi_{\uparrow} \\ \psi_{\downarrow} \end{pmatrix}, \quad (2.53)$$

where the two components ψ_{\uparrow} and ψ_{\downarrow} depend on choice of the coordinate system. When rotating an angle θ around an axis \mathbf{n} , the spinor ψ transforms as [119]

$$\psi \mapsto \exp\left(i\frac{\theta}{2}\mathbf{n} \cdot \boldsymbol{\sigma}\right)\psi = \cos\left(\frac{\theta}{2}\right)\psi + i\mathbf{n} \cdot \boldsymbol{\sigma} \sin\left(\frac{\theta}{2}\right)\psi, \quad (2.54)$$

where $\boldsymbol{\sigma} = (\sigma_x, \sigma_y, \sigma_z)$, is the vector of Pauli matrices,

$$\sigma_x = \begin{pmatrix} 0 & 1 \\ 1 & 0 \end{pmatrix}, \quad (2.55a)$$

$$\sigma_y = \begin{pmatrix} 0 & -i \\ i & 0 \end{pmatrix}, \quad (2.55b)$$

$$\sigma_z = \begin{pmatrix} 1 & 0 \\ 0 & -1 \end{pmatrix}. \quad (2.55c)$$

Note that under 2π rotation, $\psi \rightarrow -\psi$, which is why spinor fields are fermionic.

Before we can compute the spin density from the transformation properties of the field, we first need the Lagrangian density. Since the Hamiltonian is an operator, so too is the Lagrangian L , and consequently also the action, $S = \int_{-\infty}^{\infty} dt L(t)$. To obtain the Hamiltonian density, and thereby the Lagrangian density, I write

$$\mathcal{H} = \int_{\mathbb{R}^3} d^3r h(\mathbf{r}). \quad (2.56)$$

The Lagrangian density is then²

$$\mathcal{L} = \pi^\dagger \frac{\partial}{\partial t} \psi + \left(\frac{\partial}{\partial t} \psi^\dagger \right) \pi - h, \quad (2.57)$$

where π^\dagger and π are the conjugate momentum densities for ψ and ψ^\dagger , respectively. The notation π^\dagger is not literal. One does not have to choose π^\dagger to be the adjoint of π . If we do not include coupling to other fields, we can use equation (2.47), such that

$$h(\mathbf{r}) = \psi^\dagger(\mathbf{r}) \left[\frac{-\nabla^2}{2m} + U(\mathbf{r}, -i\nabla) - \mu \right] \psi(\mathbf{r}). \quad (2.58)$$

In the principle of least action³ formulation of physics, the field which is realized is that which extremizes the action,

$$S = \int_{-\infty}^{\infty} dt \int_{\mathbb{R}^3} d^3r \mathcal{L}(t, \mathbf{r}). \quad (2.59)$$

One can find an equation for the field that extremizes the action by taking the functional derivative of the action with respect to the field and setting this to zero. If the Lagrange density, and thereby action, is a function of a real scalar field φ , the functional derivative, $\delta S / \delta \varphi$, is defined to be the function that satisfies

$$\int_{-\infty}^{\infty} dt \int_{\mathbb{R}^3} d^3r \frac{\delta S}{\delta \varphi} \rho = \lim_{\varepsilon \rightarrow 0} \frac{S(\varphi + \varepsilon \rho) - S(\varphi)}{\varepsilon}, \quad (2.60)$$

-
2. Note that while \mathcal{L} is the Lagrangian *density* and L is the *total* Lagrangian, h is the Hamiltonian *density* and \mathcal{H} is the *total* Hamiltonian. The inconsistent use of calligraphic font in relation to density is chosen because the two most important quantities are \mathcal{H} and \mathcal{L} .
 3. The action does not need to be minimal, so a better name is *the stationary action principle*.

for all real scalar fields ρ . When φ is a complex field, the Lagrangian can be written in terms of two real fields, $\varphi = \varphi_R + i\varphi_I$, and the action must be extremized with respect to both of the real fields, φ_R and φ_I . Equivalently, one can treat the field φ and its complex conjugate, φ^\dagger as two separate fields and extremize with respect to both. The electron field is a spinor field, which means that it can be written in terms of two complex fields, ψ_\uparrow and ψ_\downarrow , as defined in equation (2.53). The action must therefore be extremized with respect to ψ_\uparrow , ψ_\downarrow , ψ_\uparrow^\dagger , and ψ_\downarrow^\dagger , treating them all separately.

One can freely perform partial integrations in the expression for action and I assume that surface terms vanish. As a result, the differentiation operators can be moved around such that the Lagrangian density is a function of only the four fields, ψ_\uparrow , ψ_\downarrow , ψ_\uparrow^\dagger , and ψ_\downarrow^\dagger , and their first derivatives in time and space. When the Lagrangian density, \mathcal{L} , can be written as a function of fields and their first derivatives, taking the functional derivative of the action with respect to a field φ gives

$$\frac{\delta S}{\delta \varphi} = \frac{\partial \mathcal{L}}{\partial \varphi} - \frac{\partial}{\partial t} \left[\frac{\partial \mathcal{L}}{\partial (\partial_t \varphi)} \right] - \nabla \cdot \left[\frac{\partial \mathcal{L}}{\partial (\nabla \varphi)} \right], \quad (2.61)$$

where $\partial_t = \partial/\partial t$ is differentiation with respect to time. Setting equation (2.61) to zero is also known as the Euler-Lagrange equation [115, 116].

The Euler-Lagrange equations must reproduce the Heisenberg equation, and this fact can be used to determine the proper Lagrangian density. If the Lagrangian density is

$$\mathcal{L} = \psi^\dagger \left[i \frac{\partial}{\partial t} + \frac{\nabla^2}{2m} - U + \mu \right] \psi, \quad (2.62)$$

I get from equation (2.61) that

$$\frac{\delta S}{\delta \psi^\dagger} = \left[i \frac{\partial}{\partial t} + \frac{\nabla^2}{2m} - U + \mu \right] \psi. \quad (2.63)$$

Therefore, setting the functional derivative of the action equal to zero reproduces the Heisenberg equation for ψ ,

$$i \frac{\partial \psi}{\partial t} = -[\mathcal{H}, \psi]_- = \left[\frac{-\nabla^2}{2m} + U - \mu \right] \psi. \quad (2.64)$$

One can also verify that the Heisenberg equation for ψ^\dagger is reproduced by extremizing the action with respect to ψ . Note that this means that any operator that can be written as a polynomial in the field operators also satisfies the Heisenberg equation. This can be proved by induction, using the fact that

$$\frac{\partial}{\partial t}(AB) = \left[\frac{\partial}{\partial t} A \right] B + A \left[\frac{\partial}{\partial t} B \right] = i[\mathcal{H}, A]B + iA[\mathcal{H}, B]_- = i[\mathcal{H}, AB]_- \quad (2.65)$$

Thus the principle of least action is entirely equivalent to the formulation of quantum mechanics presented in section 2.2.

Comparing with equation (2.57), we see that the conjugate momentum densities are $\pi^\dagger = i\psi^\dagger$ and $\pi = 0$. One could equivalently choose a more symmetrical Lagrangian density with $\pi^\dagger = i\psi^\dagger/2$ and $\pi = -i\psi/2$. The symmetric and asymmetric Lagrangians are equivalent as they produce the same action. This can be seen by performing a partial integration. In the symmetric case, π and π^\dagger are adjoint operators, which is more in line with what the notation suggests. Note that \mathcal{L} is a non-relativistic Lagrangian. Relativity is considered in section 2.6.

One key advantage of the principle of least action formulation of physics is that it allows for simple derivations of conservation laws. Let $\psi = (\psi_1, \dots, \psi_n)^T$ be an n -tuple of fields and let θ be a single parameter which characterizes a transformation of ψ . For instance, θ can be an angle when the transformation is a rotation. Assume further that ψ extremizes the action and that the Lagrangian density is a function of ψ and its first derivatives in time and space, $\mathcal{L}(\psi, \partial_t\psi, \nabla\psi)$. Finally, let $\tilde{\psi}(\theta, t, \mathbf{r})$ be the field after the transformation and $\tilde{\psi}(0, t, \mathbf{r}) = \psi(t, \mathbf{r})$. The derivative of the $\mathcal{L}(\tilde{\psi}, \partial_t\tilde{\psi}, \nabla\tilde{\psi})$ with respect to θ , evaluated at $\theta = 0$, is then

$$\begin{aligned} \frac{d\mathcal{L}}{d\theta} &= \sum_{i=1}^n \left\{ \frac{\partial\mathcal{L}}{\partial\psi_i} \frac{\partial\tilde{\psi}_i}{\partial\theta} + \frac{\partial\mathcal{L}}{\partial(\partial_t\psi_i)} \frac{\partial}{\partial t} \left[\frac{\partial\tilde{\psi}_i}{\partial\theta} \right] + \frac{\partial\mathcal{L}}{\partial(\nabla\psi_i)} \cdot \nabla \left[\frac{\partial\tilde{\psi}_i}{\partial\theta} \right] \right\} \\ &= \sum_{i=1}^n \left\{ \frac{\partial\mathcal{L}}{\partial\psi_i} - \frac{\partial}{\partial t} \left[\frac{\partial\mathcal{L}}{\partial(\partial_t\psi_i)} \right] - \nabla \cdot \left[\frac{\partial\mathcal{L}}{\partial(\nabla\psi_i)} \right] \right\} \frac{\partial\tilde{\psi}_i}{\partial\theta} \\ &\quad + \sum_{i=1}^n \left\{ \frac{\partial}{\partial t} \left[\frac{\partial\mathcal{L}}{\partial(\partial_t\psi_i)} \frac{\partial\tilde{\psi}_i}{\partial\theta} \right] + \nabla \cdot \left[\frac{\partial\mathcal{L}}{\partial(\nabla\psi_i)} \frac{\partial\tilde{\psi}_i}{\partial\theta} \right] \right\}. \quad (2.66) \end{aligned}$$

The first term on the right-hand side is zero by assumption since ψ extremizes the action. The transformation is called a symmetry if the Lagrangian density is either invariant or changed by a gradient term, meaning that

$$\frac{d\mathcal{L}}{d\theta} = \frac{\partial q_0}{\partial t} + \nabla \cdot \mathbf{q}. \quad (2.67)$$

When the transformation is a symmetry, equation (2.66) becomes a conservation law,

$$\frac{\partial \rho}{\partial t} + \nabla \cdot \mathbf{j} = 0, \quad (2.68)$$

where the conserved “charge” density is

$$\rho = q_0 - \sum_{i=1}^n \frac{\partial \mathcal{L}}{\partial(\partial_t \psi_i)} \frac{\partial \tilde{\psi}_i}{\partial \theta}, \quad (2.69)$$

and the conserved current is

$$\mathbf{j} = \mathbf{q} - \sum_{i=1}^n \frac{\partial \mathcal{L}}{\partial(\nabla \psi_i)} \frac{\partial \tilde{\psi}_i}{\partial \theta}. \quad (2.70)$$

The Lagrange density is not invariant under spatial rotations, $\mathbf{x} \mapsto R_1 \mathbf{x}$. Rather, as explained above, the Lagrangian is invariant under the combined rotation of space and spinors, $\psi(\mathbf{x}) \mapsto R_2 \psi(R_1 \mathbf{x})$, where R_2 rotates the spinor and R_1 rotates the spatial position. For a rotation around an axis \mathbf{n} , R_2 is given by equation (2.54) and

$$R_1 = \exp(\theta \mathbf{n} \cdot \Lambda), \quad (2.71)$$

where

$$\Lambda_x = \begin{pmatrix} 0 & 0 & 0 \\ 0 & 0 & -1 \\ 0 & 1 & 0 \end{pmatrix}, \quad (2.72a)$$

$$\Lambda_y = \begin{pmatrix} 0 & 0 & 1 \\ 0 & 0 & 0 \\ -1 & 0 & 0 \end{pmatrix}, \quad (2.72b)$$

$$\Lambda_z = \begin{pmatrix} 0 & -1 & 0 \\ 1 & 0 & 0 \\ 0 & 0 & 0 \end{pmatrix}. \quad (2.72c)$$

For a small rotation by an angle θ , the spinor field, therefore, transforms as

$$\begin{aligned}\psi(\mathbf{x}) &\mapsto \left(1 + i\frac{\theta}{2}\mathbf{n} \cdot \boldsymbol{\sigma}\right)\psi(\mathbf{x} + \theta\mathbf{n} \cdot \boldsymbol{\Lambda}\mathbf{x}) \\ &= \psi(\mathbf{x}) + \theta\left[\frac{i}{2}\mathbf{n} \cdot \boldsymbol{\sigma}\psi(\mathbf{x}) + (\mathbf{n} \cdot \boldsymbol{\Lambda})\mathbf{x} \cdot \nabla\psi(\mathbf{x})\right] + \mathcal{O}(\theta^2).\end{aligned}\quad (2.73)$$

So

$$\frac{\partial\tilde{\psi}}{\partial\theta} = \frac{i}{2}\mathbf{n} \cdot \boldsymbol{\sigma}\psi(\mathbf{x}) + (\mathbf{n} \cdot \boldsymbol{\Lambda})\mathbf{x} \cdot \nabla\psi(\mathbf{x})\quad (2.74)$$

The field ψ^\dagger also transforms, but we can freely choose the asymmetric form of the Lagrangian density with $\partial\mathcal{L}/\partial(\partial_t\psi^\dagger) = 0$, such that $\partial\tilde{\psi}^\dagger/\partial\theta$ does not enter in equation (2.69). When using this asymmetric form, $\partial\mathcal{L}/\partial(\partial_t\psi) = \pi = i\psi^\dagger$, so the conserved charge density associated with rotation is

$$\begin{aligned}\rho(\mathbf{x}) &= -i\psi^\dagger(\mathbf{x})\left[\frac{i}{2}\mathbf{n} \cdot \boldsymbol{\sigma}\psi(\mathbf{x}) + (\mathbf{n} \cdot \boldsymbol{\Lambda})\mathbf{x} \cdot \nabla\psi(\mathbf{x})\right] \\ &= \psi^\dagger(\mathbf{x})\frac{1}{2}\mathbf{n} \cdot \boldsymbol{\sigma}\psi(\mathbf{x}) + \psi^\dagger(\mathbf{x})(\mathbf{n} \times \mathbf{x}) \cdot (-i\nabla)\psi(\mathbf{x}) \\ &= \mathbf{n} \cdot [\mathbf{S}(\mathbf{x}) + \mathbf{L}(\mathbf{x})],\end{aligned}\quad (2.75)$$

where we used that $(\mathbf{n} \cdot \boldsymbol{\Lambda})\mathbf{x} = (\mathbf{n} \times \mathbf{x})$ and defined the spin angular momentum density \mathbf{S} and orbital angular momentum density, \mathbf{L} , respectively as

$$\mathbf{S}(\mathbf{x}) = \frac{1}{2}\psi^\dagger(\mathbf{x})\boldsymbol{\sigma}\psi(\mathbf{x}),\quad (2.76a)$$

$$\mathbf{L}(\mathbf{x}) = \psi^\dagger(\mathbf{x})[\mathbf{x} \times (-i\nabla)]\psi(\mathbf{x}).\quad (2.76b)$$

Note that both the orbital and spin angular momentum can in principle be nonzero even for a static field. This is not to say that \mathbf{S} and \mathbf{L} do not represent rotation in the sense of flow around an axis.

It is difficult to see how the spin \mathbf{S} makes intuitive sense as a measure of dynamic rotation around an axis without a geometric understanding of spinors. Luckily, it is possible to find a geometric understanding of spinors in the fascinating field of geometric algebra [120, 121]. In geometric algebra, spinors can be understood as rotors combined with dilation. As the name suggests, a rotor defines a rotation. Using geometric algebra notation, a spinor ψ transforms vectors according to

$\mathbf{v} \mapsto \psi \mathbf{v} \psi^\dagger$, where the dagger is used to denote the geometric algebra reverse operation. That is, while vectors define arrows with an amplitude and a direction, spinors define rotations and dilations of vectors. In the case of the electron field, the spinors define a rotation that depends on the coordinate system one works with. One can think of the electron as defining a rotation from *your* coordinate system to the *electron's* coordinate system. The z -axis of the electron's coordinate system is pointing in the direction defined of $\psi^\dagger \sigma \psi$ with the notation used here. Now, consider how the electron field changes in time, which is given by equation (2.64). For simplicity, take the situation in which

$$i \frac{\partial \psi}{\partial t} = E \psi \implies \psi(t) = e^{-iEt} \psi(t). \quad (2.77)$$

In this case, the spin $\psi^\dagger \sigma \psi$ is constant. If we convert equation (2.77) to the formulation of spinors as rotors in geometric algebra, multiplying ψ by a factor $\exp(i\varphi)$ is the same as rotating the electron coordinate system in the xy -plane. That is, the spinor defines a rotation to a coordinate system that is rotating around the axis which points in the direction given by $\psi^\dagger \sigma \psi$. Hence, in the geometric picture, there is a clear rotation around the spin axis.

As a side note, the geometric understanding of spinors also gives insight into their special rotation properties, which makes them fermionic through the spin-statistics theorem. The fact that spinors act on vectors from both sides, $\mathbf{v} \mapsto \psi \mathbf{v} \psi^\dagger$ is why they essentially rotate with half the speed of vectors. It is why they transform according to the 2-dimensional representation of the rotation group, which is why they acquire a minus sign under 2π rotation. This minus sign is why they are fermionic.

2.6 The Electron Magnetic Moment and Spin-Orbit Coupling

The fact that angular momentum is a conserved quantity means that it can be used to encode and send information. If you suddenly observe an increased amount of angular momentum, you know that it must have come from somewhere. When you send a specified amount of upwards-pointing angular momentum down an insulated wire, you can be certain that it will be received at the other end. If you and the receiver have agreed that upwards-pointing angular momentum

means 1, you have just sent a bit of information. This is in a sense, and in overly simplified terms, the basis for spintronics.

However, in order for this to work, one needs a convenient way to manipulate angular momentum. That is, while electronics work by using the electric field to manipulate the conserved scalar quantity called electric charge, spintronics require an analogous way to manipulate angular momentum. Fortunately, manipulation of angular momentum is possible, both through the magnetic field and the electric field. In particular, both the electric field and the magnetic field can be used to manipulate the spin of electrons.

Understanding how the electron spin interacts not only with the magnetic field, but also with the electric field, requires the theory of relativity. In relativistic theories, one cannot meaningfully separate the electric field and the magnetic field. Even if a stationary observer measures no magnetic field, another observer might measure a non-zero magnetic field as a consequence of the fact that this observer is in motion relative to the first observer [122]. As a result, one should instead consider a more fundamental field, (V, \mathbf{A}) , which is sometimes referred to as *the photon field* [123] or the electromagnetic 4-potential [122]. The photon field is a 4-vector field because one must treat time and space on the same footing in relativistic theories. The electric field, \mathbf{E} , and the magnetic field, \mathbf{B} , are determined from the photon field and can be calculated from

$$\mathbf{E} = -\nabla V - \frac{\partial \mathbf{A}}{\partial t}, \quad (2.78a)$$

$$\mathbf{B} = \nabla \times \mathbf{A}. \quad (2.78b)$$

Fundamentally, the same interaction that allows electric charge to be moved in electronic devices also allows spin to be manipulated in spintronics devices. A single interaction between the electron field and the photon field gives, in the non-relativistic limit, three different types of interactions: the normal electromagnetic interaction responsible for the Lorentz force, the interaction between the electron spin and the magnetic field, and the spin-orbit interaction.

In this section, I derive the interaction between the electron spin and the electromagnetic field. To do so, I start with the relativistic description of electrons and take the non-relativistic limit. Taking the non-relativistic limit means that we neglect terms with small operator

norms on the subset of non-relativistic states. That is, I assume that the system is well described by a subset of Hilbert space, $\mathcal{V}_{\text{NR}} \subset \mathcal{V}$ where the energy is dominated by the rest mass energy. The operator norm of an operator T on \mathcal{V}_{NR} is defined as the smallest real number c satisfying [105]

$$|\langle \psi | T | \psi \rangle| < c \langle \psi | \psi \rangle \quad (2.79)$$

for all $|\psi\rangle \in \mathcal{V}_{\text{NR}}$. The aim is to write the Lagrangian as a series expansion in operators with increasingly small operator norms on the non-relativistic subset of the Hilbert space. In terms of the relativistic corrections, I keep only the terms that couple spin to the magnetic and electric fields, and only the lowest order in which they occur. For a consistent description of electrons, one should keep all terms that are of the same order. However, the aim here is not full consistency. The potentials in real materials are often too complicated to evaluate even the lowest order term exactly, so including higher order terms are not necessary. The point is rather to determine the form of the most important terms in the Hamiltonian, such that we know which effects to add in an effective description of real systems, even if the strengths of these effects must be determined empirically.

In the relativistic description of the electron field, the electron field consists of two coupled spinor fields: ψ_L and ψ_R . These are known as the left-chiral and right-chiral Weyl spinors, respectively [116]. Both transform in the same way under rotation, but they transform differently under Lorentz boosts. For a general rotation of angle θ around the \mathbf{n} axis and a Lorentz boost η in the \mathbf{v} -direction, then

$$\psi_{R/L} \mapsto \exp\left(i\frac{\theta}{2}\mathbf{n}\cdot\boldsymbol{\sigma} \pm \frac{\eta}{2}\mathbf{v}\cdot\boldsymbol{\sigma}\right)\psi_{R/L}. \quad (2.80)$$

Let

$$\psi = \begin{pmatrix} \psi_L \\ \psi_R \end{pmatrix}. \quad (2.81)$$

The Lagrangian density, known as the Dirac Lagrangian [116, 124], is then given by

$$\mathcal{L} = \psi^\dagger \left[i \left(\frac{\partial}{\partial t} + iqV \right) + i\gamma_0 \boldsymbol{\gamma} \cdot (\nabla - iq\mathbf{A}) - \gamma_0 m \right] \psi, \quad (2.82)$$

where q is the electric charge and (V, \mathbf{A}) is the photon field and the 4×4 gamma matrices are

$$\gamma_0 = \begin{pmatrix} 0 & 1 \\ 1 & 0 \end{pmatrix}, \quad \text{and} \quad \boldsymbol{\gamma} = \begin{pmatrix} 0 & \boldsymbol{\sigma} \\ -\boldsymbol{\sigma} & 0 \end{pmatrix}. \quad (2.83)$$

We are mainly interested in the conserved quantity associated with rotation. Using that the Lagrangian is invariant under rotation and the Weyl-spinors transform according to equation (2.80), the same derivation as in section 2.5 shows that the spin density operator is

$$S = \psi^\dagger \frac{1}{2} \begin{pmatrix} \boldsymbol{\sigma} & 0 \\ 0 & \boldsymbol{\sigma} \end{pmatrix} \psi. \quad (2.84)$$

In order to obtain a non-relativistic description one must decouple the bispinor field into two spinor fields by using the fact that the rest mass m is large compared to other energies in the non-relativistic limit. This is difficult in the Weyl basis because the dominant mass term, $-\psi^\dagger \gamma_0 m \psi$, couples the left-chiral and right-chiral Weyl spinors. Instead, it is more convenient to use the Dirac bispinor

$$\psi_D = \frac{1}{\sqrt{2}} \begin{pmatrix} 1 & 1 \\ 1 & -1 \end{pmatrix} \begin{pmatrix} \psi_L \\ \psi_R \end{pmatrix} = \begin{pmatrix} u \\ v \end{pmatrix}. \quad (2.85)$$

Written in terms of the Dirac bispinor, the Lagrange density is

$$\mathcal{L} = \psi_D^\dagger \left[\left(i \frac{\partial}{\partial t} - qV \right) - \boldsymbol{\alpha} \cdot (-i\nabla - q\mathbf{A}) - \beta m \right] \psi_D, \quad (2.86)$$

where

$$\beta = \begin{pmatrix} 1 & 0 \\ 0 & -1 \end{pmatrix}, \quad \text{and} \quad \boldsymbol{\alpha} = \begin{pmatrix} 0 & \boldsymbol{\sigma} \\ \boldsymbol{\sigma} & 0 \end{pmatrix}. \quad (2.87)$$

One way to decouple the relativistic Dirac theory is to perform a Foldy-Wouthuysen transformation [125–127]. This is done by iteratively transforming the bispinors through unitary transformations and successively removing off-diagonal terms. A unitary transformation, by definition, is one which preserves inner products. Normally, a Foldy-Wouthuysen transformation is performed by transforming state vectors, $|\psi\rangle$ with well-defined inner products. Here, however, we want to transform the bispinor operators, and inner products are not

defined for the space of operators. Nevertheless, one can perform a transformation that preserves an expression reminiscent of the inner product in L^2 ,

$$N_{\text{tot}} = \int_{\mathbb{R}^3} d^3x \psi_D^\dagger \psi_D. \quad (2.88)$$

This expression is the operator for the total number of particles.

By ensuring that our two new decoupled spinor fields,⁴ ψ_e and ψ_p , also satisfy

$$N_{\text{tot}} = \int_{\mathbb{R}^3} d^3x \begin{pmatrix} \psi_e^\dagger & \psi_p^\dagger \end{pmatrix} \begin{pmatrix} \psi_e \\ \psi_p \end{pmatrix}, \quad (2.89)$$

one ensures that $\psi_e^\dagger \psi_e$ and $\psi_p^\dagger \psi_p$ can still be used to count the number of particles. Note however, that this does not mean that the equality $\psi_D^\dagger(\mathbf{x})\psi_D(\mathbf{x}) = \psi_e^\dagger(\mathbf{x})\psi_e(\mathbf{x}) + \psi_p^\dagger(\mathbf{x})\psi_p(\mathbf{x})$ holds locally, so $\psi_e^\dagger \psi_e$ and $\psi_p^\dagger \psi_p$ need not be density operators in the same sense as $\psi_D^\dagger \psi_D$. Because I consider quantum field theory rather than just a free Dirac particle, I do not perform a Foldy-Wouthuysen transformation. Instead, I use the Dirac equation to rewrite the Lagrangian in terms of two decoupled spinor fields, ψ_e and ψ_p , and then I ensure that the new fields can be interpreted as matter fields by ensuring that equation (2.89) is satisfied and that the total number operator is preserved for each of the two new fields. The result is consistent with what one obtains from a Foldy-Wouthuysen transformation [126].

In order to ensure that the total number operator is conserved, note that the total number of e -particles is conserved if the Lagrangian density has the form $\mathcal{L} = \mathcal{L}_e + \mathcal{L}_p$ with

$$\mathcal{L}_e = \psi_e^\dagger i \frac{\partial \psi_e}{\partial t} - h_e, \quad (2.90)$$

and similarly for \mathcal{L}_p . In this case, given that \mathcal{L}_e and \mathcal{L}_p are symmetric under global $U(1)$ -transformations, $\psi_{e/p} \mapsto \exp(i\varphi)\psi_{e/p}$, Noethers theorem states that the conserved charge densities are

$$\rho_{e/p} = -i\psi_{e/p}^\dagger \dot{\psi}_{e/p} = \dot{\psi}_{e/p}^\dagger \psi_{e/p}. \quad (2.91)$$

4. I use the subscripts e and p to indicate that ψ_e is the electron field and ψ_p is related to the positron field. Note, however, that ψ_p is not exactly the positron field. A positron is defined as the absence of what I refer to as a p -particle. The positron field would therefore be ψ_p^\dagger .

Therefore, the total charges

$$N_{e/p} = \int_{\mathbb{R}^3} d^3x \rho_{e/p} = \int_{\mathbb{R}^3} d^3x \psi_{e/p}^\dagger \psi_{e/p} \quad (2.92)$$

are conserved. We see that $N_{e/p}$ can be identified as the total number of e -particles and p -particles respectively. Note again that this does not mean that $q\psi_e^\dagger(\mathbf{x})\psi_e(\mathbf{x})$ is the electric charge density of the ψ_e -field, as we will see.

To motivate the definitions of ψ_e and ψ_p , consider the Dirac equation, which is obtained by extremizing the action with respect ψ_D^\dagger ,

$$\frac{\delta S}{\delta \psi_D^\dagger} = \left[\left(i \frac{\partial}{\partial t} - qV \right) - \boldsymbol{\alpha} \cdot (-i\nabla - q\mathbf{A}) - \beta m \right] \psi_D = 0. \quad (2.93)$$

A general solution may be written as a sum of terms with positive energies and terms with negative energies. These are related to particle and antiparticle solutions, respectively, and I will use them to define ψ_e and ψ_p . To write the Dirac equation in terms of energies, I Fourier transform in time, such that

$$\psi_D(E) = \int_{-\infty}^{\infty} dt \psi_D(t) e^{iEt}. \quad (2.94)$$

After a Fourier transformation in time equation (2.93) becomes

$$\begin{aligned} (E + i\boldsymbol{\alpha} \cdot \nabla - \beta m) \psi_D(E) \\ = -q \int_{-\infty}^{\infty} d\varepsilon [V(\varepsilon) + \boldsymbol{\alpha} \cdot \mathbf{A}(\varepsilon)] \psi_D(E - \varepsilon). \end{aligned} \quad (2.95)$$

If we assume that the right-hand side, as well as the term $\boldsymbol{\alpha} \cdot \nabla \psi_E$, are both much smaller than $m\psi_D$, we see that equation (2.95) only has non-zero solutions when E is close to $\pm m$. Moreover, in the non-relativistic limit, $V(\varepsilon) + \boldsymbol{\alpha} \cdot \mathbf{A}(\varepsilon)$ is negligible when $|\varepsilon| \approx 2m$, so the solutions close to $\varepsilon = m$ and $\varepsilon = -m$ do not couple. In other words, there is some cutoff energy $E_c \ll m$ for which one can define

$$\psi_\pm(E) = \begin{cases} \psi_D(E \pm m) & \text{if } |E| < E_c, \\ 0 & \text{otherwise,} \end{cases} \quad (2.96)$$

such that $\psi_D(E) = \psi_+(E - m) + \psi_-(E + m)$ and

$$\begin{aligned} (E + i\boldsymbol{\alpha} \cdot \nabla - \beta m) \psi_{\pm}(E \mp m) \\ = -q \int_{-\infty}^{\infty} d\varepsilon [V(\varepsilon) + \boldsymbol{\alpha} \cdot \mathbf{A}(\varepsilon)] \psi_{\pm}(E \mp m - \varepsilon). \end{aligned} \quad (2.97)$$

To avoid the convolution on the right-hand side, I inverse Fourier transform back to time coordinates, such that

$$\left[\left(i \frac{\partial}{\partial t} - qV \right) - \boldsymbol{\alpha} \cdot (-i\nabla - q\mathbf{A}) - \beta m \pm m \right] \psi_{\pm} = 0. \quad (2.98)$$

Inserting $\psi_D(t) = \exp(-imt)\psi_+(t) + \exp(imt)\psi_-(t)$ into the Dirac Lagrangian (2.86), one gets cross-terms involving both ψ_+ and ψ_- . However, these terms will also be proportional to $\exp(\pm 2imt)$. Since $\psi_{\pm}(t)$ and the photon field by assumption vary slowly in time compared to $\exp(\pm 2imt)$, these terms will have a negligible influence on the action.⁵ It is the action,

$$S = \int_{-\infty}^{\infty} dt \int_{\mathbb{R}^3} d^3x \mathcal{L}(t, x), \quad (2.99)$$

that matters. Therefore, I assume that I can neglect the cross terms. As a result, the Dirac Lagrangian becomes

$$\mathcal{L} = \mathcal{L}_e + \mathcal{L}_p, \quad (2.100)$$

where the electron Lagrangian and positron Lagrangian are

$$\mathcal{L}_{e/p} = \psi_{\pm}^{\dagger} \left[\left(i \frac{\partial}{\partial t} - qV \right) - \boldsymbol{\alpha} \cdot (-i\nabla - q\mathbf{A}) - \beta m \pm m \right] \psi_{\pm}, \quad (2.101)$$

respectively.

Equation (2.101) looks similar to equation (2.90), but it is written in terms of bispinor fields rather than spinor fields. The next step is therefore to extract proper spinor fields from ψ_{\pm} . I will only consider

5. There can in principle be cross-terms in \mathcal{L} , like $\psi_{\pm}^{\dagger}(t)\mathbf{A}(t)\psi_{\pm}(t)$, that are not negligible if \mathbf{A} oscillates with frequency $2m$. In physical terms, a (+)-particle can become a (-)-particle through an oscillation with frequency $2m$ in the photon field. This could for example be the creation of an electron-positron pair through the annihilation of a very energetic photon. I do not include such effects here, since I assume that the photon field does not oscillate that rapidly.

the electron Lagrangian \mathcal{L}_e . The derivation of the positron Lagrangian, \mathcal{L}_p , follows the same steps, but I don't show this derivation because, for the purposes of condensed matter physics, positrons are not of much relevance. Despite the fact that matter, like electrons, and anti-matter, like positrons, are on equal footing in the theoretical model, our observable universe is made almost entirely of matter [128]. Therefore, when studying the physics of condensed matter, the electron is the main player.

Inserting $\psi_+ = (u_+, v_+)^T$ into equation (2.98) I get

$$\left(i\frac{\partial}{\partial t} - qV\right)u_+ = \boldsymbol{\sigma} \cdot (-i\nabla - q\mathbf{A})v_+, \quad (2.102a)$$

$$\left(i\frac{\partial}{\partial t} - qV + 2m\right)v_+ = \boldsymbol{\sigma} \cdot (-i\nabla - q\mathbf{A})u_+. \quad (2.102b)$$

To solve for v_+ in terms of u_+ , I apply the operator

$$P = \sum_{n=0}^{\infty} \frac{(-1)^n}{(2m)^{n+1}} \left(i\frac{\partial}{\partial t} - qV\right)^n \quad (2.103)$$

to equation (2.102b) and use that

$$\begin{aligned} P\left(i\frac{\partial}{\partial t} - qV + 2m\right)v_+ &= -\sum_{n=0}^{\infty} \frac{(-1)^{n+1}}{(2m)^{n+1}} \left(i\frac{\partial}{\partial t} - qV\right)^{n+1} v_+ \\ &\quad + \sum_{n=0}^{\infty} \frac{(-1)^n}{(2m)^n} \left(i\frac{\partial}{\partial t} - qV\right)^n v_+ = v_+, \end{aligned} \quad (2.104)$$

which is true provided that the series converges. In the non-relativistic limit $|(i\partial/\partial t - qV)^n v_+|/(2m)^n \rightarrow 0$, so the series does converge. As a result,

$$v_+ = P\boldsymbol{\sigma} \cdot (-i\nabla - q\mathbf{A})u_+. \quad (2.105)$$

Inserting equation (2.105) into the electron Lagrangian, I get

$$\begin{aligned} \mathcal{L}_e &= u_+^\dagger \left(i\frac{\partial}{\partial t} - qV\right)u_+ - u_+^\dagger \boldsymbol{\sigma} \cdot (-i\nabla - q\mathbf{A})P\boldsymbol{\sigma} \cdot (-i\nabla - q\mathbf{A})u_+ \\ &\quad + [P\boldsymbol{\sigma} \cdot (-i\nabla - q\mathbf{A})u_+]^\dagger \left(i\frac{\partial}{\partial t} - qV + 2m\right)P\boldsymbol{\sigma} \cdot (-i\nabla - q\mathbf{A})u_+ \\ &\quad - [P\boldsymbol{\sigma} \cdot (-i\nabla - q\mathbf{A})u_+]^\dagger \boldsymbol{\sigma} \cdot (-i\nabla - q\mathbf{A})u_+. \end{aligned} \quad (2.106)$$

Performing the partial integrations such that all differentiation operators act to the rightmost u_+ , I get that

$$\begin{aligned} \mathcal{L}_e = & u_+^\dagger \left(i \frac{\partial}{\partial t} - qV \right) u_+ - u_+^\dagger \boldsymbol{\sigma} \cdot (-i\nabla - q\mathbf{A}) P \boldsymbol{\sigma} \cdot (-i\nabla - q\mathbf{A}) u_+ \\ & + u_+^\dagger \boldsymbol{\sigma} \cdot (-i\nabla - q\mathbf{A}) P \left(i \frac{\partial}{\partial t} - qV + 2m \right) P \boldsymbol{\sigma} \cdot (-i\nabla - q\mathbf{A}) u_+ \\ & - u_+^\dagger \boldsymbol{\sigma} \cdot (-i\nabla - q\mathbf{A}) P \boldsymbol{\sigma} \cdot (-i\nabla - q\mathbf{A}) u_+. \end{aligned} \quad (2.107)$$

From equation (2.104) one can see that the second and third terms cancel, so

$$\mathcal{L}_e = u_+^\dagger \left[i \frac{\partial}{\partial t} - qV - \boldsymbol{\sigma} \cdot (-i\nabla - q\mathbf{A}) P \boldsymbol{\sigma} \cdot (-i\nabla - q\mathbf{A}) \right] u_+. \quad (2.108)$$

We now have an expression for the electron Lagrangian in terms of a spinor field u_+ , and one can get the effective electron Lagrangian to a given order in E_c/m , where E_c is the largest energy scale below m , by terminating the series expression of P . However, u_+ is not an appropriate choice for the spinor electron field because it does not give the correct total number of electrons. The total number of electrons is

$$\begin{aligned} N_e = & \int_{\mathbb{R}^3} d^3x \psi_+^\dagger \psi_+ = \int_{\mathbb{R}^3} d^3x \left\{ u_+^\dagger u_+ \right. \\ & \left. + [P \boldsymbol{\sigma} \cdot (-i\nabla - q\mathbf{A}) u_+]^\dagger P \boldsymbol{\sigma} \cdot (-i\nabla - q\mathbf{A}) u_+ \right\}. \end{aligned} \quad (2.109)$$

Hence, we want a spinor electron field ψ_e which is normalized such that

$$\int_{\mathbb{R}^3} d^3x \psi_e^\dagger \psi_e = N_e. \quad (2.110)$$

In order to make the expansion in inverse mass more clear, I reinstate SI units when comparing terms. To convert to SI-units, the kinetic momentum operator, $(-i\nabla - q\mathbf{A})$, must be multiplied by the speed of light, c , mass m must be multiplied by c^2 and differentiation with respect to time and space must be multiplied by the reduced Planck constant, \hbar . As discussed above, I only want the lowest order corrections, so I consider a description valid to first order in E_c/mc^2 . To this order, the number of electrons is

$$N_e = \int_{\mathbb{R}^3} d^3x u_+^\dagger \left\{ 1 + \frac{c^2}{4m^2c^4} [\boldsymbol{\sigma} \cdot (-i\hbar\nabla - q\mathbf{A})]^2 \right\} u_+. \quad (2.111)$$

Choosing

$$\psi_e = \left\{ 1 + \frac{1}{8m^2c^2} [\boldsymbol{\sigma} \cdot (-i\hbar\nabla - q\mathbf{A})]^2 \right\} u_+, \quad (2.112)$$

or, equivalently,

$$u_+ = \left\{ 1 - \frac{1}{8m^2c^2} [\boldsymbol{\sigma} \cdot (-i\hbar\nabla - q\mathbf{A})]^2 \right\} \psi_e, \quad (2.113)$$

ensures that equation (2.110) is satisfied to first order. Inserting this into equation (2.108), I get that to first order in E_c/mc^2 ,

$$\mathcal{L}_e = \psi_e^\dagger \left(\varepsilon - \frac{\Pi^2}{2m} + \frac{\Pi^4}{8m^3c^2} - \frac{\Pi^2\varepsilon}{8m^2c^2} - \frac{\varepsilon\Pi^2}{8m^2c^2} + \frac{\Pi\varepsilon\Pi}{4m^2c^2} \right) \psi_e \quad (2.114)$$

where

$$\varepsilon = i\hbar \frac{\partial}{\partial t} - qV, \quad (2.115a)$$

$$\Pi = \boldsymbol{\sigma} \cdot (-i\hbar\nabla - q\mathbf{A}). \quad (2.115b)$$

From here I again go back to natural units, setting $c = 1$ and $\hbar = 1$.

Consider first the second term in equation (2.114). Using the relation that if \mathbf{a} and \mathbf{b} are two vectors, then

$$(\mathbf{a} \cdot \boldsymbol{\sigma})(\mathbf{b} \cdot \boldsymbol{\sigma}) = \mathbf{a} \cdot \mathbf{b} + i(\mathbf{a} \times \mathbf{b}) \cdot \boldsymbol{\sigma}, \quad (2.116)$$

I get that

$$\begin{aligned} \Pi^2 \psi_e &= [(-i\nabla - q\mathbf{A})^2 + i(-i\nabla - q\mathbf{A}) \times (-i\nabla - q\mathbf{A}) \cdot \boldsymbol{\sigma}] \psi_e \\ &= [(-i\nabla - q\mathbf{A})^2 + q(\nabla \times \mathbf{A}) \cdot \boldsymbol{\sigma}] \psi_e \\ &= [(-i\nabla - q\mathbf{A})^2 + q\mathbf{B} \cdot \boldsymbol{\sigma}] \psi_e, \end{aligned} \quad (2.117)$$

where I used that the magnetic field is $\mathbf{B} = \nabla \times \mathbf{A}$. From this one can also evaluate the term proportional to Π^4 . One can see that this will only give corrections to the kinetic energy and higher-order interactions between spin and \mathbf{B} . I am only interested in including the most important interactions between spin and the electromagnetic field, so I ignore the term proportional to Π^4 .

Next, the three remaining terms can be evaluated using that

$$\begin{aligned}
[\varepsilon, \Pi]_- \psi_e &= \left[i \frac{\partial}{\partial t} - qV, \boldsymbol{\sigma} \cdot (-i\nabla - q\mathbf{A}) \right]_- \psi_e \\
&= -i \left(\left[\frac{\partial}{\partial t}, \boldsymbol{\sigma} \cdot q\mathbf{A} \right]_- - [qV, \boldsymbol{\sigma} \cdot \nabla]_- \right) \psi_e \\
&= iq\boldsymbol{\sigma} \cdot \left(-\frac{\partial \mathbf{A}}{\partial t} - \nabla V \right) \psi_e = iq\boldsymbol{\sigma} \cdot \mathbf{E} \psi_e, \quad (2.118)
\end{aligned}$$

where I used that the electric field is $\mathbf{E} = -\partial \mathbf{A} / \partial t - \nabla V$. Hence,

$$\begin{aligned}
\frac{\Pi \varepsilon \Pi}{4m^2} - \frac{\Pi^2 \varepsilon}{8m^2} - \frac{\varepsilon \Pi^2}{8m^2} &= \frac{\Pi \varepsilon \Pi}{4m^2} - \frac{\Pi \varepsilon \Pi}{8m^2} - \frac{\Pi \varepsilon \Pi}{8m^2} \\
&+ \frac{iq\boldsymbol{\sigma} \cdot \mathbf{E} \Pi}{8m^2} - \frac{\Pi iq\boldsymbol{\sigma} \cdot \mathbf{E}}{8m^2} = \frac{iq\boldsymbol{\sigma} \cdot \mathbf{E} \Pi}{8m^2} - \frac{\Pi iq\boldsymbol{\sigma} \cdot \mathbf{E}}{8m^2}. \quad (2.119)
\end{aligned}$$

This is again a product of Pauli matrices and therefore again an opportunity to use equation (2.116),

$$\begin{aligned}
i[\boldsymbol{\sigma} \cdot \mathbf{E}, \Pi]_- \psi_e &= i[\boldsymbol{\sigma} \cdot \mathbf{E}, \boldsymbol{\sigma} \cdot (-i\nabla - q\mathbf{A})]_- \psi_e \\
&= \{-(\nabla \cdot \mathbf{E}) - i\boldsymbol{\sigma} \cdot (\nabla \times \mathbf{E}) - 2\boldsymbol{\sigma} \cdot [\mathbf{E} \times (-i\nabla - q\mathbf{A})]\} \psi_e. \quad (2.120)
\end{aligned}$$

The term proportional to $\nabla \cdot \mathbf{E}$ gives rise to a term in the Lagrangian known as the Darwin term [126, 129] and does not provide any coupling between spin and the electromagnetic field, so I ignore it here. Inserting this result back into the Lagrangian, I finally get that the electron Lagrangian density, written in terms of a single spinor field, is

$$\begin{aligned}
\mathcal{L}_e &= \psi_e^\dagger \left(i \frac{\partial}{\partial t} - qV - \frac{(-i\nabla - q\mathbf{A})^2}{2m} + \frac{q\boldsymbol{\sigma} \cdot \mathbf{B}}{2m} \right. \\
&\quad \left. - \frac{iq\boldsymbol{\sigma} \cdot (\nabla \times \mathbf{E})}{8m^2} - \frac{q\boldsymbol{\sigma} \cdot [\mathbf{E} \times (-i\nabla - q\mathbf{A})]}{4m^2} \right) \psi_e. \quad (2.121)
\end{aligned}$$

One can also identify the Hamiltonian density, h_e , from

$$\mathcal{L}_e = \pi^\dagger \frac{\partial \psi_e}{\partial t} - h_e, \quad (2.122)$$

where $\pi = i\psi_e^\dagger$ is the conjugate momentum density of ψ and the Hamiltonian density is

$$h_e = \psi_e^\dagger \left\{ qV + \frac{(-i\nabla - q\mathbf{A})^2}{2m} + \frac{q\boldsymbol{\sigma}}{2m} \cdot \mathbf{B} + \frac{q(\nabla \cdot \mathbf{E})}{8m^2} + \frac{iq\boldsymbol{\sigma} \cdot (\nabla \times \mathbf{E})}{8m^2} + \frac{q\boldsymbol{\sigma} \cdot [\mathbf{E} \times (-i\nabla - q\mathbf{A})]}{4m^2} \right\} \psi_e. \quad (2.123)$$

Because of the form of equation (2.122) and the fact that the Lagrangian is symmetric under global $U(1)$ -transformation, $\psi_e \mapsto \exp(i\varphi)\psi_e$, one can also see that the total number of electrons is conserved, as required. Because of the form of equation (2.122), we also know from section 2.5 that the Lagrangian density is consistent with the Heisenberg equation and that the spin angular momentum density of the field is $\mathbf{S} = (1/2)\psi_e^\dagger \boldsymbol{\sigma} \psi_e$.

The different terms in the Hamiltonian density have different physical interpretations. The first term is just the electric potential energy. The second term is the non-relativistic limit of the kinetic energy since the kinetic momentum operator is $(-i\nabla - q\mathbf{A})$. The third term is the Zeeman energy [25]. The Zeeman energy is not a relativistic correction, since it does not vanish in the limit $mc^2 \rightarrow \infty$. It is responsible for the coupling between the magnetic field \mathbf{B} and electron spin $\mathbf{S} = (1/2)\psi_e^\dagger \boldsymbol{\sigma} \psi_e$,

$$h_Z = \psi_e^\dagger \frac{q\boldsymbol{\sigma}}{2m} \cdot \mathbf{B} \psi_e = \frac{q}{m} \mathbf{S} \cdot \mathbf{B}. \quad (2.124)$$

It also defines a magnetic moment associated with the spin and thereby a g -factor [130]. The potential energy of a magnetic moment $\boldsymbol{\mu}$ in a magnetic field \mathbf{B} is

$$h_z = -\boldsymbol{\mu} \cdot \mathbf{B}, \quad (2.125)$$

and the relationship between the magnetic moment, the g -factor, g , and the spin angular momentum is [130]

$$\boldsymbol{\mu} = g \frac{q\mathbf{S}}{2m}. \quad (2.126)$$

Hence, from equation (2.123), we see that the g -factor associated with the spin at the level of operators is exactly $g = -2$. Note, however,

that to compute measured Zeeman energies one must evaluate the expectation value of the Zeeman energy operator. Therefore, the effective g -factor will be slightly different. This is because

$$\langle h_Z \rangle = \left\langle \frac{q}{m} \mathbf{S} \cdot \mathbf{B} \right\rangle \neq \frac{q}{m} \langle \mathbf{S} \rangle \cdot \langle \mathbf{B} \rangle. \quad (2.127)$$

The photon field (V, \mathbf{A}) is also a quantum field. Taking the expectation value requires taking into consideration the evolution of the photon field, not to mention the coupling to all the other fields in the standard model. To evaluate $\langle h_Z \rangle$ one can use the perturbative Green's function technique discussed in section 5.2 and treat the cubic interaction terms as perturbations. This has been done to high accuracy and with excellent agreement with experiments, and one gets an effective g -factor which is slightly different from -2 , $g = -2.00231930436$ [130, 131].

The fourth and fifth terms of equation (2.123) together constitute the spin-orbit interaction,

$$h_{\text{SO}} = \psi_e^\dagger \left(\frac{iq\boldsymbol{\sigma} \cdot (\nabla \times \mathbf{E})}{8m^2} + \frac{q\boldsymbol{\sigma} \cdot [\mathbf{E} \times (-i\nabla - q\mathbf{A})]}{4m^2} \right) \psi_e. \quad (2.128)$$

With only static charges, such that $\partial B/\partial t = 0$, the electric field is curl-free and the first term vanishes. The spin-orbit interaction couples the electron spin, through the Pauli matrices $\boldsymbol{\sigma}$, to the electric field \mathbf{E} , and makes it possible to manipulate spin angular momentum using the electric field. Since electric fields can be easier to localize in space [132, 133] compared to magnetic fields [134–136], it can be advantageous to rely on the spin-orbit interaction rather than the Zeeman interaction when designing spin-based technology.

2.7 Quantum Electrodynamics

The Hamiltonian derived in section 2.6,

$$\begin{aligned} \mathcal{H} = \int_{\mathbb{R}^3} d^3x \psi_e^\dagger \left\{ qV + \frac{(-i\nabla - q\mathbf{A})^2}{2m} + \frac{q\boldsymbol{\sigma} \cdot \mathbf{B}}{2m} \right. \\ \left. + \frac{iq\boldsymbol{\sigma} \cdot (\nabla \times \mathbf{E})}{8m^2} + \frac{q\boldsymbol{\sigma} \cdot [\mathbf{E} \times (-i\nabla - q\mathbf{A})]}{4m^2} - \mu \right\} \psi_e, \end{aligned} \quad (2.129)$$

is not enough for a complete description of the electron field. It includes terms that couple the electron field to the photon field (V, \mathbf{A}) . A

complete model must also determine how this field evolves in time. Moreover, for a proper quantum mechanical treatment of electrons one must treat the photon field quantum mechanically. This means that the photon field is also a field of operators, and the temporal evolution of these operators can be determined by extremizing the action. Note that since the electric and magnetic fields should be observable, they should be symmetric operators, meaning that $\mathbf{E}^\dagger = \mathbf{E}$ and $\mathbf{B}^\dagger = \mathbf{B}$. This also means that V and \mathbf{A} are symmetric, since $\mathbf{E} = -\nabla V - \partial\mathbf{A}/\partial t$ and $\mathbf{B} = \nabla \times \mathbf{A}$. Furthermore, the electromagnetic field is a vector field, which implies that operators should commute by the spin-statistics theorem [117].

The full Lagrangian density is

$$\mathcal{L} = \mathcal{L}_e + \mathcal{L}_{\text{em}} + \mathcal{L}_{\text{rest}} = \mathcal{L}_e + \frac{1}{2}(\mathbf{E} \cdot \mathbf{E} + \mathbf{B} \cdot \mathbf{B}) + \mathcal{L}_{\text{rest}}, \quad (2.130)$$

where \mathcal{L}_e is the electron Lagrangian density from before, $\mathcal{L}_{\text{em}} = (\mathbf{E} \cdot \mathbf{E} + \mathbf{B} \cdot \mathbf{B})/2$ is the Lagrangian for the photon field and $\mathcal{L}_{\text{rest}}$ is the Lagrangian density for the other, remaining fields. In the most fundamental description, the standard model, this would be for example the quark fields and the other lepton fields. In a higher-level description, $\mathcal{L}_{\text{rest}}$ could include an effective proton field, or, at an even higher level, it could be the Lagrangian describing the ions in a crystalline solid. The coupling between the electron field and the photon field is simpler if we use the Dirac Lagrangian,

$$\begin{aligned} \mathcal{L}_e + \mathcal{L}_{\text{em}} = \psi_D^\dagger \left[i \frac{\partial}{\partial t} + i\boldsymbol{\alpha} \cdot \nabla - \beta m \right] \psi_D + \frac{1}{2}(\mathbf{E} \cdot \mathbf{E} + \mathbf{B} \cdot \mathbf{B}) \\ - q\psi_D^\dagger V\psi_D + q\psi_D^\dagger \boldsymbol{\alpha} \cdot \mathbf{A}\psi_D, \end{aligned} \quad (2.131)$$

where I isolated the interaction terms. This is the Lagrange density of quantum electrodynamics [137]. One can get a theory with fewer variables by first solving for the photon operators. That is, one can write the photon operators as functions of the other field operators, thereby getting a new effective Lagrangian that only depends on the other fields.

To find the equations for the photon field, one can extremize the action with respect to V and \mathbf{A} . Extremizing the action of the interaction terms $-q\psi_D^\dagger V\psi_D$ and $q\psi_D^\dagger \boldsymbol{\alpha} \cdot \mathbf{A}\psi_D$ is easy because they are linear

in V and \mathbf{A} . First, I extremize the action of \mathcal{L}_{em} with respect to V . The magnetic field, $\mathbf{B} = \nabla \times \mathbf{A}$, does not depend on V , so we need only consider the electric field, $\mathbf{E} = -\nabla V - \partial \mathbf{A} / \partial t$. The Lagrangian density of the photon field only depends on ∇V , and the relevant term in the Euler-Lagrange equation (2.61) is

$$-\nabla \cdot \left[\frac{\partial \mathcal{L}_{\text{em}}}{\partial (\nabla V)} \right] = -\nabla \cdot \left[\nabla V + \frac{\partial \mathbf{A}}{\partial t} \right]. \quad (2.132)$$

Hence, if $-\rho_{\text{rest}}$ is the functional derivative of the action of $\mathcal{L}_{\text{rest}}$ with respect to V , then

$$\frac{\delta S}{\delta V} = -\nabla^2 V - \nabla \cdot \frac{\partial \mathbf{A}}{\partial t} - q\psi_D^\dagger \psi_D - \rho_{\text{rest}} = 0. \quad (2.133)$$

By similarly extremizing the action with respect to \mathbf{A} one gets the set of equations for the photon field given by

$$\nabla^2 V + \frac{\partial \nabla \cdot \mathbf{A}}{\partial t} = -q\psi_D^\dagger \psi_D - \rho_{\text{rest}}, \quad (2.134a)$$

$$\nabla^2 \mathbf{A} - \frac{\partial^2 \mathbf{A}}{\partial t^2} - \nabla \left(\frac{\partial V}{\partial t} + \nabla \cdot \mathbf{A} \right) = -q\psi_D^\dagger \boldsymbol{\alpha} \psi_D - \mathbf{j}_{\text{rest}}, \quad (2.134b)$$

where \mathbf{j}_{rest} is the functional derivative of the action of $\mathcal{L}_{\text{rest}}$ with respect to \mathbf{A} . One should interpret ρ_{rest} and \mathbf{j}_{rest} as the electric charge density and electric current density of the other fields, respectively.

Equation (2.134) can be solved such that the photon field operators can be written as a function of the Dirac bispinors as well as ρ_{rest} and \mathbf{j}_{rest} . One way to do so is to utilize the gauge symmetry equation (2.131), which is the fact that the Lagrangian is invariant under the transformation [116]

$$\psi_D \mapsto e^{iq\lambda} \psi_D, \quad (2.135a)$$

$$V \mapsto V - \frac{\partial \lambda}{\partial t}, \quad (2.135b)$$

$$\mathbf{A} \mapsto \mathbf{A} + \nabla \lambda, \quad (2.135c)$$

and similar transformations for the other fields, for any scalar-valued operator function $\lambda(t, \mathbf{r})$. Note that since we are still interpreting ψ_D , V , and \mathbf{A} as field operators, the act of changing gauge means that the annihilation operator $\psi_D(t, \mathbf{r})$ not only acts on the Dirac field by

annihilating an electron (or positron) but it also acts on the photon field. However, $\psi_D^\dagger \psi_D$ and $\psi_D^\dagger \boldsymbol{\alpha} \psi_D$ still act only on the Dirac field because the effects on the photon field cancel.

Using the freedom to choose λ , one can demand that

$$\frac{\partial V}{\partial t} + \nabla \cdot \mathbf{A} = 0. \quad (2.136)$$

This is called the Lorenz gauge condition and has the advantage of decoupling the equations for V and \mathbf{A} , such that

$$\left(\frac{\partial^2}{\partial t^2} - \nabla^2 \right) V = q \psi_D^\dagger \psi_D + \rho_{\text{rest}}, \quad (2.137a)$$

$$\left(\frac{\partial^2}{\partial t^2} - \nabla^2 \right) \mathbf{A} = q \psi_D^\dagger \boldsymbol{\alpha} \psi_D + \mathbf{j}_{\text{rest}}. \quad (2.137b)$$

Equation (2.137) are solved by

$$V = V_e + V_{\text{rest}} + V_{\text{ext}}, \quad (2.138a)$$

$$\mathbf{A} = \mathbf{A}_e + \mathbf{A}_{\text{rest}} + \mathbf{A}_{\text{ext}}, \quad (2.138b)$$

where

$$V_e(t, \mathbf{x}) = \frac{q}{4\pi} \int_{\mathbb{R}^3} d^3 y \frac{\psi_D^\dagger(t_{\text{ret}}, \mathbf{y}) \psi_D(t_{\text{ret}}, \mathbf{y})}{|\mathbf{x} - \mathbf{y}|}, \quad (2.139a)$$

$$V_{\text{rest}}(t, \mathbf{x}) = \frac{1}{4\pi} \int_{\mathbb{R}^3} d^3 y \frac{\rho_{\text{rest}}(t_{\text{ret}}, \mathbf{y})}{|\mathbf{x} - \mathbf{y}|}, \quad (2.139b)$$

$$\mathbf{A}_e(t, \mathbf{x}) = \frac{q}{4\pi} \int_{\mathbb{R}^3} d^3 y \frac{\psi_D^\dagger(t_{\text{ret}}, \mathbf{y}) \boldsymbol{\alpha} \psi_D(t_{\text{ret}}, \mathbf{y})}{|\mathbf{x} - \mathbf{y}|}, \quad (2.139c)$$

$$\mathbf{A}_{\text{rest}}(t, \mathbf{x}) = \frac{1}{4\pi} \int_{\mathbb{R}^3} d^3 y \frac{\mathbf{j}_{\text{rest}}(t_{\text{ret}}, \mathbf{y})}{|\mathbf{x} - \mathbf{y}|}, \quad (2.139d)$$

are so-called Liénard–Wiechert potentials [138, 139]. Here, $t_{\text{ret}} = t - |\mathbf{x} - \mathbf{y}|$ is called the retarded time. I will just approximate $t = t_{\text{ret}}$ since the difference is small when speeds are small compared to the speed of light. The external potentials V_{ext} and \mathbf{A}_{ext} satisfy the homogeneous solution,

$$\left(\frac{\partial^2}{\partial t^2} - \nabla^2 \right) V_{\text{ext}} = 0, \quad (2.140a)$$

$$\left(\frac{\partial^2}{\partial t^2} - \nabla^2 \right) \mathbf{A}_{\text{ext}} = 0. \quad (2.140b)$$

When considering subsystems spanned by the field operators of only a finite region in space, I will add the contributions from external sources to the external potentials. Note that V_{ext} and \mathbf{A}_{ext} cannot be chosen entirely freely. Otherwise, one could set the photon field operators to zero in the absence of charges, which is not true. Depending on the ensemble of states under consideration, it might be a good approximation to set V_{ext} and \mathbf{A}_{ext} to zero, but it is not something that is valid in general. The point of this exercise is not to fully determine photon operators in terms of electron operators. Instead, the point is to extract how the photon field evolves in space and time as a function of the other fields. By extracting this dependence, it becomes much simpler to evaluate expectation values. Since the V_{ext} and \mathbf{A}_{ext} do not couple to ψ_D , $\langle V_{\text{ext}} \psi_D^\dagger \psi_D \rangle = \langle V_{\text{ext}} \rangle \langle \psi_D^\dagger \psi_D \rangle$, and similarly for expectation values involving \mathbf{A}_{ext} .

Next, I would like to express the photon field in terms of the electron spinor field, ψ_e , rather than the Dirac bispinors, ψ_D . This can be done by simply inserting the expressions obtained in section 2.6, namely $\psi_D^T = (u, P\boldsymbol{\sigma} \cdot (-i\nabla - q\mathbf{A})u)$ and $u = \left\{1 - \frac{1}{8m^2} [\boldsymbol{\sigma} \cdot (-i\nabla - q\mathbf{A})]^2\right\} \psi_e$. However, I am again only interested in relativistic corrections which couple spin to the electric or magnetic field. As a result, it is simpler to take the functional derivative of the non-relativistic action defined by using equation (2.129). Doing this I find that the charge density operator is

$$\rho_e = q\psi_D^\dagger \psi_D \approx q\psi_e^\dagger \psi_e + \frac{q}{4m^2} \nabla \cdot [\psi_e^\dagger \boldsymbol{\sigma} \times (-i\nabla - q\mathbf{A})\psi_e]. \quad (2.141)$$

and the electric current density operator is

$$\begin{aligned} \mathbf{j}_e = q\psi_D^\dagger \boldsymbol{\alpha} \psi_D \approx & \frac{q}{2m} \psi_e^\dagger (-i\nabla - q\mathbf{A})\psi_e + \frac{q}{2m} [(-i\nabla - q\mathbf{A})\psi_e]^\dagger \psi_e \\ & - \frac{q}{2m} \nabla \times (\psi_e^\dagger \boldsymbol{\sigma} \psi_e) + \frac{q}{4m^2} \psi_e^\dagger \mathbf{E} \times \boldsymbol{\sigma} \psi_e - \frac{\partial}{\partial t} \left[\frac{iq}{8m^2} \nabla \times (\psi_e^\dagger \boldsymbol{\sigma} \psi_e) \right] \\ & + \frac{\partial}{\partial t} \left[\frac{q}{4m^2} \psi_e^\dagger \boldsymbol{\sigma} \times (-i\nabla - q\mathbf{A})\psi_e \right]. \end{aligned} \quad (2.142)$$

The terms proportional to $1/m^2$ are the relativistic corrections that come from the spin-orbit coupling. Inserting equations (2.141) and (2.142) as well as the charge and current densities from the other fields into equation (2.139) and then inserting V and \mathbf{A} into the final Lagrangian,

we get a new theory without electron-photon coupling but with electron-electron coupling as well as coupling between the electron field and all the other charged fields.

Note that even though both \mathcal{L}_{em} and $\mathcal{L}_{\text{rest}}$ depend on ψ_e after inserting the solutions of V and \mathbf{A} , extremizing the action with respect to ψ_e still only requires the electron Lagrangian density \mathcal{L}_e . This is because a version of the chain rule also works for functional derivatives [140]. Using this chain rule, taking the functional derivative of the action S with respect to ψ_e gives

$$\frac{\delta S}{\delta \psi_e} = \left. \frac{\delta S}{\delta \psi_e} \right|_{V, \mathbf{A}} + \frac{\delta S}{\delta V} \frac{\partial V}{\partial \psi_e} + \frac{\delta S}{\delta \mathbf{A}} \cdot \frac{\partial \mathbf{A}}{\partial \psi_e}, \quad (2.143)$$

where the subscript on the first term on the right-hand side means that the functional derivative should be taken while keeping V and \mathbf{A} constant. Since the action is already extremized with respect to V and \mathbf{A} , the last two terms on the right-hand side vanish, and

$$\frac{\delta S}{\delta \psi_e} = \left. \frac{\delta S}{\delta \psi_e} \right|_{V, \mathbf{A}}. \quad (2.144)$$

When V and \mathbf{A} are kept constant, the only part of the Lagrangian that depends on ψ_e is the electron Lagrangian. To specify the electron dynamics one therefore still only has to specify the electron Hamiltonian.

Quantum Theory of Solids

Building upon the foundation laid in the previous chapter, the aim of this chapter is to derive models for crystalline solid states of matter. In such materials, atoms are placed in an approximate lattice. The distance between neighboring atoms is on the order of angstroms (10^{-10} m) [141]. As a result, the electromagnetic field varies on a very short length scale, and the real space Hamiltonian can be difficult to work with. Instead, it is often better to use lattice models, which I derive in section 3.1. One can apply lattice models to study a wide range of the rich physics found in solid state systems, from topological insulators [142, 143] to quantum spin liquids [144–146]. For the work presented in this thesis, it is of special interest to use lattice models to study magnetic and superconducting materials. I show how magnetism and superconductivity are captured by lattice models in sections 3.2 and 3.3, respectively. Finally, in section 3.4 I show how to include the effect of external fields.

3.1 Lattice Models

In crystalline solid states of matter, atoms are placed in an approximate lattice [141]. That is, there is a periodic lattice of charged ions, but the ions can move and there may be defects in the lattice. Both the dynamics of the charged ions and the impurities are important for the behavior of solid states of matter. These effects can be added as corrections to an otherwise perfectly periodic lattice. I define a lattice vector \mathbf{R}_a as being such that the lattice is invariant under the translation of \mathbf{R}_a , neglecting any impurities and dynamics in the lattice. This means that there can in general be multiple ions associated with each lattice site. The Hamiltonian for the electrons has been derived in section 2.6 to be

$$\mathcal{H} = \int_{\mathbb{R}^3} d^3x \psi^\dagger \left\{ qV + \frac{(-i\nabla - q\mathbf{A})^2}{2m} + \frac{q\boldsymbol{\sigma}}{2m} \cdot \mathbf{B} + \frac{iq\boldsymbol{\sigma} \cdot (\nabla \times \mathbf{E})}{8m^2} + \frac{q\boldsymbol{\sigma} \cdot [\mathbf{E} \times (-i\nabla - q\mathbf{A})]}{4m^2} - \mu \right\} \psi. \quad (3.1)$$

As a reminder, the electron field $\psi = (\psi_\uparrow, \psi_\downarrow)^T$ is a 2-component spinor field, μ is the chemical potential, m is the electron mass, q is electric charge, V is the electric potential, \mathbf{A} is the vector potential, $\mathbf{E} = -\nabla V - \partial\mathbf{A}/\partial t$ is the electric field and $\mathbf{B} = \nabla \times \mathbf{A}$ is the magnetic field. When deriving equation (3.1) I neglected all relativistic corrections except for the spin-orbit interaction. However, treating even only the spin-orbit interaction consistently is no simple task, as it requires relativistic corrections to the electron charge density and the electron charge current density, given by equations (2.141) and (2.142), respectively.

If we collect the potentials from the other fields, such as the ions, and from external sources as

$$V_{\text{env}} = V_{\text{ext}} + V_{\text{rest}}, \quad (3.2a)$$

$$\mathbf{A}_{\text{env}} = \mathbf{A}_{\text{ext}} + \mathbf{A}_{\text{rest}}, \quad (3.2b)$$

where V_{rest} , \mathbf{A}_{rest} is given by equation (2.139) and V_{ext} and \mathbf{A}_{ext} are the external potentials, we can write the Hamiltonian as

$$\begin{aligned} \mathcal{H} = & \sum_{\sigma_1, \sigma_2 \in \uparrow\downarrow} \int_{\mathbb{R}^3} d^3x \psi_{\sigma_1}^\dagger(\mathbf{x}) M_{\sigma_1\sigma_2}(\mathbf{x}) \psi_{\sigma_2}(\mathbf{x}) \\ & + \sum_{\sigma_1, \sigma_2, \sigma_3, \sigma_4 \in \uparrow\downarrow} \int_{\mathbb{R}^3} d^3x \int_{\mathbb{R}^3} d^3y \psi_{\sigma_1}^\dagger(\mathbf{x}) \psi_{\sigma_2}^\dagger(\mathbf{y}) N_{\sigma_1\sigma_2\sigma_3\sigma_4}(\mathbf{x}, \mathbf{y}) \psi_{\sigma_3}(\mathbf{y}) \psi_{\sigma_4}(\mathbf{x}), \end{aligned} \quad (3.3)$$

where

$$\begin{aligned} M = & qV_{\text{env}} + \frac{(-i\nabla - q\mathbf{A}_{\text{env}})^2}{2m} + \frac{q\boldsymbol{\sigma}}{2m} \cdot \mathbf{B}_{\text{env}} \\ & + \frac{iq\boldsymbol{\sigma} \cdot (\nabla \times \mathbf{E}_{\text{env}})}{8m^2} + \frac{q\boldsymbol{\sigma} \cdot [\mathbf{E}_{\text{env}} \times (-i\nabla - q\mathbf{A}_{\text{env}})]}{4m^2} - \mu \end{aligned} \quad (3.4)$$

and N can be derived from combining equations (2.131) and (3.1) with equations (2.139), (2.141) and (2.142). Both M and N involve differentiation operators, but they do not include any electron field operators. They do, however, include charge and current operators for the field describing the ions.

The fact that the electromagnetic field associated with the ions varies very rapidly in space makes equation (3.3) difficult to work with. In order to derive a simpler effective model, one can use creation and

annihilation operators associated with the eigenstates of a self-adjoint operator different from the position operator. One observation that motivates another set of eigenstates is that close to an atom in the lattice, the Hamiltonian is well approximated by an atomic Hamiltonian,

$$\mathcal{H}_a = \int_{\mathbb{R}^3} d^3x \psi^\dagger \left\{ qV_a + \frac{(-i\nabla - q\mathbf{A}_a)^2}{2m} + \frac{q\boldsymbol{\sigma} \cdot \mathbf{B}_a}{2m} + \frac{iq\boldsymbol{\sigma} \cdot (\nabla \times \mathbf{E}_a)}{8m^2} + \frac{q\boldsymbol{\sigma} \cdot [\mathbf{E}_a \times (-i\nabla - q\mathbf{A}_a)]}{4m^2} - \mu \right\} \psi, \quad (3.5)$$

where V_a , \mathbf{A}_a , \mathbf{E}_a , and \mathbf{B}_a are the electromagnetic potentials and fields associated with the atom. This Hamiltonian is self-adjoint, and so it has a complete set of (possibly generalized) eigenstates. Some of these eigenstates, called orbitals, might also be tightly localized around the atom, such that they are good approximations for the eigenstates of the full Hamiltonian as well. One possibly tempting approach is to write states in terms of eigenstates of atomic Hamiltonians but shifted in space such that they match the atoms in the lattice. However, there is a problem with this.

Take for instance a crystalline material with a single atom in the unit cell, and let $\{|n\rangle\}$ be the eigenstates of the associated atomic Hamiltonian. In this case, a seemingly reasonable choice for basis is to use $\{|n\rangle\}$, but shifted in space, since this will well approximate the eigenstates of the full Hamiltonian, at least the states in $\{|n\rangle\}$ which are sufficiently localized. That is, for a general state $|\psi\rangle$, one might want to write

$$|\psi\rangle = \sum_{n,m} b_{nm} |n, \mathbf{R}_m\rangle, \quad (3.6)$$

where $|n, \mathbf{R}_m\rangle$ is orbital n shifted in space to lattice site \mathbf{R}_m , meaning that $\langle \mathbf{x} | n, \mathbf{R}_m \rangle = \langle \mathbf{x} - \mathbf{R}_m | n \rangle$. However, this does not work because the set $\{|n, \mathbf{R}_m\rangle\}$ is not an orthonormal basis. As a consequence, the coefficients $\{b_{nm}\}$ cannot be uniquely determined. This can be seen easily from the fact that a single set of atomic orbitals, $\{|n\rangle\}$, spans all of the single-particle Hilbert space. Thus, the coefficients $\{b_{nm}\}$ can be determined for any fixed choice of m . One alternative is to instead approximate states by their projection onto the subspace spanned by the few smallest orbitals from each atom. This can be a good

approximation if the electrons are tightly bound around each lattice site.

A choice for a proper complete orthonormal basis, which is similar in nature to translated atomic orbitals, is to choose a set of so-called *Wannier states* [147, 148]. These are also localized in space around the lattice sites [148], and they can be motivated by Bloch's theorem [141, 149]. Bloch's theorem concerns the eigenstates of systems with periodic potentials. The Hamiltonians of periodic systems commute with the translation operator that shifts space according to a lattice vector. The eigenstates of the lattice translation operator can be labeled by reciprocal vectors, \mathbf{k} , meaning they live in the space defined by the Fourier transform of the lattice vectors. Furthermore, they can be restricted to the first Brillouin zone [141]. This means that the eigenstates of a periodic Hamiltonian also can be labeled by \mathbf{k} . A general eigenstate of a periodic Hamiltonian can therefore be written $|\psi_{n\mathbf{k}}\rangle$. Bloch's theorem states that [141]¹

$$\langle \mathbf{x} | \psi_{n\mathbf{k}} \rangle = e^{-i\mathbf{k} \cdot \mathbf{R}_m} \langle \mathbf{x} + \mathbf{R}_m | \psi_{n\mathbf{k}} \rangle. \quad (3.7)$$

This is just an immediate consequence of the fact that $|\psi_{n\mathbf{k}}\rangle$ is an eigenstate of the translation operator $T_{\mathbf{R}_n} : \mathbf{x} \mapsto \mathbf{x} + \mathbf{R}_n$ with eigenvalue $\exp(-i\mathbf{k} \cdot \mathbf{R}_n)$, so

$$\langle \mathbf{x} | \psi_{n\mathbf{k}} \rangle = \langle \mathbf{x} + \mathbf{R}_m | T_{\mathbf{R}_m} | \psi_{n\mathbf{k}} \rangle = e^{-i\mathbf{k} \cdot \mathbf{R}_m} \langle \mathbf{x} + \mathbf{R}_m | \psi_{n\mathbf{k}} \rangle. \quad (3.8)$$

The Wannier states are defined in terms of the eigenstates of the periodic Hamiltonian as [148]

$$|\varphi_{n\mathbf{R}_m}\rangle = \frac{1}{\sqrt{N}} \sum_{\mathbf{k}} e^{-i\mathbf{k} \cdot \mathbf{R}_m} |\psi_{n\mathbf{k}}\rangle, \quad (3.9)$$

where the sum goes over the first Brillouin zone and N is the number of lattice points. Unlike the multiple sets of translated atomic orbitals above, the set of Wannier states is orthonormal, since

$$\begin{aligned} \langle \varphi_{n\mathbf{R}_a} | \varphi_{m\mathbf{R}_b} \rangle &= \frac{1}{N} \sum_{\mathbf{k}, \mathbf{q}} e^{i\mathbf{k} \cdot \mathbf{R}_a - i\mathbf{q} \cdot \mathbf{R}_b} \langle \psi_{n\mathbf{k}} | \psi_{m\mathbf{q}} \rangle \\ &= \frac{1}{N} \sum_{\mathbf{k}} e^{i\mathbf{k} \cdot (\mathbf{R}_a - \mathbf{R}_b)} \langle \psi_{n\mathbf{k}} | \psi_{m\mathbf{k}} \rangle \delta_{nm} = \delta_{\mathbf{R}_a \mathbf{R}_b} \delta_{nm}, \end{aligned} \quad (3.10)$$

1. There are really two eigenstates of the position operator at every point. Therefore, $|\mathbf{x}\rangle$ should also include a spin index, $|\mathbf{x}, \sigma\rangle$, which I omitted here for notational brevity.

where I used that the eigenstates of the Hamiltonian are assumed orthonormal, so $\langle \psi_{n,\mathbf{k}} | \psi_{m,\mathbf{q}} \rangle = \delta_{n,m} \delta_{\mathbf{k},\mathbf{q}}$.

To write the Hamiltonian in terms of creation and annihilation operators for the Wannier states, one can relate the field operators in equation (3.3) to the creation and annihilation operators, $\{c_{n\mathbf{R}_m}^\dagger\}$ and $\{c_{n\mathbf{R}_m}\}$, using equation (2.37). There are two field operators per spatial position, corresponding to two eigenstates of the position operators, $|\mathbf{r}, \uparrow\rangle$ and $|\mathbf{r}, \downarrow\rangle$. Defining the Wannier functions $\varphi_{\sigma n \mathbf{R}_m}(\mathbf{r}) = \langle \mathbf{r}, \sigma | \varphi_{n \mathbf{R}_m} \rangle$ and using that $\varphi_{\sigma n \mathbf{R}_m}(\mathbf{r}) = \varphi_{\sigma n}(\mathbf{r} - \mathbf{R}_m)$, where I assumed there is a lattice site at the origin and defined $\varphi_{\sigma n} \equiv \varphi_{\sigma n 0}$, equation (3.3) can be written as

$$\begin{aligned} \mathcal{H} = & \sum_{n,m} \sum_{\mathbf{R}_a, \mathbf{R}_b} M_{n\mathbf{R}_a m \mathbf{R}_b} c_{n\mathbf{R}_a}^\dagger c_{m\mathbf{R}_b} \\ & + \sum_{n,m,p,q} \sum_{\mathbf{R}_a, \mathbf{R}_b, \mathbf{R}_c, \mathbf{R}_d} N_{n\mathbf{R}_a m \mathbf{R}_b p \mathbf{R}_c q \mathbf{R}_d} c_{n\mathbf{R}_a}^\dagger c_{m\mathbf{R}_b}^\dagger c_{p\mathbf{R}_c} c_{q\mathbf{R}_d}, \end{aligned} \quad (3.11)$$

where the matrix elements are

$$M_{n\mathbf{R}_a m \mathbf{R}_b} = \sum_{\sigma_1, \sigma_2 \in \{\uparrow, \downarrow\}} \int_{\mathbb{R}^3} d^3 r \varphi_{\sigma_1 n}^*(\mathbf{x} - \mathbf{R}_a) M_{\sigma_1 \sigma_2}(\mathbf{x}) \varphi_{\sigma_2 m}(\mathbf{x} - \mathbf{R}_b) \quad (3.12)$$

and

$$\begin{aligned} N_{n\mathbf{R}_a m \mathbf{R}_b p \mathbf{R}_c q \mathbf{R}_d} = & \sum_{\sigma_1, \sigma_2, \sigma_3, \sigma_4 \in \{\uparrow, \downarrow\}} \int_{\mathbb{R}^3} d^3 x \int_{\mathbb{R}^3} d^3 y \varphi_{\sigma_1 n}^*(\mathbf{x} - \mathbf{R}_a) \\ & \times \varphi_{\sigma_2 m}^*(\mathbf{y} - \mathbf{R}_b) N_{\sigma_1 \sigma_2 \sigma_3 \sigma_4}(\mathbf{x}, \mathbf{y}) \varphi_{\sigma_3 p}(\mathbf{y} - \mathbf{R}_c) \varphi_{\sigma_4 q}(\mathbf{x} - \mathbf{R}_d). \end{aligned} \quad (3.13)$$

Wannier states can in principle be defined for any orthonormal set of eigenstates for a periodic Hamiltonian. The full Hamiltonian is not periodic, so one should use the eigenstates of the periodic Hamiltonian that best approximates the full Hamiltonian. This is obtained by setting the external potentials to zero and setting the ions in their equilibrium configurations with no impurities in the lattice. That being said, determining the Wannier functions is often not feasible for realistic systems. A popular simplifying approximation is to approximate the Wannier functions by the orbitals from above. This is known as the tight binding approximation [141].

Another simplifying assumption is to assume that only one or a few orbitals are relevant to the dynamics of the system. The orbitals of an atom can be sorted into discrete energy levels. The orbitals with lower energies are generally more tightly packed around the atom. As the number of electrons in the system is increased, the orbitals with the lowest energies will be filled first. Take an electron in one of these states with energy ε . In order to excite this electron to another orbital, one would need to raise its energy by $E_{\text{unoccupied}} - \varepsilon$, where $E_{\text{unoccupied}}$ is the energy of the first unoccupied state. This is because each electron state can only be occupied once, by virtue of electrons being fermions. If $E_{\text{unoccupied}} - \varepsilon$ is larger than all the relevant energy scales in the system, such as the temperature, the state with energy ε will simply remain fully occupied, not contributing to the dynamics of the system. Similarly, unoccupied states with energies much larger than $E_{\text{unoccupied}}$ will simply remain unoccupied.

Hence, a reasonable assumption is often that only a fixed number of Wannier states contribute to the dynamics of the system. The remaining states have energies that are either too large or too small, so they remain either almost completely empty or almost completely occupied at all times. In other words, we do not need to know how operators such as the Hamiltonian act on all possible state vectors in Fock space. It is sufficient to know how they act on states where the majority of Wannier states are either fully occupied or fully empty. If a Wannier state $|\varphi_{nR_a}\rangle$ is always fully empty, we can set $c_{nR_a}^\dagger c_{nR_a} = 0$, since this is true for all the states one needs to consider. Similarly, if the state is always fully occupied, we can set $c_{nR_a}^\dagger c_{nR_a} = 1$. Thus, some of the quartic terms become quadratic terms, and some quadratic terms become constants. In essence, it is equivalent to adding the spin and electric charge associated with the occupied states when computing V_{env} and A_{env} . Considering only a subspace of Fock space defined by the occupation of Wannier states is similar to considering a subspace spanned by only a few orbitals at each ion, as discussed above. The difference with considering a subspace of Wannier states rather than a subspace of orbitals is that the Wannier states are orthonormal, so the Wannier states also works as an orthonormal basis for the subspace, allowing us to use creation and annihilation operators for the Wannier states.

Another observation that can be used to simplify the problem is that the integrals in equations (3.12) and (3.13) are smaller when the lattice sites are further apart from each other. For example, one possible simplification is to set equation (3.13) to zero unless $\mathbf{R}_a = \mathbf{R}_b = \mathbf{R}_c = \mathbf{R}_d$. If there is only one atom per lattice site, and if one assumes that only one active orbital per spin per lattice site, the model with these simplifications become

$$\mathcal{H} = - \sum_{i,j} \sum_{\sigma_1, \sigma_2 \in \{\uparrow, \downarrow\}} c_{i\sigma_1}^\dagger t_{\sigma_1\sigma_2}^{ij} c_{j\sigma_2} + \sum_i \sum_{\sigma_1, \sigma_2, \sigma_3, \sigma_4 \in \{\uparrow, \downarrow\}} U_{\sigma_1\sigma_2\sigma_3\sigma_4}^i c_{i\sigma_1}^\dagger c_{i\sigma_2}^\dagger c_{i\sigma_3} c_{i\sigma_4}, \quad (3.14)$$

for some $t_{\sigma_1\sigma_2}^{ij}$ and $U_{\sigma_1\sigma_2\sigma_3\sigma_4}^i$, where the sums goes over the lattice sites. Since $c_{i\sigma}c_{i\sigma} = c_{i\sigma}^\dagger c_{i\sigma}^\dagger = 0$, the last sum is only nonzero when $\sigma_3 \neq \sigma_4$ and $\sigma_1 \neq \sigma_2$. Hence,

$$\mathcal{H} = - \sum_{i,j} \sum_{\sigma_1, \sigma_2 \in \{\uparrow, \downarrow\}} c_{i\sigma_1}^\dagger t_{\sigma_1\sigma_2}^{ij} c_{j\sigma_2} + \sum_i U^i n_{i\uparrow} n_{i\downarrow}, \quad (3.15)$$

where $n_{i\sigma} = c_{i\sigma}^\dagger c_{i\sigma}$. This is known as the (single orbital) Hubbard model [150, 151].

3.2 Magnetism

Different Wannier states have different spins, and from above we know that there is a magnetic moment associated with each spin. In a magnetic system, there is an effective interaction between the spins at different lattice sites. This tends to either align the magnetic moments in the same direction, in which case the material is called ferromagnetic, or it tends to align the magnetic moments in opposite directions, in which case the material is called either antiferromagnetic or ferrimagnetic [141]. The material is antiferromagnetic if the oppositely aligned magnetic moments are of equal magnitude, giving a net zero magnetic moment. Otherwise, the material is ferrimagnetic.

There does not need to be any intrinsic magnetic interactions in the system for a material to be magnetic. In fact, even the simple single orbital Hubbard model from above,

$$\mathcal{H} = - \sum_{i,j} \sum_{\sigma \in \{\uparrow, \downarrow\}} t^{ij} c_{i\sigma}^\dagger c_{j\sigma} + U \sum_i n_{i\uparrow} n_{i\downarrow}, \quad (3.16)$$

displays magnetic properties [151]. Here I have removed the vector potential, the magnetic field, and the spin-orbit coupling potential from the model, which means that the hopping term becomes $t_{\sigma_1\sigma_2}^{ij} = \delta_{\sigma_1\sigma_2}t^{ij}$. I also assumed for simplicity that the on-site potential U is independent of lattice site. To see why equation (3.16) displays magnetic properties, note that by tracing back the definition of U in the simplest case with no relativistic corrections, it is equal to an integral of strictly positive terms, meaning that U is positive. As a result, the energy from U is minimized when there is at most one electron at every lattice site. On the other hand, if t^{ij} is positive, the term $-t^{ij}c_{i\sigma}^\dagger c_{j\sigma}$ favors states in which site j has an occupied state with spin σ while site i does not.

If we assume a system with half-filling, meaning that there is on average 1 electron on each site, the minimum energy is for a state $|\psi\rangle$ where every site is occupied by exactly one electron, and the spin alternates between neighboring sites.² The fact that there is only one particle per site means that $n_{i\uparrow}n_{i\downarrow}|\psi\rangle = 0$ for all i , and the fact that the spins alternate means that tunneling between neighboring sites is still allowed, meaning that $t^{ij}c_{i\sigma}^\dagger c_{j\sigma}|\psi\rangle \neq 0$ for neighboring i and j . The amplitude of t^{ij} decreases with relative distance, so neighboring sites are most important. Hence, the Hubbard model at half-filling is an antiferromagnet, even if there are no magnetic fields in the Hamiltonian. At different filling fractions, the Hubbard model can also show ferromagnetic properties [152].

When studying magnetic materials, one popular choice for an effective Hamiltonian is the so-called *Heisenberg model* [114, 150],

$$\mathcal{H} = \sum_{ij} J_{ij} \mathbf{S}_i \cdot \mathbf{S}_j, \quad (3.17)$$

where J_{ij} is a constant and \mathbf{S}_i is the spin at lattice site i . This model is also something I employ in my work (paper VI), so I will derive it here from the half-filled Hubbard model. Because I restrict the filling fraction to half-filling, I consider only the subspace of Fock-space with N particles, where $2N$ is the total number of lattice sites. As a result, if

2. Note that this antiferromagnetic state is not an eigenstate of the Hamiltonian, and therefore not the ground state. A proper quantum ground state is a bit more complicated, but the qualitative feature of predominately alternating spins is the same.

we assume that t^{ii} is independent of i , then

$$-\sum_i \sum_{\sigma \in \{\uparrow, \downarrow\}} t^{ii} c_{i\sigma}^\dagger c_{j\sigma} = -t^{ii} N \quad (3.18)$$

is just a constant. We can remove this term by a constant energy shift, so

$$\mathcal{H} = -\sum_{i \neq j} \sum_{\sigma \in \{\uparrow, \downarrow\}} t^{ij} c_{i\sigma}^\dagger c_{j\sigma} + U \sum_i n_{i\uparrow} n_{i\downarrow}, \quad (3.19)$$

where the first sum now goes over all pairs (i, j) of lattice sites where $i \neq j$. Next, I want to treat the first sum as a perturbation. That is, I assume that $U \gg t^{ij}$ for all i and j .

Let

$$\mathcal{H}_0 = U \sum_i n_{i\uparrow} n_{i\downarrow}. \quad (3.20)$$

Any state in which there is exactly one electron per site is an eigenstate of \mathcal{H}_0 with the minimum eigenvalue equal to 0. There are 2^N orthogonal such states, spanning a space \mathcal{V}_0 . Similarly, any state in which there is exactly one site with two electrons will be an eigenstate with eigenvalue U . The set of all such states spans \mathcal{V}_1 . Let P_n be the projection operator which maps states onto their projection on \mathcal{V}_n , where \mathcal{V}_n is space spanned by all states with n doubly occupied lattice sites. The projection operators satisfy $P_i P_j = \delta_{ij} P_i$. Using the projection operators, we can write

$$\mathcal{H}_0 = \sum_{n=0}^{\lfloor N/2 \rfloor} n U P_n. \quad (3.21)$$

When U is large, the lowest energy eigenstates of \mathcal{H} must have a large projection onto \mathcal{V}_0 . The aim when deriving an effective Hamiltonian is to define a subspace in which all relevant states can be expected to live in. That is, the probability for a state in the statistical ensemble to be outside this space is vanishingly small. Then, one can neglect all terms in the Hamiltonian which has a negligible operator norm when acting on this subspace, as explained above. Since states in \mathcal{V}_n are multiplied by nU when acted upon by \mathcal{H}_0 , a first guess for such a subspace might be \mathcal{V}_0 . This is a good approximation to zeroth order

in t^{ij}/U . However, all states in \mathcal{V}_0 are degenerate to zeroth order, so the zeroth order problem is trivial.

To go above zeroth order, one must consider states which are superpositions of states in \mathcal{V}_0 , \mathcal{V}_1 , and so on. In order to identify a relevant subspace, I define a similarity transformation on the projection operators,

$$\tilde{P}_n = SP_nS^{-1}. \quad (3.22)$$

If we can find S such that

$$\mathcal{H} = \sum_{n=0}^{\lfloor N/2 \rfloor} \tilde{P}_n \mathcal{H} \tilde{P}_n, \quad (3.23)$$

it means that all states in the space defined by \tilde{P}_n are only mapped by \mathcal{H} to states in the same space. Let this space be $\tilde{\mathcal{V}}_n$. In particular, all eigenstates are in $\tilde{\mathcal{V}}_n$ for some n , and the eigenstates in $\tilde{\mathcal{V}}_n$ form a complete basis for $\tilde{\mathcal{V}}_n$. Since the Hamiltonian defines the time-evolution operator, it means that if we start with a statistical ensemble of states in the space defined by \tilde{P}_n , then they will remain in this space. This can be used to identify the subspace containing all the lowest energy eigenstates, which enables us to do perturbation theory.

If we let S be a function of the perturbation strength t^{ij}/U , and $\lim_{t^{ij}/U \rightarrow 0} S = 1$, the lowest energy states should be in $\tilde{\mathcal{V}}_0$. We can therefore use it as an effective Hamiltonian

$$\mathcal{H}_{\text{eff}} = \tilde{P}_0 \mathcal{H} \tilde{P}_0. \quad (3.24)$$

To derive \tilde{P}_0 , I introduce some notation for this section, which is inspired by the general theory of effective Hamiltonians by Soliverez [153]. For an operator, A , I define the operation

$$\langle A \rangle = \sum_{n=0}^{\lfloor N/2 \rfloor} P_n A P_n \quad (3.25)$$

Clearly, $\langle \mathcal{H}_0 \rangle = \mathcal{H}_0$ but $\langle \mathcal{H} \rangle \neq \mathcal{H}$. I define also the operation

$$h(A) = \sum_{i \neq j} \frac{P_i A P_j}{(i-j)U} \quad (3.26)$$

Note, using equation (3.21), as well as $P_i P_j = \delta_{ij}$ and $\sum_n P_n = 1$, that

$$\begin{aligned}
h([\mathcal{H}_0, A]_-) &= h\left(\sum_{n=0}^{\lfloor N/2 \rfloor} U n [P_n A - A P_n]\right) \\
&= \sum_{i \neq j} \sum_{n=0}^{\lfloor N/2 \rfloor} U \frac{n P_i P_n A P_j - P_i A P_n P_j n}{(i-j)U} = \sum_{i \neq j} \frac{i P_i A P_j - P_i A P_j j}{(i-j)} \\
&= \sum_{i \neq j} P_i A P_j = \sum_{ij} P_i A P_j - \sum_i P_i A P_i = A - \langle A \rangle \quad (3.27)
\end{aligned}$$

Next, I define

$$\mathcal{H}_S = S^{-1} \mathcal{H} S, \quad (3.28)$$

as well as

$$W_S = \mathcal{H}_S - \mathcal{H}_0 \quad \text{and} \quad W = \mathcal{H} - \mathcal{H}_0. \quad (3.29)$$

This means that W is the perturbation. Since,

$$S W_S = \mathcal{H} S - S \mathcal{H}_0 \quad \text{and} \quad W S = \mathcal{H} S - \mathcal{H}_0 S, \quad (3.30)$$

we see that

$$[\mathcal{H}_0, S]_- = S W_S - W S. \quad (3.31)$$

From equations (3.22) and (3.23), we have that

$$\mathcal{H}_S = S^{-1} \sum_{n=0}^{\lfloor N/2 \rfloor} S P_n S^{-1} \mathcal{H} S P_n S S^{-1} = \langle \mathcal{H}_S \rangle, \quad (3.32)$$

so

$$\langle W_S \rangle = \langle \mathcal{H}_S - \mathcal{H}_0 \rangle = \langle \mathcal{H}_S \rangle - \langle \mathcal{H}_0 \rangle = \mathcal{H}_S - \mathcal{H}_0 = W_S. \quad (3.33)$$

Thus,

$$0 = \langle [\mathcal{H}_0, S]_- \rangle = \langle S \rangle W_S - \langle W S \rangle, \quad (3.34)$$

where I used that

$$\langle \mathcal{H}_0 A \rangle = \sum_{n,m=0}^{\lfloor N/2 \rfloor} n U P_n P_m A P_m = \sum_{m=0}^{\lfloor N/2 \rfloor} m U P_m A P_m = \langle A \mathcal{H}_0 \rangle, \quad (3.35)$$

for all A . Inserting equation (3.31) into equation (3.27), we also see that

$$S = \langle S \rangle + h(SW_S - WS). \quad (3.36)$$

Equations (3.34) and (3.36) are valid for any similarity transformation such that equation (3.23) holds, and does not uniquely specify S . To proceed we must provide additional restrictions on S . First, we want $\lim_{t^{ij}/U \rightarrow \infty} S = 1$. That is, in the absence of the perturbation, $\tilde{P}_n = P_n$. Another requirement I make is that $\langle S \rangle = 1$. This simplifies the equations and means that if a state $|\psi\rangle$ is entirely in \mathcal{V}_n , meaning that $P_i|\psi\rangle = \delta_{in}|\psi\rangle$, then the projection of $S|\psi\rangle$ onto \mathcal{V}_n is equal to $|\psi\rangle$. Inserting this into equations (3.34) and (3.36), I get that

$$S = 1 + h(SW_S - WS), \quad (3.37a)$$

$$W_S = \langle WS \rangle. \quad (3.37b)$$

One can use equation (3.37) to write S as a perturbation expansion in W , and then one can use that to obtain W_S , which gives \mathcal{H}_S and in turn \mathcal{H}_{eff} through equation (3.24).

$$\mathcal{H}_{\text{eff}} = SP_0S^{-1}\mathcal{H}SP_0S^{-1} = SP_0\mathcal{H}_SP_0S^{-1}. \quad (3.38)$$

To zeroth order in W , $S = 1$, so to first order in W , $W_S = \langle W \rangle$. However,

$$\langle W \rangle = - \sum_{i \neq j} \sum_{\sigma \in \{\uparrow, \downarrow\}} t^{ij} \langle c_{i\sigma}^\dagger c_{j\sigma} \rangle = 0. \quad (3.39)$$

Inserting this into equation (3.37a), $S = 1 + h(-W)$, so $W_S = \langle Wh(-W) \rangle$. We are interested in

$$\mathcal{H}_{\text{eff}} = SP_0\mathcal{H}_SP_0S^{-1} = SP_0(\mathcal{H}_0 + W_S)P_0S^{-1}. \quad (3.40)$$

Since $P_n\mathcal{H}_0P_n = nUP_n$, the first term is zero. To second order in W , the second term is

$$\begin{aligned} SP_0W_S P_0S^{-1} &= -P_0Wh(W)P_0 \\ &= -P_0 \sum_{i \neq j} \sum_{a \neq b} \sum_{c \neq d} \sum_{\sigma_1 \in \{\uparrow, \downarrow\}} \sum_{\sigma_2 \in \{\uparrow, \downarrow\}} t^{ab} t^{cd} c_{a\sigma_1}^\dagger c_{b\sigma_1} \frac{P_i c_{c\sigma_2}^\dagger c_{d\sigma_2} P_j}{(i-j)U} P_0 \\ &= -P_0 \sum_{i \neq 0} \sum_{a \neq b} \sum_{c \neq d} \sum_{\sigma_1 \in \{\uparrow, \downarrow\}} \sum_{\sigma_2 \in \{\uparrow, \downarrow\}} t^{ab} t^{cd} c_{a\sigma_1}^\dagger c_{b\sigma_1} \frac{P_i c_{c\sigma_2}^\dagger c_{d\sigma_2} P_0}{iU} \end{aligned} \quad (3.41)$$

The only nonzero terms have $i = 1$, since $c_{c\sigma_2}^\dagger c_{d\sigma_2}$ creates a state in \mathcal{V}'_1 when acting on a state in \mathcal{V}'_0 . For this reason, I can also remove P_i . Hence,

$$P_0 W_S P_0 = -\frac{1}{U} \sum_{a \neq b} \sum_{c \neq d} \sum_{\sigma_1 \in \{\uparrow, \downarrow\}} \sum_{\sigma_2 \in \{\uparrow, \downarrow\}} t^{ab} t^{cd} P_0 c_{a\sigma_1}^\dagger c_{b\sigma_1} c_{c\sigma_2}^\dagger c_{d\sigma_2} P_0. \quad (3.42)$$

Because of the projection operators, only terms with $a = d$ and $b = c$ contribute. Since $t^{ab} = (t^{ba})^*$ if one assumes that \mathcal{H} is Hermitian, this means that, by also applying the fermionic commutation relations,

$$\begin{aligned} P_0 W_S P_0 &= -\frac{1}{U} \sum_{a \neq b} \sum_{\sigma_1 \in \{\uparrow, \downarrow\}} \sum_{\sigma_2 \in \{\uparrow, \downarrow\}} |t^{ab}|^2 P_0 c_{a\sigma_1}^\dagger c_{b\sigma_1} c_{b\sigma_2}^\dagger c_{a\sigma_2} P_0 \\ &= \sum_{i \neq j} \sum_{\sigma_1 \in \{\uparrow, \downarrow\}} \sum_{\sigma_2 \in \{\uparrow, \downarrow\}} \frac{|t^{ij}|^2}{U} P_0 c_{i\sigma_1}^\dagger c_{i\sigma_2} (c_{j\sigma_2}^\dagger c_{j\sigma_1} - \delta_{\sigma_1 \sigma_2}) P_0. \end{aligned} \quad (3.43)$$

The second term in equation (3.43) is just a constant because the sum of electrons is constant and equal to one on all lattice sites. One can therefore remove this term through a constant shift in the chemical potential. The first term can be written in terms of the spin operator. The spin operator for lattice site i is defined as

$$S_i = \begin{pmatrix} c_{i\uparrow}^\dagger & c_{i\downarrow}^\dagger \end{pmatrix} \frac{\boldsymbol{\sigma}}{2} \begin{pmatrix} c_{i\uparrow} \\ c_{i\downarrow} \end{pmatrix} = \frac{1}{2} \begin{pmatrix} S_i^+ + S_i^- \\ -iS_i^+ + iS_i^- \\ n_{i\uparrow} - n_{i\downarrow} \end{pmatrix}, \quad (3.44)$$

where $S_i^+ = c_{i\uparrow}^\dagger c_{i\downarrow}$, $S_i^- = c_{i\downarrow}^\dagger c_{i\uparrow}$ and $n_{i\sigma} = c_{i\sigma}^\dagger c_{i\sigma}$. Taking the dot product of two spin operators, I get

$$\begin{aligned} 2S_i \cdot S_j &= S_i^+ S_j^- + S_i^- S_j^+ + \frac{1}{2} (n_{i\uparrow} n_{j\uparrow} + n_{i\downarrow} n_{j\downarrow} - n_{i\uparrow} n_{j\downarrow} - n_{i\downarrow} n_{j\uparrow}) \\ &= S_i^+ S_j^- + S_i^- S_j^+ + n_{i\uparrow} n_{j\uparrow} + n_{i\downarrow} n_{j\downarrow} - \frac{1}{2} (n_{i\uparrow} + n_{i\downarrow}) (n_{j\uparrow} + n_{j\downarrow}) \\ &= \sum_{\sigma_1 \in \{\uparrow, \downarrow\}} \sum_{\sigma_2 \in \{\uparrow, \downarrow\}} c_{i\sigma_1}^\dagger c_{i\sigma_2} c_{j\sigma_2}^\dagger c_{j\sigma_1} - \frac{1}{2} (n_{i\uparrow} + n_{i\downarrow}) (n_{j\uparrow} + n_{j\downarrow}). \end{aligned} \quad (3.45)$$

When projecting onto \mathcal{V}'_0 , where all lattice sites are occupied exactly once, one can use that $n_{j\uparrow} + n_{j\downarrow} = 1$. Hence, the last term in equation (3.45) is just a constant when projected onto \mathcal{V}'_0 . Applying this to

the last two terms in equation (3.45), I get that

$$2P_0 \mathbf{S}_i \cdot \mathbf{S}_j P_0 = P_0 \sum_{\sigma_1 \in \{\uparrow, \downarrow\}} \sum_{\sigma_2 \in \{\uparrow, \downarrow\}} c_{i\sigma_1}^\dagger c_{i\sigma_2} c_{j\sigma_2}^\dagger c_{j\sigma_1} P_0 \quad (3.46)$$

which is exactly the expression in equation (3.43). Hence, to second order in the perturbation,

$$\mathcal{H}_{\text{eff}} = P_0 \sum_{i \neq j} \frac{2|t^{ij}|^2}{U} \mathbf{S}_i \cdot \mathbf{S}_j P_0. \quad (3.47)$$

In other words, the effective Hamiltonian for the half-filled Hubbard model with strong on-site repulsion U is effectively the same as the Heisenberg model with $J_{ij} = |t^{ij}|^2/U$, acting on the space of states with one electron on each lattice site. The coupling J_{ij} is strictly positive. Minimizing the energy associated with different lattice sites is therefore done by aligning the spins such that $\mathbf{S}_i \cdot \mathbf{S}_j$ is negative, meaning that the model is the antiferromagnetic Heisenberg model.

The single orbital Hubbard model was derived from a simple picture of electrons only interacting through an electrostatic potential and only one orbital per spin on each lattice site. Real materials are often much more complicated. Even if we exclude the effect of spin-orbit coupling and the Zeeman effect, real materials often consist of multiple different types of atoms with different numbers of orbitals.

For a more realistic multi-orbital version of the Hubbard model, consider a system with N ions, possibly different types. I label the ions with integers and let ion i have $2n_i$ different Wannier states, not counting those which are always either approximately occupied or approximately unoccupied. I assume that the Wannier states are spin-degenerate so that there are two Wannier states with opposite spins and equal spatial profiles. I label the creation operators with ion number $i \in 1, \dots, N$, Wannier state $m \in \{1, n_i\}$ and spin $\sigma \in \{\uparrow, \downarrow\}$. I also assume that there are only electrostatic forces, meaning no Zeeman effect and no spin-orbit coupling. In this case, I derived in section 3.1 that the Hamiltonian is

$$\mathcal{H} = \mathcal{H}_T + \mathcal{H}_U \quad (3.48)$$

where

$$\mathcal{H}_T = - \sum_{i,j=1}^N \sum_{m_1=1}^{n_i} \sum_{m_2=1}^{n_j} \sum_{\sigma \in \{\uparrow, \downarrow\}} t_{m_1 m_2}^{ij} c_{i m_1 \sigma}^\dagger c_{j m_2 \sigma} \quad (3.49)$$

and

$$\mathcal{H}_U = \sum_{i,j,k,l=1}^N \sum_{m_1=1}^{n_i} \sum_{m_2=1}^{n_j} \sum_{m_3=1}^{n_k} \sum_{m_4=1}^{n_l} \times \sum_{\sigma_1, \sigma_2 \in \{\uparrow, \downarrow\}} U_{m_1 m_2 m_3 m_4}^{ijkl} c_{im_1 \sigma_1}^\dagger c_{jm_2 \sigma_2}^\dagger c_{km_3 \sigma_2} c_{lm_4 \sigma_1}. \quad (3.50)$$

Here,

$$t_{m_1 m_2}^{ij} = \int_{\mathbb{R}^3} d^3 x \phi_{im_1}^*(\mathbf{x}) \left[\frac{\nabla^2}{2m} - qV_{\text{env}}(\mathbf{x}) \right] \phi_{jm_2}(\mathbf{x}), \quad (3.51)$$

and

$$U_{m_1 m_2 m_3 m_4}^{ijkl} = \int_{\mathbb{R}^3} d^3 x \int_{\mathbb{R}^3} d^3 y \frac{q^2 \phi_{im_1}^*(\mathbf{x}) \phi_{jm_2}^*(\mathbf{y}) \phi_{km_3}(\mathbf{y}) \phi_{lm_4}(\mathbf{x})}{4\pi |\mathbf{x} - \mathbf{y}|}, \quad (3.52)$$

where V_{env} includes the contribution from the always occupied states in the lowest orbitals and ϕ_{im_1} is the Wannier function for Wannier state m_1 at ion i .

Next, I assume again that equation (3.52) is small unless $i = j = k = l$. This amounts to assuming that the Wannier states have small amplitudes at neighboring ions. The factor $1/|\mathbf{x} - \mathbf{y}|$ will favor the contribution where $\mathbf{x} \approx \mathbf{y}$, and the terms in equation (3.50) in which all four Wannier states have large amplitudes at approximately the same position are the terms in which all four Wannier states are located around the same ion. Restricting \mathcal{H}_U to terms with $i = j = k = l$ often also means that we can assume that the Wannier functions enter in pairs. This is because Wannier states are orthogonal. For instance, the Wannier states are often assumed to resemble orbitals, which can be written in terms of spherical harmonics of different degrees. For instance, the relevant Wannier states might resemble s -orbitals and d -orbitals. The spatial symmetry of the d -orbitals means that only even powers can give a non-zero result when integrating over space.

I define

$$U_{m_1 m_2}^i = \int_{\mathbb{R}^3} d^3 x \int_{\mathbb{R}^3} d^3 y \frac{q^2 |\phi_{im_1}(\mathbf{x})|^2 |\phi_{im_2}(\mathbf{y})|^2}{4\pi |\mathbf{x} - \mathbf{y}|}, \quad (3.53a)$$

$$J_{m_1 m_2}^i = \int_{\mathbb{R}^3} d^3 x \int_{\mathbb{R}^3} d^3 y \frac{q^2 \phi_{im_1}^*(\mathbf{x}) \phi_{im_2}^*(\mathbf{y}) \phi_{im_1}(\mathbf{y}) \phi_{im_2}(\mathbf{x})}{4\pi |\mathbf{x} - \mathbf{y}|}, \quad (3.53b)$$

such that

$$\begin{aligned} \mathcal{H}_U = & \sum_{i=1}^N \sum_{m_1=1}^{n_i} \sum_{m_2=1}^{n_i} \sum_{\sigma_1, \sigma_2 \in \{\uparrow, \downarrow\}} U_{m_1 m_2}^i c_{i m_1 \sigma_1}^\dagger c_{i m_2 \sigma_2}^\dagger c_{i m_2 \sigma_2} c_{i m_1 \sigma_1} \\ & + \sum_{i=1}^N \sum_{m_1=1}^{n_i} \sum_{m_2=1}^{n_i} \sum_{\sigma_1, \sigma_2 \in \{\uparrow, \downarrow\}} J_{m_1 m_2}^i c_{i m_1 \sigma_1}^\dagger c_{i m_2 \sigma_2}^\dagger c_{i m_1 \sigma_2} c_{i m_2 \sigma_1}. \end{aligned} \quad (3.54)$$

Using the anticommutation relation for fermionic operators,

$$\begin{aligned} \mathcal{H}_U = & \sum_{i=1}^N \sum_{m_1=1}^{n_i} \sum_{\sigma \in \{\uparrow, \downarrow\}} (J_{m_1 m_1}^i - U_{m_1 m_1}^i) n_{i m_1 \sigma} \\ & + \sum_{i=1}^N \sum_{m_1=1}^{n_i} \sum_{m_2=1}^{n_i} \sum_{\sigma_1, \sigma_2 \in \{\uparrow, \downarrow\}} U_{m_1 m_2}^{ij} n_{i m_1 \sigma_1} n_{i m_2 \sigma_2} \\ & - \sum_{i=1}^N \sum_{m_1=1}^{n_i} \sum_{m_2=1}^{n_i} \sum_{\sigma_1, \sigma_2 \in \{\uparrow, \downarrow\}} J_{m_1 m_2}^i c_{i m_1 \sigma_1}^\dagger c_{i m_1 \sigma_2}^\dagger c_{i m_2 \sigma_2} c_{i m_2 \sigma_1}, \end{aligned} \quad (3.55)$$

where $n_{i m_1 \sigma_1} = c_{i m_1 \sigma_1}^\dagger c_{i m_1 \sigma_1}$. I use equation (3.45) to rewrite equation (3.55) as

$$\begin{aligned} \mathcal{H}_U = & \sum_{i=1}^N \sum_{m_1=1}^{n_i} \sum_{\sigma \in \{\uparrow, \downarrow\}} (J_{m_1 m_1}^i - U_{m_1 m_1}^i) n_{i m_1 \sigma} \\ & - \sum_{i=1}^N \sum_{m_1=1}^{n_i} \sum_{m_2=1}^{n_i} \sum_{\sigma_1, \sigma_2 \in \{\uparrow, \downarrow\}} 2 J_{m_1 m_2}^i \mathbf{S}_{i m_1} \cdot \mathbf{S}_{i m_2} \\ & + \sum_{i=1}^N \sum_{m_1=1}^{n_i} \sum_{m_2=1}^{n_i} \sum_{\sigma_1, \sigma_2 \in \{\uparrow, \downarrow\}} \left(U_{m_1 m_2}^i - \frac{1}{2} J_{m_1 m_2}^i \right) n_{i m_1 \sigma_1} n_{i m_2 \sigma_2}. \end{aligned} \quad (3.56)$$

where $\mathbf{S}_{i m_1}$ is the spin operator for the Wannier state m_1 at ion i .

Next, let

$$T_{m_1 m_2}^{ij} = t_{m_1 m_2}^{ij} + \delta_{m_1 m_2} \delta_{ij} (J_{m_1 m_1}^i - U_{m_1 m_1}^i), \quad (3.57)$$

such that one can absorb the first term in equation (3.56) into the hopping term. Hence the complete Hamiltonian in this lattice system

is

$$\begin{aligned}
\mathcal{H} = & - \sum_{i,j=1}^N \sum_{m_1=1}^{n_i} \sum_{m_2=1}^{n_j} \sum_{\sigma \in \{\uparrow, \downarrow\}} T_{m_1 m_2}^{ij} c_{im_1 \sigma}^\dagger c_{jm_2 \sigma} \\
& - \sum_{i=1}^N \sum_{m_1=1}^{n_i} \sum_{m_2=1}^{n_i} \sum_{\sigma_1, \sigma_2 \in \{\uparrow, \downarrow\}} 2J_{m_1 m_2}^i \mathbf{S}_{im_1} \cdot \mathbf{S}_{im_2} \\
& + \sum_{i=1}^N \sum_{m_1=1}^{n_i} \sum_{m_2=1}^{n_i} \sum_{\sigma_1, \sigma_2 \in \{\uparrow, \downarrow\}} \left(U_{m_1 m_2}^i - \frac{1}{2} J_{m_1 m_2}^i \right) n_{im_1 \sigma_1} n_{im_2 \sigma_2}. \quad (3.58)
\end{aligned}$$

The second term is a Heisenberg-like coupling between the spins of different Wannier states at the same lattice site. It is called an exchange coupling because it is a result of the exchange rules of identical particles [25, 150]. That is, despite our description containing no explicit spin-coupling, the fact that the state vector must be antisymmetric under the exchange of identical fermions gives rise to an effective spin interaction. In short, the total state vector must be antisymmetric under the exchange of both spatial and spin coordinates. If it is symmetric in the exchange of spins, for instance if the two spins are equal, then it must be antisymmetric in the exchange of spatial coordinates. An odd function must be zero at the origin. In the same way, a state vector that is odd in the exchange of spatial coordinates \mathbf{r}_1 and \mathbf{r}_2 must be zero when $\mathbf{r}_1 = \mathbf{r}_2$. On the other hand, if the state vector is antisymmetric under spin exchange, which can only happen when the spins are opposite in a so-called spin-singlet state, the state vector can be nonzero also for $\mathbf{r}_1 = \mathbf{r}_2$. In other words, when two electrons have the same spin direction, their spatial overlap is different by virtue of the fermionic symmetry properties, leading to different Coulomb interactions. The difference in energy for the different exchange symmetries is equal to $J_{m_1 m_2}^i$, as calculated above. If $J_{m_1 m_2}^i > 0$, the term $-2J_{m_1 m_2}^i \mathbf{S}_{im_1} \cdot \mathbf{S}_{im_2}$ favors ferromagnetic alignment between the spin at orbital m_1 and m_2 .

For an example of a magnetic system that is also metallic, consider a system where there are $n_{\text{loc}} + 1$ Wannier states at each of the N identical ions in the system. Of these, the first n_{loc} are localized tightly around the ions, such that tunneling terms involving these states are small. The last Wannier state extends more broadly in space and therefore has larger tunneling terms associated with them. Consider the n_{loc}

localized states. The on-site Coulomb repulsion, given by the term proportional to $U_{m_1 m_2}^i - J_{m_1 m_2}^i/2$, will be strongest for $m_1 = m_2$ since these have the largest spatial overlap. As a result, each of the localized states will preferably be half-filled with one particle. This is the same as for the single-orbital Hubbard model above. If we assume that all the n_{loc} localized states are half-filled, we can also ignore the last term in equation (3.58). If m_1 is one of the localized states, then summing over spins returns a constant multiplied by the number of states in m_2 . This can just be absorbed into $T_{m_2 m_2}^{ii}$. Similarly if m_2 is one of the localized states. The spins of the n_{loc} localized states will interact ferromagnetically through the exchange interaction, provided that $J_{m_1 m_2}^i > 0$, so we can assume that all the spins in the localized states point in the same direction at each lattice site. Finally, the spins at different lattice sites will interact through the weak tunneling. In the above example of the single-orbital Hubbard model, we saw that weak tunneling gave rise to an effective antiferromagnetic Heisenberg coupling of the spins. Let

$$\mathbf{S}_i = \sum_{n=1}^{n_{\text{loc}}} \mathbf{S}_{in} \quad (3.59)$$

be the total spin associated with the n_{loc} localized states, let $c_{i\sigma} = c_{i(n_{\text{loc}}+1)\sigma}$ be the annihilation operator associated with the delocalized state at site i with spin σ and

$$\mathbf{s}_i = \mathbf{S}_{i(n_{\text{loc}}+1)} \quad (3.60)$$

be the spin operator associated with the delocalized state. One can write the effective Hamiltonian as

$$\mathcal{H}_{\text{eff}} = - \sum_{i,j=1}^N T^{ij} c_{i\sigma}^\dagger c_{j\sigma} + \sum_{i,j=1}^N J_{\text{eff}}^{ij} \mathbf{S}_i \cdot \mathbf{S}_j - \sum_{i=1}^N 2J_{\text{int}}^i \mathbf{S}_i \cdot \mathbf{s}_i, \quad (3.61)$$

for some effective coupling between localized spins given by J_{eff}^{ij} . Equation (3.61) is often referred to as an s - d model [154–157], because the localized Wannier states are often the d -orbitals while the delocalized itinerant electron states are often the s -orbitals.

Exchange coupling is a short-range effect. Here, I only included exchange coupling between states at the same atom. More broadly,

important magnetic effects can come from exchange coupling between nearest neighbors, called direct exchange [158, 159], or longer-ranged exchange effects, such as superexchange [53, 160] and double exchange [161, 162], which occur through intermediary atoms. If one includes spin-orbit coupling, one can also get an effective antisymmetric exchange effect, called the Dzyaloshinskii–Moriya interaction [163–165]. Spins will also interact through magnetic effects, of course. From equation (2.142) we know that the curl of the spin density gives rise to an electric current density, and thereby a magnetic field. The magnetic field, in turn, couples to the spin. The complete picture of magnetic effects is therefore complicated, and which effects are more important will depend on the atomic structure of the material. Some materials will be ferromagnetically ordered, and others will be antiferromagnetic or ferrimagnetic ordered, or have no magnetic order at all. Moreover, some materials display simple parallel magnetic alignment, while others exhibit more complicated topological structures, such as skyrmions [165, 166] arising from antisymmetric exchange interactions.

In the work presented in this thesis, it has often been important with an effective quadratic model for the itinerant electrons because it is assumed in the quasiclassical theory (see chapter 6). To obtain such a model, one can approximate the spin operator for the localized spins by their expectation value, such that

$$\mathcal{H}_{\text{eff}} = - \sum_{i,j=1}^N T^{ij} c_{i\sigma}^\dagger c_{j\sigma} - \sum_{i=1}^N \mathbf{h}_i \cdot \mathbf{s}_i, \quad (3.62)$$

where $\mathbf{h}_i = 2J_{\text{int}}\langle \mathbf{S}_i \rangle$. Note that $\langle \mathbf{S}_i \rangle$ can still depend on time, and the temporal evolution can depend on the itinerant electrons. Equation (3.62) is reasonable if the relevant states in the ensemble have localized spins not too different from the expectation values. In other words, the energy of the system should increase rapidly as the spin deviates from the expectation value, such that for energies up to the thermal energy all states have localized spins that deviate negligibly from the expectation values.

3.3 Superconductivity

So far we have treated the contribution to the photon field from the ions as constant. However, the lattice is dynamic in real materials, and

this can have important consequences. One consequence, which will be further discussed in section 5.2.1, is that it leads to the dissipation of energy. Another consequence, which is the focus of this section, is that it can lead to superconductivity. Each ion is a complicated combination of multiple protons, neutrons, and low-energy, localized, electrons. On an even more fundamental level, each proton and neutron consist of multiple quark and gluon fields. For our purposes, it suffices with a more primitive effective description of ions as independent, spinless particles. Each ion has a kinetic energy, which I take to be non-relativistic. Additionally, since they are charged, they have electric potential energy.

The quantum mechanical Lagrangian for N spinless particles with position operators $\{\mathbf{R}_i\}$, conjugate momentum operators $\{\mathbf{P}_i\}$, masses $\{M_i\}$ and charges $\{Q_i\}$ in a vector potential \mathbf{A} and an electric scalar potential V is given by

$$L_{\text{ions}} = \sum_{i=1}^N \left\{ \frac{1}{2} \mathbf{P}_i \cdot \frac{\partial \mathbf{R}_i}{\partial t} + \frac{1}{2} \frac{\partial \mathbf{R}_i}{\partial t} \cdot \mathbf{P}_i - \frac{[\mathbf{P}_i - Q_i \mathbf{A}(\mathbf{R}_i)]^2}{2M_i} - Q_i V(\mathbf{R}_i) \right\} \quad (3.63)$$

since

$$\mathcal{H}_{\text{ion}} = \sum_{i=1}^N \left\{ \frac{[\mathbf{P}_i - Q_i \mathbf{A}(\mathbf{R}_i)]^2}{2M_i} + Q_i V(\mathbf{R}_i) \right\} \quad (3.64)$$

is the Hamiltonian. The conjugate momentum operators are $\mathbf{P}_i = M_i \partial \mathbf{R}_i / \partial t + Q_i \mathbf{A}(\mathbf{R}_i)$. This implies a commutation relation for \mathbf{R}_i and \mathbf{P}_i . Let R_i^α denote component $\alpha \in \{x, y, z\}$ of \mathbf{R}_i , and similarly for \mathbf{P}_i and \mathbf{A} . We know from the Heisenberg equation that

$$\frac{\partial R_i^\alpha}{\partial t} = i[\mathcal{H}_{\text{ion}}, R_i^\alpha]. \quad (3.65)$$

If we assume that R_i^α commutes with R_j^β and P_j^β , as long as $i \neq j$, I get that

$$\begin{aligned}
M_i \frac{\partial R_i^\alpha}{\partial t} &= \frac{i}{2} \sum_{\beta \in \{x,y,z\}} \left[P_i^\beta P_i^\beta R_i^\alpha - P_i^\beta Q_i A^\beta(\mathbf{R}_i) R_i^\alpha - Q_i A^\beta(\mathbf{R}_i) P_i^\beta R_i^\alpha \right. \\
&\quad \left. - R_i^\alpha P_i^\beta P_i^\beta + R_i^\alpha P_i^\beta Q_i A^\beta(\mathbf{R}_i) + R_i^\alpha Q_i A^\beta(\mathbf{R}_i) P_i^\beta \right] \\
&= -\frac{i}{2} \sum_{\beta \in \{x,y,z\}} \left\{ \left[R_i^\alpha, P_i^\beta \right]_- \left[P_i^\beta - Q_i A^\beta(\mathbf{R}_i) \right] \right. \\
&\quad \left. + \left[P_i^\beta - Q_i A^\beta(\mathbf{R}_i) \right] \left[R_i^\alpha, P_i^\beta \right]_- \right\} = P_i^\alpha - Q_i A^\alpha(\mathbf{R}_i). \quad (3.66)
\end{aligned}$$

This is true if the position operator \mathbf{R}_i and the momentum operator \mathbf{P}_i must satisfy the commutation relation

$$\left[R_i^\alpha, P_i^\beta \right]_- = i \delta_{\alpha\beta}. \quad (3.67)$$

Including the electron field, the photon field, and the ions, the full action is

$$S = \int_{-\infty}^{\infty} dt \left(L_{\text{ions}} + \int_{\mathbb{R}^3} d^3r [\mathcal{L}_e + \mathcal{L}_{\text{em}}] \right), \quad (3.68)$$

where \mathcal{L}_e and \mathcal{L}_{em} are the Lagrangian densities for the electron field and the photon fields, respectively. Minimizing with respect to V and \mathbf{A} , I get

$$V(t, \mathbf{x}) = \frac{1}{4\pi} \int_{\mathbb{R}^3} d^3y \frac{\rho(t_{\text{ret}}, \mathbf{y})}{|\mathbf{x} - \mathbf{y}|} + V_{\text{ext}}(t, \mathbf{x}), \quad (3.69a)$$

$$\mathbf{A}(t, \mathbf{x}) = \frac{1}{4\pi} \int_{\mathbb{R}^3} d^3y \frac{\mathbf{j}(t_{\text{ret}}, \mathbf{y})}{|\mathbf{x} - \mathbf{y}|} + \mathbf{A}_{\text{ext}}(t, \mathbf{x}), \quad (3.69b)$$

as shown in section 2.7. Here,

$$\rho(t, \mathbf{r}) = \rho_e(t, \mathbf{r}) + \sum_{i=1}^N Q_i \delta(\mathbf{r} - \mathbf{R}_i[t]) \quad (3.70a)$$

$$\mathbf{j}(t, \mathbf{r}) = \mathbf{j}_e(t, \mathbf{r}) + \sum_{i=1}^N Q_i \frac{\partial \mathbf{R}_i}{\partial t} \delta(\mathbf{r} - \mathbf{R}_i[t]), \quad (3.70b)$$

where ρ_e and \mathbf{j}_e are the charge and current densities for the electron field, which are given by equations (2.141) and (2.142). Assuming that charges move slowly compared to the speed of light, I set $t_{\text{ret}} = t$.

We started with a theory involving the electron field, the photon field, and ions. By inserting equation (3.69) into the action, we remove the coupling to the photon field in favor of new couplings. The initial theory involves coupling between the photon field and both the electron field and the ions, but not between electrons and ions. In the new theory, we get electron-electron coupling through quartic terms, we get ion-ion coupling and we get electron-ion coupling. We can do this trick one more time and get a theory involving only the electron field. To do so, we must minimize the action with respect to ion position operators R_i . We do not need to include the dependence of the action on R_i through the photon field. This is because a version of the chain rule also works with functional derivative, as explained in section 2.7.

Minimizing the action with respect to R_i , I get

$$\frac{\partial}{\partial t} [P_i - Q_i A(R_i)] = Q_i \left\{ E(R_i) + \frac{1}{2} \left[\frac{\partial R_i}{\partial t} \times B(R_i) - B(R_i) \times \frac{\partial R_i}{\partial t} \right] \right\}, \quad (3.71)$$

which, unsurprisingly, is similar to Newton's second law for a charged particle in an electromagnetic field. This equation can also be obtained by using the Heisenberg equation. Assuming no external field, one can separate E into one contribution that comes from the ions, E_{ion} and one that comes from the electron field, E_e , and similarly for $B = B_{\text{ion}} + B_e$. In the presence of an external field, one can include this into E_e and B_e .

In general, an ion will be in a superposition of different eigenstates of the velocity operator, $\partial R_i / \partial t$. To determine E_{ion} , consider a state in which the i 'th ion is in rest, meaning that $\partial R_i / \partial t = 0$. In this case, the electric field generated from this ion is

$$E_{i,0}(\mathbf{r}) = \frac{(\mathbf{r} - \mathbf{R}_i) Q_i}{4\pi |\mathbf{r} - \mathbf{R}_i|^3}, \quad (3.72)$$

and the magnetic field is $B_{i,0} = \mathbf{0}$, as can be derived from equations (3.69) and (3.70) together with $E = -\nabla V - \partial A / \partial t$ and $B = \nabla \times A$. From this, one can derive the electric and magnetic field from the i 'th ion in any eigenstate of $\partial R_i / \partial t$. Since $\partial R_i / \partial t = \mathbf{v}_i$ is equivalent to a multiplication of a constant in this state, we may perform a Lorentz transformation to the rest frame in which we know that the electric field is $E_{i,0}$ and the magnetic field is $B_{i,0} = \mathbf{0}$. This implies that the

electromagnetic field in the “lab frame”, where the velocity of the i 'th ion is \mathbf{v}_i , is

$$\mathbf{E}_i = \gamma \mathbf{E}_{i,0} - (\gamma - 1) \frac{(\mathbf{E}_{i,0} \cdot \mathbf{v}_i) \mathbf{v}_i}{\mathbf{v}_i \cdot \mathbf{v}_i} \quad (3.73a)$$

$$\mathbf{B}_i = \gamma \frac{\mathbf{v}_i \times \mathbf{E}_{i,0}}{c^2}, \quad (3.73b)$$

where $\gamma = \sqrt{1 - \mathbf{v}_i \cdot \mathbf{v}_i / c^2}$. I reintroduced the speed of light c . We see that when we are considering superpositions of states with $|\mathbf{v}_i| \ll c$ we can neglect the contribution from the magnetic field, since

$$|\mathbf{v}_i \times \mathbf{B}| < \frac{|\mathbf{v}_i \times (\mathbf{v}_i \times \mathbf{E}_{i,0})|}{c^2} \ll |\mathbf{E}_{i,0}|. \quad (3.74)$$

We can also approximate $\mathbf{E}_i \approx \mathbf{E}_{i,0}$, since $\gamma = 1 + \mathcal{O}(\mathbf{v}_i \cdot \mathbf{v}_i / c^2)$, such that

$$\mathbf{E}_{\text{ion}} = \sum_{i=1}^N \mathbf{E}_{i,0} \quad (3.75)$$

and $\mathbf{B}_{\text{ion}} = \mathbf{0}$. Finally, equation (3.73a) implies that the contribution to the electric field coming from the vector potential, which is zero in the rest frame, is negligible. That is, $|\partial \mathbf{A}_i / \partial t| \ll |\mathbf{E}_i|$. With these simplifications, equation (3.71) becomes

$$\begin{aligned} \frac{\partial P_i}{\partial t} = Q_i \left\{ \mathbf{E}_{\text{ion}}(\mathbf{R}_i) + \left(\mathbf{E}_e + \frac{\partial \mathbf{A}_e}{\partial t} \right) (\mathbf{R}_i) \right. \\ \left. + \frac{1}{2} \left[\frac{\partial \mathbf{R}_i}{\partial t} \times \mathbf{B}_e(\mathbf{R}_i) - \mathbf{B}_e(\mathbf{R}_i) \times \frac{\partial \mathbf{R}_i}{\partial t} \right] \right\}, \quad (3.76) \end{aligned}$$

The next step is to linearize the equations. However, this requires knowing how the electron field depends on the ion positions. Again I categorize the electrons as being either itinerant, if they are free to move from ion to ion, or localized, if they are mainly localized around a single ion. Previously, I argued that the lowest energy Wannier states are most localized, and that given sufficient energy gaps to the unoccupied states, these are always approximately fully occupied. This picture does not hold when taking into account ion movement. The electric field from the ions changes significantly close to the ions when

they move. Therefore, the energies of the states with large amplitudes near the ion cores will also have energies that change significantly. As a result one can no longer say that the smallest Wannier states will forever remain approximately fully occupied. Instead, I assume that the localized electrons, while no longer static, still stay localized in the sense that they move with the ions. That is, I assume that the electrons can be categorized into itinerant electrons and electrons that follow the ions. Further, I assume that electrons that follow the ions do so in perfect synchrony. This assumption is motivated by the fact that electrons are much lighter than ions. Assuming that the ions move sufficiently slowly, the localized electrons will configure themselves in the instantaneous ground state orbitals. This effectively screens the electric field coming from the ions, and I assume the dynamics of the localized electrons can be captured by renormalizing the charges of the ions. As the itinerant electrons are more delocalized in space, they will be less sensitive to small movements in the ion placement. Therefore, I assume that the linear response to the electric field from the itinerant electrons, E_e , can be neglected in equation (3.78).

I define the equilibrium positions $\{\mathbf{R}_i^{\text{eq}}\}$ to be a solution of equation (3.71) with $\partial\mathbf{R}_i/\partial t = 0$ and $\mathbf{E} = \mathbf{E}_{\text{ion}}$. This means that

$$\sum_{j \neq i} \frac{Q_j}{4\pi} \frac{(\mathbf{R}_i^{\text{eq}} - \mathbf{R}_j^{\text{eq}})}{|\mathbf{R}_i^{\text{eq}} - \mathbf{R}_j^{\text{eq}}|^3} = 0 \quad (3.77)$$

for all i , where Q_j is now the renormalized ion charge, taking into account the localized electrons. Let $\mathbf{u}_i = \mathbf{R}_i - \mathbf{R}_i^{\text{eq}}$ be the displacement away from the equilibrium position. I assume that these displacements are small compared to the distance between ions, such that I can linearize \mathbf{E}_{ion} , which now includes the field from the localized electrons, in \mathbf{u}_i . I also keep only zeroth order terms in the coupling to the itinerant electron field, meaning that the coupling to \mathbf{B}_e is assumed negligible. From this, I obtain

$$\frac{\partial P_i^\alpha}{\partial t} = \sum_{j=1}^N \sum_{\beta \in \{x,y,z\}} F_{ij}^{\alpha\beta} (u_i^\beta - u_j^\beta) + Q_i \left(E_e^\alpha + \frac{\partial A_e}{\partial t} \right) (\mathbf{R}_i^{\text{eq}}), \quad (3.78)$$

where $\alpha \in \{x, y, z\}$, $F_{ii} = 0$ and

$$F_{ij}^{\alpha\beta} = \frac{Q_i Q_j}{4\pi} \frac{\partial}{\partial (R_i^\beta - R_j^\beta)} \left[\frac{R_i^\alpha - R_j^\alpha}{|\mathbf{R}_i - \mathbf{R}_j|^3} \right]_{(\mathbf{R}_i, \mathbf{R}_j) = (\mathbf{R}_i^{\text{eq}}, \mathbf{R}_j^{\text{eq}})}, \quad (3.79)$$

when $i \neq j$.

If one assumes that all ions are identical with renormalized charges equal to Q_{ion} and masses equal to M_{ion} , then $F_{ij}^{\alpha\beta}$ depends only on the relative distance $\mathbf{R}_i - \mathbf{R}_j$. In this case, the equation can be linearized in the positional degrees of freedom through a Fourier transformation. I define

$$\mathbf{u}_k = \sum_{i=1}^N \mathbf{u}_i e^{-i\mathbf{k} \cdot \mathbf{R}_i^{\text{eq}}}, \quad (3.80a)$$

$$\mathbf{P}_k = \sum_{i=1}^N \mathbf{P}_i e^{-i\mathbf{k} \cdot \mathbf{R}_i^{\text{eq}}}, \quad (3.80b)$$

$$F_k^{\alpha\beta} = \sum_{i=1}^N F_{ij}^{\alpha\beta} e^{-i\mathbf{k} \cdot (\mathbf{R}_i^{\text{eq}} - \mathbf{R}_j^{\text{eq}})}, \quad (3.80c)$$

$$-(\nabla V_e)_k = \sum_{i=1}^N \left(\mathbf{E}_e + \frac{\partial \mathbf{A}_e}{\partial t} \right) (\mathbf{R}_i^{\text{eq}}) e^{-i\mathbf{k} \cdot \mathbf{R}_i^{\text{eq}}}, \quad (3.80d)$$

where the choice of j is arbitrary in equation (3.80c) and $-(\nabla V_e)_k$ is the contribution to the electric field coming from the scalar potential V_e . Inserting this into equation (3.78), I get that

$$\frac{\partial P_k^\alpha}{\partial t} = - \sum_{\beta \in \{x,y,z\}} (F_k^{\alpha\beta} - F_0^{\alpha\beta}) u_k^\beta - Q_{\text{ion}} (\nabla V_e)_k^\alpha, \quad (3.81)$$

$F_k^{\alpha\beta} = F_k^{\beta\alpha}$, so I can diagonalize $F_k^{\alpha\beta} - F_0^{\alpha\beta} = \sum_\gamma S^{\alpha\gamma} \lambda_k^\gamma (S^T)^\gamma{}^\beta$, and define $\tilde{P}_k^\alpha = \sum_\gamma (S^T)^{\alpha\gamma} P_k^\gamma$, $\tilde{u}_k^\alpha = \sum_\gamma (S^T)^{\alpha\gamma} u_k^\gamma$ and $(\nabla \tilde{V}_e)_k^\alpha = \sum_\gamma (S^T)^{\alpha\gamma} (\nabla V_e)_k^\gamma$, such that

$$\frac{\partial \tilde{P}_k^\alpha}{\partial t} = -\lambda_k^\alpha \tilde{u}_k^\alpha - Q_{\text{ion}} (\nabla \tilde{V}_e)_k^\alpha. \quad (3.82)$$

To decouple $\tilde{\mathbf{u}}_k$ and $\tilde{\mathbf{P}}_k$, one can introduce the phonon operators,

$$a_k^\alpha = \sqrt{\frac{M_{\text{ion}} \omega_k^\alpha}{2}} \left(\tilde{u}_k^\alpha + \frac{i}{M_{\text{ion}} \omega_k^\alpha} \tilde{p}_k^\alpha \right), \quad (3.83a)$$

$$(a_k^\alpha)^\dagger = \sqrt{\frac{M_{\text{ion}} \omega_k^\alpha}{2}} \left(\tilde{u}_{-k}^\alpha - \frac{i}{M_{\text{ion}} \omega_k^\alpha} \tilde{p}_{-k}^\alpha \right), \quad (3.83b)$$

where $\omega_k^\alpha = \sqrt{M_{\text{ion}}/\lambda_k^\alpha}$. From the commutation relation, equation (3.67), it follows that a_k^α and $(a_k^\alpha)^\dagger$ satisfy the bosonic commutation relations,

$$[a_k^\alpha, (a_q^\beta)^\dagger]_- = N\delta_{kq}\delta_{\alpha\beta}, \quad [a_k^\alpha, a_q^\beta]_- = [(a_q^\beta)^\dagger, (a_k^\alpha)^\dagger]_- = 0. \quad (3.84)$$

Combining equation (3.82) with $M_{\text{ion}}\partial\tilde{u}_k^\alpha/\partial t = \tilde{P}_k^\alpha - Q_{\text{ion}}\tilde{A}_{e,k}^\alpha$, where $\tilde{A}_{e,k}$ is the Fourier transform of the vector potential coming from the itinerant electron field, and inserting equation (3.83), I get

$$\frac{\partial a_k^\alpha}{\partial t} = -i\omega_k^\alpha a_k^\alpha - Q_{\text{ion}}\sqrt{\frac{1}{2M_{\text{ion}}\omega_k^\alpha}} \left(i(\nabla\tilde{V}_e)_k^\alpha + \omega_k^\alpha \tilde{A}_{e,k}^\alpha \right), \quad (3.85a)$$

$$\frac{\partial (a_k^\alpha)^\dagger}{\partial t} = i\omega_k^\alpha (a_k^\alpha)^\dagger + Q_{\text{ion}}\sqrt{\frac{1}{2M_{\text{ion}}\omega_k^\alpha}} \left(i(\nabla\tilde{V}_e)_{-k} - \omega_k^\alpha \tilde{A}_{e,-k}^\alpha \right). \quad (3.85b)$$

These equations are solved by

$$a_k^\alpha(t) = b_k^\alpha e^{-i\omega_k^\alpha(t-t_0)} - \frac{Q_{\text{ion}}}{\sqrt{2M_{\text{ion}}\omega_k^\alpha}} \int_{t_0}^t d\tau e^{-i\omega_k^\alpha(t-\tau)} \left(i(\nabla\tilde{V}_e)_k^\alpha + \omega_k^\alpha \tilde{A}_{e,k}^\alpha \right) (\tau), \quad (3.86a)$$

$$(a_k^\alpha)^\dagger(t) = (b_k^\alpha)^\dagger e^{i\omega_k^\alpha(t-t_0)} + \frac{Q_{\text{ion}}}{\sqrt{2M_{\text{ion}}\omega_k^\alpha}} \int_{t_0}^t d\tau e^{i\omega_k^\alpha(t-\tau)} \left(i(\nabla\tilde{V}_e)_{-k} - \omega_k^\alpha \tilde{A}_{e,-k}^\alpha \right) (\tau), \quad (3.86b)$$

for some constant operators b_k^α and $(b_k^\alpha)^\dagger$. One can rewrite equation (3.86) by using partial integration together with $\omega_k^\alpha e^{\pm i\omega_k^\alpha(t-\tau)} = \pm i\partial[e^{\pm i\omega_k^\alpha(t-\tau)}]/\partial\tau$. Doing this, I get

$$a_k^\alpha(t) = \left[b_k^\alpha - \frac{iQ_{\text{ion}}\tilde{A}_{e,k}^\alpha(t_0)}{\sqrt{2M_{\text{ion}}\omega_k^\alpha}} \right] e^{-i\omega_k^\alpha(t-t_0)} + \frac{iQ_{\text{ion}}}{\sqrt{2M_{\text{ion}}\omega_k^\alpha}} \left[\tilde{A}_{e,k}^\alpha(t) + \int_{t_0}^t d\tau e^{-i\omega_k^\alpha(t-\tau)} \tilde{E}_{e,k}^\alpha(\tau) \right], \quad (3.87a)$$

$$(a_k^\alpha)^\dagger(t) = \left[(b_k^\alpha)^\dagger + \frac{iQ_{\text{ion}}\tilde{A}_{e,-k}^\alpha(t_0)}{\sqrt{2M_{\text{ion}}\omega_k^\alpha}} \right] e^{i\omega_k^\alpha(t-t_0)} - \frac{iQ_{\text{ion}}}{\sqrt{2M_{\text{ion}}\omega_k^\alpha}} \left[\tilde{A}_{e,-k}^\alpha(t) + \int_{t_0}^t d\tau e^{i\omega_k^\alpha(t-\tau)} \tilde{E}_{e,-k}^\alpha(\tau) \right], \quad (3.87b)$$

where $\tilde{E}_{e,-k}^\alpha = -(\nabla\tilde{V}_e)^\alpha - \partial\tilde{A}_{e,k}^\alpha/\partial t$ is the electric field from the electrons, in addition to any external fields.

Using that $\omega_{-k} = \omega_k$ and inserting equation (3.86) into equation (3.83), I get that the position operators become

$$\begin{aligned} \tilde{u}_k^\alpha(t) = & \tilde{u}_k^\alpha(t_0) \cos[\omega_k^\alpha(t-t_0)] + \frac{[\tilde{P}_k^\alpha(t_0) - Q_{\text{ion}}\tilde{A}_{e,k}^\alpha(t_0)]}{M_{\text{ion}}\omega_k^\alpha} \sin[\omega_k^\alpha(t-t_0)] \\ & + \frac{Q_{\text{ion}}}{M_{\text{ion}}\omega_k^\alpha} \int_{t_0}^t d\tau \sin[\omega_k^\alpha(t-\tau)] \tilde{E}_{e,k}^\alpha(\tau). \end{aligned} \quad (3.88)$$

Notice that the expectation value, $\langle \tilde{u}_k^\alpha(t) \rangle$, evolves in time like one would expect from classical charged particles in an electric field $\langle E_e(t) \rangle$. This is because I linearized the equation for $\tilde{u}_k^\alpha(t)$.

Inserting equation (3.88) back into the Lagrangian in terms such as $q\psi_e^\dagger V\psi_e$ removes the coupling between the electron field and the ions in favor of new electron-electron coupling. At first glance, the qualitative features of this result look similar to what was obtained when solving for the photon field operators. However, there is an important difference. To see why, consider the term in the electron Hamiltonian proportional to $q\psi_e^\dagger V\psi_e$. This term is often the strongest interaction with the electromagnetic field. If we do not take into account relativistic corrections, the charge density in the electron field is $q\psi_e^\dagger\psi_e$. Using equations (3.69) and (3.70) the energy is, not taking into account the external field,

$$\begin{aligned} \mathcal{H}_U = & \frac{q^2}{4\pi} \int_{\mathbb{R}^3} d^3x \int_{\mathbb{R}^3} d^3y \frac{\psi_e^\dagger(\mathbf{x})\psi_e^\dagger(\mathbf{y})\psi_e(\mathbf{y})\psi_e(\mathbf{x})}{|\mathbf{x}-\mathbf{y}|} \\ & + \frac{qQ_{\text{ion}}}{4\pi} \sum_{i=1}^N \int_{\mathbb{R}^3} d^3x \frac{\psi_e^\dagger(\mathbf{x})\psi_e(\mathbf{x})}{|\mathbf{x}-\mathbf{R}_i|} \end{aligned} \quad (3.89)$$

The first is a repulsive Coulomb interaction between equal charges, $q^2 = |q|^2$, and the second term is an attractive Coulomb interaction between opposite charges, $qQ_{\text{ion}} = -|qQ_{\text{ion}}|$. The second term can be

rewritten in terms of \mathbf{u}_i ,

$$\begin{aligned} \frac{qQ_{\text{ion}}}{4\pi} \sum_{i=1}^N \int_{\mathbb{R}^3} d^3x \frac{\psi_e^\dagger(\mathbf{x})\psi_e(\mathbf{x})}{|\mathbf{x} - \mathbf{R}_i|} &= \frac{qQ_{\text{ion}}}{4\pi} \sum_{i=1}^N \int_{\mathbb{R}^3} d^3x \frac{\psi_e^\dagger(\mathbf{x})\psi_e(\mathbf{x})}{|\mathbf{x} - \mathbf{R}_i^{\text{eq}}|} \\ &+ \frac{qQ_{\text{ion}}}{4\pi} \sum_{i=1}^N \int_{\mathbb{R}^3} d^3x \frac{\psi_e^\dagger(\mathbf{x} + \mathbf{u}_i)\psi_e(\mathbf{x} + \mathbf{u}_i) - \psi_e^\dagger(\mathbf{x})\psi_e(\mathbf{x})}{|\mathbf{x} - \mathbf{R}_i^{\text{eq}}|}. \end{aligned} \quad (3.90)$$

The latter term gives rise to the phonon-mediated electron-electron interaction, while the first term is the coupling between electrons and the equilibrium distribution of ions, which should be used when defining the lattice model through Wannier states, as discussed in section 3.1.

When inserting the creation and annihilation operators for the Wannier states, both the interaction obtained directly from the electromagnetic field and the phonon-mediated interaction produce terms on the form

$$\mathcal{H}_U = \sum_{i,j,k,l} \sum_{\sigma_1, \sigma_2, \sigma_3, \sigma_4 \in \{\uparrow, \downarrow\}} U_{\sigma_1 \sigma_2 \sigma_3 \sigma_4}^{ijkl} c_{i\sigma_1}^\dagger c_{j\sigma_2}^\dagger c_{k\sigma_3} c_{l\sigma_4}. \quad (3.91)$$

While the electrostatic part of the direct interaction gives rise to repulsive $U_{\sigma_1 \sigma_2 \sigma_3 \sigma_4}^{ijkl}$, since equal charges repel, the phonon-mediated interaction can also produce attractive interactions through negative $U_{\sigma_1 \sigma_2 \sigma_3 \sigma_4}^{ijkl}$. This can give rise to superconductivity [45, 167]. Superconductivity can also arise from other sources of attractive interactions [167]. Another example is that attractive interactions between itinerant electrons can be mediated through localized electrons. As we saw earlier, the itinerant electrons can couple to the localized electrons through exchange interaction, and the localized electrons interact with each other. Just like we have done for the ions, one can isolate the evolution of the localized electron operators to obtain effective interactions between itinerant electrons. The resulting, so-called *magnon-mediated* interaction can also be attractive and give rise to superconductivity [168–171]. The interaction is called magnon-mediated because spin-wave excitations are called magnons, just like lattice vibration excitations are called phonons. In passing, I also note that the strength of the exchange interaction between localized spins also depends on relative distance. Therefore, the motion of the ions will result in magnon-phonon coupling. However, here I only consider phonons.

When only considering the subset of itinerant electrons states, it is reasonable to assume that ψ_e changes slowly on the length scale of \mathbf{u} . As a result, the second term on the right-hand side of equation (3.90) can be approximated as

$$\begin{aligned}\mathcal{H}_{SC} &= \frac{qQ_{\text{ion}}}{4\pi} \sum_{i=1}^N \int_{\mathbb{R}^3} d^3x \frac{\mathbf{u}_i \cdot \nabla[\psi_e^\dagger(\mathbf{x})\psi_e(\mathbf{x})]}{|\mathbf{x} - \mathbf{R}_i^{\text{eq}}|} \\ &= - \sum_{i=1}^N Q_{\text{ion}} \mathbf{u}_i \cdot \frac{q}{4\pi} \nabla_{\mathbf{R}_i^{\text{eq}}} \int_{\mathbb{R}^3} d^3x \frac{\psi_e^\dagger(\mathbf{x})\psi_e(\mathbf{x})}{|\mathbf{x} - \mathbf{R}_i^{\text{eq}}|} \\ &= \sum_{i=1}^N Q_{\text{ion}} \mathbf{u}_i \cdot \mathbf{E}_e(\mathbf{R}_i^{\text{eq}}) = \sum_k \sum_{\alpha \in \{x,y,z\}} Q_{\text{ion}} \tilde{u}_k^\alpha \tilde{E}_{e,-k}^\alpha\end{aligned}\quad (3.92)$$

where I assumed that the main contribution to the electric field comes from the electric potential, so

$$\begin{aligned}\mathbf{E}_e(\mathbf{R}_i^{\text{eq}}) &= -\frac{q\nabla_{\mathbf{R}_i^{\text{eq}}}}{4\pi} \int_{\mathbb{R}^3} d^3x \frac{\psi_e^\dagger(\mathbf{x})\psi_e(\mathbf{x})}{|\mathbf{x} - \mathbf{R}_i^{\text{eq}}|} \\ &= \sum_{j=1}^N \sum_{\sigma \in \{\uparrow, \downarrow\}} \mathbf{b}(\mathbf{R}_i^{\text{eq}} - \mathbf{R}_j^{\text{eq}}) c_{j\sigma}^\dagger c_{j\sigma},\end{aligned}\quad (3.93)$$

for some function \mathbf{b} . For simplicity, I assume that there are only two itinerant states per lattice site, one for each spin. One can also consider more states, which can give so-called multi-orbital superconductors [172–174]. Fourier transforming and changing basis using the S^T matrix from above, I get

$$\tilde{E}_{e,k}^\alpha = \sum_{k'} \frac{\tilde{b}_{k'}^\alpha}{N} \sum_{\sigma \in \{\uparrow, \downarrow\}} c_{k'\sigma}^\dagger c_{(k'+k)\sigma},\quad (3.94)$$

where $\mathbf{b}_k = \sum_{i=1}^N \mathbf{b}(\mathbf{R}_i^{\text{eq}} - \mathbf{R}_j^{\text{eq}}) e^{-i\mathbf{k} \cdot (\mathbf{R}_i^{\text{eq}} - \mathbf{R}_j^{\text{eq}})}$ and $\tilde{b}_k^\alpha = \sum_{\gamma} (S^T)^{\alpha\gamma} b_k^\gamma$.

To evaluate \mathcal{H}_{SC} we must next use equation (3.88). The ion displacement depends non-locally in time on the electron field, which makes it complicated. Consider the temporal evolution of $\tilde{E}_{e,k}^\alpha$. We can get an estimate for this by looking at the full Hamiltonian for the itinerant electrons,

$$\mathcal{H} = \sum_{k,\sigma} (\epsilon_k - \mu) c_{k\sigma}^\dagger c_{k\sigma} + \sum_{k_1, k_2, \sigma_1, \sigma_2} c_{k_1\sigma_1}^\dagger t_{\sigma_1\sigma_2}^{k_1 k_2} c_{k_2\sigma_2} + \mathcal{H}_{SC}\quad (3.95)$$

The time dependence of $c_{k\sigma}(t)$ can be found from the Heisenberg equation, which from the fermionic commutation relations can be written as

$$\frac{\partial c_{k\sigma}}{\partial t} = -i(\varepsilon_k - \mu)c_{k\sigma} - i \sum_{k_1, \sigma_1} t_{\sigma\sigma_1}^{kk_1} c_{k_1\sigma_1} + i[c_{k\sigma}, \mathcal{H}_{SC}]_-. \quad (3.96)$$

If we neglect the last term under the assumption that the electron-phonon interaction is small, and diagonalize $t_{\sigma\sigma_1}^{kk_1} c_{k_1\sigma_1} = \sum_{k_2\sigma_2} P_{\sigma\sigma_2}^{kk_2} \lambda_{\sigma_2}^{k_2} (P^{-1})_{\sigma_2\sigma_1}^{k_2k_1}$, then the solution to equation (3.96) is

$$c_{k\sigma}(t) = e^{-i(\varepsilon_k - \mu)t} \left[c_{k\sigma}(0) + \sum_{k_1 k_2 \sigma_1 \sigma_2} P_{\sigma\sigma_2}^{kk_2} \left(e^{-i\lambda_{\sigma_2}^{k_2} t} - 1 \right) (P^{-1})_{\sigma_2\sigma_1}^{k_2k_1} c_{k_1\sigma_1}(0) \right]. \quad (3.97)$$

If the system varies in space, such as through an inhomogeneous external field, then $t_{\sigma\sigma_1}^{kk_1}$ will have non-zero components with $k \neq k_1$ and thereby couple electrons with different momenta. If the variation is over a characteristic length-scale of L , then the maximal relevant values of $|\mathbf{k} - \mathbf{k}_1|$ is around $1/L$. Hence, if the system varies slowly in space, only momenta close to each other are coupled. If we were to include the last term in equation (3.96), we would also get contributions from $c_{k_1\sigma_1}^\dagger$, as we will see later. This does not affect the arguments below, so the same results also hold if we were to include this term.

Inserting this into the expression for $\tilde{E}_{e,k}^\alpha$ and into equation (3.88), the relevant terms are proportional to

$$\begin{aligned} & \int_{t_0}^t d\tau \sin[\omega_k^\alpha(t - \tau)] e^{i\gamma\tau} c_{k_1\sigma_1}^\dagger(0) c_{k_2\sigma_2}(0) \\ &= \frac{i}{2} \int_{t_0}^t d\tau \left(e^{-i\omega_k^\alpha(t-\tau)} - e^{i\omega_k^\alpha(t-\tau)} \right) e^{i\gamma\tau} c_{k_1\sigma_1}^\dagger(0) c_{k_2\sigma_2}(0). \quad (3.98) \end{aligned}$$

The time t_0 can be chosen freely. In particular, we can let $t_0 \rightarrow -\infty$. In this case, it is clear that equation (3.98) will be very small unless $\gamma \approx \pm\omega_k^\alpha$. Physically this means that the oscillations of the electrons must match the natural frequency of the phonon mode. When they match perfectly, such that $\gamma = \pm\omega_k^\alpha$, it seems from equations (3.88) and (3.98) that the amplitudes of the displacement vectors \mathbf{u}_i will grow

to infinity. This clearly violates the assumption that $|\mathbf{u}_i|$ is small for all i . In practice, there will be some mechanism to stop the amplitudes from growing too large. Nevertheless, it should be reasonable to assume that the sum of terms on the form of equation (3.98) are dominated by the terms with $\gamma \approx \pm\omega_k^\alpha$. This means that

$$\int_{t_0}^t d\tau \sin[\omega_k^\alpha(t-\tau)] e^{i\gamma\tau} c_{k_1\sigma_1}^\dagger(0) c_{k_2\sigma_2}(0) = V(\omega_k^\alpha, \gamma) e^{i\gamma t} c_{k_1\sigma_1}^\dagger(0) c_{k_2\sigma_2}(0), \quad (3.99)$$

where $V(\omega_k^\alpha, \gamma)$ is a function which is peaked around $\omega_k^\alpha = \pm\gamma$.

From equation (3.97), we see that one can write

$$c_{k_1\sigma_1}^\dagger(t) c_{k_2\sigma_2}(t) = \sum_{k_3 k_4 \sigma_3 \sigma_4} e^{i\gamma_{\sigma_3\sigma_4}^{k_3 k_4} t} A_{\sigma_3\sigma_4}^{k_3 k_4} c_{k_3\sigma_3}^\dagger(0) c_{k_4\sigma_4}(0), \quad (3.100)$$

for some $\gamma_{\sigma_3\sigma_4}^{k_3 k_4}$ and $A_{\sigma_3\sigma_4}^{k_3 k_4}$, which also depend on k_1, k_2, σ_1 and σ_2 . If we assume that the variation in $V(\omega_k^\alpha, \gamma_{\sigma_3\sigma_4}^{k_3 k_4})$ is small, such that $V(\omega_k^\alpha, \gamma_{\sigma_3\sigma_4}^{k_3 k_4}) \approx V(\omega_k^\alpha, \varepsilon_{k_1} - \varepsilon_{k_2})$ since only states which are close in energy are coupled in time, we can use equation (3.99) to obtain

$$\int_{t_0}^t d\tau \sin[\omega_k^\alpha(t-\tau)] c_{k_1\sigma_1}^\dagger(\tau) c_{k_2\sigma_2}(\tau) = V(\omega_k^\alpha, \varepsilon_{k_1} - \varepsilon_{k_2}) c_{k_1\sigma_1}^\dagger(t) c_{k_2\sigma_2}(t). \quad (3.101)$$

Inserting equation (3.94) into equation (3.88) finally gives

$$\tilde{u}_k^\alpha = \frac{Q_{\text{ion}}}{M_{\text{ion}} \omega_k^\alpha} \sum_{k'} \frac{\tilde{b}_{k'}^\alpha}{N} V(\omega_k^\alpha, \varepsilon_{k'} - \varepsilon_{k+k'}) \sum_{\sigma \in \{\uparrow, \downarrow\}} c_{k'\sigma}^\dagger c_{(k'+k)\sigma}, \quad (3.102)$$

This means that \mathcal{H}_{SC} can be computed from equation (3.92) as

$$\begin{aligned} \mathcal{H}_{SC} &= \sum_{kk_1 k_2} \sum_{\sigma_1 \sigma_2} V_{kk_1 k_2} c_{k_1\sigma_1}^\dagger c_{(k_1+k)\sigma_1} c_{k_2\sigma_2}^\dagger c_{(k_2-k)\sigma_2} \\ &= \sum_{kk_1 k_2} \sum_{\sigma_1 \sigma_2} V_{kk_1 k_2} c_{k_1\sigma_1}^\dagger c_{k_2\sigma_2}^\dagger c_{(k_2-k)\sigma_2} c_{(k_1+k)\sigma_1}, \end{aligned} \quad (3.103)$$

where

$$V_{kk_1 k_2} = \frac{Q_{\text{ion}}^2}{M_{\text{ion}}} \sum_{\alpha} \frac{\tilde{b}_{k_1}^\alpha \tilde{b}_{k_2}^\alpha}{N^2} V(\omega_k^\alpha, \varepsilon_{k_1} - \varepsilon_{k+k_1}). \quad (3.104)$$

To proceed, I again consider the relevant subspace of state vectors the operator can act on. For a term in equation (3.103) to be non-zero, the states with momenta $\mathbf{k}_2 - \mathbf{k}$ and $\mathbf{k}_1 + \mathbf{k}$ must be occupied while the states with momenta k_1 and k_2 must be empty. The Fermi surface is defined by all the \mathbf{k} -values satisfying $\varepsilon_{\mathbf{k}} = \mu$. When $t_{\sigma_1\sigma_2}^{k_1k_2} = 0$,³ $\mathcal{H}_{SC} = 0$, and the temperature is absolute zero, then all states with energy below the Fermi surface are fully occupied while all states above the Fermi level are fully empty. Hence, in this case, the \mathbf{k}_1 -state with energy ε_{k_1} must be below the Fermi level while the $(\mathbf{k}_1 + \mathbf{k})$ -state with energy ε_{k+k_1} must be above the Fermi level. From equation (3.104), we know that the terms are only significantly different from zero when $\varepsilon_{k+k_1} - \varepsilon_{k_1} \approx \omega_{\mathbf{k}}^\alpha$. Hence, only \mathbf{k}_1 -states within a shell of width equal to about $2\omega_{\mathbf{k}}^\alpha$ around the Fermi surface will contribute at zero temperature when $t_{\sigma_1\sigma_2}^{k_1k_2} = \mathcal{H}_{SC} = 0$. Taking into account finite temperature and non-zero \mathcal{H}_{SC} and $t_{\sigma_1\sigma_2}^{k_1k_2}$, the separation between occupied and unoccupied states in the ensemble is less abrupt. Some states in a shell of width determined by the temperature and the magnitude of \mathcal{H}_{SC} and $t_{\sigma_1\sigma_2}^{k_1k_2}$ will be sometimes occupied and sometimes unoccupied. In this case, one still only needs to consider terms where \mathbf{k}_1 is within a shell around the Fermi level, except now the width of the shell is determined by $\omega_{\mathbf{k}}^\alpha$, the temperature, $t_{\sigma_1\sigma_2}^{k_1k_2}$ and \mathcal{H}_{SC} .

The conditions we have for $V_{kk_1k_2}c_{k_1\sigma_1}^\dagger c_{k_2\sigma_2}^\dagger c_{(k_2-k)\sigma_2} c_{(k_1+k)\sigma_1}$ to be non-zero are that \mathbf{k}_1 and $\mathbf{k}_1 + \mathbf{k}$ must be around the Fermi level, \mathbf{k}_2 and \mathbf{k}_1 are empty states and $\mathbf{k}_2 - \mathbf{k}$ and $\mathbf{k}_1 + \mathbf{k}$ are filled states. The number of \mathbf{k} -values for which all these conditions are satisfied is maximized when $\mathbf{k}_2 = -\mathbf{k}_1$. This is because, given an inversion symmetric Fermi surface, $\mathbf{k}_2 - \mathbf{k} = -(\mathbf{k}_1 + \mathbf{k})$ will automatically be inside the Fermi surface if $\mathbf{k}_1 + \mathbf{k}$ is inside the Fermi surface. This is often the case, so for simplicity I only include these values of \mathbf{k}_2 , then

$$\mathcal{H}_{SC} = \sum_{k_1k_2} \sum_{\sigma_1\sigma_2} V_{(k_2-k_1)k_1(-k_1)} c_{k_1\sigma_1}^\dagger c_{-k_1\sigma_2}^\dagger c_{-k_2\sigma_2} c_{k_2\sigma_1}, \quad (3.105)$$

This is essentially the famous BCS Hamiltonian, named after Bardeen, Cooper and Schrieffer who discovered the first microscopic theory of superconductivity [52]. The difference is that the conventional BCS

3. Note that $t_{\sigma_1\sigma_2}^{k_1k_2}$ does not include the diagonal terms $\varepsilon_{\mathbf{k}}$, as can be seen from equation (3.95).

Hamiltonian has $\sigma_1 = -\sigma_2$. We have no good reason to set $\sigma_1 = -\sigma_2$ at this point, but we shall see that this happens naturally at the level of mean-field theory.

As will become especially clear when discussing Green's functions, it is much easier to work with quadratic Hamiltonians. One way to make \mathcal{H}_{SC} quadratic is through mean-field theory. The assumption in the mean-field theory for superconductivity is that for all pairs of relevant states, $|\psi\rangle$ and $|\varphi\rangle$, $\langle\psi|c_{-k_2\sigma_2}c_{k_2\sigma_1}|\varphi\rangle \approx \langle\psi|\langle c_{-k_2\sigma_2}c_{k_2\sigma_1}\rangle|\varphi\rangle$. Hence, we can treat $c_{-k_2\sigma_2}c_{k_2\sigma_1} - \langle c_{-k_2\sigma_2}c_{k_2\sigma_1}\rangle$ as a small parameter. Linearizing equation (3.105) in this small parameter, it becomes

$$\begin{aligned} \mathcal{H}_{\text{SC}} = & -\frac{1}{2} \sum_k \sum_{\sigma_1\sigma_2} \left[\Delta_k^{\sigma_1\sigma_2} c_{k\sigma_1}^\dagger c_{-k\sigma_2}^\dagger + (\Delta_k^{\sigma_1\sigma_2})^* c_{-k\sigma_2} c_{k\sigma_1} \right] \\ & + \frac{1}{2} \sum_k \sum_{\sigma_1\sigma_2} \Delta_k^{\sigma_1\sigma_2} \langle c_{k\sigma_1}^\dagger c_{-k\sigma_2}^\dagger \rangle \end{aligned} \quad (3.106)$$

where

$$\Delta_{k_1}^{\sigma_1\sigma_2} = -2 \sum_{k_2} V_{(k_2-k_1)k_1(-k_1)} \langle c_{-k_2\sigma_2} c_{k_2\sigma_1} \rangle. \quad (3.107)$$

Again assuming that the Fermi surface is inversion symmetric, meaning that $\varepsilon_{-k} = \varepsilon_k$, it follows from equation (3.104) that $V_{(k_2-k_1)k_1(-k_1)} = V_{(-k_2-k_1)k_1(-k_1)}$. Hence,

$$\Delta_{k_1}^{\sigma_1\sigma_2} = - \sum_{k_2} V_{(k_2-k_1)k_1(-k_1)} \langle c_{-k_2\sigma_2} c_{k_2\sigma_1} - c_{-k_2\sigma_1} c_{k_2\sigma_2} \rangle, \quad (3.108)$$

which means that $\Delta_k^{\uparrow\uparrow} = \Delta_k^{\downarrow\downarrow} = 0$ and $\Delta_k^{\uparrow\downarrow} = -\Delta_k^{\downarrow\uparrow}$. Note, importantly, that this does not mean that $\langle c_{-k_2\uparrow} c_{k_2\uparrow} \rangle$ or $\langle c_{-k_2\downarrow} c_{k_2\downarrow} \rangle$ are zero. Such correlations can be non-zero. They are especially important for superconducting spintronics because they can carry dissipationless spin-currents [65]. The symmetry properties of the phonon-mediated interaction mean that only the spin-singlet expectation values, $\langle c_{-k_2\sigma_2} c_{k_2\sigma_1} - c_{-k_2\sigma_1} c_{k_2\sigma_2} \rangle$, contribute to the Hamiltonian, but the system can still carry spin-triplet correlation. One way this can happen is if the superconductor is proximized by a ferromagnetic (paper I) or antiferromagnetic material (papers IX and X).

The last term in equation (3.106) is a scalar. When $\Delta_k^{\sigma_1\sigma_2}$ varies in space or time, it can give a non-uniform shift to the free energy. However, I here assume that it can be safely ignored. The full Hamiltonian

is therefore

$$\mathcal{H} = \sum_{k,\sigma} (\varepsilon_k - \mu) c_{k\sigma}^\dagger c_{k\sigma} + \sum_{k_1, k_2, \sigma_1, \sigma_2} c_{k_1 \sigma_1}^\dagger t_{\sigma_1 \sigma_2}^{k_1 k_2} c_{k_2 \sigma_2} - \sum_k \left[\Delta_k^{\uparrow\downarrow} c_{k\uparrow}^\dagger c_{-k\downarrow}^\dagger + (\Delta_k^{\uparrow\downarrow})^* c_{-k\downarrow} c_{k\uparrow} \right]. \quad (3.109)$$

The presence of $\Delta_k^{\uparrow\downarrow}$ is what makes the system superconducting. As mentioned in chapter 1, a superconducting system has a few characteristic properties. The most famous is probably that it can carry dissipationless current. This can be seen in papers I–V where current flows through superconducting junctions despite no drop in electric potentials. The other feature, which is often considered to be more fundamental [45] is that it expels magnetic fields. This is the Meissner effect [45, 47] and can be understood as a consequence of the fact that the photon field effectively acquires mass in superconductors through the Higgs mechanism [53, 54]. That is, if instead of deriving an effective theory for the electron field by solving for the photon field, as I did above, one instead derives an effective theory for the photon field, then the photon field would have an effective mass term as a result superconductivity. This effective mass gives the photon field a short range.

Conventional superconductors repel magnetic fields through the Meissner effect, but a sufficiently strong magnetic field will be able to penetrate through the superconductor. Superconductors can be categorized based on how they respond to strong magnetic fields. So-called type-I superconductors will repel all magnetic fields until the field strength becomes more than some critical value [45]. When the field strength reaches this value, the superconductivity breaks down, and the material becomes a normal metal. Type-II superconductors, on the other hand, will have an intermediate range of magnetic field strengths in which superconductivity and magnetic fields can coexist in the same material [45]. This is done through the proliferation of vortices, which is central in papers I, II and VIII. Vortices are lines where the superconductivity is suppressed and the magnetic field is strong. Away from these lines, the strength of the superconductivity recovers over a length scale given by the superconducting coherence length, while the strength of the magnetic field is suppressed over a

length scale given by the magnetic penetration depth. The ratio of the superconducting penetration depth to the superconducting coherence length determines whether a superconductor is type-I or type-II. However, all type-I superconductors can effectively be made into type-II superconductors if they are made thin [175].

It is worth pointing out that when the system is superconducting in the mean-field theory, such that $\langle c_{-k_2\sigma_2} c_{k_2\sigma_1} \rangle \neq 0$, then the states describing the system do not have a definite number of particles. What this means is that the state vectors $|\psi\rangle$ are superpositions of states with different numbers of particles. To see why, consider the fact that if $|\psi\rangle$ is a superposition of states with n particles, then $c_{-k_2\sigma_2} c_{k_2\sigma_1} |\psi\rangle$ is a superposition of states with $n - 2$ particles, all of which are therefore orthogonal to all the states constituting $|\psi\rangle$, so $\langle \psi | c_{-k_2\sigma_2} c_{k_2\sigma_1} | \psi \rangle = 0$. On the other hand, the original Hamiltonian before the mean-field treatment, equation (3.105), commutes with the number operator. Therefore ground states of the original Hamiltonian are also eigenstates of the number operator.

3.4 External Fields

In this section, I consider how to include external electric and magnetic fields into the quantum theory of solids. First, I summarize the derivation so far. In section 2.6 I showed that the Hamiltonian for an electron system can be written in terms of the field operators as

$$\mathcal{H} = \int_{\mathbb{R}^3} d^3x \psi^\dagger \left\{ qV + \frac{(-i\nabla - q\mathbf{A})^2}{2m} + \frac{q\boldsymbol{\sigma}}{2m} \cdot \mathbf{B} + \frac{iq\boldsymbol{\sigma} \cdot (\nabla \times \mathbf{E})}{8m^2} + \frac{q\boldsymbol{\sigma} \cdot [\mathbf{E} \times (-i\nabla - q\mathbf{A})]}{4m^2} - \mu \right\} \psi. \quad (3.110)$$

and in section 3.1 I explained that the rapidly oscillating fields from the ions in solids mean that it is convenient to use lattice models where ψ is written as a sum of annihilation operators for Wannier states. In section 2.7 I showed how the photon field, (V, \mathbf{A}) , can be written as a sum of various contributions: the contribution from electrons, the contribution from other charge sources in the system and the contribution from external fields. The contribution from electrons gave rise to electron-electron interactions in the model, and in section 3.2 I showed

that this could give rise to magnetism through exchange interactions. In solids, the most prominent source of charge, other than electrons, is from the ions constituting the lattice. This is what motivated the use of lattice models in the first place, and in section 3.3, we saw that the dynamics of these charges can give rise to superconductivity. In this section, I consider the third and final ingredient of the photon field in solids, which is the field from external sources. I assume that the external fields vary slowly in space compared to the distance between ions.

As was discussed in section 2.7, what I have called the external fields, V_{ext} and \mathbf{A}_{ext} , are also operators and can generally not be set to zero even in the absence of external sources. However, since the dependency of the photon field on the charge distribution in the system has been removed, there is no coupling between ψ and $(V_{\text{ext}}, \mathbf{A}_{\text{ext}})$. As a result, when it comes to the computation of observables, the only necessary quantities to know are the expectation values of $(V_{\text{ext}}, \mathbf{A}_{\text{ext}})$, such as $\langle V_{\text{ext}} \rangle$, $\langle V_{\text{ext}}^2 \rangle$, and so on. In the absence of charges, one can choose $\langle V_{\text{ext}} \rangle = 0$ and $\langle \mathbf{A}_{\text{ext}} \rangle = 0$.

3.4.1 Electrostatic Potential and the Zeeman Effect

For our purposes, there are four important effects of the external electromagnetic field. Two that are simple to include in the lattice models and two that are more difficult. The two simple effects are the Zeeman effect and the energy shift from the electrostatic potential. In terms of the field operators, these are

$$\mathcal{H}_V + \mathcal{H}_Z = \int_{\mathbb{R}^3} d^3x \psi^\dagger \left(qV_{\text{ext}} + \frac{q\sigma}{2m} \cdot \mathbf{B}_{\text{ext}} \right) \psi, \quad (3.111)$$

where $\mathbf{B}_{\text{ext}} = \nabla \times \mathbf{A}_{\text{ext}}$. Like before, I label the Wannier states depending on their spin-projection. That is, if there are $2N_s$ Wannier states per lattice site, one can write the field operators in terms of the annihilation operators for Wannier states, $\{c_{nm\sigma}\}$, as

$$\psi_\sigma(\mathbf{r}) = \sum_{n=1}^{N_s} \sum_{m=1}^{N_l} \varphi_{\sigma n}(\mathbf{r} - \mathbf{R}_m) c_{nm\sigma}, \quad (3.112)$$

where N_l is the number of lattice sites, and $\varphi_{\sigma n}(\mathbf{r} - \mathbf{R}_m) = \langle \mathbf{r}, \sigma | \varphi_{n\sigma \mathbf{R}_m} \rangle$, where $|\varphi_{n\sigma \mathbf{R}_m} \rangle$ is the n th Wannier state with spin σ associated with the

lattice site at \mathbf{R}_m . In other words, I choose the Wannier states such that they have uniform spin-projection in space, and $\langle \mathbf{r}, \sigma_1 | \varphi_{n\sigma_2 \mathbf{R}_m} \rangle = 0$ when $\sigma_1 \neq \sigma_2$. Inserting this I get,

$$\mathcal{H}_V + \mathcal{H}_Z = \sum_{\sigma_1, \sigma_2} \sum_{n_1, n_2} \sum_{m_1, m_2} t_{n_1 n_2 \sigma_1 \sigma_2}^{m_1 m_2} c_{n_1 m_1 \sigma_1}^\dagger c_{n_2 m_2 \sigma_2}, \quad (3.113)$$

where

$$t_{n_1 n_2 \sigma_1 \sigma_2}^{m_1 m_2} = \int_{\mathbb{R}^3} d^3 x \varphi_{\sigma_1 n_1}^*(\mathbf{x} - \mathbf{R}_{m_1}) \left\{ \delta_{\sigma_1 \sigma_2} q V_{\text{ext}}(\mathbf{x}) + \left[\frac{q\boldsymbol{\sigma}}{2m} \cdot \mathbf{B}_{\text{ext}}(\mathbf{x}) \right]_{\sigma_1 \sigma_2} \right\} \varphi_{\sigma_2 n_2}(\mathbf{x} - \mathbf{R}_{m_2}). \quad (3.114)$$

I write $V_{\text{ext}}(\mathbf{r}) = V_{\text{ext}}(\mathbf{R}_{m_1}) + \Delta V_{\text{ext}}(\mathbf{r})$ and $\mathbf{B}_{\text{ext}}(\mathbf{r}) = \mathbf{B}_{\text{ext}}(\mathbf{R}_{m_1}) + \Delta \mathbf{B}_{\text{ext}}(\mathbf{r})$, where $\Delta V_{\text{ext}}(\mathbf{r}) = V_{\text{ext}}(\mathbf{r}) - V_{\text{ext}}(\mathbf{R}_{m_1})$ and $\Delta \mathbf{B}_{\text{ext}}(\mathbf{r}) = \mathbf{B}_{\text{ext}}(\mathbf{r}) - \mathbf{B}_{\text{ext}}(\mathbf{R}_{m_1})$. Since V_{ext} and \mathbf{B}_{ext} are assumed to change slowly over the length-scale of neighboring lattice sites, we have that $|\Delta V_{\text{ext}}(\mathbf{r})| \ll |V_{\text{ext}}(\mathbf{R}_{m_1})|$ and $|\Delta \mathbf{B}_{\text{ext}}(\mathbf{r})| \ll |\mathbf{B}_{\text{ext}}(\mathbf{R}_{m_1})|$ for all relevant values of \mathbf{r} . Consider first the dominant constant terms. Since Wannier states are orthogonal, the constant electric potential contribution is

$$\int_{\mathbb{R}^3} d^3 x \varphi_{\sigma_1 n_1}^*(\mathbf{x} - \mathbf{R}_{m_1}) q V_{\text{ext}}(\mathbf{R}_{m_1}) \varphi_{\sigma_2 n_2}(\mathbf{x} - \mathbf{R}_{m_2}) = \delta_{n_1 n_2} \delta_{m_1 m_2} q V_{\text{ext}}(\mathbf{R}_{m_1}). \quad (3.115)$$

I assume that two Wannier functions, $\varphi_{\sigma_1 n_1}^*(\mathbf{x} - \mathbf{R}_{m_1})$ and $\varphi_{\sigma_2 n_2}^*(\mathbf{x} - \mathbf{R}_{m_2})$, are orthogonal if $n_1 \neq n_2$ or $m_1 \neq m_2$. From the orthogonality of the Wannier states, this assumption is true when $\sigma_1 = \sigma_2$. For simplicity, I assume that the same is true when $\sigma_1 \neq \sigma_2$. This means that

$$t_{n_1 n_2 \sigma_1 \sigma_2}^{m_1 m_2} = \delta_{n_1 n_2} \delta_{m_1 m_2} \left\{ \delta_{\sigma_1 \sigma_2} q V_{\text{ext}}(\mathbf{R}_{m_1}) + \left[\frac{q\boldsymbol{\sigma}}{2m} \cdot \mathbf{B}_{\text{ext}}(\mathbf{R}_{m_1}) \right]_{\sigma_1 \sigma_2} \int_{\mathbb{R}^3} d^3 x \varphi_{\sigma_1 n_1}^*(\mathbf{x}) \varphi_{\sigma_2 n_1}(\mathbf{x}) \right\}. \quad (3.116)$$

If the Wannier states come in two spin-degenerate pairs, then the integral in the last term is 1, and

$$t_{n_1 n_2 \sigma_1 \sigma_2}^{m_1 m_2} = \delta_{n_1 n_2} \delta_{m_1 m_2} \left\{ \delta_{\sigma_1 \sigma_2} q V_{\text{ext}}(\mathbf{R}_{m_1}) + \left[\frac{q\boldsymbol{\sigma}}{2m} \cdot \mathbf{B}_{\text{ext}}(\mathbf{R}_{m_1}) \right]_{\sigma_1 \sigma_2} \right\},$$

(3.117)

but in general, the spatial overlap between two different spin-states can be different from 1. This can for instance be the case if there is strong atomic spin-orbit coupling in the system. In this case, there will be an effective, direction-dependent g -factor, such that

$$t_{n_1 n_2 \sigma_1 \sigma_2}^{m_1 m_2} = \delta_{n_1 n_2} \delta_{m_1 m_2} \left\{ \delta_{\sigma_1 \sigma_2} q V_{\text{ext}}(\mathbf{R}_{m_1}) + g_{\sigma_1 \sigma_2} \left[\frac{q \boldsymbol{\sigma}}{4m} \cdot \mathbf{B}_{\text{ext}}(\mathbf{R}_{m_1}) \right]_{\sigma_1 \sigma_2} \right\}. \quad (3.118)$$

Some systems have strong, anisotropic g -factor [176, 177].

The contributions from ΔV_{ext} and $\Delta \mathbf{B}_{\text{ext}}$ will give small contributions to $t_{n_1 n_2 \sigma_1 \sigma_2}^{m_1 m_2}$ also when $\mathbf{m}_1 \neq \mathbf{m}_2$. Often, this contribution will be negligible compared to the hopping term which comes from the kinetic energy. However, in some circumstances, it might give rise to new kinds of hopping which are not present in the absence of the external field, such as hoppings that do not preserve orbital angular momentum. This is in fact an important contributor to Rashba spin-orbit coupling, as is explained below.

3.4.2 Peierls Substitution

The two more complicated effects from external fields are spin-orbit coupling and the orbital effect. By the latter, I mean how the vector potential enters the kinetic term,

$$\mathcal{H}_K = \int_{\mathbb{R}^3} d^3 x \psi^\dagger \left[\frac{(-i\nabla - q\mathbf{A})^2}{2m} \right] \psi. \quad (3.119)$$

A popular approximation for including how a slowly varying external vector potential affects the kinetic energy is called the Peierls substitution [178, 179]. The Peierls substitution amounts to giving the kinetic hopping term a phase shift proportional to the strength of the external vector potential and the distance between the hopping sites.

To see how the Peierls substitution can be justified, we can go back to how the Wannier states are defined. The Wannier states are defined through the eigenstates of a periodic Hamiltonian. That is, if

$\{|\psi_{nk}\rangle\}$ is a complete set of eigenstates of a periodic Hamiltonian, the corresponding Wannier states are given by

$$|\varphi_{nR_m}\rangle = \frac{1}{\sqrt{N}} \sum_{\mathbf{k}} e^{-i\mathbf{k}\cdot\mathbf{R}_m} |\psi_{nk}\rangle, \quad (3.120)$$

where N is the number of lattice sites. The Bloch states $\{|\psi_{nk}\rangle\}$ can also be written in terms of the Wannier states through an inverse Fourier transform,

$$|\psi_{nk}\rangle = \frac{1}{\sqrt{N}} \sum_{\mathbf{k}} e^{i\mathbf{k}\cdot\mathbf{R}_m} |\varphi_{nR_m}\rangle. \quad (3.121)$$

The fact that one needs a periodic Hamiltonian to define the Bloch states means that the Hamiltonian cannot include the external vector potential. However, one can define a new set of orthonormal state vectors that are related to the original Wannier states. Writing the Hamiltonian first in terms of creation operators for these state vectors gives a simple recipe for including external vector potentials in the Hamiltonian with Wannier states.

Let the original, periodic, single-particle Hamiltonian be

$$\mathcal{H}_1 = \frac{(\mathbf{p} - q\mathbf{A}_{\text{ion}})^2}{2m} + U(\mathbf{r}, \mathbf{p} - q\mathbf{A}_{\text{ion}}), \quad (3.122)$$

where \mathbf{A}_{ion} is the periodic vector potential coming from the equilibrium distribution of ions and localized electrons and where $U(\mathbf{r}, \mathbf{p})$ includes the electromagnetic field from the ions in their equilibrium configuration, including the spin-orbit coupling from the electric field generated by the ions. That is,

$$U(\mathbf{r}, \mathbf{p}) = qV_{\text{ion}}^{\text{eq}}(\mathbf{r}) + \frac{iq\mathbf{s} \cdot (\nabla \times \mathbf{E}_{\text{ion}}^{\text{eq}})}{4m^2} + \frac{q\mathbf{s} \cdot (\mathbf{E}_{\text{ion}}^{\text{eq}} \times \mathbf{p})}{2m^2}, \quad (3.123)$$

where \mathbf{s} is the spin operator. If I include a vector potential \mathbf{A}_{ext} , the single particle Hamiltonian becomes

$$\tilde{\mathcal{H}}_1 = \frac{(\mathbf{p} - q\mathbf{A})^2}{2m} + U(\mathbf{r}, \mathbf{p} - q\mathbf{A}), \quad (3.124)$$

where $\mathbf{A} = \mathbf{A}_{\text{ion}} + \mathbf{A}_{\text{ext}}$.

If the eigenstates of the periodic Hamiltonian in equation (3.122) are given by $\{|\psi_{nk}\rangle\}$, and related to the Wannier states $\{|\varphi_{nk}\rangle\}$ through equation (3.121), I can define a new set of states as

$$|\tilde{\psi}_{nk}\rangle = \frac{1}{\sqrt{N}} \sum_{\mathbf{k}} e^{i\mathbf{k}\cdot\mathbf{R}_m} |\tilde{\varphi}_{n\mathbf{R}_m}\rangle, \quad (3.125)$$

where

$$\langle \mathbf{r}, \sigma | \tilde{\varphi}_{n\mathbf{R}_m} \rangle = \exp \left[iq \int_{\mathcal{C}(\mathbf{r})} d\gamma \mathbf{A}_{\text{ext}}(\mathbf{r}'(\gamma)) \cdot \frac{\partial \mathbf{r}'}{\partial \gamma} \right] \langle \mathbf{r}, \sigma | \varphi_{n\mathbf{R}_m} \rangle. \quad (3.126)$$

Here $\mathcal{C}(\mathbf{r})$ is some path that starts at some \mathbf{r}_0 and ends in \mathbf{r} . The path is parametrized by γ , so $\partial \mathbf{r}' / \partial \gamma$ is the tangent vector to the path. Note that $\{|\tilde{\varphi}_{n\mathbf{R}_m}\rangle\}$ is an orthonormal set, since

$$\langle \tilde{\varphi}_{n_1\mathbf{R}_{m_1}} | \tilde{\varphi}_{n_1\mathbf{R}_{m_1}} \rangle = \sum_{\sigma} \int_{\mathbb{R}^3} \langle \tilde{\varphi}_{n_1\mathbf{R}_{m_1}} | \mathbf{r}, \sigma \rangle \langle \mathbf{r}, \sigma | \tilde{\varphi}_{n_1\mathbf{R}_{m_1}} \rangle = \langle \varphi_{n_1\mathbf{R}_{m_1}} | \varphi_{n_1\mathbf{R}_{m_1}} \rangle. \quad (3.127)$$

I will show that the kinetic energy term of equation (3.124) is simplified when using $\{|\tilde{\varphi}_{n\mathbf{R}_m}\rangle\}$. However, before that, I note that one must take care to define the family of paths $\{\mathcal{C}(\mathbf{r})\}$. The aim is to choose $\{\mathcal{C}(\mathbf{r})\}$ such that

$$\langle \mathbf{r}, \sigma | (\mathbf{p} - q\mathbf{A}) | \tilde{\varphi}_{n\mathbf{R}_m} \rangle \approx e^{i\theta(\mathbf{r})} \langle \mathbf{r}, \sigma | \mathbf{p} - q\mathbf{A}_{\text{ion}} | \varphi_{n\mathbf{R}_m} \rangle, \quad (3.128)$$

where

$$\theta(\mathbf{r}) = q \int_{\mathcal{C}(\mathbf{r})} d\gamma \mathbf{A}_{\text{ext}}(\mathbf{r}'(\gamma)) \cdot \frac{\partial \mathbf{r}'}{\partial \gamma}. \quad (3.129)$$

The idea is that $\nabla\theta$ should cancel the term proportional to $q\mathbf{A}_{\text{ext}}$. This is easy in one dimension, but in multiple dimensions it turns out not to be equally straightforward. The reason why it is more difficult in multiple dimensions is that $\nabla\theta$ will depend on how the path changes as a function of \mathbf{r} . Therefore, taking a straight path from \mathbf{r}_0 to \mathbf{r} , for example, will result in the transverse components of $\nabla\theta$ depending on \mathbf{A}_{ext} at all points between \mathbf{r}_0 and \mathbf{r} . I assume that \mathbf{A} changes slowly, but I cannot assume that \mathbf{A} is constant in the whole material.

Regardless of the family of paths, it is true that the kinetic energy can be written

$$\begin{aligned}\mathcal{H}_K &= \sum_{\sigma} \sum_{n_1, n_2} \sum_{m_1, m_2} t_{n_1 n_2}^{m_1, m_2} c_{n_1 m_1 \sigma} c_{n_2 m_2 \sigma} \\ &= \sum_{\sigma} \sum_{n_1, n_2} \sum_{m_1, m_2} \tilde{t}_{n_1 n_2}^{m_1, m_2} \tilde{c}_{n_1 m_1 \sigma} \tilde{c}_{n_2 m_2 \sigma},\end{aligned}\quad (3.130)$$

where $\{c_{nm\sigma}\}$ is the set of annihilation operators for $\{|\varphi_{n\mathbf{R}_m}\rangle\}$, $\{\tilde{c}_{nm\sigma}\}$ is the set of annihilation operators for $\{|\tilde{\varphi}_{n\mathbf{R}_m}\rangle\}$,

$$t_{n_1 n_2}^{m_1, m_2} = \langle \varphi_{n_1 \mathbf{R}_{m_1}} | \frac{(\mathbf{p} - q\mathbf{A})^2}{2m} | \varphi_{n_2 \mathbf{R}_{m_2}} \rangle, \quad (3.131)$$

and

$$\tilde{t}_{n_1 n_2}^{m_1, m_2} = \langle \tilde{\varphi}_{n_1 \mathbf{R}_{m_1}} | \frac{(\mathbf{p} - q\mathbf{A})^2}{2m} | \tilde{\varphi}_{n_2 \mathbf{R}_{m_2}} \rangle. \quad (3.132)$$

In a tight-binding approximation, where all the relevant Wannier states are localized around ions, one may approximate

$$\tilde{c}_{n_1 m_1 \sigma} = \sum_{n_2 m_2} \langle \tilde{\varphi}_{n_1 \mathbf{R}_{m_1}} | \varphi_{n_2 \mathbf{R}_{m_2}} \rangle c_{n_2 m_2 \sigma} \approx e^{-i\theta(\mathbf{R}_{m_1})} c_{n_1 m_1 \sigma}. \quad (3.133)$$

That is, I assume that I can neglect the coupling between different Wannier states that comes from the spatial inhomogeneity of θ . This is valid under the assumption that the changes in $\theta(\mathbf{r})$ over the domains of the Wannier functions are small compared to 1. When this is true, I get from equation (3.130) that

$$t_{n_1 n_2}^{m_1, m_2} = e^{i[\theta(\mathbf{R}_{m_1}) - \theta(\mathbf{R}_{m_2})]} \tilde{t}_{n_1 n_2}^{m_1, m_2}. \quad (3.134)$$

Next, I must choose a family of paths in order to compute $\tilde{t}_{n_1 n_2}^{m_1, m_2}$. The states $\{|\tilde{\varphi}_{n\mathbf{R}_m}\rangle\}$ are only used to help compute $t_{n_1 n_2}^{m_1, m_2}$. I am therefore free to choose the paths differently depending on which $t_{n_1 n_2}^{m_1, m_2}$ I want to compute, as long as I am consistent with the prefactor $e^{i[\theta(\mathbf{R}_{m_1}) - \theta(\mathbf{R}_{m_2})]}$. In order to compute all hopping parameters $t_{n_1 n_2}^{m_1, m_2}$ where $\mathbf{R}_{m_2} = \mathbf{R}_i$, I choose the path $\mathcal{C}(\mathbf{r})$ to go in a straight line from \mathbf{r}_0 to \mathbf{R}_i , and then in a straight line from \mathbf{R}_i to \mathbf{r} . When I compute $\nabla\theta(\mathbf{r})$, the only part of the path which depends on \mathbf{r} is the segment from \mathbf{R}_i to \mathbf{r} . Therefore,

$$(\mathbf{r} - \mathbf{R}_i) \cdot \nabla\theta = q(\mathbf{r} - \mathbf{R}_i) \cdot \mathbf{A}_{\text{ext}}(\mathbf{r}), \quad (3.135)$$

while

$$(\mathbf{r} - \mathbf{R}_i) \times \nabla \theta = \frac{q}{|\mathbf{r} - \mathbf{R}_i|} \int_0^{|\mathbf{r} - \mathbf{R}_i|} d\gamma (\mathbf{r} - \mathbf{R}_i) \times \mathbf{A}_{\text{ext}} \left(\mathbf{R}_i + \frac{\mathbf{r} - \mathbf{R}_i}{|\mathbf{r} - \mathbf{R}_i|} \gamma \right). \quad (3.136)$$

Since I only need to evaluate $\nabla \theta$ when $|\mathbf{r} - \mathbf{R}_i|$ is on the atomic length scale, I can set \mathbf{A}_{ext} constant in the interval from \mathbf{R}_i to \mathbf{r} , such that $\nabla \theta(\mathbf{r}) = q \mathbf{A}_{\text{ext}}(\mathbf{r})$. Inserting this into the definition of $\tilde{t}_{n_1 n_2}^{m_1 i}$, I get that

$$\tilde{t}_{n_1 n_2}^{m_1 i} = \langle \varphi_{n_1 \mathbf{R}_{m_1}} | \frac{(\mathbf{p} - q \mathbf{A} + q \mathbf{A}_{\text{ext}})^2}{2m} | \varphi_{n_2 \mathbf{R}_i} \rangle, \quad (3.137)$$

which is just the hopping amplitude in the absence of the external vector potential. Since \mathbf{A}_{ext} is approximately constant between \mathbf{R}_i and \mathbf{R}_{m_1} , $\theta(\mathbf{R}_{m_1}) - \theta(\mathbf{R}_i) = q(\mathbf{R}_{m_1} - \mathbf{R}_i) \cdot \mathbf{A}_{\text{ext}}(\mathbf{R}_i)$. Therefore,

$$\tilde{t}_{n_1 n_2}^{m_1 i} = e^{iq(\mathbf{R}_{m_1} - \mathbf{R}_i) \cdot \mathbf{A}_{\text{ext}}(\mathbf{R}_i)} \langle \varphi_{n_1 \mathbf{R}_{m_1}} | \frac{(\mathbf{p} - q \mathbf{A}_{\text{ion}})^2}{2m} | \varphi_{n_2 \mathbf{R}_i} \rangle. \quad (3.138)$$

This is the Peierls substitution. The hopping amplitude in the presence of a slowly changing external vector potential is equal to the hopping amplitude in the absence of the external vector potential multiplied by a phase factor $\exp[iq(\mathbf{R}_{m_1} - \mathbf{R}_i) \cdot \mathbf{A}_{\text{ext}}(\mathbf{R}_i)]$.

3.4.3 Rashba Spin-Orbit Coupling

The final effect of external fields to be discussed in this section is the effect of spin-orbit coupling. The most obvious contribution to spin-orbit coupling from an external electric field is the term

$$\mathcal{H}_{\text{SOC}} = \int_{\mathbb{R}^3} d^3 x \psi^\dagger \left\{ \frac{iq \boldsymbol{\sigma} \cdot (\nabla \times \mathbf{E}_{\text{ext}})}{8m^2} + \frac{q \boldsymbol{\sigma} \cdot [\mathbf{E}_{\text{ext}} \times (-i\nabla - q\mathbf{A})]}{4m^2} \right\} \psi. \quad (3.139)$$

If we ignore the first term, which is only non-zero with time-dependent external fields because $\nabla \times \mathbf{E}_{\text{ext}} = -\partial \mathbf{B}_{\text{ext}} / \partial t$, by using that that $\boldsymbol{\sigma} \cdot [\mathbf{E}_{\text{ext}} \times (-i\nabla - q\mathbf{A})] = \mathbf{E}_{\text{ext}} \cdot [(-i\nabla - q\mathbf{A}) \times \boldsymbol{\sigma}]$ and inserting the Wannier states, I get

$$\mathcal{H}_{\text{SOC}} = \sum_{\sigma_1 \sigma_2} \sum_{n_1 n_2} \sum_{m_1 m_2} \tilde{t}_{n_1 n_2 \sigma_1 \sigma_2}^{m_1 m_2} c_{n_1 m_1 \sigma_1}^\dagger c_{n_2 m_2 \sigma_2} \quad (3.140)$$

where, if I assume that E_{ext} is approximately constant between \mathbf{R}_{m_1} and \mathbf{R}_{m_2} ,

$$t_{n_1 n_2 \sigma_1 \sigma_2}^{m_1 m_2} = \frac{qE_{\text{ext}}}{4m^2} \int_{\mathbb{R}^3} d^3x \varphi_{\sigma_1 n_1}^*(\mathbf{x} - \mathbf{R}_{m_1}) [(-i\nabla - q\mathbf{A}) \times \boldsymbol{\sigma}]_{\sigma_1 \sigma_2} \varphi_{\sigma_2 n_2}(\mathbf{x} - \mathbf{R}_{m_2}). \quad (3.141)$$

To simplify this expression, I can use that the Wannier states have the largest overlap in space in the region between \mathbf{R}_{m_1} and \mathbf{R}_{m_2} , and if I assume that the $\varphi_{\sigma_2 n_2}$ decay most quickly in the radial direction, then the component of the gradient which is parallel to the displacement vector $\mathbf{d}_{m_1 m_2} = \mathbf{R}_{m_1} - \mathbf{R}_{m_2}$ will dominate. Therefore,

$$t_{n_1 n_2 \sigma_1 \sigma_2}^{m_1 m_2} = \lambda_{n_1 n_2}(|\mathbf{d}_{m_1 m_2}|) E_{\text{ext}} \cdot [\mathbf{d}_{m_1 m_2} \times \boldsymbol{\sigma}]_{\sigma_1 \sigma_2} \quad (3.142)$$

for some function $\lambda_{n_1 n_2}(|\mathbf{d}_{m_1 m_2}|)$. Spin-orbit coupling on the form of equation (3.142) is called Rashba spin-orbit coupling [180]. There are also other types, such as the Dresselhaus spin-orbit coupling [181].

Equation (3.142) is the correct form, but the experimental values for λ are often much larger than one would obtain from inserting reasonable approximations for the Wannier states in equation (3.141) [182, 183]. This is because there can be other much stronger contributions to spin-orbit coupling in real materials. In fact, we have already looked at one important contribution. The electric potential from an external field,⁴ qV_{ext} , can give rise to strong Rashba spin-orbit coupling in materials with strong atomic spin-orbit coupling, $qs \cdot (\mathbf{E}_{\text{ion}}^{\text{eq}} \times \mathbf{p})/2m^2$.

To illustrate how this can happen, consider a system in which there are some Wannier states corresponding to itinerant electrons at each lattice site. If the material has strong atomic spin-orbit coupling, the atomic spin-orbit coupling can give rise to a spin-splitting between the Wannier states depending on their orbital angular momentum. This is for instance the case if the Wannier states in question are similar to p -orbitals. In other words, the atomic spin-orbit coupling leads to an on-site coupling between orbital and spin angular momentum. In the absence of an external electric field, the Wannier states at different

4. I use the term *external field* in a broad sense. It does not have to be applied externally in a lab, it is simply external to the field in the atomic Hamiltonian and the field from the itinerant electrons. For example, it can come from the asymmetric charge distribution associated with an interface between two materials.

lattice sites mostly couple to each other if they have the same orbital angular momentum due to symmetry [183]. However, an external electric field can act as a symmetry-breaking field, allowing hopping between states with different orbital angular momentum. This gives rise to an effective spin-orbit coupling similar to equation (3.142).

To illustrate the physical picture, take an electron in some combination of orbital angular momentum, L_1 , and spin angular momentum, S_1 . Because of the external electric field, it can hop to another Wannier state on a neighboring lattice site with another orbital angular momentum, L_2 . However, due to the atomic spin-orbit coupling, the particle can transition from (L_2, S_1) to for example (L_1, S_2) . The end result is a transition from one lattice site to another together with a transition from one spin-state to another, just like equation (3.142). The difference is that the magnitude of the transition amplitude can be much stronger than the naive derivation of equation (3.142) would suggest. The magnitude of $\lambda_{n_1 n_2}(|\mathbf{d}_{m_1 m_2}|)$ depends on which orbitals constitute the itinerant electrons and the strength of the atomic spin-orbit coupling [183]. In practice, it is often more convenient to take $\lambda_{n_1 n_2}(|\mathbf{d}_{m_1 m_2}|)$ as an unknown free parameter that can be determined from experiments.

Green's functions

The previous chapter was about how to write down the Hamiltonian for various crystalline solid states of matter. This chapter is about how to use the Hamiltonian to compute observables through Green's functions. The concept of Green's functions has a precise mathematical definition [184], but in theoretical condensed matter physics it is typically used to refer to correlation functions more broadly [185], where the correlation functions may or may not be Green's functions in the mathematical sense. In this chapter, I start by defining Green's functions in the mathematical sense, which I use to motivate the Green's functions of condensed matter physics. I discuss how these Green's functions are related to observables, and how they can be computed through differential equations. Next, I discuss how Green's functions simplify in thermal equilibrium and show examples of some key systems related to my work.

4.1 Definition of Green's functions

Green's functions are mathematically useful because they allow one to easily solve a wide range of linear differential equations [184]. Let $V \subseteq \mathbb{C}^m$ and $u, f: \mathbb{R}^n \rightarrow V$ be two vector-valued functions satisfying

$$\mathcal{L}u = f, \quad (4.1)$$

where \mathcal{L} is a linear differential operator, meaning that for two functions u and v , $\mathcal{L}(u+v) = \mathcal{L}u + \mathcal{L}v$. A Green's function $G(x, y)$ is by definition a matrix-valued distribution which satisfies¹

$$(\mathcal{L}G)_{mn}(x, y) = \delta_{mn}\delta(x - y), \quad (4.2)$$

where $\delta(x - y)$ is the Dirac delta distribution, δ_{mn} is the Kronecker delta and \mathcal{L} acts only on the x -dependence of G . Note that even if \mathcal{L} contains differential operators, such that u must be a continuously differentiable function, when \mathcal{L} acts on G these differential operators

1. In modern mathematical terminology, this is often referred to as a *fundamental solution*, whereas the term "Green's function" is instead reserved for a related function which takes into account boundary conditions and the domain geometry [184].

must be interpreted in the distributional sense [184]. Having found the Green's function, one can then use the linearity of \mathcal{L} to easily construct the solution to equation (4.1) for any right-hand side as

$$u(x) = \int_{\mathbb{R}^n} dy G(x, y) f(y). \quad (4.3)$$

One can also derive an additional equation for G in terms of the adjoint operator \mathcal{L}^\dagger . Under the assumption that the domain of \mathcal{L} is a complete Hilbert space, the uniqueness of \mathcal{L}^\dagger is guaranteed by Riez representation theorem [105]. The adjoint is defined by

$$\int_{\mathbb{R}^n} dx v^\dagger(x) (\mathcal{L}u)(x) = \int_{\mathbb{R}^n} dx (\mathcal{L}^\dagger v)^\dagger(x) u(x) \quad (4.4)$$

for all square-integrable u and v . Using this definition,

$$\begin{aligned} \int_{\mathbb{R}^n} dx v^\dagger(x) u(x) &= \int_{\mathbb{R}^n} dx dy v^\dagger(x) \mathcal{L}G(x, y) u(y) \\ &= \int_{\mathbb{R}^n} dx dy [\mathcal{L}^\dagger v]^\dagger(x) G(x, y) u(y) \\ &= \int_{\mathbb{R}^n} dx dy [G^\dagger(y, x) \mathcal{L}^\dagger v(x)]^\dagger u(y). \end{aligned} \quad (4.5)$$

Hence,

$$G^\dagger(y, x) \mathcal{L}^\dagger = \delta(y - x). \quad (4.6)$$

This equation must again be interpreted in the distributional sense. I use the convention that matrices are promoted to the correct size through tensor products with the correct identity matrices. That is, the right-hand side must be interpreted as $m \times m$ matrix with $\delta(y - x)$ along the diagonal.

In theoretical condensed matter physics, the main differential equation of interest is the Heisenberg equation (2.20), or, equivalently, the Schrödinger equation (2.10). As shown in the previous chapters, we often consider Hamiltonians written in terms of creation and annihilation operators. As an example, consider a system that can be written in terms of N fermionic or bosonic annihilation operators $\{c_1, c_2, \dots, c_N\}$, satisfying $[c_\lambda, c_\mu^\dagger]_\pm = \delta_{\lambda\mu}$, when the operators are evaluated at the same time. Here, the upper sign is for the fermionic system and the

lower sign is for the bosonic system. If the Hamiltonian is quadratic, the Hamiltonian can in the Heisenberg picture be written

$$\mathcal{H}(t) = \sum_{\lambda, \mu=1}^N M_{\lambda\mu}(t) c_{\lambda}^{\dagger}(t) c_{\mu}(t) = c^{\dagger}(t) M(t) c(t), \quad (4.7)$$

where $c^{\dagger} = (c_1^{\dagger}, \dots, c_N^{\dagger})$ and $M^{\dagger} = M$. In this case equation (2.20) reads

$$\left(i \frac{\partial}{\partial t} - M\right) c = 0 \quad (4.8)$$

Green's functions are not necessarily unique, and for this equation there are multiple. Written in terms of correlation functions, two possible Green's functions are

$$G_{\lambda\mu}^R(t, t') = -i\theta(t - t') \left\langle \left[c_{\lambda}(t), c_{\mu}^{\dagger}(t') \right]_{\pm} \right\rangle, \quad (4.9a)$$

$$G_{\lambda\mu}^A(t, t') = +i\theta(t' - t) \left\langle \left[c_{\lambda}(t), c_{\mu}^{\dagger}(t') \right]_{\pm} \right\rangle. \quad (4.9b)$$

These are known as the retarded and advanced Green's functions, respectively. That they satisfy equation (4.2) follows from the commutation relation $[c_{\lambda}(t), c_{\mu}^{\dagger}(t)]_{\pm} = \delta_{\lambda\mu}$. For instance,

$$i \frac{\partial}{\partial t} G_{\lambda\mu}^R(t, t') = \delta(t - t') \left\langle \left[c_{\lambda}(t), c_{\mu}^{\dagger}(t') \right]_{\pm} \right\rangle \quad (4.10)$$

$$-i\theta(t - t') \left\langle \left[(Mc)_{\lambda}(t), c_{\mu}^{\dagger}(t') \right]_{\pm} \right\rangle \quad (4.11)$$

$$= \delta(t - t') \delta_{\lambda\mu} + M(t) G_{\lambda\mu}^R(t, t'). \quad (4.12)$$

In the sense of equation (4.4), the operator $(i\partial/\partial t - M)$ is self-adjoint. As a result, one must have that $[G^R(t', t)]^{\dagger}$ is also a valid Green's function. Indeed, we can see from equation (4.9) that

$$\left[G_{\lambda\mu}^A(t, t') \right]^* = -i\theta(t' - t) \left\langle \left[c_{\mu}(t'), c_{\lambda}^{\dagger}(t) \right]_{\pm} \right\rangle = G_{\mu\lambda}^R(t', t), \quad (4.13)$$

so the advanced and retarded Green's functions transform into each other under Hermitian conjugation and interchange of temporal coordinates.

One application of these Green's functions is in linear response theory [114]. Assume $M(t) = M_0 + V(t)$ with $V(t) = 0$ for $t < 0$, and

let $c = c_0 + d$, where $c_0 = \exp(-iMt)c(0)$. Assuming that both V and d are small, and neglecting the product Vd , equation (4.8) becomes

$$\left(i\frac{\partial}{\partial t} - M_0\right)d = Vc_0 \quad (4.14)$$

This is on the form of equation (4.1), so the solution can read of from equation (4.3) as

$$d(t) = \int_0^t dt' G_0^R(t, t')V(t')c_0(t'), \quad (4.15)$$

where the Green's function G_0^R is evaluated in the unperturbed system with $M = M_0$. A related formula within linear response theory is the Kubo formula [114, 186, 187], which relates expectation values of observables to perturbations in a similar way.

That being said, the reason we are interested in G^R and G^A is not primarily because they are Green's functions. In condensed matter physics, we are typically interested in them because they are correlation functions. This is because a wide range of observables, such as electron density, spin densities, and their associated currents, can be expressed in terms of correlation functions evaluated at equal times. That is, observables can often be written as

$$O(t) = \sum_{\mu\lambda} B_{\lambda\mu}(t) \langle c_\lambda^\dagger(t)c_\mu(t) \rangle \quad (4.16)$$

for some matrix B . In terms of the so-called *lesser Green's function*,

$$G_{\lambda\mu}^<(t, t') = \pm i \langle c_\mu^\dagger(t')c_\lambda(t) \rangle, \quad (4.17)$$

where again the upper sign is for fermions and the lower sign is for bosons, the observable can be written

$$O(t) = \mp i \text{Tr} [B(t)G^<(t, t)]. \quad (4.18)$$

Unlike the retarded and advanced Green's functions, the lesser Green's function is not a Green's function in the mathematical sense. However, it is common in many-body physics to use the term "Green's function" to refer to correlation functions like $G^<$. For this reason, I will also refer to these functions as Green's functions.

As an alternative to the lesser Green's function, observables can also be computed using the *greater Green's function*,

$$G_{\lambda\mu}^>(t, t') = -i \langle c_\lambda(t) c_\mu^\dagger(t') \rangle. \quad (4.19)$$

Because using $c_\mu^\dagger(t) c_\lambda(t) = \mp c_\lambda(t) c_\mu^\dagger(t) \pm \delta_{\lambda\mu}$,

$$\begin{aligned} O(t) &= \sum_{\mu\lambda} B_{\lambda\mu}(t) \langle c_\lambda^\dagger(t) c_\mu(t) \rangle = \pm \text{Tr}[B(t)] \mp \sum_{\lambda\mu} B_{\lambda\mu}(t) \langle c_\mu(t) c_\lambda^\dagger(t) \rangle \\ &= \pm \text{Tr}[B(t)] \mp i \text{Tr}[B(t) G^>(t, t)]. \end{aligned} \quad (4.20)$$

Yet another alternative, which I have used in particular in relation to the quasiclassical Green's function formalism (see chapter 6), is to use the *Keldysh Green's function*,

$$G^K = G^> + G^<, \quad (4.21)$$

since

$$O(t) = \mp \frac{i}{2} \text{Tr}[B(t) G^K(t, t)] \pm \frac{1}{2} \text{Tr}[B(t)]. \quad (4.22)$$

Another useful correlation function is the so-called *anomalous retarded Green's function*,

$$F_{\lambda\mu}^R(t, t') = -i\theta(t - t') \langle [c_\lambda(t), c_\mu(t')]_{\pm} \rangle. \quad (4.23)$$

One can similarly define anomalous advanced, lesser, greater, and Keldysh Green's functions. With the anomalous Green's function, one can apply the Green's function approach to more general systems with Hamiltonians given by

$$\begin{aligned} \mathcal{H}(t) &= \frac{1}{2} \sum_{\lambda, \mu=1}^N \left(M_{\lambda\mu}(t) c_\lambda^\dagger c_\mu + M_{\lambda\mu}^*(t) c_\mu^\dagger c_\lambda \right. \\ &\quad \left. + \Delta_{\lambda\mu}(t) c_\lambda^\dagger c_\mu^\dagger + \Delta_{\lambda\mu}^*(t) c_\mu c_\lambda \right). \end{aligned} \quad (4.24)$$

In this case, the Heisenberg equation becomes

$$\left[\begin{pmatrix} i & \\ & -i \end{pmatrix} \frac{\partial}{\partial t} - \begin{pmatrix} M & \Delta \\ \Delta^* & M^* \end{pmatrix} \right] \begin{pmatrix} c \\ c^\dagger \end{pmatrix} = 0, \quad (4.25)$$

where c^\dagger must be interpreted as a column vector. In the fermionic case, the commutation relation means that $\Delta_{\mu\lambda} = -\Delta_{\lambda\mu}$, while in the bosonic case $\Delta_{\mu\lambda} = \Delta_{\lambda\mu}$. Let $\alpha = (c, c^\dagger)^T$. The associated Green's functions can then be written

$$\hat{G}_{\lambda\mu}^R(t, t') = -i(\tau_z)_{\lambda\lambda}\theta(t - t') \left\langle \left[\alpha_\lambda(t), \alpha_\mu^\dagger(t') \right]_{\pm} \right\rangle, \quad (4.26a)$$

$$\hat{G}_{\lambda\mu}^A(t, t') = +i(\tau_z)_{\lambda\lambda}\theta(t' - t) \left\langle \left[\alpha_\lambda(t), \alpha_\mu^\dagger(t') \right]_{\pm} \right\rangle, \quad (4.26b)$$

where $\tau_z = \text{diag}(1, \dots, 1, -1, \dots, -1)$. The anomalous Green's function is especially useful in the context of superconductivity. As I showed in section 3.3, the mean-field Hamiltonian of a superconducting system is of the form given by equation (4.24).

The operator c_λ annihilates an electron state, but alternatively one could say that it creates a hole state. Therefore, one could say that the Green's functions equation (4.26) are Green's functions in particle-hole space. Another name for this is that they are Green's functions in Nambu space [185].

4.2 Equilibrium Green's functions

By "equilibrium", I mean that the system is both stationary and in thermal equilibrium. For our purposes, the latter means that the system is in a canonical or grand canonical ensemble. In this case one can compute the lesser Green's function, and therefore observables, from only the retarded or advanced Green's function. To see why, note that one can write

$$G_{\lambda\mu}^R(t, t') - G_{\lambda\mu}^A(t, t') = G_{\lambda\mu}^>(t, t') - G_{\lambda\mu}^<(t, t'). \quad (4.27)$$

In a stationary system the Hamiltonian \mathcal{H} is time independent, so from the Heisenberg equation (2.20), an operator A evaluated at time t is

$$A(t) = e^{i\mathcal{H}t} A(0) e^{-i\mathcal{H}t} = e^{i\mathcal{H}t} A_0 e^{-i\mathcal{H}t}. \quad (4.28)$$

Hence, if Z is the partition function, β is inverse temperature, $\{|n\rangle\}$ is the complete set of eigenstates of \mathcal{H} and $\{\varepsilon_n\}$ is the corresponding set

of eigenvalues, then

$$\begin{aligned}\langle c_\lambda(t)c_\mu^\dagger(t') \rangle &= Z^{-1} \sum_n e^{-\beta\varepsilon_n} \langle n|c_\lambda(t)c_\mu^\dagger(t')|n \rangle & (4.29) \\ &= Z^{-1} \sum_{n,m} e^{-\beta\varepsilon_n} e^{i(\varepsilon_n - \varepsilon_m)(t-t')} \langle n|c_{\lambda,0}|m \rangle \langle m|c_{\mu,0}^\dagger|n \rangle. & (4.30)\end{aligned}$$

Next, by Fourier transforming in relative time, I get

$$\begin{aligned}G_{\lambda\mu}^>(\varepsilon) &= -i \int_{-\infty}^{\infty} d(t-t') \langle c_\lambda(t)c_\mu^\dagger(t') \rangle e^{i\varepsilon(t-t')} \\ &= -iZ^{-1} \sum_{n,m} e^{-\beta\varepsilon_n} \langle n|c_{\lambda,0}|m \rangle \langle m|c_{\mu,0}^\dagger|n \rangle 2\pi\delta(\varepsilon + \varepsilon_n - \varepsilon_m) \\ &= -iZ^{-1} \sum_{n,m} e^{-\beta\varepsilon_m} \langle m|c_{\mu,0}^\dagger|n \rangle \langle n|c_{\lambda,0}|m \rangle 2\pi\delta(\varepsilon + \varepsilon_n - \varepsilon_m) e^{\beta(\varepsilon_m - \varepsilon_n)} \\ &= -ie^{\beta\varepsilon} \int_{-\infty}^{\infty} d(t-t') \langle c_\mu^\dagger(t')c_\lambda(t) \rangle e^{i\varepsilon(t-t')} = \mp e^{\beta\varepsilon} G_{\lambda\mu}^<(\varepsilon) & (4.31)\end{aligned}$$

Inserting this into equation (4.27), we see that

$$G_{\lambda\mu}^<(\varepsilon) = -\frac{G_{\lambda\mu}^R(\varepsilon) - G_{\lambda\mu}^A(\varepsilon)}{1 \pm e^{\beta\varepsilon}} = iA_{\lambda\mu}(\varepsilon)f_\pm(\varepsilon), \quad (4.32)$$

where

$$f_\pm(\varepsilon) = \frac{1}{1 \pm e^{\beta\varepsilon}} \quad (4.33)$$

is the Fermi-Dirac distribution in the fermionic case and the Bose-Einstein distribution in the bosonic case, and

$$A_{\lambda\mu} = i(G_{\lambda\mu}^R - G_{\lambda\mu}^A) \quad (4.34)$$

is the spectral function [114, 185]. Equation (4.32) is an example of the fluctuation-dissipation theorem [188, 189]. Similarly, from equation (4.27) I get

$$G_{\lambda\mu}^>(\varepsilon) = \frac{G_{\lambda\mu}^R(\varepsilon) - G_{\lambda\mu}^A(\varepsilon)}{1 \pm e^{-\beta\varepsilon}} = -iA_{\lambda\mu}(\varepsilon)[1 - f_\pm(\varepsilon)]. \quad (4.35)$$

The Fermi-Dirac (Bose-Einstein) distribution f_+ (f_-) gives the average number of particles in states with energy ε . On the other hand,

$-iG_{\lambda\lambda}^<(t, t) = \langle c_{\lambda}^{\dagger}(t)c_{\lambda}(t) \rangle$ is the number of particles in state λ . By writing

$$-iG_{\lambda\lambda}^<(t, t) = \int_{-\infty}^{\infty} \frac{d\varepsilon A_{\lambda\lambda}(\varepsilon)}{2\pi} f_{\pm}(\varepsilon), \quad (4.36)$$

we see that one can interpret $A_{\lambda\lambda}(\varepsilon) d\varepsilon / 2\pi$ as being how much of the state λ which is in the energy-interval $(\varepsilon, \varepsilon + d\varepsilon)$. In order to compute observables, one must in general know both the number of states with the relevant properties and the occupancy of these states. In thermal equilibrium, it is sufficient to determine the spectral function since occupancy follows from the Fermi-Dirac and Bose-Einstein distributions.

4.3 Example: Non-interacting systems

The Hamiltonian for a non-interacting system of particles can, as shown in section 2.4, be written

$$\mathcal{H} = \sum_{\lambda=1}^{\infty} \xi_{\lambda} c_{\lambda}^{\dagger} c_{\lambda}, \quad (4.37)$$

where ξ_{λ} also includes the chemical potential. In this case $M_{\lambda\mu} = \xi_{\lambda} \delta_{\lambda\mu}$. Hence, the retarded and advanced Green's functions solve

$$i \frac{\partial}{\partial t} G_{\lambda\mu}^X(t, t') - \xi_{\lambda} G_{\lambda\mu}^X(t, t') = \delta(t - t') \delta_{\lambda\mu}, \quad (4.38)$$

where X is either R or A . Multiplying the equation by $-ie^{i\xi_{\lambda}t}$, using the product rule of differentiation,² and integrating from t_0 to t , I get that

$$G_{\lambda\mu}^X(t, t') = e^{-i\xi_{\lambda}(t-t_0)} G_{\lambda\mu}^X(t_0, t') - i\delta_{\lambda\mu} e^{-i\xi_{\lambda}(t-t_0)} [\theta(t' - t_0) - \theta(t' - t)]. \quad (4.39)$$

The retarded Green's function, $G_{\lambda\mu}^R(t_0, t')$, is zero when $t' > t_0$. Choosing $t' > t_0$, such that $\theta(t' - t_0) - \theta(t' - t) = 1 - \theta(t' - t) = \theta(t - t')$, and setting $X = R$, I get

$$G_{\lambda\mu}^R(t, t') = -i\theta(t - t') \delta_{\lambda\mu} e^{-i\xi_{\lambda}(t-t')}. \quad (4.40)$$

2. The product rule of differentiation holds in the sense of distributional derivatives when working with products of normal functions and distributions. Here, the Green's function is a distribution while $e^{i\xi_{\lambda}t}$ is a smooth function. Note that one can generally not multiply distributions, so there is no product rule for differentiation for products of distributions.

Similarly, the advanced Green's function, $G_{\lambda\mu}^A(t_0, t')$, is zero when $t' < t_0$. Choosing $t' < t_0$, such that $\theta(t' - t_0) - \theta(t' - t) = -\theta(t' - t)$, and setting $X = A$, I get

$$G_{\lambda\mu}^A(t, t') = i\theta(t' - t)\delta_{\lambda\mu}e^{-i\xi_\lambda(t-t')}. \quad (4.41)$$

These results could also have been obtained by inserting $c_\lambda(t) = e^{-\xi_\lambda t}c_\lambda(0)$ into the definitions of the Green's functions in equation (4.9).

To find the spectral function, note that $i[G_{\lambda\mu}^R(t, t') - G_{\lambda\mu}^A(t, t')] = e^{-i\xi_\lambda(t-t')}$, so the spectral function is $A_{\lambda\mu}(\varepsilon) = 2\pi\delta(\varepsilon - \xi_\lambda)\delta_{\lambda\mu}$. From this, the equilibrium lesser Green's function in Fourier space is $G_{\lambda\mu}^<(\varepsilon) = 2\pi i\delta(\varepsilon - \xi_\lambda)\delta_{\lambda\mu}f_\pm(\varepsilon)$, which means that

$$G_{\lambda\mu}^<(t, t') = \int_{-\infty}^{\infty} \frac{d\varepsilon}{2\pi} e^{-i\varepsilon(t-t')} G_{\lambda\mu}^<(\varepsilon) = i\delta_{\lambda\mu}f_\pm(\xi_\lambda)e^{-i\xi_\lambda(t-t')}. \quad (4.42)$$

Fourier transforming equations (4.40) and (4.41) in relative coordinates, I get

$$G_{\lambda\mu}^{R/A}(\varepsilon) = \int_{-\infty}^{\infty} d(t-t') G_{\lambda\mu}^{R/A}(t, t') = \lim_{\eta \rightarrow 0} \frac{\delta_{\lambda\mu}}{\varepsilon - \xi_\lambda \pm i\eta}, \quad (4.43)$$

where the infinitesimal η is needed to make the inverse Fourier transforms converge. It is also needed to get the correct spectral function. Note that the limit $\eta \rightarrow 0$ must be taken outside of the integral in the inverse Fourier transform. Also, note that a non-zero value of η will make the Green's function go to zero as $|t - t'| \rightarrow \infty$. Therefore, $\eta > 0$ can be used to model systems with dissipation.

Knowing the Green's function, we can compute observables. For instance, the if the particles are electrons with charge q , the total electric charge is $Q = q \sum_\lambda \langle c_\lambda^\dagger c_\lambda \rangle = -iq \sum_\lambda G_{\lambda\lambda}^<(t, t)$. Using equation (4.42), the total electric charge is

$$Q = -iq \sum_\lambda G_{\lambda\lambda}^<(t, t) = q \sum_\lambda f_+(\xi_\lambda). \quad (4.44)$$

That is, each state contributes $q f_+(\xi_\lambda)$ to the charge. At zero temperature, $f_+(\xi_\lambda) = \theta(-\xi_\lambda)$, so all states with negative energy, meaning states below the Fermi level, adds q to the total charge, as expected.

From this example we also have a general formula to compute Green's function in quadratic systems with Hamiltonian

$$\mathcal{H} = \sum_{\lambda,\mu=1}^{\infty} M_{\lambda\mu} c_{\lambda}^{\dagger} c_{\mu}, \quad (4.45)$$

where M does not depend on time, such that

$$i \frac{\partial}{\partial t} G_{\lambda\mu}^X(t, t') - \sum_{\gamma} M_{\lambda\gamma} G_{\gamma\mu}^X(t, t') = \delta(t - t') \delta_{\lambda\mu}. \quad (4.46)$$

The first step is to diagonalize $M_{\lambda\mu} = \sum_{\gamma} S_{\lambda\gamma} \xi_{\gamma} S_{\gamma\mu}^{-1}$ and define $\bar{G}^X = S^{-1} G^X S$. Next, multiply equation (4.46) with S^{-1} from the left and S from the right, such that

$$i \frac{\partial}{\partial t} \bar{G}_{\lambda\mu}^X(t, t') - \xi_{\lambda} \bar{G}_{\lambda\mu}^X(t, t') = \delta(t - t') \delta_{\lambda\mu}. \quad (4.47)$$

This is solved by equations (4.40) and (4.41), so

$$G_{\lambda\mu}^R(t, t') = -i\theta(t - t') \sum_{\gamma} S_{\lambda\gamma} e^{-i\xi_{\gamma}(t-t')} S_{\gamma\mu}^{-1}, \quad (4.48a)$$

$$G_{\lambda\mu}^A(t, t') = i\theta(t' - t) \sum_{\gamma} S_{\lambda\gamma} e^{-i\xi_{\gamma}(t-t')} S_{\gamma\mu}^{-1}. \quad (4.48b)$$

In practice, it can be difficult to determine S , but it is significantly easier in translationally invariant systems. For small systems, one can alternatively diagonalize systems with spatial variation numerically.

4.3.1 Magnets

Consider the itinerant electrons in a magnet. It can be a ferromagnet or an antiferromagnet. Assume that there are N lattice sites and $2N_s$ orbitals, or Wannier states, per lattice site. That is N_s states per spin. Remember that each lattice site includes one whole unit cell, meaning that there can be several atoms at each lattice site. Even if there is only one Wannier state or orbital per spin at each atom, there can be more than two Wannier states at each lattice site.

I assume that the spins of the localized electrons can be treated as constant and that the exchange interaction with the localized electrons is the same at each lattice site, but it might vary between Wannier

states. Let $c_{im\sigma}$ be the annihilation operator for Wannier state m with spin σ at lattice site i . I assume that the only spin dependence is in the exchange coupling to the localized electrons or the Zeeman energy from a uniform external field, which enters in the same way in the Hamiltonian (see chapter 3). In this case, the Hamiltonian can be written

$$\mathcal{H} = \sum_{i,j=1}^N \sum_{m,n=1}^{N_s} \sum_{\sigma} t_{ij}^{mn} c_{im\sigma}^{\dagger} c_{jn\sigma} - \sum_m \sum_{i=1}^{N_s} \sum_{\sigma_1\sigma_2} c_{im\sigma_1}^{\dagger} [\mathbf{h}^m \cdot \boldsymbol{\sigma}]_{\sigma_1\sigma_2} c_{im\sigma_2}. \quad (4.49)$$

If the system is translationally invariant, then t_{ij}^{mn} depend only on the relative distance, meaning that $t_{ij}^{mn} = t_{(i+l)(j+l)}^{mn}$ for any l . In this case, performing a discrete Fourier transform results in

$$\mathcal{H} = \frac{1}{N} \sum_{k=1}^N \sum_{m,n=1}^{N_s} \sum_{\sigma_1\sigma_2} c_{km\sigma_1}^{\dagger} c_{kn\sigma_2} [\delta_{\sigma_1\sigma_2} t_k^{mn} - \delta_{mn} (\mathbf{h}^m \cdot \boldsymbol{\sigma})_{\sigma_1\sigma_2}], \quad (4.50)$$

where

$$c_{kn\sigma_2} = \sum_{i=1}^N c_{in\sigma_2} e^{-ik \cdot \mathbf{R}_i}, \quad (4.51a)$$

$$c_{kn\sigma_2}^{\dagger} = \sum_{i=1}^N c_{in\sigma_2}^{\dagger} e^{ik \cdot \mathbf{R}_i}, \quad (4.51b)$$

$$t_k^{mn} = \sum_{i=1}^N t_{ij}^{mn} e^{ik \cdot (\mathbf{R}_i - \mathbf{R}_j)}. \quad (4.51c)$$

For a simple, ferromagnetic system, where $N_s = 1$, equation (4.50) is already diagonal if we choose the z -axis to point along the direction of \mathbf{h}^1 . In this case, the Green's functions in the momentum basis are

$$G_{k_1 k_2 \uparrow \uparrow}^{R/A}(\epsilon) = \lim_{\eta \rightarrow 0} \frac{\delta_{k_1 k_2}}{\epsilon - t_k^{11} + h^1 \pm i\eta}, \quad (4.52a)$$

$$G_{k_1 k_2 \downarrow \downarrow}^{R/A}(\epsilon) = \lim_{\eta \rightarrow 0} \frac{\delta_{k_1 k_2}}{\epsilon - t_k^{11} - h^1 \pm i\eta}, \quad (4.52b)$$

$$G_{k_1 k_2 \uparrow \downarrow}^{R/A} = G_{k_1 k_2 \downarrow \uparrow}^{R/A} = 0, \quad (4.52c)$$

where

$$G_{k_1 k_2 \sigma_1 \sigma_2}^R(t, t') = -\frac{i\theta(t-t')}{N} \left\langle \left[c_{k_1 1 \sigma_1}(t), c_{k_2 1 \sigma_2}^\dagger(t') \right] \right\rangle, \quad (4.53)$$

and $G_{k_1 k_2 \sigma_1 \sigma_2}^A(t, t') = [G_{k_2 k_1 \sigma_2 \sigma_1}^R(t', t)]^*$. The factor $1/N$ comes from how I defined the Fourier transform.

From the Green's function one can compute the magnetization from the itinerant electrons in a ferromagnet. Each electron with spin up has a magnetic moment equal to $-g\mu_B/2$ in the z -direction, where g is the Landé g -factor and $\mu_B = e/2m$ is the Bohr magneton [25] (see sections 2.6 and 3.4). Electrons with spin down have the same magnetic moment but in the opposite direction. Assuming isotropic g -factor, the total magnetic moment is therefore

$$\mathbf{M} = \frac{ig\mu_B}{2} \sum_{k=1}^N \sum_{\sigma_1 \sigma_2} \sigma_{\sigma_1 \sigma_2} G_{kk\sigma_1 \sigma_2}^<(t, t). \quad (4.54)$$

Equation (4.52c) means that \mathbf{M} is parallel to \mathbf{h}^1 . Using equations (4.52a) and (4.52b), the magnetization in the z -direction is

$$M_z = -\frac{g\mu_B}{2} \sum_{k=1}^N [f_+(t_k^{11} - h^1) - f_+(t_k^{11} + h^1)]. \quad (4.55)$$

At low temperatures $f_+(t_k^{11} \mp h^1) \approx \theta(-t_k^{11} \pm h^1)$. Therefore, the sum in equation (4.55) counts the number of states with $t_k^{11} \in (-h^1, h^1)$. We can convert the sum to an integral. Let the density of states per spin be³

$$N(E) = \sum_k \delta(t_k^{11} - E). \quad (4.56)$$

Then,

$$\sum_k f(t_k^{11}) = \int_{-\infty}^{\infty} dE f(E) \sum_k \delta(t_k^{11} - E) = \int_{-\infty}^{\infty} dE f(E) N(E). \quad (4.57)$$

Hence, the magnetization is

$$M_z = -\frac{g\mu_B}{2} \int_{-\infty}^{\infty} dE N(E) [f_+(E - h^1) - f_+(E + h^1)]. \quad (4.58)$$

3. Not to be confused with the number of lattice sites.

If the density of states is approximately constant and equal to $N(0)$ in from $E = -h^1$ to $E = h^1$, then

$$M_z = -g\mu_B N(0)h^1. \quad (4.59)$$

The choice of z -axis was arbitrary. More generally,

$$\mathbf{M} = -g\mu_B N(0)\mathbf{h}^1. \quad (4.60)$$

For an antiferromagnetic system, on the other hand, we need to choose a unit cell consisting of at least two orbitals in order for the exchange coupling to be independent of lattice site. Let there be two Wannier states per orbital per lattice site, such that $h^1 = -h^2 = h$, and let $c_k^\dagger = (c_{k1\uparrow}^\dagger, c_{k1\downarrow}^\dagger, c_{k2\uparrow}^\dagger, c_{k2\downarrow}^\dagger)$ be the 4-tuple of creation operators with crystal momentum \mathbf{k} . Assuming that $t_k^{11} = t_k^{22} = a_k$ and $t_k^{12} = t_k^{21} = b_k$, the Hamiltonian can be written

$$\mathcal{H} = \frac{1}{N} \sum_{k=1}^N c_k^\dagger \begin{pmatrix} a_k - h & \cdot & b_k & \cdot \\ \cdot & a_k + h & \cdot & b_k \\ b_k & \cdot & a_k + h & \cdot \\ \cdot & b_k & \cdot & a_k - h \end{pmatrix} c_k \quad (4.61)$$

Diagonalizing this Hamiltonian can be done by defining

$$\bar{c}_k = \frac{1}{\sqrt{2\eta_k}} \left[\begin{pmatrix} -\sigma_0 & \sigma_0 \\ \sigma_0 & \sigma_0 \end{pmatrix} \bar{s}_k - \begin{pmatrix} \sigma_z & \sigma_z \\ \sigma_z & -\sigma_z \end{pmatrix} \Delta s_k \right] c_k, \quad (4.62)$$

where σ_0 is the 2×2 identity matrix, $\eta_k = \sqrt{h^2 + b_k^2}$, $\bar{s}_k = (s_k^+ + s_k^-)/2$ and $\Delta s_k = (s_k^+ - s_k^-)/2$, where $s_k^\pm = \sqrt{\eta_k \pm h}$. Inserting this into equation (4.63), I get

$$\mathcal{H} = \frac{1}{N} \sum_{k=1}^N \bar{c}_k^\dagger \begin{pmatrix} a_k - \eta_k & \cdot & \cdot & \cdot \\ \cdot & a_k - \eta_k & \cdot & \cdot \\ \cdot & \cdot & a_k + \eta_k & \cdot \\ \cdot & \cdot & \cdot & a_k + \eta_k \end{pmatrix} \bar{c}_k. \quad (4.63)$$

From this diagonal Hamiltonian, one can derive the Green's functions. Let $G_{k_1 k_2}^R(t, t') = -i\theta(t - t') \langle [c_{k_1}(t) c_{k_2}^\dagger(t')]_+ \rangle / N$ be a matrix of retarded Green's functions, where the commutator of 4-tuples A and B^\dagger is defined by $([A B^\dagger]_+)_{ij} = [A_i B_j^\dagger]_+$. The advanced Green's function

matrix is similarly defined as $G_{k_1 k_2}^A(t, t') = i\theta(t' - t)\langle [c_{k_1}(t) c_{k_2}^\dagger(t')]_+ \rangle / N$. In Fourier space, equations (4.62) and (4.63) implies that

$$G_{k_1 k_2}^{R/A}(\varepsilon) = \lim_{\delta \rightarrow 0} \frac{1}{(\varepsilon \pm i\delta - a_k)^2 - \eta_k^2} \times \begin{pmatrix} \varepsilon \pm i\delta - a_k - h & \cdot & b_k & \cdot \\ \cdot & \varepsilon \pm i\delta - a_k + h & \cdot & b_k \\ b_k & \cdot & \varepsilon \pm i\delta - a_k + h & \cdot \\ \cdot & b_k & \cdot & \varepsilon \pm i\delta - a_k - h \end{pmatrix}. \quad (4.64)$$

4.3.2 Superconductors

In section 3.3, I derived the BCS Hamiltonian for superconductors,

$$\mathcal{H} = \frac{1}{N} \sum_{k, \sigma} \xi_k c_{k\sigma}^\dagger c_{k\sigma} + \frac{1}{N} \sum_{k_1, k_2, \sigma_1, \sigma_2} c_{k_1 \sigma_1}^\dagger t_{\sigma_1 \sigma_2}^{k_1 k_2} c_{k_2 \sigma_2} - \frac{1}{N} \sum_k \left[\Delta_k^{\uparrow\downarrow} c_{k\uparrow}^\dagger c_{-k\downarrow}^\dagger + (\Delta_k^{\uparrow\downarrow})^* c_{-k\downarrow} c_{k\uparrow} \right]. \quad (4.65)$$

If the system is invariant under translation, $t_{\sigma_1 \sigma_2}^{k_1 k_2} \propto \delta_{k_1 k_2}$. Furthermore, if there is no spin-dependent hopping, which could come from spin-orbit coupling, for instance, then $t_{\sigma_1 \sigma_2}^{k_1 k_2} = t_{k_1} \delta_{k_1 k_2} \delta_{\sigma_1 \sigma_2}$. In this case, we can therefore just absorb t_k into ξ_k . Defining the 4-tuple⁴ $c_k^\dagger = (c_{k\uparrow}^\dagger, c_{k\downarrow}^\dagger, c_{-k\downarrow}, -c_{-k\uparrow})$, the Hamiltonian can be written

$$\mathcal{H} = \frac{1}{2N} \sum_k c_k^\dagger \begin{pmatrix} \xi_k & \cdot & -\Delta_k^{\uparrow\downarrow} & \cdot \\ \cdot & \xi_k & \cdot & -\Delta_{-k}^{\uparrow\downarrow} \\ -(\Delta_k^{\uparrow\downarrow})^* & \cdot & -\xi_k & \cdot \\ \cdot & -(\Delta_{-k}^{\uparrow\downarrow})^* & \cdot & -\xi_k \end{pmatrix} c_k, \quad (4.66)$$

if one neglects the constant that comes from using the anticommutation relation. For simplicity, assume $\varepsilon_{-k} = \varepsilon_k$ and $\Delta_k^{\uparrow\downarrow} = \Delta_{-k}^{\uparrow\downarrow}$. Let

4. There are two different conventions when defining the 4-tuples of creation and annihilation operators in relation to superconductivity, and in my work I have used both. The other alternative is $c_k^\dagger = (c_{k\uparrow}^\dagger, c_{k\downarrow}^\dagger, c_{-k\uparrow}, c_{-k\downarrow})$. The advantage of this is that the 4-tuple looks more symmetric. On the other hand, the one I use in the main text results in different and possibly more intuitive Green's functions.

$\tau_z = \text{diag}(1, 1, -1, -1)$ be the third Pauli matrix in Nambu-space. The retarded and advanced Green's function matrices in the superconducting system, which includes the anomalous Green's functions, are defined as

$$\hat{G}_{k_1 k_2}^R(t, t') = -\frac{i}{N} \tau_z \theta(t - t') \langle [c_{k_1}(t) c_{k_2}^\dagger(t')]_+ \rangle, \quad (4.67a)$$

$$\hat{G}_{k_1 k_2}^A(t, t') = +\frac{i}{N} \tau_z \theta(t' - t) \langle [c_{k_1}(t) c_{k_2}^\dagger(t')]_+ \rangle. \quad (4.67b)$$

Let $\hat{\Delta} = \text{antidiag}(\Delta_k^{\uparrow\downarrow} \sigma_0, -[\Delta_k^{\uparrow\downarrow}]^* \sigma_0)$, where σ_0 is the 2×2 identity matrix. From above, and as will be more explicitly shown in chapter 6, these Green's functions solve

$$i\tau_z \frac{\partial}{\partial t} \hat{G}_{kk'}^{R/A}(t, t') - (\xi_k - \hat{\Delta}) \hat{G}_{kk'}^{R/A}(t, t') = \delta_{kk'} \delta(t - t'). \quad (4.68)$$

Fourier transforming in relative time, the equation becomes

$$[\tau_z(\varepsilon \pm i\delta) - \xi_k + \hat{\Delta}] \hat{G}_{kk'}^{R/A}(\varepsilon) = \delta_{kk'}, \quad (4.69)$$

where I have added the infinitesimal δ , which is the same as η above. Hence,

$$\begin{aligned} \hat{G}_{kk'}^{R/A}(\varepsilon) &= \delta_{kk'} [\tau_z(\varepsilon \pm i\delta) - \xi_k + \hat{\Delta}]^{-1} \\ &= \delta_{kk'} \frac{\tau_z(\varepsilon \pm i\delta) + \xi_k + \hat{\Delta}}{(\varepsilon \pm i\delta)^2 - \xi_k^2 - |\Delta_k^{\uparrow\downarrow}|^2}. \end{aligned} \quad (4.70)$$

The full Green's functions,

$$\hat{G}_{kk'}^{R/A}(\varepsilon) = \begin{pmatrix} G_{kk'}^{R/A}(\varepsilon) & F_{kk'}^{R/A}(\varepsilon) \\ -[F_{kk'}^{R/A}(-\varepsilon)]^* & [G_{kk'}^{R/A}(-\varepsilon)]^* \end{pmatrix}, \quad (4.71)$$

contain both the normal Green's functions, $G_{kk'}^{R/A}$, and the anomalous Green's functions, $F_{kk'}^{R/A}$. The anomalous Green's function gives a self-consistency equation for the gap parameter $\Delta_k^{\uparrow\downarrow}$, since, from section 3.3,⁵

$$\begin{aligned} \Delta_k^{\uparrow\downarrow}(t) &= -N \sum_{k_2} V_{(k_2-k_1)k_1(-k_1)} \langle c_{-k_2\sigma_2}(t) c_{k_2\sigma_1}(t) - c_{-k_2\sigma_1}(t) c_{k_2\sigma_2}(t) \rangle \\ &= i \sum_{k_2} N^2 V_{(k_2-k_1)k_1(-k_1)} \text{Tr}[F_{k_2 k_2}^<](t, t). \end{aligned} \quad (4.72)$$

5. Compared to section 3.3, there is an extra factor of N here. This is because of how I defined the Hamiltonian here.

To obtain the spectral function, and thereby the density of states, we only need the normal Green's function,

$$G_{kk'}^{R/A}(\varepsilon) = \delta_{kk'} \sigma_0 \frac{\varepsilon \pm i\delta + \xi_k}{(\varepsilon \pm i\delta)^2 - \xi_k^2 - |\Delta_k^{\uparrow\downarrow}|^2}. \quad (4.73)$$

The spectral function is

$$A_{kk'}(\varepsilon) = i[G_{kk'}^R(\varepsilon) - G_{kk'}^A(\varepsilon)] = \frac{2\delta [|\Delta_k^{\uparrow\downarrow}|^2 + (\varepsilon + \xi_k)^2 + \delta^2]}{4\varepsilon^2\delta^2 + (\varepsilon^2 - |\Delta_k^{\uparrow\downarrow}|^2 - \delta^2 - \xi_k^2)^2}. \quad (4.74)$$

As explained above, $A_{kk}(\varepsilon)/2\pi$ is how much of the state with crystal momentum k -state that has energy in the energy-interval $(\varepsilon, \varepsilon + d\varepsilon)$. Therefore, the density of states in the energy-interval $(\varepsilon, \varepsilon + d\varepsilon)$ is

$$\begin{aligned} N(\varepsilon) &= \sum_k \frac{A_{kk}(\varepsilon)}{2\pi} \\ &= \lim_{\delta \rightarrow 0} \int_{-\infty}^{\infty} \frac{d\xi}{\pi} N_0(\xi) \frac{[|\Delta_k^{\uparrow\downarrow}|^2 + (\varepsilon + \xi)^2 + \delta^2] \delta}{4\varepsilon^2\delta^2 + (\varepsilon^2 - |\Delta_k^{\uparrow\downarrow}|^2 - \delta^2 - \xi^2)^2} \end{aligned} \quad (4.75)$$

where

$$N_0(E) = \sum_k \delta(\xi_k - E) \quad (4.76)$$

is the normal state density of states. As $\delta \rightarrow 0$, the integrand in equation (4.75) becomes zero at all points except at $\xi^2 = \varepsilon^2 - |\Delta_k^{\uparrow\downarrow}|^2$, where it blows up to infinity. When $\varepsilon^2 - |\Delta_k^{\uparrow\downarrow}|^2 < 0$, the integrand goes to zero everywhere, so $N(\varepsilon) = 0$ when $|\varepsilon| < |\Delta_k^{\uparrow\downarrow}|$. For $|\varepsilon| > |\Delta_k^{\uparrow\downarrow}|$, we can use that the integral of the Cauchy distribution is one. That is,

$$\int_{-\infty}^{\infty} \frac{dx}{\pi} \frac{\gamma}{\gamma^2 + (x - x_0)^2} = 1, \quad (4.77)$$

for arbitrary γ and x_0 , which define the width and center of the Cauchy distribution, respectively. By splitting the integral into positive and negative ξ and define $x = \xi^2$, one can write

$$N(\varepsilon) = I_+ + I_-, \quad (4.78)$$

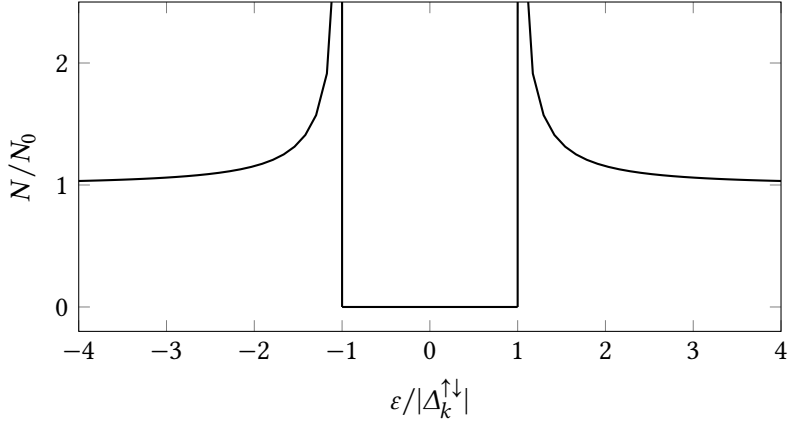


Figure 4.1: The density of states for a bulk superconductor, where N_0 is evaluated at energy $\sqrt{\varepsilon^2 - |\Delta_k^{\uparrow\downarrow}|^2}$.

where

$$I_{\pm} = \lim_{\delta \rightarrow 0} \int_0^{\infty} \frac{dx}{2\pi\sqrt{x}} N_0(\pm\sqrt{x}) \frac{[|\Delta_k^{\uparrow\downarrow}|^2 + (\varepsilon \pm \sqrt{x})^2] \delta}{4\varepsilon^2\delta^2 + [x - (\varepsilon^2 - |\Delta_k^{\uparrow\downarrow}|^2)]^2} \quad (4.79)$$

As $\delta \rightarrow 0$, the integrand becomes increasingly more like a Cauchy distribution with center at $x_0 = (\varepsilon^2 - |\Delta_k^{\uparrow\downarrow}|^2)$ and width $2\varepsilon\delta$. Hence, we can set $x = x_0$ everywhere except the denominator.

Using that $|\Delta_k^{\uparrow\downarrow}|^2 + (\varepsilon \pm \sqrt{x_0})^2 = 2\varepsilon(\varepsilon \pm \sqrt{x_0})$, I get that

$$\begin{aligned} I_{\pm} &= \frac{N_0(\pm\sqrt{x_0})(\varepsilon \pm \sqrt{x_0})}{2\sqrt{x_0}} \lim_{\delta \rightarrow 0} \int_0^{\infty} \frac{dx}{\pi} \frac{2\varepsilon\delta}{(2\varepsilon\delta)^2 + (x - x_0)^2} \\ &= \frac{N_0(\pm\sqrt{x_0})(\varepsilon \pm \sqrt{x_0})}{2\sqrt{x_0}}. \end{aligned} \quad (4.80)$$

If we assume that $N_0(-\sqrt{x_0}) = N_0(\sqrt{x_0})$, then, for $|\varepsilon| > |\Delta_k^{\uparrow\downarrow}|$,

$$N(\varepsilon) = I_+ + I_- = N_0\left(\sqrt{\varepsilon^2 - |\Delta_k^{\uparrow\downarrow}|^2}\right) \frac{\varepsilon}{\sqrt{\varepsilon^2 - |\Delta_k^{\uparrow\downarrow}|^2}}. \quad (4.81)$$

Combining the results, the density of states in a superconductor is

$$N(\varepsilon) = \begin{cases} 0 & \text{if } |\varepsilon| < |\Delta_k^{\uparrow\downarrow}|, \\ N_0\left(\sqrt{\varepsilon^2 - |\Delta_k^{\uparrow\downarrow}|^2}\right) \frac{\varepsilon}{\sqrt{\varepsilon^2 - |\Delta_k^{\uparrow\downarrow}|^2}} & \text{if } |\varepsilon| > |\Delta_k^{\uparrow\downarrow}|, \end{cases} \quad (4.82)$$

which is illustrated in figure 4.1. As we can see, there is a gap in the spectrum equal to $2|\Delta_k^{\uparrow\downarrow}|$, which is why $|\Delta_k^{\uparrow\downarrow}|$ is often called the gap parameter.

Green's Function Perturbation Theory

For a system out of equilibrium, determining the lesser Green's function is more difficult. However, one can often compute approximate Green's functions through perturbation theory. In this chapter, I show some perturbation techniques that have been central in my work. I also provide examples that are relevant to my work and to the next chapter.

First, I consider a general approach that is applicable as long as the Hamiltonian is quadratic. This approach is similar to the linear response discussed above, but it is valid to all orders in the perturbation. It relies on the fact that the retarded and advanced Green's functions are in fact Green's functions in the mathematical sense. The end result is the Dyson equations [114], and as an example of this perturbation theory, I consider elastic impurity scattering.

Next, I consider another more general approach to perturbation theory. This is based on the interaction picture of quantum mechanics and is applicable to perturbations of any order, not only quadratic perturbations. I used this approach in the project on spin-pumping (paper VI), where the perturbation is linear in creation and annihilation operators. As an example, I use this approach to consider dissipation through interactions with an open environment. This leads to the relaxation time approximation, which is heavily used in the projects related to quasiclassical Green's functions.

5.1 Quadratic Hamiltonians

Consider a system with an Hamiltonian which is quadratic in annihilation operators,

$$\mathcal{H}(t) = \frac{1}{2} \sum_{\lambda, \mu=1}^N \left(M_{\lambda\mu}(t) c_{\lambda}^{\dagger} c_{\mu} \mp M_{\lambda\mu}^*(t) c_{\lambda} c_{\mu}^{\dagger} + \Delta_{\lambda\mu}(t) c_{\lambda}^{\dagger} c_{\mu}^{\dagger} \mp \Delta_{\lambda\mu}^*(t) c_{\lambda} c_{\mu} \right). \quad (5.1)$$

In this case, we know from above that the vector of annihilation and creation operators, c , satisfies

$$\left[i\tau_z \frac{d}{dt} - A(t) \right] c = 0, \quad (5.2)$$

where $\tau_z = \text{diag}(1, \dots, 1, -1, \dots, -1)$ and

$$A = \begin{pmatrix} M & \Delta \\ \Delta^* & M^* \end{pmatrix}. \quad (5.3)$$

The retarded and advanced Green's functions are also Green's functions in the mathematical sense, so they solve

$$\left[i\tau_z \frac{d}{dt} - A(t) \right] \hat{G}^X(t, t') = \delta(t - t'), \quad (5.4)$$

where X is either R or A .

I define A_0 , V and c_0 such that

$$A = A_0 + V, \quad (5.5)$$

and c_0 is the solution to

$$\left[i\tau_z \frac{\partial}{\partial t} - A_0(t) \right] c_0 = 0. \quad (5.6)$$

Let \hat{G}_0^R , \hat{G}_0^A and $\hat{G}_0^<$ be the corresponding Green's functions. In applications, A_0 might be time-independent or simple enough for c_0 to be analytically solvable, while V might be a perturbation that is assumed small. Let the tuple of annihilation and creation operators be $c = c_0 + d$. By inserting this into equation (5.2), I get

$$\left[i\tau_z \frac{\partial}{\partial t} - A(t) \right] d(t) = V(t)c_0(t) \quad (5.7)$$

Hence, using the mathematical Green's function properties of \hat{G}^R and \hat{G}^A ,

$$d(t) = \int_{-\infty}^{\infty} d\tilde{t} \hat{G}^R(t, \tilde{t}) V(\tilde{t}) c_0(\tilde{t}), \quad (5.8a)$$

$$d^\dagger(t) = \int_{-\infty}^{\infty} d\tilde{t} c_0^\dagger(\tilde{t}) V(\tilde{t}) \hat{G}^A(\tilde{t}, t). \quad (5.8b)$$

Inserting this into the definition of $\hat{G}^<$,

$$\hat{G}_{\lambda\mu}^<(t, t') = \pm i \left\langle [c_0^\dagger(t') + d^\dagger(t')]_\mu [c_0(t) + d(t)]_\lambda \right\rangle, \quad (5.9)$$

one gets

$$\begin{aligned}
\hat{G}^<(t, t') &= \hat{G}_0^<(t, t') + \int_{-\infty}^{\infty} d\tilde{t} \hat{G}^R(t, \tilde{t}) V(\tilde{t}) G_0^<(\tilde{t}, t') \\
&+ \int_{-\infty}^{\infty} d\tilde{t} \hat{G}_0^<(t, \tilde{t}) V(\tilde{t}) \hat{G}^A(\tilde{t}, t') \\
&+ \int_{-\infty}^{\infty} dt_1 \int_{-\infty}^{\infty} dt_2 \hat{G}^R(t, t_1) V(t_1) \hat{G}_0^<(t_1, t_2) V(t_2) \hat{G}^A(t_2, t'). \quad (5.10)
\end{aligned}$$

This notation can be simplified by using the circle product,

$$(A \circ B)(t, t') = \int_{-\infty}^{\infty} d\tilde{t} A(t, \tilde{t}) B(\tilde{t}, t'), \quad (5.11)$$

and defining $\Sigma(t, t') = V(t)\delta(t - t')$, such that

$$\hat{G}^< = \hat{G}_0^< + \hat{G}^R \circ \Sigma \circ \hat{G}_0^< + \hat{G}_0^< \circ \Sigma \circ \hat{G}^A + \hat{G}^R \circ \Sigma \circ \hat{G}_0^< \circ \Sigma \circ \hat{G}^A. \quad (5.12)$$

Hence, to first order in V one can immediately see that

$$\hat{G}^< = \hat{G}_0^< + \hat{G}_0^R \circ \Sigma \circ \hat{G}_0^< + \hat{G}_0^< \circ \Sigma \circ \hat{G}_0^A. \quad (5.13)$$

When $\hat{G}_0^<$, \hat{G}_0^R and \hat{G}_0^A are all known, equation (5.13) gives a convenient way to compute the first order correction to the lesser Green's function in the presence of a perturbation.

For the higher order components, one can derive similar relations between \hat{G}^R , \hat{G}^A , \hat{G}_0^R and \hat{G}_0^A . This can be done using equation (4.6). That is,

$$-\frac{\partial \hat{G}_0^X(t, t')}{\partial t'} i\tau_z - \hat{G}_0^X(t, t') A_0(t') = \delta(t - t'), \quad (5.14)$$

where $X \in \{R, A\}$. Hence, if $Y \in \{R, A\}$, and $t \neq t'$

$$\begin{aligned}
\hat{G}_0^X(t, t') &= \int_{-\infty}^{\infty} d\tilde{t} \hat{G}_0^X(t, \tilde{t}) \left[i\tau_z \frac{\partial}{\partial \tilde{t}} - A(\tilde{t}) \right] \hat{G}_0^Y(\tilde{t}, t') \\
&= \left[\hat{G}_0^X(t, \tilde{t}) i\tau_z \hat{G}_0^Y(\tilde{t}, t') \right]_{-\infty}^{\infty} \\
&+ \int_{-\infty}^{\infty} d\tilde{t} \left[-\frac{\partial \hat{G}_0^X(t, \tilde{t})}{\partial \tilde{t}} i\tau_z - \hat{G}_0^X(t, \tilde{t}) A_0(\tilde{t}) \right] \hat{G}_0^Y(\tilde{t}, t') - \left[\hat{G}_0^X \circ \Sigma \circ \hat{G}_0^Y \right](t, t') \\
&= \left[\hat{G}_0^X(t, \tilde{t}) i\tau_z \hat{G}_0^Y(\tilde{t}, t') \right]_{-\infty}^{\infty} + \hat{G}^Y(t, t') - \left[\hat{G}_0^X \circ \Sigma \circ \hat{G}_0^Y \right](t, t'). \quad (5.15)
\end{aligned}$$

If $X = Y$, the first term on the right-hand side is zero because of the step functions in the definitions of the retarded and advanced Green's functions. Hence,

$$\hat{G}^X = \hat{G}_0^X + \hat{G}_0^X \circ \Sigma \circ \hat{G}^X. \quad (5.16)$$

By symmetry, considering $-V$ as a perturbation to $A_0 + V$, or by doing a similar derivation as above, one also gets

$$\hat{G}^X = \hat{G}_0^X + \hat{G}^X \circ \Sigma \circ \hat{G}_0^X. \quad (5.17)$$

These equations are known as Dyson equations. One can insert these equations recursively into the equation for $\hat{G}^<$ to obtain

$$\hat{G}^< = \sum_{n,m=0}^{\infty} (\hat{G}_0^{R\circ})^n \hat{G}_0^< (\circ\hat{G}_0^A)^m, \quad (5.18)$$

where $(\hat{G}_0^{R\circ})^0 = (\circ\hat{G}_0^A)^0 = 1$. Note that this is the same series as one would get by recursive insertion of the right-hand sides of

$$\hat{G}^< = \hat{G}_0^< + \hat{G}_0^R \circ \Sigma \circ \hat{G}^< + \hat{G}_0^< \circ \Sigma \circ \hat{G}^A, \quad (5.19a)$$

$$\hat{G}^< = \hat{G}_0^< + \hat{G}^R \circ \Sigma \circ \hat{G}_0^< + \hat{G}^< \circ \Sigma \circ \hat{G}_0^A. \quad (5.19b)$$

Therefore, assuming that the series converges, equation (5.19) must also hold. Equations (5.16), (5.17) and (5.19) can be combined by writing

$$\begin{pmatrix} \hat{G}^R & \hat{G}^< \\ & \hat{G}^A \end{pmatrix} = \begin{pmatrix} \hat{G}_0^R & \hat{G}_0^< \\ & \hat{G}_0^A \end{pmatrix} + \begin{pmatrix} \hat{G}_0^R & \hat{G}_0^< \\ & \hat{G}_0^A \end{pmatrix} \circ \Sigma \circ \begin{pmatrix} \hat{G}^R & \hat{G}^< \\ & \hat{G}^A \end{pmatrix}, \quad (5.20a)$$

$$\begin{pmatrix} \hat{G}^R & \hat{G}^< \\ & \hat{G}^A \end{pmatrix} = \begin{pmatrix} \hat{G}_0^R & \hat{G}_0^< \\ & \hat{G}_0^A \end{pmatrix} + \begin{pmatrix} \hat{G}^R & \hat{G}^< \\ & \hat{G}^A \end{pmatrix} \circ \Sigma \circ \begin{pmatrix} \hat{G}_0^R & \hat{G}_0^< \\ & \hat{G}_0^A \end{pmatrix}. \quad (5.20b)$$

With this one can calculate the Green's functions and thereby calculate observables in systems that are out of equilibrium. However, this method only works if the Hamiltonian is quadratic in creation and annihilation operators. This is not always the case. For instance, in paper VI about spin-pumping in antiferromagnet/superconductor bilayers, the external rotating magnetic field gives rise to a linear term in the Hamiltonian. Moreover, as we have seen in previous chapters, electron-electron interactions will give rise to quartic terms, which are

also not covered by the method presented above. For such situations, one can use a more versatile approach based on the interaction picture of quantum mechanics.¹

The analogous derivation for $\hat{G}^>$ gives the same result as equation (5.20), but with $\hat{G}^>$ instead of $\hat{G}^<$. Therefore, one can also write down the Dyson equations for the Keldysh Green's function, $\hat{G}^K = \hat{G}^< + \hat{G}^>$. That is, if

$$\check{G} = \begin{pmatrix} \hat{G}^R & \hat{G}^K \\ & \hat{G}^A \end{pmatrix}, \quad (5.21)$$

it is also true that

$$\check{G} = \check{G}_0 + \check{G}_0 \circ \Sigma \circ \check{G}, \quad (5.22a)$$

$$\check{G} = \check{G}_0 + \check{G} \circ \Sigma \circ \check{G}_0. \quad (5.22b)$$

Finally, note that the same derivation also works in the other direction. That is, if

$$\left[i\tau_z \frac{\partial}{\partial t} - A_0(t) \right] \check{G}_0(t, t') = \delta(t - t') \quad (5.23)$$

and

$$\check{G} = \check{G}_0 + \check{G}_0 \circ \Sigma \circ \check{G}, \quad (5.24)$$

then inserting $\check{G}_0 = \check{G} - \check{G}_0 \circ \Sigma \circ \check{G}$ into equation (5.23) yields

$$\left[i\tau_z \frac{\partial}{\partial t} - A_0(t) \right] \check{G}(t, t') - [\Sigma \circ \check{G}](t, t') = \delta(t - t'). \quad (5.25)$$

That is, by identifying a self-energy through the Dyson equation, one can derive a differential equation for the Green's function. This is especially useful in the context of impurity scattering (section 5.1.1), where equation (5.25) allows us to get an equation for the impurity-averaged Green's function.

1. Note that this also does not cover everything. Superconductivity comes from an attractive electron-electron interaction manifesting as a quartic term in the Hamiltonian. However, perturbative approaches such as those presented in section 5.2 are incapable of reproducing the superconducting state because it is separated from the normal state by a phase transition.

5.1.1 Example: Impurity scattering

Consider a fermionic lattice model. On each lattice point, there might be multiple degrees of freedom, such as spin or orbital degrees of freedom. Assuming there are N such degrees of freedom, I collect them into a vector of creation and annihilation operators, such that for lattice point i

$$c_i^\dagger = \begin{pmatrix} c_{i1}^\dagger & c_{i2}^\dagger & \cdots & c_{iN}^\dagger & c_{i1} & c_{i2} & \cdots & c_{iN} \end{pmatrix}, \quad (5.26)$$

where $c_{i\lambda}$ annihilates a state λ on lattice site i . A general quadratic Hamiltonian can then be written

$$\mathcal{H} = \frac{1}{2} \sum_{ij} c_i^\dagger M_{ij} c_j. \quad (5.27)$$

I collect the degrees of freedom associated with each lattice point in the Green's functions, such that the retarded, advanced, and Keldysh Green's functions associated with lattice sites i and j are

$$\hat{G}_{ij}^R(t, t') = -i\theta(t - t') \left\langle \left[c_i(t), c_j^\dagger(t') \right]_+ \right\rangle \quad (5.28a)$$

$$\hat{G}_{ij}^A(t, t') = +i\theta(t' - t) \left\langle \left[c_i(t), c_j^\dagger(t') \right]_+ \right\rangle \quad (5.28b)$$

$$\hat{G}_{ij}^K(t, t') = -i \left\langle \left[c_i(t), c_j^\dagger(t') \right]_- \right\rangle, \quad (5.28c)$$

where the commutators of two vectors A and B^\dagger is a matrix given by

$$\left([A, B^\dagger]_\pm \right)_{ij} = [A_i, B_j^\dagger]_\pm. \quad (5.29)$$

Again, I also collect these in a larger $4N \times 4N$ matrix,

$$\check{G}_{ij} = \begin{pmatrix} \hat{G}_{ij}^R & \hat{G}_{ij}^K \\ & \hat{G}_{ij}^A \end{pmatrix}. \quad (5.30)$$

This Green's function solves the equation

$$i\tau_z \frac{\partial}{\partial t} \check{G}_{ij}(t, t') - \sum_k \tau_z M_{ik}(t) \check{G}_{kj}(t, t') = \delta(t - t') \delta_{ij}, \quad (5.31)$$

where I use the convention that the multiplication of two matrices of different sizes means that the smaller is promoted to the size of the larger through a tensor product with a unity matrix.

Next, assume that there are N_{imp} impurities, where impurity i is located on lattice site number r_i and gives rise to an energy term in the Hamiltonian equal to $c_i^\dagger U_i c_i$, where U_i is a matrix. This means that

$$\tau_z M(t) = \tau_z M_0(t) + \tau_z V_{\text{imp}} \quad (5.32)$$

where

$$[\tau_z V_{\text{imp}}]_{ij} = \delta_{ij} \sum_{k=1}^{N_{\text{imp}}} \begin{pmatrix} U_k & \\ & U_k^* \end{pmatrix} \delta_{ir_k}. \quad (5.33)$$

Computing the Green's function for any single impurity configuration is difficult because it depends on the specific location of each impurity. However, computing this configuration-specific Green's function is often not necessary. Instead of estimating results for observables that are specific to a given impurity configuration, we are instead interested in impurity-averaged observables. In fact, impurity averaging can often be imposed by the physical properties of the system itself. This is because of so-called *self-averaging* occurring due to inelastic scattering [114]. Each inelastic scattering changes the electron phase by a small random amount, giving rise to a finite coherence length for the electrons. As a result, measuring observables is effectively like measuring an incoherent average of subsystems with a size given by the coherence length. Even if the system is smaller than the coherence length, such that no self-averaging takes place, it is simpler and often more desirable to solve for impurity-averaged quantities, as the precise impurity configuration of a sample is difficult to determine. An exception is systems with engineered impurities.

I define the impurity-average as

$$\langle A \rangle_{\text{imp}} = \sum_{\{r_i\}} \int d\{U_i\} p(\{r_i, U_i\}) A(\{r_i, U_i\}), \quad (5.34)$$

where $p(\{r_i, U_i\})$ is the probability that the impurities are located at $\{r_i\}$ with impurity strengths $\{U_i\}$. Let O be an observable. Of particular interest are observables that are linear functionals of the Keldysh Green's function,

$$O(t) = \sum_{ij} \text{Tr}[B_{ij}(t) \hat{G}_{ij}^K(t, t)], \quad (5.35)$$

for some set of matrices B_{ij} that do not depend on the impurity configuration. The impurity-averaged observable can be computed from the impurity averaged Green's function,

$$\begin{aligned} \langle O(t) \rangle_{\text{imp}} &= \left\langle \sum_{ij} \text{Tr} \left[B_{ij}(t) \hat{G}_{ij}^K(t, t) \right] \right\rangle_{\text{imp}} \\ &= \sum_{ij} \text{Tr} \left[B_{ij}(t) \langle \hat{G}_{ij}^K \rangle_{\text{imp}}(t, t) \right]. \end{aligned} \quad (5.36)$$

In order to derive an equation for the impurity-averaged Green's function, I first relate the impurity-averaged Green's function to the Green's function in the absence of impurities through the Dyson equations. This will give an effective impurity self-energy term Σ_{imp} through

$$\langle \check{G} \rangle_{\text{imp}} = \check{G}_0 + \check{G}_0 \circ \Sigma_{\text{imp}} \circ \langle \check{G} \rangle_{\text{imp}}, \quad (5.37)$$

where \check{G}_0 is the Green's function in the absence of impurities, solving

$$i\tau_z \frac{\partial}{\partial t} \check{G}_0(t, t') - \tau_z M_0(t) \check{G}_0(t, t') = \delta(t - t'). \quad (5.38)$$

Using equation (5.25) then gives us that the impurity-averaged Green's function solves

$$\begin{aligned} i\tau_z \frac{\partial}{\partial t} \langle \check{G} \rangle_{\text{imp}}(t, t') - \tau_z M_0(t) \langle \check{G} \rangle_{\text{imp}} \\ - \left[\Sigma_{\text{imp}} \circ \langle \check{G} \rangle_{\text{imp}} \right](t, t') = \delta(t - t'). \end{aligned} \quad (5.39)$$

Let \check{G}_0 be the Green's function in the absence of impurities and let $\Sigma(t, t') = \tau_z V_{\text{imp}} \delta(t - t')$. In this case, the Dyson equations become

$$\check{G} = \check{G}_0 + \check{G}_0 \circ \Sigma \circ \check{G}, \quad (5.40a)$$

$$\check{G} = \check{G}_0 + \check{G} \circ \Sigma \circ \check{G}_0. \quad (5.40b)$$

Next, I take the impurity average of equation (5.40b), yielding

$$\langle \check{G} \rangle_{\text{imp}} = \check{G}_0 + \langle \check{G} \circ \Sigma \rangle_{\text{imp}} \circ \check{G}_0. \quad (5.41)$$

Inserting equation (5.40a), I get

$$\langle \check{G} \rangle_{\text{imp}} = \check{G}_0 + \check{G}_0 \circ \left(\langle \Sigma \rangle_{\text{imp}} + \langle \Sigma \circ \check{G} \circ \Sigma \rangle_{\text{imp}} \right) \circ \check{G}_0. \quad (5.42)$$

In order to arrive at equation (5.37), I must express the rightmost \check{G}_0 in terms of $\langle \check{G} \rangle_{\text{imp}}$. This can be done by multiplying equation (5.41) from the left with $\sum_{n=0}^{\infty} (-\langle \check{G} \circ \Sigma \rangle_{\text{imp}})^n$, where the power series must be interpreted in the terms of the circle product, and using that

$$\left[\sum_{n=0}^{\infty} (-\langle \check{G} \circ \Sigma \rangle_{\text{imp}})^n \right] \circ [1_{\circ} + \langle \check{G} \circ \Sigma \rangle_{\text{imp}}] = 1_{\circ}, \quad (5.43)$$

where 1_{\circ} is the circle product identity satisfying $1_{\circ} \circ A = A$ for all A . That is, $1_{\circ}(t, t') = \delta(t - t')$. Combining this with equation (5.41) I get

$$\check{G}_0 = \left[\sum_{n=0}^{\infty} (-\langle \check{G} \circ \Sigma \rangle_{\text{imp}})^n \right] \circ \langle \check{G} \rangle_{\text{imp}}. \quad (5.44)$$

Inserting equation (5.44) into equation (5.42) I finally get

$$\begin{aligned} \langle \check{G} \rangle_{\text{imp}} = \check{G}_0 + \check{G}_0 \circ (\langle \Sigma \rangle_{\text{imp}} + \langle \Sigma \circ \check{G} \circ \Sigma \rangle_{\text{imp}}) \\ \circ \left[\sum_{n=0}^{\infty} (-\langle \check{G} \circ \Sigma \rangle_{\text{imp}})^n \right] \circ \langle \check{G} \rangle_{\text{imp}}. \end{aligned} \quad (5.45)$$

Comparing with equation (5.37), the impurity self-energy can be identified as

$$\Sigma_{\text{imp}} = (\langle \Sigma \rangle_{\text{imp}} + \langle \Sigma \circ \check{G} \circ \Sigma \rangle_{\text{imp}}) \circ \left[\sum_{n=0}^{\infty} (-\langle \check{G} \circ \Sigma \rangle_{\text{imp}})^n \right]. \quad (5.46)$$

I am interested in the self-energy to second order in Σ , so I can use that $\check{G} = \check{G}_0 + \mathcal{O}(\Sigma) = \langle \check{G} \rangle_{\text{imp}} + \mathcal{O}(\Sigma)$. Therefore, to second order in Σ ,

$$\Sigma_{\text{imp}} = \langle \Sigma \rangle_{\text{imp}} + \langle \Sigma \circ \langle \check{G} \rangle_{\text{imp}} \circ \Sigma \rangle_{\text{imp}} - \langle \Sigma \rangle_{\text{imp}} \circ \langle \check{G} \rangle_{\text{imp}} \circ \langle \Sigma \rangle_{\text{imp}}. \quad (5.47)$$

This is known as the self-consistent Born approximation [190, 191].

Since $\Sigma(t, t') = \tau_z V_{\text{imp}} \delta(t - t')$, the first order term is

$$\begin{aligned} \langle \Sigma_{ij} \rangle_{\text{imp}}(t, t') &= \left\langle \delta_{ij} \sum_{k=1}^{N_{\text{imp}}} \begin{pmatrix} U_k & \\ & U_k^* \end{pmatrix} \delta_{i r_k} \right\rangle_{\text{imp}} \delta(t - t') \\ &= \delta_{ij} n_i \left(\langle U \rangle_{\text{imp}} \quad \langle U \rangle_{\text{imp}}^* \right) \delta(t - t'). \end{aligned} \quad (5.48)$$

where I assumed that all impurity locations are distributed equally in space, such that the impurity density $n_i = N_{\text{imp}} \langle \delta_{k r_i} \rangle_{\text{imp}}$ is independent

of impurity number k . I also defined the average impurity potential as $\langle U \rangle_{\text{imp}} = \sum_{k=1}^{N_{\text{imp}}} \langle U_k \rangle_{\text{imp}} / N_{\text{imp}}$. I do not assume that the impurities have the same distributions. For instance, the impurities can have different matrix structures. They can be magnetic with different magnetization orientations, or they can be located on different sublattices, for instance.

I assume that the impurities are independent, such that $\langle U_i U_j \rangle_{\text{imp}} = \langle U_i \rangle_{\text{imp}} \langle U_j \rangle_{\text{imp}}$ and $\langle \delta_{kr_i} \delta_{kr_j} \rangle_{\text{imp}} = \langle \delta_{kr_i} \rangle_{\text{imp}} \langle \delta_{kr_j} \rangle_{\text{imp}}$ when $i \neq j$. This simplifies the second-order term, since it means that

$$\begin{aligned}
& \left\langle \left(\Sigma \circ \langle \check{G} \rangle_{\text{imp}} \circ \Sigma \right)_{ij} \right\rangle_{\text{imp}} \\
&= \left\langle \sum_{n=1}^{N_{\text{imp}}} \sum_{m=1}^{N_{\text{imp}}} \begin{pmatrix} U_n & \\ & U_n^* \end{pmatrix} \delta_{ir_n} \langle \check{G}_{ij} \rangle_{\text{imp}} \begin{pmatrix} U_m & \\ & U_m^* \end{pmatrix} \delta_{jr_m} \right\rangle_{\text{imp}} \\
&= \left\langle \sum_{n=1}^{N_{\text{imp}}} \begin{pmatrix} U_n & \\ & U_n^* \end{pmatrix} \delta_{ir_n} \right\rangle_{\text{imp}} \langle \check{G}_{ij} \rangle_{\text{imp}} \left\langle \sum_{m \neq n} \begin{pmatrix} U_m & \\ & U_m^* \end{pmatrix} \delta_{jr_m} \right\rangle_{\text{imp}} \\
&\quad + \left\langle \sum_{n=1}^{N_{\text{imp}}} \begin{pmatrix} U_n & \\ & U_n^* \end{pmatrix} \delta_{ir_n} \langle \check{G}_{ij} \rangle_{\text{imp}} \begin{pmatrix} U_n & \\ & U_n^* \end{pmatrix} \delta_{jr_n} \right\rangle_{\text{imp}}. \quad (5.49)
\end{aligned}$$

The first term on the right-hand side is almost equal to the last term in equation (5.47). That is,

$$\begin{aligned}
& \left\langle \left(\Sigma \circ \langle \check{G} \rangle_{\text{imp}} \circ \Sigma \right)_{ij} \right\rangle_{\text{imp}} - \left(\langle \Sigma \rangle_{\text{imp}} \circ \langle \check{G} \rangle_{\text{imp}} \circ \langle \Sigma \rangle_{\text{imp}} \right)_{ij} \\
&= \left\langle \sum_{n=1}^{N_{\text{imp}}} \begin{pmatrix} U_n & \\ & U_n^* \end{pmatrix} \delta_{ir_n} \langle \check{G}_{ij} \rangle_{\text{imp}} \begin{pmatrix} U_n & \\ & U_n^* \end{pmatrix} \delta_{jr_n} \right\rangle_{\text{imp}} \\
&\quad - \sum_{n=1}^{N_{\text{imp}}} \left\langle \begin{pmatrix} U_n & \\ & U_n^* \end{pmatrix} \delta_{ir_n} \right\rangle_{\text{imp}} \langle \check{G}_{ij} \rangle_{\text{imp}} \left\langle \begin{pmatrix} U_n & \\ & U_n^* \end{pmatrix} \delta_{jr_n} \right\rangle_{\text{imp}} \\
&= \delta_{ij} \frac{n_i}{N_{\text{imp}}} \sum_{n=1}^{N_{\text{imp}}} \left\langle \begin{pmatrix} U_n & \\ & U_n^* \end{pmatrix} \langle \check{G}_{ii} \rangle_{\text{imp}} \begin{pmatrix} U_n & \\ & U_n^* \end{pmatrix} \right\rangle_{\text{imp}} \\
&\quad - \frac{n_i n_j}{N_{\text{imp}}} \left(\langle U \rangle_{\text{imp}} \langle U \rangle_{\text{imp}}^* \right) \langle \check{G}_{ij} \rangle_{\text{imp}} \left(\langle U \rangle_{\text{imp}} \langle U \rangle_{\text{imp}}^* \right). \quad (5.50)
\end{aligned}$$

The last term can be neglected under the assumptions that $n_i \ll N_{\text{imp}}$ and $\langle \check{G}_{ij} \rangle_{\text{imp}}$ decays sufficiently quickly as a function of the relative distance between lattice points i and j .

To proceed, one must define the type of impurities under consideration. As a concrete example, consider non-magnetic impurities in a system with a sublattice degree of freedom, as in the antiferromagnetic systems considered in papers IX and X. In this case, half of the impurities are located on sublattice A , such that $U_n = \rho_A V_n$, where ρ_A is a diagonal matrix with ones for the elements corresponding to the A -lattice and zeroes for the remaining elements corresponding to the B -lattice. The strength of impurity n is real and equal to V_n . Similarly, if impurity n is located on the B -lattice, we have $U_n = \rho_B V_n$. I assume that V_n is distributed equally for impurities on the A and B sublattices. Note that $\langle U \rangle_{\text{imp}} = \langle V_n \rangle_{\text{imp}} / 2$ is scalar since $\rho_A + \rho_B = 1$. If the last term in equation (5.50) is neglected, I get that the impurity self-energy is

$$\begin{aligned} (\Sigma_{\text{imp}})_{ij}(t, t') &= \delta_{ij} \delta(t - t') \frac{n_i \langle V_n \rangle_{\text{imp}}}{2} \\ &+ \delta_{ij} \frac{n_i \langle V_n^2 \rangle_{\text{imp}}}{2} \left[\rho_A \langle \check{G}_{ij} \rangle_{\text{imp}}(t, t') \rho_A + \rho_B \langle \check{G}_{ij} \rangle_{\text{imp}}(t, t') \rho_B \right]. \end{aligned} \quad (5.51)$$

5.2 Interaction Picture and Time Ordering

The interaction picture is equivalent to the Heisenberg picture and Schrödinger picture, but with the time dependence being partially on the state vectors and partially on the operators. That is, the interaction picture can be viewed as a hybrid between the Heisenberg picture and the Schrödinger picture, which were described in section 2.2. As I will show in this section, the interaction picture is particularly useful in the context of perturbation theory.

Consider an expectation value in the Schrödinger picture,

$$\langle A \rangle_{\psi}(t) = \langle \psi_S(t) | A_S(t) | \psi_S(t) \rangle, \quad (5.52)$$

where $|\psi_S(t)\rangle$ solves the Schrödinger equation (2.10). Next, let the Hamiltonian in the Schrödinger picture be

$$\mathcal{H}_S(t) = \mathcal{H}_{0,S} + \mathcal{V}_S(t), \quad (5.53)$$

where I assume that $\mathcal{H}_{0,S}$ is time-independent, and define a time-evolution operator U_0 which solve

$$i\frac{\partial}{\partial t}U_0(t, t_0) = \mathcal{H}_{0,S}U_0(t, t_0) \quad (5.54)$$

with $U_0(t, t) = 1$. This would be the full time evolution operator if $\mathcal{V}_S = 0$. Inserting this into equation (5.52), I get

$$\begin{aligned} \langle A \rangle_{\psi}(t) &= \langle \psi_S(t) | U_0(t, t_0) U_0(t_0, t) A_S(t) U_0(t, t_0) U_0(t_0, t) | \psi_S(t) \rangle \\ &= \langle \psi_I(t) | A_I(t) | \psi_I(t) \rangle, \end{aligned} \quad (5.55)$$

where

$$|\psi_I(t)\rangle = U_0(t_0, t) |\psi_S(t)\rangle, \quad (5.56a)$$

$$A_I(t) = U_0(t_0, t) A_S(t) U_0(t, t_0). \quad (5.56b)$$

These are the state vector and the operator in the interaction picture, respectively. That is, operators in the interaction picture are defined the same as operators in the Heisenberg with $\mathcal{H} = \mathcal{H}_0$. On the other hand, the state vectors solve

$$\begin{aligned} i\frac{\partial}{\partial t} |\psi_I(t)\rangle &= \left[i\frac{\partial}{\partial t} U_0(t_0, t) \right] |\psi_S(t)\rangle + U_0(t_0, t) \left[i\frac{\partial}{\partial t} |\psi_S(t)\rangle \right], \\ &= -\mathcal{H}_{0,S} |\psi_I(t)\rangle + U_0(t_0, t) \mathcal{H}_S(t) U_0(t, t_0) |\psi_I(t)\rangle = \mathcal{V}_I(t) |\psi_I(t)\rangle, \end{aligned} \quad (5.57)$$

where I used that $U_0(t_0, t) \mathcal{H}_{S,0} U_0(t, t_0) = \mathcal{H}_{S,0}$, and where

$$\mathcal{V}_I(t) = U_0(t_0, t) \mathcal{V}_S(t) U_0(t, t_0), \quad (5.58)$$

for some choice of t_0 . The operator \mathcal{V}_I can be thought of as \mathcal{V}_S evaluated in the Heisenberg picture of the unperturbed system with $\mathcal{H}_S = \mathcal{H}_{0,S}$.

It is convenient to choose t_0 such that it is possible to determine a relevant ensemble of states at this time. Typically, this is most easily done if $\mathcal{V}_S(t)$ is zero at times before t_0 . In practice, one often assumes that $\lim_{t \rightarrow \infty} \mathcal{V}_S(t) = 0$ and let $t_0 \rightarrow -\infty$, which is also what I do here. In this case, the states $\lim_{t \rightarrow -\infty} \{ |\psi_I(t)\rangle \}$ can for example be assumed to be occupied according to the grand canonical ensemble with $\mathcal{H}_S = \mathcal{H}_{0,S}$ if one chooses $\lim_{t \rightarrow -\infty} |\psi_I(t)\rangle = |\psi_H\rangle$ to be the state vector in the Heisenberg picture.

It is also useful to define the *S-matrix* as the time evolution operator for state vectors in the interaction picture,

$$|\psi_I(t)\rangle = S(t, t_0)|\psi_I(t_0)\rangle. \quad (5.59)$$

Let

$$\langle A(t) \rangle_0 = \langle \psi_H | A_I(t) | \psi_H \rangle, \quad (5.60)$$

be the expectation value in the unperturbed system, meaning that it is equal to the expectation value when $\mathcal{V}_S(t) = 0$ for all t . The full expectation value can then be written in terms of the S-matrix and the unperturbed expectation value as

$$\langle A(t) \rangle = \langle S(-\infty, t) A(t) S(t, -\infty) \rangle_0. \quad (5.61)$$

Correlation functions in the interaction picture can be derived from the Schrödinger picture definition,

$$\begin{aligned} \langle B(t) A(t') \rangle &= \langle \psi_S(t) | B_S(t) U(t, t') A_S(t') | \psi_S(t') \rangle \\ &= \langle \psi_I(t) | B_I(t) U_0(t_0, t) U(t, t') U_0(t', t_0) A_I(t') | \psi_I(t') \rangle, \end{aligned} \quad (5.62)$$

where U is the full time evolution operator. To simplify this expression, I first show that

$$U_0(t_0, t) U(t, t') U_0(t', t_0) = S(t, t'). \quad (5.63)$$

From equation (2.12), we know that

$$U(t + \Delta t, t) = 1 - i\mathcal{H}_{0,S} - i\mathcal{V}_S(t) + \mathcal{O}(\Delta t^2). \quad (5.64)$$

Using that $U_0(t_0, t + \Delta t) \mathcal{H}_{0,S} U_0(t, t_0) = \mathcal{H}_{0,S} + \mathcal{O}(\Delta t)$, that $U_0(t_0, t + \Delta t) \mathcal{V}_S(t) U_0(t, t_0) = \mathcal{V}_I(t) + \mathcal{O}(\Delta t)$ and, because $\mathcal{H}_{0,S}$ is time-independent,

$$\begin{aligned} U_0(t_0, t + \Delta t) U_0(t, t_0) &= U_0(t, t_0) U_0(t_0, t + \Delta t) = U_0(t, t + \Delta t) \\ &= 1 + i\mathcal{H}_{0,S} \Delta t + \mathcal{O}(\Delta t^2), \end{aligned} \quad (5.65)$$

we see that

$$\begin{aligned} U_0(t_0, t + \Delta t) U(t + \Delta t, t) U_0(t, t_0) &= 1 + i\mathcal{H}_{0,S} \Delta t - i\mathcal{H}_{0,S} - i\mathcal{V}_S(t) + \mathcal{O}(\Delta t^2) \\ &= S(t + \Delta t, t) + \mathcal{O}(\Delta t^2). \end{aligned} \quad (5.66)$$

Moreover, if we let $\Delta t = (t - t')/N$ we can write

$$\begin{aligned} & U_0(t_0, t)U(t, t')U_0(t', t_0) \\ &= \prod_{n=1}^N U_0(t_0, t' + n\Delta t)U(t' + n\Delta t, t' + [n-1]\Delta t)U_0(t' + [n-1]\Delta t, t_0), \end{aligned} \quad (5.67)$$

for any N . Let $E = U_0(t_0, t + \Delta t)U(t + \Delta t, t)U_0(t, t_0) - S(t + \Delta t, t)$ and note that are N terms in equation (5.67) that are linear in E . As each of these is proportional to $\Delta t^2 \propto 1/N^2$, the sum of linear terms will vanish in the limit $N \rightarrow \infty$. Similarly, there are $\binom{N}{k} = N(N-1)\dots(N-k+1)/k! < N^k$ terms proportional to $E^k \propto 1/N^{2k}$. As a result, taking the limit $N \rightarrow \infty$ in equation (5.67), I get

$$\begin{aligned} U_0(t_0, t)U(t, t')U_0(t', t_0) &= \lim_{N \rightarrow \infty} \prod_{n=1}^N S(t' + n\Delta t, t' + [n-1]\Delta t) \\ &= \lim_{N \rightarrow \infty} S(t, t') = S(t, t'). \end{aligned} \quad (5.68)$$

Inserting this into the expression for correlation functions, I get

$$\langle B(t)A(t') \rangle = \langle \psi_I(t) | B_I(t) S(t, t') A_I(t') | \psi_I(t') \rangle. \quad (5.69)$$

Next, I derive an expression for S which can be used to obtain an iterative procedure to approximate Green's functions. Inserting equation (5.59) into equation (5.57) I get a differential equation for S , which can be integrated to obtain

$$S(t, t_0) = 1 - i \int_{t_0}^t \tilde{d}\tilde{t} \mathcal{V}_I(\tilde{t}) S(\tilde{t}, t_0). \quad (5.70)$$

One can insert the right-hand side into S recursively to obtain

$$S(t, t_0) = 1 + \sum_{n=1}^{\infty} (-i)^n \int_{t_0}^t dt_1 \int_{t_0}^{t_1} dt_2 \dots \int_{t_0}^{t_{n-1}} dt_n \prod_{j=1}^n \mathcal{V}_I(t_j). \quad (5.71)$$

Note that the order of $\mathcal{V}_I(t_1)\mathcal{V}_I(t_2)\dots\mathcal{V}_I(t_n)$, matters, since in general one may have $[\mathcal{V}_I(t_1), \mathcal{V}_I(t_2)]_- \neq 0$ when $t_1 \neq t_2$. One can simplify this

integral by using the time ordering symbol,² \mathcal{T} , and time anti-ordering, $\bar{\mathcal{T}}$, defined as

$$\mathcal{T}\{A_1(t_1)A_2(t_2)\cdots A_n(t_n)\} = (\mp 1)^{s(p)} A_{p_1}(t_{p_1})\cdots A_{p_n}(t_{p_n}) \quad (5.72a)$$

$$\bar{\mathcal{T}}\{A_1(t_1)A_2(t_2)\cdots A_n(t_n)\} = (\mp 1)^{s(q)} A_{q_1}(t_{q_1})\cdots A_{q_n}(t_{q_n}) \quad (5.72b)$$

where p and q are the permutations such that $t_{p_n} < t_{p_{n-1}}$ and $t_{q_n} > t_{q_{n-1}}$, respectively. The upper and lower signs are for fermionic and bosonic operators, respectively, and $s(p)$ and $s(q)$ are the number of inversions required to perform the permutation. The latter means that $(-1)^{s(p)}$ is the sign of permutation p . I assume that \mathcal{V}_I does not include terms with an odd number of fermionic operators. In this case, if $t > t_0$,

$$\begin{aligned} & \int_{t_0}^t dt_1 \int_{t_0}^{t_1} dt_2 \cdots \int_{t_0}^{t_{n-1}} dt_n \prod_{j=1}^n \mathcal{V}_I(t_j) \\ &= \int_{t_0}^t dt_1 \int_{t_0}^{t_1} dt_2 \cdots \int_{t_0}^{t_{n-1}} dt_n \mathcal{T} \left\{ \prod_{j=1}^n \mathcal{V}_I(t_j) \right\} \\ &= \frac{1}{n!} \int_{t_0}^t dt_1 \int_{t_0}^{t_1} dt_2 \cdots \int_{t_0}^t dt_n \mathcal{T} \left\{ \prod_{j=1}^n \mathcal{V}_I(t_j) \right\}, \end{aligned} \quad (5.73)$$

because of the symmetry of the integrand in the $n!$ subregions of the n -dimensional hypercube with lengths $t - t_0$. Next, I define the time-ordered exponential as

$$\begin{aligned} & \mathcal{T} \exp \left[-i \int_{t_0}^t d\tilde{t} \mathcal{V}_I(\tilde{t}) \right] \\ &= 1 + \sum_{n=1}^{\infty} \frac{(-i)^n}{n!} \int_{t_0}^t dt_1 \int_{t_0}^{t_1} dt_2 \cdots \int_{t_0}^t dt_n \mathcal{T} \left\{ \prod_{j=1}^n \mathcal{V}_I(t_j) \right\} \end{aligned} \quad (5.74)$$

and similarly for the anti-time ordering. Comparing with the S-matrix, one can see that

$$S(t, t_0) = \begin{cases} \mathcal{T} \exp \left[-i \int_{t_0}^t d\tilde{t} \mathcal{V}_I(\tilde{t}) \right] & \text{if } t > t_0, \\ \bar{\mathcal{T}} \exp \left[-i \int_{t_0}^t d\tilde{t} \mathcal{V}_I(\tilde{t}) \right] & \text{if } t < t_0. \end{cases} \quad (5.75)$$

2. Despite not actually being an operator, it is often also referred to as the *time ordering operator*.

Because of the time orderings in equation (5.75), it is useful to define a time-ordered Green's function,

$$\begin{aligned} G_{\lambda\mu}^T(t, t') &= -i \left\langle \mathcal{T} c_\lambda(t) c_\mu^\dagger(t') \right\rangle \\ &= -i\theta(t - t') \left\langle c_\lambda(t) c_\mu^\dagger(t') \right\rangle \pm i\theta(t' - t) \left\langle c_\mu^\dagger(t') c_\lambda(t) \right\rangle \\ &= \theta(t - t') G_{\lambda\mu}^>(t, t') + \theta(t' - t) G_{\lambda\mu}^<(t, t'), \end{aligned} \quad (5.76)$$

and the time anti-ordered Green's function,

$$\begin{aligned} G_{\lambda\mu}^{\bar{T}}(t, t') &= -i \left\langle \bar{\mathcal{T}} c_\lambda(t) c_\mu^\dagger(t') \right\rangle \\ &= \theta(t - t') G_{\lambda\mu}^<(t, t') + \theta(t' - t) G_{\lambda\mu}^>(t, t'). \end{aligned} \quad (5.77)$$

Differentiating G^T and $-G^{\bar{T}}$, one can see that these are also Green's functions in the mathematical sense, just like G^R and G^A . It is also useful to note the relations

$$G^R(t, t') = \theta(t - t') [G^>(t, t') - G^<(t, t')] \quad (5.78a)$$

$$= G^T(t, t') - G^<(t, t'), \quad (5.78b)$$

$$G^A(t, t') = \theta(t' - t) [G^<(t, t') - G^>(t, t')] \quad (5.78c)$$

$$= G^T(t, t') - G^>(t, t'), \quad (5.78d)$$

$$G^T + G^{\bar{T}} = G^> + G^<. \quad (5.78e)$$

Defining $t_{\max} = \max(t, t')$, one can see from equation (5.61) that

$$\begin{aligned} G_{\lambda\mu}^T(t, t') &= -i \left\langle S(-\infty, t_{\max}) \mathcal{T} \left[c_\lambda(t) c_\mu^\dagger(t') S(t_{\max}, -\infty) \right] \right\rangle_0 \\ &= -i \left\langle S(-\infty, \infty) \mathcal{T} \left[c_\lambda(t) c_\mu^\dagger(t') S(\infty, -\infty) \right] \right\rangle_0. \end{aligned} \quad (5.79)$$

This expression is useful when considering systems at zero temperature where the state vector can be assumed to be a non-degenerate ground state of \mathcal{H}_0 at $t = -\infty$. If the perturbation \mathcal{V}_I can be assumed to be turned on adiabatically, such that the system always stays in the ground state of \mathcal{H}_0 , the states $|\psi_I(-\infty)\rangle$ and $|\psi_I(\infty)\rangle$ must both be ground states of \mathcal{H}_0 . If this ground state can be assumed unique up to a phase, it means that

$$\langle \psi_I(\infty) | = \langle \psi_I(-\infty) | S(-\infty, \infty) = e^{i\varphi} \langle \psi_I(-\infty) |, \quad (5.80)$$

so

$$G_{\lambda\mu}^T(t, t') = -ie^{i\varphi} \left\langle \mathcal{T} \left[c_\lambda(t) c_\mu^\dagger(t') S(\infty, -\infty) \right] \right\rangle_0. \quad (5.81)$$

From this, one can evaluate G^T to any order in \mathcal{V}_I by expanding S in powers of \mathcal{V}_I . This is made possible by combining the two different S -matrices in equation (5.79), such that the Green's function can be expressed in terms of a single time-ordering symbol.

The reason why it is important to have a common time-ordering for the whole expectation value is that it allows the expression to be conveniently reduced to products of time-ordered Green's functions by the use of Wick's theorem. Assuming \mathcal{H}_0 is quadratic, Wick's theorem allows time-ordered expectation values of $2N$ creation and annihilation operators to be written in terms of products of N time-ordered expectation values of 2 operators. This means that each term in the exponential expansion of equation (5.81) can be written in terms of products of the, presumably known, unperturbed Green's functions, $G_{0,\lambda\mu}^T(t, t') = -i \left\langle \mathcal{T} \left[c_\lambda(t) c_\mu^\dagger(t') \right] \right\rangle_0$.

Deriving Wick's theorem is not too difficult if the unperturbed Hamiltonian is time-independent in the Schrödinger picture and can be diagonalized such that

$$\mathcal{H}_0 = \sum_{\lambda=1}^N \varepsilon_\lambda c_\lambda^\dagger c_\lambda, \quad (5.82)$$

which I assume to be the case. I also assume that the unperturbed system was in thermal equilibrium, such that occupation follows a Boltzmann distribution, for example because the states are in a grand canonical ensemble. From the first assumption, the Heisenberg equation immediately gives that in the interaction picture,

$$c_\lambda(t) = e^{-i\varepsilon_\lambda(t-t_0)} c_\lambda(t_0), \quad c_\lambda^\dagger(t) = e^{i\varepsilon_\lambda(t-t_0)} c_\lambda^\dagger(t_0), \quad (5.83)$$

because operators in the interaction picture evolve in time according to the unperturbed Hamiltonian. Hence,

$$\left[c_\lambda(t), c_\mu^\dagger(t') \right]_{\pm} = \delta_{\lambda\mu} e^{-i\varepsilon_\lambda(t-t')}, \quad \left[c_\lambda(t), c_\mu(t') \right]_{\pm} = 0. \quad (5.84)$$

Let α_λ denote either c_λ when $\lambda \in \{1, \dots, N\}$ or c_λ^\dagger when $\lambda \in \{N+1, \dots, 2N\}$, and define s_λ to be -1 if $\alpha_\lambda = c_\lambda$ and 1 if $\alpha_\lambda = c_\lambda^\dagger$. From

equation (5.83) one can see that

$$\langle \alpha_\lambda(t) \alpha_\mu(t') \rangle_0 = [\alpha_\lambda(t), \alpha_\mu(t')]_{\pm} (1 \pm e^{s_\lambda \varepsilon_\lambda \beta}), \quad (5.85)$$

where the upper and lower signs are for fermions and bosons, respectively, and where β is the inverse temperature. The next ingredient needed to derive Wick's theorem is that, for any operator A ,

$$\begin{aligned} \langle \alpha_\lambda(t_1) A(t_2, t_3, \dots, t_n) \rangle_0 &= Z^{-1} \sum_n e^{-\beta \varepsilon_n} \langle n | \alpha_\lambda(t_1) A(t_2, t_3, \dots, t_n) | n \rangle \\ &= Z^{-1} \sum_{nm} e^{-\beta \varepsilon_n} \langle n | \alpha_\lambda(t_1) | m \rangle \langle m | A(t_2, t_3, \dots, t_n) | n \rangle \\ &= Z^{-1} \sum_{nm} e^{-\beta(\varepsilon_m + s_\lambda \varepsilon_\lambda)} \langle m | A(t_2, t_3, \dots, t_n) | n \rangle \langle n | \alpha_\lambda(t_1) | m \rangle \\ &= \langle A(t_2, t_3, \dots, t_n) \alpha_\lambda(t_1) \rangle_0 e^{-\beta s_\lambda \varepsilon_\lambda}, \quad (5.86) \end{aligned}$$

where the sum goes over a complete set of states, and where in the third equality I used that $|n\rangle$ must differ from $|m\rangle$ by an excitation with energy $s_\lambda \varepsilon_\lambda$. By using that $\alpha_\lambda(t_1) \alpha_\mu(t_2) = [\alpha_\lambda(t_1), \alpha_\mu(t_2)]_{\pm} \mp \alpha_\mu(t_2) \alpha_\lambda(t_1)$ one can also see that

$$\begin{aligned} \alpha_{\lambda_1}(t_1) \alpha_{\lambda_2}(t_2) \cdots \alpha_{\lambda_n}(t_n) &= [\alpha_{\lambda_1}(t_1), \alpha_{\lambda_2}(t_2)]_{\pm} \alpha_{\lambda_3}(t_3) \cdots \alpha_{\lambda_n}(t_n) \\ &\mp \alpha_{\lambda_2}(t_2) \alpha_{\lambda_1}(t_1) \alpha_{\lambda_3}(t_3) \cdots \alpha_{\lambda_n}(t_n) \\ &= \sum_{k=2}^n (\mp 1)^k [\alpha_{\lambda_1}(t_1), \alpha_{\lambda_k}(t_k)]_{\pm} \alpha_{\lambda_2}(t_2) \cdots \widehat{\alpha_{\lambda_i}(t_i)} \cdots \alpha_{\lambda_n}(t_n) \\ &\quad + (\mp 1)^{n+1} \alpha_{\lambda_2}(t_2) \cdots \alpha_{\lambda_n}(t_n) \alpha_{\lambda_1}(t_1), \quad (5.87) \end{aligned}$$

where $\widehat{\alpha_{\lambda_i}(t_i)}$ means that this factor should be excluded. Hence, if n is even, taking the expectation value of equation (5.87), moving the last term to the left-hand side, using equations (5.85) and (5.86) and dividing by $(1 \pm e^{s_\lambda \varepsilon_\lambda \beta})$, I get

$$\begin{aligned} \langle \alpha_{\lambda_1}(t_1) \alpha_{\lambda_2}(t_2) \cdots \alpha_{\lambda_n}(t_n) \rangle &= \sum_{k=2}^n (\mp 1)^k \langle \alpha_{\lambda_1}(t_1) \alpha_{\lambda_k}(t_k) \rangle \langle \alpha_{\lambda_2}(t_2) \cdots \widehat{\alpha_{\lambda_k}(t_k)} \cdots \alpha_{\lambda_n}(t_n) \rangle. \quad (5.88) \end{aligned}$$

This formula also works when using a basis that does not diagonalize the Hamiltonian. For a general quadratic Hamiltonian,

$$\mathcal{H} = \psi^\dagger M \psi, \quad (5.89)$$

where $\psi^\dagger = (d_1^\dagger, d_2^\dagger, \dots, d_N^\dagger, d_1, \dots, d_N)$ is a vector of creation and annihilation operators and M is a $2N \times 2N$ matrix, one can relate ψ to a diagonal basis through a linear transformation $\psi_\lambda = \sum_\mu P_{\lambda\mu} \alpha_\mu$. Hence, by summing over repeated indices,

$$\begin{aligned}
\langle \psi_{\lambda_1}(t_1) \psi_{\lambda_2}(t_2) \cdots \psi_{\lambda_n}(t_n) \rangle &= P_{\lambda_1 \mu_1} \cdots P_{\lambda_n \mu_n} \langle \alpha_{\mu_1}(t_1) \cdots \alpha_{\mu_n}(t_n) \rangle \\
&= \sum_{k=2}^n (\mp 1)^k \langle P_{\lambda_1 \mu_1} \alpha_{\mu_1}(t_1) P_{\lambda_k \mu_k} \alpha_{\mu_k}(t_k) \rangle \\
&\times \langle P_{\lambda_2 \mu_2} \alpha_{\mu_2}(t_2) \cdots P_{\lambda_k \mu_k} \widehat{\alpha_{\mu_k}(t_k)} \cdots P_{\lambda_n \mu_n} \alpha_{\mu_n}(t_n) \rangle \\
&= \sum_{k=2}^n (\mp 1)^k \langle \psi_{\lambda_1}(t_1) \psi_{\lambda_k}(t_k) \rangle \langle \psi_{\lambda_2}(t_2) \cdots \widehat{\psi_{\lambda_k}(t_k)} \cdots \psi_{\lambda_n}(t_n) \rangle. \quad (5.90)
\end{aligned}$$

This is an example of Wick's theorem [192, 193]

Applying equation (5.90) formula recursively, one ends up with products of only expectation values of two operators when the total number of operators is even. Note that equation (5.90) also applies to an odd number of operators. This means that when $\langle \psi_\lambda(t) \rangle = 0$ for all λ and t , which is often the case for fermionic ψ_λ , then all expectation values of odd number of operators are zero.

Note that the relative order between operators within each expectation value stays the same, meaning that the expectation value of a time-ordered set of operators can be written in terms of products of time-ordered Green's functions. This is the important part that makes Wick's theorem especially useful for time-ordered Green's functions. Moreover, the sign is equal to the sign of the permutation. This means that for instance, the first order correction to a quadratic perturbation with $\mathcal{V}_I(t) = V(t) c_\eta(t) c_\gamma^\dagger(t)$ is, using equation (5.81),

$$\begin{aligned}
e^{-i\varphi} G_{\lambda\mu}^T(t, t') &= -i \langle \mathcal{T} c_\lambda(t) c_\mu^\dagger(t') \rangle_0 \\
&- \left\langle \mathcal{T} \int_{-\infty}^{\infty} d\tilde{t} V(\tilde{t}) c_\lambda(t) c_\mu^\dagger(t') c_\eta(\tilde{t}) c_\gamma^\dagger(\tilde{t}) \right\rangle_0 \\
&= G_{0,\lambda\mu}^T(t, t') + \int_{-\infty}^{\infty} d\tilde{t} V(\tilde{t}) \left[G_{0,\lambda\mu}^T(t, t') G_{0,\eta\gamma}^T(\tilde{t}, \tilde{t}) \right. \\
&\quad \left. - G_{0,\lambda\gamma}^T(t, \tilde{t}) G_{0,\eta\mu}^T(\tilde{t}, t') \right], \quad (5.91)
\end{aligned}$$

where I have assumed for simplicity that the anomalous Green's function is zero.

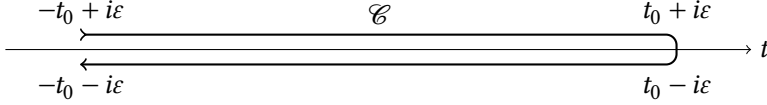


Figure 5.1: A sketch of the Schwinger-Keldysh contour.

However, equation (5.81) does not work at finite temperatures, because then the system does not occupy a single non-degenerate state satisfying equation (5.80). To study systems at finite temperatures, one can use the Schwinger-Keldysh contour and contour-ordered Green's functions [185]. The Schwinger-Keldysh contour, \mathcal{E} , is illustrated in figure 5.1. It starts $t = -t_0 + i\varepsilon$, follows parallel to the real line to $t_0 + i\varepsilon$, crosses the real line down to $t_0 - i\varepsilon$ and then follows the real line back to $-t_0 - i\varepsilon$. One then takes $t_0 \rightarrow \infty$ and $\varepsilon \rightarrow 0^+$. To make clear that I am working with complex times defined on the Schwinger-Keldysh contour, I use τ instead of t . Contour-ordering, $\mathcal{T}_{\mathcal{E}}$, is defined in the same way as time-ordering. The contour-ordered Green's function is therefore, in the limit $\varepsilon \rightarrow 0^+$,

$$G^c(\tau_1, \tau_2) \rightarrow \begin{cases} G^T[\text{Re}(\tau_1), \text{Re}(\tau_2)] & \text{if } \text{Im}(\tau_1) > 0, \text{Im}(\tau_2) > 0 \\ G^<[\text{Re}(\tau_1), \text{Re}(\tau_2)] & \text{if } \text{Im}(\tau_1) > 0, \text{Im}(\tau_2) < 0 \\ G^>[\text{Re}(\tau_1), \text{Re}(\tau_2)] & \text{if } \text{Im}(\tau_1) < 0, \text{Im}(\tau_2) > 0 \\ G^{\bar{T}}[\text{Re}(\tau_1), \text{Re}(\tau_2)] & \text{if } \text{Im}(\tau_1) < 0, \text{Im}(\tau_2) < 0 \end{cases} \quad (5.92)$$

The relationship between Wick's theorem and time-ordered Green's functions works equivalently for contour-ordered Green's functions. Therefore, if S_c denote

$$S_c = \mathcal{T}_{\mathcal{E}} \exp \left[-i \int_{\mathcal{E}} d\tau \mathcal{V}_I(\tau) \right], \quad (5.93)$$

such that the contour-ordered Green's function becomes

$$G_{\lambda\mu}^c(\tau_1, \tau_2) = -i \left\langle \mathcal{T}_{\mathcal{E}} \left[c_{\lambda}(\tau_1) c_{\mu}^{\dagger}(\tau_2) \right] \right\rangle = -i \left\langle \mathcal{T}_{\mathcal{E}} \left[c_{\lambda}(\tau_1) c_{\mu}^{\dagger}(\tau_2) S_c \right] \right\rangle_0, \quad (5.94)$$

one can again expand the exponential in S_c and apply Wick's theorem to get a series expansion of G^c in terms of the unperturbed contour-ordered Green's function.

As an example, consider how this can be applied to find the lowest order correction to a linear perturbation of a bosonic system, which is how it is used to study spin-pumping in paper VI. Let

$$\mathcal{H}_0 = \sum_{\lambda\mu} M_{\lambda\mu} c_\lambda^\dagger c_\mu \quad (5.95)$$

and

$$\mathcal{V}_I(t) = \sum_\lambda \left[h_\lambda^*(t) c_\lambda(t) + h_\lambda(t) c_\lambda^\dagger(t) \right]. \quad (5.96)$$

The first-order correction is zero because it is odd in creation and annihilation operators. To second order, the correction to the contour-ordered Green's function is

$$\begin{aligned} G_{\lambda\mu}^c(\tau_1, \tau_2) - G_{0,\lambda\mu}^c(\tau_1, \tau_2) &= \frac{i}{2} \int_{\mathcal{C}} d\tau_3 \int_{\mathcal{C}} d\tau_4 \sum_{\gamma,\nu} \left\langle \mathcal{T}_{\mathcal{C}} \left\{ c_\lambda(\tau_1) c_\mu^\dagger(\tau_2) \right. \right. \\ &\quad \times \left. \left[h_\gamma^*(\tau_3) c_\gamma(\tau_3) + h_\gamma(\tau_3) c_\gamma^\dagger(\tau_3) \right] \left[h_\nu^*(\tau_4) c_\nu(\tau_4) + h_\nu(\tau_4) c_\nu^\dagger(\tau_4) \right] \right\} \Bigg|_0 \\ &= i \int_{\mathcal{C}} d\tau_3 \int_{\mathcal{C}} d\tau_4 \sum_{\gamma,\nu} \left\langle \mathcal{T}_{\mathcal{C}} \left[c_\lambda(\tau_1) c_\mu^\dagger(\tau_2) h_\gamma^*(\tau_3) h_\nu(\tau_4) c_\gamma(\tau_3) c_\nu^\dagger(\tau_4) \right] \right\} \Bigg|_0 \end{aligned} \quad (5.97)$$

Applying Wick's theorem, I get

$$\begin{aligned} G_{\lambda\mu}^c(\tau_1, \tau_2) - G_{0,\lambda\mu}^c(\tau_1, \tau_2) &= -i \int_{\mathcal{C}} d\tau_3 \int_{\mathcal{C}} d\tau_4 \sum_{\gamma,\nu} h_\gamma^*(\tau_3) h_\nu(\tau_4) \left\{ G_{0,\lambda\mu}^c(\tau_1, \tau_2) G_{0,\gamma\nu}^c(\tau_3, \tau_4) \right. \\ &\quad \left. + G_{0,\lambda\nu}^c(\tau_1, \tau_4) G_{0,\gamma\mu}^c(\tau_3, \tau_2) \right\}. \end{aligned} \quad (5.98)$$

The first term is zero, since

$$\begin{aligned} -i \int_{\mathcal{C}} d\tau_3 \int_{\mathcal{C}} d\tau_4 \sum_{\gamma,\nu} h_\nu(\tau_4) h_\gamma^*(\tau_3) G_{0,\gamma\nu}^c(\tau_3, \tau_4) \\ = \left(\int_{-\infty}^{\infty} dt_4 + \int_{\infty}^{-\infty} dt_4 \right) (\Sigma \bullet_{\mathcal{C}} G^c)_{\nu\nu}(t, t) = 0, \end{aligned} \quad (5.99)$$

where $\Sigma_{\lambda\mu}(t_1, t_2) = -ih_\lambda(t_1)h_\mu^*(t_2)$ and the contour bullet product is

$$(A \bullet_{\mathcal{C}} B)_{\lambda\mu}(\tau_1, \tau_2) = \sum_Y \int_{\mathcal{C}} d\tau_3 A_{\lambda Y}(\tau_1, \tau_3) B_{Y\mu}(\tau_3, \tau_2). \quad (5.100)$$

Hence,

$$\begin{aligned} & G_{\lambda\mu}^c(\tau_1, \tau_2) - G_{0,\lambda\mu}^c(\tau_1, \tau_2) \\ &= - \sum_{Y,\nu} i \int_{\mathcal{C}} d\tau_4 G_{0,\lambda\nu}^c(\tau_1, \tau_4) \int_{\mathcal{C}} d\tau_3 h_\nu(\tau_4) h_Y^*(\tau_3) G_{0,Y\mu}^c(\tau_3, \tau_2). \end{aligned} \quad (5.101)$$

The form of the right-hand side is

$$D = A \bullet_{\mathcal{C}} B \bullet_{\mathcal{C}} C, \quad (5.102)$$

Splitting up the integral and using equation (5.92), one can write the integral in terms of real-time variables. For example, the lesser function can be obtained by keeping τ_1 on the upper branch in the Schwinger-Keldysh contour and τ_2 on the lower branch in the contour, giving

$$\begin{aligned} (A \bullet_{\mathcal{C}} B)_{\lambda\mu}^< (t_1, t_2) &= \sum_Y \int_{-\infty}^{\infty} dt_3 \left[A_{\lambda Y}^T(t_1, t_3) B_{Y\mu}^< (t_3, t_2) \right. \\ &\quad \left. - A_{\lambda Y}^< (t_1, t_3) B_{Y\mu}^{\bar{T}}(t_3, t_2) \right]. \end{aligned} \quad (5.103)$$

Using equation (5.78), one can also write this as

$$\begin{aligned} (A \bullet_{\mathcal{C}} B)_{\lambda\mu}^< (t_1, t_2) &= \sum_Y \int_{-\infty}^{\infty} dt_3 \left[A_{\lambda Y}^R(t_1, t_3) B_{Y\mu}^< (t_3, t_2) \right. \\ &\quad \left. + A_{\lambda Y}^< (t_1, t_3) B_{Y\mu}^A(t_3, t_2) \right]. \end{aligned} \quad (5.104)$$

This is a special case of the Langreth rules [185, 194]. More generally, if

$$C(\tau_1, \tau_2) = (A \bullet B)(\tau_1, \tau_2), \quad (5.105a)$$

$$D(\tau_1, \tau_2) = (A \bullet B \bullet C)(\tau_1, \tau_2), \quad (5.105b)$$

where A and B are contour-ordered functions, then the corresponding advanced, retarded, and lesser Green's functions satisfy [185]

$$C^{</>} = A^R \circ B^{</>} + A^{</>} \circ B^A, \quad (5.106a)$$

$$C^{R/A} = A^{R/A} \circ B^{R/A}, \quad (5.106b)$$

$$D^{</>} = A^R \circ B^R \circ C^{</>} + A^R \circ B^{</>} \circ C^A + A^{</>} \circ B^A \circ C^A, \quad (5.106c)$$

$$D^{R/A} = A^{R/A} \circ B^{R/A} \circ C^{R/A}, \quad (5.106d)$$

As a result, if we again write $\Sigma_{\lambda\mu}(t_1, t_2) = -ih_\lambda(t_1)h_\mu^*(t_2)$,

$$G^< = G_0^< + G_0^R \circ \Sigma \circ G_0^< + G_0^< \circ \Sigma \circ G_0^A, \quad (5.107)$$

which is on the same form as the first-order correction obtained from the Dyson equation (5.19).

5.2.1 Example: Dissipation

Real physical systems are never perfectly closed, and there is generally some degree of interaction with the environment. As a result, a good model should in principle include a Hamiltonian which describes the environment, not just the small subsystem that may be of interest in the lab. In other words, one should generally consider a Hamiltonian

$$\mathcal{H} = \mathcal{H}_s + \mathcal{H}_e + \mathcal{H}_{se}, \quad (5.108)$$

where \mathcal{H}_s is the system Hamiltonian, \mathcal{H}_e is the Hamiltonian for the environment and \mathcal{H}_{se} is the interaction between the system and environment. For a perfectly isolated system, $\mathcal{H}_{se} = 0$. Otherwise, $\mathcal{H}_{se} \neq 0$, and its treatment will generally depend on the nature of the interaction. Often, the interaction can be assumed to be weak, and one can apply the perturbation techniques discussed above.

As an example, consider a fermionic system where there are interactions with fermionic degrees of freedom in the environment. Let $\{c_\lambda\}$ be the annihilation operators of the system, let $\{d_\lambda\}$ be the annihilation operators of the environment, and let the interaction be

$$\mathcal{H}_{se} = \sum_{\mu\lambda} \left(\Gamma_{\mu\lambda} c_\mu^\dagger d_\lambda + \Gamma_{\mu\lambda}^* d_\lambda^\dagger c_\mu \right). \quad (5.109)$$

This interaction could for instance come from interaction with a substrate or the localized electron states when studying a system of itinerant electrons. To reduce the number of terms, I assume that the anomalous Green's function is zero.

In order to evaluate

$$G_{\lambda\mu}^c(\tau_1, \tau_2) = -i \left\langle \mathcal{T}_{\mathcal{E}} \left[c_{\lambda}(\tau_1) c_{\mu}^{\dagger}(\tau_2) \right] \right\rangle, \quad (5.110)$$

one can use the interaction picture approach detailed above. As with the impurity scattering example, the goal is to determine a self-energy term Σ such that

$$G^c = G_0^c + G_0^c \bullet_{\mathcal{E}} \Sigma \bullet_{\mathcal{E}} G^c, \quad (5.111)$$

where G_0^c is the Green's function evaluated in the absence of dissipation. If \mathcal{H}_s is quadratic, one can from this derive an equation of motion for the Green's function which includes dissipation, in a similar way as was done for impurities in section 5.1.1. If \mathcal{H}_s , \mathcal{H}_e and \mathcal{H}_{se} are all quadratic, we could of course use an approach similar to what was done in section 5.1.1. However, with the approach based on the interaction picture, we do not need to make such a restrictive assumption on \mathcal{H}_e , and the same approach works for more complicated \mathcal{H}_{se} . For instance, electron-phonon coupling is an important source of dissipation in many systems, and this comes from a cubic interaction term coupling fermionic and bosonic degrees of freedom, as can be seen from section 3.3. Because \mathcal{H}_e is not assumed quadratic in d_{λ} , the derivation presented above for Wick's theorem is no longer valid in general when evaluating expectation values of d_{λ} operators. However, this is not a problem here because I only consider expectation values up to second order in d_{λ} , and the derivation of Wick's theorem is valid for the c_{λ} operators.

From section 5.2, we know that

$$\begin{aligned} G_{\lambda\mu}^c(\tau_1, \tau_2) &= -i \left\langle \mathcal{T}_{\mathcal{E}} \left[c_{\lambda}(\tau_1) c_{\mu}^{\dagger}(\tau_2) S_c \right] \right\rangle_0 = G_{0,\lambda\mu}^c(\tau_1, \tau_2) \\ &- \sum_{\gamma\nu} \int_{\mathcal{E}} d\tau \left\langle \mathcal{T}_{\mathcal{E}} \left[c_{\lambda}(\tau_1) c_{\mu}^{\dagger}(\tau_2) \right] \left[\Gamma_{\gamma\nu} c_{\gamma}^{\dagger}(\tau) d_{\nu}(\tau) + \Gamma_{\gamma\nu}^* d_{\nu}^{\dagger}(\tau) c_{\gamma}(\tau) \right] \right\rangle_0 \\ &+ \dots \quad (5.112) \end{aligned}$$

The second term on the right-hand side is zero because $\langle c_\lambda(\tau_1)c_\mu^\dagger(\tau_2)c_\gamma(\tau) \rangle_0 = 0$ is odd in c_λ -operators. The lowest order correction to the Green's function is therefore quadratic in the coupling constants $\Gamma_{\lambda\mu}$. This second order correction is

$$\begin{aligned}
& G_{\lambda\mu}^c(\tau_1, \tau_2) - G_{0,\lambda\mu}^c(\tau_1, \tau_2) \\
&= -i \frac{(-i)^2}{2} \sum_{\gamma\nu} \sum_{mn} \int_{\mathcal{E}} d\tau \int_{\mathcal{E}} d\tau' \left\langle \mathcal{T}_{\mathcal{E}} \left[c_\lambda(\tau_1) c_\mu^\dagger(\tau_2) \right] \right. \\
&\quad \times \left[\Gamma_{\gamma\nu} c_\gamma^\dagger(\tau) d_\nu(\tau) + \Gamma_{\gamma\nu}^* d_\nu^\dagger(\tau) c_\gamma(\tau) \right] \\
&\quad \left. \times \left[\Gamma_{mn} c_m^\dagger(\tau') d_n(\tau') + \Gamma_{mn}^* d_n^\dagger(\tau') c_m(\tau') \right] \right\rangle_0. \quad (5.113)
\end{aligned}$$

Using Wick's theorem, the term proportional to $G_{0,\lambda\mu}^c(\tau_1, \tau_2)$ on the right-hand side is zero for the same reason as the first term on the right-hand side of equation (5.98). The last two terms are identical after renaming the summation variables and time coordinates, so

$$G^c = G_0^c + G_0^c \bullet_{\mathcal{E}} \Gamma G_e^c \Gamma^\dagger \bullet_{\mathcal{E}} G_0^c. \quad (5.114)$$

where $G_{e,\lambda\mu}^c(\tau_1, \tau_2) = -i \left\langle \mathcal{T}_{\mathcal{E}} \left[d_\lambda(\tau_1) d_\mu^\dagger(\tau_2) \right] \right\rangle_0$. Also to second order in Γ , one can write

$$G^c = G_0^c + G_0^c \bullet_{\mathcal{E}} \Gamma G_e^c \Gamma^\dagger \bullet_{\mathcal{E}} G^c. \quad (5.115)$$

Hence, the self-energy which correctly captures dissipation through this interaction with the environment to second order in Γ is

$$\Sigma_{\text{inel}} = \Gamma G_e^c \Gamma^\dagger. \quad (5.116)$$

Using the Langreth rules, one can express the self-energy for the matrix of retarded, advanced, and Keldysh Green's functions as

$$\check{\Sigma}_{\text{inel}} = \begin{pmatrix} \Gamma G_e^R \Gamma^\dagger & \Gamma G_e^K \Gamma^\dagger \\ \Gamma G_e^A \Gamma^\dagger & \end{pmatrix}. \quad (5.117)$$

To proceed, I must make some simplifying assumptions regarding the environment. One such assumption is that the coupling to the environment is local, such that $\Gamma G_e^R \Gamma^\dagger$ is proportional to the identity

matrix. I also assume that $G_e^R(t_1, t_2)$ does not depend on the center-of-mass time $(t_1 + t_2)/2$.

Next, let $\Gamma G_e^R(\varepsilon)\Gamma^\dagger = r(\varepsilon) - i\delta(\varepsilon)$, where $G_e^R(\varepsilon)$ is obtained from $G_e^R(t_1, t_2)$ by a Fourier transform in relative time. The real part, $r(\varepsilon)$, can be neglected in the differential equation for the Green's function compared to the other real energies in the system. This is because the interaction with the environment is assumed to be weak. The imaginary part, on the other hand, cannot be neglected unless there are other, larger imaginary terms in the equation of motion for the Green's function. This is often not the case because the Hamiltonian is assumed Hermitian. A possible exception is the impurity self-energy that comes from impurity-averaging, as shown in section 5.1.1.

Next, I assume that the environment is at thermal equilibrium. Using the results from section 4.2 this implies that

$$\Gamma G_e^K(\varepsilon)\Gamma^\dagger = -2i\delta(\varepsilon) \tanh(\beta_e\varepsilon/2), \quad (5.118)$$

since $G_e^A(\varepsilon) = [G_e^R(\varepsilon)]^\dagger$. Here, β_e is the inverse temperature of the fermions in the environment, which are annihilated by the d_λ -operators. Hence, the self-energy is

$$\check{\Sigma}_{\text{inel}}(\varepsilon) = \begin{pmatrix} -i\delta(\varepsilon) & -2i\delta(\varepsilon) \tanh(\beta_e\varepsilon/2) \\ & i\delta(\varepsilon) \end{pmatrix}. \quad (5.119)$$

Another simplification that is often useful, is to assume that $\delta(\varepsilon)$ is independent of ε as long as $|\varepsilon|$ is less than all the relevant energies of the system under consideration. This is sometimes referred to as the relaxation time approximation [195].

Another relevant source of dissipation is electron-phonon scatterings. In this case \mathcal{H}_{se} is cubic, as explained above. The derivation is therefore more complicated and involves more terms than the one presented here, but the general procedure is the same. The end result is also the same for our purposes [185], except that the inverse temperature β_e is now the inverse temperature of the phonons.

Quasiclassical Keldysh Theory

One of the most striking features of our physical world, possibly only rivaled by the extraordinary effectiveness of symmetry arguments in physics, is the efficacy of effective theories. It is often possible to model a system with great precision without knowing the details of the underlying constituents. One can model the movement of a tsunami without knowing where there are fish or rocks that obstruct the flow of water [196, 197], one can model the flow of water around rocks without knowing how the water molecules bounce around [198, 199], and one can model the motion of ions without knowing about the quark and gluon constituents. The history of physics has largely been about going from large scales, like fluids, to increasingly smaller scales, like molecules, atoms, electrons, and eventually quarks. This would not have been possible if one needed to know about the detailed motion of atoms in order to predict the behavior of fluids. Hence, the efficacy of effective theories is arguably the reason why humanity has been able to study physics in the first place.

Effective theories can emerge when there is a hierarchy of scales, but this need not always be the case. If one tries to model atmospheric convection using the Lorenz equation [200], even an arbitrarily small perturbation in the initial condition will often lead to wildly different predictions [201]. This is an example of a chaotic system [202], which is a system where approximate knowledge of initial conditions does not give approximate predictions for the future. As a result, any long time-scale or length-scale prediction in chaotic systems is impossible without knowing the exact details of the microscopic initial condition.

Luckily, the behavior of electrons in crystalline solids is generally not chaotic. Therefore, if there is a hierarchy of scales it can be possible to derive effective theories. An example is the quasiclassical Keldysh Green's function formalism [203, 204], which is the topic of this chapter and the main tool in many of the articles presented in this thesis. The quasiclassical Keldysh formalism separates the quantum effects occurring at length scales comparable to the Fermi wavelength from other length scales. This is useful because, while quantum mechanics can be reasonably manageable when systems are translationally invariant, the equations become considerably more difficult to solve

when systems include inhomogeneous external fields or multiple materials. Quasiclassical Keldysh theory allows efficient treatment of such systems, as I will show in this chapter.

In this chapter, I will derive quasiclassical Keldysh theory in the general case, based on the theory from the previous chapters. I have also done so in detail in paper IX for the special case of antiferromagnetic metals. Antiferromagnetic metals are extra challenging compared to normal metals because one must consider two sublattices, while in conventional derivations of quasiclassical theory one often starts from continuous models. Here, I will take a more general approach and do the derivation in a different way compared to the derivation in paper IX. For instance, I will not derive the equations for two materials simultaneously, which was done in paper IX in order to also derive boundary conditions. Instead, I will be much more general when it comes to material properties and end up with equations that are applicable to many systems. Additionally, I will also derive the normalization condition.

6.1 Green's functions in Wigner coordinates

I consider again systems that can be modeled with a quadratic Hamiltonian. As we have seen, this includes superconductors, ferromagnets, antiferromagnets, spin-orbit coupling, impurities, and various external fields. As before, let $2N_s$ be the number of Wannier states per lattice site, and remember that each lattice site contains one unit cell that may include more than one atom. There are N_s Wannier states per spin, and the states need not be spin-degenerate. Let the annihilation operator for Wannier state m with spin σ and crystal momentum k be $c_{km\sigma}$. The most general quadratic Hamiltonian for such a system can be written

$$\begin{aligned} \mathcal{H} = & \sum_{k,m_1,m_2} \sum_{\sigma_1,\sigma_2} \frac{t_{k\sigma_1\sigma_2}^{m_1m_2}}{N} c_{km_1\sigma_1}^\dagger c_{km_2\sigma_2} + \sum_{k_1,k_2,m_1,m_2} \sum_{\sigma_1,\sigma_2} \frac{V_{k_1k_2\sigma_1\sigma_2}^{m_1m_2}}{N} c_{k_1m_1\sigma_1}^\dagger c_{k_2m_2\sigma_2} \\ & + \frac{1}{2N} \sum_{k_1,k_2,m_1,m_2} \sum_{\sigma_1,\sigma_2} \left[\Delta_{k_1k_2\sigma_1\sigma_2}^{m_1m_2} c_{k_1m_1\sigma_1}^\dagger c_{-k_2m_2\sigma_2}^\dagger + (\Delta_{k_2k_1\sigma_2\sigma_1}^{m_2m_1})^* c_{-k_1m_1\sigma_1} c_{k_2m_2\sigma_2} \right]. \end{aligned} \quad (6.1)$$

I define the Green's functions in terms of the $4N_s$ -tuple of creation and annihilation operators,

$$c_k^\dagger = \left(c_{k1\uparrow}^\dagger \quad c_{k1\downarrow}^\dagger \quad c_{k2\uparrow}^\dagger \quad \cdots \quad c_{kN_s\downarrow}^\dagger \quad c_{-k1\downarrow} \quad -c_{-k1\uparrow} \quad \cdots \quad -c_{-kN_s\uparrow} \right), \quad (6.2)$$

such that

$$\hat{G}_{k_1 k_2}^R(t, t') = -\frac{i}{N} \theta(t - t') \tau_z \left\langle \left[c_{k_1}(t), c_{k_2}^\dagger(t') \right]_+ \right\rangle, \quad (6.3a)$$

$$\hat{G}_{k_1 k_2}^A(t, t') = +\frac{i}{N} \theta(t' - t) \tau_z \left\langle \left[c_{k_1}(t), c_{k_2}^\dagger(t') \right]_+ \right\rangle, \quad (6.3b)$$

$$\hat{G}_{k_1 k_2}^K(t, t') = -\frac{i}{N} \tau_z \left\langle \left[c_{k_1}(t), c_{k_2}^\dagger(t') \right]_- \right\rangle, \quad (6.3c)$$

where $\tau_z = \text{diag}(1, 1, \dots, 1, -1, -1, \dots, -1)$ is again the third Pauli matrix in Nambu space. The Green's functions can be combined into a larger Green's function,

$$\check{G}_{k_1 k_2}(t, t') = \begin{pmatrix} \hat{G}_{k_1 k_2}^R(t, t') & \hat{G}_{k_1 k_2}^K(t, t') \\ \hat{G}_{k_1 k_2}^A(t, t') & \hat{G}_{k_1 k_2}^R(t, t') \end{pmatrix}. \quad (6.4)$$

The differential equation for these Green's functions can again be found from the Heisenberg equation for c_k^\dagger ,

$$i \frac{\partial c_k^\dagger}{\partial t} \tau_z + [\mathcal{H}, c_k^\dagger]_- \tau_z = 0, \quad (6.5)$$

where the commutator must be taken element-wise.

From $[AB, C]_- = A[B, C]_+ - [A, C]_+ B$ together with the anti-commutation relations for fermionic operators, $[c_{k_2 m_2 \sigma_2}, c_{k_1 m_1 \sigma_1}]_+ = [c_{k_2 m_2 \sigma_2}^\dagger, c_{k_1 m_1 \sigma_1}^\dagger]_+ = 0$ and

$$\begin{aligned} [c_{k_2 m_2 \sigma_2}, c_{k_1 m_1 \sigma_1}^\dagger]_+ &= \sum_{i,j} e^{-ik_2 \cdot R_i} e^{ik_1 \cdot R_j} [c_{i m_2 \sigma_2}, c_{j m_1 \sigma_1}^\dagger]_+ \\ &= \delta_{\sigma_1 \sigma_2} \delta_{m_1 m_2} \sum_i e^{i(k_1 - k_2) \cdot R_i} = N \delta_{\sigma_1 \sigma_2} \delta_{m_1 m_2} \delta_{k_1 k_2}, \end{aligned} \quad (6.6)$$

where N is the number of lattice sites, I get that

$$\left[c_{k_1 m_1 \sigma_1}^\dagger c_{k_2 m_2 \sigma_2}, c_{k_3 m_3 \sigma_3} \right]_+ = -N c_{k_2 m_2 \sigma_2} \delta_{k_1 k_3} \delta_{m_1 m_3} \delta_{\sigma_1 \sigma_3}, \quad (6.7a)$$

$$\left[c_{k_1 m_1 \sigma_1}^\dagger c_{k_2 m_2 \sigma_2}, c_{k_3 m_3 \sigma_3}^\dagger \right]_+ = N c_{k_1 m_1 \sigma_1}^\dagger \delta_{k_2 k_3} \delta_{m_2 m_3} \delta_{\sigma_2 \sigma_3}, \quad (6.7b)$$

$$\begin{aligned} \left[c_{k_1 m_1 \sigma_1}^\dagger c_{-k_2 m_2 \sigma_2}^\dagger, c_{k_3 m_3 \sigma_3} \right]_+ &= N c_{k_1 m_1 \sigma_1}^\dagger \delta_{-k_2 k_3} \delta_{m_2 m_3} \delta_{\sigma_2 \sigma_3} \\ &\quad - N c_{-k_2 m_2 \sigma_2}^\dagger \delta_{k_1 k_3} \delta_{m_1 m_3} \delta_{\sigma_1 \sigma_3}, \end{aligned} \quad (6.7c)$$

$$\begin{aligned} \left[c_{-k_1 m_1 \sigma_1} c_{k_2 m_2 \sigma_2}, c_{k_3 m_3 \sigma_3}^\dagger \right]_+ &= N c_{-k_1 m_1 \sigma_1} \delta_{k_2 k_3} \delta_{m_2 m_3} \delta_{\sigma_2 \sigma_3} \\ &\quad - N c_{k_2 m_2 \sigma_2} \delta_{-k_1 k_3} \delta_{m_1 m_3} \delta_{\sigma_1 \sigma_3}, \end{aligned} \quad (6.7d)$$

$$\left[c_{k_1 m_1 \sigma_1}^\dagger c_{-k_2 m_2 \sigma_2}^\dagger, c_{k_3 m_3 \sigma_3}^\dagger \right] = \left[c_{-k_1 m_1 \sigma_1} c_{k_2 m_2 \sigma_2}, c_{k_3 m_3 \sigma_3} \right]_+ = 0. \quad (6.7e)$$

Therefore,

$$\begin{aligned} \left[\mathcal{H}, c_{k_3 m_3 \sigma_3} \right]_- &= - \sum_{m_2} \sum_{\sigma_2} t_{k_3 \sigma_3 \sigma_2}^{m_3 m_2} c_{k_3 m_2 \sigma_2} - \sum_{k_2, m_2, \sigma_2} V_{k_3 k_2 \sigma_3 \sigma_2}^{m_3 m_2} c_{k_2 m_2 \sigma_2} \\ &\quad - \sum_{k_2, m_2, \sigma_2} \Delta_{k_3 k_2 \sigma_3 \sigma_2}^{m_3 m_2} c_{-k_2 m_2 \sigma_2}^\dagger. \end{aligned} \quad (6.8)$$

Moreover, since $\left[\mathcal{H}, c_{k_3 m_3 \sigma_3}^\dagger \right]_- = -(\left[\mathcal{H}, c_{k_3 m_3 \sigma_3} \right]_-)^\dagger$,

$$\begin{aligned} \left[\mathcal{H}, c_{k_3 m_3 \sigma_3}^\dagger \right]_- &= \sum_{m_2} \sum_{\sigma_2} (t_{k_3 \sigma_3 \sigma_2}^{m_3 m_2})^* c_{k_3 m_2 \sigma_2}^\dagger + \sum_{k_2, m_2, \sigma_2} (V_{k_3 k_2 \sigma_3 \sigma_2}^{m_3 m_2})^* c_{k_2 m_2 \sigma_2}^\dagger \\ &\quad + \sum_{k_2, m_2, \sigma_2} (\Delta_{k_3 k_2 \sigma_3 \sigma_2}^{m_3 m_2})^* c_{-k_2 m_2 \sigma_2}. \end{aligned} \quad (6.9)$$

Combining equations (6.8) and (6.9) the equation for c_k becomes

$$i \frac{\partial c_k^\dagger}{\partial t} \tau_z + c_k^\dagger H_{0,k} + \sum_{k'} c_{k'}^\dagger V_{k'k} = 0, \quad (6.10)$$

where

$$H_{0,k} = \begin{pmatrix} t_{k\uparrow\uparrow}^{11} & \cdots & t_{k\uparrow\downarrow}^{1N_s} & 0 & \cdots & 0 \\ \vdots & \ddots & \vdots & \vdots & \ddots & \vdots \\ t_{k\downarrow\uparrow}^{N_s 1} & \cdots & t_{k\downarrow\downarrow}^{N_s N_s} & 0 & \cdots & 0 \\ 0 & \cdots & 0 & (t_{-k\downarrow\downarrow}^{11})^* & \cdots & -(t_{-k\downarrow\uparrow}^{1N_s})^* \\ \vdots & \ddots & \vdots & \vdots & \ddots & \vdots \\ 0 & \cdots & 0 & -(t_{-k\uparrow\downarrow}^{N_s 1})^* & \cdots & (t_{-k\uparrow\uparrow}^{N_s N_s})^* \end{pmatrix}, \quad (6.11)$$

and

$$V_{k'k} = \begin{pmatrix} V_{k'k\uparrow\uparrow}^{11} & \cdots & V_{k'k\uparrow\downarrow}^{1N_s} & -\Delta_{k'k\uparrow\downarrow}^{11} & \cdots & \Delta_{k'k\uparrow\uparrow}^{1N_s} \\ \vdots & \ddots & \vdots & \vdots & \ddots & \vdots \\ V_{k'k\downarrow\uparrow}^{N_s 1} & \cdots & V_{k'k\downarrow\downarrow}^{N_s N_s} & -\Delta_{k'k\downarrow\downarrow}^{N_s 1} & \cdots & \Delta_{k'k\downarrow\uparrow}^{N_s N_s} \\ -(\Delta_{-k'-k\downarrow\uparrow}^{11})^* & \cdots & -(\Delta_{-k'-k\downarrow\downarrow}^{1N_s})^* & (V_{-k'-k\downarrow\downarrow}^{11})^* & \cdots & -(V_{-k'-k\downarrow\uparrow}^{1N_s})^* \\ \vdots & \ddots & \vdots & \vdots & \ddots & \vdots \\ (\Delta_{-k'-k\uparrow\uparrow}^{N_s 1})^* & \cdots & (\Delta_{-k'-k\uparrow\downarrow}^{N_s N_s})^* & -(V_{-k'-k\uparrow\downarrow}^{N_s 1})^* & \cdots & (V_{-k'-k\uparrow\uparrow}^{N_s N_s})^* \end{pmatrix}, \quad (6.12)$$

where I used that $(t_{k_3\sigma_2\sigma_3}^{m_3 m_2})^* = t_{k_3\sigma_2\sigma_3}^{m_2 m_3}$, $(V_{k_3 k_2 \sigma_3 \sigma_2}^{m_3 m_2})^* = V_{k_2 k_3 \sigma_2 \sigma_3}^{m_2 m_3}$ and $\Delta_{k_3 k_2 \sigma_3 \sigma_2}^{m_3 m_2} = -\Delta_{-k_2 -k_3 \sigma_2 \sigma_3}^{m_2 m_3}$, which follows from the Hermiticity of the Hamiltonian. Using these relations, it also follows from taking the complex conjugate of equation (6.10) that

$$-i\tau_z \frac{\partial c_k}{\partial t} + \sum_{k'} \tau_z [H_{0,k} \delta_{kk'} + V_{kk'}] \tau_z c_{k'} = 0. \quad (6.13)$$

Differentiating the retarded and advanced Green's functions with respect to t' and using equation (6.10), I get

$$i \frac{\partial \hat{G}_{k_1 k_2}^{R/A}(t, t')}{\partial t'} \tau_z = -\delta(t - t') \delta_{k_1 k_2} - \sum_{k'} \hat{G}_{k_1 k'}^{R/A}(t, t') [\delta_{k' k_2} H_{0, k_2}(t') + V_{k' k_2}(t')]. \quad (6.14)$$

Similarly,

$$i \frac{\partial \hat{G}_{k_1 k_2}^K(t, t')}{\partial t'} \tau_z = - \sum_{k'} \hat{G}_{k_1 k'}^K(t, t') [\delta_{k' k_2} H_{0, k_2}(t') + V_{k' k_2}(t')]. \quad (6.15)$$

Differentiating with respect to t and using equation (6.13), I get

$$i\tau_z \frac{\partial \hat{G}_{k_1 k_2}^{R/A}(t, t')}{\partial t} = \delta(t - t') \delta_{k_1 k_2} + \sum_{k'} [H_{0, k_1}(t') \delta_{k_1 k'} + V_{k_1 k'}(t')] \hat{G}_{k' k_2}^{R/A}(t, t'), \quad (6.16)$$

and

$$i\tau_z \frac{\partial \hat{G}_{k_1 k_2}^K(t, t')}{\partial t} = + \sum_{k'} [H_{0, k_1}(t') \delta_{k_1 k'} + V_{k_1 k'}(t')] \hat{G}_{k' k_2}^K(t, t'). \quad (6.17)$$

combining these results,

$$i\tau_z \frac{\partial \check{G}_{k_1 k_2}(t, t')}{\partial t} - \sum_{k'} [H_{0, k_1}(t') \delta_{k_1 k'} + V_{k_1 k'}(t')] \check{G}_{k' k_2}(t, t') = \delta(t - t') \delta_{k_1 k_2}, \quad (6.18a)$$

$$i \frac{\partial \check{G}_{k_1 k_2}(t, t')}{\partial t'} \tau_z + \sum_{k'} \check{G}_{k_1 k'}(t, t') [\delta_{k' k_2} H_{0, k_2}(t') + V_{k' k_2}(t')] = -\delta(t - t') \delta_{k_1 k_2}. \quad (6.18b)$$

In section 5.1.1, I showed that one can convert the equations for the full Green's function into equations for impurity-averaged Green's functions by replacing the impurity-potential in $V_{k_1 k_2}$ with the impurity self-energy, $\check{\Sigma}_{\text{imp}}$, which depend on the type of impurity as well as $\check{G}_{k_1 k_2}$. Moreover, in section 5.2.1, I showed that we can include the effect of dissipation to the environment by including a self-energy term $\check{\Sigma}_{\text{inel}}$. Both $\check{\Sigma}_{\text{imp}}$ and $\check{\Sigma}_{\text{inel}}$ are special in that they are non-diagonal in Keldysh space, meaning that they include a Keldysh component in addition to the usual retarded and advanced components. Including these effects, the equations for the Green's functions become

$$i\tau_z \frac{\partial \check{G}_{k_1 k_2}(t, t')}{\partial t} - \sum_{k'} (\check{\Sigma}_{k_1 k'} \circ \check{G}_{k' k_2})(t, t') = \delta(t - t') \delta_{k_1 k_2}, \quad (6.19a)$$

$$i \frac{\partial \check{G}_{k_1 k_2}(t, t')}{\partial t'} \tau_z + \sum_{k'} (\check{G}_{k_1 k'} \circ \check{\Sigma}_{k' k_2})(t, t') = -\delta(t - t') \delta_{k_1 k_2}, \quad (6.19b)$$

where the circle-product is an integral over the internal time coordinate,

$$(A \circ B)(t_1, t_2) = \int_{-\infty}^{\infty} dt' A(t_1, t') B(t', t_2), \quad (6.20)$$

and

$$\check{\Sigma}_{k_1 k_2}(t, t') = [H_{0, k_1} \delta_{k_1 k_2} + V_{k_1 k_2}(t)] \delta(t - t') + \check{\Sigma}_{\text{imp}, k_1 k_2} + \check{\Sigma}_{\text{inel}, k_1 k_2}.$$

However, this is not always the case. To include the possibility of $\xi_{j,k} \neq \xi_{j,-k}$, I write

$$D_k = \begin{pmatrix} \check{\xi}_{1,k} & & & & & \\ & \ddots & & & & \\ & & \check{\xi}_{2N_s,k} & & & \\ & & & \check{\xi}_{2N_s+1,k} & & \\ & & & & \ddots & \\ & & & & & \check{\xi}_{4N_s,k} \end{pmatrix}. \quad (6.23)$$

where $\check{\xi}_{2N_s+i,k} = \check{\xi}_{i,-k}$.

The similarity transformation defined by S_k transforms into the basis of the different energy bands in the system. There are $2N_s$ different, possibly degenerate, energy bands, and the Fermi surface is defined to be the set of crystal momenta for which $\check{\xi}_{i,k} = 0$ for at least one $i \in \{1, \dots, 2N_s\}$. The Fermi surface need in principle not be a single continuous surface, and the different bands can cross the Fermi level, meaning that $\check{\xi}_{i,k} = 0$, at different values of k . I transform onto the energy band basis by defining $\check{G}'_{k_1 k_2} = S_{k_1} \check{G}_{k_1 k_2} S_{k_2}^\dagger$, and $\check{\Sigma}'_{k_1 k_2} = S_{k_1} \check{\Sigma}_{k_1 k_2} S_{k_2}^\dagger$. Performing a similarity transformation on equation (6.19), I get

$$i\tau_z \frac{\partial \check{G}'_{k_1 k_2}}{\partial t} - \sum_{k'} \check{\Sigma}'_{k_1 k'} \circ \check{G}'_{k' k_2} = \delta(t - t') \delta_{k_1 k_2}, \quad (6.24a)$$

$$i \frac{\partial \check{G}'_{k_1 k_2}}{\partial t'} \tau_z + \sum_{k'} \check{G}'_{k_1 k} \circ \check{\Sigma}'_{k' k_2} = -\delta(t - t') \delta_{k_1 k_2}. \quad (6.24b)$$

The idea of quasiclassical theory is that the variation is slow in the center of mass (COM) position compared to the Fermi wavelength. This means that we should write the Green's functions as functions of COM position and COM time. The set of COM coordinates, $(\mathbf{R}, \mathbf{k}, T, \varepsilon)$, where \mathbf{R} is COM position, T is COM time, \mathbf{k} is crystal momentum and ε is energy, is also known as Wigner coordinates [185]. Consider first the time coordinate. Let \mathcal{F}_t denote Fourier transform in relative time, such that

$$\check{G}'_{k_1 k}(T, \varepsilon) = \mathcal{F}_t\{\check{G}'_{k_1 k}\}(T, \varepsilon) = \int_{-\infty}^{\infty} dt \check{G}'_{k_1 k}(T+t/2, T-t/2) e^{i\varepsilon t}. \quad (6.25)$$

Consider

$$\mathcal{F}_t\{A \circ B\}(T, \varepsilon) = \int_{-\infty}^{\infty} dt (A \circ B)(T + t/2, T - t/2) e^{i\varepsilon t}. \quad (6.26)$$

Let $a(T, t) = A(T + t/2, T - t/2)$ and $b(T, t) = B(T + t/2, T - t/2)$, such that

$$(A \circ B)(T + t/2, T - t/2) = \int_{-\infty}^{\infty} dt' a(T + t'/2, t - t') b(T - [t - t']/2, t'). \quad (6.27)$$

Taylor expanding $a(T + t'/2, t - t')$ around $a(T, t - t')$ and $b(T - [t - t']/2, t')$ around $b(T, t')$, I get that

$$(A \circ B)(T + t/2, T - t/2) = \sum_{n,m=0}^{\infty} \frac{1}{n!m!} \left[\left(-\frac{t}{2} \right)^m \frac{\partial^n a}{\partial T^n} \right] * \left[\left(\frac{t}{2} \right)^n \frac{\partial^m b}{\partial T^m} \right], \quad (6.28)$$

where $*$ denotes regular convolution in the relative time variable. The Fourier transform of a convolution is the product of the Fourier transforms, and $\mathcal{F}_t\{(\pm t/2)^n f\} = [\mp(i/2)\partial/\partial\varepsilon]^n \mathcal{F}_t\{f\}$, so

$$\mathcal{F}_t\{A \circ B\} = \sum_{n,m=0}^{\infty} \frac{1}{n!m!} \left(\frac{i}{2} \right)^m \left(-\frac{i}{2} \right)^n \left[\frac{\partial^m}{\partial \varepsilon^m} \frac{\partial^n}{\partial T^n} \mathcal{F}_t\{A\} \right] \left[\frac{\partial^n}{\partial \varepsilon^n} \frac{\partial^m}{\partial T^m} \mathcal{F}_t\{B\} \right]. \quad (6.29)$$

This is often written more compactly as

$$\mathcal{F}_t\{A \circ B\} = \exp\left(\frac{i}{2}\partial_\varepsilon^A \partial_T^B - \frac{i}{2}\partial_\varepsilon^B \partial_T^A\right) AB, \quad (6.30)$$

where it is understood that A and B are written as functions of ε and T on the right-hand side, and where the superscripts on the differential operators indicate which functions they act on. I use the circle product to also denote the product

$$A \circ B = \exp\left(\frac{i}{2}\partial_\varepsilon^A \partial_T^B - \frac{i}{2}\partial_\varepsilon^B \partial_T^A\right) AB \quad (6.31)$$

when A and B are functions of ε and T . Fourier transforming equation (6.24) in relative temporal coordinates, I get

$$\varepsilon\tau_z \circ \check{G}'_{k_1 k_2} - \sum_{k'} \check{\Sigma}'_{k_1 k'} \circ \check{G}'_{k' k_2} = \delta_{k_1 k_2}, \quad (6.32a)$$

$$\check{G}'_{k_1 k_2} \circ \varepsilon\tau_z - \sum_{k'} \check{G}'_{k_1 k'} \circ \check{\Sigma}'_{k' k_2} = \delta_{k_1 k_2}. \quad (6.32b)$$

Quasiclassical theory is often derived from continuous models [203–207], but real materials are often better described by lattice models. Since I here consider a lattice model with a finite number of lattice sites, the crystal momenta takes discrete values. As a result, we must take care when defining the COM spatial positions. For instance, one cannot easily use the symmetric definition in terms of $\check{G}_{(k+p/2)(k-p/2)}$ because we cannot evaluate $\check{G}_{(k+p/2)(k-p/2)}$ for all p . I define

$$\check{G}'_{Rk} = \sum_p \check{G}'_{(k+p)k} e^{i\mathbf{p}\cdot\mathbf{R}} \quad (6.33)$$

and

$$\begin{aligned} \check{\Sigma}'_{Rk}(T, \varepsilon) &= \sum_p \check{\Sigma}'_{(k+p)k}(T, \varepsilon) e^{i\mathbf{p}\cdot\mathbf{R}} \\ &= D_k + V'_{Rk}(T) + \check{\Sigma}'_{\text{imp}, Rk}(T, \varepsilon) + \check{\Sigma}'_{\text{inel}, Rk}(T, \varepsilon). \end{aligned} \quad (6.34)$$

To rewrite equation (6.24) in terms of COM coordinates, one must evaluate the sum over internal momenta, $\sum_{k'} \check{\Sigma}'_{k_1 k'} \circ \check{G}'_{k' k_2}$ as a function of COM coordinates. This can be done in the discrete case by using the Newton Forward differences formula, like was done in paper IX. However, here I instead define continuous variables to simplify this step.

In order to define functions of continuous momentum and position coordinates, I assume that the variation in \check{G}'_{Rk} and $\check{\Sigma}'_{Rk}$ between neighboring positions \mathbf{R} and momenta \mathbf{k} is small. More precisely, I assume that there exist λ_R and λ_k which are larger than the distance between neighboring lattice sites and neighboring momenta, respectively, such that

$$\left| \check{G}'_{(R+r)(k+p)} - \check{G}'_{Rk} \right| \ll \left| \check{G}'_{Rk} \right| \quad (6.35)$$

as long as $|\mathbf{r}| < \lambda_R$ and $|\mathbf{p}| < \lambda_p$, where the norm is an appropriate Matrix norm, such as the Frobenius norm.

In the absence of impurity scattering or dissipation, it is not clear that this assumption is valid. For instance, if $\check{\Sigma}'_{k_1 k_2} = D_k \delta_{k_1 k_2}$, then $\check{G}'_{k_1 k_2} = \delta_{k_1 k_2} [\tau_z \varepsilon - D_{k_1}]^{-1}$, so $\check{G}'_{Rk} = [\tau_z \varepsilon - D_k]^{-1}$ which diverges at $\varepsilon = \xi_{i, \pm k}$ for all $i \in \{1, \dots, 2N_s\}$. Close to these energies it is therefore not true that

\check{G}'_{Rk} varies slowly with k . On the other hand, if we include dissipation and impurity scattering, this will remove the divergence. For instance, if we use the relaxation time approximation when including dissipation, we effectively add an imaginary constant to the energy, $\varepsilon \rightarrow \varepsilon + i\delta$, thereby shifting the divergence away from the real axis. To get an order of magnitude estimate for when the assumption of slow variation in \mathbf{k} -space is valid, consider the case when the retarded part of the self-energy is $\check{\Sigma}'_{k_1k_2} = D_k\delta_{k_1k_2} + i\delta\tau_z$. In this case, the retarded and advanced Green's functions are $\check{G}'_{Rk} = [\tau_z(\varepsilon + i\delta) - D_k]^{-1}$. The Green's function is strongly peaked at $\xi_{i,\pm k} = \varepsilon$. Consider one of the energy bands which crosses $\xi_{i,\pm k} = \varepsilon$, and let \mathbf{k}_1 be such that $\xi_{i,k_1} = \varepsilon$ and \mathbf{k}_2 be in the neighborhood such that $\xi_{i,k_2} \approx \xi_{i,k_1} + \Delta\mathbf{k} \cdot \nabla_k \xi_{i,k_1}$, where $\Delta\mathbf{k} = \mathbf{k}_2 - \mathbf{k}_1$. I find that

$$\frac{|\check{G}'_{Rk_2} - \check{G}'_{Rk_1}|}{|\check{G}'_{Rk_1}|} \lesssim \frac{|\Delta\mathbf{k} \cdot \nabla_k \xi_{i,k_1}|}{\delta}. \quad (6.36)$$

In quasiclassical theory, $\nabla_k \xi_{i,k_1}$ will be on the order of the Fermi velocity, v_F . On the other hand, neighboring momenta differ by $2\pi/L$, where L is the length of the system. Therefore,

$$\frac{|\check{G}'_{Rk_2} - \check{G}'_{Rk_1}(T, \varepsilon)|}{|\check{G}'_{Rk_1}|} \lesssim \frac{2\pi(1/\delta)v_F}{L} = 2\pi \frac{l_{\text{inel}}}{L}, \quad (6.37)$$

where inelastic l_{inel} is the inelastic mean free path, since $1/\delta$ is the inelastic scattering rate. Therefore, the assumption of slow variation in \mathbf{k} -space is justified when the inelastic mean free path is much shorter than the system size L . This is not always the case, as the inelastic mean free path can be several centimeters (see paper VIII). Note that elastic impurity scattering has similar effects because it also gives rise to an imaginary self-energy term, and the elastic mean free path is often much smaller than the inelastic mean free path. Therefore, it can be sufficient that the system is much shorter than the elastic mean free path. When the assumption of slow variation is not valid in \mathbf{k} -space, one can do the derivation using a lattice model, like in paper IX.

With the assumption of slow variation on the scale of nearest neighbor COM position and momentum, I define the continuous Green's

function as

$$\check{G}'(\mathbf{R}, \mathbf{k}, T, \varepsilon) = \sum_i \sum_p \frac{\check{G}'_{R_i p}}{C_R(\mathbf{R})C_k(\mathbf{k})} e^{-(R_i - R)^2/\lambda_R^2} e^{-(\mathbf{p} - \mathbf{k})^2/\lambda_k^2}, \quad (6.38)$$

where λ_R and λ_k is larger than the nearest neighbor distances in position and momentum space, respectively, and such that the relative variation in $\check{G}'_{R_i p}$ over this scale is negligible. In order for the continuous Green's function to satisfy $\check{G}'(\mathbf{R}, \mathbf{k}, T, \varepsilon) \approx \check{G}'_{Rk}(T, \varepsilon)$, I choose

$$C_R(\mathbf{R}) = \sum_i e^{-(R_i - R)^2/\lambda_R^2}, \quad (6.39a)$$

$$C_k(\mathbf{k}) = \sum_p e^{-(\mathbf{p} - \mathbf{k})^2/\lambda_k^2}. \quad (6.39b)$$

From equation (6.38), one can compute $\sum_{k'} \check{\Sigma}'_{k_1 k'} \circ \check{G}'_{k' k_2}$ in Wigner coordinates. In COM coordinates, this sum becomes

$$\begin{aligned} & \sum_p \sum_{k'} \check{\Sigma}'_{(k+p)k'} \circ \check{G}'_{k'k} e^{i\mathbf{p} \cdot \mathbf{R}} = \sum_{p'} \sum_{k'} \check{\Sigma}'_{(k'+p')k'} e^{i\mathbf{p}' \cdot \mathbf{R}} \circ \check{G}'_{k'k} e^{i(\mathbf{k}' - \mathbf{k}) \cdot \mathbf{R}} \\ & = \sum_{k'} \check{\Sigma}'_{Rk'} \circ \check{G}'_{k'k} e^{i(\mathbf{k}' - \mathbf{k}) \cdot \mathbf{R}} = \sum_{\tilde{k}} \check{\Sigma}'_{R(k+\tilde{k})} \circ \check{G}'_{(k+\tilde{k})k} e^{i\tilde{k} \cdot \mathbf{R}} \\ & \approx \sum_{\tilde{k}} \check{\Sigma}'(\mathbf{R}, \mathbf{k} + \tilde{\mathbf{k}}) \check{G}'_{(k+\tilde{k})k} e^{i\tilde{k} \cdot \mathbf{R}} \\ & = \sum_{\alpha} \frac{\nabla_{\tilde{k}}^{\alpha} \check{\Sigma}'(\mathbf{R}, \mathbf{k})}{\alpha!} \circ \sum_{\tilde{k}} (\tilde{\mathbf{k}})^{\alpha} \check{G}'_{(k+\tilde{k})k} e^{i\tilde{k} \cdot \mathbf{R}} \\ & = \sum_{\alpha} \frac{\nabla_{\tilde{k}}^{\alpha} \check{\Sigma}'(\mathbf{R}, \mathbf{k})}{\alpha!} (-i\nabla_R)^{\alpha} \circ \sum_{\tilde{k}} \check{G}'_{(k+\tilde{k})k} e^{i\tilde{k} \cdot \mathbf{R}} \\ & \approx \sum_{\alpha} \frac{(-i)^{|\alpha|}}{\alpha!} \nabla_{\tilde{k}}^{\alpha} \check{\Sigma}'(\mathbf{R}, \mathbf{k}) \circ \nabla_R^{\alpha} \check{G}'(\mathbf{R}, \mathbf{k}), \quad (6.40) \end{aligned}$$

where the sum over α goes over multi-indices. That is, $\alpha = (\alpha_1, \alpha_2, \alpha_3)$ is a multi-index, where α_i is an integer and goes from 0 to ∞ for all $i \in \{1, 2, 3\}$. If $\mathbf{k} = (k_1, k_2, k_3)$ is a vector, then $(\mathbf{k})^{\alpha} = k_1^{\alpha_1} k_2^{\alpha_2} k_3^{\alpha_3}$. The same applies to the vectors of differential operators, ∇_k and ∇_R . Moreover, $\alpha! = \alpha_1! \alpha_2! \alpha_3!$ and $|\alpha| = \alpha_1 + \alpha_2 + \alpha_3$. I use the bullet operator,

•, to denote

$$(\check{\Sigma}' \bullet \check{G}')(\mathbf{R}, \mathbf{k}) = \sum_{\alpha} \frac{(-i)^{|\alpha|}}{\alpha!} \nabla_{\mathbf{k}}^{\alpha} \check{\Sigma}'(\mathbf{R}, \mathbf{k}) \circ \nabla_{\mathbf{R}}^{\alpha} \check{G}'(\mathbf{R}, \mathbf{k}). \quad (6.41)$$

Sometimes this notation is shortened to [204]

$$\check{\Sigma}' \bullet \check{G}' = \exp\left(-i \nabla_{\mathbf{k}}^{\check{\Sigma}'} \nabla_{\mathbf{R}}^{\check{G}'}\right) \check{\Sigma}' \circ \check{G}', \quad (6.42)$$

although one should keep in mind that the series expansion of the exponential must go over all multi-indices. This form of the bullet product is also known as the gradient expansion [185, 204], since it is a series expansion in differential operators. With this notation, the equations for the Green's functions in the Wigner coordinates become

$$\varepsilon \tau_z \circ \check{G}' - \check{\Sigma}' \bullet \check{G}' = 1, \quad (6.43a)$$

$$\check{G}' \circ \varepsilon \tau_z - \check{G}' \bullet \check{\Sigma}' = 1. \quad (6.43b)$$

6.2 The Quasiclassical Green's Function and the Eilenberger Equation

While equation (6.43) is written in compact notation, solving it is very difficult. Equation (6.43) involves an infinite series of differential operators of increasing order. Since \check{G}' is strongly peaked in momentum-space close to the Fermi level, it is also not always true that one can truncate the series expansions of the exponential operators to obtain a set of partial differential equations of reasonable order. Even if we could truncate the series expansions, solving it for all possible momenta, positions, energies and time would be computationally difficult. Luckily, we can define a so-called quasiclassical Green's function as an integral over momenta close to the peaks, thereby truncating the gradient expansion and removing the radial part of the momentum from the problem.

The quasiclassical Green's function is defined as an integral over momenta close to the Fermi level. However, in the general treatment considered here, we can have more than one energy band crossing the Fermi level. In simple normal metals or antiferromagnetic metals,

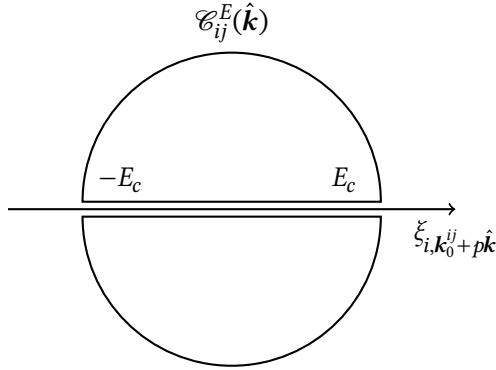


Figure 6.1: A sketch of the Eilenberger contour [205].

there are two spin-degenerate bands crossing the Fermi level at the same place. In strongly polarized ferromagnets, on the other hand, the spin bands are shifted with respect to each other, giving two different regions in \mathbf{k} -space where the energy bands cross the Fermi level [208, 209]. More generally, there might be multiple energy bands that cross the Fermi level, and some energy bands may cross the Fermi level in only some \mathbf{k} -directions. For a general description that includes the possibility of multiple conduction bands which crosses the Fermi level at various places, we must integrate over multiple sets of momenta. To do this, I generalize the Eilenberger contour, first introduced by Eilenberger [205].

I assume that the energy bands are continuous. This means that we can define continuous surfaces in momentum space where $\xi_{i, \mathbf{p}}$ are constant. If we take into account the periodicity of crystal momentum and apply periodic boundaries to the first Brillouin zone the isosurfaces of constant $\xi_{i, \mathbf{p}}$ must be closed due to the continuity of $\xi_{i, \mathbf{p}}$. I define a *Fermi surface* of the i 'th energy band to be a closed surface in momentum space such that $\xi_{i, \mathbf{p}} = 0$ at all points in this surface. The requirement of a closed Fermi surface is only true in the general case when one takes into consideration the periodic boundary conditions in momentum space. An energy band might have multiple Fermi surfaces, only one Fermi surface, or no Fermi surface.

Let $\xi_{i, \mathbf{p}}$ be an energy band with at least one Fermi surface. We can label these Fermi surfaces from 1 to $n_{F,i}$. Let \mathbf{k}_0^i be a crystal momentum

in the volume enclosed by Fermi surface j . I assume for that \mathbf{k}_0^{ij} is chosen such that for each unit vector $\hat{\mathbf{k}}$, $\xi_{i,\mathbf{k}_0^{ij}+p\hat{\mathbf{k}}}$ crosses the Fermi surface for exactly one p , if we take into account the periodic boundaries. I denote the value p for which this happens as $p_F^{ij}(\hat{\mathbf{k}})$. Next, I define the Eilenberger contour $\mathcal{C}_{ij}^E(\hat{\mathbf{k}})$ to be the set of two closed semicircular paths in the complex plane, as sketched in figure 6.1. That is, $\mathcal{C}_{ij}^E(\hat{\mathbf{k}})$ consists of two paths, each following the real $\xi_{i,\mathbf{k}_0^{ij}+p\hat{\mathbf{k}}}$ -line from $\xi_{i,\mathbf{k}_0^{ij}+p\hat{\mathbf{k}}} = -E_c$ to $\xi_{i,\mathbf{k}_0^{ij}+p\hat{\mathbf{k}}} = E_c$, where they split into two semicircular arcs in the upper and lower parts of the complex plane, before the paths close at $\xi_{i,\mathbf{k}_0^{ij}+p\hat{\mathbf{k}}} = -E_c$. The arc must be sufficiently far from all the zeroes of D so that $\check{\Sigma}' \approx D$.

This is a key assumption of the quasiclassical theory. The distance to the extrema of the energy band must be at least E_c by definition, and in order for $\check{\Sigma}' \approx D$, E_c must be much larger than all the other energies in $\check{\Sigma}'$. That is, if $\check{\Sigma}' = D + \check{\Omega}$, then $E_c \gg |\check{\Omega}|$. This also gives a restriction to other Fermi surfaces in the system. Take any energy band, $\xi_{n,p}$, where $n \neq i$. If a root of this energy band is inside $\mathcal{C}_{ij}^E(\hat{\mathbf{k}})$, then it must be relatively close to $\mathbf{k}_0^{ij} + p_F^{ij}\hat{\mathbf{k}}$, such that $\xi_{n,\mathbf{k}_0^{ij}+\hat{\mathbf{k}}p_F^{ij}(\hat{\mathbf{k}})} \ll E_c$. This will be more clear in the derivation that follows, but it has an important consequence for how we can define the quasiclassical Green's functions.

Since $\check{\Sigma}' \approx D$ at the arcs, and D is independent of COM time T and COM position \mathbf{R} , equation (6.43) is solved by $\check{G}' = (\varepsilon\tau_z - D)^{-1}$ at the arcs. Quasiclassical theory only applies to $|\varepsilon| \ll E_c$, so $\check{G}' = -D^{-1}$ at the arcs. This means that larger $|\varepsilon|$ must be treated separately when computing observables, as shown in section 6.6. The usefulness of quasiclassical theory is that it separates the expressions for observables into one part containing the so-called quasiclassical Green's function, which depends on the full self-energy $\check{\Sigma}'$, but which is easier to compute than the full Green's function \check{G}' , and another part away from the Fermi surface where the full Green's function is easier to compute.

The fact that zeroes of different energy bands must be either close in momentum space or far away, means that we cannot have two different Fermi surfaces which are close to each other in some region of momentum space and far away in another. If two Fermi surfaces are close in some regions, then they must be close everywhere. This means that we can collect sets of Fermi surfaces by proximity, as illustrated in

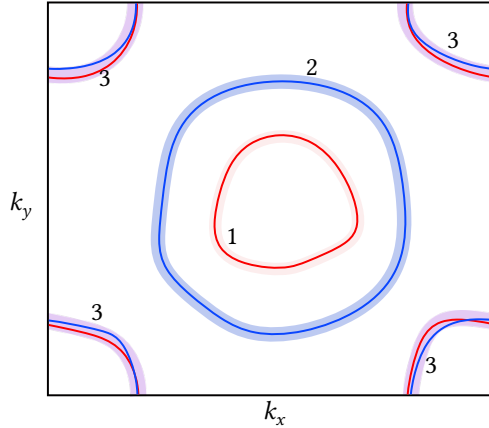


Figure 6.2: A sketch of 4 Fermi surfaces in a 2D plane in the first Brillouin zone. The Fermi surfaces can be collected in three groups ($N_q = 3$) by proximity, labeled 1, 2 and 3 in the figure. The Fermi surfaces in the same group must be close compared to the distances to the edges of the energy bands, while Fermi surfaces in different groups must be far away from each other.

figure 6.2. Let the number of different collections of Fermi surfaces be N_q , and let $\Xi_i = \{\xi_{i_1}, \xi_{i_2}, \dots\}$ be the set of energy bands that have a Fermi surface in collection i , where $i \in \{1, \dots, N_q\}$. For each collection of Fermi surfaces, we must choose one energy band to define the quasiclassical Green's function, which I choose to be ξ_{i_1} . For notational simplicity, I define $\eta_i(p) = \xi_{i_1, \mathbf{k}_0^{i_1} + p\hat{\mathbf{k}}}$ and $\mathcal{C}_i^E = \mathcal{C}_{i_1}^E$. I define the i 'th quasiclassical Green's function to be¹

$$\check{g}_i(\mathbf{R}, \hat{\mathbf{k}}, T, \varepsilon) = \frac{i}{2\pi} \oint_{\mathcal{C}_i^E} d\eta_i \check{G}'(\mathbf{R}, \mathbf{k}_0^{i_1} + p\hat{\mathbf{k}}, T, \varepsilon), \quad (6.44)$$

where $i \in \{1, \dots, N_q\}$. I assume that the energy bands that cross the Fermi level in \mathcal{C}_i^E are monotonously increasing or decreasing, which means that they only cross the Fermi level once inside this region. However, different bands may cross at different points and have different slopes.

1. The prefactor $i/2\pi$ is often replaced with $1/\pi$ in the literature. The reason for the extra factor $1/2$ in this work is that the Eilenberger contour is the sum of two paths, so the integral goes over the real line twice.

The quasiclassical equations of motion are obtained by integrating equation (6.43) over \mathcal{C}_i^E . Since \mathcal{C}_i^E is the sum of two closed paths, one can use the residue theorem to evaluate the integral. The path in the upper half of the complex plane is positively oriented while the path in the lower half plane is negatively oriented. Therefore, the integral of a function $f(\eta_i)$ becomes

$$\frac{i}{2\pi} \oint_{\mathcal{C}_i^E} d\eta_i f(\eta_i) = - \sum_{\eta_i'} \text{Im}(\eta_i') \text{Res}(f, \eta_i'), \quad (6.45)$$

where the sum goes over all the poles of f inside the contours and $\text{Res}(f, \eta_i')$ is the residue of f at η_i' . The right-hand sides of equation (6.43) have no poles and the first terms on the left-hand sides only depend on momentum through \check{G}' . Therefore,

$$\varepsilon\tau_z \circ \check{g}_i - \frac{i}{2\pi} \oint_{\mathcal{C}_i^E} d\eta_i \check{\Sigma}' \cdot \check{G}' = 0, \quad (6.46a)$$

$$\check{g}_i \circ \varepsilon\tau_z - \frac{i}{2\pi} \oint_{\mathcal{C}_i^E} d\eta_i \check{G}' \cdot \check{\Sigma}' = 0. \quad (6.46b)$$

Let $\check{\Sigma}' = D + \check{\Omega}$. To evaluate the second terms on the left-hand sides of equations (6.46a) and (6.46b), I will use that if $f(\eta_i)$ has no poles inside the contours and are approximately the same on all the poles of \check{G}' , then

$$\begin{aligned} \frac{i}{2\pi} \oint_{\mathcal{C}_i^E} d\eta_i f(\eta_i) \check{G}'(\mathbf{k}_0^{i1} + p\hat{\mathbf{k}}) &= - \sum_{\eta_i'} \text{Im}(\eta_i') f(\eta_i') \text{Res}(\check{G}', \eta_i') \\ &= f(0) \check{g}_i + \mathcal{O}(a \partial_{\eta_i} f \check{g}_i), \end{aligned} \quad (6.47)$$

where a is an order of estimate for the distances between the poles of \check{G}' . If $|a \partial_{\eta_i} f_{ij}| \ll |f_{ij}(0)|$ for all matrix elements f_{ij} of f , then we can ignore the second term compared to the first, such that

$$\frac{i}{\pi} \oint_{\mathcal{C}_i^E} d\eta_i f(\eta_i) \check{G}'(\xi_j, p\hat{\mathbf{k}}) \approx f(0) \check{g}_i. \quad (6.48)$$

This approximation is *not* valid when $f = D$, since elements of D go through zero close to the poles. For this reason, we have no way to evaluate

$$\frac{i}{2\pi} \oint_{\mathcal{C}_i^E} d\eta_i D \check{G}' \quad \text{and} \quad \frac{i}{2\pi} \oint_{\mathcal{C}_i^E} d\eta_i \check{G}' D. \quad (6.49)$$

The trick to obtaining quasiclassical equations of motion is to remove this term by essentially subtracting equation (6.46b) from equation (6.46a). In a simple normal metal where D is proportional to the identity matrix, this is straightforward. In an antiferromagnet or other systems with multiple energy bands, not all energy bands cross the Fermi surface, as in paper IX, which makes it slightly more complicated. In this even more general case presented here, where the energy bands can also have different slopes as they cross the Fermi surface, and where they can cross at different momenta, the procedure becomes even more difficult.

From before, Ξ_i is the set of the bands which crosses the Fermi level in the region specified by \mathcal{E}_i^E . I define the diagonal matrix D_0 such that $D_{0,ij} = 0$ if $i \neq j$ and

$$D_{0,mn} = \begin{cases} \xi_{n,\mathbf{k}_0^{i_1} + p\hat{\mathbf{k}}} & \text{if } \xi_n \in \Xi_i, \\ \xi_{i_1,\mathbf{k}_0^{i_1} + p\hat{\mathbf{k}}} & \text{otherwise.} \end{cases} \quad (6.50)$$

Since $|a\partial_{\eta_i}(D - D_0)_{ij}| \ll |(D - D_0)_{ij}(0)|$ whenever $(D - D_0)_{ij}$ is not identically equal to zero,

$$\frac{i}{\pi} \oint_{\mathcal{E}_i^E} d\eta_i (D - D_0) \check{G}' = (D - D_0)(0) \check{g}_i(\hat{\mathbf{k}}), \quad (6.51)$$

and similarly for the integral of $\check{G}'(D - D_0)$. The non-zero components of $D - D_0$ correspond to the energy bands which do not cross the Fermi level in the part of momentum space under consideration. This means that the elements are larger than E_c in magnitude, and therefore much larger than the elements of \check{Q} and D_0 , which are on the order $a \ll E_c$. It follows from equation (6.51) and the similar equation from the integral of $\check{G}'(D - D_0)$ that $(\check{g}_i)_{nm} = \mathcal{O}(a/E_c)$ unless both n and m correspond to one of the energy bands going through the Fermi level in \mathcal{E}_i^E .

Above I defined the Fermi momentum $p_F^{i_1}(\hat{\mathbf{k}})$, such that $\xi_{i_1,\mathbf{k}_0^{i_1} + p_F^{i_1}(\hat{\mathbf{k}})\hat{\mathbf{k}}} = 0$. I assume that at all the roots, the energy bands that cross the Fermi level, $\xi_n \in \Xi_i$, are well approximated by

$$\xi_{n,\mathbf{k}_0^{i_1} + p\hat{\mathbf{k}}} \approx \xi_{n,p_F^{i_1}(\hat{\mathbf{k}})\hat{\mathbf{k}}} + (\hat{\mathbf{k}} \cdot \mathbf{v}_F^n) \left[p - p_F^{i_1}(\hat{\mathbf{k}}) \right] \quad (6.52)$$

where $\hat{\mathbf{k}} \cdot \mathbf{v}_F^n = \partial \xi_{n,\mathbf{k}_0^{i_1} + p\hat{\mathbf{k}}} / \partial p|_{p=p_F^{i_1}(\hat{\mathbf{k}})}$. This assumption is valid provided that the gradient of ξ_n is approximately constant on all the poles, which

means that the relative change is small. When the functional form of ξ_n is known, such as in paper IX, this assumption can be related to the parameters of the system, such as the chemical potential. With this,

$$D_0 = D_0|_{p=p_F^{i_1}(\hat{\mathbf{k}})} + (\hat{\mathbf{k}} \cdot \nabla_k D_0)|_{p=p_F^{i_1}(\hat{\mathbf{k}})} \left[p - p_F^{i_1}(\hat{\mathbf{k}}) \right] \quad (6.53)$$

at all the poles.

We can remove the difficult terms in equation (6.46) if we multiply equations (6.46a) and (6.46b) by $(\hat{\mathbf{k}} \cdot \mathbf{v}_F^{i_1}) (\hat{\mathbf{k}} \cdot \nabla_k D_0)|_{p=p_F^{i_1}(\hat{\mathbf{k}})}^{-1}$ from the left and right, respectively, and take the difference. I define

$$F_i(\hat{\mathbf{k}}) = (\hat{\mathbf{k}} \cdot \mathbf{v}_F^{i_1}) (\hat{\mathbf{k}} \cdot \nabla_k D_0)|_{p=p_F^{i_1}(\hat{\mathbf{k}})}^{-1} \quad (6.54)$$

The terms in question then become

$$\begin{aligned} \frac{i}{\pi} \oint_{\mathcal{C}_i^E} d\eta_i (F_i D \check{G}' - \check{G}' D F_i) &= \left[F_i (D - D_0)|_{p_F^{i_1}} + F_i D_0|_{p_F^{i_1}}, \check{g}_i \right]_- \\ &= \left[F_i D|_{p_F^{i_1}}, \check{g}_i \right]_- . \end{aligned} \quad (6.55)$$

The diagonal matrix F_i can be understood as a flatness factor since the terms are determined by the slopes of the bands. Matrix elements corresponding to bands that are flatter than ξ_{i_1} have magnitudes larger than 1, while sharper bands have magnitudes less than 1. Note that the matrix elements can also be negative, if the bands have slopes of different signs, such as in weak antiferromagnets close to where the two energy bands cross (see paper IX). The flatness is also related to the density of states, so one could also think of F_i as correcting for the difference in the density of states for the different bands.

Since we have assumed that the gradient of D_0 is approximately constant at the poles, and since $\nabla_R D = 0$, we can also evaluate the next terms in the Gradient expansion.

$$\frac{i}{\pi} \oint_{\mathcal{C}_i^E} d\eta_i (-i F_i \nabla_k D \cdot \nabla_R \check{G}' + i \nabla_k \check{G}' \cdot \nabla_R D F_i) = -i F_i \nabla_k D \cdot \nabla_R \check{g}_i. \quad (6.56)$$

It is not necessary that the gradient of D is approximately constant. The terms in D not corresponding to an energy band that crosses the

Fermi level in \mathcal{E}_i^E are large. In particular, they are larger than E_c . As a result, the relative variation in these terms can be assumed small, so the gradient expansion can be truncated at the lowest order, in contrast to the gradient expansion of D_0 . Additionally, the elements of the Green's function corresponding to these terms are negligible because of the magnitude of D for these elements, since $(\check{g}_i)_{nm} = \mathcal{O}(a/E_c)$ unless both n and m correspond to one of the energy bands going through the Fermi level in \mathcal{E}_i^E . Hence, one can replace $\nabla_k D$ with $\nabla_k D_0$.

It also follows from the fact that $\nabla_k D_0$ is approximately constant at the poles, together with the fact that the Green's function changes slowly as a function of COM position, that we can neglect the higher order terms in the gradient expansion. I define the characteristic length L as the smallest scalar satisfying

$$|\nabla_R \check{g}_i| < \frac{|\check{g}_i|}{L}. \quad (6.57)$$

The scalar L should also satisfy $|\nabla_R^2 \check{g}_i| < \frac{|\nabla_R \check{g}_i|}{L}$ and similar for higher order derivatives. The fact that the gradient of D_0 is approximately constant on the poles means that $|\partial^2 \xi_i / \partial p^2| \ll |\partial \xi_i / \partial p|_{p=p_F^{i_1}} / |p - p_F^{i_1}|$. Assuming that the second order derivatives of ξ_i in all directions are similar in magnitude, the next order in the gradient expansion satisfies

$$|\nabla_k^2 D \nabla_R^2 \check{g}_i| \ll \frac{\nabla_k D \cdot \nabla_R \check{g}_i}{|p - p_{F,j}|L}. \quad (6.58)$$

Hence, the higher order terms are negligible as long as $|p - p_F^{i_1}|L$ is not negligible compared to 1. The distance between poles is on the order a , as explained above. This means $p - p_F^{i_1} = \mathcal{O}(a/v_F^{i_1})$, where $v_F^{i_1}$ is the amplitude of the Fermi velocity of the band used to define the quasiclassical Green's function. Hence, $(p - p_F^{i_1})L = \mathcal{O}(aL/v_F^{i_1})$. The inverse energy $1/a$ defines a time scale. For instance, if the dominant energy in the system is the elastic scattering rate, then $1/a$ is maximally on the order of the time between scatterings and $v_F^{i_1}/a$ is the mean free path for particles at the Fermi level i in energy band i_1 . The statement that $(p - p_F^{i_1})L = \mathcal{O}(L/[v_F^{i_1}/a])$ is not too small in this case means that L should not be negligible compared to the mean free path. Note that L can be on the order of the mean free path with no issue. Under this

assumption,

$$\frac{i}{2\pi} \oint_{\mathcal{E}_i^E} d\eta_i (F_i D \cdot \check{G}' - \check{G}' \cdot D F_i) = \left[F_i D \Big|_{p_F^{i_1}, \check{g}_i} \right]_- - i F_i \nabla_k D_0 \cdot \nabla_R \check{g}_i. \quad (6.59)$$

To complete the derivation of the quasiclassical equation of motion, we only need to evaluate

$$\frac{i}{\pi} \oint_{\mathcal{E}_i^E} d\eta_i (F_i \check{\Omega} \cdot \check{G}' - \check{G}' \cdot \check{\Omega} F_i). \quad (6.60)$$

I assume that $\check{\Omega}$ is approximately constant on all the poles. This means that $|\partial^2 \check{\Omega} / \partial p^2| \ll |\partial \check{\Omega} / \partial p|_{p=p_F^{i_1}} / |p - p_F^{i_1}|$. For the same reason as with the gradient of D_0 above, this means that higher order terms in the gradient expansion of $\check{\Omega} \cdot \check{G}'$ are negligible after integration, so

$$\frac{i}{\pi} \oint_{\mathcal{E}_i^E} d\eta_i F_i \check{\Omega} \cdot \check{G}' \approx F_i \check{\Omega} \circ \check{g}_i. \quad (6.61)$$

When evaluating the higher order terms in the gradient expansion of $\check{G}' \cdot \check{\Omega} F_i$, we can use the fact that $\partial_{p_F^{i_1}}$ is approximately constant combined with the fact that the contour integral of a total derivative is always zero, which implies that

$$\begin{aligned} \oint_{\mathcal{E}_i^E} d\eta_i A(\hat{\mathbf{k}} \cdot \nabla_k) B &= \oint_{\mathcal{E}_i^E} d\eta_i A(\hat{\mathbf{k}} \cdot \nabla_k \eta_j) \frac{\partial B}{\partial \eta_i} \\ &= \oint_{\mathcal{E}_i^E} d\eta_i \frac{\partial}{\partial \eta_i} (A \hat{\mathbf{k}} \cdot \nabla_k \eta_j) B \approx \oint_{\mathcal{E}_i^E} d\eta_i [(\hat{\mathbf{k}} \cdot \nabla_k) A] B. \end{aligned} \quad (6.62)$$

With this trick, the momentum derivative of \check{G}' , which is strongly peaked in momentum space, can be moved over to $\check{\Omega}$. Since $\check{\Omega}$ should change as slowly in space as \check{g}_i , the same arguments as above imply that we can neglect the higher order terms in the gradient expansion of $\check{G}' \cdot \check{\Omega} F_i$ as well. Hence, the full equations for the quasiclassical Green's function become

$$i F_i (\nabla_k D_0) \cdot \nabla_R \check{g}_i + \left[F_i \varepsilon \tau_z - F_i D \Big|_{p_F^{i_1}, \check{g}_i} \right]_- - F_i \check{\Omega} \circ \check{g}_i + \check{g}_i \circ \check{\Omega} F_i = 0, \quad (6.63)$$

which can be seen as a generalization of the Eilenberger equation [205]. Each collection of proximized Fermi surfaces gives a quasiclassical

Green's function, and the number of such Green's functions is N_q . Note that the different Green's functions can couple, but only through \check{Q} . For instance, the impurity term in \check{Q} or the superconducting term can couple the different quasiclassical Green's functions and quasiclassical Green's functions at different momentum directions. In particular, impurity scattering will couple all momentum directions, typically making the quasiclassical Green's function more isotropic in space.

With the general framework presented here, there can be multiple sets of Fermi surfaces at different points in momentum space, and the same energy band can cross the Fermi level multiple times. This means that the theory can be applied to for instance normal metal, weak ferromagnets, strongly polarized ferromagnets [208], including half-metals (paper I), antiferromagnetic metals (paper IX), systems with antiferromagnetic insulators [210], Rashba superconductors [211] and systems with spin-density waves [212]. Additionally, because I have included the possibility of different flatness for different bands as they cross the Fermi surfaces, the quasiclassical theory takes into account the different density of states of different bands, making it capable of modeling for instance flatband superconductors [213].

6.3 Normalization Condition

The different components of the quasiclassical Green's functions are not independent. This is partly because the definition of $\hat{G}_{k_1 k_2}^{R/A/K}$ includes two copies of the normal and anomalous Green's functions, not to mention the fact that $\hat{G}_{k_1 k_2}^R$ and $\hat{G}_{k_1 k_2}^A$ are related through $\hat{G}_{k_1 k_2}^A(t_1, t_2) = \tau_z [\hat{G}_{k_2 k_1}^R(t_2, t_1)]^\dagger \tau_z$. In addition to this, the components are related through a normalization condition, which is what I will show in this section. To do so, I will in part follow Shelankov's method [206], but I will generalize it to work with how I defined the more generalized quasiclassical Green's function in the previous section. Additionally, I will change some key steps and make some important changes to various definitions, for instance in order to make mathematical limits well-defined. For example, unlike how I defined quasiclassical Green's functions above, Shelankov did not use the Eilenberger contour. Using the Eilenberger contour to define quasiclassical Green's functions, rather than the divergent definition in Ref. [206], and changing the

definition of the trajectory Green's functions, I find that the proof simplifies.

Consider a collection of Fermi surfaces number i . Let $\mathbf{v}_F^n = \nabla_{\mathbf{k}} \xi_n, \mathbf{p} |_{\mathbf{p}=\mathbf{k}_0^{i_1} + p_F^{i_1} \hat{\mathbf{k}}}$ when $\xi_n \in \Xi_i$ and $\mathbf{v}_F^n = \nabla_{\mathbf{k}} \xi_{i_1}, \mathbf{p} |_{\mathbf{p}=\mathbf{k}_0^{i_1} + p_F^{i_1} \hat{\mathbf{k}}}$ otherwise, where ξ_{i_1} is the energy band used to define the quasiclassical Green's function \check{g}_i . Next, let the trajectory Green's function be

$$\check{g}_{i,mn}^t(y_1, y_2, \mathbf{R}, \hat{\mathbf{k}}) = \frac{i}{2\pi} \int_{\mathcal{C}_i(y_1-y_2)} d\eta_i e^{i\eta_i(y_1-y_2)/(\hat{\mathbf{k}} \cdot \mathbf{v}_F^{i_1})} \times \check{G}'_{mn} \left(\mathbf{R} + \frac{y_1 \mathbf{v}_F^m}{\hat{\mathbf{k}} \cdot \mathbf{v}_F^m}, \mathbf{k}_0^{i_1} + p \hat{\mathbf{k}} \right) \quad (6.64)$$

where $\mathcal{C}_i(y_1 - y_2)$ is one of the two semi-circles in the definition of the quasiclassical Green's function. In particular, $\mathcal{C}_i(y_1 - y_2)$ is the path which goes first from $\eta_i = \xi_{i_1, \mathbf{k}_0^{i_1} + p \hat{\mathbf{k}}} = -E_c$ to $\eta_i = E_c$ along the real line. Then, if $(y_1 - y_2)/(\hat{\mathbf{k}} \cdot \mathbf{v}_F^{i_1}) > 0$, the path goes up into the upper part of the complex plane and follows a semicircular path, closing the contour at $\xi_{i_1, \mathbf{k}_0^{i_1} + p \hat{\mathbf{k}}} = -E_c$. Otherwise, if $(y_1 - y_2)/(\hat{\mathbf{k}} \cdot \mathbf{v}_F^{i_1}) < 0$, the path goes down into the lower part of the complex plane and follows a semicircular path, closing the contour at $\xi_{i_1, \mathbf{k}_0^{i_1} + p \hat{\mathbf{k}}} = -E_c$. Because we are again working with closed contours, we can use the residue theorem to evaluate the trajectory Green's function.

By definition of $\mathcal{C}_i(y_1 - y_2)$, the contours only contain poles with $\text{Re}[i\xi_{i_1}(y_1 - y_2)/(\hat{\mathbf{k}} \cdot \mathbf{v}_F^{i_1})] < 0$. As a result,

$$\lim_{y_2 \rightarrow \pm\infty} \check{g}_{i,mn}^t(y_1, y_2, \mathbf{R}, \hat{\mathbf{k}}) = 0. \quad (6.65)$$

Moreover, by comparing the trajectory Green's function to the quasiclassical Green's function, it is clear that

$$\begin{aligned} & \lim_{y \rightarrow 0^+} \left[\check{g}_i^t(0, -y, \mathbf{R}, \hat{\mathbf{k}}) + \check{g}_i^t(0, y, \mathbf{R}, \hat{\mathbf{k}}) \right] \\ &= \frac{i}{2\pi} \left(\int_{\mathcal{C}_i(y)} d\eta_i + \int_{\mathcal{C}_i(-y)} d\eta_i \right) \check{G}' \left(\mathbf{R}, \mathbf{k}_0^{i_1} + p \hat{\mathbf{k}} \right) \\ &= \frac{i}{2\pi} \int_{\mathcal{C}_i^E} d\eta_i \check{G}' \left(\mathbf{R}, \mathbf{k}_0^{i_1} + p \hat{\mathbf{k}} \right) = \check{g}_i(\mathbf{R}, \hat{\mathbf{k}}), \end{aligned} \quad (6.66)$$

where \mathcal{C}_i^E is the Eilenberger contour from before.

Next, consider the difference, $\lim_{y \rightarrow 0^+} [\check{g}_i^t(0, -y, \mathbf{R}, \hat{\mathbf{k}}) - \check{g}_i^t(0, y, \mathbf{R}, \hat{\mathbf{k}})]$. The part of the contours following the real line cancel because they are the same for $\mathcal{C}_i(y)$ and $\mathcal{C}_i(-y)$. The remaining parts of the contours combine into one large circular path with a diameter equal to $2E_c$. That is,

$$\lim_{y \rightarrow 0^+} [\check{g}_i^t(0, -y, \mathbf{R}, \hat{\mathbf{k}}) - \check{g}_i^t(0, y, \mathbf{R}, \hat{\mathbf{k}})] = \frac{i}{2\pi} \int_{\mathcal{C}_i^c} d\eta_i \check{G}'(\mathbf{R}, \mathbf{k}_0^{i_1} + p\hat{\mathbf{k}}), \quad (6.67)$$

where \mathcal{C}_i^c starts from $-E_c$ and then goes for a full circular path in an either clockwise or counterclockwise direction, depending on the sign of $\hat{\mathbf{k}} \cdot \mathbf{v}_F^{i_1}$. If $\hat{\mathbf{k}} \cdot \mathbf{v}_F^{i_1} > 0$ the path is counterclockwise, meaning that it has a positive orientation. On the other hand, if $\hat{\mathbf{k}} \cdot \mathbf{v}_F^{i_1} < 0$, the path is clockwise and therefore has a negative orientation. Since the entirety of the path is a distance E_c from the poles, we can set $\check{G}' = -D^{-1}$ in the integrand. This makes it easy to evaluate the integral, since $1/\xi_{n, \mathbf{k}_0^{i_1} + p\hat{\mathbf{k}}}$ has exactly zero or one simple pole inside the contour. The energy bands which cross the Fermi level are the only ones with a pole inside the contour, so $\lim_{y \rightarrow 0^+} [\check{g}_i^t(0, -y, \mathbf{R}, \hat{\mathbf{k}}) - \check{g}_i^t(0, y, \mathbf{R}, \hat{\mathbf{k}})]_{mn} = 0$ if $\xi_m \notin \Xi_i$ or if $m \neq n$. One can freely deform the contour as long as one does not cross any poles. Hence, I can deform the contour close to the poles and use equation (6.53) to evaluate the integral for $\xi_m \in \Xi_i$. With this,

$$\begin{aligned} \lim_{y \rightarrow 0^+} [\check{g}_i^t(0, -y, \mathbf{R}, \hat{\mathbf{k}}) - \check{g}_i^t(0, y, \mathbf{R}, \hat{\mathbf{k}})]_{mn} &= -\frac{i}{2\pi} \int_{\mathcal{C}_i^c} d\eta_i [D^{-1}]_{mn} \\ &= \delta_{mn} \begin{cases} \text{sign}(\hat{\mathbf{k}} \cdot \mathbf{v}_F^{i_1}) F_{i,mm}(\hat{\mathbf{k}}) & \text{if } \xi_{m,p\hat{\mathbf{k}}} \in \Xi_i, \\ 0 & \text{if } \xi_{m,p\hat{\mathbf{k}}} \notin \Xi_i, \end{cases} \end{aligned} \quad (6.68)$$

where F_i is given by equation (6.54) and $\text{sign}(x) = \theta(x) - \theta(-x)$ is the sign function. To write this more compactly, I define the diagonal matrix K_i as

$$K_{i,mn} = \delta_{mn} \begin{cases} 1 & \text{if } \xi_m \in \Xi_i, \\ 0 & \text{if } \xi_m \notin \Xi_i, \end{cases} \quad (6.69)$$

such that

$$\lim_{y \rightarrow 0^+} [\check{g}_i^t(0, -y, \mathbf{R}, \hat{\mathbf{k}}) - \check{g}_i^t(0, y, \mathbf{R}, \hat{\mathbf{k}})] = \text{sign}(\hat{\mathbf{k}} \cdot \mathbf{v}_F^{i_1}) K_i F_i(\hat{\mathbf{k}}). \quad (6.70)$$

One can also generalize this to

$$\lim_{y \rightarrow 0^+} [\check{g}_i^t(x, x - y, \mathbf{R}, \hat{\mathbf{k}}) - \check{g}_i^t(x, x + y, \mathbf{R}, \hat{\mathbf{k}})] = \text{sign}(\hat{\mathbf{k}} \cdot \mathbf{v}_F^{i_1}) K_i F_i(\hat{\mathbf{k}}), \quad (6.71)$$

which follows from the definition of the trajectory Green's function and the fact that D is independent of the COM position.

Next, we need differential equations for the trajectory Green's function. Differentiating the trajectory Green's function with respect to y_1 and assuming $y_1 \neq y_2$, I get

$$\begin{aligned} i(\hat{\mathbf{k}} \cdot \mathbf{v}_F^{i_1}) \frac{\partial \check{g}_{i,mn}^t}{\partial y_1} &= \frac{i}{2\pi} \int_{\mathcal{C}_i(y_1 - y_2)} d\eta_i e^{i\eta_i(y_1 - y_2)/(\hat{\mathbf{k}} \cdot \mathbf{v}_F^{i_1})} \\ &\times \left[-\eta_i \check{G}'_{mn} \left(\mathbf{R} + \frac{y_1 \mathbf{v}_{F,m}}{\hat{\mathbf{k}} \cdot \mathbf{v}_{F,m}}, \mathbf{k}_0^{i_1} + p\hat{\mathbf{k}} \right) \right. \\ &\quad \left. + \frac{\hat{\mathbf{k}} \cdot \mathbf{v}_F^{i_1}}{\hat{\mathbf{k}} \cdot \mathbf{v}_F^m} i(\mathbf{v}_F^m \cdot \nabla_R) \check{G}'_{mn} \left(\mathbf{R} + \frac{y_1 \mathbf{v}_F^m}{\hat{\mathbf{k}} \cdot \mathbf{v}_F^m}, \mathbf{k}_0^{i_1} + p\hat{\mathbf{k}} \right) \right]. \end{aligned} \quad (6.72)$$

Next, note that $\hat{\mathbf{k}} \cdot \mathbf{v}_F^{i_1} / \hat{\mathbf{k}} \cdot \mathbf{v}_F^m = F_{i,mm}(\hat{\mathbf{k}})$ and

$$\eta_i = \xi_{i_1, \mathbf{k}_0^{i_1} + p\hat{\mathbf{k}}} = F_i D_0 - F D_0|_{p=p_F^{i_1}}, \quad (6.73)$$

at all the relevant poles by assumption. Hence,

$$\begin{aligned} i(\hat{\mathbf{k}} \cdot \mathbf{v}_F^{i_1}) \frac{\partial \check{g}_{i,mn}^t}{\partial y_1} &= i(F_i \nabla_k D_0)_{mm} \cdot \nabla_R \check{g}_{i,mn}^t \\ &+ (F_i D_0|_{p=p_F^{i_1}})_{mm} \check{g}_{i,mn}^t - \frac{i F_{i,mm}}{2\pi} \int_{\mathcal{C}_i(y_1 - y_2)} d\eta_i e^{i\eta_i(y_1 - y_2)/(\hat{\mathbf{k}} \cdot \mathbf{v}_F^{i_1})} \\ &\quad \times D_{0,mm} \check{G}'_{mn} \left(\mathbf{R} + \frac{y_1 \mathbf{v}_F^m}{\hat{\mathbf{k}} \cdot \mathbf{v}_F^m}, \mathbf{k}_0^{i_1} + p\hat{\mathbf{k}} \right) \end{aligned} \quad (6.74)$$

Combining this with equation (6.43a), which can be written

$$F_i \varepsilon \tau_z \cdot \check{G}' - F_i D_0 \cdot \check{G}' - F(D - D_0) \cdot \check{G}' - F_i \check{\Omega} \cdot \check{G}' = 1, \quad (6.75)$$

gives a differential equation for the trajectory Green's function. Because of the contour integral, one can also truncate the gradient expansion by the same reasoning as presented in the above section. That

is, after integrating over the contour I can truncate the contribution from $D_0 \bullet \check{G}'$ at first order and I can truncate the contributions from $\check{\Omega} \bullet \check{G}'$ and $(D - D_0) \bullet \check{G}'$ at zeroth order. That is,

$$\begin{aligned} & (F_i \varepsilon \tau_z)_{mm} \circ \check{g}_{i,mn}^t + i(F_i \nabla_k D_0)_{mm} \cdot \nabla_R \check{g}_{i,mn}^t \\ & - \frac{iF_{i,mm}}{2\pi} \int_{\mathcal{C}_i(\gamma_1 - \gamma_2)} d\eta_i e^{i\eta_i(\gamma_1 - \gamma_2)/(\hat{\mathbf{k}} \cdot \mathbf{v}_F^{i_1})} D_{0,mm} \check{G}'_{mn} \left(\mathbf{R} + \frac{\gamma_1 \mathbf{v}_F^m}{\hat{\mathbf{k}} \cdot \mathbf{v}_F^m}, \mathbf{k}_0^{i_1} + p\hat{\mathbf{k}} \right) \\ & = [F_i(D - D_0)]_{mm} \check{g}_{i,mn}^t + \sum_l (F_i \check{\Omega})_{ml} \circ \check{g}_{i,ln}^t. \end{aligned} \quad (6.76)$$

Combining this with equation (6.74), I get

$$i \left(\hat{\mathbf{k}} \cdot \mathbf{v}_F^{i_1} \right) \frac{\partial \check{g}_i^t}{\partial \gamma_1} = -F_i \varepsilon \tau_z \circ \check{g}_i^t + F_i D|_{p=p_F^{i_1}} \check{g}_i^t + F \check{\Omega} \circ \check{g}_i^t = F_i \check{H} \circ \check{g}_i^t, \quad (6.77)$$

where

$$\check{H} = -\varepsilon \tau_z + D|_{p=p_F^{i_1}} + \check{\Omega}. \quad (6.78)$$

Similarly, differentiating the trajectory Green's function with respect to γ_2 and assuming $\gamma_1 \neq \gamma_2$ such that the contours do not change, I get

$$\begin{aligned} & i \left(\hat{\mathbf{k}} \cdot \mathbf{v}_F^{i_1} \right) \frac{\partial \check{g}_{i,mn}^t}{\partial \gamma_2} = \frac{i}{2\pi} \int_{\mathcal{C}_i(\gamma_1 - \gamma_2)} d\eta_i e^{i\eta_i(\gamma_1 - \gamma_2)/(\hat{\mathbf{k}} \cdot \mathbf{v}_F^{i_1})} \\ & \times \check{G}'_{mn} \left(\mathbf{R} + \frac{\gamma_1 \mathbf{v}_F^m}{\hat{\mathbf{k}} \cdot \mathbf{v}_F^m}, \mathbf{k}_0^{i_1} + p\hat{\mathbf{k}} \right) \eta_i \\ & = -\check{g}_{i,mn}^t (F_i D_0|_{p=p_F^{i_1}})_{nn} + \frac{i}{2\pi} \int_{\mathcal{C}_i(\gamma_1 - \gamma_2)} d\xi_{j,p\hat{\mathbf{k}}} e^{i\xi_{j,p\hat{\mathbf{k}}}(\gamma_1 - \gamma_2)/(\hat{\mathbf{k}} \cdot \mathbf{v}_{F,j})} \\ & \times \check{G}'_{mn} \left(\mathbf{R} + \frac{\gamma_1 \mathbf{v}_F^m}{\hat{\mathbf{k}} \cdot \mathbf{v}_F^m}, \mathbf{k}_0^{i_1} + p\hat{\mathbf{k}} \right) D_{0,nn} F_{i,nn}, \end{aligned} \quad (6.79)$$

which can be combined with

$$\begin{aligned} & -\frac{i}{2\pi} \int_{\mathcal{C}_i(\gamma_1 - \gamma_2)} d\eta_i e^{i\eta_i(\gamma_1 - \gamma_2)/(\hat{\mathbf{k}} \cdot \mathbf{v}_F^{i_1})} \check{G}'_{mn} \left(\mathbf{R} + \frac{\gamma_1 \mathbf{v}_F^m}{\hat{\mathbf{k}} \cdot \mathbf{v}_F^m}, \mathbf{k}_0^{i_1} + p\hat{\mathbf{k}} \right) D_{0,nn} F_{i,nn} \\ & = -\check{g}_{i,mn}^t \circ (\varepsilon \tau_z F_i)_{nn} + \check{g}_{i,mn}^t [F_i(D - D_0)]_{nn} + \sum_l \check{g}_{i,mn}^t \circ (\check{\Omega} F_i)_{ln}. \end{aligned} \quad (6.80)$$

to obtain

$$i(\hat{\mathbf{k}} \cdot \mathbf{v}_F^{i_1}) \frac{\partial \check{g}_i^t}{\partial y_2} = -\check{g}_i^t \circ \check{H} F_i. \quad (6.81)$$

Next, consider the quantity

$$A(y_1, y_2, y_3) = [\check{g}_i^t(y_1, y_2) F_i^{-1}] \circ \check{g}_i^t(y_2, y_3) = \check{g}_i^t(y_1, y_2) \circ [F_i^{-1} \check{g}_i^t(y_2, y_3)]. \quad (6.82)$$

Differentiating with respect to y_2 , assuming $y_1 \neq y_2$ and $y_2 \neq y_3$ and using equations (6.77) and (6.81), I get

$$\begin{aligned} i(\hat{\mathbf{k}} \cdot \mathbf{v}_F^{i_1}) \frac{\partial A}{\partial y_2} &= -\check{g}_i^t(y_1, y_2) \circ H \circ \check{g}_i^t(y_2, y_3) \\ &+ \check{g}_i^t(y_1, y_2) \circ H \circ \check{g}_i^t(y_2, y_3) = 0. \end{aligned} \quad (6.83)$$

For any combination of y_1 and y_3 there are up to three regions of different y_2 values, and A must be constant within each region because of equation (6.83). One can determine the value of A in all possible regions with equations (6.65) and (6.71), and then use this to determine the normalization condition.

Consider first $y_1 > y_3$. If $y_1 > y_3 > y_2$, one can take the limit $y_2 \rightarrow -\infty$ and use equation (6.65), which implies that $A = 0$ in this region. To find A when $y_1 > y_2 > y_3$, let $y_3 = y_2 - \delta$, such that

$$A(y_1, y_2, y_2 - \delta) = [\check{g}_i^t(y_1, y_2) F_i^{-1}] \circ \check{g}_i^t(y_2, y_2 - \delta). \quad (6.84)$$

Equation (6.71) then implies that

$$\lim_{\delta \rightarrow 0^+} A(y_1, y_2, y_2 - \delta) = \check{g}_i^t(y_1, y_2) K_i \text{sign}(\hat{\mathbf{k}} \cdot \mathbf{v}_F^{i_1}), \quad (6.85)$$

so

$$A(y_1, y_2, y_3) = \check{g}_i^t(y_1, y_3) K_i \text{sign}(\hat{\mathbf{k}} \cdot \mathbf{v}_F^{i_1}), \quad (6.86)$$

when $y_1 > y_2 > y_3$. Finally, to find A when $y_2 > y_1 > y_3$, let $y_2 = y_1 + \delta$. Again, using equation (6.71),

$$\begin{aligned} \lim_{\delta \rightarrow 0^+} A(y_1, y_1 + \delta, y_3) &= \check{g}_i^t(y_1, y_3) K_i \text{sign}(\hat{\mathbf{k}} \cdot \mathbf{v}_F^{i_1}) \\ &- K_i \text{sign}(\hat{\mathbf{k}} \cdot \mathbf{v}_F^{i_1}) \check{g}_i^t(y_1, y_3) = 0, \end{aligned} \quad (6.87)$$

because $[\check{g}_i^t, K]_- = 0$ within quasiclassical theory. This is because the only non-zero elements of $[\check{g}_i^t, K_i]_-$ are the elements that correspond to the energy bands that do not cross the Fermi level. These are $\mathcal{O}(a/E_c)$, as previously discussed, and therefore negligible.

Next, consider $y_3 > y_1$. First, if $y_3 > y_1 > y_2$, then $A = 0$ again since one can let $y_2 \rightarrow -\infty$ and use equation (6.65). If $y_3 > y_2 > y_1$, one can let $y_2 = y_1 + \delta$. Equation (6.71) then implies that

$$\lim_{\delta \rightarrow 0^+} A(y_1, y_1 + \delta, y_3) = -K_i \text{sign}(\hat{\mathbf{k}} \cdot \mathbf{v}_F^{i1}) \check{g}_i^t(y_1, y_3), \quad (6.88)$$

and if $y_2 > y_3 > y_1$, setting $y_3 = y_2 - \delta$, using equation (6.71) and again letting $\delta \rightarrow 0^+$ again reveals that $A = 0$. Combining these results,

$$A(y_1, y_2, y_3) = \begin{cases} K_i \text{sign}(\hat{\mathbf{k}} \cdot \mathbf{v}_F^{i1}) \check{g}_i^t(y_1, y_3) & \text{if } y_1 > y_2 > y_3, \\ -K_i \text{sign}(\hat{\mathbf{k}} \cdot \mathbf{v}_F^{i1}) \check{g}_i^t(y_1, y_3) & \text{if } y_3 > y_2 > y_1, \\ 0 & \text{otherwise.} \end{cases} \quad (6.89)$$

We are now ready to derive the normalization condition. Let

$$\check{g}_i^\pm(\mathbf{R}, \hat{\mathbf{k}}) = \lim_{y \rightarrow 0^+} \check{g}_i^t(0, \pm y, \mathbf{R}, \hat{\mathbf{k}}). \quad (6.90)$$

We already know from equation (6.66) that the quasiclassical Green's function is

$$\check{g}_i = \check{g}_i^+ + \check{g}_i^-, \quad (6.91)$$

and from equation (6.70), we know that

$$\check{g}_i^- - \check{g}_i^+ = K_i F_i \text{sign}(\hat{\mathbf{k}} \cdot \mathbf{v}_F^{i1}). \quad (6.92)$$

Setting $y_1 = 0$, using that $\lim_{y \rightarrow 0^+} \check{g}_i^t(0, \pm y) = \lim_{y \rightarrow 0^+} \check{g}_i^t(\mp y, 0)$, and taking the limits $y_2 \rightarrow 0$ and $y_3 \rightarrow 0$ in the different regions, equation (6.89) gives

$$\check{g}_i^\pm \circ [F_i^{-1} \check{g}_i^\pm] = \mp K_i \text{sign}(\hat{\mathbf{k}} \cdot \mathbf{v}_F^{i1}) \check{g}_i^\pm, \quad (6.93a)$$

$$\check{g}_i^\pm \circ [F_i^{-1} \check{g}_i^\mp] = 0. \quad (6.93b)$$

Hence,

$$\begin{aligned}\check{g}_i \circ [F_i^{-1} \check{g}_i] &= \check{g}_i^+ \circ [F_i^{-1} \check{g}_i^+] + \check{g}_i^+ \circ [F_i^{-1} \check{g}_i^-] + \check{g}_i^- \circ [F_i^{-1} \check{g}_i^+] + \check{g}_i^- \circ [F_i^{-1} \check{g}_i^-] \\ &= K_i \text{sign}(\hat{\mathbf{k}} \cdot \mathbf{v}_F^i) (\check{g}_i^- - \check{g}_i^+) = K_i \text{sign}(\hat{\mathbf{k}} \cdot \mathbf{v}_F^i) K_i F_i \text{sign}(\hat{\mathbf{k}} \cdot \mathbf{v}_F^i).\end{aligned}\quad (6.94)$$

Thus, the generalized normalization condition for the quasiclassical Green's function is

$$\check{g}_i \circ [F_i^{-1} \check{g}_i] = [\check{g}_i F_i^{-1}] \circ \check{g}_i = K_i F_i. \quad (6.95)$$

For a normal metal with only two spin-degenerate bands, this reduces to the well-known $\check{g} \circ \check{g} = 1$. If it is more preferable with a normalization equal to unity, for instance because it could be advantageous in terms of parametrization, it is possible to scale the Green's function. Defining $\check{g}_i^F = F_i^{-1/2} \check{g}_i F_i^{-1/2}$ and removing all the zero elements, the generalized normalization condition becomes $\check{g}_i^F \circ \check{g}_i^F = 1$.

6.4 The Dirty Limit

When the impurity self-energy is dominant over other self-energy terms, except for H_0 , it can be possible to simplify the equations for the quasiclassical Green's function. This is known as the dirty limit, which has been assumed in much of my work. Since real materials often can have relatively short mean free paths, the diffusive equations can give excellent agreement with observations, as in paper VIII. To derive these equations, we must first look at the impurity self-energy.

In section 5.1.1, I showed that the impurity self-energy is

$$\begin{aligned}\check{\Sigma}_{\text{imp},ij}(t_1, t_2) &= \delta_{ij} n_i \langle U \rangle_{\text{imp}} \delta(t - t') \\ &\quad + \delta_{ij} \frac{n_i}{N_{\text{imp}}} \sum_{n=1}^{N_{\text{imp}}} \langle U_n \check{G}_{ii}(t_1, t_2) U_n \rangle_{\text{imp}},\end{aligned}\quad (6.96)$$

where the matrix U_n is the impurity potential associated with the n 'th impurity, which has the same matrix structure as $H_{0,0}$ in equation (6.11), N_{imp} is the number of impurities, n_i is the impurity density, $\langle \cdot \rangle_{\text{imp}}$ denotes impurity-averaging, which is defined in section 5.1.1, \check{G}_{ii} is the impurity-averaged Green's function, and $\langle U \rangle_{\text{imp}} = \sum_{k=1}^{N_{\text{imp}}} \langle U_k \rangle_{\text{imp}} / N_{\text{imp}}$

is the average impurity-averaged impurity potential. Note that different impurities can have different potentials, even if all impurities are nonmagnetic. For instance, if one unit cell includes more than one atom, U_n can depend on which atom has the impurity. This is the case in antiferromagnets, for instance.

To relate this to the quasiclassical theory, we must write the self-energy in the basis of the energy bands and transform it to Wigner coordinates. Because of how I defined the Green's functions in section 6.1, the relationship between the self-energies and Green's functions in real space and those in momentum space is

$$\check{\Sigma}_{k_1 k_2} = \frac{1}{N} \sum_{ij} e^{-ik_1 R_i} \check{\Sigma}_{ij} e^{ik_2 R_j}, \quad (6.97a)$$

$$\check{G}_{k_1 k_2} = \frac{1}{N} \sum_{ij} e^{-ik_1 R_i} \check{G}_{ij} e^{ik_2 R_j}. \quad (6.97b)$$

Equation (6.97a) means that, if $\check{\Sigma}_{ij}$ is proportional to δ_{ij} , then $\check{\Sigma}_{(k+p)k} = \sum_i \check{\Sigma}_{ii} \exp(-i\mathbf{p} \cdot \mathbf{R}_i)/N$, so

$$\check{\Sigma}_{R_i k} = \sum_p \check{\Sigma}_{(k+p)k} e^{i\mathbf{p} \cdot \mathbf{R}} = \check{\Sigma}_{ii}. \quad (6.98)$$

The first-order term in the impurity self-energy is simple. It is invariant under spatial and temporal translation, so it can be included in H_0 . If not, one can use that in Wigner coordinates the term becomes

$$\check{\Sigma}_{\text{imp}1, Rk}(T, \varepsilon) = n_i \langle U \rangle_{\text{imp}} \quad (6.99)$$

which is a constant matrix. Writing in the basis of the energy bands defined by H_0 amounts to taking the bullet product with S_k from the left and S_k^\dagger from the right, which in this case is simply

$$\check{\Sigma}'_{\text{imp}1, Rk}(T, \varepsilon) = n_i S_k \langle U \rangle_{\text{imp}} S_k^\dagger. \quad (6.100)$$

The second-order term involves more work, as one must first rewrite \check{G}_{ii} in terms of the quasiclassical Green's function. This is because we ultimately want equations that only involve the quasiclassical Green's

function. By Fourier transforming, I find that

$$\begin{aligned}\check{G}_{ii} &= \frac{1}{N} \sum_{k_1 k_2} \check{G}_{k_1 k_2} e^{i\mathbf{R}_i \cdot (\mathbf{k}_1 - \mathbf{k}_2)} = \frac{1}{N^2} \sum_R \sum_{k_1 k_2} \check{G}_{Rk_2} e^{i\mathbf{R}_i \cdot (\mathbf{k}_1 - \mathbf{k}_2)} e^{-i\mathbf{R} \cdot (\mathbf{k}_1 - \mathbf{k}_2)} \\ &= \frac{1}{N} \sum_{k_2} \check{G}_{R, k_2} \quad (6.101)\end{aligned}$$

I define $S(\mathbf{k})$ as a continuous function with $S(\mathbf{k}) \approx S_k$ similar to how I defined the continuous Green's functions and self-energies above. Then, $\check{G}(\mathbf{R}, \mathbf{k})$ and $\check{G}'(\mathbf{R}, \mathbf{k})$ is related through

$$\check{G}' = S \bullet \check{G} \bullet S^\dagger, \quad (6.102)$$

and $S^\dagger \bullet S = S^\dagger S = 1$, where the bullet product is defined through equation (6.41). Since S only depends on momentum and not position, $\check{G} \bullet S^\dagger = \check{G} S^\dagger$. Moreover, assuming that S changes slowly with \mathbf{k} compared to the characteristic length scale, L , meaning that $|\nabla_k S| L \ll |S|$, one can neglect the higher order terms in the gradient expansion of $S \bullet \check{G}$, since the gradient expansion only in this case only involves differentiation of \check{G} with respect to position. This means that

$$\check{G}'(\mathbf{R}, \mathbf{k}) = S(\mathbf{k}) \check{G}_{Rk}(\mathbf{R}, \mathbf{k}) S^\dagger(\mathbf{k}). \quad (6.103)$$

Similarly,

$$\check{\Sigma}'_{\text{imp}}(\mathbf{R}, \mathbf{k}) = S(\mathbf{k}) \check{\Sigma}_{\text{imp}}(\mathbf{R}, \mathbf{k}) S^\dagger(\mathbf{k}). \quad (6.104)$$

Therefore, the second-order self-energy term is

$$\begin{aligned}\check{\Sigma}'_{\text{imp}2}(\mathbf{R}, \mathbf{k}) &= \frac{n_i}{N_{\text{imp}}} \sum_{n=1}^{N_{\text{imp}}} \frac{1}{N} \sum_p \left\langle S(\mathbf{k}) U_n S^\dagger(\mathbf{p}) \right. \\ &\quad \left. \times \check{G}'(\mathbf{R}, \mathbf{p}) S(\mathbf{p}) U_n S^\dagger(\mathbf{k}) \right\rangle_{\text{imp}}, \quad (6.105)\end{aligned}$$

The momentum sum can be approximated as an integral, since the variation is small between nearest neighbor momenta by assumption. Using that $1/N = V_e d^3 p / (2\pi)^3$, where V_e is the volume of a single

unit cell,

$$\check{\Sigma}'_{\text{imp}2}(\mathbf{R}, \mathbf{k}) = \frac{V_e n_i}{N_{\text{imp}}} \sum_{n=1}^{N_{\text{imp}}} \int \frac{d^3 p}{(2\pi)^3} \left\langle S(\mathbf{k}) U_n S^\dagger(\mathbf{p}) \right. \\ \left. \times \check{G}'(\mathbf{R}, \mathbf{p}) S(\mathbf{p}) U_n S^\dagger(\mathbf{k}) \right\rangle_{\text{imp}}, \quad (6.106)$$

Next, the integral over all momenta can be separated into integrals over momenta close to the N_q collections of Fermi surfaces and a remainder. The radial part can then be split into the Eilenberger contours and a remainder. The momentum integrals over the Eilenberger can be rewritten as integrals over the energies $\xi_{i_1, \mathbf{k}_0^{i_1} + p\hat{\mathbf{k}}}$ by the introduction of

$$N_i(\hat{\mathbf{k}}, p) = \frac{p^2}{2\pi^2(\partial\eta_i/\partial p)} = \frac{p^2}{2\pi^2(\partial\xi_{i_1, \mathbf{k}_0^{i_1} + p\hat{\mathbf{k}}}/\partial p)}. \quad (6.107)$$

That is, \check{G}_{ii} can be written

$$\check{G}_{ii} = \int \frac{d^3 p}{(2\pi)^3} S^\dagger(\mathbf{p}) \check{G}'(\mathbf{R}_i, \mathbf{p}) S(\mathbf{p}) \\ = \int_{\mathcal{E}_0} \frac{d^3 p}{(2\pi)^3} S^\dagger(\mathbf{p}) \check{G}'(\mathbf{R}_i, \mathbf{p}) S(\mathbf{p}) \\ - i\pi \int \frac{d\Omega_k}{4\pi} \sum_i \frac{i}{\pi} \oint_{\mathcal{E}_i^E} d\eta_i N_i(\hat{\mathbf{k}}, p) S^\dagger(\mathbf{k}_0^{i_1} + p\hat{\mathbf{k}}) \check{G}'(\mathbf{R}_i, \mathbf{k}_0^{i_1} + p\hat{\mathbf{k}}) S(\mathbf{k}_0^{i_1} + p\hat{\mathbf{k}}), \quad (6.108)$$

where $d\Omega_k$ is the differential solid angle in momentum space and \mathcal{E}_0 the domain left after removing all of the Eilenberger contours. The quantity $N_i(\hat{\mathbf{k}}, p)$ is similar to the normal state density of states, except that it only includes the states close to the i 'th collection of Fermi surfaces. I have already assumed that N_i and S are approximately constant at all the poles of the Green's function for any given Eilenberger contour, so

$$\check{G}_{ii} = \int_{\mathcal{E}_0} \frac{d^3 p}{(2\pi)^3} S^\dagger(\mathbf{p}) \check{G}'(\mathbf{R}_i, \mathbf{p}) S(\mathbf{p}) \\ - i\pi \sum_i \int \frac{d\Omega_k}{4\pi} N_i(\hat{\mathbf{k}}, p_F^{i_1}) S^\dagger(\mathbf{k}_0^{i_1} + p_F^{i_1} \hat{\mathbf{k}}) \check{g}_i(\mathbf{R}_i, \hat{\mathbf{k}}) S(\mathbf{k}_0^{i_1} + p_F^{i_1} \hat{\mathbf{k}}). \quad (6.109)$$

The first term on the right-hand side of equation (6.109) is not necessarily negligible compared to the contributions from the quasiclassical Green's functions. This is because $\check{G}' \approx -D^{-1}$ for $\mathbf{p} \in \mathcal{C}_0$. However, similar to the first order term $\Sigma_{\text{imp}1}$, the first term on the right-hand side of equation (6.109) is a constant matrix that only depends on H_0 and the impurity potentials. In principle, it can therefore be absorbed into H_0 , effectively renormalizing H_0 . Alternatively, it can in principle introduce important effects depending on the matrix structure of S and U_n , especially in the dirty limit where the impurity scattering time is assumed small. However, here, I assume that both this and the first-order term can be safely ignored, for example by absorbing them into H_0 , such that the impurity self-energy becomes

$$\begin{aligned} \check{\Sigma}'_{\text{imp}}(\mathbf{R}, \mathbf{k}) = & - \sum_i \int \frac{d\Omega_k}{4\pi} \frac{i\pi V_e n_i N_i(\hat{\mathbf{k}}, p_F^{i_1})}{N_{\text{imp}}} \\ & \times \sum_{n=1}^{N_{\text{imp}}} \left\langle S(\mathbf{k}) U_n S^\dagger(\mathbf{k}_0^{i_1} + p_F^{i_1} \hat{\mathbf{k}}) \check{g}_i(\mathbf{R}_i, \hat{\mathbf{k}}) S(\mathbf{k}_0^{i_1} + p_F^{i_1} \hat{\mathbf{k}}) U_n S^\dagger(\mathbf{k}) \right\rangle_{\text{imp}}. \end{aligned} \quad (6.110)$$

I assume that the impurities included in $\check{\Sigma}'_{\text{imp}}$ are nonmagnetic, and any magnetic impurities are included in a separate self-energy term. This does not mean that U_n is proportional to the identity matrix, however. If the unit cell at each lattice contains multiple atoms, U_n will not be proportional to the identity matrix. In addition to the matrix structure of U_n , $\check{\Sigma}'_{\text{imp}}$ will also depend on the momentum dependence of S . In a simple normal metal with only two degenerate energy bands crossing the Fermi level, a constant density of states, N_0 at the Fermi level, $S = 1$, and only one atom per lattice site, such that non-magnetic impurities all have U_n proportional to the identity matrix, the impurity self-energy all becomes

$$\check{\Sigma}'_{\text{imp}}(\mathbf{R}, \mathbf{k}) = -\frac{i}{2\tau_{\text{imp}}} \int \frac{d\Omega_k}{4\pi} \check{g}(\mathbf{R}, \hat{\mathbf{p}}) = -\frac{i}{2\tau_{\text{imp}}} \langle \check{g} \rangle_{\mathbf{k}}(\mathbf{R}), \quad (6.111)$$

where

$$\tau_{\text{imp}} = \left(2\pi V_e n_i N_0 \langle U_n^2 \rangle_{\text{imp}} \right)^{-1} \quad (6.112)$$

is the impurity scattering time, and where I defined the angular average in momentum space as $\langle \cdot \rangle_k$. In an antiferromagnet, I have previously derived both S and U_n in sections 4.3.1 and 5.1.1, respectively. If one considers an antiferromagnetic metal, where only one of the two spin-degenerate bands crosses the Fermi level, I find that

$$\check{\Sigma}'_{\text{imp}} = -\frac{i}{2\tau_{\text{imp}}} \left(\langle \check{g} \rangle_p + \frac{\hbar^2}{\eta_{k_F}^2} \tau_z \sigma_z \langle \check{g} \rangle_k \tau_z \sigma_z \right), \quad (6.113)$$

where $\tau_{\text{imp}} = \left(\pi V_e n_i N_0 \langle V_n^2 \rangle_{\text{imp}} \right)^{-1}$ and V_n is the strength of the impurities. A detailed derivation of this result is presented in paper IX.

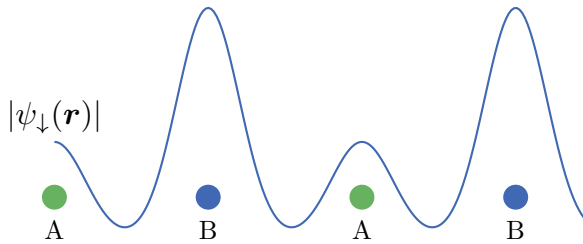


Figure 6.3: Exaggerated sketch of the spatial distribution of the conduction electron state with spin down. The overlap is larger with the B-sublattice than with the A-sublattice. As a result, the conduction band electrons with spin-down will be affected more strongly by non-magnetic impurities on the B-sublattice than by non-magnetic impurities on the A-sublattice.

To understand the physical origin of the fact that the non-magnetic impurity self-energy becomes spin-dependent in antiferromagnets, consider figure 6.3, which is taken from paper X. Figure 6.3 shows an exaggerated sketch of the spatial distribution of an electron state in the spin-down conduction band of an antiferromagnet. The amplitude of conduction band electrons is larger on one sublattice compared to the other, depending on the spin. For example, figure 6.3 in the wave function corresponds to a particle with spin down and the amplitude is larger on the B lattice compared to the A lattice. On the other hand, the wave function corresponding to a particle with spin up will have a larger amplitude on the A lattice compared to the B lattice. As a result, if a non-magnetic impurity is located on the B lattice, it will affect

spin-down particles more strongly than spin-up particles. In other words, the effect on conduction band electrons from non-magnetic impurities on sublattice A (B) act like superpositions of non-magnetic impurities and impurities with magnetization in the $+z(-z)$ -direction.

Another situation can be found in materials with strong spin-orbit coupling, such as Rashba superconductors [211], where $S(\mathbf{p})$ will depend on the direction of \mathbf{p} , and as a result, the impurity self-energy will depend on the p -wave part of the quasiclassical Green's function, $\langle \hat{\mathbf{k}} \check{g} \rangle_k$. In general, the impurity self-energy can be written

$$\check{\Sigma}'_{\text{imp}} = - \sum_{j=1}^{N_q} \frac{i}{2\tau_{\text{imp},j}} (\langle \check{g}_j \rangle_k + \check{X}_j), \quad (6.114)$$

for some $\{\tau_{\text{imp},j}\}$ and $\{\check{X}_j\}$ which depend on the system. The special cases mentioned above can be reproduced by setting $N_q = 1$ and $\check{X}_j = 0$, $\check{X}_j = \frac{\hbar^2}{\eta_{k_F}^2} \tau_z \sigma_z \langle \check{g}_j \rangle_p \tau_z \sigma_z$ or $X_j \propto \langle \hat{\mathbf{k}} \check{g} \rangle_k$.

From section 6.2, the equation for the i 'th quasiclassical Green's function is

$$iF_i(\nabla_k D_0) \cdot \nabla_R \check{g}_i + \left[F_i \varepsilon \tau_z - F_i D \Big|_{p_F}^{\check{g}_i} \right]_{-}^{\circ} - F_i \check{\Omega} \circ \check{g}_i + \check{g}_i \circ \check{\Omega} F_i = 0, \quad (6.115)$$

As all the Fermi surfaces associated with Green's function \check{g}_i must be close in momentum space everywhere, it is reasonable to assume that the gradients of the energy bands are approximately parallel. This is because the gradient $\nabla_k \xi_n$ is orthogonal to the surface defined by $\xi_n = 0$. Similar surfaces must have similar normal vectors. I therefore assume that the Fermi velocities for the bands crossing the Fermi level inside \mathcal{C}_i^E are parallel, meaning that $\nabla_K D_0 = C \mathbf{v}_F^{i1}$ for some matrix C . They can still be different in amplitude and point in opposite directions, but they must be parallel, so I still include the possibility of different densities of states. Using equation (6.54), this implies that

$$F_i(\hat{\mathbf{k}}) \nabla_K D_0 = \left(\hat{\mathbf{k}} \cdot \mathbf{v}_F^{i1} \right) \left(\hat{\mathbf{k}} \cdot \nabla_k D_0 \right) \Big|_{p=p_F^{i1}(\hat{\mathbf{k}})}^{-1} \nabla_K D_0 = \mathbf{v}_F^{i1} \quad (6.116)$$

Hence, the equation for the quasiclassical Green's function becomes

$$\begin{aligned} i\mathbf{v}_F^{i1} \cdot \nabla_R \check{g}_i + \left[F_i \varepsilon \tau_z - F_i D \Big|_{p_F}^{\check{g}_i} \right]_{-}^{\circ} - F_i \check{\Omega}_0 \circ \check{g}_i + \check{g}_i \circ \check{\Omega}_0 F_i \\ - F_i \check{\Sigma}'_{\text{imp}} \circ \check{g}_i + \check{g}_i \circ \check{\Sigma}'_{\text{imp}} F_i = 0, \end{aligned} \quad (6.117)$$

where I defined $\check{\Omega}_0 = \check{\Omega} - \check{\Sigma}'_{\text{imp}}$.

Next, I assume that $\check{\Omega}_0$ can be decomposed into one s -wave component, $\check{\Omega}_0^s = \langle \check{\Omega}_0 \rangle_k$ and one p -wave component, $\mathbf{v}_F^{i_1} \cdot \check{\Omega}_0^p$, where $\check{\Omega}_0^p = \langle \mathbf{v}_F^{i_1} \check{\Omega}_0 / (\mathbf{v}_F^{i_1} \cdot \mathbf{v}_F^{i_1}) \rangle_k$. The p -wave component will come from terms in the Hamiltonian that involve more than one lattice site. It can for instance come from an external vector potential, giving rise to a position-dependent correction to the hopping amplitude through the Peierls substitution, as shown in section 3.4.2. Since this correction is not invariant under translation, it cannot be included in H_0 and must instead be included in $\check{\Omega}_0$. A p -wave component in $\check{\Omega}_0$ can also come from Rashba spin-orbit coupling, which also involves more than one lattice site, as shown in section 3.4.3. There can also be other sources depending on the system. For instance, in paper IX it is shown that a spatially inhomogeneous magnetic order in an antiferromagnetic metal will give rise to a p -wave component in the self-energy. In principle, there can also be higher spherical harmonics, but I assume that these are negligible. For simplicity, I also assume that the flatness factor is constant along the Fermi surface, such that $F_i(\hat{\mathbf{k}}) = F_i^s = \langle F_i \rangle_k$. Finally, I also assume that $D|_{p_F}^{i_1}$ can be written as a sum of s -wave and p -wave contributions, as

$$D|_{p_F}^{i_1} = D|_{p_F}^s + \mathbf{v}_F^{i_1} \cdot D|_{p_F}^p. \quad (6.118)$$

From the p -wave components of $\check{\Omega}_0$ and $D|_{p_F}^{i_1}$, I define the covariant derivative,

$$\tilde{\nabla} \circ \check{g}_i = \nabla_R \check{g}_i + iF_i \left(\check{\Omega}_0^p + D|_{p_F}^p \right) \circ \check{g}_i - i\check{g}_i \circ \left(\check{\Omega}_0^p + D|_{p_F}^p \right) F_i, \quad (6.119)$$

such that

$$\begin{aligned} i\mathbf{v}_F^{i_1} \cdot \tilde{\nabla} \circ \check{g}_i + \left[F_i \varepsilon \tau_z - F_i D|_{p_F}^s, \check{g}_i \right]_- - F_i \check{\Omega}_0^s \circ \check{g}_i + \check{g}_i \circ \check{\Omega}_0^s F_i \\ - F_i \check{\Sigma}'_{\text{imp}} \circ \check{g}_i + \check{g}_i \circ \check{\Sigma}'_{\text{imp}} F_i = 0. \end{aligned} \quad (6.120)$$

Moreover, I define the matrix current

$$\check{\mathbf{j}}_i = \langle \mathbf{v}_F^{i_1} \check{g}_i \rangle_k \quad (6.121)$$

and the isotropic, s -wave part of the quasiclassical Green's function, $\check{g}_i^s = \langle \check{g}_i \rangle_k$.

Many observables depend only on the s -wave component or the p -wave component of the Green's function. For example, if a particle contributes the same to an observable regardless of its momentum, such as when the observable is a density like electric charge density or spin density, then the observable depends only on the s -wave component. Similarly, if the observable is a vector quantity, then it is often only the matrix current that is necessary. The advantage of the dirty limit is that it allows us to get closed equations for the isotropic Green's function and the matrix current by taking angular averages of the Eilenberger equation (6.120).

Taking the angular average of equation (6.120), I get

$$i\tilde{\nabla} \circ \check{j}_i + \left[F_i \varepsilon \tau_z - F_i D \Big|_{p_F}^{s, \check{g}_i^s} \right]_{-}^{\circ} - F_i \check{\Omega}_0^s \circ \check{g}_i^s + \check{g}_i^s \circ \check{\Omega}_0^s F_i - F_i \check{\Sigma}'_{\text{imp}} \circ \check{g}_i^s + \check{g}_i^s \circ \check{\Sigma}'_{\text{imp}} F_i = 0. \quad (6.122)$$

We need another equation to determine j_i , which can be obtained by assuming that

$$\tau_{\text{imp},i} \nabla \cdot \left(\langle \mathbf{v}_F^{i_1} \otimes \mathbf{v}_F^{i_1} \check{g}_i \rangle_k \right) \approx \tau_{\text{imp},i} \nabla \cdot \left(\langle \mathbf{v}_F^{i_1} \otimes \mathbf{v}_F^{i_1} \rangle_k \right) \check{g}_i^s = \nabla \cdot (D_i \check{g}_i^s), \quad (6.123)$$

where $D_i = \tau_{\text{imp},i} \langle \mathbf{v}_F^{i_1} \otimes \mathbf{v}_F^{i_1} \rangle_k$ is the diffusion tensor, and where \otimes denotes tensor product. For a spherically symmetric Fermi surface, the diffusion tensor is simply $D_i = \text{diag}(1, 1, 1) \times \tau_{\text{imp},i} |\mathbf{v}_F^{i_1}|^2 / 3$. This assumption means that the variation d -wave component is small compared to the variation in the s -wave component. The consistency of this assumption should be checked with the normalization condition as well as the Eilenberger equation. For example, if there are large d -wave terms in the Eilenberger equation, which I have assumed not to be the case, then equation (6.123) would not hold. Also, if the quasiclassical Green's function varies on the scale of the mean free path, then it is also possible that equation (6.123) does not hold. This can in principle happen for some components depending on the form of the impurity self-energy. However, when this happens the impurity-self energy will also tend to strongly suppress the offending components, making them negligible in the dirty limit. Therefore, the equations can be simplified by using the fact that these components vanish, and it is still

valid to use equation (6.123) in this case. We show this explicitly in paper IX, but it should also hold more generally. Using equation (6.123) and multiplying equation (6.120) with $\mathbf{v}_F^{i_1}$ before taking the angular average, I get

$$\begin{aligned} \frac{i}{\tau_{\text{imp},i}} \tilde{\nabla} \circ (D_i \check{g}_i^s) + \left[F_i \varepsilon \tau_z - F_i D \Big|_{p_F^{i_1}}^s, \check{\mathbf{j}}_i \right]_- - F_i \check{\Omega}_0^s \circ \check{\mathbf{j}}_i + \check{\mathbf{j}}_i \circ \check{\Omega}_0^s F_i \\ - F_i \check{\Sigma}'_{\text{imp}} \circ \check{\mathbf{j}}_i + \check{\mathbf{j}}_i \circ \check{\Sigma}'_{\text{imp}} F_i = 0, \end{aligned} \quad (6.124)$$

As mentioned, the consistency of equation (6.123) should be tested from the normalization condition. Assuming that the Green's function depends on $\hat{\mathbf{k}}$ through the Fermi velocity $\mathbf{v}_F^{i_1}$, one can in general write \check{g}_i as a multipole expansion in $\mathbf{v}_F^{i_1}$. Let $\hat{\mathbf{v}}_F^{i_1} = (\sin \theta \cos \varphi, \sin \theta \sin \varphi, \cos \theta)$ be the unit vector in the direction of $\mathbf{v}_F^{i_1}$. The multipole expansion of \check{g}_i is then

$$\check{g}_i = \sum_{l=0}^{\infty} \sum_{m=-l}^l \check{C}_l^m Y_l^m(\theta, \varphi), \quad (6.125)$$

where C_l^m are matrix-valued coefficients that do not depend on $\mathbf{v}_F^{i_1}$ and $Y_l^m(\theta, \varphi)$ are the spherical harmonics. The monopole, or s -wave, term is

$$\check{C}_0^0 Y_0^0 = \check{g}_i^s, \quad (6.126)$$

while the p -wave, or dipole, term is

$$\check{g}_i^p = \sum_{m=-1}^1 \check{C}_1^m Y_1^m(\theta, \varphi) = \frac{\hat{\mathbf{v}}_F^{i_1} \cdot \check{\mathbf{j}}_i}{\sqrt{\langle |\mathbf{v}_F^{i_1}|^2 \rangle_k}}, \quad (6.127)$$

under the assumptions that $\langle \mathbf{v}_F^{i_1} \rangle_k = 0$ and $\langle (\mathbf{v}_F^{i_1})_\alpha (\mathbf{v}_F^{i_1})_\beta \rangle_k = \delta_{\alpha\beta} \langle (\mathbf{v}_F^{i_1})_\alpha^2 \rangle_k$, where $(\mathbf{v}_F^{i_1})_\alpha$ is component α of $\mathbf{v}_F^{i_1}$. Conventionally, the spherical harmonics are normalized such that the integral over all solids angles of $(Y_l^m)^* Y_l^m$ is one. This means that, for instance, $\check{C}_0^0 = \sqrt{4\pi} \check{g}_i^s$.

The spherical harmonics form an orthonormal basis set, so all functions of spherical angles can be written as multipole expansion. In particular, the product of two spherical harmonics, $Y_{l_1}^{m_1}$ and $Y_{l_2}^{m_2}$, can

be written as a sum of spherical harmonics using so-called Clebsch-Gordan coefficients [214, 215], $\{c_{l_1 m_1 l_2 m_2}^{LM}\}$,

$$Y_{l_1}^{m_1} Y_{l_2}^{m_2} = \sum_{L=|l_1-l_2|}^{l_1+l_2} \sqrt{\frac{(2l_1+1)(2l_2+1)}{4\pi(2L+1)}} c_{l_1 0 l_2 0}^{L0} c_{l_1 m_1 l_2 m_2}^{L(m_1+m_2)} Y_L^{m_1+m_2}. \quad (6.128)$$

The normalization condition for \check{g}_i can be written

$$\check{g}_i \circ (F_i^{-1} \check{g}_i) = \sum_{l_1=0}^{\infty} \sum_{m_1=-l_1}^{l_1} \sum_{l_2=0}^{\infty} \sum_{m_2=-l_2}^{l_2} \check{C}_{l_1}^{m_1} \circ (F_i^{-1} \check{C}_{l_1}^{m_1}) Y_{l_1}^{m_1} Y_{l_2}^{m_2} = K_i F_i. \quad (6.129)$$

Using equation (6.128) together with the orthogonality of the spherical harmonics, one can equate the different spherical harmonics on each side. The right-hand side only contains an s -wave component, since I have assumed that F_i is independent of $\hat{\mathbf{k}}$. The Clebsch-Gordan coefficients can be read of from tables [215], but here we only need the first few terms, as we assume that everything above p -wave is negligible. Products with s -wave spherical harmonics are trivial, as these are isotropic. The first non-trivial products are therefore products of two p -waves. Using the Clebsch-Gordan coefficients, these are

$$Y_1^0 Y_1^0 = \frac{1}{\sqrt{4\pi}} Y_0^0 + \frac{1}{\sqrt{5\pi}} Y_2^0, \quad (6.130a)$$

$$Y_1^1 Y_1^{-1} = -\frac{1}{\sqrt{4\pi}} Y_0^0 + \frac{1}{\sqrt{20\pi}} Y_2^0, \quad (6.130b)$$

$$Y_1^{\pm 1} Y_1^0 = \sqrt{\frac{3}{20\pi}} Y_2^{\pm 1}, \quad (6.130c)$$

$$Y_1^{\pm 1} Y_1^{\pm 1} = \sqrt{\frac{3}{10\pi}} Y_2^{\pm 2}. \quad (6.130d)$$

In other words, the product of two p -wave spherical harmonics is a sum of an s -wave and a d -wave ($l = 2$).

Let $\check{g}_i = \check{g}_i^s + \check{g}_i^p + \check{g}_i^d + \dots$, where \check{g}_i^d is the d -wave part of the quasiclassical Green's function, and let $\langle \cdot \rangle_{s/p/d}$ denote projection onto s -wave p -wave and d -wave spherical harmonics, respectively. Including up to d -wave, the different components of the normalization condition

reads

$$\check{g}_i^s \circ (F_i^{-1} \check{g}_i^s) + \langle \check{g}_i^p \circ (F_i^{-1} \check{g}_i^p) \rangle_s + \langle \check{g}_i^d \circ (F_i^{-1} \check{g}_i^d) \rangle_s = K_i F_i, \quad (6.131a)$$

$$\check{g}_i^s \circ (F_i^{-1} \check{g}_i^p) + \check{g}_i^p \circ (F_i^{-1} \check{g}_i^s) + \langle \check{g}_i^p \circ (F_i^{-1} \check{g}_i^d) \rangle_p + \langle \check{g}_i^d \circ (F_i^{-1} \check{g}_i^p) \rangle_p = 0, \quad (6.131b)$$

$$\langle \check{g}_i^p \circ (F_i^{-1} \check{g}_i^p) \rangle_d + \check{g}_i^s \circ (F_i^{-1} \check{g}_i^d) + \check{g}_i^d \circ (F_i^{-1} \check{g}_i^s) + \langle \check{g}_i^d \circ (F_i^{-1} \check{g}_i^d) \rangle_d = 0. \quad (6.131c)$$

If the assumption of isotropic F_i is relaxed, one would get values different from 0 on the right-hand sides of the second and third equations. The assumption needed to derive equation (6.124) was that \check{g}_i^d is negligible compared to \check{g}_i^s . From equation (6.131c), we see that if $\check{g}_i^s = \mathcal{O}(F_i)$, then $\check{g}_i^d = \mathcal{O}(\langle \check{g}_i^p \circ (F_i^{-1} \check{g}_i^p) \rangle_d)$. Hence, consistency requires that $|\check{g}_i^p \circ (F_i^{-1} \check{g}_i^p)| \ll 1$, which means that the square amplitude of the matrix current, $|\check{j}_i|^2$, is much less than the average of the square amplitude of the Fermi velocity, $\langle |\mathbf{v}_F^{i1}|^2 \rangle_k$.

From equation (6.130) we also see that $\langle \check{g}_i^p \circ (F_i^{-1} \check{g}_i^p) \rangle_d$ and $\langle \check{g}_i^p \circ (F_i^{-1} \check{g}_i^p) \rangle_s$ are similar in magnitude. Therefore, keeping only up to first order in \check{g}_i^p , the normalization conditions become

$$\check{g}_i^s \circ (F_i^{-1} \check{g}_i^s) = K_i F_i, \quad (6.132a)$$

$$\check{g}_i^s \circ (F_i^{-1} \check{g}_i^p) + \check{g}_i^p \circ (F_i^{-1} \check{g}_i^s) = 0. \quad (6.132b)$$

Equation (6.132b) means that

$$\check{g}_i^s \circ (F_i^{-1} \check{j}_i) + \check{j}_i \circ (F_i^{-1} \check{g}_i^s) = 0. \quad (6.133)$$

The problem of finding $\check{g}_i(\mathbf{R}, \hat{\mathbf{k}}, T, \varepsilon)$ for all possible momentum directions $\hat{\mathbf{k}}$ has been reduced to finding just the isotropic part $\check{g}_i^s(\mathbf{R}, T, \varepsilon)$ and the matrix current $\check{j}_i(\mathbf{R}, T, \varepsilon)$. This is already a significant simplification. We went from infinitely many coupled matrix equations, one for each direction of $\hat{\mathbf{k}}$, to a maximum of 4, depending on the number of spatial dimensions and thereby the number of components of \check{j}_i .

So far, this is in principle valid for any value of elastic scattering time, $\tau_{\text{imp},i}$, but it assumes that the square of the d -wave component of the quasiclassical Green's function is small. Physically, one can expect this when the impurity scattering time is small. When considering the

diffusive limit, where one assumes that $1/\tau_{\text{imp},i}$ is not much larger than all other energy scales except E_c , equation (6.124) can be simplified further. Multiplying the equation by $\tau_{\text{imp},i}$, and assuming that the terms proportional to $\tau_{\text{imp},i}\varepsilon$, $\tau_{\text{imp},i}\check{\Omega}_0$ and $\tau_{\text{imp},i}D|_{p_F}^{s,ii}$ are negligible compared to the terms proportional to $\tau_{\text{imp},i} \circ \check{\Sigma}_{\text{imp}}$, I get

$$i\check{\nabla} \circ (D_i \check{g}_i^s) + \tau_{\text{imp},i} \check{J}_i \circ \check{\Sigma}'_{\text{imp}} F_i - \tau_{\text{imp},i} F_i \check{\Sigma}'_{\text{imp}} \circ \check{J}_i = 0. \quad (6.134)$$

Inserting equation (6.114), I get

$$\begin{aligned} & \sum_{j=1}^{N_q} \frac{\tau_{\text{imp},i}}{2\tau_{\text{imp},j}} (F_i \check{g}_j^s \circ \check{J}_i - \check{J}_i \circ \check{g}_j^s F_i) \\ &= -\check{\nabla} \circ (D_i \check{g}_i^s) - \sum_{j=1}^{N_q} \frac{\tau_{\text{imp},i}}{2\tau_{\text{imp},j}} (F_i \check{X}_j \circ \check{J}_i - \check{J}_i \circ \check{X}_j F_i). \end{aligned} \quad (6.135)$$

By using the normalization condition, equation (6.132a), I get a recursive equation for \check{J}_i ,

$$\begin{aligned} \check{J}_i &= -2F_i^{-1} \check{g}_i^s \circ [F_i^{-2} \check{\nabla} \circ (D_i \check{g}_i^s)] + 2F_i^{-1} \check{g}_i^s \circ [F_i^{-2} \check{J}_i \circ \check{g}_i^s F_i] \\ &\quad - 2F_i^{-1} \check{g}_i^s \circ \left[F_i^{-2} \sum_{j=1}^{N_q} \frac{\tau_{\text{imp},i}}{2\tau_{\text{imp},j}} (F_i \check{X}_j \circ \check{J}_i - \check{J}_i \circ \check{X}_j F_i) \right] \\ &\quad - F_i^{-1} \check{g}_i^s \circ \left[F_i^{-2} \sum_{j \neq i} \frac{\tau_{\text{imp},i}}{\tau_{\text{imp},j}} (F_i \check{g}_j^s \circ \check{J}_i - \check{J}_i \circ \check{g}_j^s F_i) \right] \end{aligned} \quad (6.136)$$

where I used that $K_i \check{J}_i = \check{J}_i$. Solving equations (6.122), (6.132a), (6.133) and (6.136) simultaneously can be done for any system where the impurity scattering time can be assumed small and $|\check{J}_i|^2 \ll \langle |v_F^{ii}|^2 \rangle_k$. Depending on \check{X}_j , one should also verify that the components which vary on a length scale on the order of the mean free path become negligible, such that it is valid to use equation (6.123). Numerical algorithms for how to solve these equations are presented in chapter 7.

To end this section, I show how the equations simplify in the special cases that are more commonly found in the literature, where $F = 1$ and $N_q = 1$. Let $\check{g}^s = \check{g}_1^s$ and $\check{J} = \check{J}_1$. Taking the second term on the right-hand side of equation (6.136) over to the left-hand side, using equation (6.133) and dividing by 2, the equation becomes

$$\check{J} = -\check{g}^s \circ \check{\nabla} \circ (D \check{g}^s) - \frac{\check{g}_i^s}{2} \circ [\check{X}, \check{J}]_- . \quad (6.137)$$

Setting $\check{X} = \tau_z \sigma_z \check{g}^s \tau_z \sigma_z h^2 / \eta_{k_F}^2$ reproduces the result for antiferromagnetic metals, presented in paper IX. On the other hand, setting $\check{X} = 0$ reproduces the well-known result for diffusive normal metals, $\check{\mathbf{j}} = -\check{g}^s \circ \check{\nabla} \circ (D\check{g}^s)$. Removing unnecessary indices and inserting $F = 1$ and $\check{\Sigma}_{\text{imp}} = -i(\check{g}^s + \check{X})/2\tau_{\text{imp}}$ into the other equation (6.122), it becomes

$$i\check{\nabla} \circ \check{\mathbf{j}} + \left[\varepsilon\tau_z - D|_{p_F}^s - \check{\Omega}_0^s + \frac{i}{2\tau_{\text{imp}}} \check{X}, \check{g}^s \right]_{-}^{\circ} = 0. \quad (6.138)$$

Again, setting $\check{X} = \tau_z \sigma_z \check{g}^s \tau_z \sigma_z h^2 / \eta_{k_F}^2$ and $\check{X} = 0$ reproduces the results for diffusive antiferromagnetic metals and normal metals, respectively. That is, the equations reduce to the Usadel equation [216] for normal metals when $\check{X} = 0$.

6.5 Boundary conditions

We are often interested in applying quasiclassical theory to mesoscopic heterostructures. The boundary between two different materials in such heterostructures represents regions in which there is rapid spatial variation. Even if the number of atoms in the unit cell happens to be the same in both materials, the energy bands, defined by H_0 , will typically differ. It was an underlying assumption behind the quasiclassical theory that H_0 is invariant under spatial translation. This renders the quasiclassical equations invalid in systems that involve multiple materials. To remedy this, one must perform the quasiclassical treatment in each material independently, and connect the solutions through boundary conditions.

The validity of the diffusive equations rests on the assumption that the matrix current is small compared to the Fermi velocity. This must also be true close to the boundaries. The different components of the matrix current can be used to calculate quantities such as the electric current or spin currents. Therefore, the assumption that the matrix current is small also implies that physical currents are small compared to some measures. This, in turn, means that the currents across interfaces between neighboring materials should also be small.

I believe it is instructive to first consider a single system with no neighboring materials, meaning that all boundaries have vacuum on the other side. There is a rapid variation at the edges associated with

the fact that the unit cells at the edges do not have the same number of neighbors as those in the interior, in addition to the fact that the unit cells themselves might include fewer atoms. This means that H_0 looks different at the boundary atoms.

In order to regain the spatial invariance of H_0 , I extend the lattice to infinity in all directions. The electrons should not propagate beyond the physical lattice, so I add a spin-independent potential, R , which is zero inside the material but quickly grows to infinity at the physical boundary. Since this potential means that no states are occupied beyond the physical boundary, we can freely choose H_0 to be the same also at all lattice sites.

To extend the description to include multiple materials, one can treat each material separately by similarly extending the lattice through their physical boundaries and impose potentials that keep all particles confined to the physical lattice, giving a physically identical description. Because materials are now in spatial proximity, two additional effects must be taken into consideration. First, the fields from one material can propagate into the other. For instance, if one material is magnetic, the neighboring material can feel a magnetic field that is strongly localized at the interface. This can effectively give a magnetic component to the potential R . Second, there can be hopping between states at neighboring lattice sites across the interface. That is, particles can hop from one lattice site to another, even if the two participating lattice sites belong to different materials. This intermaterial hopping will typically be much weaker than intramaterial hopping, but it can lead to interesting effects, such as leakage of superconductivity into neighboring materials, known as the superconductive proximity effect [217]. Hence, such hopping must be included in the boundary condition.

Formally, the essence of how I carry out the derivation of the boundary condition is that I integrate the Usadel-type equation, equation (6.122), which is

$$\begin{aligned} i\tilde{\nabla} \circ \check{\mathbf{j}}_i + \left[F_i \varepsilon \tau_z - F_i D \Big|_{\rho_F}^s \Big|_{\check{g}_i^s} \right]_+ - F_i \check{\Omega}_0^s \circ \check{g}_i^s + \check{g}_i^s \circ \check{\Omega}_0^s F_i \\ - F_i \check{\Sigma}_{\text{imp}} \circ \check{g}_i^s + \check{g}_i^s \circ \check{\Sigma}_{\text{imp}} F_i = 0, \quad (6.139) \end{aligned}$$

over a small volume enclosing a part of the interface. The effects discussed above manifest as a strongly localized self-energy term at

the boundary, $\check{\Omega}_0^s = \check{A} + \check{B}\delta(x - x_0)$, where x_0 is the location of the boundary. Using the divergence theorem to evaluate the gradient of the matrix current, \check{j}_i , together with the fact that the matrix current must be zero outside the material, and letting the volume of the integration domain go to zero, one is left with

$$\hat{n} \cdot \check{j}_i = i(F_i \check{B} \circ \check{g}_i^s - \check{g}_i^s \circ \check{B}F_i), \quad (6.140)$$

where \hat{n} is the outwards pointing unit vector. With a vacuum or insulator on the other side of the boundary, \check{B} will come from the potential R , but in the more general case it can include tunneling to the other material.

The derivation sketched above is not mathematically justified. Under the assumptions used to derive equation (6.139), one cannot include potentials that are rapidly varying on the atomic length scale. Moreover, even though \check{j}_i is mathematically well-defined outside of the material because we extended the lattice, it, together with \check{g}_i^s , quickly goes to zero as the center of mass position leaves the material. Therefore, a proper derivation should start from the more general equation (6.24). That is, a proper derivation must take into account the discrete nature of the lattice and evaluate terms like $D \cdot \check{G}$ explicitly.

Starting from the full microscopic description, I performed the derivation of boundary conditions in antiferromagnetic metals in paper IX. As can be seen in paper IX, a discrete lattice gives rise to finite differences in the equations for the quasiclassical Green's functions, rather than the continuous derivatives that can be obtained when the Green's function is approximated as a continuous function that can be assumed to vary slowly in space. The derivation in the more general formalism presented here is not substantially changed compared to the derivation presented in paper IX. I therefore refer to paper IX for the more detailed calculations. Here, I simply derive the self-energy term \check{B} .

To derive \check{B} , I start from a description of N_m materials. In each material, labeled α , there is some self-energy, $\check{\Omega}^\alpha$, together with a geometric term R^α , which is large outside of the material and zero inside the material, as discussed above. Additionally, there is a tunneling term, $T^{\alpha\beta}$, between every pair of materials. The tunneling term $T^{\alpha\beta}$ only has nonzero components if materials α and β shares a boundary.

For a multimaterial system, the Green's functions are defined as

$$\hat{G}_{k_1 k_2}^{\alpha\beta,R}(t, t') = -\frac{i}{N}\theta(t-t')\tau_z \left\langle \left[c_{\alpha, k_1}(t), c_{\beta, k_2}^\dagger(t') \right]_+ \right\rangle, \quad (6.141a)$$

$$\hat{G}_{k_1 k_2}^{\alpha\beta,A}(t, t') = +\frac{i}{N}\theta(t'-t)\tau_z \left\langle \left[c_{\alpha, k_1}(t), c_{\beta, k_2}^\dagger(t') \right]_+ \right\rangle, \quad (6.141b)$$

$$\hat{G}_{k_1 k_2}^{\alpha\beta,K}(t, t') = -\frac{i}{N}\tau_z \left\langle \left[c_{\alpha, k_1}(t), c_{\beta, k_2}^\dagger(t') \right]_- \right\rangle, \quad (6.141c)$$

where c_{α, k_1} is the tuple of creation and annihilation operators for crystal momentum k_1 in material α . Note that the number of operators in c_{α, k_1} can depend on α , so intermaterial Green's functions are not necessarily square. From equation (6.24), the equations for the Green's function $\check{G}^{\alpha\beta}$, reads

$$i\tau_z \frac{\partial \check{G}^{\alpha\beta}}{\partial t} - (\check{\Omega}^\alpha + R^\alpha) \bullet \check{G}^{\alpha\beta} - \sum_\gamma T^{\alpha\gamma} \bullet \check{G}^{\gamma\beta} = \delta(t-t')\delta_{\alpha\beta}, \quad (6.142a)$$

$$i \frac{\partial \check{G}^{\alpha\beta}}{\partial t'} \tau_z + \check{G}^{\alpha\beta} \bullet (\check{\Omega}^\beta + R^\beta) + \sum_\gamma \check{G}^{\alpha\gamma} \bullet T^{\gamma\beta} = -\delta(t-t')\delta_{\alpha\beta}. \quad (6.142b)$$

The sum goes over all the N_m materials, and the bullet products, \bullet , also include sums over internal momenta.

The next step is to remove the intermaterial Green's functions, which can be done through the Dyson equation, derived in chapter 5. Treating the tunneling amplitude as a perturbation, the Dyson equation implies that (see paper IX)

$$i\tau_z \frac{\partial \check{G}^{\alpha\alpha}}{\partial t} - \left(\check{\Omega}^\alpha + R^\alpha + \sum_\gamma T^{\alpha\gamma} \bullet \check{G}_0^{\gamma\gamma} \bullet T^{\gamma\alpha} \right) \bullet \check{G}^{\alpha\alpha} = \delta(t-t'), \quad (6.143a)$$

$$i \frac{\partial \check{G}^{\alpha\alpha}}{\partial t'} \tau_z + \check{G}^{\alpha\alpha} \bullet \left(\check{\Omega}^\alpha + R^\alpha + \sum_\gamma T^{\alpha\gamma} \bullet \check{G}_0^{\gamma\gamma} \bullet T^{\gamma\alpha} \right) = -\delta(t-t'), \quad (6.143b)$$

where $\check{G}_0^{\alpha\alpha}$ is the Green's function obtained by setting $T^{\beta\gamma} = 0$ for all pairs (β, γ) . Note that this does not mean that $\check{G}_0^{\alpha\alpha}$ is the Green's function in the absence of tunneling. That is, $\check{G}_0^{\alpha\alpha}$ can still depend

on $\check{G}^{\beta\beta}$ for $\beta \neq \alpha$. For example, if α is a superconductor and β is a neighboring normal metal, $\check{G}_0^{\beta\beta}$ can still have superconducting correlations by virtue of the proximity effect. This is because the impurity self-energy is present in $\check{\Omega}^\beta$, and $\check{G}_0^{\beta\beta}$ depend on $\check{\Omega}^\beta$. Since the impurity self energy depends on $\check{G}^{\beta\beta}$, and $\check{G}^{\beta\beta}$ depend on the tunneling term, this means that $\check{G}_0^{\beta\beta}$ also depend on the neighboring materials.

Using the above-mentioned approach of deriving boundary conditions, with calculations similar to those performed in paper IX, the boundary self-energy for the interface between material α and β , $\check{B}^{\alpha\beta}$, can be identified as

$$\check{B}^{\alpha\beta} = R^\alpha - i \sum_j \mathcal{T}^{\alpha\beta} \check{g}_{0,j}^{s,\beta\beta} \mathcal{T}^{\beta\alpha}, \quad (6.144)$$

where $\check{g}_{0,j}^{s,\beta\beta}$ is the isotropic part of the j 'th quasiclassical Green's function in material β with tunneling amplitudes set to zero, and $\mathcal{T}^{\alpha\beta}$ are renormalized tunneling amplitudes. Hence, the boundary condition for the i 'th quasiclassical Green's function in material α at the interface with material β is

$$\begin{aligned} \hat{n} \cdot \check{\mathbf{j}}_i = F_i & \left(\sum_j \mathcal{T}^{\alpha\beta} \check{g}_{0,j}^{s,\beta\beta} \mathcal{T}^{\beta\alpha} + iR^\alpha \right) \circ \check{g}_i^s \\ & - \check{g}_i^s \circ \left(\sum_j \mathcal{T}^{\alpha\beta} \check{g}_{0,j}^{s,\beta\beta} \mathcal{T}^{\beta\alpha} + iR^\alpha \right) F_i. \end{aligned} \quad (6.145)$$

To second order in tunneling amplitudes, equation (6.145) becomes

$$\begin{aligned} \hat{n} \cdot \check{\mathbf{j}}_i = F_i & \left(\sum_j \mathcal{T}^{\alpha\beta} \check{g}_j^{s,\beta\beta} \mathcal{T}^{\beta\alpha} + iR^\alpha \right) \circ \check{g}_i^s \\ & - \check{g}_i^s \circ \left(\sum_j \mathcal{T}^{\alpha\beta} \check{g}_j^{s,\beta\beta} \mathcal{T}^{\beta\alpha} + iR^\alpha \right) F_i, \end{aligned} \quad (6.146)$$

which reduces to the Kupriyanov-Lukichev boundary condition for normal metals [218], its generalization to spin-active boundaries [209], or its generalization to antiferromagnetic systems (paper IX), when there is only one quasiclassical Green's function in each material and there are only two energy bands with the same density of states near

the Fermi level, meaning that F_i is proportional to the identity matrix. One can also use the Dyson equation to write $\check{g}_{0,j}^{s,\beta\beta}$ as a series expansion in $\check{g}_j^{s,\beta\beta}$, thereby producing boundary conditions that are valid to higher order in tunneling amplitudes. This should in principle provide generalizations to the Nazarov boundary condition [219, 220].

6.6 Observables in quasiclassical theory

In order to apply quasiclassical theory to make predictions about real physical systems, one must know how to compute observables. From chapter 4 we know that observables can be written as linear combinations of the Keldysh Green's function. This can be related to the quasiclassical Green's function, although the full expression also involves high-energy components. I derived a general expression for observables in the quasiclassical theory for antiferromagnetic metals in paper IX. The generalization to the quasiclassical theory presented here is relatively straightforward. Therefore, I outline the main steps and refer to paper IX for the more detailed calculations.

We are interested in observables that can be written as linear combinations of the expectation values of pairs of fermionic operators. Using the $4N_s$ -tuples defined in equation (6.2) and the commutation relation for fermionic operators, all such observables can be written

$$Q(t) = C(t) + \frac{1}{N^2} \sum_{k_1 k_2} \left(\langle c_{k_1}^\dagger(t) B_{k_1 k_2}(t) c_{k_2}(t) \rangle - \langle c_{k_2}^T(t) B_{k_1 k_2}^T(t) (c_{k_1}^\dagger)^T(t) \rangle \right), \quad (6.147)$$

for some real scalar $C(t)$ and some set of $4N_s \times 4N_s$ matrices $B_{k_1 k_2}(t)$. One can relate this to the Keldysh Green's function,

$$\hat{G}_{k_1 k_2}^K(t, t') = -\frac{i}{N} \tau_z \left\langle \left[c_{k_1}(t), c_{k_2}^\dagger(t') \right]_- \right\rangle, \quad (6.148)$$

such that

$$Q(t) = C(t) - iN^{-1} \sum_{k_1 k_2} \text{Tr} \left[B_{k_1 k_2}(t) \tau_z \hat{G}_{k_2 k_1}^K(t, t) \right]. \quad (6.149)$$

Like before, we can relate this Green's function to the energy basis Green's function through a similarity transformation, $\hat{G}_{k_1 k_2}^K =$

$S_{k_1} \hat{G}_{k_1 k_2}^K S_{k_2}^\dagger$. Defining $B'_{k_1 k_2} = S_{k_1} B_{k_1 k_2} S_{k_2}^\dagger$, the expression for the observable Q becomes

$$Q(t) = C(t) - iN^{-1} \sum_{k_1 k_2} \text{Tr} \left[B'_{k_1 k_2}(t) \tau_z \hat{G}_{k_2 k_1}^K(t, t) \right]. \quad (6.150)$$

Fourier transforming, writing in terms of Wigner coordinates and assuming that the spatial variation in \hat{G}^K is small, such that it is sufficient to keep the lowest order in the gradient expansion, I get that

$$Q(t) = C(t) - iN^{-1} \sum_{Rk} \int_{-\infty}^{\infty} \frac{d\varepsilon}{2\pi} \text{Tr} \left[B'(\mathbf{R}, \mathbf{k}, t) \tau_z \hat{G}'^K(\mathbf{R}, \mathbf{k}, t, \varepsilon) \right]. \quad (6.151)$$

Typically, one is interested in local densities, such as charge density, spin densities or various current densities. Quantities like total electrical charge can then be computed by integrating the density over a volume. Letting the density of $Q(t)$ be $q(\mathbf{R}, t)$, we can get an expression for $q(\mathbf{R}, t)$ by writing $B'(\mathbf{R}, \mathbf{k}) = A(\mathbf{R}, \mathbf{k})/V_e$, where V_e is the volume associated with each lattice site. With this, the density becomes

$$q(\mathbf{R}, t) = c(\mathbf{R}, t) - i \frac{N}{V_e} \sum_k \int_{-\infty}^{\infty} \frac{d\varepsilon}{2\pi} \text{Tr} \left[A(\mathbf{R}, \mathbf{k}, t) \tau_z \hat{G}'^K(\mathbf{R}, \mathbf{k}, t, \varepsilon) \right], \quad (6.152)$$

where c is the density of C . Like in section 6.4, we can write the sum over momenta as an integral, using that $1/N = V_e d^3k / (2\pi)^3$, such that

$$q(\mathbf{R}, t) = c(\mathbf{R}, t) - i \int_{-\infty}^{\infty} \frac{d\varepsilon}{2\pi} \int \frac{d^3k}{(2\pi)^3} \text{Tr} \left[A(\mathbf{R}, \mathbf{k}, t) \tau_z \hat{G}'^K(\mathbf{R}, \mathbf{k}, t, \varepsilon) \right]. \quad (6.153)$$

The next step is to split up the energy integral. This is necessary because quasiclassical theory is only applicable to energies ε that are small compared to the Fermi energy. When working in the diffusive limit, it is only advantageous to restrict ε to be well below the impurity scattering rate, as this can simplify the equations (see section 6.4). Let a be a cutoff energy that is such that the quasiclassical Green's function

can be obtained for energies satisfying $|\varepsilon| < a$, and consider first the contributions from energies $|\varepsilon| < a$. Let

$$q_{qc} = -i \int_{-a}^a \frac{d\varepsilon}{2\pi} \int \frac{d^3k}{(2\pi)^3} \text{Tr} \left[A(\mathbf{R}, \mathbf{k}, t) \tau_z \hat{G}'^K(\mathbf{R}, \mathbf{k}, t, \varepsilon) \right]. \quad (6.154)$$

As in section 6.4, one can split the integral over momenta into one contribution from the quasiclassical Green's functions and one rest component,

$$\begin{aligned} q_{qc} = & -i \int_{-a}^a \frac{d\varepsilon}{2\pi} \int_{\mathcal{E}_0} \frac{d^3k}{(2\pi)^3} \text{Tr} \left[A(\mathbf{R}, \mathbf{k}, t) \tau_z \hat{G}'^K(\mathbf{R}, \mathbf{k}, t, \varepsilon) \right] \\ & + \int_{-a}^a \frac{d\varepsilon}{2\pi} \sum_{i=1}^{N_q} \pi \int \frac{d\Omega_k}{4\pi} N_i(\hat{\mathbf{k}}) \text{Tr} \left[A(\mathbf{R}, \mathbf{k}_0^{i_1} + p_F^{i_1} \hat{\mathbf{k}}, t) \tau_z \hat{g}_i^K(\mathbf{R}, \hat{\mathbf{k}}, t, \varepsilon) \right], \end{aligned} \quad (6.155)$$

where the sum goes over all the N_q quasiclassical Green's functions and \mathcal{E}_0 is the integral over all the remaining parts of the momentum space. The quantity N_i can, as before, be thought of as the normal state density of states for the first energy band in the i 'th collection of Fermi levels. The integral over \mathcal{E}_0 can be neglected because only the Keldysh Green's function is involved. This is justified by the fact that the Keldysh Green's function goes to zero as $\sim 1/\xi^2$, where ξ is energy. Hence,

$$q_{qc} = \int_{-a}^a d\varepsilon \sum_{i=1}^{N_q} \left\langle \frac{N_i(\hat{\mathbf{k}})}{2} \text{Tr} \left[A(\mathbf{R}, \mathbf{k}_0^{i_1} + p_F^{i_1} \hat{\mathbf{k}}, t) \tau_z \hat{g}_i^K(\mathbf{R}, \hat{\mathbf{k}}, t, \varepsilon) \right] \right\rangle. \quad (6.156)$$

The remaining part of the integral can be simplified because only energies $|\varepsilon| > a$ are considered. Assuming that a is sufficiently large compared to the thermal energy, all states at these energies are either fully occupied or fully empty, meaning that the Keldysh Green's function is fully determined by the spectral function. In addition, choosing a much larger than the superconducting gap, it is reasonable to neglect the effect of superconductivity on the spectral function. This makes it possible to evaluate the integral over momenta and energies $|\varepsilon| > a$. The detailed calculations are shown in paper IX, but in essence, the

idea is the following. The integral over momenta and energies $|\varepsilon| > a$ counts the number of states with energies in the intervals $(-\infty, -a)$ and (a, ∞) . This number can be changed by changes in the retarded part of the self-energy, $\hat{\Omega}^R$. For example, an increase in the electrochemical potential, such as by an applied electric potential, will shift the whole spectrum, giving fewer states in the region $(-\infty, -a)$ and more states in the region (a, ∞) . For the bands which cross the Fermi level, this means that fewer high-energy states are occupied.² Assuming that the density of states is approximately constant in the region $(-a, a)$, the contribution from high-energy states to the observable, neglecting a constant that can be absorbed into c , is equal to

$$- \sum_{i=1}^{N_q} \left\langle N_i(\hat{\mathbf{k}}) \text{Tr} \left[A(\mathbf{R}, \mathbf{k}_0^{i_1} + p_F^{i_1} \hat{\mathbf{k}}, t) \tau_z K_i \left(\hat{\Omega}^R(\mathbf{R}, \mathbf{k}_0^{i_1} + p_F^{i_1} \hat{\mathbf{k}}, t) + [\hat{\Omega}^R(\mathbf{R}, \mathbf{k}_0^{i_1} + p_F^{i_1} \hat{\mathbf{k}}, t)]^\dagger \right) K_i \right] \right\rangle, \quad (6.157)$$

where the factors K_i comes from the fact that it is only some of the energy bands that cross the Fermi level at the different locations in momentum space. Combining the results and removing the arguments for notational simplicity, the final, general expression for observables in quasiclassical theory is

$$q = c + \int_{-a}^a d\varepsilon \sum_{i=1}^{N_q} \left\langle \frac{N_i}{2} \text{Tr} [A \tau_z \hat{\delta}_i^K] \right\rangle - \sum_{i=1}^{N_q} \left\langle N_i \text{Tr} [A \tau_z K_i (\hat{\Omega}^R + [\hat{\Omega}^R]^\dagger) K_i] \right\rangle \quad (6.158)$$

For not only the detailed steps in the last calculations but also a few examples of specific observables, such as charge and spin density, I refer to section XIV in paper IX. Finally, note that the last term in equation (6.158) is needed to make observables gauge invariant.

2. This is not to say that the total number of occupied states is necessarily changed. There are fewer occupied states with energies $(-\infty, -a) \cup (a, \infty)$, but there can be more occupied states with energies $(-a, a)$.

Numerics

In the previous chapters I showed, starting from the fundamentals of quantum mechanics, how to model mesoscopic condensed matter systems. The end results were partial differential equations. Solving these equations, one can obtain the quasiclassical Green's function, which in turn can be used to compute quantities such as charge and spin densities or charge and spin currents. This chapter is dedicated to how to solve these equations numerically. The equations in question, equations (6.122), (6.132a), (6.133) and (6.136), together with the boundary conditions presented in section 6.5, constitute a coupled set of non-linear matrix differential equations. An analytical solution to these equations can only be found under certain ideal conditions, and even when analytical expressions can be found, numerical integration techniques might be required to present the solutions graphically. In addition to the above-mentioned equations, a complete theoretical model might require solving additional equations for parameters that enter the equations.

The two most common examples of such parameters are the superconducting gap parameter and the electromagnetic potentials. As derived in section 3.3, superconductivity can be treated in a mean-field approach. This results in a self-energy term in equation (6.122) that depends on the quasiclassical Green's function. As a result, one gets an additional equation that must be solved simultaneously in order to ensure consistency between the quasiclassical Green's function and parameters used to compute the quasiclassical Green's function. As we saw in section 3.4.2, an external electromagnetic vector potential will also contribute to the Hamiltonian. As this term gives a correction to the kinetic hopping term, it will be included in the covariant derivative in equations (6.122) and (6.136). The external vector potential should involve all the non-equilibrium contributions, so it should also involve the contributions from the current and charge distributions associated with the itinerant electrons. Hence, the electromagnetic vector and scalar potentials must be consistent with the electric charge density and charge current through the Maxwell equations. The electric charge density and the electric charge current can be computed from the quasiclassical Green's function. An example of where the

quasiclassical equation, gap equation, and Maxwell's equations are solved self-consistently can be found in paper VIII. The aim of this section is to provide the tools necessary to perform such calculations.

In this chapter, I will consider only time-independent systems, which means that circle-products reduce to normal matrix products, $A \circ B = AB$. The equations become much harder to solve in the general case in time-dependent systems. In the general time-dependent case, one must use equation (6.31), which means that the equations are partial differential equations of infinite order in time and energy. I consider how to solve the equations in time-dependent systems in paper V.

7.1 Parametrization

The equations are partial differential equations of matrices. However, not all of the matrix components are independent. This is because of certain symmetries in the definition of the Green's functions. Hence, one does not have to solve for all the matrix elements separately. Moreover, by choosing a clever parametrization scheme one can ensure that the normalization condition is automatically satisfied. This simultaneously removes this equation from the problem and gives fewer unknown parameters to solve for. Such a parametrization scheme is therefore advantageous compared to solving for the different matrix elements of the Green's function directly.

The symmetries of the Green's function, and therefore also the form of the parametrization, depends on the convention used for defining the Green's function. As previously shown, the Green's functions are defined as

$$\hat{G}_{k_1 k_2}^R(t, t') = -\frac{i}{N} \theta(t - t') \tau_z \left\langle \left[c_{k_1}(t), c_{k_2}^\dagger(t') \right]_+ \right\rangle, \quad (7.1a)$$

$$\hat{G}_{k_1 k_2}^A(t, t') = +\frac{i}{N} \theta(t' - t) \tau_z \left\langle \left[c_{k_1}(t), c_{k_2}^\dagger(t') \right]_+ \right\rangle, \quad (7.1b)$$

$$\hat{G}_{k_1 k_2}^K(t, t') = -\frac{i}{N} \tau_z \left\langle \left[c_{k_1}(t), c_{k_2}^\dagger(t') \right]_- \right\rangle, \quad (7.1c)$$

and the difference between the different conventions is determined by how the tuple of creation and annihilation operators are chosen. The two most common choices are

$$c_k^\dagger = \left(c_{k1\uparrow}^\dagger \quad c_{k1\downarrow}^\dagger \quad c_{k2\uparrow}^\dagger \quad \cdots \quad c_{kN_s\downarrow}^\dagger \quad c_{-k1\downarrow} \quad -c_{-k1\uparrow} \quad \cdots \quad -c_{-kN_s\uparrow} \right),$$

(7.2)

and

$$c_k^\dagger = \left(c_{k1\uparrow}^\dagger \quad c_{k1\downarrow}^\dagger \quad c_{k2\uparrow}^\dagger \quad \cdots \quad c_{kN_s\downarrow}^\dagger \quad c_{-k1\uparrow} \quad c_{-k1\downarrow} \quad \cdots \quad c_{-kN_s\downarrow} \right), \quad (7.3)$$

where $2N_s$ is the number of Wannier states associated with each unit cell. In chapter 6 I chose the equation (7.2), but in my work I have used both. Using that

$$\begin{aligned} \left\langle \left[c_{k_1,i}(t), c_{k_2,j}^\dagger(t') \right]_{\pm} \right\rangle^* &= \left\langle \left[(c_{k_2,j})^\dagger(t'), (c_{k_1,i})^\dagger(t) \right]_{\pm} \right\rangle \\ &= \pm \left\langle \left[(c_{k_1,i})^\dagger(t), (c_{k_2,j})^\dagger(t') \right]_{\pm} \right\rangle, \end{aligned} \quad (7.4)$$

one can deduce symmetries for the Green's functions. For instance, one gets that when using equation (7.3) that, after transforming to Wigner coordinates,

$$\hat{G}_{Rk}^{R/A}(t, t') = \begin{pmatrix} G_{Rk}^{R/A}(t, t') & F_{Rk}^{R/A}(t, t') \\ [F_{R(-k)}^{R/A}(t, t')]^* & [G_{R(-k)}^{R/A}(t, t')]^* \end{pmatrix}, \quad (7.5)$$

and

$$\hat{G}_{Rk}^K(t, t') = \begin{pmatrix} G_{Rk}^K(t, t') & F_{Rk}^K(t, t') \\ -[F_{R(-k)}^K(t, t')]^* & -[G_{R(-k)}^K(t, t')]^* \end{pmatrix}. \quad (7.6)$$

When using the convention of equation (7.2), the symmetries can be obtained from equations (7.5) and (7.6), since the Green's functions in the different are related through a similarity transformation.

If $\check{G}_{R,k} = \check{G}_{R,-k}$, I get from integrating over an Eilenberger contour, \mathcal{C}_i^E , that the quasiclassical Green's function satisfies

$$\hat{g}_i^{R/A}(\varepsilon) = \begin{pmatrix} g_i^{R/A}(\varepsilon) & f_i^{R/A}(\varepsilon) \\ -[f_i^{R/A}(-\varepsilon)]^* & -[g_i^{R/A}(-\varepsilon)]^* \end{pmatrix}, \quad (7.7)$$

and

$$\hat{g}_i^K(\varepsilon) = \begin{pmatrix} g_i^K(\varepsilon) & f_i^K(\varepsilon) \\ [f_i^{R/A}(-\varepsilon)]^* & [g_i^{R/A}(-\varepsilon)]^* \end{pmatrix}, \quad (7.8)$$

where I used that there is an extra imaginary factor i in the definition of the quasiclassical Green's function and that the Fourier transform, \mathcal{F}_t satisfies $\mathcal{F}_t\{A^*\}(\varepsilon) = [\mathcal{F}_t\{A\}(-\varepsilon)]^*$. Written in terms the Pauli matrices in Nambu space, $\{\tau_x, \tau_y, \tau_z\}$, these identities can be written $\hat{g}^{R/A}(\varepsilon) = -\tau_x[\hat{g}^{R/A}(-\varepsilon)]^* \tau_x$ and $\hat{g}^K(\varepsilon) = \tau_x[\hat{g}^K(-\varepsilon)]^* \tau_x$.

While this special case of $\check{G}_{R,k} = \check{G}_{R,-k}$ is often assumed, it is not assumed in my derivation presented in chapter 6. Therefore, these symmetries do not follow in the general case. In the general case, the symmetries depend on the structure of the Fermi surfaces in momentum space. For simplicity, I assume here that $\check{G}_{R,k} = \check{G}_{R,-k}$. In this case, one can similarly deduce from equation (7.1) that

$$\hat{g}_i^A(\varepsilon) = -\tau_z[\hat{g}_i^R(\varepsilon)]^\dagger \tau_z. \quad (7.9)$$

A parameterization of the quasiclassical Green's function should take into account the symmetries as well as the normalization condition

$$\check{g}_i \circ (F_i^{-1} \check{g}_i) = K_i F_i. \quad (7.10)$$

The Keldysh part of this equation,

$$\check{g}_i^R \circ (F_i^{-1} \check{g}_i^K) + \check{g}_i^K \circ (F_i^{-1} \check{g}_i^A) = 0, \quad (7.11)$$

is automatically satisfied if we write

$$\check{g}_i^K = \check{g}_i^R \circ (F_i^{-1/2} h_i F_i^{1/2}) - (F_i^{1/2} h_i F_i^{-1/2}) \circ \check{g}_i^A. \quad (7.12)$$

for any h_i , as long as the retarded and advanced parts of the normalization condition are satisfied. Here, h_i is known as the distribution function, and in thermal equilibrium it is simply $h_i(\varepsilon) = \tanh(\beta\varepsilon/2)$, where β is inverse temperature, as shown in section 4.2. From equation (7.8), there are certain symmetries the distribution function must satisfy, and the distribution function can in turn be parametrized.

The two most common parametrization schemes used for the retarded and advanced quasiclassical Green's functions are the Ricatti parametrization [221, 222] and the θ -parametrization [223]. In my work I have exclusively chosen the former. As shown in section 6.3, the quasiclassical Green's function can always be transformed such that

$$\check{g}_i^S \check{g}_i^S = \check{g}_i^S \circ \check{g}_i^S = 1, \quad (7.13)$$

where I used the assumption of time independence in the first equality. In the Ricatti-parametrization, the retarded quasiclassical Green's function is written

$$\hat{g}_i^R = \begin{pmatrix} N_i & 0 \\ 0 & \tilde{N}_i \end{pmatrix} \begin{pmatrix} 1 + \gamma_i \tilde{\gamma}_i & 2\gamma_i \\ -2\tilde{\gamma}_i & -(1 + \tilde{\gamma}_i \gamma_i) \end{pmatrix} \quad (7.14)$$

when using the equation (7.3) convention. Here, the \sim -operator is defined as $\tilde{\gamma}_i(\varepsilon) = \gamma_i^*(-\varepsilon)$ and $N_i = (1 - \gamma_i \tilde{\gamma}_i)^{-1}$. How the Ricatti parametrization will look when using the equation (7.3) convention will generally depend on which spin bands are present in the quasiclassical Green's function \hat{g}_i^R . In the normal case where γ_i includes one of each spin band, then

$$\hat{g}_i^R = \begin{pmatrix} N_i & 0 \\ 0 & i\sigma_y \tilde{N}_i \end{pmatrix} \begin{pmatrix} 1 + \gamma_i \tilde{\gamma}_i & -2\gamma_i i\sigma_y \\ -2\tilde{\gamma}_i & (1 + \tilde{\gamma}_i \gamma_i) i\sigma_y \end{pmatrix}. \quad (7.15)$$

7.2 Discretization

When the quasiclassical Green's functions have been parametrized, the result is a set of coupled non-linear partial differential equations for complex scalar parameters. The next step when solving the equations numerically is then to discretize the equations. The word *discretize* typically means to approximate something continuous by discrete values, but here I use the word to refer specifically to the process of turning a coupled set of partial differential equations into a larger set of algebraic equations or ordinary differential equations. In my work I have mainly transformed partial differential equations into algebraic equations when solving the equations numerically. When solving the time-dependent equations, as in papers V and VII, it could be beneficial to not discretize in the time dimension, such that the end product is a set of coupled ordinary differential equations. This is because one often only has one boundary condition in the time-dimension. The two main discretization schemes I have utilized in my work have been the finite element method and collocation methods.

7.2.1 The Finite Element Method

A general set of N partial differential equations can be formulated

$$R(u_1, u_2, \dots, u_N) = 0, \quad (7.16)$$

where R is some operator that takes as input the N unknown functions u_1 to u_N and returns a tuple of N functions. The aim is then to determine $\{u_1, \dots, u_N\}$ such that all the N functions are identically equal to zero. Equation (7.16) is typically accompanied by a set of boundary conditions. Sometimes, these can be incorporated by looking for solutions in a vector space of functions where the boundary conditions are satisfied, but more generally one must additionally solve a set of equations

$$B(u_1, u_2, \dots, u_N)|_{r \in \partial\Omega} = 0, \quad (7.17)$$

where Ω is the domain of the functions and $\partial\Omega$ is the boundary of Ω .

One way to think about why the problem of analytically solving a partial differential equation is difficult, is that the difficulty comes from the fact that the relevant vector spaces of functions are normally infinite-dimensional. For any choice of basis functions $\{\varphi_i\}$, the functions in $\{u_1, \dots, u_N\}$ can be written

$$u_j = \sum_{i=1}^{\infty} a_j^i \varphi_i. \quad (7.18)$$

Inserting this into equation (7.16) converts the problem into an algebraic problem for the scalar coefficients $\{a_j^i\}$. This is what we want, since there are numerical techniques for solving coupled sets of algebraic equations. Unfortunately, the number of these equations scales with the dimensionality of the vector space. The infinite dimensionality of function spaces means that one must solve a set of infinitely many algebraic equations, which is not feasible to do numerically.

A natural approach to make the equations solvable is to write $\{u_j\}$ as a linear combination of a finite number of basis functions, $\{\varphi_1, \dots, \varphi_n\}$. That is, instead of looking for solutions in the whole space of functions, one instead looks for solutions in a finite-dimensional subspace of functions. This is the main idea behind a wide class of numerical methods for solving differential equations, including spectral methods [224], pseudo-spectral methods [225] and finite-element methods [226, 227]. However, the chance of finding the exact solution in a finite-dimensional subspace is vanishingly small. Inserting

$$u_j = \sum_{i=1}^n a_j^i \varphi_i \quad (7.19)$$

into equation (7.16) will in typically yield products such as $\varphi_i \varphi_j$ which may not lie in the finite-dimensional subspace. Thus, one cannot hope to solve equations (7.16) and (7.17) exactly with this approach. Instead, the best one can hope for is an approximate solution.

To find such an approximate solution, $\{\tilde{u}_j\}$, one must turn equations (7.16) and (7.17) into $n \times N$ algebraic equations which can be used to uniquely determine $\{\tilde{a}_j^i\}$. The idea is that if $\{\tilde{a}_j^i\}$ can be chosen to such that

$$\tilde{u}_j = \sum_{i=1}^n \tilde{a}_j^i \varphi_i \quad (7.20)$$

minimizes R in the finite-dimensional subspace, then, as long as R is sufficiently nice, the difference between $\{u_j\}$ and $\{\tilde{u}_j\}$ should also be small.

In the finite element method, the way of turning equations (7.16) and (7.17) into algebraic equations is to take the inner product of each of the components of R with each of the basis functions. That is,

$$\int_{\Omega} dx \varphi_k^*(x) \left[R_j \left(\sum_{i=1}^n \tilde{a}_1^i \varphi_i, \dots, \sum_{i=1}^n \tilde{a}_N^i \varphi_i \right) \right] (x) = 0, \quad (7.21)$$

for all $k \in \{1, \dots, n\}$ and $j \in \{1, \dots, N\}$. This gives the appropriate number of equations. Equation (7.21) is closely related to what is called the weak formulation of equation (7.16). In the weak formulation, $\{u_1, \dots, u_N\}$ must solve

$$\int_{\Omega} dx v^*(x) [R_j(u_1, \dots, u_N)] (x) = 0, \quad (7.22)$$

for all functions v in the space of test functions [184], meaning infinitely differential functions with compact support. Equation (7.22) is known as the weak formulation because if the set $\{u_1, \dots, u_N\}$ solves equation (7.16), then it must also solve equation (7.22), but the reverse is not true. That is, one can in some cases find solutions to equation (7.22) that are not solutions to equation (7.16). In particular equation (7.22) can have solutions in the space of distributions even when equation (7.16) has no solutions. This happens for instance in systems with shocks, and examples can be found in my work on the two-layer shallow water equations [1, 2]. Equation (7.21) can be viewed as an approximation to

the weak formulation where both the test functions and the solution is restricted to a finite-dimensional subspace of functions.

The equations should also incorporate the boundary conditions. Certain boundary conditions, such as periodic boundaries or boundary conditions where either the value or the derivative is set to zero, can be incorporated by choosing the set of basis functions such that all linear combinations satisfy the boundary conditions. Otherwise, it can be possible to rewrite equation (7.21) using partial integration such that it incorporates the boundary conditions.

For a concrete example, take the diffusive differential equations from quasiclassical theory, as derived in section 6.4. In the most general, but time-independent case, these were

$$i\tilde{\nabla} \cdot \check{\mathbf{j}}_i + \left[F_i \varepsilon \tau_z - F_i D \Big|_{p_F}^s, \check{g}_i^s \right]_- - F_i \check{Q}_0^s \check{g}_i^s + \check{g}_i^s \check{Q}_0^s F_i - F_i \check{\Sigma}'_{\text{imp}} \check{g}_i^s + \check{g}_i^s \check{\Sigma}'_{\text{imp}} F_i = 0, \quad (7.23)$$

and

$$\begin{aligned} \check{\mathbf{j}}_i = & -2F_i^{-1} \check{g}_i^s \left[F_i^{-2} \tilde{\nabla} (D_i \check{g}_i^s) \right] + 2F_i^{-1} \check{g}_i^s \left[F_i^{-2} \check{\mathbf{j}}_i \check{g}_i^s F_i \right] \\ & - 2F_i^{-1} \check{g}_i^s \left[F_i^{-2} \sum_{j=1}^{N_q} \frac{\tau_{\text{imp},j}}{2\tau_{\text{imp},j}} (F_i \check{X}_j \check{\mathbf{j}}_i - \check{\mathbf{j}}_i \check{X}_j F_i) \right] \\ & - F_i^{-1} \check{g}_i^s \left[F_i^{-2} \sum_{j \neq i} \frac{\tau_{\text{imp},j}}{\tau_{\text{imp},j}} (F_i \check{g}_j^s \check{\mathbf{j}}_i - \check{\mathbf{j}}_i \check{g}_j^s F_i) \right]. \end{aligned} \quad (7.24)$$

Choosing a parametrization scheme for \check{g}_i , with parameters $\{u_1, \dots, u_N\}$, and extracting an appropriate amount of matrix elements of the equations, the equations can be more compactly written

$$\nabla \cdot \mathbf{j} + f(u_1, \dots, u_N, \mathbf{j}) = 0, \quad (7.25a)$$

$$\mathbf{j}(u_1, \dots, u_N) = \mathbf{g}(u_1, \dots, u_N, \mathbf{j}), \quad (7.25b)$$

where \mathbf{j} is a tuple of N vectors, and f and \mathbf{g} are some functions that can be determined from equations (7.23) and (7.24). The divergence of \mathbf{j} should be taken element-wise, meaning that one should take the divergence of each of the N -vectors. When there is only one quasiclassical Green's function, \mathbf{j} can for example be chosen to be N different components of the matrix current $\check{\mathbf{j}}_1$. When there are

multiple quasiclassical Green's functions, \mathbf{j} will contain elements from all matrix currents, $\check{\mathbf{j}}_1, \dots, \check{\mathbf{j}}_{N_q}$, and the set of parameters, $\{u_1, \dots, u_N\}$, must parametrize all the isotropic Green's functions, $\check{g}_1^s, \dots, \check{g}_{N_q}^s$. From section 6.5 we also know that the boundary condition is

$$\hat{\mathbf{n}} \cdot \mathbf{j}|_{r \in \partial\Omega} = b(u_1, \dots, u_N), \quad (7.26)$$

for some function b .

The first step to solving equation (7.25) numerically using the finite element method is to choose a set of basis functions, $\{\varphi_1, \dots, \varphi_n\}$, and write

$$u_j = \sum_{i=1}^n a_j^i \varphi_i. \quad (7.27)$$

Next, multiply the i 'th element of equation (7.25a) with φ_l^* , where $l \in \{1, \dots, n\}$ and integrate over the domain Ω to obtain

$$\int_{\Omega} d^d x \varphi_l^*(\mathbf{x}) [\nabla \cdot \mathbf{j}_i(\mathbf{x}) + f_i(\mathbf{x})] = 0, \quad (7.28)$$

where d is the number of spatial dimensions of Ω . Performing a partial integration of the first term and using equation (7.26) together with the divergence theorem, I get

$$\int_{\partial\Omega} d^{d-1} x \varphi_l(\mathbf{x}) b_i(\mathbf{x}) + \int_{\Omega} d^d x \{ \varphi_l^*(\mathbf{x}) f_i(\mathbf{x}) - [\mathbf{j}_i(\mathbf{x}) \cdot \nabla] \varphi_l^*(\mathbf{x}) \} = 0. \quad (7.29)$$

After performing the integrations, one is left with $N \times n$ algebraic equations that can be solved for the unknown coefficients. In practice, the integrations are performed numerically using collocation methods discussed in section 7.2.2.

Because the equations are non-linear, finding the solutions must typically be done iteratively, and the integrations might be necessary at each step. How this step is performed in practice is presented in section 7.3. With the general quasiclassical theory presented here, this also involves solving equation (7.25b) to obtain the matrix current at each point. From the coefficients, one can compute the Green's function, and then one can in turn compute the superconducting gap

parameter or observables like densities and currents. In general, one might then have to insert these values into Maxwell's equations to obtain updated values for the electromagnetic potentials, and then one should solve equation (7.29) again with the updated parameters. This should be repeated until there is consistency between the parameters used in equation (7.29) and the values obtained from the solution of equation (7.29) (see section 7.5).

The recipe presented above is the same for finite element methods and spectral methods. The difference is just in the choice of basis functions. In spectral methods the basis functions are chosen to be global, meaning they are generally non-zero on the whole domain. A popular choice of basis functions is the Fourier basis, $\{\exp(ikx)\}$. On the other hand, the basis functions in finite element methods are local, being only non-zero on small, finite elements. While the basis functions of spectral methods are typically smooth and of high order, the basis functions of finite element methods are typically polynomials of low degrees with discontinuous derivatives. The strength of spectral methods is that they have excellent convergence properties when the solution is smooth. On the other hand, the local basis functions of finite element methods give these methods great versatility. Even very complex geometries can be divided into small elements, while global basis functions on such domains can be difficult to define. It is possible to combine the strengths of spectral methods and finite element methods in so-called spectral element methods [228].

The finite element method has been used in papers I–IV. The domain was divided into cells, and a number of basis functions were defined for each cell. The basis functions were nonzero only in the nearest cells, and they were polynomials of a small degree. Exactly how the cells and basis functions were defined depended on the dimensionality. For example, for two-dimensional systems I typically chose square cells with 9 second-order polynomials at each cell.

In this section, I have not discussed the problem of error estimation. That is, how large is the difference between the exact solution of equation (7.16) and the solution of equation (7.21). I have only presented how to determine the finite element solution, but a proper introduction to the finite element method should also show that the approximate so-

lution converges to the exact solution as the number of basis functions increases. Such analysis can be found in textbooks such as [227].

7.2.2 Collocation Methods

Collocation methods are similar to finite element methods in the sense that one approximates functions by elements of finite-dimensional subspaces of functions. In fact, finite element methods typically use collocation methods to determine the basis functions. Collocation methods refer to the general idea of using an equation on a specific collection of points, so-called collocation points, in order to determine the appropriate element from the subspace of functions [229]. The basis functions of finite element methods, for example, are typically chosen to be in the set of polynomials up to a certain degree such that they are equal to 1 or 0 on the different nodes in the cells. However, in the finite element approach, one uses an inner product of the equation and the basis functions in order to convert the continuous partial differential equation into a discrete set of algebraic equations. The collocation method approach to this step would have been to instead demand that the equations are satisfied on a set of collocation points rather than the whole domain.

For another way to use collocation methods to discretize the equations, consider the one-dimensional version of the quasiclassical equations,

$$\frac{\partial j}{\partial x} + f(u_1, \dots, u_N, j) = 0, \quad (7.30a)$$

$$j(u_1, \dots, u_N) = g(u_1, \dots, u_N, j), \quad (7.30b)$$

where $x \in (x_L, x_R)$, with boundary condition

$$j(x_L) = b_L(u_1, \dots, u_N), \quad (7.31a)$$

$$j(x_R) = b_R(u_1, \dots, u_N), \quad (7.31b)$$

Integrating equation (7.30a) from $x = a$ to $x = b$ gives

$$j(b) - j(a) + \int_a^b dx f(x) = 0. \quad (7.32)$$

The integral can be approximated by collocation methods. Let L be a function in the space of polynomials of degree $p - 1$. In order to

choose L such that it approximates f , take p different x -values in the interval (a, b) , $\{x_1, \dots, x_p\}$, and choose L such that

$$L(x_i) = f(x_i) \quad (7.33)$$

for all $i \in \{1, \dots, p\}$. This determines L uniquely, and L can be written in terms of Lagrange polynomials [229]. Let

$$l_i(x) = \prod_{j \neq i} \frac{x - x_j}{x_i - x_j}. \quad (7.34)$$

Then,

$$L(x) = \sum_{i=1}^p f(x_i) l_i(x), \quad (7.35)$$

so

$$\int_a^b dx f(x) \approx \int_a^b dx L(x) = \sum_{i=1}^p f(x_i) \int_a^b dx l_i(x) = \sum_{i=1}^p f(x_i) w_i, \quad (7.36)$$

where $w_i = \int_a^b dx l_i(x)$. Hence, one can approximate

$$j(b) - j(a) + \sum_{i=1}^p w_i f(x_i) = 0. \quad (7.37)$$

With this approximation, one can convert the set of partial differential equations into a finite set of algebraic equations. Let $\{x_L, x_2, \dots, x_{n-1}, x_R\}$ be a set of n points on the interval (x_L, x_R) . Take a set of n different 2-tuples from this set of points, $\{(a_1, b_1), \dots, (a_n, b_n)\}$, where $a_i \in \{x_L, x_2, \dots, x_{n-1}\}$ and $b_i \in \{x_2, \dots, x_{n-1}, x_R\}$ for all n . Integrating over the interval (a_i, b_i) and using the above approximation with Lagrange polynomials gives

$$j(b_i) - j(a_i) + \sum_j w_j^i f(x_j) = 0, \quad (7.38)$$

where the sum goes from $x_j = a_i$ to $x_j = b_i$ and the weights are

$$w_j^i = \int_{a_i}^{b_i} dx \prod_{k \neq j} \frac{x - x_k}{x_j - x_k}, \quad (7.39)$$

where the product also goes from $x_k = a_i$ to $x_k = b_i$, not including $x_k = x_j$. When $a_i = x_L$ or $b_i = x_R$, one should use the boundary condition in equation (7.31) to evaluate j .

Performing this integration for all n intervals gives $n \times N$ equations. However, the number of unknown variables are $2nN$, since to evaluate j and f at all N points, one must know not only the parameters $\{u_1, \dots, u_N\}$, but also their derivatives, $\{\partial_x u_1, \dots, \partial_x u_N\}$. To get the same amount of equations as unknowns, one can convert the set of second-order partial differential equations to a set of twice as many first-order differential equations. Let $v_i = \partial_x u_i$,

$$j_{\text{ext}} = \begin{pmatrix} j_1 \\ \vdots \\ j_N \\ u_1 \\ \vdots \\ u_N \end{pmatrix} \quad \text{and} \quad f_{\text{ext}} = \begin{pmatrix} f_1 \\ \vdots \\ f_N \\ -v_1 \\ \vdots \\ -v_N \end{pmatrix}. \quad (7.40)$$

Since, $\partial_x j_{\text{ext}} + f_{\text{ext}} = 0$, we have that

$$j_{\text{ext}}(b_i) - j_{\text{ext}}(a_i) + \sum_j w_j^i f_{\text{ext}}(x_j) = 0, \quad (7.41)$$

which gives the correct number of equations. Assuming the distances between points are small, the differences between f and the polynomials used to determine w_j^i are small.

To determine the value of the of the parameters, $\{u_1, \dots, u_N\}$, and their derivatives, $\{\partial_x u_1, \dots, \partial_x u_N\}$, at a collection of n points, $\{x_L, x_2, \dots, x_{n-1}, x_R\}$, define a set of n intervals, compute the corresponding weights through equation (7.39) and solve equation (7.41), where the boundary conditions are used to determine j at the boundaries and equation (7.31b) is used to determine the matrix current. Assuming that the differential equation is well-behaved, the difference between the solution to equation (7.41) and the solution to equations (7.30) and (7.31) will also be small. More precisely, if one defines a sequence of increasingly large sets of points, such that the limit is dense in (x_L, x_R) , and a sequence of functions that interpolates the solution found with the above-mentioned method. Assuming this limit of functions converges, the limit solves the differential equation.

I have used this approach in papers VIII and X, where I have chosen the points to be unilaterally spaced, and with most of the intervals having lengths corresponding to 5 points. The weights, w_j^i , are in this case the same as for Boole's quadrature rule [230]. There are not n different intervals of length 5 in a set of n points. To get the appropriate number of intervals I also used additional smaller intervals near the boundaries.

7.3 Solving Nonlinear equations

Having converted the partial differential equation to a large set of nonlinear algebraic equations, the next step is to solve this set numerically. One method to achieve this is known as the Newton-Rhapson method [231]. This method is conceptually simple, but requires a good initial guess for the solution. Any general set of M algebraic equations of M unknown complex parameters, u_1, \dots, u_M can be written

$$R_i(u_1, \dots, u_M) = 0, \quad (7.42)$$

where i goes from 1 to M . More compactly, one can write

$$R(u) = 0, \quad (7.43)$$

where $R = (R_1, \dots, R_M)$ and $u = (u_1, \dots, u_M)$.¹ Assuming that \tilde{u} solves equation (7.43) and that R is at least once continuously differentiable in all variables at $u = \tilde{u}$, Taylor's theorem for multivariate functions [232] states that

$$R_i(\tilde{u}) = R_i(u) + \sum_{j=1}^M \left. \frac{\partial R_i}{\partial u_j} \right|_u (\tilde{u}_j - u_j) + h(u) = 0 \quad (7.44)$$

where $\lim_{u \rightarrow \tilde{u}} h(u)/|u - \tilde{u}| = 0$. Under the assumption that u_0 is close to \tilde{u} , one can neglect $h(u_0)$ since it is at least second order in $|u_0 - \tilde{u}|$. Hence, multiplying equation (7.44) by $J^{-1}(\tilde{u})$, where

$$J_{ij}(a) = \left. \frac{\partial R_i}{\partial u_j} \right|_{u=a} \quad (7.45)$$

1. In order to be consistent, I do not use bold font to denote tuples of numbers unless they are geometric vectors in the standard physical sense.

is Jacobian at $u = a$, I get

$$\tilde{u} \approx u_0 - J^{-1}(u_0)R(u_0). \quad (7.46)$$

In general, $u_1 = u_0 - J^{-1}(u_0)R(u_0)$ will not be a solution to equation (7.43), but often it is a better guess than u_0 . An even better guess can in turn be expected from redoing the same calculation with u_1 instead of u_0 , that is, letting $u_2 = u_1 - J^{-1}(u_1)R(u_1)$. This is the essence of the Newton-Rhapson method. Let u_0 be an initial guess and define

$$u_{n+1} = u_n - J^{-1}(u_n)R(u_n), \quad (7.47)$$

for $n \geq 0$. Under the assumption that this sequence converges and $\lim_{n \rightarrow \infty} J^{-1}(u_n) \neq 0$, the limit $u = \lim_{n \rightarrow \infty} u_n$ is a solution to equation (7.43).

The convergence of this method is covered by the Newton-Kantorovich theorem [233–235]. The theorem states that the Newton-Rhapson method with initial guess u_0 will converge to a solution \tilde{u} if the Jacobian is Lipschitz continuous on a ball of radius $|u_0 - \tilde{u}|$ around \tilde{u} and if the inverse of the Jacobian, J^{-1} is bounded from above in the same domain. To illustrate how, let

$$\|J\|_F = \sqrt{\sum_{i,j=1}^M |J_{ij}|^2} \quad (7.48)$$

be the Frobenius norm and let $B_{\tilde{u}}(|u_0 - \tilde{u}|)$ be the ball of radius $|u_0 - \tilde{u}|$ around \tilde{u} . The Jacobian is Lipschitz continuous on $B_{\tilde{u}}(|u_0 - \tilde{u}|)$ if there exists a positive real number L such that

$$\|J(a) - J(b)\|_F < L|a - b|, \quad (7.49)$$

for all a, b in $B_{\tilde{u}}(|u_0 - \tilde{u}|)$. Moreover, J^{-1} is bounded from above on $B_{\tilde{u}}(|u_0 - \tilde{u}|)$ if there exists a positive real number ρ such that

$$\|J^{-1}(a)\|_F < \rho, \quad (7.50)$$

for all a in $B_{\tilde{u}}(|u_0 - \tilde{u}|)$.

From the fundamental theorem of calculus,

$$\begin{aligned} R(a) - R(b) &= \int_0^1 dt \frac{d}{dt} R[b + t(a - b)] \\ &= \int_0^1 dt J[b + t(a - b)](a - b). \end{aligned} \quad (7.51)$$

Setting $a = \tilde{u}$, $b = u_n$, using that $R(\tilde{u}) = 0$, multiplying with $J^{-1}(u_n)$ from the left and using that $J^{-1}(u_n)R(u_n) = u_n - u_{n+1}$, I get

$$u_{n-1} - u_n = J^{-1}(u_n) \int_0^1 dt J[u_n + t(\tilde{u} - u_n)](\tilde{u} - u_n). \quad (7.52)$$

Subtracting $\tilde{u} - u_n = J^{-1}(u_n)J(u_n)(\tilde{u} - u_n)$ from both sides of the equation, taking the norm and using equations (7.49) and (7.50), I get

$$|\tilde{u} - u_{n-1}| = \left| J^{-1}(u_n) \int_0^1 dt \{J[u_n + t(\tilde{u} - u_n)] - J(u_n)\}(\tilde{u} - u_n) \right| < \rho L |\tilde{u} - u_n|^2 \int_0^1 dt t = \frac{\rho L |\tilde{u} - u_n|^2}{2}. \quad (7.53)$$

Hence, the Newton-Rhapson method is quadratically convergent.

From equation (7.53) one can see that whether or not u_{n+1} will be a better estimate for the solution \tilde{u} compared to u_n depends on the magnitude of $|\tilde{u} - u_n|$ as well as the magnitudes of the Lipschitz constant L and the upper bound ρ . In particular, the method is only guaranteed to converge from an initial guess u_0 if $\rho L |\tilde{u} - u_0|/2 < 1$. As a result, an important aspect of using the Newton-Rhapson method is to ensure that the initial guess is close to a solution. In the quasiclassical Green's function formalism, one possible initial guess is to use the known results for bulk systems. Under the assumption that the effects from neighboring materials or boundaries are small, this can be a good estimate for the solution. A better estimate can be obtained by taking advantage of the fact that one must usually solve the equations for many different energies in order to compute observables. At large energies, the influence of the various self-energies in the system, such as the superconducting gap, becomes less important, and a good estimate can be found by simply setting them to zero. This typically means setting the matrix current and the quasiclassical Green's function equal to a bulk homogeneous solution. In the general framework with flatness factor F_i , the Eilenberger equation (6.63), the normalization condition (6.95) and the symmetry-requirements discussed in section 7.1 are solved by $\hat{g}_i^R = K_i F_i \tau_z$.² One way to get

2. Actually, $\hat{g}_i^R = K_i F_i \tau_z$ is not a unique solution to these equations. To determine that $\hat{g}_i^R = K_i F_i \tau_z$ is correct, one should start from the known full Green's func-

good convergence is therefore to start by solving the equations at large energies, where this initial guess is particularly good, and then progressively use the solution at larger energies as initial guesses for the smaller energies. This works under the assumption that the solution changes only by a small amount between consecutive energies. Choosing an initial guess using this method requires that one knows where in energy space the quasiclassical Green's function changes rapidly, which is not always trivial. In particular, this method is not guaranteed to work well if the set of energies is chosen adaptively.

7.4 Forward-Mode Automatic Differentiation

A central part of the Newton-Raphson method is to evaluate the Jacobian. This involves differentiating all of the equations with respect to all of the parameters. In this section, I briefly explain forward-mode automatic differentiation [236], which is how I have determined Jacobians in my work. The idea behind automatic differentiation is that functions are often composed of elementary functions, such as polynomials and exponentials, for which the derivatives are well-known. Therefore, it is possible to differentiate through the chain rule.

Forward-mode automatic differentiation can be implemented rather elegantly by defining objects called *dual numbers* [237, 238]. Much like complex numbers, dual numbers contain two parts; one normal part and one dual part. The normal part is often called the real part, but to avoid confusion with complex numbers I use the term “normal part”. Similar to how the unit imaginary number is denoted i , the unit dual part is denoted ε . An arbitrary dual number, u , can therefore be written

$$u = a + b\varepsilon. \tag{7.54}$$

Here, a and b are the normal and dual parts of u , respectively, and a and b can in general be complex numbers. Continuing the analogy with complex numbers, instead of $i^2 = -1$, the unit dual part satisfies $\varepsilon^2 = 0$. In other words, ε can be thought of as an infinitesimal, and this makes dual numbers especially useful in the context of differentiation.

tions obtained by setting $V_{k_1 k_2} = 0$ in equation (6.18) an integrating using the Eilenberger contour.

Let $f(x)$ be an analytic function of either real or complex numbers. Because f is analytic, one can write f as

$$f(x + y) = \sum_{n=0}^{\infty} \frac{f^{(n)}(x)}{n!} y^n, \quad (7.55)$$

where $f^{(n)}(x)$ is the n 'th derivative of f evaluated at x . Evaluating $f(x + \varepsilon)$ using the Taylor series of f , one can see that

$$f(x + \varepsilon) = f(x) + f'(x)\varepsilon. \quad (7.56)$$

Therefore, evaluating a function at $x + \varepsilon$ and taking the dual part of the results produces the derivative of f at x , $f'(x)$. Interpreting the dual part as the derivative is consistent with the product rule, since

$$\begin{aligned} [f(x) + f'(x)\varepsilon][g(x) + g'(x)\varepsilon] &= f(x)g(x) \\ &+ [f(x)g'(x) + g(x)f'(x)]\varepsilon, \end{aligned} \quad (7.57)$$

and the chain rule, since equation (7.55) also implies that

$$f[g(x + \varepsilon)] = f[g(x) + g'(x)\varepsilon] = f[g(x)] + f'[g(x)]g'(x)\varepsilon. \quad (7.58)$$

In order to use dual numbers to compute derivatives numerically, one must define the dual number as a data type and define addition, subtraction, multiplication, and division between dual numbers. These operators follow from the property that $\varepsilon^2 = 0$ and $a\varepsilon + b\varepsilon = (a + b)\varepsilon$. Simply evaluating the function at $x + \varepsilon$ will then return the derivative at x . This works also if the function is defined in terms of if-statements or for-loops. To speed up the computation, one can also overload common analytic functions, such as trigonometric functions, exponentials, logarithms, and polynomials.

7.5 Fixed-Point Acceleration

What makes solving the quasiclassical equations particularly difficult to solve in some situations, is that the parameters of the equations can depend on the solution integrated over all energies. In particular, the gap depends on the energy integral of the anomalous Green's function, and the electromagnetic potentials depend on the electric charge density and charge current, which in turn depends on the

energy integral of the isotropic quasiclassical green's function and the matrix current.

In general, there are various parameters that define the system, some will depend on the quasiclassical Green's function and others are externally fixed, like the size of the system or external spin-splitting fields. Let $P = (P_1, \dots, P_n)$ be the collection of parameters that depend on the quasiclassical Green's function. In general, P must solve

$$P = f(P) \tag{7.59}$$

for some function f . The function f involves solving the quasiclassical equations many times for different energies and integrating the results. Evaluating $f(P)$ is therefore computationally costly.

The conceptually simplest method of ensuring that equation (7.59) is satisfied is to first make an initial guess P_0 and perform fixed-point iterations

$$P_{n+1} = f(P_n). \tag{7.60}$$

However, this procedure can be extremely inefficient, requiring possibly hundreds of evaluations of the computationally costly function f . For a more effective algorithm, one can write the problem as a root-finding problem,

$$g(P) = f(P) - P = 0. \tag{7.61}$$

From section 7.3 we know that this problem can be solved with quadratic convergence through the Newton-Rhapson method,

$$P_{n+1} = P_n - J^{-1}(P_n)g(P_n), \tag{7.62}$$

where J is the Jacobian. The Newton-Rhapson method has better convergence, but it requires determining the Jacobian. Since f , and by extension g , is a computationally complex function, involving solving the quasiclassical equations and numerically integrating the results over all energies, differentiating g analytically is not feasible. Instead, a crude estimate for the derivative can sometimes be obtained by using finite differences combined with equation (7.60).

For simplicity, consider the case of a single parameter P . Let P_n be some estimate for the parameter. The slow fixed-point iteration

defined by equation (7.60) is performed for at least two steps, such that

$$P_{n+1} = f(P_n), \quad (7.63a)$$

$$P_{n+2} = f(P_{n+1}). \quad (7.63b)$$

To estimate the derivative, one can then use forward differences, such that

$$J(P_n) = \left. \frac{\partial g}{\partial P} \right|_{P=P_n} \approx \frac{g_i(P_{n+1}) - g_i(P_n)}{P_{n+1} - P_n} = -\frac{P_{n+2} - 2P_{n+1} + P_n}{P_{n+1} - P_n}. \quad (7.64)$$

Inserting this into equation (7.62), the updated estimate for the parameter can be evaluated as

$$P_{n+3} = P_n - \frac{(P_{n+1} - P_n)^2}{P_{n+2} - 2P_{n+1} + P_n}. \quad (7.65)$$

This procedure of using finite differences as estimates for the derivative in the Newton-Raphson method is known as Steffensen's method [239]. One can accelerate the convergence by letting every k 'th iteration be given by equation (7.65) rather than equation (7.60), where k is some suitable integer. In theory it has quadratic convergence, but in practice it requires consecutive steps in equation (7.60) to be sufficiently small such that the finite difference estimate is a good approximation to the derivative. Unfortunately, the number of parameters that depend on the quasiclassical Greens function is almost never 1. Even if the only unknown parameter is the superconducting gap parameter, solving the equations requires knowing the superconducting gap parameter at every point. Therefore, the number of unknown parameters, if different from 0, is typically very large. Using Steffensen's method to evaluate the Jacobian properly in this case requires differentiating the expression for the gap parameter at every point with respect to changes in the gap parameter at every other point. This would be much less efficient than simply using equation (7.60).

One approach is to treat the parameters as single parameters meaning that the acceleration step is

$$P_{n+3,i} = P_{n,i} - \frac{(P_{n+1,i} - P_{n,i})^2}{P_{n+2,i} - 2P_{n+1,i} + P_{n,i}}. \quad (7.66)$$

for all i . In my experience, this has worked in some cases as long as the acceleration step is not performed too often. However, it should not be expected to work when changing one parameter strongly affects the remaining parameters. That is, one should not expect this to work well when the off-diagonal elements of the Jacobian are significant. For instance, if the phases of the superconducting gap parameter change between different iterations, the naive implementation of the Steffensen acceleration method for the multivariate problem is less reliable. For better convergence in the general case, one should use a method that takes into account the multivariate nature of the problem, such as the Anderson acceleration method [240] or another quasi-Newton method [241].³ The quasi-Newton methods update not only the estimate for the root but also the estimate for the Jacobian. For example, Broyden's method [241, 242] for solving $g(P) = 0$ updates the solution and the Jacobian according to

$$P_{n+1} = P_n - J_n^{-1}g(P_n), \quad (7.67a)$$

$$J_{n+1} = J_n + \frac{[g(P_{n+1}) - g(P_n) - J_n(P_{n+1} - P_n)](P_{n+1} - P_n)^T}{(P_{n+1} - P_n)^T(P_{n+1} - P_n)}. \quad (7.67b)$$

There are also quasi-Newton methods that update the inverse Jacobian J^{-1} directly, such that one does not need to invert the Jacobian when computing P_{n+1} [241].

3. Fang, Saad [241] showed that the Anderson acceleration method can be interpreted as a quasi-Newton method.

Research Highlights

8

While considerable work has gone into the preparation of this thesis, the bulk of my work is contained in the papers presented at the end of the thesis. Since these are presented in their entirety, and since I have already discussed the contents of many of them above, I have decided not to review each paper individually. Instead, I give a short summary of some highlights and overarching themes.

The projects contained in the appended papers can be separated into two categories. First are the projects that apply existing theory, either to uncover the physics of previously unexplored systems or reproduce experimental results. The latter can be found in paper VIII, where, despite few free parameters, the quasiclassical theory was able to reproduce experimental scanning tunneling spectroscopy measurements to an astonishing level of accuracy.

One common theme in this first category of projects is the study of vortices. Vortices are topological defects in superconducting condensates that may come from applied magnetic fields. These vortices are important to the physics of superconductors [243]. For example, vortices, being topological in nature, cannot suddenly vanish and can therefore be used as information carriers. They can move in response to electric currents, and their movement is a source of electrical resistance in the otherwise excellently conducting superconductors. Vortices are associated with a few important characteristics. First, the superconducting condensate is completely suppressed in the center of a vortex, and there is a phase winding in the gap parameter around the vortex. There are also circulating supercurrents around the vortex.

One question we studied in relation to vortices was regarding the existence of vortices in pure odd-frequency spin-triplet superconducting condensates. This was done in paper I, where we theoretically applied a uniform magnetic field to a superconducting condensate in a dirty half-metal in a superconductor/half-metal/superconductor junction, illustrated in figure 8.1. Conduction electrons in half-metals all have the same spin, so only spin-triplet superconducting correlations are possible in such systems. Moreover, in diffusive half-metals only odd-frequency spin-triplet correlations are possible.

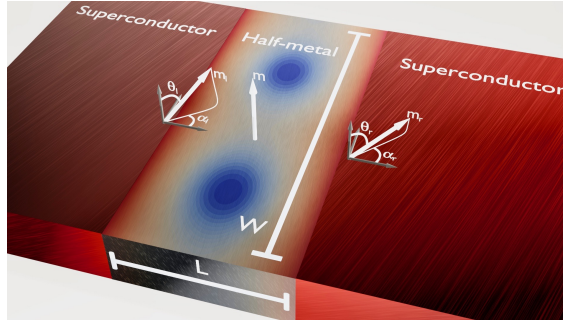


Figure 8.1: Taken from paper I. Illustration of a superconductor/half-metal/superconductor junction with an applied magnetic field corresponding to two flux quanta, $\pi\hbar/e$, where e is the electron charge. A plot of the local density of states is shown on top of the half-metal. The blue dots are regions with density of states equal to that of the normal state, and can be identified as two vortex cores. The different symbols are explained in paper I.

After solving the equations, it is straightforward to study the directly observable aspects of vortices. That is, by computing the local density of states and electric current, it is straightforward to identify locations with circulating supercurrents and cores where the local density of states is equal to that of a normal metal. One of our results was that, although spin-triplet odd-frequency condensates have different magnetic properties compared to spin-singlet superconducting condensates, they also show normal-state cores with circulating, resistance-free electrical current in the presence of magnetic fields. What was less clear was how these vortices are related to the superconducting order parameter.

In conventional superconductors, the expectation value of the Cooper pair annihilation operator, $\langle c_{k\uparrow}c_{-k\downarrow} \rangle$, is often used as an order parameter¹ and vortices are topological defects in this parameter. I have omitted the sum over momentum for simplicity. On the other hand, there is no non-zero (equal-time) expectation value of Cooper pair annihilation operators in purely odd-frequency condensates in the same way. Instead, one can go to the Heisenberg picture and con-

1. While the term *order parameter* is often used, it should be noted that expectation value of the Cooper pair annihilation operator is not gauge invariant.

sider the more general correlation function $\langle c_{k\uparrow}(t_1)c_{-k\uparrow}(t_2) \rangle$.² One can characterize odd-frequency superconducting condensates by non-zero values of $\langle c_{k\uparrow}(t_1)c_{-k\uparrow}(t_2) \rangle$ for $t_1 \neq t_2$, but it is not immediately clear which choice of t_1 and t_2 to use or how this relates to vortices.

Different choices of t_1 and t_2 are used when defining order parameters from $\langle c_{k\uparrow}(t_1)c_{-k\uparrow}(t_2) \rangle$ in different contexts. What we found was that not all choices lead to topological defects in the gap parameter that corresponded to vortices as characterized by the observable normal state density of states and circulating supercurrents. The best choice in relation to vortices seems to be

$$\Psi_2(t) = \lim_{t' \rightarrow t} \frac{\partial}{\partial t'} \langle c_{k\uparrow}(t')c_{-k\uparrow}(t) \rangle. \quad (8.1)$$

In my experience, topological defects in this quantity always correspond to physical vortices. On the other hand, other choices of t_1 and t_2 can give rise to topological defects in the order parameter that do not correspond to physical vortices, as seen in figure 8.2. This quantity can, at least in some cases, be considered the expectation value of the annihilation operator for a composite boson. When viewing odd-frequency superconductors as condensates of composite bosons, Ψ_2 is the natural choice for an order parameter. This is because the Heisenberg equation tells us that

$$\Psi_2 = i \langle [\mathcal{H}(t), c_{k\uparrow}(t)]_{-c_{-k\uparrow}(t)} \rangle. \quad (8.2)$$

Writing out the Hamiltonian and using the fermionic anticommutation relation, one is left with the expectation value of products of annihilation and creation operators. Depending on the terms in \mathcal{H} responsible for the odd-frequency superconductivity, this can for example be the expectation value for a composite boson consisting of a Cooper pair and a magnon [67]. In our case, where the odd-frequency superconductivity comes from the proximity to a conventional even-frequency spin-singlet superconductor, the picture with composite bosons is less clear. Nevertheless, we found that Ψ_2 is still the optimal choice for an order parameter, at least when it comes to vortices.

2. One can also call this a Cooper pair that is non-local in time. While one can talk about temporally non-local Cooper pairs, their connection to superconducting condensates is not the same as it is for standard Cooper pairs. It should also be noted that conventional even-frequency superconductors also have these temporally non-local Cooper pairs.

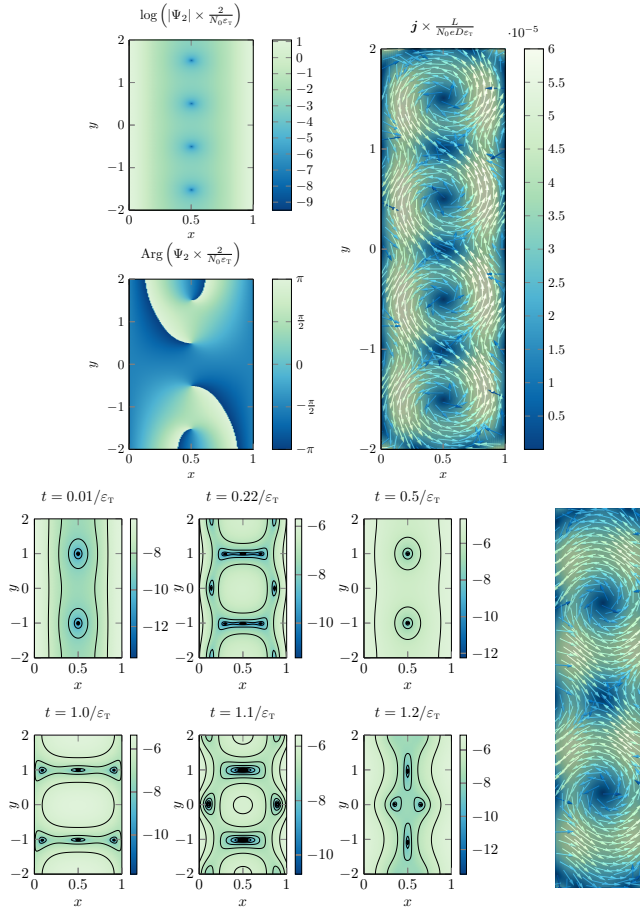


Figure 8.2: Taken from paper I. The top right figure shows the electric current circulating 4 vortices. The positions corresponds to the topological defects in Ψ_2 , as shown in the top left figures, which show the amplitude and phase of Ψ_2 . The bottom right figure shows the electric current in a system with two vortices, and the six plots to the left shows essentially $\langle c_{k\uparrow}(t)c_{-k\uparrow}(0) \rangle$ for different choices of t . In this case, different values of t can give additional topological defects which do not correspond to physical vortices. See paper I for more details.

The second category consists of the projects where we either developed new theory or used our newly developed theory to study new systems. Part of my main motivation going into my Ph.D. have been projects of this kind. In particular, I wanted to contribute to the difficult problem of solving the Usadel equation in time-dependent systems. The reason why this problem is so challenging is that the Usadel equation, as derived above, involves circle products defined as

$$A \circ B = \exp\left(\frac{i}{2}\partial_\varepsilon^A \partial_T^B - \frac{i}{2}\partial_\varepsilon^B \partial_T^A\right) AB. \quad (8.3)$$

In other words, the equations are complicated differential equations of infinite order. As such, it is much simpler to consider time-invariant systems where equation (8.3) reduces to $A \circ B = AB$.

If we want the systems we study to be used in real computers, where voltages and currents change rapidly, and often not periodically in time, it is important to know how the systems evolve in time under such conditions. Unfortunately, the presence of circle products means that no general algorithm exists for solving the equations in general time-dependent cases. While there were known ways to solve the equations when the temporal variation is slow or periodic, there was no way to find transient solutions to sudden changes. In paper V, we found a way to solve the equations with arbitrary time-dependence. The catch is that it only works if the proximity effect is weak. However, the regime of weak proximity effect is often a reasonable assumption, and one typically has to assume this in order to solve the equations analytically.

We applied the methodology to a superconductor/normal metal/superconductor (S/N/S) junction with a sudden applied magnetic field. It is well-known that an applied magnetic field to an S/N/S junction will strongly suppress the superconductivity. It was therefore surprising when we found that there was a certain period of time where the applied magnetic field had the complete opposite effect. Instead of suppressing the superconductivity, it strongly enhanced it (see figure 8.3). This effect can be understood from the process which mediates superconductivity to the normal metal. This process is called Andreev reflection [244], and what happens is that the applied magnetic field shifts the energies of the electrons such that the largest density of states and the largest Andreev reflection probabilities overlap, giving a

substantial increase in the superconductivity. After a time determined by the rate of inelastic scattering, the electrons fall down to the lowest unoccupied energy states, and the superconductivity is strongly suppressed as expected.

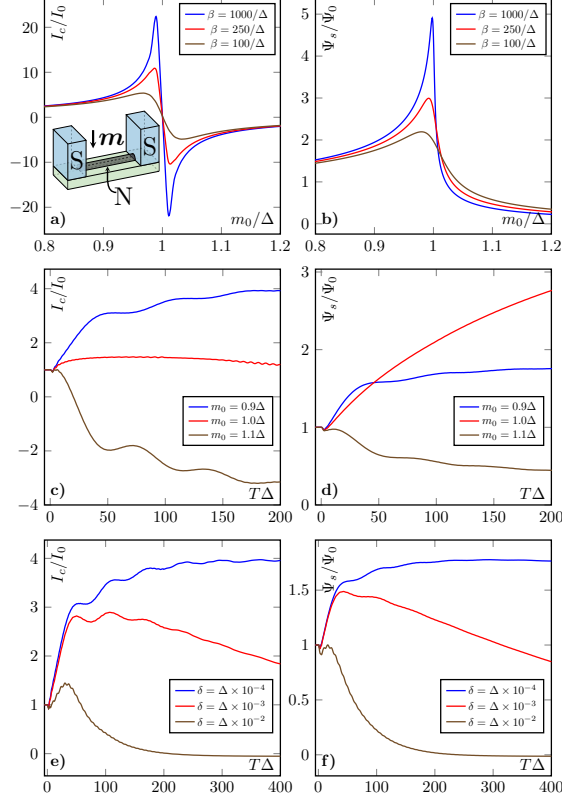


Figure 8.3: Taken from paper V. The supercurrent (left column) and superconducting pair correlation function (right column) in a S/N/S junction with a suddenly applied magnetic field, sketched in the top light panel. Notice the strong enhancement of superconductivity when strength of the Zeeman splitting m_0 is approximately equal to the magnitude of the gap, Δ . (c)-(f) shows the temporal evolution with different parameters, where T is time after the magnetic field is applied.

Another application of this methodology can be found in paper VII, where we used the time-dependent Usadel equation to ask the ques-

tion of whether an effect similar to spin-pumping [245, 246] (see also paper VI) can be achieved using electric fields. Spin-pumping is a popular way to generate spin from rotating magnetic fields. It would be interesting if a similar effect was possible with electric fields, as there are certain important advantages when using electric fields rather than magnetic fields, such as the fact that electric fields can be easier to localize than magnetic fields [132–136]. Using the newly developed methodology, we found that this is indeed possible and that it should be observable with currently known materials (see figure 8.4).

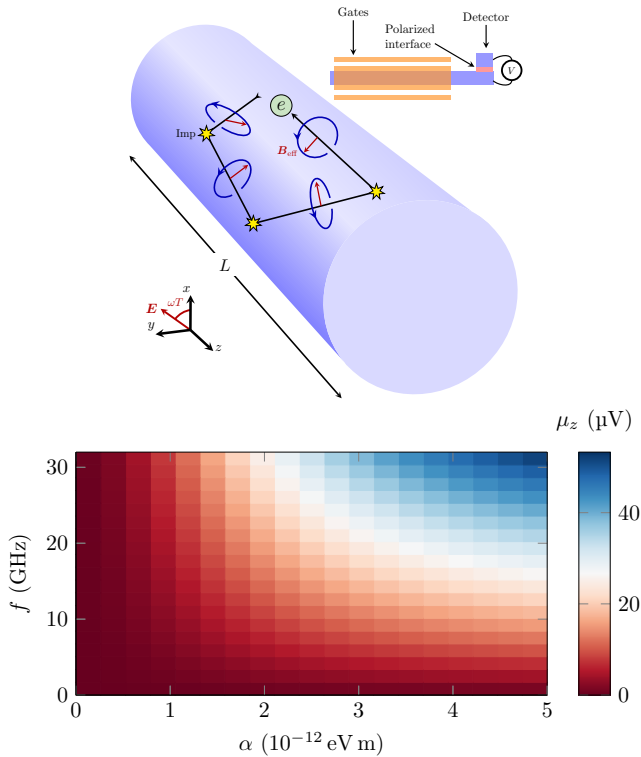


Figure 8.4: Taken from paper VII. Top: sketch of a nanowire in a rotating electric field with angular frequency ω . The figure show how the effective magnetic field for a moving electron, B_{eff} , changes due to collisions with impurities. Bottom: spin-voltage as a function of frequency $f = \omega/2\pi$ and Rashba parameter α .

Another big project that falls under the category of new theory development has led to paper IX. In this paper, we developed a quasiclassical theory that is applicable to antiferromagnetic metals. Unlike ferromagnets, antiferromagnets are not covered by the standard quasiclassical theory for normal metals because the magnetic moments oscillate on the atomic length scale. One approach that has previously been used to model antiferromagnetic metals is to just treat them as normal metals, using the justification that the magnetic field is compensated on the length scale of the superconducting coherence length. While this sounds reasonable, it is not capable of explaining why the critical temperature in superconductor/antiferromagnetic metal structures is strongly suppressed and almost constant when the length of the antiferromagnet is more than about the mean free path [247–249]. To explain this observation, one needs a proper theory for superconducting antiferromagnetic metals. Many of the key insights that lead to paper IX are also what allowed me to derive the more general theory presented in chapter 6. Armed with the quasiclassical theory for antiferromagnetic metals, we studied superconductor/antiferromagnetic metal bilayers in paper X (see figure 8.5), which provided a neat physical explanation for the above-mentioned observations of critical temperatures in such structures.

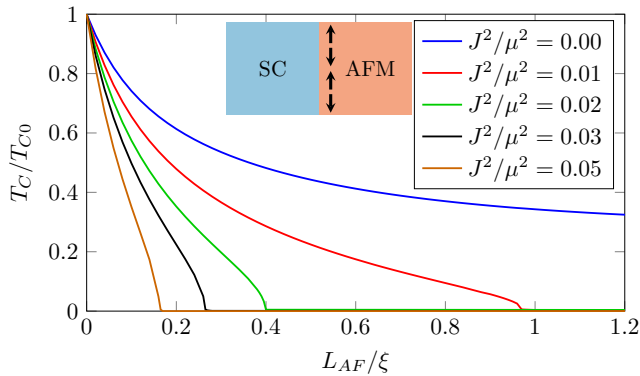


Figure 8.5: Taken from paper X. The critical temperature in superconductor/antiferromagnet (S/AF) bilayers as a function of AF thickness, L_{AF} . The critical temperature decreases faster as the strength of the AF exchange coupling, J , increases.

Conclusion and Outlook

Starting from the foundations of quantum mechanics as symmetric, and sometimes self-adjoint, operators acting on state vectors in an abstract Hilbert space, I have shown the origin of spin, and how other conservation laws arise in quantum field theories. By starting from fully relativistic quantum electrodynamics, I also showed how the coupling between spin and the electromagnetic field emerges. Additionally, I showed how quantum field theories give rise to lattice models in crystalline states of matter. Furthermore, I discussed how the effective interactions between electrons, either mediated directly through the electromagnetic field or through a combination of both the electromagnetic field and the movement of ions, can give rise to magnetism and superconductivity. Then, I showed how to turn these models into solvable equations through Green's function techniques, and derived a general quasiclassical framework that can model heterostructures where each material have multiple Fermi surfaces and different density of states associated with different energy bands. To complete the picture of how to study mesoscopic systems, I showed how the equations can be solved using numerical techniques and summarized some of my work. While I am happy with everything I have learned and achieved during my time as a graduate student, there still remains much I would have liked to explore further. Here, I conclude my thesis by discussing possible future research directions.

In particular, as much of my time has been spent on deriving new theory, I would have liked more time to explore applications. For example, there are likely interesting, unexplored physics in the realm of transient phenomena in mesoscopic heterostructures. As such systems have long been unfeasible to study with quasiclassical Keldysh theory, much remains unexplored in this domain. In the simple example of a superconductor/normal metal/superconductor Josephson junction, we found a surprising and interesting sudden increase in superconductivity after an applied magnetic field. There are likely further fascinating physics to discover in more complicated systems. For example, how do different Josephson junctions react to sudden applied voltages, or how do the vortices in two-dimensional Josephson junctions form and

find their equilibrium positions after an application of an out-of-plane magnetic field?

Superconductor/antiferromagnet structures are much less explored than superconductor/ferromagnet structures, which was an important motivation for the derivation of quasiclassical theory capable of modeling such systems. We explored equilibrium superconductor/antiferromagnet bilayers in paper X, but it could be interesting to explore trilayers and nonequilibrium, or even time-dependent physics in such structures. Although we showed that spin-singlet superconducting correlations are short-ranged in diffusive metallic antiferromagnets, we also showed that some spin-triplet correlations are long-ranged. This is analogous to the situation in ferromagnets and means that metallic antiferromagnets can be useful in the context of superconducting spintronics.

In this thesis, I also derived a more general quasiclassical theory that can also be used in systems with multiple energy bands with different flatness. It could for example be interesting to apply this to flatband superconductors. Clean flatband superconductors have theoretically been shown to exhibit extraordinary magnetic resilience, surviving magnetic fields beyond the Chandrasekhar-Clogston limit [213]. With the theory presented in chapter 6, one could explore whether this prediction survives in the presence of impurities, and one could model more complex structures involving flatband superconductors in various heterostructures and with various geometries.

Bibliography

1. **E.H. Fyhn, K.Y. Lervåg, Å. Ervik, Ø. Wilhelmsen.**
A consistent reduction of the two-layer shallow-water equations to an accurate one-layer spreading model.
Physics of Fluids **31**, 122103 (2019).
DOI: 10.1063/1.5126168
2. **K.Y. Lervåg, H.L. Skarsvåg, E. Aursand, J.A. Ouassou, M. Hammer, G. Reigstad, Å. Ervik, E.H. Fyhn, M.A. Gjennestad, P. Aursand, Ø. Wilhelmsen.**
A combined fluid-dynamic and thermodynamic model to predict the onset of rapid phase transitions in LNG spills.
Journal of Loss Prevention in the Process Industries **69**, 104354 (2021).
DOI: 10.1016/j.jlp.2020.104354
3. **R. Keranen.**
Inventions in Computing: From the Abacus to Personal Computers (Cavendish Square Publishing, LLC, 2016).
ISBN: 9781502623027
4. **T. Haigh.**
The history of information technology.
Annual Review of Information Science and Technology **45**, 431–487 (2011).
DOI: 10.1002/aris.2011.1440450116
5. **A.M. Turing.**
On computable numbers, with an application to the Entscheidungsproblem.
J. of Math **58**, 5 (1936).
6. **A. Reprintsev.**
Turing Completeness in Oracle SQL Revealed: Executing Business Logic in the Database Engine 235–242 (Apress, Berkeley, CA, 2018).
ISBN: 9781484233726
DOI: 10.1007/978-1-4842-3372-6_10

7. **L.F. Menabrea, A. Lovelace.**
Scientific memoirs v. 3, 666–731 (London, Richard and John E. Taylor, 1843).
8. **M.V. Wilkes, W. Renwick.**
The EDSAC (Electronic delay storage automatic calculator).
Mathematics of Computation **4**, 61–65 (1950).
DOI: 10.1090/s0025-5718-1950-0037589-7
9. **B.J. Copeland.**
The Modern History of Computing in The Stanford Encyclopedia of Philosophy.
(ed E.N. Zalta)
Winter 2020
(Metaphysics Research Lab, Stanford University, 2020).
10. **R.H. Dennard, F.H. Gaensslen, H.-N. Yu, V.L. Rideout, E. Bassous, A. LeBlanc.**
Design Of Ion-implanted MOSFET's with Very Small Physical Dimensions.
Proceedings of the IEEE **87**, 668–678 (1974).
11. **R. Schaller.**
Moore's law: past, present and future.
IEEE Spectrum **34**, 52–59 (1997).
DOI: 10.1109/6.591665
12. **C.E. Leiserson, N.C. Thompson, J.S. Emer, B.C. Kuszmaul, B.W. Lampson, D. Sanchez, T.B. Schardl.**
There's plenty of room at the Top: What will drive computer performance after Moore's law?
Science **368**, eaam9744 (2020).
DOI: 10.1126/science.aam9744
13. **A. Technica.**
The 40th birthday of—maybe—the first microprocessor, the Intel 4004.
URL: <https://arstechnica.com/information-technology/2011/11/the-40th-birthday-ofmaybe-the-first-microprocessor/>.
Accessed: 2023-04-04.

14. **W. Knight.**
How Apple's Monster M1 Ultra Chip Keeps Moore's Law Alive.
URL: <https://www.wired.com/story/apple-m1-ultra-chip-moores-law/>.
Accessed: 2023-04-04.
15. **CPU-World.**
Intel Pentium D 840 specifications.
URL: [https://www.cpu-world.com/CPUs/Pentium_D/Intel-Pentium%20D%20840%20HH80551PG0882MN%20\(BX80551PG3200FN%20-%20BX80551PG3200FT\).html](https://www.cpu-world.com/CPUs/Pentium_D/Intel-Pentium%20D%20840%20HH80551PG0882MN%20(BX80551PG3200FN%20-%20BX80551PG3200FT).html).
Accessed: 2023-04-04.
16. **H. Yan, H. Wu.**
Joule Heating and Chip Materials in Encyclopedia of Microfluidics and Nanofluidics (ed D. Li) 886–896 (Springer US, Boston, MA, 2008).
ISBN: 978-0-387-48998-8
DOI: 10.1007/978-0-387-48998-8_758
17. **D. Dibra, M. Stecher, S. Decker, A. Lindemann, J. Lutz, C. Kadow.**
On the Origin of Thermal Runaway in a Trench Power MOSFET.
IEEE Transactions on Electron Devices **58**, 3477–3484 (2011).
DOI: 10.1109/ted.2011.2160867
18. **S. Lin.**
Best Power Supply for Your NVIDIA RTX 4090 Graphics Card: Do you need ATX 3.0?
URL: <https://www.msi.com/blog/best-power-supply-for-your-nvidia-rtx-4090-graphics-card-do-you-need-atx-3-0>.
Accessed: 2023-04-04.
19. **N. Jones.**
How to stop data centres from gobbling up the world's electricity.
Nature **561**, 163–166 (2018).
DOI: 10.1038/d41586-018-06610-y

20. **B. Jones, A. Goodkind, R. Berrens.**
Economic estimation of Bitcoin mining's climate damages demonstrates closer resemblance to digital crude than digital gold.
 Scientific Reports **12**, 14512 (2022).
 DOI: 10.1038/s41598-022-18686-8
21. **V.K. Joshi.**
Spintronics: A contemporary review of emerging electronics devices.
 Engineering Science and Technology, an International Journal **19**, 1503–1513 (2016).
 DOI: 10.1016/j.jestch.2016.05.002
22. **I. Žutić, J. Fabian, S. Das Sarma.**
Spintronics: Fundamentals and applications.
 Reviews of Modern Physics **76**, 323–410 (2004).
 DOI: 10.1103/revmodphys.76.323
23. **A. Hirohata, K. Yamada, Y. Nakatani, I.-L. Prejbeanu, B. Diény, P. Pirro, B. Hillebrands.**
Review on spintronics: Principles and device applications.
 Journal of Magnetism and Magnetic Materials **509**, 166711 (2020).
 DOI: 10.1016/j.jmmm.2020.166711
24. **S. Bader, S. Parkin.**
Spintronics.
 Annual Review of Condensed Matter Physics **1**, 71–88 (2010).
 DOI: 10.1146/annurev-conmatphys-070909-104123
25. **D.J. Griffiths.**
Introduction to Quantum Mechanics 2nd ed. (Cambridge University Press, Cambridge, 2017).
 ISBN: 9781107179868
 DOI: 10.1017/9781316841136
26. **R.H. Arpaci-Dusseau, A.C. Arpaci-Dusseau.**
Operating Systems: Three Easy Pieces 1.00 (Arpaci-Dusseau Books, 2018).
 ISBN: 9781985086593

27. **R.E. Camley, J. Barnaś.**
Theory of giant magnetoresistance effects in magnetic layered structures with antiferromagnetic coupling.
Physical Review Letters **63**, 664–667 (1989).
DOI: 10.1103/physrevlett.63.664
28. **S.S.P. Parkin.**
Giant Magnetoresistance in Magnetic Nanostructures.
Annual Review of Materials Science **25**, 357–388 (1995).
DOI: 10.1146/annurev.ms.25.080195.002041
29. **P.A. Grünberg.**
Nobel Lecture: From spin waves to giant magnetoresistance and beyond.
Reviews of Modern Physics **80**, 1531–1540 (2008).
DOI: 10.1103/revmodphys.80.1531
30. **M.N. Baibich, J.M. Broto, A. Fert, F.N. Van Dau, F. Petroff, P. Etienne, G. Creuzet, A. Friederich, J. Chazelas.**
Giant Magnetoresistance of (001)Fe/(001)Cr Magnetic Superlattices.
Physical Review Letters **61**, 2472–2475 (1988).
DOI: 10.1103/physrevlett.61.2472
31. **G. Binasch, P. Grünberg, F. Saurenbach, W. Zinn.**
Enhanced magnetoresistance in layered magnetic structures with antiferromagnetic interlayer exchange.
Physical Review B **39**, 4828–4830 (1989).
DOI: 10.1103/physrevb.39.4828
32. **M. Julliere.**
Tunneling between ferromagnetic films.
Physics Letters A **54**, 225–226 (1975).
DOI: 10.1016/0375-9601(75)90174-7
33. **J. Mathon, A. Umerski.**
Theory of tunneling magnetoresistance of an epitaxial Fe/MgO/Fe(001) junction.
Physical Review B **63**, 220403 (2001).
DOI: 10.1103/physrevb.63.220403

34. **J.-G.J. Zhu, C. Park.**
Magnetic tunnel junctions.
Materials Today **9**, 36–45 (2006).
DOI: 10.1016/s1369-7021(06)71693-5
35. **A. Spessot, H. Oh.**
1T-1C Dynamic Random Access Memory Status, Challenges, and Prospects.
IEEE Transactions on Electron Devices **67**, 1382–1393 (2020).
DOI: 10.1109/ted.2020.2963911
36. **H.B. Peek.**
The emergence of the compact disc.
IEEE Communications Magazine **48**, 10–17 (2010).
DOI: 10.1109/mcom.2010.5394021
37. **L. Heide.**
Shaping a technology: American punched card systems 1880-1914.
IEEE Annals of the History of Computing **19**, 28–41 (1997).
DOI: 10.1109/85.627897
38. **R.H. Dee.**
Magnetic Tape for Data Storage: An Enduring Technology.
Proceedings of the IEEE **96**, 1775–1785 (2008).
DOI: 10.1109/jproc.2008.2004311
39. **G. Sollman.**
Evolution of the minifloppy (TM) product family.
IEEE Transactions on Magnetics **14**, 160–166 (1978).
DOI: 10.1109/tmag.1978.1059748
40. **M.V. Reimer, H.Y. Schenk-Mathes, M.F. Hoffmann, T. Elwert.**
Recycling Decisions in 2020, 2030, and 2040—When Can Substantial NdFeB Extraction be Expected in the EU?
Metals **8**, 867 (2018).
DOI: 10.3390/met8110867

41. **S. Wang, C. He, J. Tang, X. Lu, C. Shen, H. Yu, L. Du, J. Li, R. Yang, D. Shi, G. Zhang.**
New Floating Gate Memory with Excellent Retention Characteristics.
Advanced Electronic Materials 5, 1800726 (2019).
DOI: 10.1002/aelm.201800726
42. **T.D. Nguyen, E. Ehrenfreund, Z.V. Vardeny.**
Spin-Polarized Light-Emitting Diode Based on an Organic Bipolar Spin Valve.
Science 337, 204–209 (2012).
DOI: 10.1126/science.1223444
43. **J. Åkerman.**
Toward a Universal Memory.
Science 308, 508–510 (2005).
DOI: 10.1126/science.1110549
44. **S. Datta, B. Das.**
Electronic analog of the electro-optic modulator.
Applied Physics Letters 56, 665–667 (1990).
DOI: 10.1063/1.102730
45. **K. Fossheim, A. Sudbø.**
Superconductivity: Physics and Applications (John Wiley & Sons Ltd, Chichester, 2004).
ISBN: 9870470844523
46. **D. van Delft, P. Kes.**
The discovery of superconductivity.
Physics Today 63, 38–43 (2010).
DOI: 10.1063/1.3490499
47. **W. Meissner, R. Ochsenfeld.**
Ein neuer Effekt bei Eintritt der Supraleitfähigkeit.
Naturwissenschaften 21, 787–788 (1933).
DOI: 10.1007/bf01504252
48. **A. Abrikosov.**
The magnetic properties of superconducting alloys.
Journal of Physics and Chemistry of Solids 2, 199–208 (1957).
DOI: 10.1016/0022-3697(57)90083-5

49. **R.S. Keizer, S.T. Gönnenwein, T.M. Klapwijk, G. Miao, G. Xiao, A. Gupta.**
A spin triplet supercurrent through the half-metallic ferromagnet CrO₂.
Nature **439**, 825–827 (2006).
DOI: 10.1038/nature04499
50. **J.M.D. Coey, M. Venkatesan.**
Half-metallic ferromagnetism: Example of CrO₂ (invited).
Journal of Applied Physics **91**, 8345–8350 (2002).
DOI: 10.1063/1.1447879
51. **J. Linder, J.W. Robinson.**
Superconducting spintronics.
Nature Physics **11**, 307–315 (2015).
DOI: 10.1038/nphys3242
52. **J. Bardeen, L.N. Cooper, J.R. Schrieffer.**
Microscopic Theory of Superconductivity.
Physical Review **106**, 162–164 (1957).
DOI: 10.1103/physrev.106.162
53. **P.W. Anderson.**
Plasmons, Gauge Invariance, and Mass.
Physical Review **130**, 439–442 (1963).
DOI: 10.1103/physrev.130.439
54. **P.W. Higgs.**
Broken Symmetries and the Masses of Gauge Bosons.
Physical Review Letters **13**, 508–509 (1964).
DOI: 10.1103/physrevlett.13.508
55. **A.I. Buzdin, L.N. Bulaevskii, M.L. Kulich, S.V. Panyukov.**
Magnetic superconductors.
Soviet Physics Uspekhi **27**, 927 (1984).
DOI: 10.1070/pu1984v027n12abeh004085
56. **W.A. Fertig, D.C. Johnston, L.E. DeLong, R.W. McCallum, M.B. Maple, B.T. Matthias.**
Destruction of Superconductivity at the Onset of Long-Range Magnetic Order in the Compound ErRh₄B₄.
Physical Review Letters **38**, 987–990 (1977).
DOI: 10.1103/physrevlett.38.987

57. **J.W. Lynn, G. Shirane, W. Thomlinson, R.N. Shelton.**
Competition between Ferromagnetism and Superconductivity in HoMo₆S₈.
 Physical Review Letters **46**, 368–371 (1981).
 DOI: 10.1103/physrevlett.46.368
58. **M. Ishikawa, Ø. Fischer.**
Magnetic ordering in the superconducting state of rare earth molybdenum sulphides, (RE)_{1.2}Mo₆S₈ (RE = Tb, Dy and Er).
 Solid State Communications **24**, 747–751 (1977).
 DOI: 10.1016/0038-1098(77)91182-6
59. **D.E. Moncton, D.B. McWhan, P.H. Schmidt, G. Shirane, W. Thomlinson, M.B. Maple, H.B. MacKay, L.D. Woolf, Z. Fisk, D.C. Johnston.**
Oscillatory Magnetic Fluctuations near the Superconductor-to-Ferromagnet Transition in ErRh₄B₄.
 Physical Review Letters **45**, 2060–2063 (1980).
 DOI: 10.1103/physrevlett.45.2060
60. **S. Saxena, P. Agarwal, K. Ahilan, F. Grosche, R. Haselwimmer, M. Steiner, E. Pugh, I. Walker, S. Julian, P. Monthoux, et al.**
Superconductivity on the border of itinerant-electron ferromagnetism in UGe₂.
 Nature **406**, 587–592 (2000).
 DOI: 10.1038/35020500
61. **N.T. Huy, A. Gasparini, D.E. de Nijs, Y. Huang, J.C.P. Klaasse, T. Gortenmulder, A. de Visser, A. Hamann, T. Görlach, H.v. Löhneysen.**
Superconductivity on the Border of Weak Itinerant Ferromagnetism in UCoGe.
 Physical Review Letters **99**, 067006 (2007).
 DOI: 10.1103/physrevlett.99.067006
62. **M. Sgrist, K. Ueda.**
Phenomenological theory of unconventional superconductivity.
 Reviews of Modern Physics **63**, 239–311 (1991).
 DOI: 10.1103/revmodphys.63.239

63. **R Holm, W Meissner.**
Messungen mit Hilfe von flüssigem Helium. XIII: Kontaktwiderstand zwischen Supraleitern und Nichtsupraleitern.
Zeitschrift für Physik 74, 715–735 (1932).
DOI: 10.1007/bf01340420
64. **P. De Gennes, E. Guyon.**
Superconductivity in “normal” metals.
Physics Letters 3, 168–169 (1963).
DOI: 10.1016/0031-9163(63)90401-3
65. **F.S. Bergeret, A.F. Volkov, K.B. Efetov.**
Long-Range Proximity Effects in Superconductor-Ferromagnet Structures.
Physical Review Letters 86, 4096–4099 (2001).
DOI: 10.1103/physrevlett.86.4096
66. **J. Linder, A.V. Balatsky.**
Odd-frequency superconductivity.
Reviews of Modern Physics 91, 045005 (2019).
DOI: 10.1103/revmodphys.91.045005
67. **H.P. Dahal, E Abrahams, D Mozyrsky, Y Tanaka, A.V. Balatsky.**
Wave function for odd-frequency superconductors.
New Journal of Physics 11, 065005 (2009).
DOI: 10.1088/1367-2630/11/6/065005
68. **F.S. Bergeret, A.F. Volkov, K.B. Efetov.**
Odd triplet superconductivity and related phenomena in superconductor-ferromagnet structures.
Reviews of Modern Physics 77, 1321–1373 (2005).
DOI: 10.1103/revmodphys.77.1321
69. **A. Kadigrobov, R.I. Shekhter, M. Jonson.**
Quantum spin fluctuations as a source of long-range proximity effects in diffusive ferromagnet-super conductor structures.
Europhysics Letters 54, 394 (2001).
DOI: 10.1209/epl/i2001-00107-2

70. **J.W.A. Robinson, J.D.S. Witt, M.G. Blamire.**
Controlled Injection of Spin-Triplet Supercurrents into a Strong Ferromagnet.
Science **329**, 59–61 (2010).
DOI: 10.1126/science.1189246
71. **T.S. Khaire, M.A. Khasawneh, W.P. Pratt, N.O. Birge.**
Observation of Spin-Triplet Superconductivity in Co-Based Josephson Junctions.
Physical Review Letters **104**, 137002 (2010).
DOI: 10.1103/physrevlett.104.137002
72. **R. Fermin, D. van Dinter, M. Hubert, B. Woltjes, M. Silaev, J. Aarts, K. Lahabi.**
Superconducting Triplet Rim Currents in a Spin-Textured Ferromagnetic Disk.
Nano Letters **22**, 2209–2216 (2022).
DOI: 10.1021/acs.nanolett.1c04051
73. **Z. Niu.**
A spin triplet supercurrent in half metal ferromagnet/superconductor junctions with the interfacial Rashba spin-orbit coupling.
Applied Physics Letters **101**, 062601 (2012).
DOI: 10.1063/1.4743001
74. **A.A. Mazanik, I.V. Bobkova.**
Supercurrent-induced long-range triplet correlations and controllable Josephson effect in superconductor/ferromagnet hybrids with extrinsic spin-orbit coupling.
Physical Review B **105**, 144502 (2022).
DOI: 10.1103/physrevb.105.144502
75. **F.S. Bergeret, I.V. Tokatly.**
Singlet-Triplet Conversion and the Long-Range Proximity Effect in Superconductor-Ferromagnet Structures with Generic Spin Dependent Fields.
Physical Review Letters **110**, 117003 (2013).
DOI: 10.1103/physrevlett.110.117003

76. **S.H. Jacobsen, J. Linder.**
Giant triplet proximity effect in π -biased Josephson junctions with spin-orbit coupling.
Physical Review B **92**, 024501 (2015).
DOI: 10.1103/physrevb.92.024501
77. **S.H. Jacobsen, I. Kulagina, J. Linder.**
Controlling superconducting spin flow with spin-flip immunity using a single homogeneous ferromagnet.
Scientific reports **6**, 1–9 (2016).
DOI: 10.1038/srep23926
78. **N. Banerjee, J.A. Ouassou, Y. Zhu, N.A. Stelmashenko, J. Linder, M.G. Blamire.**
Controlling the superconducting transition by spin-orbit coupling.
Physical Review B **97**, 184521 (2018).
DOI: 10.1103/physrevb.97.184521
79. **K.-R. Jeon, C. Ciccarelli, A.J. Ferguson, H. Kurebayashi, L.F. Cohen, X. Montiel, M. Eschrig, J.W. Robinson, M.G. Blamire.**
Enhanced spin pumping into superconductors provides evidence for superconducting pure spin currents.
Nature materials **17**, 499–503 (2018).
DOI: 10.1038/s41563-018-0058-9
80. **J.J. He, K. Hiroki, K. Hamamoto, N. Nagaosa.**
Spin supercurrent in two-dimensional superconductors with Rashba spin-orbit interaction.
Communications Physics **2**, 128 (2019).
DOI: 10.1038/s42005-019-0230-9
81. **J. Nagamatsu, N. Nakagawa, T. Muranaka, Y. Zenitani, J. Akimitsu.**
Superconductivity at 39 K in magnesium diboride.
Nature **410**, 63–64 (2001).
DOI: 10.1038/35065039

82. **J. Hirsch, M. Maple, F. Marsiglio.**
Superconducting materials classes: Introduction and overview.
Physica C: Superconductivity and its Applications 514. Superconducting Materials: Conventional, Unconventional and Undetermined, 1–8 (2015).
DOI: 10.1016/j.physc.2015.03.002
83. **C. Chu, L. Deng, B. Lv.**
Hole-doped cuprate high temperature superconductors.
Physica C: Superconductivity and its Applications 514. Superconducting Materials: Conventional, Unconventional and Undetermined, 290–313 (2015).
DOI: 10.1016/j.physc.2015.02.047
84. **P. Dai, B. Chakoumakos, G. Sun, K. Wong, Y. Xin, D. Lu.**
Synthesis and neutron powder diffraction study of the superconductor $\text{HgBa}_2\text{Ca}_2\text{Cu}_3\text{O}_8 + \delta$ by Tl substitution.
Physica C: Superconductivity 243, 201–206 (1995).
DOI: 10.1016/0921-4534(94)02461-8
85. **Y.-J. Feng, M.-J. Jiang, H.-B. Ding, H.-L. Tian, Z.-H. Lu, G.-H. Zhong, C.-L. Yang, X.-J. Chen, H.-Q. Lin.**
High-Temperature Superconductivity in HfS_3 up to 253 K at a Pressure of 140 GPa by Doping Holes.
The Journal of Physical Chemistry C 126, 20702–20709 (2022).
DOI: 10.1021/acs.jpcc.2c06650
86. **J. Bi, Y. Nakamoto, P. Zhang, K. Shimizu, B. Zou, H. Liu, M. Zhou, G. Liu, H. Wang, Y. Ma.**
Giant enhancement of superconducting critical temperature in substitutional alloy (La, Ce) Hf_3 .
Nature Communications 13, 5952 (2022).
DOI: 10.1038/s41467-022-33743-6
87. **A. Drozdov, M. Erements, I. Troyan, V. Ksenofontov, S.I. Shylin.**
Conventional superconductivity at 203 kelvin at high pressures in the sulfur hydride system.
Nature 525, 73–76 (2015).
DOI: 10.1038/nature14964

88. **A. Drozdov, P. Kong, V. Minkov, S. Besedin, M. Kuzovnikov, S Mozaffari, L Balicas, F. Balakirev, D. Graf, V. Prakapenka, et al.**
Superconductivity at 250 K in lanthanum hydride under high pressures.
 Nature **569**, 528–531 (2019).
 DOI: 10.1038/s41586-019-1201-8
89. **D.S. Holmes, A.L. Ripple, M.A. Manheimer.**
Energy-Efficient Superconducting Computing—Power Budgets and Requirements.
 IEEE Transactions on Applied Superconductivity **23**, 1701610–1701610 (2013).
 DOI: 10.1109/tasc.2013.2244634
90. **M.A. Manheimer.**
Cryogenic Computing Complexity Program: Phase 1 Introduction.
 IEEE Transactions on Applied Superconductivity **25**, 1–4 (2015).
 DOI: 10.1109/tasc.2015.2399866
91. **J.A. Flores-Livas, L. Boeri, A. Sanna, G. Profeta, R. Arita, M. Eremets.**
A perspective on conventional high-temperature superconductors at high pressure: Methods and materials.
 Physics Reports **856**. A perspective on conventional high-temperature superconductors at high pressure: Methods and materials, 1–78 (2020).
 DOI: 10.1016/j.physrep.2020.02.003
92. **D.S. Holmes.**
Cryogenic Electronics and Quantum Information Processing in 2021 IEEE International Roadmap for Devices and Systems Outbriefs.
 (IEEE Computer Society, Santa Clara, 2021), 1–93.
 ISBN: 9781665486385
 DOI: 10.1109/irds54852.2021.00012

93. **I.M. Dayton, T. Sage, E.C. Gingrich, M.G. Loving, T.F. Ambrose, N.P. Siwak, S. Keebaugh, C. Kirby, D.L. Miller, A.Y. Herr, Q.P. Herr, *et al.***
Experimental Demonstration of a Josephson Magnetic Memory Cell With a Programmable π -Junction.
IEEE Magnetics Letters **9**, 1–5 (2018).
DOI: 10.1109/lmag.2018.2801820
94. **R. Fermin, N.M.A. Scheinowitz, J. Aarts, K. Lahabi.**
Mesoscopic superconducting memory based on bistable magnetic textures.
Physical Review Research **4**, 033136 (2022).
DOI: 10.1103/physrevresearch.4.033136
95. **N.O. Birge, M. Houzet.**
Spin-Singlet and Spin-Triplet Josephson Junctions for Cryogenic Memory.
IEEE Magnetics Letters **10**, 1–5 (2019).
DOI: 10.1109/lmag.2019.2955419
96. **Y. Takeshita, F. Li, D. Hasegawa, K. Sano, M. Tanaka, T. Yamashita, A. Fujimaki.**
High-Speed Memory Driven by SFQ Pulses Based on $0-\pi$ SQUID.
IEEE Transactions on Applied Superconductivity **31**, 1–6 (2021).
DOI: 10.1109/tasc.2021.3060351
97. **K. Likharev, V. Semenov.**
RSFQ logic/memory family: a new Josephson-junction technology for sub-terahertz-clock-frequency digital systems.
IEEE Transactions on Applied Superconductivity **1**, 3–28 (1991).
DOI: 10.1109/77.80745

98. **K. Ishida, I. Byun, I. Nagaoka, K. Fukumitsu, M. Tanaka, S. Kawakami, T. Tanimoto, T. Ono, J. Kim, K. Inoue.**
SuperNPU: An Extremely Fast Neural Processing Unit Using Superconducting Logic Devices
 in *2020 53rd Annual IEEE/ACM International Symposium on Microarchitecture (MICRO)*.
 (2020),
 58–72.
 DOI: 10.1109/micro50266.2020.00018
99. **I. Ishikawa, I. Nagaoka, R. Kashima, K. Ishida, K. Fukumitsu, K. Oka, M. Tanaka, S. Kawakami, T. Tanimoto, T. Ono, A. Fujimaki, et al.**
Design of Variable Bit-Width Arithmetic Unit Using Single Flux Quantum Device
 in *2022 IEEE International Symposium on Circuits and Systems (ISCAS)*.
 (2022),
 3547–3551.
 DOI: 10.1109/iscas48785.2022.9937317
100. **C. Cao, S.M. Carroll, S. Michalakis.**
Space from Hilbert space: Recovering geometry from bulk entanglement.
 Physical Review D **95**, 024031 (2017).
 DOI: 10.1103/physrevd.95.024031
101. **C. Cao, S.M. Carroll.**
Bulk entanglement gravity without a boundary: Towards finding Einstein’s equation in Hilbert space.
 Physical Review D **97**, 086003 (2018).
 DOI: 10.1103/physrevd.97.086003
102. **S.M. Carroll, A. Singh.**
Mad-Dog Everettianism: Quantum Mechanics at Its Most Minimal in *What is Fundamental?* (eds A. Aguirre, B. Foster, Z. Merali) 95–104 (Springer International Publishing, Cham, 2019).
 ISBN: 978-3-030-11301-8
 DOI: 10.1007/978-3-030-11301-8_10

103. **S.M. Carroll.**
Reality as a Vector in Hilbert Space in Quantum Mechanics and Fundamentality : Naturalizing Quantum Theory between Scientific Realism and Ontological Indeterminacy (ed V. Allori) 211–224 (Springer International Publishing, Cham, 2022).
ISBN: 978-3-030-99642-0
DOI: 10.1007/978-3-030-99642-0_15
104. **F.A. Berezin, M. Shubin.**
The Schrödinger Equation (Springer Science & Business Media, Dordrecht, 2012).
ISBN: 9789401131544
DOI: 10.1007/978-94-011-3154-4
105. **N. Young.**
An introduction to Hilbert space (Cambridge University Press, 1988).
ISBN: 9780521337175
106. **B.C. Hall.**
Quantum Theory for Mathematicians (Springer, New York, 2013).
ISBN: 9781461471165
DOI: 10.1007/978-1-4614-7116-5
107. **C.M. Bender, S. Boettcher.**
Real Spectra in Non-Hermitian Hamiltonians Having PT Symmetry.
Physical Review Letters **80**, 5243–5246 (1998).
DOI: 10.1103/physrevlett.80.5243
108. **C.M. Bender.**
Making sense of non-Hermitian Hamiltonians.
Reports on Progress in Physics **70**, 947 (2007).
DOI: 10.1088/0034-4885/70/6/r03
109. **C.M. Bender.**
PT symmetry in quantum physics: From a mathematical curiosity to optical experiments.
Europhysics News **47**, 17–20 (2016).
DOI: 10.1051/epn/2016201

110. **C.M. Bender, D.C. Brody, M.P. Müller.**
Hamiltonian for the Zeros of the Riemann Zeta Function.
 Physical Review Letters **118**, 130201 (2017).
 DOI: 10.1103/physrevlett.118.130201
111. **C.M. Bender, D.C. Brody.**
Asymptotic analysis on a pseudo-Hermitian Riemann-zeta Hamiltonian.
 Journal of Physics A: Mathematical and Theoretical **51**, 135203 (2018).
 DOI: 10.1088/1751-8121/aab068
112. **M.H. Stone.**
On One-Parameter Unitary Groups in Hilbert Space.
 Annals of Mathematics **33**, 643–648 (1932).
 DOI: 10.2307/1968538
113. **C. Heissenberg, A. Sagnotti.**
Classical and Quantum Statistical Physics: Fundamentals and Advanced Topics, 134–140 (Cambridge University Press, Cambridge, 2022).
 DOI: 10.1017/9781108952002
114. **H. Bruus, K. Flensberg.**
Many-body Quantum Theory in Condensed Matter Physics (Oxford University Press, Oxford, 2004).
 ISBN: 9780198566335
115. **H. Goldstein, C. Poole, J. Safko.**
Classical Mechanics (Addison Wesley, 2002).
 ISBN: 9780201657029
116. **M. Kachelriess.**
Quantum Fields — From the Hubble to the Planck Scale (Oxford University Press, Oxford, 2018).
 ISBN: 9780198802877
 DOI: 10.1093/oso/9780198802877.001.0001
117. **R.F. Streater, A.S. Wightman.**
PCT, spin and statistics, and all that (Princeton University Press, Princeton, 2000).
 ISBN: 9780691070629

118. **E. Noether.**
Invariante Variationsprobleme.
Nachrichten von der Gesellschaft der Wissenschaften zu
Göttingen, Mathematisch-Physikalische Klasse, 235–257 (1918).
119. **A. Zee.**
Group Theory in a Nutshell for Physicists (Princeton University
Press, Princeton, 2016).
ISBN: 9780691162690
120. **C. Doran, A. Lasenby, J. Lasenby.**
Geometric algebra for physicists (Cambridge University Press,
Cambridge, 2003).
ISBN: 9780521480222
121. **A.N. Lasenby.**
*Geometric Algebra as a Unifying Language for Physics and
Engineering and Its Use in the Study of Gravity.*
Advances in Applied Clifford Algebras 27, 733–759 (2017).
DOI: 10.1007/s00006-016-0700-z
122. **D.J. Griffiths.**
Introduction to Electrodynamics 4th ed. (Cambridge University
Press, Cambridge, 2017).
DOI: 10.1017/9781108333511
123. **R.H. Milburn.**
Electron Scattering by an Intense Polarized Photon Field.
Physical Review Letters 10, 75–77 (1963).
DOI: 10.1103/physrevlett.10.75
124. **P.A.M. Dirac, R.H. Fowler.**
The Quantum Theory of the Electron.
Proceedings of the Royal Society of London. Series A, Con-
taining Papers of a Mathematical and Physical Character 117,
610–624 (1928).
DOI: 10.1098/rspa.1928.0023
125. **L.L. Foldy, S.A. Wouthuysen.**
*On the Dirac Theory of Spin 1/2 Particles and Its Non-Relativistic
Limit.*
Physical Review 78, 29–36 (1950).
DOI: 10.1103/physrev.78.29

126. **L.L. Foldy.**
The Electromagnetic Properties of Dirac Particles.
Physical Review **87**, 688–693 (1952).
DOI: 10.1103/physrev.87.688
127. **R. Acharya, E.C.G. Sudarshan.**
“Front” Description in Relativistic Quantum Mechanics.
Journal of Mathematical Physics **1**, 532–536 (1960).
DOI: 10.1063/1.1703689
128. **L. Canetti, M. Drewes, M. Shaposhnikov.**
Matter and antimatter in the universe.
New Journal of Physics **14**, 095012 (2012).
DOI: 10.1088/1367-2630/14/9/095012
129. **C.G. Darwin.**
The Wave Equations of the Electron.
Proceedings of the Royal Society of London. Series A, Con-
taining Papers of a Mathematical and Physical Character **118**,
654–680 (1928).
130. **B. Odom, D. Hanneke, B. D’Urso, G. Gabrielse.**
*New Measurement of the Electron Magnetic Moment Using a
One-Electron Quantum Cyclotron.*
Physical Review Letters **97**, 030801 (2006).
DOI: 10.1103/physrevlett.97.030801
131. **X. Fan, T.G. Myers, B.A.D. Sukra, G. Gabrielse.**
Measurement of the Electron Magnetic Moment.
Physical Review Letters **130**, 071801 (2023).
DOI: 10.1103/physrevlett.130.071801
132. **K.C. Nowack, F.H.L. Koppens, Y.V. Nazarov, L.M.K. Vander-
sypen.**
Coherent Control of a Single Electron Spin with Electric Fields.
Science **318**, 1430–1433 (2007).
DOI: 10.1126/science.1148092
133. **D. Liang, X.P. Gao.**
*Strong Tuning of Rashba Spin–Orbit Interaction in Single InAs
Nanowires.*
Nano Letters **12**, 3263–3267 (2012).
DOI: 10.1021/nl301325h

134. **B. Simović, P. Studerus, S. Gustavsson, R. Leturcq, K. Ensslin, R. Schuhmann, J. Forrer, A. Schweiger.**
Design of Q-band loop-gap resonators at frequencies of 34–36GHz for single electron spin spectroscopy in semiconductor nanostructures.
 Review of Scientific Instruments 77, 064702 (2006).
 DOI: 10.1063/1.2206776
135. **F.H. Koppens, C. Buizert, K.-J. Tielrooij, I.T. Vink, K.C. Nowack, T. Meunier, L. Kouwenhoven, L. Vandersypen.**
Driven coherent oscillations of a single electron spin in a quantum dot.
 Nature 442, 766–771 (2006).
 DOI: 10.1038/nature05065
136. **A.C. Torrezan, T.P. Mayer Alegre, G. Medeiros-Ribeiro.**
Microstrip resonators for electron paramagnetic resonance experiments.
 Review of Scientific Instruments 80, 075111 (2009).
 DOI: 10.1063/1.3186054
137. **M.E. Peskin, D.V. Schroeder.**
An Introduction To Quantum Field Theory (CRC Press, Boca Raton, 1995).
 ISBN: 9780201503975
138. **A. Liénard.**
Champ électrique et magnétique produit par une charge électrique concentrée en un point et animée d'un mouvement quelconque.
 L'Éclairage Electrique 16, 5 (1898).
139. **E. Wiechert.**
Elektrodynamische Elementargesetze.
 Annalen der Physik 309, 667–689 (1901).
 DOI: 10.1002/andp.19013090403
140. **W. Greiner, J. Reinhardt, D. Bromley.**
Field Quantization (Springer, Frankfurt, 1996).
 ISBN: 9783540591795

141. **C. Kittel, P. McEuen.**
Introduction to Solid State Physics (John Wiley & Sons, Hoboken, New Jersey, 2005).
ISBN: 9780471415268
142. **J.E. Moore.**
The Birth of Topological Insulators.
Nature **464**, 194–198 (2010).
DOI: 10.1038/nature08916
143. **L. Fu, C.L. Kane, E.J. Mele.**
Topological Insulators in Three Dimensions.
Physical Review Letters **98**, 106803 (2007).
DOI: 10.1103/physrevlett.98.106803
144. **C. Broholm, R.J. Cava, S.A. Kivelson, D.G. Nocera, M.R. Norman, T. Senthil.**
Quantum spin liquids.
Science **367**, eaay0668 (2020).
DOI: 10.1126/science.aay0668
145. **D.A. Huse, V. Elser.**
Simple Variational Wave Functions for Two-Dimensional Heisenberg Spin- $\frac{1}{2}$ Antiferromagnets.
Physical Review Letters **60**, 2531–2534 (1988).
DOI: 10.1103/physrevlett.60.2531
146. **L. Savary, L. Balents.**
Quantum spin liquids: a review.
Reports on Progress in Physics **80**, 016502 (2016).
DOI: 10.1088/0034-4885/80/1/016502
147. **G.H. Wannier.**
The Structure of Electronic Excitation Levels in Insulating Crystals.
Physical Review **52**, 191–197 (1937).
DOI: 10.1103/physrev.52.191
148. **W. Kohn.**
Analytic Properties of Bloch Waves and Wannier Functions.
Physical Review **115**, 809–821 (1959).
DOI: 10.1103/physrev.115.809

149. **F. Bloch.**
Über die quantenmechanik der elektronen in kristallgittern.
Zeitschrift für physik **52**, 555–600 (1929).
DOI: 10.1007/bf01339455
150. **A. Altland, B. Simons.**
Condensed Matter Field Theory (Cambridge University Press,
Cambridge, 2010).
ISBN: 9780521769754
151. **H. Tasaki.**
*The Hubbard model - an introduction and selected rigorous
results.*
Journal of Physics: Condensed Matter **10**, 4353 (1998).
DOI: 10.1088/0953-8984/10/20/004
152. **H. Tasaki.**
*Ferromagnetism in the Hubbard Model: A Constructive Ap-
proach.*
Communications in Mathematical Physics **242**, 445–472
(2003).
DOI: 10.1007/s00220-003-0952-z
153. **C.E. Soliverez.**
General theory of effective Hamiltonians.
Physical Review A **24**, 4–9 (1981).
DOI: 10.1103/physreva.24.4
154. **B. Heinrich, D. Fraitová, V. Kamberský.**
*The Influence of s-d Exchange on Relaxation of Magnons in
Metals.*
physica status solidi (b) **23**, 501–507 (1967).
DOI: 10.1002/pssb.19670230209
155. **A.H. Mitchell.**
*Ferromagnetic Relaxation by the Exchange Interaction between
Ferromagnetic Electrons and Conduction Electrons.*
Physical Review **105**, 1439–1444 (1957).
DOI: 10.1103/physrev.105.1439

156. **H.J. Skadsem, Y. Tserkovnyak, A. Brataas, G.E.W. Bauer.**
Magnetization damping in a local-density approximation.
Physical Review B **75**, 094416 (2007).
DOI: 10.1103/physrevb.75.094416
157. **H.T. Simensen, A. Kamra, R.E. Troncoso, A. Brataas.**
Magnon decay theory of Gilbert damping in metallic antiferromagnets.
Physical Review B **101**, 020403 (2020).
DOI: 10.1103/physrevb.101.020403
158. **R. Stuart, W. Marshall.**
Direct Exchange in Ferromagnets.
Physical Review **120**, 353–357 (1960).
DOI: 10.1103/physrev.120.353
159. **R. Martin, R. Scalettar, R. Resta, E. Koch, A. Oles, R. Eder, P. Prelovsek, F. Gebhard, E. Pavarini, A. Lichtenstein, V. Janis, et al.**
The Physics of Correlated Insulators, Metals, and Superconductors (eds E. Pavarini, E. Koch, R. Scalettar, R. Martin)
(Forschungszentrum Jülich GmbH Zentralbibliothek, Verlag, Jülich, 2017).
ISBN: 9783958062245
160. **P.W. Anderson.**
Antiferromagnetism. Theory of Superexchange Interaction.
Physical Review **79**, 350–356 (1950).
DOI: 10.1103/physrev.79.350
161. **M. Azhar, M. Mostovoy.**
Incommensurate Spiral Order from Double-Exchange Interactions.
Physical Review Letters **118**, 027203 (2017).
DOI: 10.1103/physrevlett.118.027203
162. **P.G. de Gennes.**
Effects of Double Exchange in Magnetic Crystals.
Physical Review **118**, 141–154 (1960).
DOI: 10.1103/physrev.118.141

163. **I. Dzyaloshinsky.**
A thermodynamic theory of “weak” ferromagnetism of antiferromagnetics.
Journal of Physics and Chemistry of Solids 4, 241–255 (1958).
DOI: 10.1016/0022-3697(58)90076-3
164. **T. Moriya.**
Anisotropic Superexchange Interaction and Weak Ferromagnetism.
Physical Review 120, 91–98 (1960).
DOI: 10.1103/physrev.120.91
165. **H. Yang, J. Liang, Q. Cui.**
First-principles calculations for Dzyaloshinskii–Moriya interaction.
Nature Reviews Physics 5, 43–61 (2023).
DOI: 10.1038/s42254-022-00529-0
166. **G. Finocchio, F. Büttner, R. Tomasello, M. Carpentieri, M. Kläui.**
Magnetic skyrmions: from fundamental to applications.
Journal of Physics D: Applied Physics 49, 423001 (2016).
DOI: 10.1088/0022-3727/49/42/423001
167. **M. Tinkham.**
Introduction to Superconductivity (Dover Publications, Mineola, 2004).
ISBN: 9780486134727
168. **N. Karchev.**
Magnon-mediated superconductivity in itinerant ferromagnets.
Journal of Physics: Condensed Matter 15, L385 (2003).
DOI: 10.1088/0953-8984/15/24/105
169. **E. Erlandsen, A. Brataas, A. Sudbø.**
Magnon-mediated superconductivity on the surface of a topological insulator.
Physical Review B 101, 094503 (2020).
DOI: 10.1103/physrevb.101.094503

170. **E. Erlandsen, A. Kamra, A. Brataas, A. Sudbø.**
Enhancement of superconductivity mediated by antiferromagnetic squeezed magnons.
Physical Review B **100**, 100503 (2019).
DOI: 10.1103/physrevb.100.100503
171. **E. Thingstad, E. Erlandsen, A. Sudbø.**
Eliashberg study of superconductivity induced by interfacial coupling to antiferromagnets.
Physical Review B **104**, 014508 (2021).
DOI: 10.1103/physrevb.104.014508
172. **S. Beck, A. Hampel, M. Zingl, C. Timm, A. Ramires.**
Effects of strain in multiorbital superconductors: The case of Sr_2RuO_4 .
Physical Review Research **4**, 023060 (2022).
DOI: 10.1103/physrevresearch.4.023060
173. **F. Parhizgar, A.M. Black-Schaffer.**
Diamagnetic and paramagnetic Meissner effect from odd-frequency pairing in multiorbital superconductors.
Physical Review B **104**, 054507 (2021).
DOI: 10.1103/physrevb.104.054507
174. **C. Triola, J. Cayao, A.M. Black-Schaffer.**
The Role of Odd-Frequency Pairing in Multiband Superconductors.
Annalen der Physik **532**, 1900298 (2020).
DOI: <https://doi.org/10.1002/andp.201900298>
175. **A.L. Fetter, P.C. Hohenberg.**
The Mixed State of Thin Superconducting Films in Perpendicular Fields.
Physical Review **159**, 330–343 (1967).
DOI: 10.1103/physrev.159.330
176. **Y. Fuseya, Z. Zhu, B. Fauqué, W. Kang, B. Lenoir, K. Behnia.**
Origin of the Large Anisotropic g Factor of Holes in Bismuth.
Physical Review Letters **115**, 216401 (2015).
DOI: 10.1103/physrevlett.115.216401

177. **J.H. Qvist, J. Danon.**
Anisotropic g-tensors in hole quantum dots: Role of transverse confinement direction.
Physical Review B **105**, 075303 (2022).
DOI: 10.1103/physrevb.105.075303
178. **R. Peierls.**
Zur theorie des diamagnetismus von leitungselektronen.
Zeitschrift für Physik **80**, 763–791 (1933).
DOI: 10.1007/bf01342591
179. **E. Brown.**
Bloch Electrons in a Uniform Magnetic Field.
Physical Review **133**, A1038–A1044 (1964).
DOI: 10.1103/physrev.133.a1038
180. **G Bihlmayer, O Rader, R Winkler.**
Focus on the Rashba effect.
New Journal of Physics **17**, 050202 (2015).
DOI: 10.1088/1367-2630/17/5/050202
181. **G. Dresselhaus.**
Spin-Orbit Coupling Effects in Zinc Blende Structures.
Physical Review **100**, 580–586 (1955).
DOI: 10.1103/physrev.100.580
182. **S. LaShell, B.A. McDougall, E. Jensen.**
Spin Splitting of an Au(111) Surface State Band Observed with Angle Resolved Photoelectron Spectroscopy.
Physical Review Letters **77**, 3419–3422 (1996).
DOI: 10.1103/physrevlett.77.3419
183. **L. Petersen, P. Hedegård.**
A simple tight-binding model of spin-orbit splitting of sp-derived surface states.
Surface Science **459**, 49–56 (2000).
DOI: 10.1016/s0039-6028(00)00441-6
184. **D. Borthwick.**
Introduction to Partial Differential Equations (Springer, Cham, 2017).
ISBN: 9783319489346

185. **J. Rammer.**
Quantum Field Theory of Non-equilibrium States (Cambridge University Press, Cambridge, 2007).
DOI: 10.1017/cbo9780511618956
186. **R. Kubo.**
Statistical-Mechanical Theory of Irreversible Processes. I. General Theory and Simple Applications to Magnetic and Conduction Problems.
Journal of the Physical Society of Japan **12**, 570–586 (1957).
DOI: 10.1143/jpsj.12.570
187. **R. Kubo, M. Yokota, S. Nakajima.**
Statistical-Mechanical Theory of Irreversible Processes. II. Response to Thermal Disturbance.
Journal of the Physical Society of Japan **12**, 1203–1211 (1957).
DOI: 10.1143/jpsj.12.1203
188. **H.B. Callen, T.A. Welton.**
Irreversibility and Generalized Noise.
Physical Review **83**, 34–40 (1951).
DOI: 10.1103/physrev.83.34
189. **R Kubo.**
The fluctuation-dissipation theorem.
Reports on Progress in Physics **29**, 255 (1966).
DOI: 10.1088/0034-4885/29/1/306
190. **M. Galperin, M.A. Ratner, A. Nitzan.**
Inelastic electron tunneling spectroscopy in molecular junctions: Peaks and dips.
The Journal of Chemical Physics **121**, 11965–11979 (2004).
DOI: 10.1063/1.1814076
191. **B.Y.-K. Hu, E.H. Hwang, S. Das Sarma.**
Density of states of disordered graphene.
Physical Review B **78**, 165411 (2008).
DOI: 10.1103/physrevb.78.165411
192. **G.C. Wick.**
The Evaluation of the Collision Matrix.
Physical Review **80**, 268–272 (1950).
DOI: 10.1103/physrev.80.268

193. **T. Evans, D. Steer.**
Wick's theorem at finite temperature.
 Nuclear Physics B 474, 481–496 (1996).
 DOI: 10.1016/0550-3213(96)00286-6
194. **D.C. Langreth.**
Linear and Nonlinear Response Theory with Applications in Linear and Nonlinear Electron Transport in Solids (eds J.T. Devreese, V.E. van Doren) 3–32 (Springer, Boston, 1976).
 ISBN: 978-1-4757-0875-2
 DOI: 10.1007/978-1-4757-0875-2_1
195. **P. Virtanen, T.T. Heikkilä, F.S. Bergeret, J.C. Cuevas.**
Theory of Microwave-Assisted Supercurrent in Diffusive SNS Junctions.
 Physical Review Letters 104, 247003 (2010).
 DOI: 10.1103/physrevlett.104.247003
196. **A. Geyer, R. Quirchmayr.**
Shallow water equations for equatorial tsunami waves.
 Philosophical Transactions of the Royal Society A 376, 20170100 (2018).
 DOI: 10.1098/rsta.2017.0100
197. **Y. Liu, Y. Shi, D.A. Yuen, E.O. Sevre, X. Yuan, H.L. Xing.**
Comparison of linear and nonlinear shallow wave water equations applied to tsunami waves over the China Sea.
 Acta Geotechnica 4, 129–137 (2009).
 DOI: 10.1007/s11440-008-0073-0
198. **R. Mittal, G. Iaccarino.**
Immersed Boundary Methods.
 Annual Review of Fluid Mechanics 37, 239–261 (2005).
 DOI: 10.1146/annurev.fluid.37.061903.175743
199. **C. Xu, Y. wei Wang, C. guang Huang, J. Huang, C. Yu.**
The effect of free surface on cloud cavitating flow around a blunt body.
 Journal of Hydrodynamics, Ser. B 29, 979–986 (2017).
 DOI: 10.1016/s1001-6058(16)60812-0

200. **E.N. Lorenz.**
Deterministic Nonperiodic Flow.
 Journal of Atmospheric Sciences **20**, 130–141 (1963).
 DOI: 10.1175/1520-0469(1963)020<0130:dnf>2.0.co;2
201. **C. Sparrow.**
The Lorenz Equations: Bifurcations, Chaos, and Strange Attractors (Springer, New York, 2012).
 ISBN: 9781461257677
 DOI: 10.1007/978-1-4612-5767-7
202. **S. Strogatz.**
Nonlinear Dynamics and Chaos: With Applications to Physics, Biology, Chemistry, and Engineering (Westview Press, Colorado, 2015).
 ISBN: 9780813349107
203. **J. Rammer, H. Smith.**
Quantum field-theoretical methods in transport theory of metals.
 Reviews of Modern Physics **58**, 323–359 (1986).
 DOI: 10.1103/revmodphys.58.323
204. **W. Belzig, F.K. Wilhelm, C. Bruder, G. Schön, A.D. Zaikin.**
Quasiclassical Green's function approach to mesoscopic superconductivity.
 Superlattices and Microstructures **25**, 1251–1288 (1999).
 DOI: 10.1006/spmi.1999.0710
205. **G. Eilenberger.**
Transformation of Gorkov's equation for type II superconductors into transport-like equations.
 Zeitschrift für Physik A Hadrons and nuclei **214**, 195–213 (1968).
 DOI: 0.1007/bf01379803
206. **A.L. Shelankov.**
On the derivation of quasiclassical equations for superconductors.
 Journal of Low Temperature Physics **60**, 29–44 (1985).
 DOI: 10.1007/bf00681651

207. **M. Amundsen, J. Linder.**
Quasiclassical theory for interfaces with spin-orbit coupling.
Physical Review B **100**, 064502 (2019).
DOI: 10.1103/physrevb.100.064502
208. **R. Grein, T. Löfwander, G. Metalidis, M. Eschrig.**
Theory of superconductor-ferromagnet point-contact spectra: The case of strong spin polarization.
Physical Review B **81**, 094508 (2010).
DOI: 10.1103/physrevb.81.094508
209. **M Eschrig, A Cottet, W Belzig, J Linder.**
General boundary conditions for quasiclassical theory of superconductivity in the diffusive limit: application to strongly spin-polarized systems.
New Journal of Physics **17**, 083037 (2015).
DOI: 10.1088/1367-2630/17/8/083037
210. **G.A. Bobkov, I.V. Bobkova, A.M. Bobkov, A. Kamra.**
Néel proximity effect at antiferromagnet/superconductor interfaces.
Physical Review B **106**, 144512 (2022).
DOI: 10.1103/physrevb.106.144512
211. **M. Houzet, J.S. Meyer.**
Quasiclassical theory of disordered Rashba superconductors.
Physical Review B **92**, 014509 (2015).
DOI: 10.1103/physrevb.92.014509
212. **A. Moor, A.F. Volkov, K.B. Efetov.**
Quasiclassical description of a superconductor with a spin density wave.
Physical Review B **83**, 134524 (2011).
DOI: 10.1103/physrevb.83.134524
213. **A. Ghanbari, E. Erlandsen, A. Sudbø, J. Linder.**
Going beyond the Chandrasekhar-Clogston limit in a flatband superconductor.
Physical Review B **105**, L060501 (2022).
DOI: 10.1103/physrevb.105.l060501

214. **T. Inui, Y. Tanabe, Y. Onodera.**
Group Theory and Its Applications in Physics (Springer, Berlin, 2012).
ISBN: 9783540604457
DOI: 10.1007/978-3-642-80021-4
215. **K. Hagiwara, K. Hikasa, K. Nakamura, M. Tanabashi, M. Aguilar-Benitez, C. Amsler, R.M. Barnett, P.R. Burchat, C.D. Carone, C. Caso, G. Conforto, et al.**
Review of Particle Properties.
Physical Review D **66**, 010001 (2002).
DOI: 10.1103/physrevd.66.010001
216. **K.D. Usadel.**
Generalized Diffusion Equation for Superconducting Alloys.
Physical Review Letters **25**, 507–509 (1970).
DOI: 10.1103/physrevlett.25.507
217. **W.L. McMillan.**
Tunneling Model of the Superconducting Proximity Effect.
Physical Review **175**, 537–542 (1968).
DOI: 10.1103/physrev.175.537
218. **M.Y. Kupriyanov, V.F. Lukichev.**
Influence of boundary transparency on the critical current of "dirty" SS'S structures.
Zh. Eksp. Teor. Fiz **94** (1988).
219. **Y.V. Nazarov.**
Novel circuit theory of Andreev reflection.
Superlattices Microstruct. **25**, 1221–1231 (1999).
DOI: 10.1006/spmi.1999.0738
220. **Y.V. Nazarov, Y.M. Blanter.**
Quantum Transport: Introduction to Nanoscience (Cambridge University Press, Cambridge, 2009).
DOI: 10.1017/cbo9780511626906

221. **M. Eschrig.**
Distribution functions in nonequilibrium theory of superconductivity and Andreev spectroscopy in unconventional superconductors.
Physical Review B **61**, 9061–9076 (2000).
DOI: 10.1103/physrevb.61.9061
222. **A. Konstandin, J. Kopu, M. Eschrig.**
Superconducting proximity effect through a magnetic domain wall.
Physical Review B **72**, 140501 (2005).
DOI: 10.1103/physrevb.72.140501
223. **D.A. Ivanov, Y.V. Fominov.**
Minigap in superconductor-ferromagnet junctions with inhomogeneous magnetization.
Physical Review B **73**, 214524 (2006).
DOI: 10.1103/physrevb.73.214524
224. **L.-L.W. Jie Shen Tao Tang.**
Spectral Methods (Springer-Verlag, Berlin, 2011).
ISBN: 9783540710400
DOI: 10.1007/978-3-540-71041-7
225. **S.A. Orszag.**
Comparison of Pseudospectral and Spectral Approximation.
Studies in Applied Mathematics **51**, 253–259 (1972).
DOI: 10.1002/sapm1972513253
226. **A. Quarteroni, A. Valli.**
Numerical Approximation of Partial Differential Equations
(Springer-Verlag, Berlin, 2008).
ISBN: 9783540852674
DOI: 10.1007/978-3-540-85268-1
227. **L.A. Peter Knabner.**
Numerical Methods for Elliptic and Parabolic Partial Differential Equations (Springer, Cham, 2021).
ISBN: 9783030793845
DOI: 110.1007/978-3-030-79385-2

228. **A.T. Patera.**
A spectral element method for fluid dynamics: Laminar flow in a channel expansion.
 Journal of Computational Physics **54**, 468–488 (1984).
 DOI: 10.1016/0021-9991(84)90128-1
229. **S.P.N. Ernst Hairer Gerhard Wanner.**
Solving Ordinary Differential Equations I: Nonstiff Problems
 (Springer-Verlag, Berlin, 1993).
 ISBN: 9783540566700
 DOI: 10.1007/978-3-540-78862-1
230. **P. Sablonnière, D. Sbibih, M Tahrichi.**
Error estimate and extrapolation of a quadrature formula derived from a quartic spline quasi-interpolant.
 BIT Numerical Mathematics **50**, 843–862 (2010).
 DOI: 10.1007/s10543-010-0278-0
231. **T.J. Ypma.**
Historical Development of the Newton–Raphson Method.
 SIAM Review **37**, 531–551 (1995).
 DOI: 10.1137/1037125
232. **G. Anastassiou, S. Dragomir.**
On Some Estimates of the Remainder in Taylor’s Formula.
 Journal of Mathematical Analysis and Applications **263**, 246–263 (2001).
 DOI: 10.1006/jmaa.2001.7622
233. **W.B. Gragg, R.A. Tapia.**
Optimal Error Bounds for the Newton-Kantorovich Theorem.
 SIAM Journal on Numerical Analysis **11**, 10–13 (1974).
 DOI: 10.1137/0711002
234. **J.M. Ortega.**
The Newton-Kantorovich Theorem.
 The American Mathematical Monthly **75**, 658–660.
 DOI: 10.2307/2313800
235. **R.A. Tapia.**
The Kantorovich Theorem for Newton’s Method.
 The American Mathematical Monthly **78**, 389–392 (1971).
 DOI: 10.1080/00029890.1971.11992771

236. **U. Kulisch, R. Hammer, D. Ratz, M. Hocks.**
Numerical Toolbox for Verified Computing I: Basic Numerical Problems Theory, Algorithms, and Pascal-XSC Programs, 69–86 (Springer, Berlin, 1993).
ISBN: 9783642784231
DOI: 10.1007/978-3-642-78423-1_5
237. **Clifford.**
Preliminary Sketch of Biquaternions.
Proceedings of the London Mathematical Society **s1-4**, 381–395 (1871).
DOI: 10.1112/plms/s1-4.1.381
238. **M.S.P. Eastham.**
On the Definition of Dual Numbers.
The Mathematical Gazette **45**, 232–233 (1961).
DOI: 10.2307/3612794
239. **L.W. Johnson, D.R. Scholz.**
On Steffensen's Method.
SIAM Journal on Numerical Analysis **5**, 296–302 (1968).
DOI: 10.1137/0705026
240. **D.G. Anderson.**
Iterative Procedures for Nonlinear Integral Equations.
Journal of the Association for Computing Machinery **12**, 547–560 (1965).
DOI: 10.1145/321296.321305
241. **H. Fang, Y. Saad.**
Two classes of multisection methods for nonlinear acceleration.
Numerical Linear Algebra with Applications **16**, 197–221 (2009).
DOI: 10.1002/nla.617
242. **C.G. Broyden.**
A class of methods for solving nonlinear simultaneous equations.
Mathematics of Computation **19**, 557–593 (1965).
DOI: 10.2307/2003941

243. **B.I. Halperin, G. Refael, E. Demler.**
Resistance in Superconductors.
International Journal of Modern Physics B **24**, 4039–4080
(2010).
DOI: 10.1142/s021797921005644x
244. **G.E. Blonder, M. Tinkham, T.M. Klapwijk.**
Transition from metallic to tunneling regimes in superconducting microconstrictions: Excess current, charge imbalance, and supercurrent conversion.
Physical Review B **25**, 4515–4532 (1982).
DOI: 10.1103/physrevb.25.4515
245. **Y. Tserkovnyak, A. Brataas, G.E.W. Bauer.**
Enhanced Gilbert Damping in Thin Ferromagnetic Films.
Physical Review Letters **88**, 117601 (2002).
DOI: 10.1103/physrevlett.88.117601
246. **Y. Tserkovnyak, A. Brataas, G.E.W. Bauer, B.I. Halperin.**
Nonlocal magnetization dynamics in ferromagnetic heterostructures.
Reviews of Modern Physics **77**, 1375–1421 (2005).
DOI: 10.1103/revmodphys.77.1375
247. **M Hübener, D Tikhonov, I.A. Garifullin, K Westerholt, H Zabel.**
The antiferromagnet/superconductor proximity effect in Cr/V/Cr trilayers.
J. Phys.: Condens. Matter **14**, 8687–8696.
DOI: 10.1088/0953-8984/14/37/305
248. **B.L. Wu, Y.M. Yang, Z.B. Guo, Y.H. Wu, J.J. Qiu.**
Suppression of superconductivity in Nb by IrMn in IrMn/Nb bilayers.
Appl. Phys. Letters **103**, 152602 (2013).
DOI: 10.1063/1.4824891

249. **C. Bell, E.J. Tarte, G. Burnell, C.W. Leung, D.-J. Kang, M.G. Blamire.**
Proximity and Josephson effects in superconductor/antiferromagnetic Nb/ γ -Fe₅₀Mn₅₀ heterostructures.
Physical Review B **68**, 144517 (14 2003).
DOI: 10.1103/physrevb.68.144517


PAPER I

Reference

Eirik Holm Fyhn and Jacob Linder,
Superconducting vortices in half-metals.
Physical Review B **100**, 224508 (2019)
DOI: 10.1103/physrevb.100.224508

CONTRIBUTIONS

EHF performed the analytical calculations and the numerical simulations, with support from JL. EHF drafted the manuscript. JL formulated the initial research goal. EHF and JL contributed to the physics discussions and the final manuscript revision. Specifically, in addition to participating in the discussion of the physics and the revision of the final manuscript, EHF wrote the initial draft, performed all the calculations, developed the code, performed the numerical simulations and produced all figures presented in the paper.

Superconducting vortices in half-metalsEirik Holm Fyhn and Jacob Linder *Center for Quantum Spintronics, Department of Physics, Norwegian University of Science and Technology, NO-7491 Trondheim, Norway*

(Received 9 April 2019; revised manuscript received 2 October 2019; published 10 December 2019)

When the impurity mean free path is short, only spin-polarized Cooper pairs which are nonlocally and antisymmetrically correlated in time may exist in a half-metallic ferromagnet. As a consequence, the half-metal acts as an odd-frequency superconducting condensate. We demonstrate both analytically and numerically that quantum vortices can emerge in half-metals despite the complete absence of conventional superconducting correlations. Because these metals are conducting in only one spin band, we show that a circulating spin supercurrent accompanies these vortices. Moreover, we demonstrate that magnetic disorder at the interfaces with the superconductor influences the position at which the vortices nucleate. This insight can be used to help determine the effective interfacial misalignment angles for the magnetization in hybrid structures since the vortex position is experimentally observable via scanning tunneling microscopy measurements. We also give a brief discussion regarding which superconducting order parameter to use for odd-frequency triplet Cooper pairs in the quasiclassical theory.

DOI: [10.1103/PhysRevB.100.224508](https://doi.org/10.1103/PhysRevB.100.224508)**I. INTRODUCTION**

New physical phenomena can emerge at the interface between materials with different quantum orders. One such example is in systems combining ferromagnetism and superconductivity, where it is possible to generate Cooper pairs that are both spin polarized and correlated nonlocally in time. This has become the basis for the field of superconducting spintronics [1], which has as one of its goals enabling new types of devices utilizing spin-polarized supercurrents [2]. On a more fundamental level, it is of interest to consider the interplay between different types of spontaneous symmetry breaking in such hybrid structures since symmetry breaking governs a wide range of physical phenomena, including mass differences of elementary particles and phase transitions.

Half-metallic ferromagnets are 100% spin polarized, meaning that only one spin band is conducting. Any supercurrent flowing through such a material, as has been observed experimentally [3], is therefore necessarily spin polarized. This makes half-metals especially interesting to study in order to understand how superconductivity adapts to a fully polarized environment. Much experimental and theoretical work was recently conducted in order to understand hybrid structures involving superconductors (S) and half-metals (H) [3–15].

One hitherto unsolved problem is whether superconducting quantum vortices can form in half-metallic materials. This is an unusual physical situation since the electrons are correlated exclusively nonlocally in time such that the half-metal, in fact, mimics a purely odd-frequency [16] superconducting state. Vortices have nonsuperconducting cores and a phase winding of an integer multiple of 2π in the superconducting order parameter, leading to circulating supercurrents [17]. In addition to being interesting from a fundamental physics point of view, understanding the behavior of vortices is useful on a practical level. Their motion is a source of nonzero electrical

resistance [18], and recently, it was proposed that vortices can be used as a means for long-range spin transport [19].

It is known that vortices can form also inside normal metals that are in proximity to a superconductor [20–23]. Cooper pairs can then leak into the normal metal through the process of Andreev reflection [24]. This is the key mechanism behind the proximity effect, which consists of weak superconductivity observed in a material placed in contact with a superconductor.

The proximity effect in half-metals is more complicated because it requires a mechanism which converts the spinless (singlet) Cooper pairs to spin-polarized (triplet) pairs. The theorized mechanism to produce such correlations involves spin mixing and spin-flip scattering at the interface [8]. Spin mixing introduces triplet correlations on the superconducting side, and spin-flip scattering mediates these correlations to the half-metallic side.

What allows us to investigate SH heterostructures in the presence of an external magnetic field is the recent derivation of general spin-active boundary conditions for the quasiclassical theory applied to diffusive systems [9,10]. This means that we can apply the quasiclassical Usadel theory in such a way that the Cooper pair conversion mechanism described above is included.

Here we apply this theory both analytically and numerically to a two-dimensional SHS junction as depicted in Fig. 1 under a constant perpendicular magnetic field. The constant magnetic field will, in general, have contributions both from the uniform magnetization in the half-metal and from a uniform applied field. We find that vortices indeed form in the purely triplet odd-frequency superconducting condensate existing in the half-metallic ferromagnet. Their location depends not only on the superconducting phase difference but also on the effective interfacial magnetization directions characterizing either magnetic disorder or artificially inserted thin ferromagnetic layers [5].

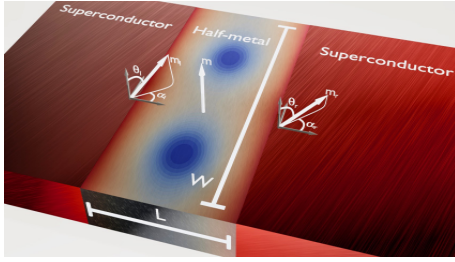


FIG. 1. Sketch of a SHS junction. The half-metal has a uniform magnetization direction \mathbf{m} . The interfaces with the left and right superconductors have effective magnetization directions \mathbf{m}_l and \mathbf{m}_r , respectively. These may come from, for instance, artificially inserted thin ferromagnetic layers or interfacial magnetic disorder. θ_l and θ_r are the associated polar angles, and α_l and α_r are the associated azimuthal angles. L and W are the length and width of the half-metal, respectively. The blue regions show the vortex cores where the DOS equals its normal-state value. Away from the cores, the DOS deviates from its normal-state value due to the superconducting proximity effect.

II. METHODOLOGY

In this section we discuss the quasiclassical Usadel theory and how it may be used to analyze the SHS junction depicted in Fig. 1. We first present the mathematical tools and end with the numerical implementation.

A. Quasiclassical theory

The SHS junction depicted in Fig. 1 can be treated in the quasiclassical formalism under the assumption that the Fermi wavelength is much shorter than all other relevant length scales. This assumption is seemingly broken in the half-metal, where the exchange field is so large that the associated energy is not negligible compared to the Fermi energy [25]. The redemption comes from the realization that the spin splitting in such system is so severe that there is effectively no interaction between different spin bands. We can then continue to use the quasiclassical theory if we, instead of including an exchange field, treat the spin bands as noninteracting. If, in addition, the system is diffusive, meaning that the scattering time is small, the isotropic part of the quasiclassical Green's function dominates and solves the Usadel equation [26–29],

$$D\bar{\nabla} \cdot (\hat{g}\bar{\nabla}\hat{g}) + i[\varepsilon\hat{\rho}_3 + \hat{\Delta}, \hat{g}] = 0. \quad (1)$$

Here D is a diffusion constant, $\hat{\rho}_3 = \text{diag}(1, 1, -1, -1)$, and $\hat{\Delta} = \text{antidiag}(+\Delta, -\Delta, +\Delta^*, -\Delta^*)$, where Δ is the superconducting gap parameter. In the superconductors D is a scalar, while in the half-metal it is $\text{diag}(D, 0)$, assuming that the conducting band is spin up. The covariant derivative is $\bar{\nabla}\hat{g} = \nabla\hat{g} - ie[\hat{\rho}_3\mathbf{A}, \hat{g}]$, where \mathbf{A} is the vector potential and

$$\hat{g} = \begin{pmatrix} \hat{g}^R & \hat{g}^K \\ 0 & \hat{g}^A \end{pmatrix} \quad (2)$$

is the quasiclassical impurity-averaged Green's function. \hat{g} is normalized such that $\hat{g}\hat{g} = 1$. We use the convention that when two matrices of different dimensionalities are multiplied, the

smaller matrix is elevated to the dimensionality of the larger matrix by the tensor product of an identity matrix of the appropriate size. In equilibrium, the components of the 8×8 Green's function in Eq. (2) are related by the identities $\hat{g}^K = (\hat{g}^R - \hat{g}^A) \tanh(\varepsilon\beta/2)$ and $\hat{g}^A = -\hat{\rho}_3\hat{g}^R\hat{\rho}_3$, which means that in this case it is sufficient to solve for the retarded component \hat{g}^R .

The Usadel equation can be made dimensionless by introducing the Thouless energy, $\varepsilon_T := D/L^2$, and measuring length scales relative to L and energies relative to ε_T .

In general, the Usadel equation has to be solved together with the Maxwell equation in a self-consistent manner. However, we are interested here in the case where the width W is smaller than the Josephson penetration depth. In this case one can ignore the screening of the magnetic field by the Josephson currents, and the magnetic field is equal to the external one [30].

To simplify the numerical and analytical calculations we assume that the magnetic field is zero inside the superconductors. This assumption is widely used [20,21] and has been shown to give good agreement with experimental results [31]. Reference [32] found that including the vector potential in the superconductors leads to corrections proportional to λ_s/L , where λ_s is the effective penetration depth in the superconductors and L is the length of the junction. Assuming λ_s/L is small, we neglect the corrections from the vector potential to the Green's function in the superconductors. We use the vector potential $e\mathbf{A} = -n\pi y/W[\theta(x) - \theta(x-L)]\mathbf{e}_x$, where $n = \Phi/\Phi_0$ is the number of flux quanta penetrating the half-metal and \mathbf{e}_x is the unit vector in the x direction.

B. Boundary conditions

The quasiclassical formalism is not applicable across boundaries because the associated length scale is too short. The Usadel equation must therefore be solved in the half-metal and superconductors separately, and the solutions must be connected through boundary conditions. These can be written

$$G_i L_i \mathbf{e}_n \cdot (\hat{g}_i^R \bar{\nabla} \hat{g}_i^R) = \hat{I}(\hat{g}_i^R, \hat{g}_j^R), \quad (3)$$

where \mathbf{e}_n is the outward-pointing normal vector for region i , G_i is the bulk conductance of material i , and L_i is the length of material i in the direction of \mathbf{e}_n . $\hat{I}(\hat{g}_i^R, \hat{g}_j^R)$ is the matrix current from material i to material j .

The matrix current for general spin-active boundaries between diffusive materials was found in 2015 by Eschrig *et al.* [9]. The expression to second order in spin-mixing angles and transmission probabilities was simplified in 2017 by Ouassou *et al.* [10], making them easier to implement and more efficient to compute. This is the expression we will use here, and it reads

$$\begin{aligned} \hat{I} = & \frac{G_0^i}{2} [\hat{g}_i, F(\hat{g}_j)] - \frac{iG_\phi^i}{2} [\hat{g}_i, \hat{m}_i] + \frac{G_2^i}{8} F(\hat{g}_j) \hat{g}_i F(\hat{g}_j) \\ & + \frac{G_{\phi 2}^i}{8} [\hat{g}_i, \hat{m}_i \hat{g}_i \hat{m}_i] + \frac{iG_\chi^i}{8} [\hat{g}_i, F(\hat{g}_j) \hat{g}_i \hat{m}_i + \hat{m}_i \hat{g}_i F(\hat{g}_j)] \\ & + \frac{iG_\chi^j}{8} [\hat{g}_i, F(\hat{g}_j \hat{m}_j \hat{g}_j - \hat{m}_j)], \end{aligned} \quad (4)$$

where, for a half-metallic ferromagnet, $F(\hat{v}) = \hat{v} + \{\hat{v}, \hat{m}\} + \hat{m}\hat{v}\hat{m}$ and $\hat{m}_k = \text{diag}(\mathbf{m}_k \cdot \boldsymbol{\sigma}, \mathbf{m}_k \cdot \boldsymbol{\sigma}^*)$. Here $\boldsymbol{\sigma} = (\sigma_1, \sigma_2, \sigma_3)^\top$ is the vector of Pauli matrices, and \mathbf{m}_k is a unit vector in the direction of the magnetization experienced by a particle being reflected in material k . Similarly, $\hat{m} = \text{diag}(\mathbf{m} \cdot \boldsymbol{\sigma}, \mathbf{m} \cdot \boldsymbol{\sigma}^*)$, where \mathbf{m} is the unit vector in the direction of the magnetization being felt by a particle which is transmitted. The interface conductances are [10]

$$\begin{aligned} G_0^i &= G_q \sum_{n=1}^N T_n^i, & G_\phi^i &= 2G_q \sum_{n=1}^N \phi_n^i, \\ G_2^i &= G_q \sum_{n=1}^N (T_n^i)^2, & G_\chi^i &= G_q \sum_{n=1}^N T_n^i \phi_n^i, \\ G_{\phi 2}^i &= 2G_q \sum_{n=1}^N (\phi_n^i)^2, \end{aligned} \quad (5)$$

where T_n^i and ϕ_n^i are, respectively, the transmission probability and spin mixing angle for tunneling channel n from material i to material j . For boundaries interfacing vacuum at $y = \pm W/2$, the matrix current is $\hat{I} = 0$.

C. Riccati parametrization

In the Riccati parametrization [33] of \hat{g}^R , the parameter is the 2×2 matrix γ and the retarded Green's function is written

$$\hat{g}^R = \begin{pmatrix} N & 0 \\ 0 & -\tilde{N} \end{pmatrix} \begin{pmatrix} 1 + \gamma \tilde{\gamma} & 2\gamma \\ 2\tilde{\gamma} & 1 + \tilde{\gamma} \gamma \end{pmatrix}, \quad (6)$$

where $N := (1 - \gamma \tilde{\gamma})^{-1}$ and tilde conjugation is $\tilde{\gamma}(\varepsilon) = \gamma^*(-\varepsilon)$.

There is only one conducting spin band in a half-metal, and as a result γ has only one nonzero element,

$$\gamma_{\text{HM}} = \begin{pmatrix} a & 0 \\ 0 & 0 \end{pmatrix}. \quad (7)$$

Substituting this into Eq. (1), we find that a solves the equation

$$\nabla^2 a + \frac{2\tilde{a}\nabla a \cdot \nabla a}{1 - a\tilde{a}} = \frac{4(1 + a\tilde{a})eA \cdot (aeA + i\nabla a)}{1 - a\tilde{a}} - 2i\varepsilon a. \quad (8)$$

In Sec. III A we will show that the Green's function in the superconductors can be taken to be the bulk Green's function. Thus, the Riccati parameter can be written as $\gamma_{\text{SC}} = \text{antidiag}(b, -b)$, where b is a function of ε and the superconducting gap parameter Δ . Inserting this and Eqs. (4) and (7) into Eq. (3), we get

$$\begin{aligned} G_{\text{HM}} \mathbf{e}_n \cdot \nabla a &= 4G_0^{\text{HM}} B C a - G_2^{\text{HM}} B^2 C^2 a (a\tilde{a} + 3) \\ &+ 2iG_\chi^{\text{SC}} B C^2 \sin \theta (b e^{-i\alpha} - \tilde{b} e^{i\alpha} a^2) \\ &+ 2iG_{\text{HM}} a \mathbf{e}_n \cdot A \mathbf{e}, \end{aligned} \quad (9)$$

where $B = b\tilde{b} - 1$, $C = 1/(1 + b\tilde{b})$, and θ and α are the angles for the magnetization directions on the superconducting side, as shown in Fig. 1. The corresponding equations for \tilde{a} and $\mathbf{e}_n \cdot \nabla \tilde{a}$ are found by tilde conjugating Eqs. (8) and (9).

From Eq. (9) it can be seen that in order to have a nonzero solution for a it is necessary that either $\sin \theta_l \neq 0$ or

$\sin \theta_r \neq 0$. This means that having the effective magnetization angles at the interface not parallel to the uniform magnetization of the half-metal is necessary for the occurrence of superconducting triplet correlations in the half-metal. This is because the creation of a long-range spin triplet requires spin mixing and spin rotation [1,8]. When spin-singlet Cooper pairs in a superconductors encounter an interface with effective magnetization direction \mathbf{m}_l , the spin-active boundary will produce spin triplets with zero spin along \mathbf{m}_l . If \mathbf{m}_l is not parallel to the magnetization of the half-metal \mathbf{m} , then the triplet with zero spin along \mathbf{m}_l will have a nonzero projection onto the spin-triplet state with spin 1 along \mathbf{m} . Hence, if the interfacial magnetization angles are not parallel to \mathbf{m} , the spin-active boundaries will produce equal spin triplets.

D. Observables

As mentioned initially, a vortex is accompanied by a normal-state density of states and a circulating supercurrent. This can be extracted from the quasiclassical Green's function. In the following it will be useful to write

$$\hat{g}^R = \begin{pmatrix} g & f \\ -\tilde{f} & -\tilde{g} \end{pmatrix}. \quad (10)$$

In the half-metal, f has only one nonzero component, f_\uparrow .

1. Local density of states

The local density of states for spin band σ at energy ε and location \mathbf{r} can be written

$$N_0(\varepsilon, \mathbf{r}) = N_0 \text{Re}\{g_{\sigma\sigma}(\varepsilon, \mathbf{r})\}, \quad (11)$$

where N_0 is the normal-state density of states at the Fermi surface. In the half-metal we can write Eq. (11) in terms of a ,

$$N(\varepsilon, \mathbf{r}) := N_\uparrow(\varepsilon, \mathbf{r}) = N_0 \frac{1 + a\tilde{a}}{1 - a\tilde{a}}. \quad (12)$$

2. Supercurrent

Written in terms of the quasiclassical Green's function, the current density is [26]

$$\mathbf{j} = \frac{N_0 e D}{4} \int_{-\infty}^{\infty} \text{Tr}(\hat{\rho}_3 [\hat{g} \tilde{\nabla} \hat{g}]^K) d\varepsilon. \quad (13)$$

Inserting Eq. (10), using the relations $\hat{g}^\Lambda = -\hat{\rho}_3 \hat{g}^{R\Lambda} \hat{\rho}_3$, $\hat{g}^K = (\hat{g}^R - \hat{g}^\Lambda) \tanh(\varepsilon\beta/2)$, Eq. (13) can be rewritten

$$\begin{aligned} \mathbf{j} &= \frac{N_0 e D}{2} \int_{-\infty}^{\infty} \tanh\left(\frac{\beta\varepsilon}{2}\right) \text{Tr}(\text{Re}[\tilde{f}^\dagger \nabla f^\dagger - f \nabla \tilde{f}]) \\ &+ 2eA \text{Im}[f \tilde{f} - \tilde{f}^\dagger f^\dagger] d\varepsilon. \end{aligned} \quad (14)$$

The spin current can be found by multiplying the matrix in the integrand of Eq. (13) by the Pauli matrix corresponding to the appropriate spin direction before taking the trace. For a half-metal magnetized in the z direction, the z component of the spin supercurrent polarization is proportional to the electric current while the remaining spin current components vanish.

3. Cooper pair correlation function

The study of vortices in diffusive half-metals naturally raises the question of how to define the superconducting order parameter. In a normal superconductor, the order parameter is $\langle \psi_\uparrow(\mathbf{r}, 0)\psi_\downarrow(\mathbf{r}, 0) \rangle$, where $\psi_\sigma(\mathbf{r}, t)$ is the field operator which destroys an electron with spin σ at position \mathbf{r} and time t . The same order parameter is used in a normal metal, but the analogous quantity for the half-metal, $\langle \psi_\uparrow(\mathbf{r}, 0)\psi_\uparrow(\mathbf{r}, 0) \rangle$, is always zero because of the Pauli exclusion principle. That is, the Cooper pair correlation function in a diffusive half-metal must vanish at equal times and is thus temporally nonlocal [16].

One approach of defining an order parameter in odd-frequency superconducting condensates, which is often used in the Bogoliubov–de Gennes formalism [34], is to keep the relative time coordinate t finite between the field operators, that is,

$$\begin{aligned} \Psi_1(\mathbf{r}, t) &:= \langle \psi_\uparrow(\mathbf{r}, t)\psi_\uparrow(\mathbf{r}, 0) \rangle \\ &= \frac{-iN_0}{2} \int_{-\infty}^{\infty} f_\uparrow(\mathbf{r}, \varepsilon) \tanh(\varepsilon\beta/2) \sin(\varepsilon t) d\varepsilon. \end{aligned} \quad (15)$$

Another frequently used strategy [35] is to make the order parameter even in time by differentiation. This yields

$$\Psi_2(\mathbf{r}) := \left. \frac{\partial \Psi_1}{\partial t} \right|_{t=0} = \frac{-iN_0}{2} \int_{-\infty}^{\infty} \varepsilon f_\uparrow(\mathbf{r}, \varepsilon) \tanh(\varepsilon\beta/2) d\varepsilon. \quad (16)$$

Below, we shall compare these two possible choices for the order parameter describing the odd-frequency superconducting condensate to see which of them correctly captures the vortex behavior.

E. Numerics

The Usadel equation was solved numerically using a finite-element scheme. See, for instance, [36] to see how to set up and solve the nonlinear Usadel equations in a finite-element scheme using the Newton-Raphson method. The program was written in JULIA [37], we used quadratic quadrilateral elements, and JUAPEM.JL [38] was used to iterate through the cells. Gauss-Legendre quadrature rules of the fourth order were used to integrate through the cells, and Romberg integration was used to integrate over energy. See, for instance, [39]. Finally, forward-mode automatic differentiation [40] was used to calculate the Jacobian.

III. RESULTS AND DISCUSSION

Here we present first an analytical solution of the Usadel equation in the weak proximity effect regime; then we show numerically that the findings are present also in the full proximity effect regime. Dimensionless quantities are used in the analytics, with length being measured relative to the length of the half-metal L and energies being measured relative to the Thouless energy $\varepsilon_T = D/L^2$, where D is the diffusion constant in the half-metal.

A. Analytics

In order to justify Eq. (9) we will show that it suffices to use the bulk solution

$$\hat{g}_{\text{BCS}} = \left[\frac{\theta(\varepsilon^2 - |\Delta|^2)}{\sqrt{\varepsilon^2 - |\Delta|^2}} \text{sgn}(\varepsilon) - \frac{\theta(|\Delta|^2 - \varepsilon^2)}{\sqrt{|\Delta|^2 - \varepsilon^2}} i \right] (\varepsilon \hat{\rho}_3 + \hat{\Delta}) \quad (17)$$

in the superconductors when a certain condition is fulfilled. Let λ (to be defined quantitatively below) be the length scale over which the Green's function recovers its bulk value in the superconductor. The criterion for neglecting the inverse proximity effect in the superconductors is then that the normal-state conductance of the superconductors for a sample of length λ is much larger than the interface conductance and that the length of each superconductor is not small compared to λ . We now proceed to prove this.

First, let

$$\hat{g} = \hat{g}_{\text{BCS}} + \delta\hat{g} \quad (18)$$

be the solution of the dimensionful Usadel equation,

$$D_{\text{sc}} \nabla \cdot (\hat{g} \nabla \hat{g}) + i[\varepsilon \hat{\rho}_3 + \hat{\Delta}, \hat{g}] = 0, \quad (19)$$

in the superconductor at $x < 0$. This gives an equation for $\delta\hat{g}$,

$$D_{\text{sc}} \nabla \cdot ([\hat{g}_{\text{BCS}} + \delta\hat{g}] \nabla \delta\hat{g}) + i[\varepsilon \hat{\rho}_3 + \hat{\Delta}, \delta\hat{g}] = 0, \quad (20)$$

where we have used the fact that \hat{g}_{BCS} solves the Eq. (19) for a bulk superconductor and assumed that the variations of the gap parameter from the bulk value are negligible. Next, we assume the inverse proximity effect to be weak, such that $\delta\hat{g} \ll \hat{g}_{\text{BCS}}$. Using $\hat{g}_{\text{BCS}} \hat{g}_{\text{BCS}} = 1$, this yields

$$D_{\text{sc}} \nabla^2 \delta\hat{g} + i\hat{g}_{\text{BCS}} [\varepsilon \hat{\rho}_3 + \hat{\Delta}, \delta\hat{g}] = 0. \quad (21)$$

$\hat{g}_{\text{BCS}} + \delta\hat{g}$ must also satisfy the normalization condition $\hat{g}^2 = 1$, so

$$(\hat{g}_{\text{BCS}} + \delta\hat{g})^2 = 1 \Rightarrow \{\hat{g}_{\text{BCS}}, \delta\hat{g}\} = 0. \quad (22)$$

Hence, using $[\varepsilon \hat{\rho}_3 + \hat{\Delta}, \hat{g}_{\text{BCS}}] = 0$,

$$\begin{aligned} \hat{g}_{\text{BCS}} [\varepsilon \hat{\rho}_3 + \hat{\Delta}, \delta\hat{g}] &= (\varepsilon \hat{\rho}_3 + \hat{\Delta}) \hat{g}_{\text{BCS}} \delta\hat{g} + \delta\hat{g} (\varepsilon \hat{\rho}_3 + \hat{\Delta}) \hat{g}_{\text{BCS}} \\ &= \{\delta\hat{g}, (\varepsilon \hat{\rho}_3 + \hat{\Delta}) \hat{g}_{\text{BCS}}\}. \end{aligned} \quad (23)$$

Finally, from

$$(\varepsilon \hat{\rho}_3 + \hat{\Delta})^2 = \varepsilon^2 - \Delta^2 \quad (24)$$

we find that $\delta\hat{g}$ is an eigenfunction of the Laplacian,

$$\nabla^2 \delta\hat{g} = \lambda^{-2} \delta\hat{g}, \quad (25)$$

where

$$\begin{aligned} \lambda^{-2} &= -\frac{2i}{D_{\text{sc}}} [\text{sgn}(\varepsilon) \sqrt{\varepsilon^2 - |\Delta|^2} \theta(\varepsilon^2 - |\Delta|^2) \\ &\quad + i\sqrt{|\Delta|^2 - \varepsilon^2} \theta(|\Delta|^2 - \varepsilon^2)]. \end{aligned} \quad (26)$$

We can choose the sign of λ to be such that $\text{Re}(\lambda) > 0$.

Using the boundary condition

$$\nabla \delta\hat{g}|_{r \in \Omega} = 0, \quad (27)$$

where Ω is the boundary not interfacing with the half-metal, we get

$$\delta\hat{g}(\varepsilon, x, y) = C[e^{-|x|/\lambda} + e^{(|x|-2L_{SC})/\lambda}], \quad (28)$$

where C is some function of y and ε to be determined by the final boundary condition. If the matrix current across this boundary is \hat{I}_{SC} , then

$$C = \frac{\hat{g}_{BCS}\hat{I}_{SC}}{(1 - e^{-2L_{SC}/\lambda})G_{SC}L_{SC}/\lambda}. \quad (29)$$

From Eq. (28) we see that $\text{Re}(\lambda)$ can be interpreted as the penetration depth of δg . Note that $\text{Re}(\lambda)$ is bounded by including the effect of inelastic scattering, which is done by the substitution $\varepsilon \rightarrow \varepsilon + i\delta$ for some positive scattering rate δ [41]. This ensures that $1/(1 - e^{-2L_{SC}/\lambda})$ remains finite as $\varepsilon \rightarrow \Delta$. From the definition of λ in Eq. (26) we see that $\text{Re}(\lambda) = \lambda$ when $\varepsilon < |\Delta|$ and $\text{Re}(\lambda) = |\lambda|/\sqrt{2}$ otherwise.

G_{SC} is the conductance over the whole length L_{SC} of the superconductor and is therefore proportional to $1/L_{SC}$. Hence, $G_{SC}L_{SC}/\text{Re}(\lambda)$ is the normal-state conductance of a superconductor of length $\text{Re}(\lambda)$. From the definition of \hat{I} in Eq. (4) we see that C , and therefore δg , becomes negligible when

$$\frac{\max(G_0^{SC}, G_\phi^{SC}, G_2^{SC}, G_{\phi_2}^{SC}, G_\chi^{SC}, G_\chi^{HM})}{G_{SC}L_{SC}/\text{Re}(\lambda)} \ll 1, \quad (30)$$

provided that the length of the superconductor L_{SC} is not small compared to the maximal penetration depth $\max[\text{Re}(\lambda)]$. A similar calculation shows that we can use \hat{g}_{BCS} also in the superconductor at $x > L$.

Taking the superconducting coherence length ξ as a measure of the inverse proximity effect penetration depth $\text{Re}(\lambda)$, we see that the criterion (30) is indeed experimentally feasible. The equation is fulfilled for a low-transparency interface and for a superconductor that is larger than the coherence length.

Next, we turn to the solution of the Usadel equation in the half-metal, Eq. (8), together with the boundary condition (9). In order to solve these equations we must make some simplifying assumptions. If we assume the proximity is weak, we can keep only terms which are linear in a and \tilde{a} and their gradients. In this case the dimensionless Usadel equation (8) decouples:

$$\nabla^2 a = 4A \cdot (aA + i\nabla a) - 2i\varepsilon a, \quad (31a)$$

$$\nabla^2 \tilde{a} = 4A \cdot (\tilde{a}A - i\nabla \tilde{a}) - 2i\varepsilon \tilde{a}. \quad (31b)$$

and so do the boundary conditions,

$$e_n \cdot \nabla a = \left\{ 4 \frac{G_0^{HM}}{G^{HM}} BC - 3 \frac{G_2^{HM}}{G^{HM}} B^2 C^2 + 2ie_n \cdot Ae \right\} a + 2i \frac{G_\chi^{SC}}{G^{HM}} BC^2 |b| \sin \theta e^{i(\phi - \alpha)}, \quad (32a)$$

$$e_n \cdot \nabla \tilde{a} = \left\{ 4 \frac{G_0^{HM}}{G^{HM}} BC - 3 \frac{G_2^{HM}}{G^{HM}} B^2 C^2 - 2ie_n \cdot Ae \right\} \tilde{a} - 2i \frac{G_\chi^{SC}}{G^{HM}} BC^2 |\tilde{b}| \sin \theta e^{-i(\phi - \alpha)}. \quad (32b)$$

Equation (31) can be further simplified in the so-called wide junction limit, where $n/W \ll 1$. If $A = 0$, the solution of Eq. (31) is constant in the y direction. Assuming this is

approximately true also for small A , we neglect the term $\partial_y^2 a$. Equation (31) can now be solved exactly, as it is a second-order ordinary differential equation with constant coefficients. The solution of Eq. (31a) is

$$a = C_1 e^{(u+k)x} + C_2 e^{(u-k)x}, \quad (33)$$

where $u = -2\pi i n y / W$, $k = \sqrt{-2i\varepsilon}$, and C_1 and C_2 are independent of x .

Determining C_1 and C_2 requires the boundary conditions, which can be written

$$\left. \frac{\partial a}{\partial x} \right|_{x=0} = -c \sin \theta_l e^{i(\phi_l - \alpha_l)} - (d - u)a, \quad (34a)$$

$$\left. \frac{\partial a}{\partial x} \right|_{x=1} = c \sin \theta_r e^{i(\phi_r - \alpha_r)} + (d + u)a, \quad (34b)$$

where

$$c = 2i \frac{G_\chi^{SC}}{G^{HM}} BC^2 |b|, \quad d = 4 \frac{G_0^{HM}}{G^{HM}} BC - 3 \frac{G_2^{HM}}{G^{HM}} B^2 C^2. \quad (35)$$

After some algebra, we find that the solution can be written

$$a = \frac{c e^{i(\phi_l - \alpha_l) + u x}}{(k - d)^2 e^k - (k + d)^2 e^{-k}} \{ (k - d) (\sin \theta_l e^{-k(1-x)} + \sin \theta_r e^{i\delta\phi - u} e^{-kx}) + (k + d) (\sin \theta_l e^{k(1-x)} + \sin \theta_r e^{i\delta\phi - u} e^{kx}) \}, \quad (36)$$

where

$$\delta\phi = \phi_r - \alpha_r - \phi_l + \alpha_l. \quad (37)$$

Note that the wide junction approximation is not applicable at small energies. This is because the solution will be slowly varying in the x direction, and therefore, $\partial_x^2 a$ is no longer negligible compared to $\partial_x^2 a$.

When $\sin \theta_l = \sin \theta_r$, a vanishes at $x = 1/2$, and

$$\frac{y}{W} = \frac{1}{n} \left(\frac{1}{2} + N - \frac{\phi_r - \alpha_r - \phi_l + \alpha_l}{2\pi} \right), \quad (38)$$

where N is any integer. This means that f_\uparrow and hence also the order parameters Ψ_1 and Ψ_2 vanish at these points. From Eq. (12) we see that the density of states is equal to the normal-state density of states at these points, indicating that these are indeed vortices. By Taylor expanding a to first order around a root located at $(1/2, \bar{y})$ we find

$$a \sim B_1 \cos(\theta + \alpha_1) + iB_2 \cos(\theta + \alpha_2), \quad (39)$$

where $x - 1/2 \sim \cos \theta$ and $y - \bar{y} \sim \sin \theta$, $B_1^2 = 5|k|^2/4 - |k|d + 2d^2$, $B_2^2 = |k|^2/4 + d^2$, $\alpha_1 = \tan^{-1}[(|k|/2 + d)/(|k| - d)]$, and $\alpha_2 = \tan^{-1}(|k|/2d)$. Hence, these roots have a phase winding of 2π , which is characteristic for vortices. These approximately n roots are the only ones for Ψ_2 , but for Ψ_1 there are relative times t for which additional roots exist. Since each vortex is associated with a quantum of magnetic flux Φ_0 , there should be, at most, n vortices when the flux is $n\Phi_0$. This suggests that Ψ_1 is less suited for finding vortices than Ψ_2 if we identify vortices by the roots of the order parameter. Using Ψ_2 suggests that when $\sin \theta_l = \sin \theta_r$ and the magnetic flux is $n\Phi_0$, there will, in the wide-junction limit, be n vortices whose location is determined by the difference in the superconducting phases and the magnetization angles.

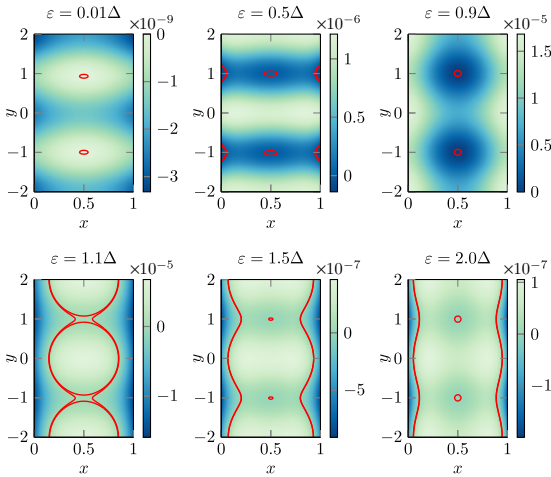


FIG. 2. The normalized difference between the local density of states and the normal-state density of states, $(N - N_0)/N_0$, for various energies. Red contour lines are added at $\pm 0.01 \times S$, where S is the number at the top of the respective color bars. Here $n = 2$, $\phi_r = \alpha_r = 0$, and $\sin \theta_r = 1$.

The situation is more complicated when $\sin \theta_l \neq \sin \theta_r$. In this case the roots of Eq. (36) depend on ε , and we will leave the discussion for how this affects the order parameter of the numerical investigation. However, some insight can still be had from the analysis. Scaling $\sin \theta$ in the boundary condition (32) is equivalent to scaling the conductance G_χ^{SC} . That is, if $\sin \theta_r < \sin \theta_l$, the proximity effect should be weaker on the right side, meaning that the vortices should be pushed to the right. This is indeed what we find numerically.

B. Numerics

We now proceed to show numerical results in the full (non-linear) proximity effect regime. We have set the parameters $|\Delta| = 4\varepsilon_T$, $G_{\text{HM}} = 3G_0^{\text{HM}}$, $G_\chi^{\text{SC}} = 0.01G_0^{\text{HM}}$, $G_2^{\text{HM}} = 0.002G_0^{\text{HM}}$, and $\phi_l = \alpha_l = 0$ common for all the numerical calculations. We obtain qualitatively similar results for other choices of the conductance parameters $G_i^{\text{HM/SC}}$. We include the effect of inelastic scattering by doing the substitution $\varepsilon \rightarrow \varepsilon + i\delta$, where $\delta = 0.001|\Delta|$ in order to avoid the divergence of \hat{g}_{BCS} at $\varepsilon = |\Delta|$ [41].

1. Local density of states

In the symmetric case ($\sin \theta_r = 1.0$), we suspect from the analysis above that for all energies, the local density of states is equal to that of the normal state in n points along the line $x = 0.5$, where n is the number of magnetic flux quanta. This is also what we find numerically, as shown in Fig. 2. Figure 2 shows the local density of states at various energies for the symmetric case with $n = 2$, with red lines close to where it is equal to the normal-state density of states. We see that there are indeed two locations where the difference between the local density of states and the normal-state density of states vanishes for all energies and that the locations of these points are exactly those predicted by the analysis.

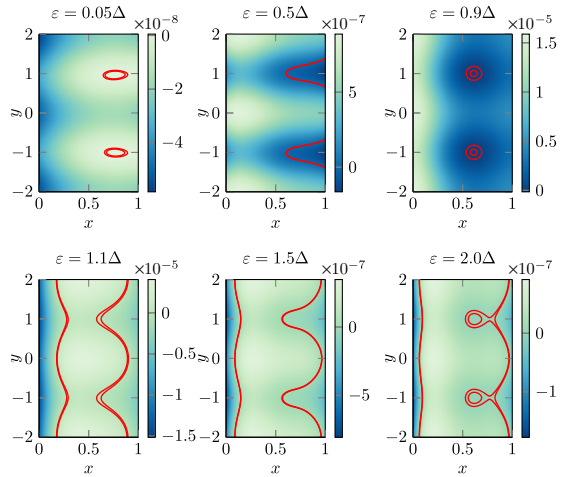


FIG. 3. The normalized difference between the local density of states and the normal-state density of states, $(N - N_0)/N_0$, for various energies. Red contour lines are added at $\pm 0.01 \times S$, where S is the number at the top of the respective color bars. Here $n = 2$, $\phi_r = \alpha_r = 0$, and $\sin \theta_r = 0.5$.

The situation is slightly different for the asymmetric case ($\sin \theta_r \neq 1$), as can be seen in Fig. 3. There is no longer a single point where $N = N_0$ for all energies. Instead, there are points where N is equal to or almost equal to N_0 for all energies, as can be seen in Fig. 3. In Secs. III B 2 and III B 3 we will see that these points also are associated with vortices. Qualitatively, the points where N stays close to N_0 are different in the asymmetric case. In the symmetric case the points at $x = 1/2$ are mostly isolated, but in the asymmetric case the point is part of a line where $N = N_0$ which stretches towards the side where $\sin \theta$ is smaller. For $n = 2$, as can be seen in Fig. 3, the location where N is close to or equal to N_0 for all energies occurs at $y = \pm W/4$, which is also the y values where the vortices are in the symmetric case.

Note that the energy dependence on the position where $N = N_0$ is not unique for the special case of a SHS junction. The same phenomenon occurs in superconductor-normal metal-superconductor junctions if the conductances at the interfaces are unequal. As mentioned above, changing $\sin \theta$ is the same as changing the conductance G_χ^{SC} .

2. Supercurrent

Figure 4 shows the current amplitude and direction for the same two cases that were discussed in Sec. III B 1. In both cases there are exactly two points where the supercurrents vanish and where the supercurrent circles around. This indicates the existence of two superconducting vortices, which is in accordance with the analysis, local density of states, and the fact that the system experiences two quanta of magnetic flux. We underline that the supercurrents accompanying the vortices induced in the half-metal are fully spin polarized and carried by triplet Cooper pairs. This is different from the nonpolarized charge supercurrents circulating vortices in previously studied hybrid structures [20–22].

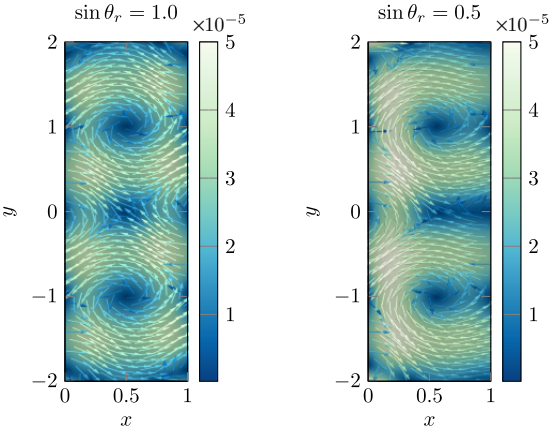


FIG. 4. Amplitude and direction of the fully spin polarized supercurrent \mathbf{j} for the symmetric case ($\sin \theta_r = 1$) and the asymmetric case ($\sin \theta_r \neq 1$). Here $n = 2$, and $\phi_r = \alpha_r = 0$. The values are given for the dimensionless supercurrent $\mathbf{j} \times (L/N_0 e D \varepsilon_T)$.

The y value of the points with circulating supercurrents is the same as what is expected from the analysis, given by Eq. (38). In the symmetric case these points are midway between the superconductors, i.e., at $x = L/2$, while in the asymmetric case they are moved slightly toward the side where $\sin \theta$ is smaller. Hence, the vortex locations as given by the supercurrents agree with the analysis as well as the results from the local density of states.

One feature of the asymmetric case worth noting is that the supercurrent is suppressed to the right of the vortex, which is towards the side where $\sin \theta$ is smaller. This is in agreement with the fact that this region had a local density of states which was closer to the normal-state value, as shown in Sec. III B 1.

3. Cooper pair correlation function

Investigating vortices in odd-frequency superconductors gives rise to the problem of choosing what order parameter to use. The Cooper pair correlation function which is normally used is not applicable as it is identically equal to zero. The two most obvious remaining choices are

$$\Psi_1(\mathbf{r}, t) := \langle \psi_\uparrow(\mathbf{r}, t) \psi_\uparrow(\mathbf{r}, 0) \rangle \quad (40)$$

and

$$\Psi_2(\mathbf{r}) := \left. \frac{\partial \langle \psi_\uparrow(\mathbf{r}, t) \psi_\uparrow(\mathbf{r}, 0) \rangle}{\partial t} \right|_{t=0}, \quad (41)$$

as mentioned above. From looking at the local density of states and the supercurrent we already know that we expect vortices and that their location should have a y value given by Eq. (38) and should be at $x = L/2$ in the symmetric case and closer to the side where $\sin \theta$ is smaller in the asymmetric case. Comparing the position of the roots of Ψ_1 and Ψ_2 with the position of the vortices, as predicted by the local density of states and the supercurrent, can be used to give an indication of how good the order parameters are as means to find vortices.

Figures 5 and 6 show Ψ_1 with various values of t for the same two cases that were shown in Secs. III B 1 and III B 2.

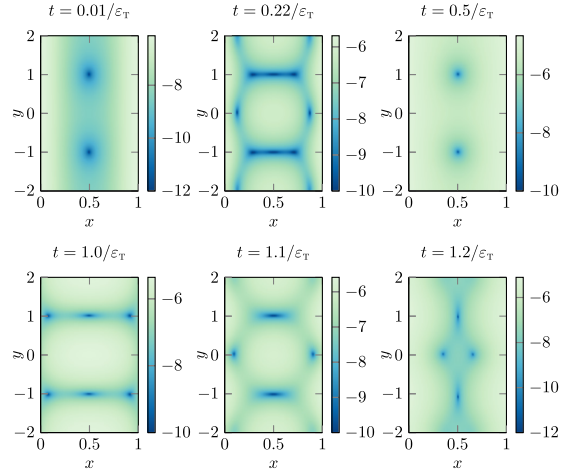


FIG. 5. Plots of $\ln[|\Psi_1(\mathbf{r}, t)| \times 2/N_0 \varepsilon_T]$ for various values of t in the symmetric case ($\sin \theta_r = 1$) with $n = 2$ and $\phi_r = \alpha_r = 0$.

Figure 5 shows the symmetric case with $n = 2$, $\phi_r = \alpha_r = 0$, and $\sin \theta_r = 1$, while Fig. 6 shows the asymmetric case with $n = 2$, $\phi_r = \alpha_r = 0$, and $\sin \theta_r = 0.5$. $\Psi_2(\mathbf{r})$ looks identical to $\Psi_1(\mathbf{r}, 0.01/\varepsilon_T)$, which is shown in the figures, but is a factor of 100 larger in magnitude. Ψ_2 is therefore not shown. In both cases, there are exactly two roots in Ψ_2 and Ψ_1 for small t , and the positions are the same as those given for the vortices by the local density of states and supercurrent. Around these two roots are a phase winding of 2π .

For larger values of t , $\Psi_1(\mathbf{r}, t)$ seems to be less suited for finding vortices. In the symmetric case there are additional roots which appear. These additional roots also have a corresponding phase winding of 2π but do not correspond to vortices when compared to the local density of states or supercurrent. The situation is even worse for large t in the asymmetric case. In addition to having extra roots, the original

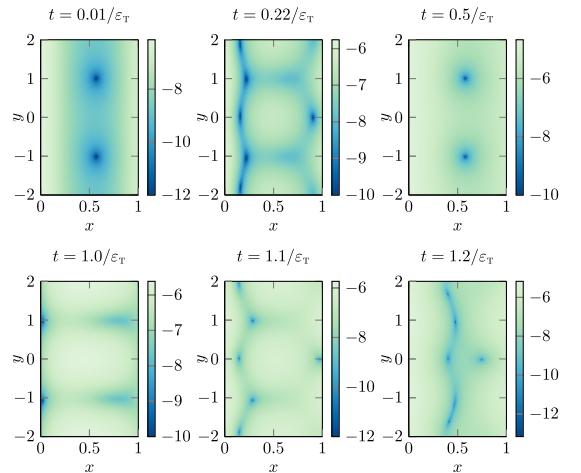


FIG. 6. Plots of $\ln[|\Psi_1(\mathbf{r}, t)| \times 2/N_0 \varepsilon_T]$ for various values of t in the asymmetric case ($\sin \theta_r = 0.5$) with $n = 2$ and $\phi_r = \alpha_r = 0$.

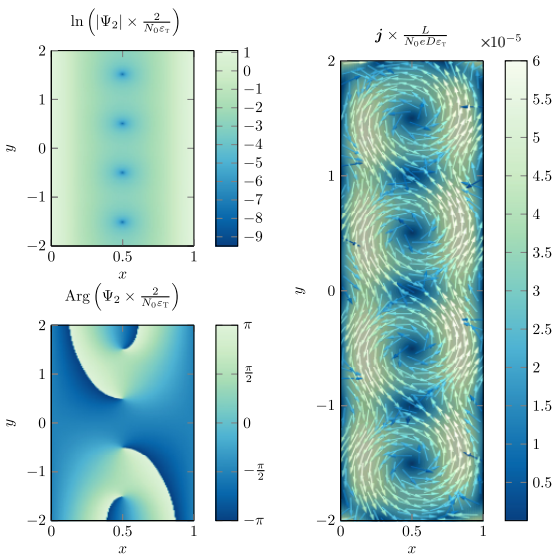


FIG. 7. Amplitude and phase of the order parameter Ψ_2 and amplitude and direction of the fully spin polarized supercurrent \mathbf{j} . Here $n = 4$, $\phi_r = \alpha_r = 0$, and $\sin \theta_r = 1$.

roots which correspond to vortices are either moved or not present. This is also the case for other choices of n , ϕ_r , α_r , and $\sin \theta_r$.

Thus, we conclude that using Ψ_2 seems best suited as an order parameter for the numerical investigation of quantum vortices in a purely odd frequency superconducting condensate. Alternatively, one could use Ψ_1 with $\epsilon_T t \ll 1$, which will give the same result since $\Psi_1 \sim \Psi_2 t$ as $t \rightarrow 0$.

Figures 7 and 8 show the phase of Ψ_2 , in addition to the supercurrent and amplitude of Ψ_2 , for a magnetic flux of $4\Phi_0$ and with $\sin \theta_r = 1$, $\phi_r = \alpha_r = 0$ and $\sin \theta_r = 0.5$, $\phi_r - \alpha_r = \pi/2$, respectively. Note that there is indeed a phase winding of 2π around the vortices, as mentioned above.

4. Vortex position

So far we have looked only at the case with $\phi_r = \alpha_r = 0$. Choosing a nonzero value for $\phi_r - \alpha_r$ moves the vortices along the y axis, and the locations correspond to those predicted by the analysis and given in Eq. (38). Figures 7 and 8 show the amplitude and phase of Ψ_2 as well as the supercurrent \mathbf{j} for a wide junction subjected to a magnetic flux of $4\Phi_0$, with $\sin \theta_r = 1$, $\phi_r - \alpha_r = 0$ and $\sin \theta_r = 0.5$, $\phi_r - \alpha_r = \pi/2$, respectively. In Fig. 8 the vortices are shifted $W/16$ down along the y axis, which is exactly what is predicted by Eq. (38). Note also that the vortices are moved towards the side where $\sin \theta$ is smaller in Fig. 8.

The dependence of the vortex position on both α and θ suggests an experimental method to determine the effective magnetization angles describing disorder in the form of interfacial misaligned moments or artificially inserted misaligned magnetic layers in half-metallic hybrid structures. For a fixed value of the magnetic flux and phase difference $\phi_r - \phi_l$ (which is tunable by the applied current), the y coordinates of the vortices give information about the azimuthal angles

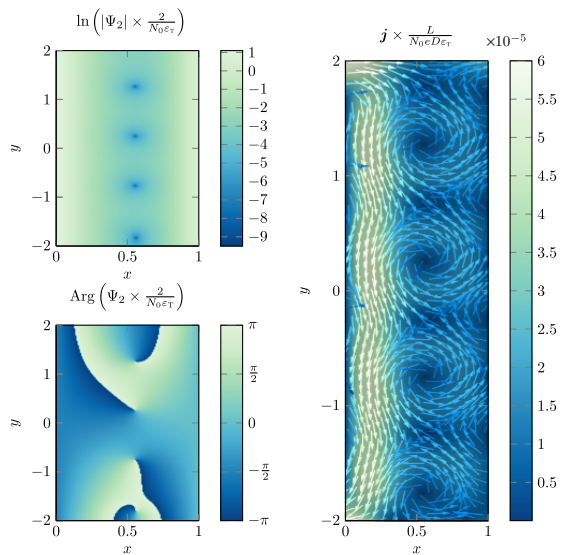


FIG. 8. Amplitude and phase of the order parameter Ψ_2 and amplitude and direction of the fully spin polarized supercurrent \mathbf{j} . Here $n = 4$, $\phi_r - \alpha_r = \pi/2$, and $\sin \theta_r = 0.5$.

α_l and α_r , while the x coordinates give information about the polar angles θ_l and θ_r . This approach could possibly be easier than trying to measure the magnetization angles directly, especially if the noncollinear magnetization angle at the interface is produced by the natural misalignment of magnetic dipoles arising from the conjunction of different atomic structures at the interface.

IV. CONCLUSION

Using the quasiclassical Usadel theory, we have found both analytically and numerically that superconducting vortices occur also in purely odd frequency superconducting condensates that exist in proximized half-metallic ferromagnets. Because half-metals have only one conducting spin band, the vortex cores are circulated by fully polarized spin supercurrents. An additional feature of vortex structures in half-metals compared to a normal metal is that the vortex position depends on the magnetization angles. We suggest that this insight can be used to help determine these angles in hybrid structures.

The study of vortices in odd-frequency superconducting condensates naturally raises the question of how to define the superconducting order parameter. Comparing the roots of the superconducting order parameter to the location vortices, we have found that the order parameter that works best is that which is made even in time by differentiation, $\frac{\partial}{\partial t} \langle \psi_\uparrow(\vec{r}, t) \psi_\uparrow(\vec{r}, 0) \rangle|_{t=0}$.

ACKNOWLEDGMENTS

We thank M. Amundsen for helpful discussions. This work was supported by the Research Council of Norway through Grant No. 240806 and its Centres of Excellence funding scheme Grant No. 262633 ‘‘QuSpin’’

- [1] J. Linder and J. W. A. Robinson, *Nat. Phys.* **11**, 307 (2015).
- [2] M. Eschrig, *Rep. Prog. Phys.* **78**, 104501 (2015).
- [3] R. S. Keizer, S. T. B. Goennenwein, T. M. Klapwijk, G. Miao, G. Xiao, and A. Gupta, *Nature (London)* **439**, 825 (2006).
- [4] Y. Kalcheim, O. Millo, M. Egilmez, J. W. A. Robinson, and M. G. Blamire, *Phys. Rev. B* **85**, 104504 (2012).
- [5] A. Singh, S. Voltan, K. Lahabi, and J. Aarts, *Phys. Rev. X* **5**, 021019 (2015).
- [6] V. Peña, Z. Sefrioui, D. Arias, C. Leon, J. Santamaria, M. Varela, S. J. Pennycook, and J. L. Martinez, *Phys. Rev. B* **69**, 224502 (2004).
- [7] M. Eschrig, T. Löfwander, T. Champel, J. C. Cuevas, J. Kopu, and G. Schön, *J. Low Temp. Phys.* **147**, 457 (2007).
- [8] M. Eschrig, J. Kopu, J. C. Cuevas, and G. Schön, *Phys. Rev. Lett.* **90**, 137003 (2003).
- [9] M. Eschrig, A. Cottet, W. Belzig, and J. Linder, *New J. Phys.* **17**, 83037 (2015).
- [10] J. A. Ouassou, A. Pal, M. Blamire, M. Eschrig, and J. Linder, *Sci. Rep.* **7**, 1932 (2017).
- [11] H. P. Dahal, E. Abrahams, D. Mozyrsky, Y. Tanaka, and A. V. Balatsky, *New J. Phys.* **11**, 65005 (2009).
- [12] C.-T. Wu and K. Halterman, *Phys. Rev. B* **98**, 054518 (2018).
- [13] S. Mironov and A. Buzdin, *Phys. Rev. B* **92**, 184506 (2015).
- [14] M. S. Anwar, F. Czeschka, M. Hesselberth, M. Porcu, and J. Aarts, *Phys. Rev. B* **82**, 100501(R) (2010).
- [15] Y. Asano, Y. Sawa, Y. Tanaka, and A. A. Golubov, *Phys. Rev. B* **76**, 224525 (2007).
- [16] J. Linder and A. V. Balatsky, [arXiv:1709.03986](https://arxiv.org/abs/1709.03986) [Rev. Mod. Phys. (to be published)].
- [17] W. K. Kwok, U. Welp, A. Glatz, A. E. Koshelev, K. J. Kihlstrom, and G. W. Crabtree, *Rep. Prog. Phys.* **79**, 116501 (2016).
- [18] B. I. Halperin, G. Refael, and E. Demler, *Int. J. Mod. Phys. B* **24**, 4039 (2010).
- [19] S. K. Kim, R. Myers, and Y. Tserkovnyak, *Phys. Rev. Lett.* **121**, 187203 (2018).
- [20] J. C. Cuevas and F. S. Bergeret, *Phys. Rev. Lett.* **99**, 217002 (2007).
- [21] F. S. Bergeret and J. C. Cuevas, *J. Low Temp. Phys.* **153**, 304 (2008).
- [22] M. Amundsen, J. A. Ouassou, and J. Linder, *Phys. Rev. Lett.* **120**, 207001 (2018).
- [23] V. S. Stolyarov, T. Cren, C. Brun, I. A. Golovchanskiy, O. V. Skryabina, D. I. Kasatonov, M. M. Khapaev, M. Y. Kupriyanov, A. A. Golubov, and D. Roditchev, *Nat. Commun.* **9**, 2277 (2018).
- [24] B. Pannetier and H. Courtois, *J. Low Temp. Phys.* **118**, 599 (2000).
- [25] P. Schlottmann, *Phys. Rev. B* **67**, 174419 (2003).
- [26] W. Belzig, F. K. Wilhelm, C. Bruder, G. Schön, and A. D. Zaikin, *Superlattices Microstruct.* **25**, 1251 (1999).
- [27] V. Chandrasekhar, in *The Physics of Superconductors* (Springer, Berlin, 2004), pp. 55–110.
- [28] J. Rammer, *Quantum Transport Theory* (Westview, Boulder, Colorado, 2004), p. 521.
- [29] K. D. Usadel, *Phys. Rev. Lett.* **25**, 507 (1970).
- [30] A. Barone and G. Paternò, *Physics and Applications of the Josephson Effect* (Wiley, New York, 1982).
- [31] F. Chiodi, M. Ferrier, S. Guéron, J. C. Cuevas, G. Montambaux, F. Fortuna, A. Kasumov, and H. Bouchiat, *Phys. Rev. B* **86**, 064510 (2012).
- [32] W. Belzig, C. Bruder, and A. L. Fauchère, *Phys. Rev. B* **58**, 14531 (1998).
- [33] N. Schopohl, [arXiv:cond-mat/9804064](https://arxiv.org/abs/cond-mat/9804064).
- [34] K. Halterman, P. H. Barsic, and O. T. Valls, *Phys. Rev. Lett.* **99**, 127002 (2007).
- [35] E. Abrahams, A. Balatsky, D. J. Scalapino, and J. R. Schrieffer, *Phys. Rev. B* **52**, 1271 (1995).
- [36] M. Amundsen and J. Linder, *Sci. Rep.* **6**, 22765 (2016).
- [37] J. Bezanson, A. Edelman, S. Karpinski, and V. B. Shah, *SIAM Rev.* **59**, 65 (2017).
- [38] K. Carlsson, JUA-FEM.JL, <https://github.com/KristofferC/JuAFEM.jl>.
- [39] T. Sauer, *Numerical Analysis*, Pearson new int. ed. (Pearson Education, Essex, United Kingdom, 2013).
- [40] J. Revels, M. Lubin, and T. Papamarkou, [arXiv:1607.07892](https://arxiv.org/abs/1607.07892).
- [41] R. C. Dynes, J. P. Garno, G. B. Hertel, and T. P. Orlando, *Phys. Rev. Lett.* **53**, 2437 (1984).

PAPER II

Reference

Eirik Holm Fyhn and Jacob Linder,
Controllable vortex loops in superconducting proximity systems.
Physical Review B **100**, 214503 (2019)
DOI: 10.1103/physrevb.100.214503

CONTRIBUTIONS

EHF performed the analytical calculations and the numerical simulations, with support from JL. EHF drafted the manuscript. EHF and JL formulated the initial idea. EHF and JL contributed to the discussions of the physics, and the revision of the final manuscript. Specifically, in addition to participating in the discussion of the physics and the revision of the final manuscript, EHF wrote the initial draft, formulated the initial idea, performed all the calculations, developed the code, performed the numerical simulations and produced all figures presented in the paper.

Controllable vortex loops in superconducting proximity systems

Eirik Holm Fyhn[✉] and Jacob Linder

Center for Quantum Spintronics, Department of Physics, Norwegian University of Science and Technology, NO-7491 Trondheim, Norway



(Received 4 June 2019; revised manuscript received 19 September 2019; published 5 December 2019)

Superconducting vortex loops have so far avoided experimental detection despite being the focus of much theoretical work. We here propose a method of creating controllable vortex loops in the superconducting condensate arising in a normal metal through the proximity effect. We demonstrate both analytically and numerically that superconducting vortex loops emerge when the junction is pierced by a current-carrying insulated wire and give an analytical expression for their radii. The vortex loops can readily be tuned big enough to hit the sample surface, making them directly observable through scanning tunneling microscopy.

DOI: [10.1103/PhysRevB.100.214503](https://doi.org/10.1103/PhysRevB.100.214503)

I. INTRODUCTION

Many key properties of physical systems are determined by topological defects, such as dislocations in solids, domain walls in ferroics, vortices in superfluids, magnetic skyrmions in condensed-matter systems, and cosmic strings in quantum field theories. In superconductors, the topological entities are vortex lines of quantized magnetic flux. The topological nature of these vortices makes them stable, which is important for potential applications, such as superconducting qubits [1–3], digital memory, and long-range spin transport [4]. Vortices have nonsuperconducting cores and a phase winding of an integer multiple of 2π in the superconducting order parameter, leading to circulating supercurrents [5].

The formation of superconducting vortex loops is topologically allowed and has theoretically been predicted to form around strong magnetic inclusions inside the superconductor [6] in cylindrically shaped current-carrying superconductors [7–9] or through vortex cutting and recombination [10,11]. However, no observation of vortex loops in superconducting systems has been found to date. One challenging aspect is that vortex loops are typically small in conventional superconductors and difficult to stabilize for an extended period of time [12]. Recently, it has been shown that vortex loops can be formed in proximity systems by inserting physical barriers around which the vortices can wrap [11].

In this paper, we present a way to create controllable vortices in mesoscopic proximity systems in a manner which makes them experimentally detectable through scanning tunneling microscopy. The system considered is a three-dimensional superconductor-normal metal-superconductor (SNS) junction pierced by a current-carrying wire which creates the inhomogeneous field responsible for the vortex loops. In planar SNS junctions with uniform applied magnetic fields, changing the superconducting phase difference between the two superconductors shifts the vortex lines in the vertical direction [13]. We here show that the corresponding effect on vortex loops in three dimensions is to change their size.

Thus, these vortex loops are easily tunable. This makes it possible to make the vortices touch the surface, leaving distinct traces which are directly observable by scanning tunneling spectroscopy [14].

Vortex loops in superconducting systems have previously been predicted using the phenomenological Ginzburg-Landau theory [6,10,11]. Here, we use a fully microscopic framework known as quasiclassical Usadel theory and solve the Usadel equation relevant for diffusive systems [15]. By showing that vortex loop formation occurs in a microscopic theory, we give valuable support to the earlier proposed mechanisms for superconducting vortex loops. Finally, we discuss how the proposed setup can be realized experimentally.

II. METHODOLOGY

In this section, we discuss the quasiclassical Usadel theory and how it may be used to analyze the SNS junction depicted in Fig. 1. We first present the mathematical tools and end with the numerical implementation.

A. Quasiclassical theory

In the Usadel theory, the system is described by a quasiclassical Green's function from which physical properties can be extracted. The SNS junction depicted in Fig. 1 can be treated in the quasiclassical formalism under the assumptions that the Fermi wavelength is much shorter than all other relevant length scales. If the system is diffusive, meaning that the scattering time is short, the isotropic part dominates and solves the Usadel equation [15–18], which, in the normal metal, can be written

$$D\bar{\nabla} \cdot (\check{g}\bar{\nabla}\check{g}) + i[\varepsilon\hat{\rho}_3 + \hat{\Delta}, \check{g}] = 0. \quad (1)$$

Here, D is a diffusion constant, $\hat{\rho}_3 = \text{diag}(1, 1, -1, -1)$, and $\hat{\Delta} = \text{antidiag}(+\Delta, -\Delta, +\Delta^*, -\Delta^*)$ where Δ is the superconducting gap parameter. The covariant derivative is $\bar{\nabla}\check{g} = \nabla\check{g} - ie[\hat{\rho}_3\mathbf{A}, \check{g}]$, where $e = -|e|$ is the electron charge, \mathbf{A} is the vector potential, and

$$\check{g} = \begin{pmatrix} \hat{g}^R & \hat{g}^K \\ 0 & \hat{g}^A \end{pmatrix} \quad (2)$$

[✉]Corresponding author: eirik.h.fyhn@ntnu.no

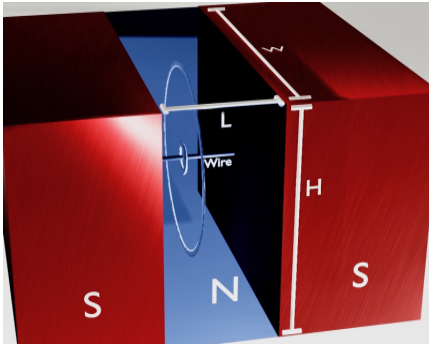


FIG. 1. Sketch of three-dimensional SNS junction considered in this paper. The height, width, and length are H , W , and L , respectively, and the junction is pierced by an insulated current-carrying wire. Contours of the superconducting vortex loops are shown at the location where they are found in our numerical simulations.

is the quasiclassical impurity-averaged Green's function. Finally, $x \in [-L/2, L/2]$, $y \in [-W/2, W/2]$ and $z \in [-H/2, H/2]$ in the normal metal.

\hat{g} is normalized such that $\hat{g}\hat{g} = 1$. We use the convention that, when two matrices of different dimensionality is multiplied, the smaller matrix is elevated to the dimensionality of the larger matrix by the tensor product of an identity matrix of the appropriate size. In equilibrium, the components of the 8×8 Green's function in Eq. (2) are related by the identities $\hat{g}^K = (\hat{g}^R - \hat{g}^A) \tanh(\varepsilon\beta/2)$ and $\hat{g}^A = -\hat{\rho}_3 \hat{g}^{R\dagger} \hat{\rho}_3$, which means that, in this case, it is sufficient to solve for the retarded component \hat{g}^R .

The quasiclassical formalism is not applicable across boundaries because the associated length scale is too short. The Usadel equation must, therefore, be solved in the normal metal and superconductors separately, and the solutions must be connected through boundary conditions. If we assume a low-transparency interface, we may use the Kupriyanov-Lukichev boundary condition,

$$\zeta_i L_i \mathbf{e}_n \cdot (\hat{g}_i^R \bar{\nabla} \hat{g}_i^R) = \frac{1}{2} [\hat{g}_i^R, \hat{g}_i^R], \quad (3)$$

where \mathbf{e}_n is the outward-pointing normal vector for region i , ζ_i is the ratio of the bulk and interface conductances of material i , and L_i is the length of material i in the direction of \mathbf{e}_n . For the boundaries interfacing vacuum, $\mathbf{e}_n \cdot \bar{\nabla} \hat{g}^R = 0$.

The Usadel equation can be made dimensionless by introducing the Thouless energy, $\varepsilon_T := D/L^2$. The Usadel equation then becomes dimensionless by performing the substitutions $(x, y, z) \rightarrow (x/L, y/L, z/L)$, $\varepsilon \rightarrow \varepsilon/\varepsilon_T$, $\Delta \rightarrow \Delta/\varepsilon_T$, and $\bar{\nabla} \rightarrow L\bar{\nabla}$.

B. Electromagnetic vector potential

The magnetic field should satisfy Biot-Savart's law,

$$\mathbf{B} = \frac{\mu}{4\pi} \int \frac{\mathbf{J}(\mathbf{r}') \times (\mathbf{r} - \mathbf{r}')}{|\mathbf{r} - \mathbf{r}'|^3} d^3r', \quad (4)$$

where μ is the permeability and \mathbf{J} is the electric current density. In general, \mathbf{J} includes the contribution the induced

currents in the normal metal and superconductors in addition to that from the insulated current-carrying wire along the x axis. However, we will make some assumptions in order to simplify the analytical and numerical calculations. First, we will assume that the width W and height H is smaller than the Josephson penetration depth. In this case, we can ignore the screening of the magnetic field by currents inside the normal metal [19]. Second, we will neglect the magnetic field produced by the supercurrents produced inside the normal metal. Third, we will assume that the magnetic field vanishes inside the superconductors due to the screening currents. These last two assumptions are widely used in the context of hybrid structures with constant applied magnetic fields [13,20,21] and has, in such conditions, been shown to give good agreement with experimental results [22]. Finally, we will assume that the part of the wire which is inside the superconductors does not contribute to the magnetic field in the normal metal.

The last two assumptions are inaccurate very close to the wire. Close to the wire, the details of screening currents will be important for the magnetic field, but, far away, we assume that the total contribution from the currents inside the superconductor is zero. A more precise model could be developed by taking into account screening currents inside the superconductors and solving the Usadel equation self-consistently with Maxwell's equation and the superconducting gap equation inside the superconductors. However, we are here interested in the solution far away from the wire, and the details of the magnetic field near the wire should not significantly alter the results. For this reason, we also model the wire as being infinitely thin.

With the assumptions presented above, we get a current density which is

$$\mathbf{J} = I\delta(y)\delta(z)[\theta(x + L/2) - \theta(x - L/2)]\mathbf{e}_x, \quad (5)$$

where θ is the Heaviside step function. Inserting Eq. (5) into Eq. (4) we get

$$\mathbf{B} = \frac{\mu I}{4\pi\rho} \left(\frac{L/2 + x}{\sqrt{(L/2 + x)^2 + \rho^2}} + \frac{L/2 - x}{\sqrt{(L/2 - x)^2 + \rho^2}} \right) \mathbf{e}_\phi \quad (6)$$

for $x \in (-L/2, L/2)$, where $\rho = \sqrt{y^2 + z^2}$ and $\mathbf{e}_\phi = (y\mathbf{e}_z - z\mathbf{e}_y)/\rho$. $\mathbf{B} = 0$ for $x < -L/2$ and $x > L/2$. A vector potential which satisfies $\mathbf{B} = \nabla \times \mathbf{A}$ is

$$\mathbf{A} = \frac{\mu I}{4\pi} \ln \left(\frac{\sqrt{(L/2 - x)^2 + \rho^2} + L/2 - x}{\sqrt{(L/2 + x)^2 + \rho^2} - L/2 - x} \right) \times [\theta(x + L/2) - \theta(x - L/2)]\mathbf{e}_x, \quad (7)$$

as can be seen from insertion or calculated directly from Biot-Savart law by using that $\nabla \times [\mathbf{J}(\mathbf{r}')/|\mathbf{r} - \mathbf{r}'|] = \mathbf{J}(\mathbf{r}') \times (\mathbf{r}' - \mathbf{r})/|\mathbf{r}' - \mathbf{r}|^3$.

C. The Riccati parametrization

In the Riccati parametrization [23] of \hat{g}^R , the parameter is the 2×2 matrix γ , and the retarded Green's function is

written

$$\hat{g}^R = \begin{pmatrix} N & 0 \\ 0 & -\tilde{N} \end{pmatrix} \begin{pmatrix} 1 + \gamma\tilde{\gamma} & 2\gamma \\ 2\tilde{\gamma} & 1 + \tilde{\gamma}\gamma \end{pmatrix}, \quad (8)$$

where $N := (1 - \gamma\tilde{\gamma})^{-1}$ and tilde conjugation is $\tilde{\gamma}(\varepsilon) = \gamma^*(-\varepsilon)$.

Since the superconducting correlations in our system are spin singlet, we may write $\gamma_N = \text{antidiag}(a, -a)$ and $\gamma_{\text{BCS}} = \text{antidiag}(b, -b)$, where γ_N and γ_{BCS} are the Riccati parameters in the normal metal and superconductors, respectively. Substituting this into Eqs. (1) and (3), we obtain the dimensionless equations,

$$\begin{aligned} \nabla^2 a = & \frac{2\tilde{a}\nabla a \cdot \nabla a}{1 + a\tilde{a}} + \frac{4(1 - a\tilde{a})LeA \cdot (aLeA + i\nabla a)}{1 + a\tilde{a}} \\ & + 2iLe(\nabla \cdot A)a - 2i\varepsilon a, \end{aligned} \quad (9)$$

and

$$\mathbf{e}_n \cdot \nabla a = \frac{(1 + a\tilde{b})(b - a)}{\zeta(b\tilde{b} + 1)} + 2iae_n \cdot A eL, \quad (10)$$

where L is the length which is used to define the Thouless energy ε_T . The corresponding equations for \tilde{a} and $\mathbf{e}_n \cdot \nabla \tilde{a}$ are found by tilde conjugating Eqs. (9) and (10).

D. Observables

As mentioned initially, a vortex is accompanied by a nonsuperconducting core and a circulating supercurrent. Both the superconducting order parameter and the supercurrent can be extracted from the quasiclassical Green's function. In the following it will be useful to write:

$$\hat{g}^R = \begin{pmatrix} g & f \\ -\tilde{f} & -\tilde{g} \end{pmatrix}. \quad (11)$$

There are only singlet correlations in the SNS system, so $f = \text{antidiag}(f_s, -f_s)$.

The local density of states for spin-band σ at energy ε and location \mathbf{r} can be written

$$N_\sigma(\varepsilon, \mathbf{r}) = N_0 \mathcal{R}[\hat{g}_{\sigma\sigma}(\varepsilon, \mathbf{r})], \quad (12)$$

where N_0 is the normal-state density of state at the Fermi surface. In the normal metal, we can write Eq. (12) in terms of a ,

$$N(\varepsilon, \mathbf{r}) := \frac{N_\uparrow(\varepsilon, \mathbf{r}) + N_\downarrow(\varepsilon, \mathbf{r})}{2} = N_0 \frac{1 - a\tilde{a}}{1 + a\tilde{a}}. \quad (13)$$

In the cores of vortices, we expect $N = N_0$ for all energies, which happens when $a(\varepsilon) \equiv 0$.

The current density is [16]

$$\mathbf{j} = \frac{N_0 e D}{4} \int_{-\infty}^{\infty} \text{Tr}[\hat{\rho}_3 [\hat{g} \tilde{\nabla} \tilde{\hat{g}}]^\text{K}] d\varepsilon. \quad (14)$$

Inserting Eq. (11), using the relations $\hat{g}^A = -\hat{\rho}_3 \hat{g}^{\text{R}\dagger} \hat{\rho}_3$, $\hat{g}^K = (\hat{g}^R - \hat{g}^A) \tanh(\varepsilon\beta/2)$, Eq. (14) can be rewritten

$$\begin{aligned} \mathbf{j} = & \frac{N_0 e D}{2} \int_{-\infty}^{\infty} \tanh\left(\frac{\beta\varepsilon}{2}\right) \text{Tr}[\text{Re}[\tilde{f}^\dagger \nabla f^\dagger - f \nabla \tilde{f}]] \\ & + 2eA \text{Im}[f \tilde{f} - \tilde{f}^\dagger f^\dagger] d\varepsilon. \end{aligned} \quad (15)$$

Written in terms of the quasiclassical Green's function, the superconducting order parameter is

$$\begin{aligned} \Psi(\mathbf{r}) := & \langle \psi_\uparrow(\mathbf{r}, 0) \psi_\downarrow(\mathbf{r}, 0) \rangle \\ = & \frac{N_0}{2} \int_{-\infty}^{\infty} f_s(\mathbf{r}, \varepsilon) \tanh(\varepsilon\beta/2) d\varepsilon. \end{aligned} \quad (16)$$

where $\psi_\sigma(\mathbf{r}, t)$ is the field operator which destroys an electron with spin σ at position \mathbf{r} and time t , N_0 is the normal-state density of states and $\beta = 1/k_B T$.

E. Numerics

The Usadel equation was solved numerically using a finite element scheme. See, for instance, Ref. [24] to see how to set up and solve the nonlinear Usadel equations in a finite element scheme by the use of the Newton-Raphson method. The program was written in JULIA [25], we used linear hexahedral elements, and JUAFEM.JL [26] was used to iterate through the cells. Gauss-Legendre quadrature rules of fourth order were used to integrate through the cells, and Romberg integration was used to integrate over energy. See, for instance, Ref. [27]. Finally, forward-mode automatic differentiation [28] was used to calculate the Jacobian.

III. RESULTS AND DISCUSSION

Here, we present first an analytical solution of the Usadel equation in the weak proximity effect regime, then we show numerically that the findings are also present in the full proximity effect regime. Dimensionless quantities are used in the analytics with distances being measured relative to the length of the half-metal L , and energies being measured relative to the Thouless energy $\varepsilon_T = D/L^2$, where D is the diffusion constant in the normal metal.

A. Analytics

Before solving the Usadel equation, we must determine the solution in the superconductors. We will show that it suffices to use the bulk solution,

$$\hat{g}_{\text{BCS}} = \left[\frac{\theta(\varepsilon^2 - |\Delta|^2)}{\sqrt{\varepsilon^2 - |\Delta|^2}} \text{sgn}(\varepsilon) - \frac{\theta(|\Delta|^2 - \varepsilon^2)}{\sqrt{|\Delta|^2 - \varepsilon^2}} i \right] (\varepsilon \hat{\rho}_3 + \hat{\Delta}), \quad (17)$$

in the superconductors when a certain condition is fulfilled. Let λ (to be defined quantitatively below) be the length scale over which the Green's function recovers its bulk value in the superconductor. The criterion for neglecting the inverse proximity effect in the superconductors is then that the normal-state conductance of the superconductors for a sample of length λ is much larger than the interface conductance and that the length of each superconductor is not small compared to λ . We now proceed to prove this.

The vector potential (7) is zero inside the superconductors, so the Usadel equation simplifies to

$$D_{\text{SC}} \nabla \cdot (\hat{g}^R \nabla \hat{g}^R) + i[\varepsilon \hat{\rho}_3 + \hat{\Delta}, \hat{g}^R] = 0, \quad (18)$$

in the superconductor at $x < -1/2$. To show that we can use the bulk solution, let

$$\hat{g}^R = \hat{g}_{\text{BCS}} + \delta\hat{g}. \quad (19)$$

This gives an equation for $\delta\hat{g}$,

$$D_{\text{SC}}\nabla \cdot (\hat{g}_{\text{BCS}} + \delta\hat{g})\nabla\delta\hat{g} + i[\varepsilon\hat{\rho}_3 + \hat{\Delta}, \delta\hat{g}] = 0, \quad (20)$$

where we have used that \hat{g}_{BCS} solves Eq. (18) for a bulk superconductor. Next, assume the inverse proximity effect to be weak such that $\delta\hat{g} \ll \hat{g}_{\text{BCS}}$. Using that $\hat{g}_{\text{BCS}}\hat{g}_{\text{BCS}} = 1$, this yields

$$D_{\text{SC}}\nabla^2\delta\hat{g} + i\hat{g}_{\text{BCS}}[\varepsilon\hat{\rho}_3 + \hat{\Delta}, \delta\hat{g}] = 0. \quad (21)$$

$\hat{g}_{\text{BCS}} + \delta\hat{g}$ must also satisfy the normalization condition $(\hat{g}^R)^2 = 1$, so

$$(\hat{g}_{\text{BCS}} + \delta\hat{g})^2 = 1 \Rightarrow \{\hat{g}_{\text{BCS}}, \delta\hat{g}\} = 0. \quad (22)$$

Hence, using that $[\varepsilon\hat{\rho}_3 + \hat{\Delta}, \hat{g}_{\text{BCS}}] = 0$,

$$\begin{aligned} \hat{g}_{\text{BCS}}[\varepsilon\hat{\rho}_3 + \hat{\Delta}, \delta\hat{g}] &= (\varepsilon\hat{\rho}_3 + \hat{\Delta})\hat{g}_{\text{BCS}}\delta\hat{g} + \delta\hat{g}(\varepsilon\hat{\rho}_3 + \hat{\Delta})\hat{g}_{\text{BCS}} \\ &= \{\delta\hat{g}, (\varepsilon\hat{\rho}_3 + \hat{\Delta})\hat{g}_{\text{BCS}}\}. \end{aligned} \quad (23)$$

Finally, from

$$(\varepsilon\hat{\rho}_3 + \hat{\Delta})^2 = \varepsilon^2 - \Delta^2, \quad (24)$$

we get that $\delta\hat{g}$ is an eigenfunction of the Laplacian,

$$\nabla^2\delta\hat{g} = \lambda^{-2}\delta\hat{g}, \quad (25)$$

where

$$\begin{aligned} \lambda^{-2} &= -\frac{2i}{D_{\text{SC}}}[\text{sgn}(\varepsilon)\sqrt{\varepsilon^2 - |\Delta|^2}\theta(\varepsilon^2 - |\Delta|^2) \\ &\quad + i\sqrt{|\Delta|^2 - \varepsilon^2}\theta(|\Delta|^2 - \varepsilon^2)]. \end{aligned} \quad (26)$$

We can choose the sign of λ to be such that $\mathcal{R}(\lambda) > 0$.

Let L_{SC} be the length of the superconductor in multiples of the length of the normal metal. Using the boundary condition,

$$\nabla\delta\hat{g}|_{r\in\Omega} = 0, \quad (27)$$

where Ω is the boundary not interfacing the normal metal, we get

$$\delta\hat{g}(\varepsilon, x, y) = C[e^{-|x+1/2|/\lambda} + e^{-2L_{\text{SC}}/\lambda+|x+1/2|/\lambda}], \quad (28)$$

where C is some function of y and ε to be determined by the final boundary condition. From the remaining boundary condition, Eq. (3), we get

$$C = \frac{\lambda\hat{g}_{\text{BCS}}[\hat{g}_{\text{BCS}} + \delta\hat{g}, \hat{g}_{\text{N}}]}{2(1 - e^{-2L_{\text{SC}}/\lambda})\zeta_{\text{SC}}L_{\text{SC}}}. \quad (29)$$

From Eq. (28), we see that $\mathcal{R}(\lambda)$ can be interpreted as the penetration depth of δg . Note that $\mathcal{R}(\lambda)$ is bounded by including the effect of inelastic scattering, which is performed by the substitution $\varepsilon \rightarrow \varepsilon + i\delta$ for some positive scattering rate δ [29]. This ensures that $1/(1 - e^{-2L_{\text{SC}}/\lambda})$ remains finite as $\varepsilon \rightarrow \Delta$. Thus, we see from Eq. (29) that C , and, therefore, δg , becomes negligible when

$$\zeta_{\text{SC}}L_{\text{SC}}/\mathcal{R}(\lambda) \gg 1 \quad (30)$$

provided that the length of the superconductor L_{SC} is not small compared to the maximal penetration depth $\max[\mathcal{R}(\lambda)]$.

ζ_{SC} is proportional to the conductance of the whole superconductor and, therefore, with $1/L_{\text{SC}}$. Therefore, $\zeta_{\text{SC}}L_{\text{SC}}/\mathcal{R}(\lambda)$ is the ratio of the normal-state conductance of a superconductor of length $\mathcal{R}(\lambda)$ to the interface conductance. Taking the superconducting coherence length ξ as a measure of the inverse proximity effect penetration depth $\mathcal{R}(\lambda)$, we see that the criterion Eq. (30) is, indeed, experimentally feasible. The equation is fulfilled for a low-transparency interface and for a superconductor that is larger than the coherence length. A similar calculation shows that we can use \hat{g}_{BCS} also in the superconductor at $x > 1/2$.

Solving for the Riccati parameter in the superconductors we get that $\gamma_{\text{BCS}} = \text{antidiag}(b, -b)$ with

$$\begin{aligned} b &= \frac{\Delta}{\varepsilon + i\sqrt{|\Delta|^2 - \varepsilon^2}}\theta(|\Delta| - |\varepsilon|) \\ &\quad + \frac{\Delta \text{sgn}(\varepsilon)}{|\varepsilon| + \sqrt{\varepsilon^2 - |\Delta|^2}}\theta(|\varepsilon| - |\Delta|). \end{aligned} \quad (31)$$

The nonlinear Usadel equation does not have a general analytical solution, but it can be solved analytically in an approximate manner far away from the wire. If we assume the proximity effect to be weak, we can keep only terms which are linear in a , \tilde{a} , and their gradients. In this case, the Usadel equation (9) decouples

$$\nabla^2 a = 4eL\mathbf{A} \cdot (aeL\mathbf{A} + i\nabla a) + 2ieL(\nabla \cdot \mathbf{A})a - 2iea. \quad (32)$$

Equation 32 can be further simplified when we only consider regions where $\rho \gg 1$ with $\rho = \sqrt{y^2 + z^2}$. The solution of Eq. (32) is constant in y and z when $\mathbf{A} = \mathbf{0}$, and by assuming this is approximately true when $|eL\mathbf{A}| \ll 1$, we can neglect the terms $\partial_y^2 a$ and $\partial_z^2 a$. Finally, we can simplify the calculations further by Taylor expanding the vector potential,

$$Le\mathbf{A} = -n\pi \frac{1}{\rho} \mathbf{e}_x + \mathcal{O}\left(\frac{1}{\rho^2}\right) \mathbf{e}_x, \quad (33)$$

where

$$n = -\frac{eL\mu I}{4\pi^2}. \quad (34)$$

We keep only the first term in the Taylor expansion.

Equation (32) can now be solved exactly, and by applying the linearized boundary conditions,

$$\mathbf{e}_n \cdot \nabla a = \frac{(b + a[b\tilde{b} - 1])}{\zeta(b\tilde{b} + 1)} + 2iae_n \cdot \mathbf{A}eL, \quad (35)$$

the solution can be written in the form

$$\begin{aligned} a &= \frac{ce^{i\phi_1+u(x-0.5)}}{(k-d)^2 e^k - (k+d)^2 e^{-k}} \{(k-d)[e^{k(x-0.5)} \\ &\quad + e^{i\delta\phi-u} e^{-k(x+0.5)}] + (k+d)[e^{k(0.5-x)} \\ &\quad + e^{i\delta\phi-u} e^{k(x+0.5)}]\}, \end{aligned} \quad (36)$$

where

$$\delta\phi = \phi_r - \phi_l, \quad (37)$$

$$c = \frac{|b|}{\zeta(b\tilde{b} + 1)}, \quad d = \frac{(b\tilde{b} - 1)}{\zeta(b\tilde{b} + 1)}, \quad (38)$$

$$u = -\frac{2\pi in}{\rho} \quad \text{and} \quad k = \sqrt{-2i\varepsilon}. \quad (39)$$

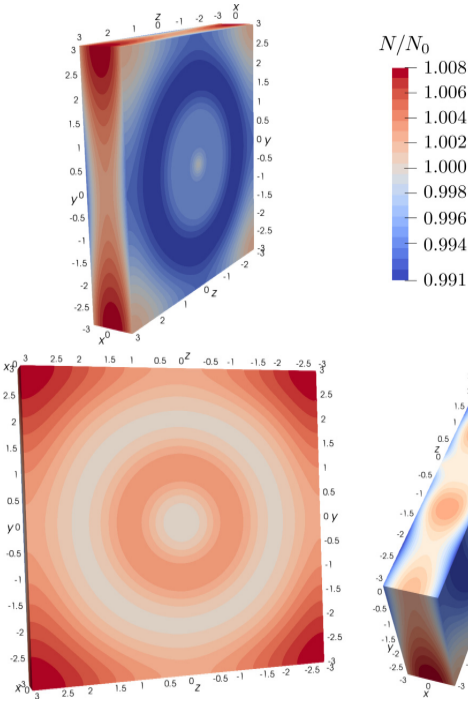


FIG. 2. Local density of states N relative to the normal-state density of states N_0 at energy $\varepsilon = 0.5|\Delta|$, where Δ is the superconducting gap parameter. The lower left shows a cross section at $x = 0$ and the lower right shows a cross section at $y = 0$. Here, $n = 1$ and the superconducting phase difference is $\phi_r = 0$.

From Eq. (36), we see that a vanishes at $x = 0$ and $i\delta\phi - u = i(2N + 1)\pi$, where N is any integer. This happens at

$$\rho = \frac{2n}{1 + 2N - \frac{\phi_r - \phi_l}{\pi}}. \quad (40)$$

This means that f and, hence, Ψ vanish at these points. By Taylor expanding a to first order around a root located at $(0, \tilde{\rho})$, we find

$$a \sim B_1 \cos(\theta + \alpha_1) + iB_2 \cos(\theta + \alpha_2), \quad (41)$$

where $x \sim \cos \theta$ and $\rho - \tilde{\rho} \sim \sin \theta$, $B_1^2 = 5|k|^2/4 - |k|d + 2d^2$, $B_2^2 = |k|^2/4 + d^2$, $\alpha_1 = \tan^{-1}[(|k|/2 + d)/(|k| - d)]$, and $\alpha_2 = \tan^{-1}(|k|/2d)$. Hence, these roots have a phase winding of 2π as is characteristic for vortices. Equation (40) is our main analytical result as it predicts how the radius of the vortex loops depends on the tunable parameters of the system: the current through the wire and the applied phase difference. Although it was obtained using approximations, we demonstrate below that it matches the full numerical solution of the exact Usadel equation very well.

Note that the radius ρ of the largest vortex loop given Eq. (40) can be made arbitrarily large by letting $\phi_r - \phi_l$ approach π . Thus, for a given sample size $L \times W \times H$ and current I , there is a superconducting phase difference for

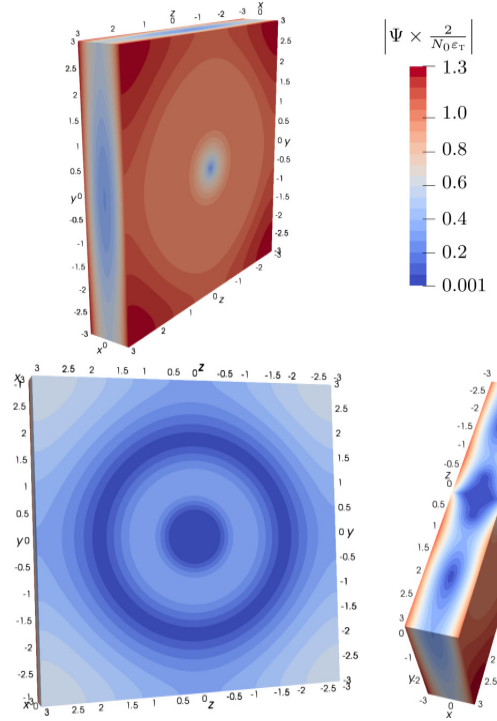


FIG. 3. Amplitude of the superconducting order parameter Ψ for $n = 1$ and superconducting phase difference $\phi_r = 0$. The lower left shows a cross section at $x = 0$, and the lower right shows a cross section at $y = 0$.

which the vortex loop hits the surface and can be directly detected experimentally.

It is expected that a change in the superconducting phase difference will change the radii of vortex loops. This is because changing the phase difference is equivalent to changing the applied supercurrent through the junction. The applied current will be deflected by the circulating currents associated with the vortices and, hence, produce a reactionary force on the vortices. See, for instance, Ref. [30]. What is more surprising, however, is that changing the superconducting phase difference can make the vortices arbitrarily large so that they can always be made to hit the surface. If this feature is generally true for other systems with vortex loops, it could prove useful for the study of systems containing vortex loops which are less obviously controllable than the one considered in the present paper but which are easier to design in a laboratory. For instance, one possibility is to grow the normal metal around a magnetic dipole. Reference [6] found that vortex loops can form around magnetic dipole inclusions in superconductors if the magnetic field is strong enough, so there are reasons to believe that vortex loops can also form around magnetic dipoles embedded in a SNS junction. The magnetic field from a dipole can, unlike the magnetic field from a wire, not be altered in strength. Nevertheless, if the field is strong enough to produce vortices, altering the

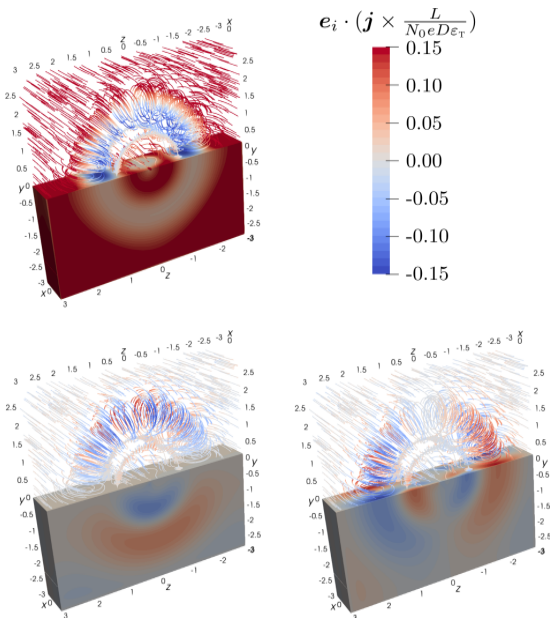


FIG. 4. Plot of the three different components of the supercurrent $e_x \cdot \mathbf{j}$ (upper left), $e_y \cdot \mathbf{j}$ (lower left), and $e_z \cdot \mathbf{j}$ (lower right). The lower half shows the value of the current on the surface in color, and the upper half shows streamlines of the current with the current strength indicated by the same color. Here, $n = 1$ and $\phi_r = 0$.

superconducting phase difference could be a way to increase the size of the vortex to the point where it touches the surface and becomes directly observable.

B. Numerics

We now proceed to show numerical results in the full (nonlinear) proximity effect regime. We have set the parameters $|\Delta| = 4\varepsilon_T$, $\zeta = 3$, $W = H = 6L$, and $\phi_l = 0$ common for all the numerical calculations. We include the effect of inelastic scattering by performing the substitution $\varepsilon \rightarrow \varepsilon + i\delta$ where $\delta = 0.001|\Delta|$ in order to avoid the divergence of \hat{g}_{BCS} at $\varepsilon = |\Delta|$ [29].

Numerically, we find that vortex loops form at the locations predicted by the analysis. There are circular paths around the origin where the superconducting order parameter vanishes, and the local density of states is equal to that of the normal state. This can be seen in Figs. 2 and 3 which shows the local density of states and the amplitude of the Cooper pair-correlation function Ψ , respectively. Around these loops, there are a circulating supercurrent as can be seen in Fig. 4, and a phase winding in the order parameter of 2π . Figure 5 shows a contour plot of $|\Psi|$, which shows the location of the vortices, together with the circulating supercurrent \mathbf{j} as well as the phase of Ψ , which shows that there is, indeed, a phase winding of 2π around the vortices.

We find that the positions of the vortex loops match with Eq. (40) for vortices with radii that are between $2L$ and $3L$. Figures 6 and 7 show how the sizes of the vortex loops depend

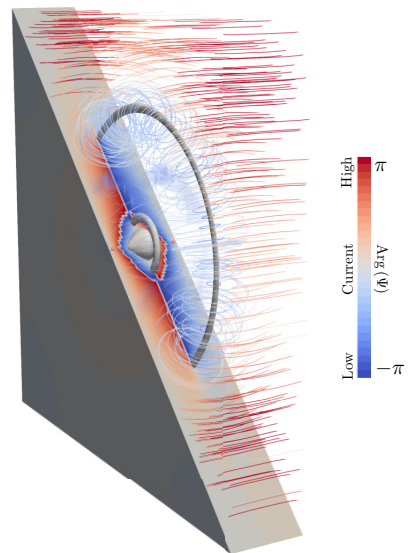


FIG. 5. Plot of the phase of the superconducting order parameter Ψ on a diagonally cut part of the normal metal, contour plot of its amplitude $|\Psi|$, and streamlines of the supercurrent \mathbf{j} . Here, $n = 1$ and $\phi_r = 0$.

on superconducting phase difference ϕ and magnetic-field strength n , respectively. We find that increasing ϕ can make the vortices arbitrarily large but does not increase the number of vortices. Increasing n , on the other hand, also increases the number of vortices, but the sizes grow only linearly with n . Note that, as the vortex loops hit the surface, they curve so as to hit normally to the surface. This is consistent with previous results [6,31] and can be understood from the circulating currents. There should be no current component normal to the surface, and the only way for the current circulating the vortices to adhere to this is if the vortices hit the surfaces at a right angle.

IV. EXPERIMENTAL REALIZATION

Normal SNS junctions are created by vertically growing first a superconducting material, such as niobium, then, a normal metal, such as copper, and finally the same superconducting material. The layers are grown, for instance, by a sputter deposition technique, such as direct current sputtering [32] or radio-frequency sputtering [33]. The setup presented here adds an extra complication by requiring an isolated conducting nanowire to penetrate the system. One possible way to achieve this could be to first grow a vertical insulated nanowire and then grow the superconductor and normal metal around it in a layerwise fashion.

Growing a wire is more complicated than growing a plane because one must localize the growth to happen at the tip of the wire, even though most of the surface area will be on the sides. Nevertheless, growing vertical nanowires has successfully been performed by methods, such as the vapor-liquid-solid method [34–36] and template-directed

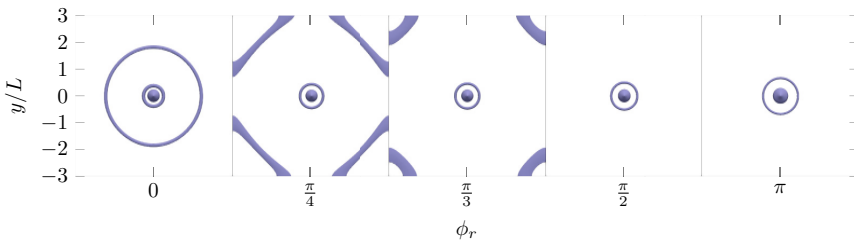


FIG. 6. Contour plot of the amplitude of the superconducting order parameter Ψ for $n = 1$ and various values of the superconducting phase difference ϕ_r .

synthesis [37]. The vapor-liquid-solid method works by using droplets of, for instance, gold which are a few angstroms in width to localize the growth [35], and template-directed synthesis works by having the wire grow inside a premade template which can later be removed [37]. The vapor-liquid-solid method has already been used to produce vertical surround-gate field-effect transistors with a precision exceeding what should be necessary for the system presented here [35].

Schmidt *et al.* [35] made nanowires using the vapor-liquid-solid method which were 40 nm in diameter and 400 nm in length. This should be on the same length scale as would be necessary for the system considered in this paper. The superconducting energy gap of niobium is $|\Delta| = 30.5 \times 10^{-4}$ eV [38], which is equivalent to about 2.46 mm^{-1} in natural units. The Fermi velocity and scattering time for copper are about $v_F = 3.70 \times 10^{-3}$ and $\tau = 10.8 \mu\text{m}$, respectively [39]. The diffusion coefficient is defined as

$$D := \frac{\tau v_F^2}{3}, \quad (42)$$

so the diffusion coefficient for copper is about $D = 49.2 \text{ pm}$. In the numerics, we have used

$$|\Delta| = 4\varepsilon_T = \frac{4D}{L^2}, \quad (43)$$

so

$$L = 283 \text{ nm} \quad (44)$$

which is on the same scale as what has been made with the vapor-liquid-solid method. Of course, other metals and superconductors could be used, giving different physical lengths corresponding to the values being used in the numerics here. Moreover, from the analysis, it seems vortex

loops would form also for other values of $|\Delta|/\varepsilon_T$. The calculation above is merely to show that the length scales used here are not unreasonable compared to what has already been experimentally achieved.

V. CONCLUSION

We have used quasiclassical Usadel theory to demonstrate that controllable superconducting vortex loops can emerge in a Josephson junction pierced by an insulated current-carrying wire. The size and number of vortices depend on the phase difference between the superconducting order parameter in the superconductors $\phi_r - \phi_l$ as well as the strength of the magnetic field. The radius of the vortices can be made arbitrarily large by tuning of the superconducting phase difference, which means that they can always be manipulated so that they intersect the surface. This makes them directly observable by scanning tunneling microscopy, which has already been used to detect normal vortices in proximized metals [14]. If this ability of the superconducting phase difference to expand vortex loops to arbitrary sizes is a general feature of SNS junctions, it could be used to detect vortex loops in systems where controlling the magnetic-field strength is not an option, such as in a system with a magnetic dipole inclusion.

ACKNOWLEDGMENTS

We thank M. Amundsen and V. Risinggård for helpful discussions. This work was supported by the Research Council of Norway through Grant No. 240806 and its Centres of Excellence Funding Scheme Grant No. 262633 “*QuSpin*.”

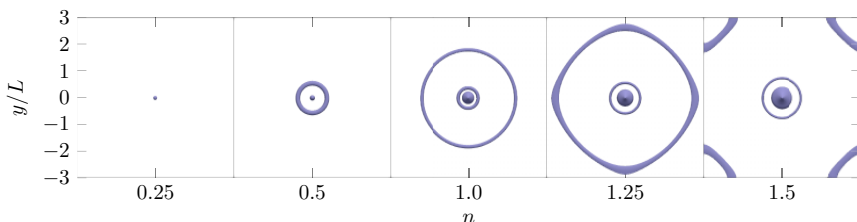


FIG. 7. Contour plot of the amplitude of the superconducting order parameter Ψ for superconducting phase difference $\phi_r = 0$ and various values of n .

- [1] K. G. Fedorov, A. V. Shcherbakova, M. J. Wolf, D. Beckmann, and A. V. Ustinov, *Phys. Rev. Lett.* **112**, 160502 (2014).
- [2] M. H. Devoret and R. J. Schoelkopf, *Science* **339**, 1169 (2013).
- [3] A. Herr, A. Fedorov, A. Shnirman, E. Il'ichev, and G. Schön, *Supercond. Sci. Technol.* **20**, S450 (2007).
- [4] S. K. Kim, R. Myers, and Y. Tserkovnyak, *Phys. Rev. Lett.* **121**, 187203 (2018).
- [5] W. K. Kwok, U. Welp, A. Glatz, A. E. Koshelev, K. J. Kihlstrom, and G. W. Crabtree, *Rep. Prog. Phys.* **79**, 116501 (2016).
- [6] M. M. Doria, A. R. De C. Romaguera, M. V. Milošević, and F. M. Peeters, *Europhys. Lett.* **79**, 47006 (2007).
- [7] A. V. Samokhvalov, *Physica C* **308**, 74 (1998).
- [8] A. Samokhvalov, *Physica C* **282-287**, 2163 (1997).
- [9] V. Kozlov and A. Samokhvalov, *Physica C* **213**, 103 (1993).
- [10] A. Glatz, V. K. Vlasko-Vlasov, W. K. Kwok, and G. W. Crabtree, *Phys. Rev. B* **94**, 064505 (2016).
- [11] G. R. Berdiyrov, M. V. Milošević, F. Kusmartsev, F. M. Peeters, and S. Savel'ev, *Sci. Rep.* **8**, 2733 (2018).
- [12] A. Schönenberger, A. Larkin, E. Heeb, V. Geshkenbein, and G. Blatter, *Phys. Rev. Lett.* **77**, 4636 (1996).
- [13] J. C. Cuevas and F. S. Bergeret, *Phys. Rev. Lett.* **99**, 217002 (2007).
- [14] V. S. Stolyarov, T. Cren, C. Brun, I. A. Golovchanskiy, O. V. Skryabina, D. I. Kasatonov, M. M. Khapaev, M. Y. Kupriyanov, A. A. Golubov, and D. Roditchev, *Nat. Commun.* **9**, 2277 (2018).
- [15] K. D. Usadel, *Phys. Rev. Lett.* **25**, 507 (1970).
- [16] W. Belzig, F. K. Wilhelm, C. Bruder, G. Schön, and A. D. Zaikin, *Superlattices Microstruct.* **25**, 1251 (2002).
- [17] V. Chandrasekhar, Proximity-Coupled Systems: Quasiclassical Theory of Superconductivity, *The Physics of Superconductors*, edited by K. H. Bennemann and J. B. Ketterson (Springer, Berlin, Heidelberg, 2004), pp. 55–110.
- [18] J. Rammer, *Quantum Transport Theory* (Westview, Boulder, CO, 2004) p. 521.
- [19] A. Barone and G. Paternò, *Physics and Applications of the Josephson Effect* (Wiley, New York, 1982).
- [20] M. Alidoust and K. Halterman, *J. Appl. Phys.* **117**, 123906 (2015).
- [21] F. S. Bergeret and J. C. Cuevas, *J. Low Temp. Phys.* **153**, 304 (2008).
- [22] F. Chiodi, M. Ferrier, S. Guéron, J. C. Cuevas, G. Montambaux, F. Fortuna, A. Kasumov, and H. Bouchiat, *Phys. Rev. B* **86**, 064510 (2012).
- [23] N. Schopohl, [arXiv:cond-mat/9804064](https://arxiv.org/abs/cond-mat/9804064).
- [24] M. Amundsen and J. Linder, *Sci. Rep.* **6**, 22765 (2016).
- [25] J. Bezanson, A. Edelman, S. Karpinski, and V. B. Shah, *SIAM Rev.* **59**, 65 (2017).
- [26] K. Carlsson, Juafem.jl [<https://github.com/KristofferC/JuAFEM.jl>] (2019).
- [27] T. Sauer, *Numerical Analysis: Pearson New International Edition* (Pearson Education Limited, Essex, U.K., 2013).
- [28] J. Revels, M. Lubin, and T. Papamarkou, [arXiv:1607.07892](https://arxiv.org/abs/1607.07892).
- [29] R. C. Dynes, J. P. Garno, G. B. Hertel, and T. P. Orlando, *Phys. Rev. Lett.* **53**, 2437 (1984).
- [30] E. B. Sonin, *Phys. Rev. B* **55**, 485 (1997).
- [31] A. R. de C. Romaguera, M. M. Doria, and F. M. Peeters, *Phys. Rev. B* **75**, 184525 (2007).
- [32] R. E. Miller, W. H. Mallison, A. W. Kleinsasser, K. A. Delin, and E. M. Macedo, *Appl. Phys. Lett.* **63**, 1423 (1993).
- [33] V. M. Krasnov, N. F. Pedersen, V. A. Oboznov, and V. V. Ryazanov, *Phys. Rev. B* **49**, 12969 (1994).
- [34] H. T. Ng, J. Han, T. Yamada, P. Nguyen, Y. P. Chen, and M. Meyyappan, *Nano Lett.* **4**, 1247 (2004).
- [35] V. Schmidt, H. Riel, S. Senz, S. Karg, W. Riess, and U. Gösele, *Small* **2**, 85 (2006).
- [36] K. Tomioka, M. Yoshimura, and T. Fukui, *Nature (London)* **488**, 189 (2012).
- [37] Y. Xia, P. Yang, Y. Sun, Y. Wu, B. Mayers, B. Gates, Y. Yin, F. Kim, and H. Yan, *Adv. Mater.* **15**, 353 (2003).
- [38] C. Kittel *et al.*, *Introduction to Solid State Physics* (Wiley, New York, 1976), Vol. 8.
- [39] D. Gall, *J. Appl. Phys.* **119**, 085101 (2016).

PAPER III

Reference

Eirik Holm Fyhn, Morten Amundsen, Ayelet Zalic, Tom Dvir, Hadar Steinberg, and Jacob Linder,




Combined Zeeman and orbital effect on the Josephson effect in rippled graphene.

Physical Review B **102**, 024510 (2020)

doi: 10.1103/physrevb.102.024510

CONTRIBUTIONS

EHF performed the analytical calculations and the numerical simulations, with support from MA and JL. EHF drafted the manuscript. AZ, TD and HS formulated the initial overarching research goal. All authors contributed to the discussions of the physics, and the revision of the final manuscript. Specifically, in addition to participating in the discussion of the physics and the revision of the final manuscript, EHF wrote the initial draft, performed all the analytical calculations, developed the code, performed the numerical simulations and produced all figures presented in the paper.

Combined Zeeman and orbital effect on the Josephson effect in rippled grapheneEirik Holm Fyhn ^{1,*}, Morten Amundsen ¹, Ayelet Zalic,² Tom Dvir,² Hadar Steinberg ² and Jacob Linder¹¹Center for Quantum Spintronics, Department of Physics, Norwegian University of Science and Technology, NO-7491 Trondheim, Norway²The Racah Institute of Physics, The Hebrew University of Jerusalem, Jerusalem 91904, Israel

(Received 16 April 2020; revised 25 May 2020; accepted 25 June 2020; published 9 July 2020)

The two-dimensional nature of graphene Josephson junctions offers the possibility of creating effective superconductor-ferromagnet-superconductor junctions with tunable Zeeman splitting caused by an in-plane magnetic field. Such junctions would be able to alternate between a conventional superconducting ground state and a ground state with an intrinsic phase difference, making them controllable $0-\pi$ Josephson junctions. However, in addition to the Zeeman splitting, an in-plane magnetic field will in general also produce an orbital effect because of height variations in graphene, colloquially known as ripples. Both the Zeeman and orbital effect will thus affect the critical current, so to be able to identify $0-\pi$ transitions it is necessary to understand their combined effect. From both analytical and numerical solutions of the Usadel equation we find that ripples can in fact produce a current response similar to that which is characteristic of a $0-\pi$ transition. Hence, additional analysis is required in order to reveal the presence of a $0-\pi$ transition caused by spin splitting in graphene with ripples. We provide a closed form analytical expression for the critical current in the presence of exchange field and ripple effects as well as an expression for the scaling of critical current zeros with junction parameters.

DOI: [10.1103/PhysRevB.102.024510](https://doi.org/10.1103/PhysRevB.102.024510)**I. INTRODUCTION**

When the spinless superconducting order of a conventional superconductor comes in contact with a ferromagnet, it can adapt by creating spin-triplet Cooper pairs [1]. The synergy between superconductivity and ferromagnetism, two seemingly incompatible orders, is a topic of fundamental interest but could also be of practical value. One interesting consequence is that it allows for spinful supercurrents. The promise of low-dissipation spin transport has helped spawn the field of superconducting spintronics [2].

In the last decade, the possibility of creating Josephson junctions with graphene has attracted interest [3–7]. Superconductor-graphene-superconductor (SGS) junctions provide an arena for understanding the interplay between superconductivity and otherwise distinct physical phenomena, such as special relativity [3] and the quantum Hall effect [8,9]. Here, we are interested in how the two-dimensional nature of monolayer graphene can be utilized to create an effective superconductor-ferromagnet-superconductor (SFS) junction with a tunable exchange field. This is done by introducing a Zeeman splitting between the spin bands in the graphene by use of a strong in-plane magnetic field. This is possible because the two-dimensional nature of the graphene minimizes the magnetic depairing effect that would otherwise quench the superconducting correlations. By using electrodes with Ising-like superconductivity, like thin NbSe_2 , one avoids destroying the superconducting state of the electrodes via the Pauli limitation.

The possibility of *in situ* control of the exchange field could open new avenues for manipulations that take advantage of the

combined effect of magnetic and superconducting order. In addition to giving rise to the possibility of Cooper pairs with nonzero total spin [2], the presence of a magnetic field gives the Cooper pairs a nonzero total momentum, as first explained by Fulde, Ferrel, Larkin and Ovchinnikov [10,11]. The total momentum of the Cooper pairs in the so-called FFLO-state is given by the strength of the exchange field, as this determines the displacement of the two Fermi surfaces corresponding to spin-up and spin-down electrons. The nonzero momentum produces spatial variations in the superconducting order parameter [12].

One consequence of the spatial variations is that the ground state of a superconductor-ferromagnet-superconductor (SFS) Josephson junction can be one in which the phases of the order parameter in the two superconductors differs by π , which is known as a π junction. Such junctions could have an important role in the design of components for quantum computing [13–15], superconducting computing [16,17], or as cryogenic memory [18].

Whether an SFS junction is a π junction or not depends on its length [19,20] as well as the strength of the exchange field, which are typically fixed parameters. If, however, the exchange field could be tuned, this would allow for a controllable switching between the 0 -junction state and π -junction state. Zeeman-effect-induced $0-\pi$ transitions have previously been observed in a Dirac semimetal with a g factor on the order of 10^3 [21]. The large g factor allowed the $0-\pi$ transition to occur before the magnetic field extinguished the superconducting correlations. Using a junction with a two-dimensional material, such as monolayer graphene, would allow for Zeeman driven $0-\pi$ transitions without the need for large g factors, since such junctions can withstand much larger in-plane magnetic fields.

*Corresponding author: eirik.h.fyhn@ntnu.no

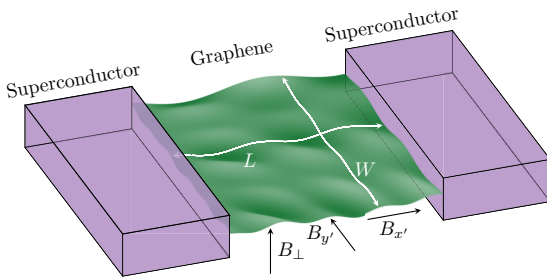


FIG. 1. Sketch of superconductor-graphene-superconductor junction with rippled graphene and external magnetic field. The magnetic field has out-of-plane component B_{\perp} and in-plane components $B_{y'}$ and $B_{x'}$.

The prospect of a graphene Josephson junction being used as a tunable SFS junction is interesting, but it also demands a thorough investigation into how the supercurrent in an SGS junction responds to the strong in-plane magnetic field necessary for an appreciable Zeeman splitting. Even though monolayer graphene is two dimensional, it will in general not be perfectly flat. It will have a curvature that depends on the underlying substrate. If the graphene is placed on SiO_2 , it will be rippled with peak-to-peak height difference of about 1 nm and typical feature size of 30 nm [22]. Hence, the in-plane magnetic field will have a component orthogonal to the graphene surface, giving rise to an orbital effect. This orthogonal component has been observed to suppress phase-coherent weak localization [23,24]. Consequently, extra care must be taken when considering phase-coherent transport experiments relying on in-plane magnetic fields. Here, we show that attention must also be paid to ripples when considering SGS junction with tunable Zeeman splitting.

One property of a $0\text{-}\pi$ transition is that the current changes sign, giving zero net current exactly at the transition [19]. Characterization of an SGS junction and the identification of a possible $0\text{-}\pi$ transition will typically be done by measuring the current response to an applied magnetic field. Therefore, it is important to know whether features in the critical current, such as the decay rate and zeros, can also be produced by an interference effect that arises from ripples in the graphene. Of particular interest is whether interference effects can give

a vanishing critical current at magnetic field strengths that are comparable to the magnetic field necessary for a $0\text{-}\pi$ transition. The Zeeman energy necessary for the transition is typically smaller for diffusive systems [12], so diffusive systems, achievable for instance with SiO_2 as substrate [25], are most promising for tunable π junctions. However, computing the supercurrent in a model with ripples in graphene is a challenging task due to the nontrivial geometry of the system.

A sketch of the system under consideration is shown in Fig. 1. In order to model this geometry, we add a spatially varying magnetic field to the equations governing diffusive SFS junctions, where the exchange field in the ferromagnet comes from the Zeeman effect. In order to fully model the disorderly ripples, one must be able to solve the equations with arbitrary magnetic field distributions. We are able to do that numerically by using the finite element method. Additionally, we extend the analytical result by Bergeret and Cuevas [26] for superconductor-normal-superconductor (SNS) junctions with uniform magnetic fields to SFS junctions with arbitrary magnetic field distributions and arbitrary exchange fields.

II. METHODOLOGY

The critical current, as well as other physical quantities such as the local density of states, can be calculated using the quasiclassical Keldysh Green's function formalism [27,28]. Previous studies of ballistic systems have investigated the interplay of the Zeeman and the orbital effect using an analytical propagator approach [29,30]. The diffusive limit considered here, however, is more appropriately described by the Usadel equation, which previously has been done to successfully model experimental results for the supercurrent in SGS junctions [31]. We use natural units throughout, meaning that $c = \hbar = 1$.

In thermal equilibrium it is sufficient to solve for the retarded Green's function \hat{g} , which is normalized to $\hat{g}^2 = 1$ and solves the Usadel equation,

$$D\tilde{\nabla} \cdot (\hat{g}\tilde{\nabla}\hat{g}) + i[\hat{\Sigma}, \hat{g}] = 0, \quad (1)$$

provided that the Fermi wavelength and the elastic impurity scattering time is much shorter than all other relevant length scales, and the Fermi wavelength is much smaller than the scattering time. Here D is the diffusion coefficient and the covariant derivative is $\tilde{\nabla}\hat{g} \equiv \nabla\hat{g} - ie\mathbf{A}[\hat{\rho}_3, \hat{g}]$, where \mathbf{A} is the vector potential and $e = -|e|$ is the electron charge. The self-energy is

$$\hat{\Sigma} = \begin{cases} (\varepsilon + i\delta)\hat{\rho}_3 + \begin{pmatrix} & & -\Delta \\ -\Delta^* & \Delta^* & \\ & & \end{pmatrix} & \text{in the superconductors,} \\ (\varepsilon + i\delta)\hat{\rho}_3 + \begin{pmatrix} \mathbf{h} \cdot \boldsymbol{\sigma} & \\ & \mathbf{h} \cdot \boldsymbol{\sigma}^* \end{pmatrix} & \text{in the ferromagnet,} \end{cases} \quad (2)$$

where ε is the energy, δ^{-1} is the inelastic scattering time, $\hat{\rho}_3 = \text{diag}(1, 1, -1, -1)$, Δ is the superconducting gap parameter, \mathbf{h} is the exchange field, and $^*\sigma$ is the vector consisting of

Pauli matrices. Defining “spin up” and “spin down” parallel to the in-plane magnetic field gives $\mathbf{h} = h\hat{\mathbf{z}}$. We here disregard the effect of the very weak \mathbf{k} -dependent spin-orbit induced

effective Zeeman-field caused by ripples in graphene, which is opposite in direction at the two inequivalent Dirac points of graphene [32].

To model rippled graphene, we will map the nonflat graphene sheet in the laboratory frame $x'y'z'$ shown in Fig. 1 with magnetic field components $B_{x'}, B_{y'}, B_{\perp}$ to a local coordinate system xyz that follows the graphene surface in the sense that the z axis is always orthogonal to the surface. The spatially constant magnetic field in the laboratory frame will then give rise to a spatially dependent magnetic field in the local coordinate system xyz .

Let x and y denote orthogonal coordinates on the graphene surface such that the superconductors are located at $x = \pm L/2$ and the interfaces with vacuum are at $y = \pm W/2$. The curved geometry of graphene will in general enter into the Usadel Eq. (1) in three ways. First, the divergence and gradient operators are altered by the curvature. For a given ripple structure, these operators can be calculated from the resulting metric tensor. However, since the curvature of rippled graphene typically is very small [22], the deviation from the Euclidean metric is negligible. Consequently, we use $\nabla \equiv \hat{\mathbf{x}} \partial/\partial x + \hat{\mathbf{y}} \partial/\partial y$. Second, the out-of-plane magnetic field component is modulated because it penetrates the graphene at varying angles. That is, if $\mathbf{B}_{\perp} = B_{\perp} \hat{\mathbf{z}}$ is the out-of-plane magnetic field $\hat{\mathbf{z}}$ is the unit vector pointing out of the plane in the external coordinate system, or ‘‘lab frame,’’ and $\hat{\mathbf{z}}$ is the unit vector orthogonal to the graphene, then

$$\mathbf{B}_{\perp} \cdot \hat{\mathbf{z}} = B_{\perp} + \beta(x, y). \quad (3)$$

Again, since the curvature is small, β is negligible compared to B_{\perp} , so we can safely disregard this correction. Third, and crucial for the effect considered here, the in-plane magnetic field has a component orthogonal to the surface. In the laboratory frame, the magnetic field can be written $\mathbf{B} = (B_{x'}, B_{y'}, B_{\perp})^T$. In the coordinate system of the curved graphene, this gives rise to a magnetic field with a z component equal to

$$\begin{aligned} \mathbf{B} \cdot \hat{\mathbf{z}} &= -B_{x'} \sin \left[\arctan \left(\frac{\partial \eta}{\partial x'} \right) \right] - B_{y'} \sin \left[\arctan \left(\frac{\partial \eta}{\partial y'} \right) \right] \\ &+ B_{\perp} + \beta \approx -B_{x'} \frac{\partial \eta}{\partial x} - B_{y'} \frac{\partial \eta}{\partial y} + B_{\perp}, \end{aligned} \quad (4)$$

where η is the height distribution of the graphene, x' and y' are the coordinates in the laboratory frame, and we have used the assumption that $\partial \eta/\partial x \approx \partial \eta/\partial x' \ll 1$ and $\partial \eta/\partial y \approx \partial \eta/\partial y' \ll 1$.

In order to capture the magnetic field given by Eq. (4), we use the vector potential

$$\mathbf{A} = \left(B_y \eta + B_{x'} \int_0^y \frac{\partial \eta}{\partial x} d\tilde{y} - B_{\perp} y \right) \hat{\mathbf{x}}. \quad (5)$$

Choosing the vector potential parallel to the x axis allows us to set $\mathbf{A} = \mathbf{0}$ in the superconductors, which means that the ground states in the superconductors have constant phases. In the following we denote the superconducting phase in the left ($x < -L/2$) and right ($x > L/2$) superconductors by ϕ_l and ϕ_r , respectively. Having established the form of the vector potential \mathbf{A} [Eq. (5)] in the local coordinate system where

graphene is flat, we will from now on omit the prime on $B_{x'}$ and $B_{y'}$ for brevity of notation.

The Usadel Eq. (1) is not valid across boundaries of different materials since the associated length scales are not negligible compared to the Fermi wavelength. Instead, the Green’s function in the different materials must be connected through a boundary condition. For low-transparency tunneling interfaces, one may use the Kupriyanov-Lukichev boundary condition [33],

$$\zeta_i L_i \hat{\mathbf{n}} \cdot (\hat{g}_i \tilde{\nabla} \hat{g}_i) = \frac{1}{2} [\hat{g}_i, \hat{g}_j], \quad (6)$$

where the subscripts i and j denote the different sides of the interface, $\hat{\mathbf{n}}$ is a normal unit vector pointing out of region i , L_i is the length of region i in the $\hat{\mathbf{n}}$ direction, and ζ_i is the ratio of the normal-state conductance of region i to the interface conductance. Equation (6) is used along the interface between the superconductors and graphene at $x = -L/2$ and $x = L/2$. Along the boundaries with vacuum at $y = \pm W/2$, the boundary condition is $\hat{\mathbf{n}} \cdot \tilde{\nabla} \hat{g} = 0$.

It has been shown that one may use the bulk solution in the superconductors,

$$\hat{g}_{\text{BCS}} = \frac{\hat{\Sigma}}{\sqrt{(\varepsilon + i\delta)^2 - |\Delta|^2}}, \quad (7)$$

when the interface conductance is much smaller than the normal-state conductance of length ξ of the superconductor [34], where

$$\xi = \sqrt{\frac{D}{\Delta}} \quad (8)$$

is the coherence length. The square root in Eq. (7) must be chosen such that it has a positive imaginary part.

Having found the Green’s function, the electrical current density can be calculated from [35]

$$\mathbf{j} = \frac{N_0 e D}{4} \int_{-\infty}^{\infty} \text{Tr}(\hat{\rho}_3 \hat{g} \tilde{\nabla} \hat{g} - \hat{g}^{\dagger} \tilde{\nabla} \hat{g}^{\dagger} \hat{\rho}_3) \tanh \left(\frac{\beta \varepsilon}{2} \right) d\varepsilon, \quad (9)$$

where N_0 is the normal density of states and β is inverse temperature. Finally, Eq. (9) allows for calculation of the critical current, given by

$$I_c = \max_{\phi_r - \phi_l} \int_{-W/2}^{W/2} \hat{\mathbf{x}} \cdot \mathbf{j}(x, y) dy, \quad (10)$$

where the choice of x is arbitrary.

In order to solve Eq. (1) numerically, we use the Riccati parametrization,

$$\hat{g} = \begin{pmatrix} N & \\ & -\tilde{N} \end{pmatrix} \begin{pmatrix} 1 + \gamma \tilde{\gamma} & 2\gamma \\ 2\tilde{\gamma} & 1 + \tilde{\gamma} \gamma \end{pmatrix}, \quad (11)$$

where $N = (1 - \gamma \tilde{\gamma})^{-1}$ and tilde conjugation is defined as $\tilde{\gamma}(\varepsilon) = \gamma^*(-\varepsilon)$. This respects the normalization and underlying symmetries of \hat{g} . The resulting equations for the 2×2 matrices γ and $\tilde{\gamma}$ are discretized by the finite element method [36] with quadratic elements, and Gauss-Legendre quadrature rules of fourth order is used to integrate over the elements. The resulting nonlinear set of algebraic equations are solved by the Newton-Raphson method [37], where the Jacobian is determined by forward-mode automatic differentiation [38].

III. RESULTS AND DISCUSSION

In order to linearize the Usadel equation, we write

$$\hat{g} = \hat{g}_0 + \hat{f}, \quad (12)$$

where \hat{g}_0 is the bulk solution. In a ferromagnet, the self-energy $\hat{\Sigma}$, given by (2), is diagonal. Hence, the bulk equation $[\hat{\Sigma}, \hat{g}_0] = 0$ is solved by any diagonal matrix satisfying $\hat{g}_0^2 = 1$. In order to find the correct solution one must solve the full Gor'kov equation. The result is that $\hat{g}_0 = \hat{\rho}_3$. If we assume that the proximity effect is weak, we can keep only linear terms in \hat{f} , yielding

$$D\hat{\rho}_3\hat{\nabla}^2\hat{f} + i[\hat{\Sigma}\hat{f}] = 0. \quad (13)$$

In order for the normalization $\hat{g}^2 = 1$ to hold to linear order in \hat{f} , we need $\{\hat{f}, \hat{\rho}_3\} = 0$. This implies that

$$\hat{f} = \begin{pmatrix} 0 & \hat{f} \\ -\hat{f} & 0 \end{pmatrix} \quad (14)$$

and

$$\hat{\nabla}\hat{f} = \nabla\hat{f} - 2ie\mathbf{A}\hat{\rho}_3\hat{f}. \quad (15)$$

In the weak proximity effect regime, the boundary conditions read

$$\zeta L\hat{\rho}_3\hat{\mathbf{n}}\cdot\hat{\nabla}\hat{f} = \frac{1}{2}[\hat{\rho}_3 + \hat{f}_s, \hat{g}_s + \hat{f}_s] = \hat{\rho}_3\hat{f}_s - \hat{g}_s\hat{f}_s, \quad (16)$$

where \hat{g}_s is the part of \hat{g}_{BCS} proportional to $\hat{\rho}_3$ and \hat{f}_s is the remaining part proportional to $\text{anti diag}(\Delta, -\Delta, \Delta^*, -\Delta^*)$. Additionally, we must have $[\hat{f}, \hat{f}_s] = 0$, since this term would be block diagonal.

Since $\hat{\Sigma}$ is diagonal in the ferromagnet, the different components of \hat{f} decouple. Only the elements which are nonzero in \hat{f}_s will have a constant term in the boundary conditions. The remaining elements must be zero. Hence, \hat{f} must be antidiagonal, just like \hat{f}_s . This in turn implies that $[\hat{\Sigma}, \hat{f}] = 2\hat{\Sigma}\hat{f}$.

In order to solve the Usadel equation for arbitrary magnetic fields, we first define

$$\hat{u} = \exp\left(-2ie\hat{\rho}_3 \int_{-L/2}^x A(x', y) dx'\right)\hat{f}. \quad (17)$$

With this, the Usadel equation can be written

$$D\hat{\rho}_3\nabla^2\hat{u} + 2i\hat{\Sigma}\hat{u} - 2Die\hat{\rho}_3\hat{u} \int_{-L/2}^x \frac{\partial B}{\partial y} dx' - 4De^2\hat{u} \left(\int_{-L/2}^x B dx'\right)^2 - 4Die \frac{\partial \hat{u}}{\partial y} \int_{-L/2}^x B dx' = 0, \quad (18)$$

where we have defined $B \equiv B_z = -\partial A/\partial y$ as the magnetic field component orthogonal to the graphene. We can neglect the terms involving B by assuming that the magnetic field is sufficiently weak. That is, for all $x \in (-L/2, L/2)$,

$$\int_{-L/2}^x B dx' \ll \Phi_0 \sqrt{\frac{\delta}{D}}, \quad (19a)$$

and

$$\int_{-L/2}^x \frac{\partial B}{\partial y} dx' \ll \frac{\Phi_0 \delta}{D}, \quad (19b)$$

where $\Phi_0 = \pi/e$ is the magnetic flux quantum.

The boundary conditions for \hat{u} at $y = \pm W/2$ is

$$\frac{\partial \hat{u}}{\partial y} \Big|_{y=\pm W/2} = -i\hat{u} \int_{-L/2}^x B dx'. \quad (20)$$

Equations (16), (18), and (20) can be solved exactly when $B = 0$ by assuming $\partial^2 \hat{u}/\partial y^2 = 0$. For B satisfying Eq. (19) we can find an approximate solution by neglecting the term $\partial^2 \hat{u}/\partial y^2$ in Eq. (18).

With these approximations, the Usadel equation becomes an ordinary differential equation,

$$\frac{\partial^2 \hat{u}}{\partial x^2} + \frac{2i\hat{\rho}_3\hat{\Sigma}}{D}\hat{u} = 0, \quad (21)$$

with solution

$$\hat{u} = e^{\hat{k}x}\hat{A} + e^{-\hat{k}x}\hat{B}, \quad (22)$$

for some coefficients \hat{A} and \hat{B} . Here

$$\hat{k} = \sqrt{-\frac{2i\hat{\rho}_3\hat{\Sigma}}{D}}, \quad (23)$$

which, since $\hat{\rho}_3\hat{\Sigma}$ is diagonal, \hat{k} can be obtained simply by taking the elementwise square root. To determine \hat{A} and \hat{B} one must use Eq. (16). The solution is

$$\hat{u} = [(\zeta L\hat{k} + \hat{\rho}_3\hat{g}_s)^2 e^{\hat{k}L} - (\zeta L\hat{k} - \hat{\rho}_3\hat{g}_s)^2 e^{-\hat{k}L}]^{-1} \times [\hat{p}(x) + e^{i\hat{\rho}_3\theta} \hat{p}(-x)]\hat{f}_s, \quad (24)$$

where

$$\theta = \phi_r - \phi_l - 2e \int_{-L/2}^{L/2} A(x, y) dx \quad (25)$$

and

$$\hat{p}(x) = (\zeta L\hat{k} + \hat{\rho}_3\hat{g}_s)e^{\hat{k}(x-L/2)} + (\zeta L\hat{k} - \hat{\rho}_3\hat{g}_s)e^{-\hat{k}(x-L/2)}. \quad (26)$$

Note that the boundary condition for the interfaces with vacuum, Eq. (20), is only approximately satisfied.

To find the current from Eq. (24) we can use that the x component of the current, as given by Eq. (9), can be written

$$\mathbf{j} \cdot \hat{\mathbf{x}} = \frac{N_0 e D}{4} \int_{-\infty}^{\infty} \text{Tr} \left(\hat{\rho}_3 \hat{u} \frac{\partial \hat{u}}{\partial x} - \hat{u}^\dagger \frac{\partial \hat{u}^\dagger}{\partial x} \hat{\rho}_3 \right) \tanh\left(\frac{\beta \varepsilon}{2}\right) d\varepsilon. \quad (27)$$

To simplify this expression, note that Eq. (24) can be written

$$\hat{u} = \begin{pmatrix} & & d(h)e^{i\phi_l} \\ & -d(-h)e^{-i\phi_l} & \\ \tilde{d}(-h)e^{-i\phi_l} & & \end{pmatrix} \quad (28)$$

where

$$d(h) = \frac{[p(x) + e^{i\theta} p(-x)]|\Delta|/\sqrt{(\varepsilon + i\delta)^2 - |\Delta|^2}}{[(\zeta Lk + g_s)^2 e^{kL} - (\zeta Lk - g_s)^2 e^{-kL}]} \quad (29)$$

with $g_s = (\varepsilon + i\delta)/\sqrt{(\varepsilon + i\delta)^2 - |\Delta|^2}$; the square roots are those which have positive imaginary parts, $k =$

$\sqrt{-2i(\varepsilon + h + i\delta)/D}$ and

$$p(x) = (\zeta Lk + g_s)e^{k(x-L/2)} + (\zeta Lk - g_s)e^{-k(x-L/2)}. \quad (30)$$

Inserting Eq. (29) into Eq. (27) gives

$$\mathbf{j} \cdot \hat{\mathbf{x}} = N_0 e D \int_{-\infty}^{\infty} \Re \left[d(h) \frac{\partial \tilde{d}(-h)}{\partial x} + d(-h) \frac{\partial \tilde{d}(h)}{\partial x} \right] \times \tanh\left(\frac{\beta \varepsilon}{2}\right) d\varepsilon. \quad (31)$$

$$\kappa_{\pm} = \frac{4|\Delta|^2 k_{\pm}}{(\varepsilon + i\delta)^2 - |\Delta|^2} \times \frac{[\zeta Lk_{\pm} \cosh(k_{\pm}L/2) - g_s \sinh(k_{\pm}L/2)] \times [g_s \cosh(k_{\pm}L/2) - \zeta Lk_{\pm} \sinh(k_{\pm}L/2)]}{[(\zeta Lk_{\pm} + g_s)^2 e^{k_{\pm}L} - (\zeta Lk_{\pm} - g_s)^2 e^{-k_{\pm}L}]^2}, \quad (34)$$

with $k_{\pm} = \sqrt{-2i(\varepsilon \pm h + i\delta)/D}$.

Equation (33) is our main analytical result and allows for evaluation of the current at arbitrary exchange field strengths and magnetic field distributions. Of particular interest is the fact that the contributions from the vector potential and exchange field decouple. One consequence of this is that a constant magnetic field gives rise to a Fraunhofer pattern in the current regardless of the strength of the exchange field, as long as the magnetic field is weak enough. This can be seen from the fact that for a constant magnetic field $eA = -\pi \Phi_{\perp} y / \Phi_0 W L$, where Φ_{\perp} is the magnetic flux from the perpendicular field, so

$$I \propto \int_{-W/2}^{W/2} \sin\left(\phi_r - \phi_l + 2\pi \frac{\Phi_{\perp} y}{\Phi_0 W}\right) dy = W \sin(\phi_r - \phi_l) \frac{\sin(\pi \Phi_{\perp} / \Phi_0)}{\pi \Phi_{\perp} / \Phi_0}. \quad (35)$$

Figure 2 shows the critical current found analytically using Eq. (33) for the case of no ripples, compared to the critical current obtained numerically from the full nonlinear Usadel equation. In addition to showing the agreement between the full solution and the analytical approximation, Fig. 2 also shows that there is an exchange-driven $0-\pi$ transition at $h \approx$

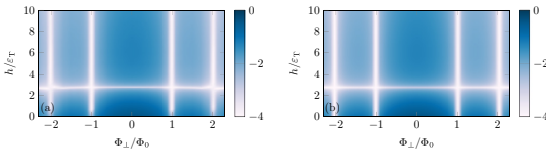


FIG. 2. Color plot of $\log_{10}(I_c/I_0)$, where I_c is the critical current and $I_0 = N_0 e W D^2 / L^3$ for various exchange fields h and out-of-plane magnetic fluxes. (a) shows the solution found numerically from the full Usadel equation, and (b) shows the analytical solution found using Eq. (33). Here, $\varepsilon_T = D/L^2$, $W = 10L$, $L = 6\xi$, $\delta/\Delta = 0.01$, and $B_x = B_y = 0$.

By evaluating \mathbf{j} at $x = 0$ we can factorize out the dependence on the vector potential, since

$$\left. \frac{\partial \tilde{d}(h)}{\partial x} \right|_{x=0} = -\frac{2i \sin \theta}{1 + e^{i\theta}} \times \left. \frac{\partial \ln p}{\partial x} d(-h) \right|_{x=0}. \quad (32)$$

Inserting this into Eq. (31) and integrating the current density over y to obtain the total current finally gives

$$I = 2N_0 e D \int_{-W/2}^{W/2} \sin\left(\phi_r - \phi_l - 2e \int_{-L/2}^{L/2} A(x, y) dx\right) dy \times \int_{-\infty}^{\infty} \Im[\kappa_+ + \kappa_-] \tanh\left(\frac{\beta \varepsilon}{2}\right) d\varepsilon, \quad (33)$$

where

$2\varepsilon_T$, where

$$\varepsilon_T = \frac{D}{L^2} \quad (36)$$

is the Thouless energy.

Since the contribution from the exchange field is independent of the vector potential, we can focus on how the magnetic field alters the critical current. With the vector potential given by Eq. (5), we get

$$\int_{L/2}^{L/2} A(x, y) dx = B_y L \bar{\eta}(y) - \Phi_{\perp} \frac{y}{W} + B_x \int_0^y [\eta(L/2, \bar{y}) - \eta(-L/2, \bar{y})] d\bar{y}, \quad (37)$$

where

$$\bar{\eta}(y) = \frac{1}{L} \int_{-L/2}^{L/2} \eta(x, y) dx \quad (38)$$

is the longitudinally averaged height. From Eq. (37) it can be observed that the contribution proportional to B_x is small for variations that are fast in the y direction, since the integrand will oscillate rapidly, and small for very slow variations, which will contribute little to $\eta(L/2, y) - \eta(-L/2, y)$. Similarly, variations that are fast in the x direction will contribute little to the term proportional to B_y . Otherwise, the contributions from the terms proportional to B_y and B_x is similar, so we set $B_x = 0$ in the following. We also set $\beta = 1000/\Delta$, corresponding to $T/T_c \approx 1.8 \times 10^{-3}$, where T_c is the critical temperature.

From Eqs. (33) and (37) we can find how big the height variations must be in order to possibly cause a vanishing critical current at $\Phi_{\perp} = 0$. In order for the critical current to vanish, the argument of the sine function in Eq. (33) must have variations of at least $\pi/2$. Otherwise, the phase difference, $\phi_r - \phi_l$, can be chosen such that the integrand is of one sign. This means that in order for there to be a root in the critical

current at $\Phi_{\perp} = 0$, the in-plane magnetic field must be at least

$$B_y = \frac{\Phi_0}{4L(\max \bar{\eta} - \min \bar{\eta})}, \quad (39)$$

assuming $B_x = 0$.

In order to apply Eq. (33) to the case of rippled graphene with vector potential given by Eq. (5), we need a model of the height distribution η of the ripples. From Eq. (37) we find that it is reasonable to categorize ripples into short ripples and long ripples, depending on whether the wavelength is shorter or longer than $2L$. Ripples with wavelength shorter than $2L$ will have a smaller contribution to $\bar{\eta}$ in Eq. (37) since the integrand oscillates between positive and negative values. For this reason, short ripples will contribute less to interference effects than long ripples with the same amplitude. On the other hand, faster variations in the y direction gives a larger magnetic field component perpendicular to the graphene surface and therefore a larger depairing effect. Short ripples are therefore expected to lead to larger deviations from the analytical approximation given by Eq. (33). In particular, they are expected to cause a faster decay, which, as we will see, is also what happens.

In general, the height distribution will be a superposition of long and short ripples. We look first at only long ripples, then at only short ripples, and finally at the combination of both short and long ripples. In order to simplify the presentation and analysis, we present solutions for height distributions that can be written as the product of cosines. We obtain qualitatively similar result for more realistic, randomized height distributions.

To model n uniform ripples in the x direction and m uniform ripples in the y direction, we use the height distribution

$$\eta(x, y) = \frac{\eta_0}{2} \cos\left(n\pi \frac{x}{L}\right) \cos\left(m\pi \frac{y}{W}\right), \quad (40)$$

where η_0 is the peak-to-peak height difference. Figures 3–5 show the critical current, given by Eq. (10), for the height distribution in Eq. (40) with $n = 1$ and $m = 2$, $m = 5$ and $m = 10$, respectively. The exchange field, h , is set to zero in order to isolate the orbital effect, such that it can be observed whether the orbital effect alone is sufficient to produce roots in the critical current. Physically, the situation with negligible exchange field would be the case if the Thouless energy, ε_T , is much larger than the Zeeman splitting $\mu_B B_y$, where μ_B is the Bohr magneton.

It can be seen from Figs. 3–5 that a height variation of only 1 nm is sufficient to produce oscillations in the critical current. In particular, the critical current is zero for $\Phi_{\perp} = 0$ and finite B_y when $m = 2$ and $m = 10$. Both zeros satisfy Eq. (39), which is $B_y = 2$ T in this case. We can conclude from this that a zero in the critical current of an SGS junction is not sufficient to identify an exchange-driven $0-\pi$ transition, since zeros can also be produced from the ripples.

Since the junction widths are equal in Figs. 3–5, larger m means a larger orthogonal component from the in-plane magnet field. Consequently, the magnetic field strengths for which the weak field assumption, Eq. (19), remains valid is reduced when m increases. This is reflected in the correspon-

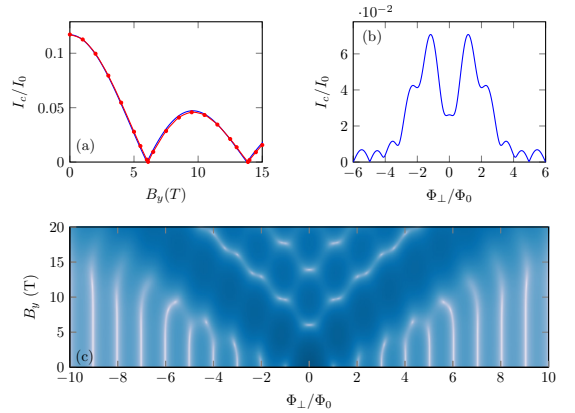


FIG. 3. Critical current I_c for various in-plane magnetic field strengths B_y and out-of-plane magnetic fluxes Φ_{\perp} for the height distribution given by Eq. (40) with $n = 1$ and $m = 2$. Here, $I_0 = N_0 e W D^2 / L^3$, $W = 10L$, $L = 10\xi = 400$ nm, $\eta_0 = 1$ nm, $\delta/\Delta = 0.02$, and $B_x = 0$. (a) shows the analytical solution of I_c against B_y for $\Phi_{\perp} = 0$ (blue line), compared to the numerical solution (red dots). (b) shows the analytical solution of I_c against Φ_{\perp} for $B_y = 5$ T and (c) shows a logarithmically scaled color plot of analytical I_c where white means zero current and deep blue corresponds to large current.

dence between the numerical simulations and the analytical predictions.

The color plots in Figs. 3–5(c) show that the critical current has especially large maxima at $\Phi_{\perp}/\Phi_0 = km/2$ for integer k . This is also reflected in Figs. 3–5(b), which show that the lobe structure has strong maxima at $\Phi_{\perp}/\Phi_0 = m/2$. To understand why, note that the orbital part of the current can be written as a Fourier transform. That is,

$$\begin{aligned} I &= C(h) \int_{-W/2}^{W/2} \sin\left(\phi_l - \phi_r + 2\pi \frac{B_y L \bar{\eta}}{\Phi_0} - 2\pi \frac{\Phi_{\perp} y}{\Phi_0 W}\right) dy \\ &= C(h) \Im \left\{ e^{i(\phi_l - \phi_r)} \int_{-W/2}^{W/2} \exp\left[2\pi i \left(\frac{B_y L \bar{\eta}}{\Phi_0} - \frac{\Phi_{\perp} y}{\Phi_0 W}\right)\right] dy \right\}, \end{aligned} \quad (41)$$

where C is a function of the exchange field. Hence, the critical current can be written as

$$I_c = C(h) \left| \mathcal{F} \left[\text{rect}(y/W) e^{2\pi i B_y L \bar{\eta} / \Phi_0} \right] \left(\frac{2\pi \Phi_{\perp}}{W \Phi_0} \right) \right|, \quad (42)$$

where rect is the rectangular function and \mathcal{F} means Fourier transform. Accordingly, a Fourier analysis of the current response to out-of-plane magnetic fields can uncover properties of the ripple structure. In this case, $\bar{\eta}$ is a cosine with wave number $m\pi/W$, so it is reasonable that the Fourier transform peaks at $2\pi \Phi_{\perp} / W \Phi_0 = km\pi/W$ with strengths that depends on B_y . For a more general ripple structure, mapping out the current response to both the in-plane and out-of-plane one could uncover information about the slow height variations that can be difficult to detect with surface probe techniques.

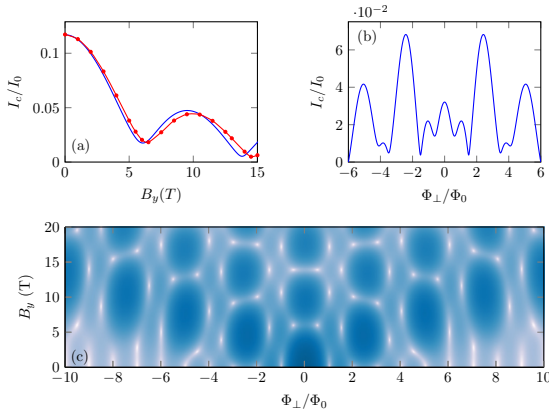


FIG. 4. Critical current I_c for various in-plane magnetic field strengths B_y and out-of-plane magnetic fluxes Φ_\perp for the height distribution given by Eq. (40) with $n = 1$ and $m = 5$. Here, $I_0 = N_0 e W D^2 / L^3$, $W = 10L$, $L = 10\xi = 400$ nm, $\eta_0 = 1$ nm, $\delta/\Delta = 0.02$, and $B_x = 0$. (a) shows the analytical solution of I_c against B_y for $\Phi_\perp = 0$ (blue line), compared to the numerical solution (red dots). (b) shows the analytical solution of I_c against Φ_\perp for $B_y = 5$ T and (c) shows a logarithmically scaled color plot of analytical I_c where white means zero current and deep blue corresponds to large current.

Obtaining $\bar{\eta}$ from measurements of the critical current is complicated by the loss of the phase information of the Fourier transform in Eq. (42). One possible resolution is to obtain the current-phase relation, as has been done for ballistic graphene by use of a SQUID [39]. In this case, one could take advantage of the fact that the current for a given in-plane magnetic field is proportional to $\sin(\phi_l - \phi_r)\Re(F) + \cos(\phi_l - \phi_r)\Im(F)$, where F is the Fourier transform in Eq. (42). It would then in theory be straightforward to find the phase of F and compute its Fourier inverse. If the only available data is the critical current, one could look at the values of Φ_\perp that gives enhanced current upon application of in-plane magnetic field to extract the most prominent Fourier components of $\bar{\eta}$ or use the variational method to approximate the function $\bar{\eta}$ that solves Eq. (42). If one can also manipulate the direction of the in-plane magnetic field, one could combine the knowledge of $\bar{\eta}$ with the corresponding function relevant for when the field is in the x direction to get even more insight into the full ripple profile η .

Figures 3–5(a) also give clues to how the full solution of the Usadel equation deviates from Eq. (33) when the magnetic field is strong. Two things seem to happen when the flux density is strong. First, compared to the analytical solution, the full solution decays more rapidly as B_y increases. That the critical current decays faster than the analytical solution predicts is unsurprising, since we neglected the depairing effect of the magnetic field in our derivation of Eq. (33).

Second, the functional dependence on B_y is slower in the numerical case, in the sense that roots and extremal values in the critical current are skewed towards larger values of B_y . A plausible explanation for this phenomenon is that the full

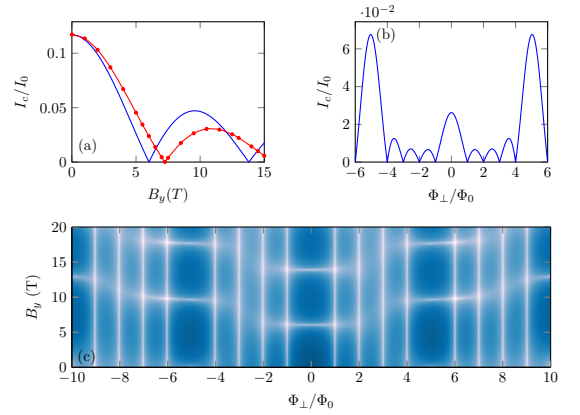


FIG. 5. Critical current I_c for various in-plane magnetic field strengths B_y and out-of-plane magnetic fluxes Φ_\perp for the height distribution given by Eq. (40) with $n = 1$ and $m = 10$. Here, $I_0 = N_0 e W D^2 / L^3$, $W = 10L$, $L = 10\xi = 400$ nm, $\eta_0 = 1$ nm, $\delta/\Delta = 0.02$, and $B_x = 0$. (a) shows the analytical solution of I_c against B_y for $\Phi_\perp = 0$ (blue line), compared to the numerical solution (red dots). (b) shows the analytical solution of I_c against Φ_\perp for $B_y = 5$ T and (c) shows a logarithmically scaled color plot of analytical I_c where white means zero current and deep blue corresponds to large current.

solution varies more slowly in the y -direction compared to the analytical approximation in Eq. (24). The analytical solution has $\partial \hat{f} / \partial y \propto B$, but it neglects the boundary condition that demands $\partial \hat{f} / \partial y = 0$ when $y = \pm W/2$. Hence, it is possible that the analytical solution overestimates the variation of f with respect to y , at least close to $y = \pm W/2$. The roots in the critical current occur because the magnetic field creates mutually canceling oscillations in the current density as a function of y . If the analytical approximation overestimates how fast these oscillations occur, it will underestimate the magnetic field required to give $I_c = 0$. The faster decay, but slower variation, is also exactly what happens in the case of uniform magnetic fields, as can be seen from Fig. 3 in Ref. [26].

Moving on to short ripples, Fig. 6 shows the critical current for the distribution given by Eq. (40) with $n = 11$, $m = 10$, and $\eta_0 = 1$ nm. With $L = 400$ nm, this corresponds to a ripple length of 40 nm, which is comparable to the short ripples observed in graphene on SiO_2 [22]. The exchange field is again set to 0. What matters for the analytical approximation is the longitudinally averaged height $\bar{\eta}$, which in this case is small because of the rapid oscillations. Hence, the analytical approximation predicts very little change in the critical current at $\Phi_\perp = 0$. On the other hand, the orbital depairing effect is quite large because of the short ripples, which is reflected in the decay of the critical current observed in the numerical solution of the full Usadel equations.

Finally, Fig. 7 shows the critical current for combinations of short and long ripples, both with and without a nonzero

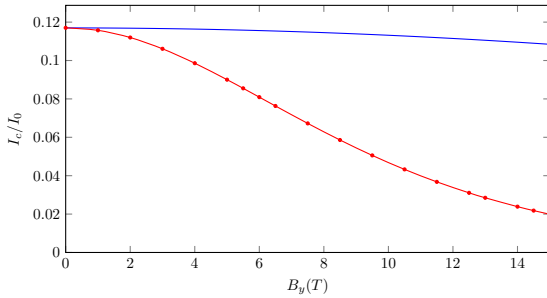


FIG. 6. Critical current I_c for $B_{\perp} = 0$ and various in-plane magnetic field strengths B_y with the height distribution given by Eq. (40) with $n = 11$ and $m = 10$. Here, $I_0 = N_0 e W D^2 / L^3$, $W = L = 10\xi = 400$ nm, $\eta_0 = 1$ nm, $\delta/\Delta = 0.02$, and $B_x = 0$. The blue line shows the analytical solution, as found by Eq. (33), and the red line with dots shows the numerical solution found by solving the full Usadel equation.

exchange field. The height distribution is in this case given by

$$\eta = 1 \text{ nm} \times \cos\left(2\pi \frac{y}{W}\right) + A \cos\left(n\pi \frac{x}{L}\right) \cos\left(n\pi \frac{y}{L}\right), \quad (43)$$

where $n = 4$ for “hBN” and “Large” and $n = 10$ for “SiO₂.” The amplitude of the short ripples are $A = 0.1$ nm, $A = 0.5$ nm, $A = 2$ nm for “hBN,” “SiO₂,” and “Large,” respec-

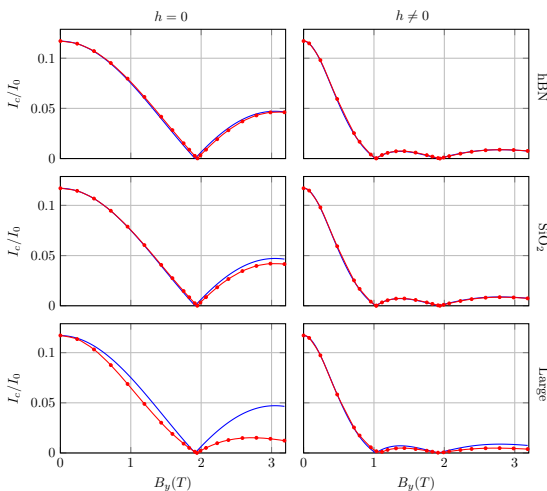


FIG. 7. Critical current I_c for $B_{\perp} = 0$ and various in-plane magnetic field strengths B_y with the height distribution given by Eq. (43) with $(A, N) = (0.1 \text{ nm}, 4)$, $(0.5 \text{ nm}, 10)$, and $(2 \text{ nm}, 4)$, respectively, from top to bottom. The exchange field is $h = 0$ in the left panels and $h = \mu_B B_y$ in the right panels, where μ_B is the Bohr magneton. Here, $I_0 = N_0 e W D^2 / L^3$, $W = 10L$, $L = 10\xi = 400$ nm, $\delta/\Delta = 0.02$, $\Delta = 1.5$ meV, and $B_x = 0$. The blue line shows the analytical solution, as found by Eq. (33), and the red line with dots shows the numerical solution found by solving the full Usadel equation.

tively. The values for “SiO₂” and “hBN” are chosen such that the short ripple sizes correspond to the observed values for SiO₂ and hBN [22]. The values for “Large” are chosen such that amplitudes of the short ripples are twice as large as the long ripples. In this case the orthogonal component of the magnetic field is much too high for the analytical solution to give accurate results.

Since n is even, the analytical solution given by Eq. (33) is equal for the three cases. The only difference is the magnitude of the additional magnetic flux density that comes from the short ripples. As mentioned above, we should expect a faster decay for larger and faster ripples. This is indeed also what we observe from the numerical results in Fig. 7. Interestingly, the location of the roots is not substantially altered by the short ripples. Even in the lowermost panels, where the short ripples are twice as large as the long ripples, the roots in the numerical solution occur not far from the values of B_y predicted by the analytical solution, even if the amplitude decays much faster.

Long ripples, as we have seen, can give rise to interference effects that produce oscillations and possibly roots in the critical current. Short ripples, on the other hand, increase the magnetic flux density and can lead to a substantial magnetic depairing effect, which manifest as a rapidly decaying critical current. Hence, the combined effect of short and long ripples can yield a rapidly decaying critical current with zeros, much like what one would expect from a ferromagnet undergoing a $0-\pi$ transition.

From Fig. 7 it can also be observed that the deviation between the analytical and numerical solutions is smaller when the exchange field is nonzero. This is as expected, since neglecting the contribution from B in Eq. (18) is a better approximation when the self-energy $\hat{\Sigma}$ is larger. Note that in Fig. 7, the presence of the exchange field induces a $0-\pi$ transition around $B_y = 1$ T, which manifests as a root in the critical current.

Since the ripples and the exchange field both give rise to oscillating and decaying critical currents, it is useful to determine whether a $0-\pi$ transition is expected to occur before or after a possible zero in the critical current coming from ripples. The exact values of B_y at which these events take place will in general depend on several parameters, but we can give some order of magnitude estimates based on Eq. (33) and numerical simulations. The first $0-\pi$ transition typically occurs around $h = 2\varepsilon_T$ but can occur at larger values if the inelastic scattering time $1/\delta$ is small. Inserting the definition of the Thouless energy ε_T and using that $h = \mu_B B_y$, this means that the Zeeman driven $0-\pi$ transition occurs at

$$B_y \approx \frac{2D}{\mu_B L^2}. \quad (44)$$

Equation (39) gives a minimal value for B_y at which a zero can be produced from the interference effect that is due to ripples. In the numerical result presented here, we see that the zero occurs for a value of B_y that is about three times larger. An order of magnitude estimate is that, for long ripples with peak-to-peak height of η_0 , the first zero in the critical current can occur at around

$$B_y \approx \frac{\Phi_0}{\eta_0 L}. \quad (45)$$

Notice that Eqs. (44) and (45) scales differently with junction length L . Therefore, it is more plausible that an observed zero in the critical current correspond to a $0-\pi$ transition when the junction is long. Alternatively, one could try to limit the presence of variations in the y -direction that are longer than L by making $W \ll L$.

From Figs. 3–5 we also observe that the ripples can substantially alter the Fraunhofer lobe structure found when varying B_{\perp} , while Fig. 2 shows that the Fraunhofer pattern is unaltered when the effect of ripples is negligible. Hence, investigating how I_c depends on B_{\perp} could also be useful when identifying $0-\pi$ transitions. As long as the junction width and diffusivity are approximately constant, a $0-\pi$ transition will give rise to a vanishing critical current for all values of out-of-plane magnetic flux densities B_{\perp} . If in addition the effect of ripples is small, one should expect that the critical current as a function of B_{\perp} is a Fraunhofer pattern at any constant value of the in-plane magnetic field B_{\parallel} . Accordingly, determining whether the minima in critical current as a function of B_{\perp} and B_{\parallel} are straight lines, as in Fig. 2, or curved, as in Figs. 3–5, can give clues as to whether ripples are important. If ripples are important, Eq. (42) could give insight to their structure.

IV. CONCLUSION

We have solved the Usadel equation analytically in the presence of an exchange field and an arbitrary magnetic field distribution, under the assumption of a weak proximity effect and a weak magnetic field. The solution has been applied to SGS junctions with the combined Zeeman effect and orbital effect coming from an in-plane magnetic field. Deviations from the analytical solution at large magnetic fields have been studied numerically. We find that the orbital effect that results from a curvature in the graphene can produce a critical current

response that is similar to what one would get by increasing the exchange field. Slow variations in the graphene height distributions give rise to interference effects that produce oscillations in the critical current, while rapid variations cause larger orbital depairing effects that lead to a faster critical current decay rate.

Since both the Zeeman splitting and orbital effects in rippled graphene can cause similar behavior, extra care must be taken when identifying possible $0-\pi$ transitions. The interference effect from ripples is reduced if the width of the junction is much smaller than the length. In addition to reducing the relative effect of ripples compared to the Zeeman splitting, which is achieved by increasing the length of the junction and minimizing the height variations, it could also be useful to look at how the critical current varies with a perpendicular magnetic field. The effect of ripples, if present, will then typically alter the Fraunhofer pattern observed at zero in-plane magnetic field. Because slow height variations are difficult to detect using surface probe techniques, we suggest the use of parallel magnetic field as a means to probe the presence of such variations.

ACKNOWLEDGMENTS

This work was supported by the Research Council of Norway through Grant No. 240806, and its Centres of Excellence funding scheme Grant No. 262633 “*QuSpin*.” J.L. and M.A. also acknowledge funding from the NV faculty at the Norwegian University of Science and Technology. H.S. is funded by a European Research Council Starting Grant (No. 637298, TUNNEL), and Israeli Science Foundation Grant No. 861/19. T.D. and A.Z. are grateful to the Azrieli Foundation for Azrieli Fellowships.

-
- [1] M. Eschrig, *Rep. Prog. Phys.* **78**, 104501 (2015).
 - [2] J. Linder and J. W. A. Robinson, *Nat. Phys.* **11**, 307 (2015).
 - [3] G.-H. Lee and H.-J. Lee, *Rep. Prog. Phys.* **81**, 056502 (2018).
 - [4] P. Kumaravdivel and X. Du, *Sci. Rep.* **6**, 24274 (2016).
 - [5] U. C. Coskun, M. Brenner, T. Hymel, V. Vakaryuk, A. Levchenko, and A. Bezryadin, *Phys. Rev. Lett.* **108**, 097003 (2012).
 - [6] K. Komatsu, C. Li, S. Autier-Laurent, H. Bouchiat, and S. Guéron, *Phys. Rev. B* **86**, 115412 (2012).
 - [7] H. B. Heersche, P. Jarillo-Herrero, J. B. Oostinga, L. M. K. Vandersypen, and A. F. Morpurgo, *Nature (London)* **446**, 56 (2007).
 - [8] F. Amet, C. T. Ke, I. V. Borzenets, J. Wang, K. Watanabe, T. Taniguchi, R. S. Deacon, M. Yamamoto, Y. Bomze, S. Tarucha, and G. Finkelstein, *Science* **352**, 966 (2016).
 - [9] J. Liu, H. Liu, J. Song, Q.-F. Sun, and X. C. Xie, *Phys. Rev. B* **96**, 045401 (2017).
 - [10] P. Fulde and R. A. Ferrell, *Phys. Rev.* **135**, A550 (1964).
 - [11] A. I. Larkin and Y. N. Ovchinnikov, *Sov. Phys. JETP* **20**, 762 (1965).
 - [12] A. I. Buzdin, *Rev. Mod. Phys.* **77**, 935 (2005).
 - [13] G. Blatter, V. B. Geshkenbein, and L. B. Ioffe, *Phys. Rev. B* **63**, 174511 (2001).
 - [14] T. Yamashita, K. Tanikawa, S. Takahashi, and S. Maekawa, *Phys. Rev. Lett.* **95**, 097001 (2005).
 - [15] M. I. Khabipov, D. V. Balashov, F. Maibaum, A. B. Zorin, V. A. Oboznov, V. V. Bolginov, A. N. Rossolenko, and V. V. Ryazanov, *Supercond. Sci. Technol.* **23**, 045032 (2010).
 - [16] A. K. Feofanov, V. A. Oboznov, V. V. Bol’ginov, J. Lisenfeld, S. Poletto, V. V. Ryazanov, A. N. Rossolenko, M. Khabipov, D. Balashov, A. B. Zorin, V. P. K. P. N. Dmitriev, and A. V. Ustinov, *Nat. Phys.* **6**, 593 (2010).
 - [17] A. V. Ustinov and V. K. Kaplunenko, *J. Appl. Phys.* **94**, 5405 (2003).
 - [18] E. C. Gingrich, B. M. Niedzielski, J. A. Glick, Y. Wang, D. L. Miller, R. Loloee, W. P. P. Jr, and N. O. Birge, *Nat. Phys.* **12**, 564 (2016).
 - [19] V. A. Oboznov, V. V. Bol’ginov, A. K. Feofanov, V. V. Ryazanov, and A. I. Buzdin, *Phys. Rev. Lett.* **96**, 197003 (2006).
 - [20] N. G. Pugach, M. Y. Kupriyanov, A. V. Vedyayev, C. Lacroix, E. Goldobin, D. Koelle, R. Kleiner, and A. S. Sidorenko, *Phys. Rev. B* **80**, 134516 (2009).

- [21] C. Li, B. de Ronde, J. de Boer, J. Ridderbos, F. Zwanenburg, Y. Huang, A. Golubov, and A. Brinkman, *Phys. Rev. Lett.* **123**, 026802 (2019).
- [22] J. Xue, J. Sanchez-Yamagishi, D. Bulmash, P. Jacquod, A. Deshpande, K. Watanabe, T. Taniguchi, P. Jarillo-Herrero, and B. J. LeRoy, *Nat. Mater.* **10**, 282 (2011).
- [23] M. B. Lundeberg and J. A. Folk, *Phys. Rev. Lett.* **105**, 146804 (2010).
- [24] S. Zihlmann, P. Makk, M. K. Rehm, L. Wang, M. Kedves, D. Indolese, K. Watanabe, T. Taniguchi, D. M. Zumbühl, and C. Schönenberger, [arXiv:2004.02690](https://arxiv.org/abs/2004.02690).
- [25] C. T. Ke, I. V. Borzenets, A. W. Draelos, F. Amet, Y. Bomze, G. Jones, M. Craciun, S. Russo, M. Yamamoto, S. Tarucha, and G. Finkelstein, *Nano Lett.* **16**, 4788 (2016).
- [26] F. Bergeret and J. Cuevas, *J. Low Temp. Phys.* **153**, 304 (2008).
- [27] K. D. Usadel, *Phys. Rev. Lett.* **25**, 507 (1970).
- [28] J. Rammer and H. Smith, *Rev. Mod. Phys.* **58**, 323 (1986).
- [29] S. Hart, H. Ren, M. Kosowsky, G. Ben-Shach, P. Leubner, C. Brüne, H. Buhmann, L. W. Molenkamp, B. I. Halperin, and A. Yacoby, *Nat. Phys.* **13**, 87 (2017).
- [30] A. Q. Chen, M. J. Park, S. T. Gill, Y. Xiao, D. Reig-i Plessis, G. J. MacDougall, M. J. Gilbert, and N. Mason, *Nat. Commun.* **9**, 1 (2018).
- [31] C. Li, S. Guéron, A. Chepelianskii, and H. Bouchiat, *Phys. Rev. B* **94**, 115405 (2016).
- [32] J.-S. Jeong, J. Shin, and H.-W. Lee, *Phys. Rev. B* **84**, 195457 (2011).
- [33] M. Yu. Kuprianov and V. F. Lukichev, *Zh. Eksp. Teor. Fiz.* **94**, 139 (1988).
- [34] E. H. Fyhn and J. Linder, *Phys. Rev. B* **100**, 214503 (2019).
- [35] W. Belzig, F. K. Wilhelm, C. Bruder, G. Schön, and A. D. Zaikin, *Superlattices Microstruct.* **25**, 1251 (1999).
- [36] M. Amundsen and J. Linder, *Sci. Rep.* **6**, 22765 (2016).
- [37] R. Burden and J. Faires, *Numerical Analysis* (Brooks/Cole, Cengage Learning, Boston, MA, 2011).
- [38] J. Revels, M. Lubin, and T. Papamarkou, [arXiv:1607.07892](https://arxiv.org/abs/1607.07892).
- [39] G. Nanda, J. L. Aguilera-Servin, P. Rakyta, A. Kormányos, R. Kleiner, D. Koelle, K. Watanabe, T. Taniguchi, L. M. K. Vandersypen, and S. Goswami, *Nano Lett.* **17**, 3396 (2017).

PAPER IV

Reference

Tom Dvir, Ayelet Zalic, Eirik Holm Fyhn, Morten Amundsen, Takashi Taniguchi, Kenji Watanabe, Jacob Linder, and Hadar Steinberg,

Planar graphene-NbSe₂ Josephson junctions in a parallel magnetic field.

Physical Review B **103**, 115401 (2021)

doi: 10.1103/physrevb.103.115401

CONTRIBUTIONS

AZ, TD and HS formulated the initial overarching research goal, wrote the initial manuscript, acquired the experimental data, designed and implemented the experimental analysis. TT and KW provided the hBN. EHF performed the analytical calculations and the numerical simulations based on the Green's function formalism, with support from JL and MA. All authors contributed to the physics discussions and the final manuscript revision. Specifically, in addition to participating in the discussion of the physics and the revision of the final manuscript, EHF developed the theoretical model, developed the code, performed the numerical simulations and produced figure 5, which shows the theoretical results.

Planar graphene-NbSe₂ Josephson junctions in a parallel magnetic field

Tom Dvir^{1,*}, Ayelet Zalic^{1,*}, Eirik Holm Fyhn², Morten Amundsen², Takashi Taniguchi³, Kenji Watanabe⁴,
Jacob Linder² and Hadar Steinberg¹

¹The Racah Institute of Physics, The Hebrew University of Jerusalem, Jerusalem 91904, Israel

²Center for Quantum Spintronics, Department of Physics, Norwegian University of Science and Technology, NO-7491 Trondheim, Norway

³International Center for Materials Nanoarchitectonics, National Institute for Materials Science, 1-1 Namiki, Tsukuba 305-0044, Japan

⁴Research Center for Functional Materials, National Institute for Materials Science, 1-1 Namiki, Tsukuba 305-0044, Japan



(Received 9 August 2020; revised 26 January 2021; accepted 28 January 2021; published 2 March 2021)

Thin transition metal dichalcogenides sustain superconductivity at large in-plane magnetic fields due to Ising spin-orbit protection, which locks their spins in an out-of-plane orientation. Here we use thin NbSe₂ as superconducting electrodes laterally coupled to graphene, making a planar, all van der Waals two-dimensional Josephson junction (2DJJ). We map out the behavior of these novel devices with respect to temperature, gate voltage, and both out-of-plane and in-plane magnetic fields. Notably, the 2DJJs sustain supercurrent up to parallel fields as high as 8.5 T, where the Zeeman energy E_Z rivals the Thouless energy E_{Th} , a regime hitherto inaccessible in graphene. As the parallel magnetic field H_{\parallel} increases, the 2DJJ's critical current is suppressed and in a few cases undergoes suppression and recovery. We explore the behavior in H_{\parallel} by considering theoretically two effects: a $0-\pi$ transition induced by tuning of the Zeeman energy and the unique effect of ripples in an atomically thin layer which create a small spatially varying perpendicular component of the field. The 2DJJs have potential utility as flexible probes for two-dimensional superconductivity in a variety of materials and introduce high H_{\parallel} as a newly accessible experimental knob.

DOI: [10.1103/PhysRevB.103.115401](https://doi.org/10.1103/PhysRevB.103.115401)

I. INTRODUCTION

By coupling graphene to exfoliated superconductors such as NbSe₂ [1–3] it is possible to realize Josephson junctions where both the normal and superconductor materials are two-dimensional (2D). Such junctions should sustain high in-plane magnetic fields. Thin NbSe₂ retains superconductivity at very high in-plane fields due to a combination of suppressed orbital depairing and Ising protection against pair breaking [4,5] and can sustain magnetic fields above 8 T without any measurable effect on the gap size [4,6]. Coupling graphene to two NbSe₂ flakes results in an all van der Waals two-dimensional Josephson junction (2DJJ). The response of such 2DJJs to in-plane magnetic field will be dictated by both spin and orbital effects. In the graphene layer, forming the weak link, the response of carrier spins to the Zeeman field may lead to interesting phenomena such as finite-momentum Cooper pairing and a $0-\pi$ transition [7–10]. However, the deviation of such devices from the ideal 2D geometry due to ripples and other deformations is significant, as it gives rise to field components perpendicular to the local sample plane, introducing orbital dephasing. The latter also occurs due to the bending of magnetic field flux lines, which cannot be considered truly parallel, as they are deflected by superconducting leads [11].

Two-dimensional Josephson devices are a useful platform for the study of finite-momentum superconducting states: Cooper pairs may survive in the spin-polarized Fermi surface

created at high magnetic fields by attaining a finite center-of-mass momentum [12,13], which translates into a spatially varying order parameter. Finite Cooper-pair momentum $q = 2E_Z/\hbar v_F$ is dictated by the Zeeman energy $E_Z = 0.5g\mu_B H$, where g is the Landé factor, v_F is the Fermi velocity, and μ_B is the Bohr magneton. The resulting oscillation of the order parameter within the junction can create π -phase junctions, where the transition to the π phase is found in junction lengths L determined by the multiples of π/q . Weak links characterized by large g factors have shown signatures of finite-momentum Cooper pairing [14] and allowed the realization of tunable Zeeman-driven $0-\pi$ transitions [15–17]. Graphene should also exhibit a Zeeman-driven $0-\pi$ transition [7–10]. However, reaching this transition requires the application of high magnetic fields due to the low g factor which limits the momentum shift of the Cooper pair. Ballistic graphene is uniquely expected to produce field-tunable switching between 0 and π phases while retaining a finite critical current [7] and is expected to exhibit triplet superconductivity [18].

However, the entirely 2D nature of the graphene sheet gives rise to a unique form of disorder due to graphene ripples in the third dimension. In the presence of applied H_{\parallel} this introduces a small component of perpendicular field with a disorderly spatial variation created by the ripple pattern. This effect can lead to critical current decay with parallel field, a non-Fraunhofer interference pattern, and suppression and recovery of the critical current mimicking a $0-\pi$ transition. The effect of ripples changes depending on ripple amplitude and wavelength and junction dimensions [19]. Thus, in any

*These authors contributed equally to this work.

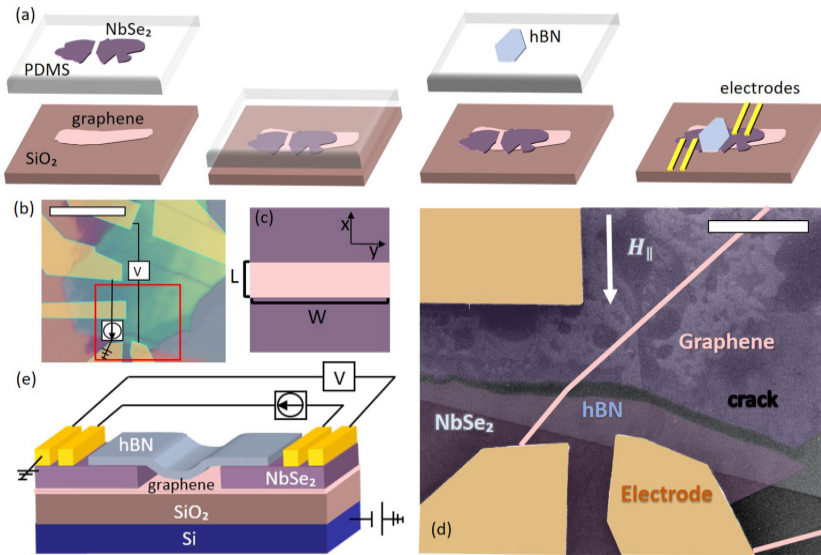


FIG. 1. (a) Fabrication of planar graphene-NbSe₂ JJs involves (1) exfoliation of graphene on SiO₂ and NbSe₂ on PDMS, (2) stamping a cracked NbSe₂ flake onto graphene, (3) stamping a thin hBN flake for encapsulation of the crack, (4) and patterning of electrodes. Steps are illustrated from left to right. (b) Optical image of junction A with schematics of current flow. NbSe₂ thickness is around 10 nm. Scale bar is 10 μm. (c) Illustration of a rectangular junction geometry. (d) A false-color SEM image of the region marked by a red square in (b), showing the actual junction geometry, with the graphene flake contour highlighted and the direction of H_{\parallel} indicated. Scale bar is 2 μm. (e) Schematic illustration of the JJ in a four-probe electronic configuration. Current flows in plane from NbSe₂ to graphene to NbSe₂. The crack is shielded from the top by hBN. Gate voltage is applied across the SiO₂ dielectric.

experiment involving graphene in a parallel field—or, indeed, we believe any 2D conductor in a parallel field—this effect should be considered. The morphology and effect of ripples are expected to change depending on the substrate and thickness of the 2D layer. Due to the high parallel fields sustained by the junction, our 2DJJ is sensitive to both long- and short-wavelength submilliradian curvature and subnanometer height variation in graphene.

We study planar NbSe₂-graphene-NbSe₂ junctions, fabricated by transferring cracked NbSe₂ on exfoliated graphene (see Fig. 1 and detailed information in the Supplemental Material, Sec. 4 [20]). The thickness of the NbSe₂ flakes used for the devices in this paper was around 5–10 nm, evaluated by optical contrast. The junctions exhibit supercurrent characteristics which are similar to diffusive graphene-based devices fabricated using evaporated superconducting electrodes, including gate-tunable critical current and a Fraunhofer-like interference in out-of-plane field [21–25]. Upon application of in-plane field, the 2DJJ critical current undergoes exponential suppression and transitions from a Fraunhofer to superconducting quantum interference device (SQUID)-like interference pattern, which is retained as the field is further increased up to 8.5 T. We focus our paper on junction A, with NbSe₂ thickness of around 10 nm and a weak link consisting of monolayer graphene. In this device we find that the supercurrent exhibits a pronounced suppression-recovery pattern, a feature which may be associated either with a $0-\pi$ transition or with the effect of graphene ripples.

II. TRANSPORT MEASUREMENTS

We begin by characterizing the transport of a 2DJJ. Figure 2(a) shows the typical current-voltage characteristics of junction A, where the I - V curves at different gate voltages exhibit a switching behavior between zero resistance and finite resistance at the junction switching current I_C . Typical of density-tunable graphene JJs [21], I_C is modulated by the gate voltage V_G and reaches a minimal, yet finite, value of $I_C \approx 0.4 \mu\text{A}$ at the Dirac point $V_G = -4$ V. This is evident in Fig. 1(b), where the differential resistance dV/dI vs I and V_G is presented as a color plot. Thus, our 2DJJs exhibit the same bipolar supercurrent expected in graphene-based Josephson devices [21].

The Thouless energy E_{Th} , defined as the inverse of the traversal time of the junction, is an energy scale characteristic of normal transport, which also governs the superconducting properties of Josephson junctions [27]. Josephson junctions vary between regimes defined as long ($\Delta/E_{Th} \gg 1$) or short ($\Delta/E_{Th} \ll 1$) and diffusive ($L > l$) or ballistic ($L < l$), where l is the mean free path in the weak link and L is the junction length. In the diffusive case $E_{Th} = \hbar D/L^2$, where D is the diffusion constant and L is the junction length. E_{Th} and l can, in principle, be extracted from the dependence of graphene normal resistance on V_G [24,25]. However, our device has an unusual geometry and noncolinear current and voltage probes, introducing uncertainties in the determination of E_{Th} . Taking l in the tens of nanometers, we estimate E_{Th} to be a few hundred μeV . The gap Δ of 10-nm-thick NbSe₂ is close to the bulk

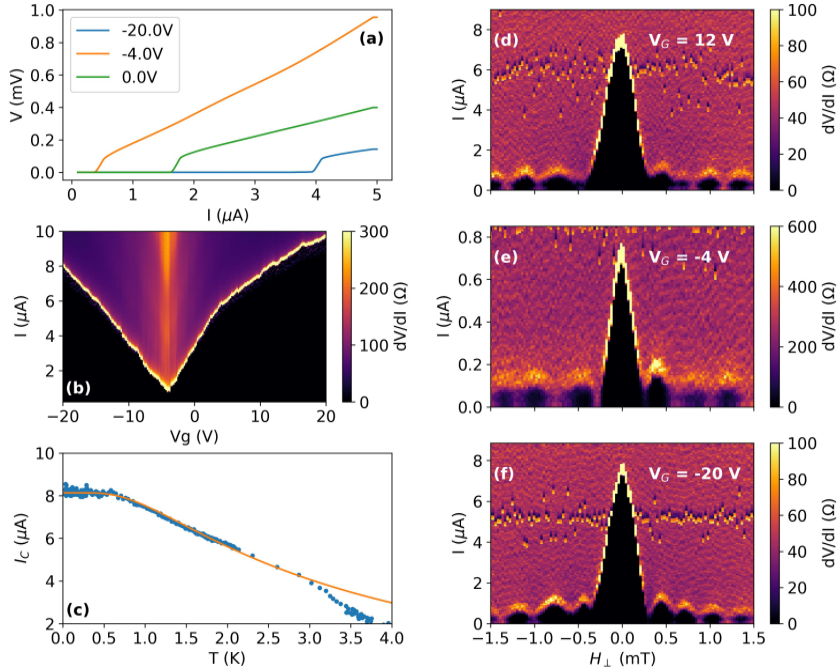


FIG. 2. (a) I - V curves of junction A (monolayer graphene) taken at different gate voltages (see legend). (b) Differential resistance dV/dI of junction A as a function of bias current and gate voltage. (c) Temperature dependence of the critical current of junction A (blue dots) and a fit to Eq. (1) (orange line), taken with a gate voltage of -20 V. (d)–(f) Differential resistance of junction A as a function of bias current and external perpendicular magnetic field, taken with gate voltages of 12 V, -4 V (Dirac point), and -20 V, respectively. All the panels show data at $H_{\parallel} = 0$ T and $T = 30$ mK.

value of 1.3 meV [28], placing junction A in an intermediate regime, leaning towards the long and diffusive.

It is predicted that in infinitely long metallic diffusive superconductor-normal-superconductor (SNS) junctions, with perfect contacts, at zero temperature $eI_C R_N = \alpha E_{Th}$ (R_N is the junction normal resistance [29]). Values near the theoretically predicted value of $\alpha = 10.82$ were seen in metal SNS junctions [29], whereas in graphene α varies widely, reaching values as much as 100 times smaller than theory [22–25]. Low values of α are attributed to an effective Thouless energy E_{Th}^* , smaller than E_{Th} determined by transport. This is possibly due to finite contact resistance and Andreev reflections across the N-S barrier, which increase the time of junction traversal [25,26]. In junction A E_{Th} is of the order of $I_C R_N$; thus, the proportionality factor α is of order unity. This indicates an effective $E_{Th}^* \approx 0.1E_{Th}$, smaller than metallic SNS junctions and larger than previously reported diffusive graphene junctions [22–25].

In the long junction limit at low temperatures theory predicts [29]

$$eI_C R_N = \alpha_1 E_{Th} \left[1 - b \exp\left(\frac{-\alpha_2 E_{Th}}{3.2k_B T}\right) \right], \quad (1)$$

where $\alpha_1 = \alpha_2 = 10.82$ and $b = 1.3$. Previous attempts to fit the temperature dependence in superconductor-graphene-superconductor (SGS) junctions led to findings of $\alpha_{1,2} = 1.1$ – 2.9 in [3,22,25]. In Fig. 2(c) we show that the temperature

dependence of the critical current in junction A fits well to an equation of this form at low temperatures up to $T \simeq 3$ K. Since we do not know the precise value of the transport E_{Th} , the fitting parameters are of limited quantitative value; nevertheless, assuming $E_{Th} \approx 300 \mu\text{eV}$, we find $\alpha_1 = 1.2$, $\alpha_2 = 2.4$, and $b = 1.2$. ($\alpha_1 < \alpha_2$ was also found for similar NbSe₂-graphene JJs [17]). These values of $\alpha_{1,2} < 10.82$ again indicate an effective $E_{Th}^* < E_{Th}$. As we will show below, measurements at parallel magnetic fields may provide another gauge for E_{Th}^* .

Next, we observe the response of the system to the application of magnetic field H_{\perp} perpendicular to the junction plane. Figures 2(d)–2(f) show dV/dI as a function of H_{\perp} and I , taken at three different gate voltages. The observed Fraunhofer-like pattern confirms a smooth current distribution across the junction. The apparent period is 0.4 mT. We compare this to the expected period $\Phi_0 / [(L + 2\lambda_L)W]$, where Φ_0 is the flux quantum, L is the average junction length, and W is the junction width. λ_L is the London penetration length, taken to be $\lambda_L = 200$ nm (known values in the literature range between ≈ 120 nm for bulk NbSe₂ [30] and 250 nm for bilayer NbSe₂ [31]). Using the above, we find the period to be ≈ 0.7 mT: larger than the observed period, likely due to flux focusing [11,23].

The junction appears to retain a homogeneous current distribution even when the Fermi energy is tuned to the Dirac point, unlike ballistic graphene devices, where transport becomes dominated by edge modes [32,33]. Close scrutiny of

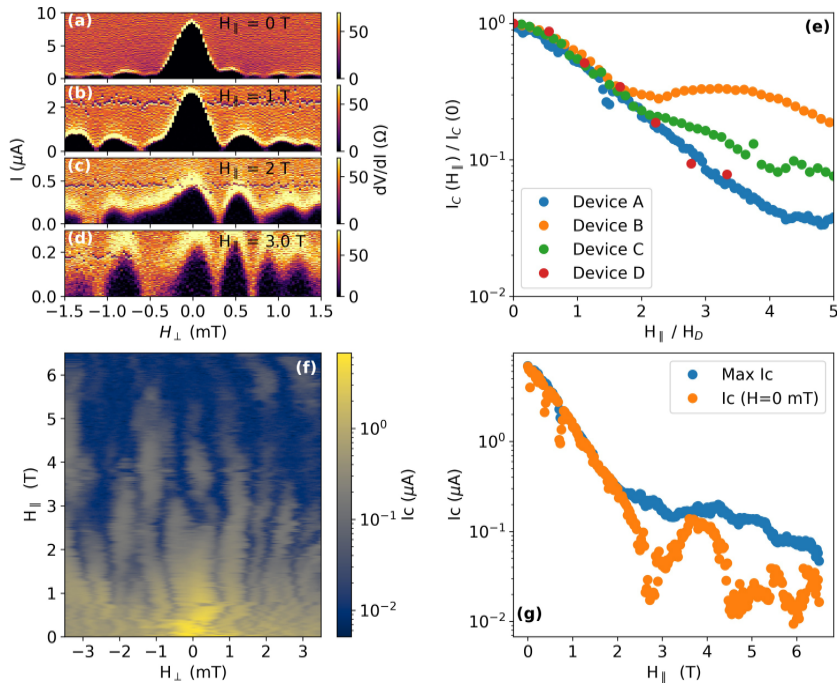


FIG. 3. (a)–(d) Differential resistance of junction A as a function of bias current and external perpendicular magnetic field, taken with applied in-plane magnetic field of 0, 1, 2, and 3 T, respectively. All measurements were conducted with $V_G = 20$ V. (e) Parallel field dependence of the maximal critical current for junctions A, B, C, and D. I_c is normalized to $I_c(H_{\parallel} = 0, H_{\perp} = 0)$, and the in-plane field is normalized by a junction-specific decay field H_D . Each value is extracted from a 2D scan of $R(V, H_{\perp})$ at a given H_{\parallel} and is defined as the maximal I_c obtained in each scan. $H_D = 0.6, 0.16, 0.4,$ and 0.9 T for junctions A, B, C, and D, respectively. The field at which exponential decay slows H_T is indicated by a dotted line for junctions A, B, and C. (f) I_c of junction A as a function of H_{\parallel} and H_{\perp} . The curves were shifted to correct for sample misalignment and were then aligned to be as continuous as possible. Logarithmic color scale. (g) Dependence of the maximal I_c (blue) and of I_c at $H_{\perp} = 0$ (orange), extracted from (f).

Figs. 2(d)–2(f), however, reveals discrepancies from the perfect interference pattern: lobes are not identical, and there is an asymmetry around $H_{\perp} = 0$. We suggest that this asymmetry in the interference pattern is due to spatial asymmetry in junction shape and disorder potential [11,34,35]. Additional asymmetry could arise due to the penetration of vortices into the junction area, breaking time reversal symmetry locally [36,37]. This will be more likely to contribute at finite H_{\parallel} . Having confirmed that 2DJJs have transport characteristics typical of diffusive SGS junctions [21], we turn our focus to the effect of in-plane magnetic field H_{\parallel} on the junction.

III. TRANSPORT IN PARALLEL MAGNETIC FIELD

Since the junction is sensitive to out-of-plane fields H_{\perp} on the scale of a few hundreds of microteslas, extreme care is needed when aligning H_{\perp} and H_{\parallel} in our vector magnet to the sample geometric tilt. We do this by measuring the out-of-plane interference pattern at any given H_{\parallel} . At low fields of up to 1.5 T in junction A, the interference pattern shows a clearly distinguishable central lobe [Figs. 3(a) and 3(b)], allowing for unambiguous identification of the absolute field orientation. At higher H_{\parallel} this is no longer possible: the central lobe is suppressed to the same magnitude as the side lobes [Figs. 3(c)

and 3(d)]. This SQUID-like supercurrent distribution may be retained up to high parallel field. Junction A, for example, retains its critical current at a field of $H_{\parallel} = 8.5$ T, showing a SQUID-like lobe structure as a function of H_{\perp} [Fig. 4(a)]. The voltage as a function of current curve shows a clear transition from the superconducting to normal state at a critical current of $I = 100$ nA for $H_{\perp} = -2$ mT [Fig. 4(b)].

Once the central lobe is no longer distinguishable, there is, in general, no straightforward indication of the true position of $H_{\perp} = 0$. Lacking this identification, we take the maximal $I_c(H_{\perp})$ (hence I_c^{\max}) as a measure for the junction critical current at each H_{\parallel} . We find that $I_c^{\max}(H_{\parallel})$ exhibits an exponential-like decay, corresponding to the suppression of the central lobe seen in Figs. 3(a)–3(c). Normalizing to $I_c^{\max}(H_{\parallel} = 0)$, we plot $I_c^{\max}(H_{\parallel})$ in Fig. 3(e) for junctions A, B, C, and D (all have monolayer graphene weak links, except junction B, which is bilayer graphene). To see the universality of the decay of $I_c(H_{\parallel})$, we normalize it by a junction-specific decay field H_D . The universal decay in I_c^{\max} persists up to a second characteristic field scale H_T , where I_c^{\max} stabilizes to the critical current of the side lobes. Depending on the sample, at $H > H_T$ the exponential decay in I_c^{\max} either becomes moderate or even turns into a small increase. For junctions

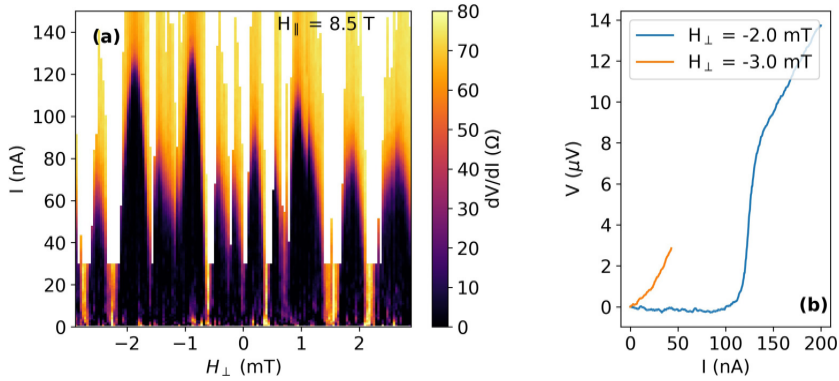


FIG. 4. High-field supercurrent. (a) The interference pattern of junction A at a parallel field of 8.5 T shows clear lobes of zero resistance (data are from a different cooldown than Fig. 3). (b) I - V curve from (a) where the critical current is maximal (blue) and minimal (orange). The measurement was set to stop when the normal state transport was observed.

A, B, and C shown in Fig. 3(e) this field is given by $H_T = 2.4$ T ($4H_D$), 0.24 T ($1.5H_D$), and 0.8 T ($2H_D$), respectively. In junction D there are not enough data points to quantify this field. The junctions thus evolve to a SQUID-like lobe structure at finite, yet device-dependent H_{\parallel} (see Supplemental Material, Sec. 3 [20]). The Zeeman effect in a uniform junction predicts universal decay with H_{\parallel} . Deviation from universal behavior at H_T could be a result of ripples or junction nonuniformity, as we will discuss.

We now turn our attention to Fig. 3(f), which depicts the evolution of I_C vs H_{\perp} and H_{\parallel} in junction A. In this junction we were able to track the evolution of the interference pattern up to $H_{\parallel} = 6.5$ T, aligning the $I_C(H_{\perp})$ curves as explained in Sec. 1 of the Supplemental Material [20], thus obtaining the map shown in Fig. 3(f).¹ The magnitude of $I_C(H_{\parallel}, H_{\perp} = 0)$, plotted in Fig. 3(g), shows a suppression and recovery pattern. These data are reminiscent of suppression-recovery patterns seen in superconductor-ferromagnet-superconductor (SFS) junctions [38–43] and in 2D systems [14,15,17], where they are interpreted as a 0 - π transition.

The salient features of the data are therefore (1) exponential decay of the critical current at low field, (2) saturation of the critical current at intermediate fields, (3) lobe structure transition from Fraunhofer-like to SQUID-like, and (4) vanishing and reappearing of the central lobe critical current in device A. In what follows, we discuss the physics in our 2DJJ by considering both the parallel field-tunable Zeeman splitting of the graphene band structure and the orbital effect of out-of-plane ripples in the graphene [19].

IV. THEORETICAL MODEL AND DISCUSSION

Lacking an intrinsic spin-orbit coupling, graphene dispersion is affected by magnetic field only through Zeeman

splitting, where the Zeeman energy is analogous to the exchange interaction in SFS JJs [19,44]. In the latter, the superconducting order parameter in the ferromagnetic layer varies as the product of an exponential decay and an oscillatory term:

$$\psi(x) = \psi_i \exp(-k_1 x) \cos(k_2 x), \quad (2)$$

where $\psi(x)$ is the order parameter at position x along the junction, ψ_i is the order parameter at the superconducting lead, and k_1 and k_2 are the inverse characteristic length scales associated with the decay and oscillation. In the diffusive limit, they are both given by $1/k_1, 1/k_2 = \sqrt{L^2 E_{Th}/E_Z} = \sqrt{2D/g\mu_B H_{\parallel}}$, where D is the diffusion coefficient.

The order parameter thus experiences a decay accompanied by oscillation, with zeros occurring periodically when $Lk_2 = \pi/2 + n\pi$ or $E_Z = (\pi/2 + n\pi)^2 E_{Th}$. This behavior of the order parameter leads to an oscillatory decay of the critical current of the junction. Following this intuition, the critical current of an SGS junction in a parallel magnetic field is thus expected to undergo an exponential suppression at low fields, in agreement with our observations. The oscillatory component of the wave function leads to a 0 - π transition: a change in the equilibrium phase difference between the two superconducting leads, accompanied by a reversal of the supercurrent.

Using the analytical solution of the Usadel equations in an SGS junction [19] to qualitatively model our system, we calculate the critical current as a function of H_{\parallel} and H_{\perp} specifically for junction A. We assume the junction length $L = 214$ nm and width $W = 4.69$ μ m [average dimensions are taken from the scanning electron microscopy (SEM) measurement shown in Fig. 1(c)]. Results are shown in Fig. 5(a). The assumed uniform supercurrent reversal manifests in the suppression of all lobes, corresponding to the disappearance of the uniform supercurrent throughout the junction at a numerically determined transition field [19]:

$$H_{\parallel} \approx \frac{2.5E_{Th}}{0.5g\mu_B} = \frac{5D\hbar}{g\mu_B L^2}. \quad (3)$$

¹Data in Figs. 3(a)–3(d) come from a different measurement than those in Fig. 3(f), taken on the same device, and show a slightly different lobe structure.

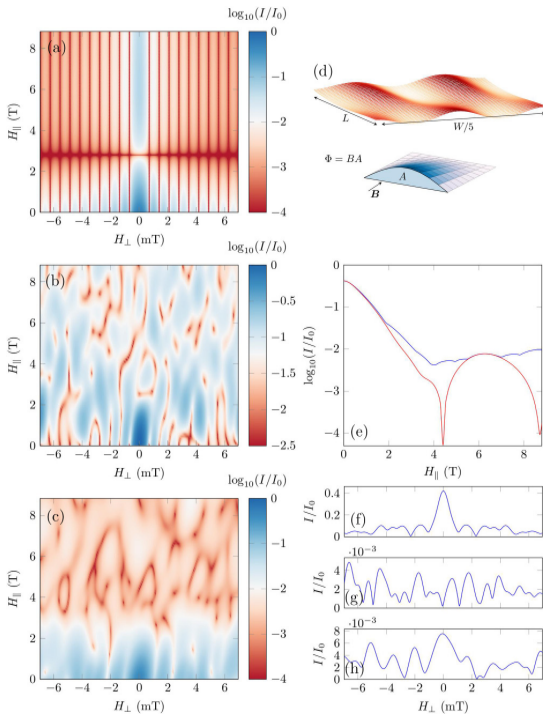


FIG. 5. (a)–(c) Calculated critical current I_C with a logarithmic color scale as a function of H_{\perp} and H_{\parallel} . (a) Simulated Zeeman effect with $E_{Th} = 64 \mu\text{eV}$ and a rectangular junction of dimensions $L = 214 \text{ nm}$, $W = 4.69 \mu\text{m}$ without ripples. (b) A rectangular junction with ripples, disregarding the Zeeman effect. (c) Our measured junction contour with varying L , $E_{Th} = 64 \mu\text{eV}$, Zeeman effect, and ripples. (d) Top: ripple profile used to generate the maps in (b) and (c). Note that the actual aspect ratio is around $W/L \approx 20$. Bottom: illustration of a long-wavelength ripple which could give rise to a zero in I_C at low fields. (e) I_C at $H_{\perp} = 0$ (red) and maximal I_C for all H_{\perp} (blue) vs H_{\parallel} ; line cuts are taken from the simulation in (c). (f)–(h) I_C vs H_{\perp} for $H_{\parallel} = 0, 4.1, \text{ and } 6.2 \text{ T}$; line cuts are from the simulation in (c).

From the experimentally observed transition field of 2.8 T, assuming $g = 2$, we find $E_{Th} = 64 \mu\text{eV}$. This falls between the order of magnitude expected for E_{Th} of hundreds of μeV which we extract from normal regime transport properties and E_{Th}^* of tens of μeV extracted from $I_C R_N$. Recalling that a lower effective E_{Th} has been attributed to Andreev reflection across an imperfect S-N interface, we point out that there is, to the best of our knowledge, no theory addressing how this would affect the Zeeman physics in the junction.

In the data in Fig. 3(f) we find that high-order lobes are retained, while the zero lobe, representing the average supercurrent, is suppressed. This indicates that the supercurrent is nonuniform. When multiple transport channels are present, they may carry positive and negative supercurrents which cancel out at $H_{\parallel} = 2.8 \text{ T}$, where the central lobe vanishes. In this regime the other lobes of the interference pattern, measuring higher moments of the supercurrent with respect

to the out-of-plane field, should not, in general, disappear. This phenomenon was seen in SFS JJs with a nonuniform ferromagnetic barrier, leading to a similar interference pattern [45–48]. Nonuniformity in supercurrent reversal can arise from local variation in E_{Th} since regions with lower E_{Th} will undergo stronger suppression due to E_Z . Such variation in E_{Th} can arise from varying junction length, as well as from local variations in contact transparency. Additionally, it could be a consequence of charge disorder, locally affecting the diffusion constant. However, the observed SQUID-like interference pattern can be reproduced only by an E_{Th} profile which sharply favors edge transport.

We now turn to the orbital effects associated with the locally varying perpendicular components of H_{\perp} . These variations may be caused either by graphene height variations or by disruptions to the parallel field due to the Meissner effect, which diverts flux lines around the superconducting electrodes (flux focusing). Because both ripples and flux focusing give rise to a spatially varying perpendicular field component, their effects on the electric current are similar. For concreteness we give an in-depth discussion of the ripple scenario but note that the underlying mechanism could, in principle, also be flux focusing.

Using the same model as discussed previously, we distinguish between the effects of short- and long-wavelength ripples [19]. Short ripples as seen in microscopy studies of graphene on SiO_2 are typically $\approx 0.3 \text{ nm}$ peak to peak, with a correlation length of 10–30 nm [49–52]. Long ripples have a wavelength larger than the junction dimensions. Intuitively, one may gauge the effect of a ripple by calculating the flux accumulated within an area defined by the ripple lateral cross section, illustrated in Fig. 5(d). To induce a full current suppression and revival at $H_{\perp} = 0$, a ripple within the junction has to accumulate a single flux quantum due to the parallel field, according to the equation

$$H_{\parallel} = \frac{\Phi_0}{\eta\lambda}, \quad (4)$$

where η is the average ripple amplitude within the junction and λ is the wavelength (or the limiting junction dimension if the ripple extends beyond the junction). For the typical short-wavelength ripple seen in graphene on SiO_2 , parallel fields of order 50 T are required to obtain an entire flux quantum within a ripple. However, the cumulative effect of many such ripples causes a faster decay of the critical current which can create exponential-like behavior, similar to the Zeeman effect [19].

Two-dimensional JJs in a parallel field are highly sensitive to long-wavelength height variations [19]. In our experimental geometry, with junction width $W \approx 4.7 \mu\text{m}$, it is possible to consider a ripple of length $\lambda \simeq W$. As a long-wavelength feature accumulates much more flux, it is possible to reach a flux quantum given a few-tesla parallel field and a small height variation of $\eta \approx 0.1 \text{ nm}$ within the junction. We note that based on atomic force microscopy and scanning tunneling microscopy studies, it is difficult to tell whether such subnanometer height variations are present over micron length scales. Such geometry is physically conceivable due to strain or curvature of the substrate and cannot be ruled out. We show the simulated supercurrent in a sample ripple configuration containing ripples in Fig. 5(b). The simulation reproduces the

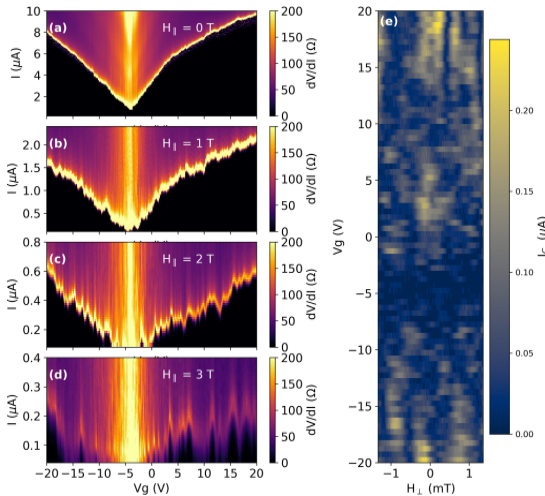


FIG. 6. (a)–(d) Differential resistance of junction A as a function of bias current and gate voltage, taken with applied in-plane magnetic field of 0, 1, 2, and 3 T, respectively. All measurements were conducted with $H_{\perp} = 0$. (e) I_C vs H_{\parallel} and V_G for junction A, taken with parallel field $H_{\parallel} = 3$ T.

features of the data highlighted previously: exponential decay followed by saturation, lobe structure transition, and a critical current dip at around $B = 3$ T. The specifics of these features, such as the location and sharpness of the critical current dip, vary with different ripple configurations; however, many different patterns can produce qualitatively similar results (see Supplemental Material, Sec. 2 [20]). Figure 5(d) illustrates the specific ripple profile used to obtain the map in Fig. 5(b). The simulation does not include ripples of wavelength smaller than around 100 nm. These, in general, cause a sharper decay of critical current with parallel field [19].

Since we expect Zeeman and ripple effects to coexist, we present a compound simulation which considers them both [Fig. 5(c)]. This simulation also accounts for varying E_{Th} due to variation in the junction length as extracted from the SEM data presented in Fig. 1(c). In the case of varying junction length our analytical model is not rigorous, but it does give a qualitative approximation. As we see in Fig. 5(e), the simulation reproduces the exponential decay, suppression, and recovery of $I_C(H_{\parallel}, H_{\perp} = 0)$. The lobe structure at $H_{\parallel} = 0, 4.1, 6.2$ T [Figs. 5(f)–5(h)] exhibits the experimentally observed transition between Fraunhofer-like and SQUID-like profiles.

V. GATE DEPENDENCE IN MAGNETIC FIELD

Finally, we observe how the application of H_{\parallel} affects the gate dependence of the critical current (Fig. 6). At zero field I_C varies smoothly with V_G [Fig. 6(a)], leading to a nearly constant $I_C R_N$ product away from the Dirac point. Upon increasing H_{\parallel} , I_C fluctuates with V_G [Figs. 6(b)–6(d)] leading to

$H_{\parallel} = 3$ T to patterns of decay and revival of $I_C(V_G)$. Observing the evolution of the interference pattern with V_G at the same field reveals a qualitative change in the number of visible lobes and in their positions [Fig. 6(e)].

The observed gate dependence of the interference pattern shows that at H_{\parallel} around the suppression-recovery field of 2.8 T, the junction enters a new regime where the critical current survives in patches at fluctuating gate values. Similar phenomenology has been observed in ballistic graphene JJs at high perpendicular field and has been attributed to chaotic billiards due to cyclotron orbits reflecting from the graphene edge [53]. However, the physics in our regime is different since the junction is diffusive and $B_{\perp} \approx 0$. Within the Zeeman effect interpretation, it could be due to local gate-driven fluctuations around the $0-\pi$ transition as in [16]. Alternatively, when ripples become important, changing gate could change the resulting interference pattern. There could also be a gate-dependent effect in the contact region between the graphene and NbSe₂. In any case, clearly, the current flow distribution in this regime depends strongly on graphene Fermi energy. This could be linked to local charge conditions such as the disorder potential landscape; however, the lobe structure continues to evolve when the graphene is at high carrier densities, where disorder potential should be screened.

VI. CONCLUSION

We conclude that the 2DJJ architecture allows the study of graphene Josephson junctions at high parallel magnetic fields, where supercurrent is sensitive to both the Zeeman effect and subnanometer graphene height variations. Junction currents evolve from a Fraunhofer-like to a SQUID-like interference pattern. We observe a supercurrent suppression and recovery feature which may be associated with a Zeeman-driven $0-\pi$ transition or with the accumulation of a single flux quantum within a micron-wavelength ripple. While in the present measurements it is difficult to distinguish between the two effects, future experiments, with graphene placed on hexagonal boron nitride (hBN), are expected to suppress the ripple contribution. In the future it will be interesting to consider devices of the 2DJJ architecture utilizing different 2D materials as contacts and weak links. For example, devices where graphene inherits a spin-orbit term from a transition metal dichalcogenide substrate. The combination of significant spin-orbit and high parallel magnetic fields in the context of a Josephson junction could give rise to topological effects [54].

The authors wish to thank M. Aprili, Y. Oreg, A. Stern, F. Pientka, and A. Di Bernardo for illuminating discussions. This work was funded by a European Research Council Starting Grant (Grant No. 637298, TUNNEL), Israeli Science Foundation Grant No. 861/19, and BSF Grant No. 2016320. T.D. and A.Z. are grateful to the Azrieli Foundation for Azrieli Fellowships. K.W. and T.T. acknowledge support from the Elemental Strategy Initiative conducted by the MEXT, Japan, Grant No. JPMXP0112101001, JSPS KAKENHI Grant No. JP20H00354 and the CREST (Grant No. JPMJCR15F3), JST.

- [1] D. K. Efetov, L. Wang, C. Handschin, K. B. Efetov, J. Shuang, R. Cava, T. Taniguchi, K. Watanabe, J. Hone, C. R. Dean, and P. Kim, Specular interband Andreev reflections at van der Waals interfaces between graphene and NbSe₂, *Nat. Phys.* **12**, 328 (2016).
- [2] M. R. Sahu, X. Liu, A. K. Paul, S. Das, P. Raychaudhuri, J. K. Jain, and A. Das, Inter-Landau-Level Andreev Reflection at the Dirac Point in a Graphene Quantum Hall State Coupled to a NbSe₂ Superconductor, *Phys. Rev. Lett.* **121**, 086809 (2018).
- [3] J. Lee, M. Kim, K. Watanabe, T. Taniguchi, G. H. Lee, and H. J. Lee, Planar graphene Josephson coupling via van der Waals superconducting contacts, *Curr. Appl. Phys.* **19**, 251 (2019).
- [4] X. Xi, Z. Wang, W. Zhao, J. H. Park, K. T. Law, H. Berger, L. Forró, J. Shan, and K. F. Mak, Ising pairing in superconducting NbSe₂ atomic layers, *Nat. Phys.* **12**, 139 (2016).
- [5] T. Dvir, F. Masee, L. Attias, M. Khodas, M. Aprili, C. H. L. Quay, and H. Steinberg, Spectroscopy of bulk and few-layer superconducting NbSe₂ with van der Waals tunnel junctions, *Nat. Commun.* **9**, 598 (2018).
- [6] T. Dvir, M. Aprili, C. H. L. Quay, and H. Steinberg, Zeeman Tunability of Andreev Bound States in van der Waals Tunnel Barriers, *Phys. Rev. Lett.* **123**, 217003 (2019).
- [7] J. Linder, T. Yokoyama, D. Huertas-Hernando, and A. Sudbø, Supercurrent Switch in Graphene π Junctions, *Phys. Rev. Lett.* **100**, 187004 (2008).
- [8] Q. Liang, Y. Yu, Q. Wang, and J. Dong, Controllable $0-\pi$ Transition in a Superconducting Graphene-Nanoribbon Junction, *Phys. Rev. Lett.* **101**, 187002 (2008).
- [9] A. G. Moghaddam and M. Zareyan, Long-range Josephson coupling through ferromagnetic graphene, *Phys. Rev. B* **78**, 115413 (2008).
- [10] Y. Asano, T. Yoshida, Y. Tanaka, and A. A. Golubov, Electron transport in a ferromagnet-superconductor junction on graphene, *Phys. Rev. B* **78**, 014514 (2008).
- [11] H. J. Suominen, J. Danon, M. Kjaergaard, K. Flensberg, J. Shabani, C. J. Palmstrøm, F. Nichele, and C. M. Marcus, Anomalous Fraunhofer interference in epitaxial superconductor-semiconductor Josephson junctions, *Phys. Rev. B* **95**, 035307 (2017).
- [12] P. Fulde and R. A. Ferrell, Superconductivity in a strong spin-exchange field, *Phys. Rev.* **135**, A550 (1964).
- [13] A. I. Larkin and Y. N. Ovchinnikov, Inhomogeneous state of superconductors, *Zh. Eksp. Teor. Fiz.* **47**, 1136 (1964) [*Sov. Phys. JETP* **20**, 762 (1965)].
- [14] A. Q. Chen, M. J. Park, S. T. Gill, Y. Xiao, D. R. Plessis, G. J. MacDougall, M. J. Gilbert, and N. Mason, Finite momentum Cooper pairing in three-dimensional topological insulator Josephson junctions, *Nat. Commun.* **9**, 3478 (2018).
- [15] S. Hart, H. Ren, M. Kosowsky, G. Ben-Shach, P. Leubner, C. Brüne, H. Buhmann, L. W. Molenkamp, B. I. Halperin, and A. Yacoby, Controlled finite momentum pairing and spatially varying order parameter in proximitized HgTe quantum wells, *Nat. Phys.* **13**, 87 (2016).
- [16] C. T. Ke, C. M. Moehle, F. K. Vries, C. Thomas, S. Metti, C. R. Guinn, R. Kallaher, M. Lodari, G. Scappucci, T. Wang, R. E. Diaz, G. C. Gardner, M. J. Manfra, and S. Goswami, Ballistic superconductivity and tunable π junctions in InSb quantum wells, *Nat. Commun.* **10**, 3764 (2019).
- [17] C. Li, B. de Ronde, J. de Boer, J. Ridderbos, F. Zwanenburg, Y. Huang, A. Golubov, and A. Brinkman, Zeeman-Effect-Induced $0-\pi$ Transitions in Ballistic Dirac Semimetal Josephson Junctions, *Phys. Rev. Lett.* **123**, 026802 (2019).
- [18] J. Linder, A. M. Black-Schaffer, and A. Sudbø, Triplet proximity effect and odd-frequency pairing in graphene, *Phys. Rev. B* **82**, 041409(R) (2010).
- [19] E. H. Fyhn, M. Amundsen, A. Zalic, T. Dvir, H. Steinberg, and J. Linder, Combined Zeeman and orbital effect on the Josephson effect in rippled graphene, *Phys. Rev. B* **102**, 024510 (2020).
- [20] See Supplemental Material at <http://link.aps.org/supplemental/10.1103/PhysRevB.103.115401> for the magnetic field alignment procedure (Sec. 1), information on the simulation of ripples in graphene (Sec. 2), measurements from additional samples (Sec. 3), and fabrication methods (Sec. 4).
- [21] H. B. Heersche, P. Jarillo-Herrero, J. B. Oostinga, L. M. K. Vandersypen, and A. F. Morpurgo, Bipolar supercurrent in graphene, *Nature (London)* **446**, 56 (2007).
- [22] D. Jeong, J. H. Choi, G. H. Lee, S. Jo, Y. J. Doh, and H. J. Lee, Observation of supercurrent in PbIn-graphene-PbIn Josephson junction, *Phys. Rev. B* **83**, 094503 (2011).
- [23] K. Komatsu, C. Li, S. Autier-Laurent, H. Bouchiat, and S. Guéron, Superconducting proximity effect in long superconductor/graphene/superconductor junctions: From specular Andreev reflection at zero field to the quantum Hall regime, *Phys. Rev. B* **86**, 115412 (2012).
- [24] C. T. Ke, I. V. Borzenets, A. W. Draeos, F. Amet, Y. Bomze, G. Jones, M. Craciun, S. Russo, M. Yamamoto, S. Tarucha, and G. Finkelstein, Critical current scaling in long diffusive graphene-based Josephson junctions, *Nano Lett.* **16**, 4788 (2016).
- [25] C. Li, S. Guéron, A. Chepelianskii, and H. Bouchiat, Full range of proximity effect probed with superconductor/graphene/superconductor junctions, *Phys. Rev. B* **94**, 115405 (2016).
- [26] J. C. Hammer, J. C. Cuevas, F. S. Bergeret, and W. Belzig, Density of states and supercurrent in diffusive SNS junctions: Roles of nonideal interfaces and spin-flip scattering, *Phys. Rev. B* **76**, 064514 (2007).
- [27] A. N. Tahvildar-Zadeh, J. K. Freericks, and B. K. Nikolić, Thouless energy as a unifying concept for Josephson junctions tuned through the Mott metal-insulator transition, *Phys. Rev. B* **73**, 184515 (2006).
- [28] E. Khestanova, J. Birkbeck, M. Zhu, Y. Cao, G. L. Yu, D. Ghazaryan, J. Yin, H. Berger, L. Forró, T. Taniguchi, K. Watanabe, R. V. Gorbachev, A. Mishchenko, A. K. Geim, and I. V. Grigorieva, Unusual suppression of the superconducting energy gap and critical temperature in atomically thin NbSe₂, *Nano Lett.* **18**, 2623 (2018).
- [29] P. Dubos, H. Courtois, B. Pannetier, F. K. Wilhelm, A. D. Zaikin, and G. Schön, Josephson critical current in a long mesoscopic SNS junction, *Phys. Rev. B* **63**, 064502 (2001).
- [30] F. D. Callaghan, M. Laulajainen, C. V. Kaiser, and J. E. Sonier, Field Dependence of the Vortex Core Size in a Multiband Superconductor, *Phys. Rev. Lett.* **95**, 197001 (2005).
- [31] E. F. Talantsev, W. P. Crump, J. O. Island, Y. Xing, Y. Sun, J. Wang, and J. L. Tallon, On the origin of critical temperature enhancement in atomically thin superconductors, *2D Mater.* **4**, 025072 (2017).

- [32] M. T. Allen, O. Shtanko, I. C. Fulga, A. R. Akhmerov, K. Watanabe, T. Taniguchi, P. Jarillo-Herrero, L. S. Levitov, and A. Yacoby, Spatially resolved edge currents and guided-wave electronic states in graphene, *Nat. Phys.* **12**, 128 (2016).
- [33] M. J. Zhu, A. V. Kretinin, M. D. Thompson, D. A. Bandurin, S. Hu, G. L. Yu, J. Birkbeck, A. Mishchenko, I. J. Vera-Marun, K. Watanabe, T. Taniguchi, M. Polini, J. R. Prance, K. S. Novoselov, A. K. Geim, and M. Ben Shalom, Edge currents shunt the insulating bulk in gapped graphene, *Nat. Commun.* **8**, 6 (2017).
- [34] A. Rasmussen, J. Danon, H. Suominen, F. Nichele, M. Kjaergaard, and K. Flensberg, Effects of spin-orbit coupling and spatial symmetries on the Josephson current in SNS junctions, *Phys. Rev. B* **93**, 155406 (2016).
- [35] A. Assouline, C. Feuillet-Palma, N. Bergeal, T. Zhang, A. Mottaghizadeh, A. Zimmers, E. Lhuillier, M. Eddrie, P. Atkinson, M. Aprili, and H. Aubin, Spin-Orbit induced phase-shift in Bi₂Se₃ Josephson junctions, *Nat. Commun.* **10**, 126 (2019).
- [36] T. Golod, A. Rydh, and V. M. Krasnov, Detection of the Phase Shift from a Single Abrikosov Vortex, *Phys. Rev. Lett.* **104**, 227003 (2010).
- [37] V. M. Krasnov, Josephson junctions in a local inhomogeneous magnetic field, *Phys. Rev. B* **101**, 144507 (2020).
- [38] T. Kontos, M. Aprili, J. Lesueur, F. Genêt, B. Stephanidis, and R. Boursier, Josephson Junction through a Thin Ferromagnetic Layer: Negative Coupling, *Phys. Rev. Lett.* **89**, 137007 (2002).
- [39] W. Guichard, M. Aprili, O. Bourgeois, T. Kontos, J. Lesueur, and P. Gandit, Phase Sensitive Experiments in Ferromagnetic-Based Josephson Junctions, *Phys. Rev. Lett.* **90**, 167001 (2003).
- [40] Y. Blum, A. Tsukernik, M. Karpovski, and A. Palevski, Oscillations of the Superconducting Critical Current in Nb-Cu-Ni-Cu-Nb Junctions, *Phys. Rev. Lett.* **89**, 187004 (2002).
- [41] V. A. Oboznov, V. V. Bol'ginov, A. K. Feofanov, V. V. Ryazanov, and A. I. Buzdin, Thickness Dependence of the Josephson Ground States of Superconductor-Ferromagnet-Superconductor Junctions, *Phys. Rev. Lett.* **96**, 197003 (2006).
- [42] V. Shelukhin, A. Tsukernik, M. Karpovski, Y. Blum, K. B. Efetov, A. F. Volkov, T. Champel, M. Eschrig, T. Löfwander, G. Schon, and A. Palevski, Observation of periodic π -phase shifts in ferromagnet-superconductor multilayers, *Phys. Rev. B* **73**, 174506 (2006).
- [43] J. W. A. Robinson, S. Piano, G. Burnell, C. Bell, and M. G. Blamire, Critical Current Oscillations in Strong Ferromagnetic π Junctions, *Phys. Rev. Lett.* **97**, 177003 (2006).
- [44] A. I. Buzdin, Proximity effects in superconductor-ferromagnet heterostructures, *Rev. Mod. Phys.* **77**, 935 (2005).
- [45] M. Kemmler, M. Weides, M. Weiler, M. Opel, S. T. B. Goennenwein, A. S. Vasenko, A. A. Golubov, H. Kohlstedt, D. Koelle, R. Kleiner, and E. Goldobin, Magnetic interference patterns in $0-\pi$ superconductor/insulator/ferromagnet/superconductor Josephson junctions: Effects of asymmetry between 0 and π regions, *Phys. Rev. B* **81**, 054522 (2010).
- [46] S. M. Frolov, D. J. Van Harlingen, V. V. Bolginov, V. A. Oboznov, and V. V. Ryazanov, Josephson interferometry and Shapiro step measurements of superconductor-ferromagnet-superconductor $0-\pi$ junctions, *Phys. Rev. B* **74**, 020503(R) (2006).
- [47] J. Pfeiffer, M. Kemmler, D. Koelle, R. Kleiner, E. Goldobin, M. Weides, A. K. Feofanov, J. Lisenfeld, and A. V. Ustinov, Static and dynamic properties of 0 , π , and $0-\pi$ ferromagnetic Josephson tunnel junctions, *Phys. Rev. B* **77**, 214506 (2008).
- [48] M. Weides, M. Kemmler, H. Kohlstedt, R. Waser, D. Koelle, R. Kleiner, and E. Goldobin, $0-\pi$ Josephson Tunnel Junctions with Ferromagnetic Barrier, *Phys. Rev. Lett.* **97**, 247001 (2006).
- [49] M. Ishigami, J. H. Chen, W. G. Cullen, M. S. Fuhrer, and E. D. Williams, Atomic structure of graphene on SiO₂, *Nano Lett.* **7**, 1643 (2007).
- [50] V. Geringer, M. Liebmann, T. Echtermeyer, S. Runte, M. Schmidt, R. Rückamp, M. C. Lemme, and M. Morgenstern, Intrinsic and Extrinsic Corrugation of Monolayer Graphene Deposited on SiO₂, *Phys. Rev. Lett.* **102**, 076102 (2009).
- [51] W. G. Cullen, M. Yamamoto, K. M. Burson, J. H. Chen, C. Jang, L. Li, M. S. Fuhrer, and E. D. Williams, High-Fidelity Conformation of Graphene to SiO₂ Topographic Features, *Phys. Rev. Lett.* **105**, 215504 (2010).
- [52] J. Xue, J. Sanchez-Yamagishi, D. Bulmash, P. Jacquod, A. Deshpande, K. Watanabe, T. Taniguchi, P. Jarillo-Herrero, and B. J. LeRoy, Scanning tunneling microscopy and spectroscopy of ultra-flat graphene on hexagonal boron nitride, *Nat. Mater.* **10**, 282 (2011).
- [53] M. B. Shalom, M. J. Zhu, V. I. Fal, A. Mishchenko, A. V. Kretinin, K. S. Novoselov, C. R. Woods, K. Watanabe, T. Taniguchi, A. K. Geim, and J. R. Prance, Quantum oscillations of the critical current and high-field superconducting proximity in ballistic graphene, *Nat. Phys.* **12**, 318 (2016).
- [54] T. Wakamura, N. J. Wu, A. D. Chepelianskii, S. Guéron, M. Och, M. Ferrier, T. Taniguchi, K. Watanabe, C. Mattevi, and H. Bouchiat, Spin-Orbit-Enhanced Robustness of Supercurrent in Graphene/WS₂ Josephson Junctions, *Phys. Rev. Lett.* **125**, 266801 (2020).

Supplemental Materials

*Tom Dvir¹, *Ayelet Zalic¹, Eirik Holm Fyhn², Morten Amundsen², Takashi Taniguchi³,
Kenji Watanabe⁴, Jacob Linder², and Hadar Steinberg¹

¹*The Racah Institute of Physics, The Hebrew University of Jerusalem, Jerusalem
91904, Israel*

²*Center for Quantum Spintronics, Department of Physics, Norwegian University of
Science and Technology, NO-7491 Trondheim, Norway*

³*International Center for Materials Nanoarchitectonics, National Institute for Materials
Science, 1-1 Namiki, Tsukuba 305-0044, Japan*

⁴*Research Center for Functional Materials, National Institute for Materials Science, 1-1
Namiki, Tsukuba 305-0044, Japan*

February 11, 2021

S1 Supplementary Section: Measurement and field alignment procedure

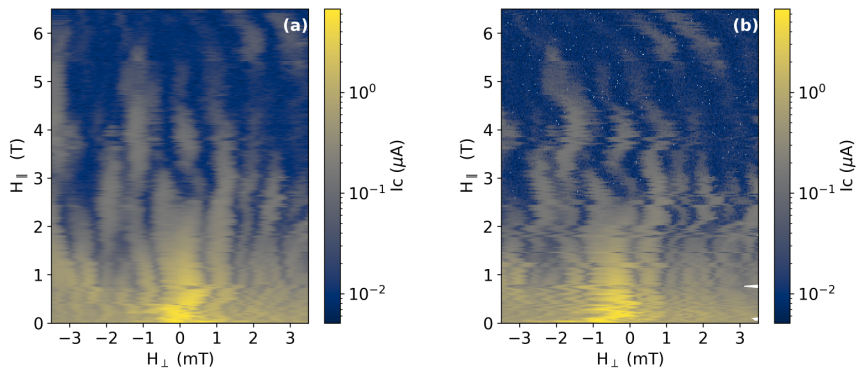
The system studied here, an SNS junction using graphene as the weak link between NbSe₂ SC leads, is very sensitive to the presence of perpendicular fields on the scale of hundreds of μT . When applying parallel magnetic field, perpendicular field can also be present, either from a small misalignment of the sample within the magnet, or from the presence of vortices and trapped magnetic flux in the leads, in the junction or in the magnet itself. At low parallel magnetic fields, the interference pattern of the supercurrent with the application of perpendicular field shows a clear maximum at zero applied field. Thus, it is possible to track the shift of this maximum with applied parallel field and find the sample misalignment. In the measurements reported in this work we have done so, and found the required amount of perpendicular field to compensate for this effect. The interference patterns reported here are always with respect to the corrected zero perpendicular field.

At higher magnetic fields, this correction is not enough, as remnant field, coming from vortices in the leads and trapped flux in the magnet affects the sample. To correct for that, we assume that a small change in the parallel field should not create a large change in the interference pattern of the junction.

*Equal contribution

Based on this assumption, when analyzing the data, we use the following alignment procedure: We shift the interference pattern measured at a given parallel field by a some amount of perpendicular field. We calculate the sum of the squared differences between an this pattern and the pattern measured in the previous parallel field. We repeat this for a series of shifts and find for which shift this difference is minimal. We choose this shift as the correct alignment for the pattern, and repeat with the pattern taken at the next step of the parallel field.

The above procedure was utilized for junction A. For other junctions, we could not determine the orientation of $H_{\perp}=0\text{T}$ at high values of H_{\parallel} due to jumps in the interference pattern. Therefore we used the maximal critical current I_C^{max} as an indicator of the junction critical current.



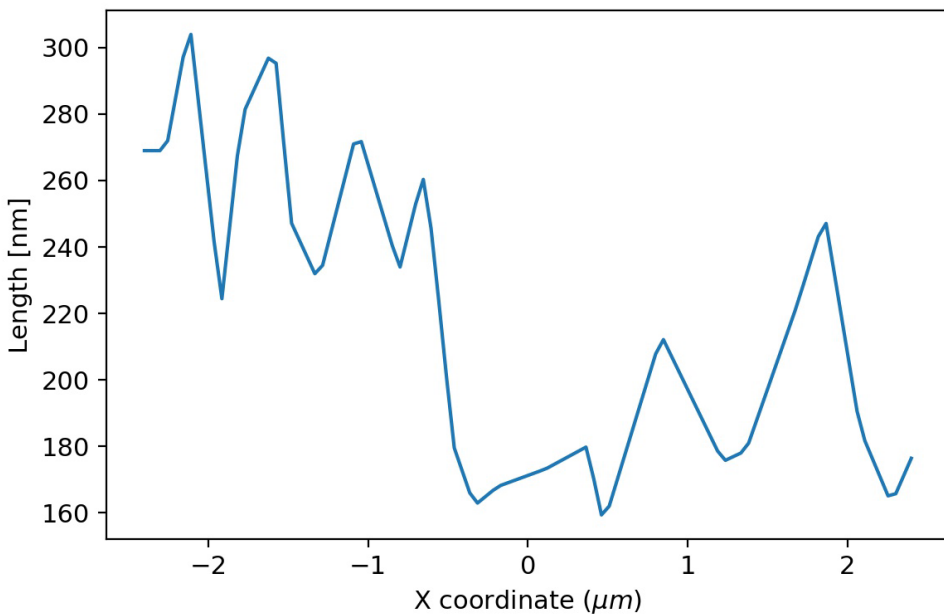
Supplementary Figure S1: (a) The 2D map of I_C of Junction A as a function of H_{\parallel} and H_{\perp} , aligned using the full alignment procedure of minimizing the squared difference between line-scans and shown also in main text Fig. 2(f). (b) The same data shown when only geometrical misalignment was taken into consideration.

S2 Supplementary Section: Simulation of ripples in graphene

We assume the presence of height variations in graphene, and in the absence of the Zeeman effect (taking $E_{Th} \gg E_Z$), theoretically calculate the critical current expected for Junction A, shown in main text Fig. 3 panel (b). We calculated this for eight different ripple profiles, generated by taking a sum of a random number of sine functions, all with randomized wavelength, amplitude and angular offsets. The wavelengths were taken from an exponential distribution (meaning that longer wavelengths are more probable) while the rest of the parameters were taken from uniform distributions. Qualitative features such as a transition in the lobe structure from Fraunhofer-like to SQUID-like, decay of the critical current and a suppression and reappearance of $I_C(H_{\perp}=0)$ appear for several of the randomly generated profiles. The specific result we chose to present in the main text was generated from the following ripple profile:

$$\eta(x, y) = 1.25 \sin 64.6y + 1.7164 \sin 3.5x - 0.7 + 0.45 \sin 37.3y + 2.136 \sin 2x + 1.3 \sin 2y + 0.3224 \sin 0.1x + 0.03 \quad (\text{S1})$$

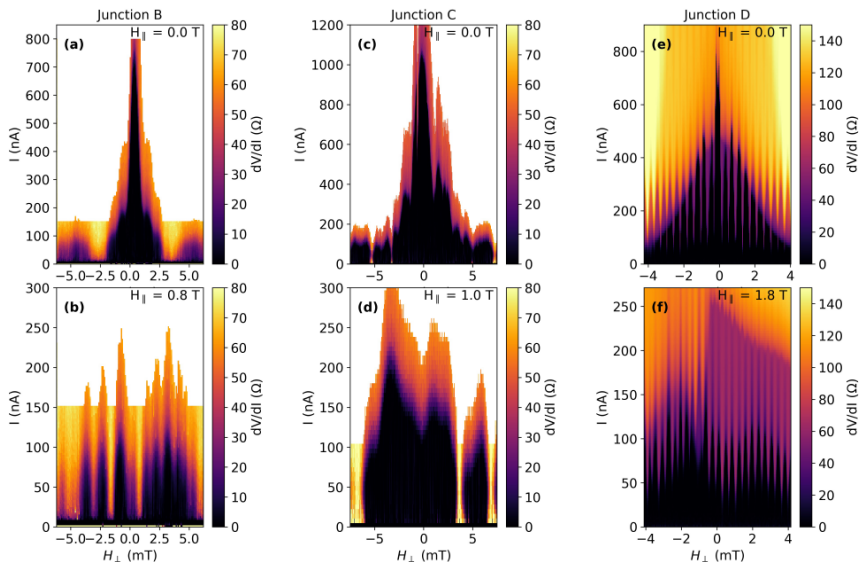
Ripple amplitude is given in nm, while the coordinates x,y are normalized and range between -0.5,0.5. The profiles were chosen with wavelengths much larger than 50 nm, in order to accommodate the use of the wide-junction approximation [1]. The junction length profile used for the combined simulation of Zeeman, ripple and junction geometry effects presented in main text Fig. 3 panel (c), is illustrated in Fig. S2.



Supplementary Figure S2: The junction length profile of Junction A as measured by SEM.

S3 Supplementary Section: Additional junctions

We present critical current measurements from devices B,C,D, showing I_C vs H_{\perp} (Junction B has a weak link of bilayer graphene, the rest are monolayer). This exhibits a Fraunhofer-like interference at low H_{\parallel} and a more SQUID-like lobe structure, with lobes having a similar maximal I_C , at higher H_{\parallel} for each device. Junction D has a nonuniform geometry with multiple graphene weak links, making it difficult to directly interpret the interference pattern. Roughly, the lobe structure at $H_{\parallel}=0$ has a large area non-uniform component leading to high frequency lobes, modulated by a slow decay due to the uniform current in an individual small junction. The later modulation becomes more uniform as H_{\parallel} increases, as in the other devices.



Supplementary Figure S3: Interference patterns from Junctions B,C,D (a-c) Interference patterns of Junctions B,C,D respectively at $H_{\parallel}=0$ T showing a pronounced central lobe in each case (d-e) Interference patterns at various values of non-zero H_{\parallel} (indicated in the panel) for device B,D,C respectively. These patterns have all lobes with similar maximal values of I_C , indicating a non-uniform current distribution

S4 Supplementary Section: Fabrication Methods

To fabricate a graphene - NbSe₂ Josephson junction (JJ), we first exfoliate graphene on marked SiO₂ and locate suitable flakes. Next, NbSe₂ is exfoliated on PDMS gel and examined to find flakes which are a few layers thick and have an observable crack, less than 500 nm wide. Chosen NbSe₂ flakes are

transferred onto graphene using the viscoelastic dry-transfer method [2]. A few nm thick hBN flake may then be transferred over the crack to serve as a protective layer and a potential top-gate dielectric. The NbSe₂ flake is contacted with standard e-beam lithography using Ti/Au contacts. Prior to evaporation of contacts surface oxide was removed using Argon ion milling. Four-probe measurements were conducted in a dilution cryostat with a base temperature of 30 mK (see main text Fig. 1).

References

- [1] F. S. Bergeret and J. C. Cuevas. The vortex state and Josephson critical current of a diffusive SNS junction. *J. Low. Temp. Phys.* 153, 304 (2008).
- [2] A. Castellanos-Gomez, M. Buscema, R. Molenaar, V. Singh, L. Janssen, H. S. J. van der Zant, and G. A. Steele. Deterministic transfer of two-dimensional materials by all-dry viscoelastic stamping. *2D Mat.* 1, 011002 (2014).


PAPER V

Reference

Eirik Holm Fyhn and Jacob Linder,
Temporarily enhanced superconductivity from magnetic fields.
Physical Review B **103**, L100502 (2021)
DOI: 10.1103/physrevb.103.l100502

CONTRIBUTIONS

EHF performed the analytical calculations and the numerical simulations, with support from JL. EHF drafted the manuscript. EHF developed the methodology. EHF and JL contributed to the discussions of the physics, and the revision of the final manuscript. Specifically, in addition to participating in the discussion of the physics and the revision of the final manuscript, EHF wrote the initial draft, developed the methodology, performed all the calculations, developed the code, performed the numerical simulations and produced all figures presented in the paper.

Temporarily enhanced superconductivity from magnetic fieldsEirik Holm Fyhn  and Jacob Linder *Center for Quantum Spintronics, Department of Physics, Norwegian University of Science and Technology, NO-7491 Trondheim, Norway* (Received 18 October 2020; revised 22 February 2021; accepted 26 February 2021; published 11 March 2021)

Contrary to the expected detrimental influence on superconductivity when applying a magnetic field, we predict that the abrupt onset of such a field can temporarily strongly enhance the superconducting order parameter. Specifically, we find that the supercurrent in a Josephson junction with a normal metal weak link can increase more than twentyfold in this way. The effect can be understood from the interplay between the energy dependence of Andreev reflection and the abrupt spin-dependent shift in the distribution functions for excitations in the system. The duration of the increase depends on the inelastic scattering rate in the system and is estimated to be in the range of nanoseconds. We demonstrate this by developing a method which solves the Usadel equation for an arbitrary time dependence. This enables the study of ultrafast time-dependent physics in heterostructures combining superconductors with different types of materials.

DOI: [10.1103/PhysRevB.103.L100502](https://doi.org/10.1103/PhysRevB.103.L100502)

Introduction. Time-dependent phenomena in superconductors encompass a variety of both applied and fundamental physics. These phenomena range from the perfect voltage-to-frequency conversion via the AC Josephson effect to excitation of the amplitude mode of the superconducting order parameter, which is the condensed-matter equivalent of the Higgs boson in the standard model.

More recently, interest in time-dependent phenomena in superconductors has been generated by experiments showing optically induced transient states with superconducting properties well above the equilibrium critical temperature [1–3]. In superconducting heterostructures it has also been shown that microwaves can greatly increase the critical current [4,5]. This was given a theoretical explanation based on quasiclassical Green's functions [6]. Another application of quasiclassical Green's functions has been to show that time-dependent exchange fields can produce odd-frequency superconductivity which survives for long distances inside ferromagnets [7,8]. This is a type of superconductivity that is interesting due to its nonlocal temporal symmetry, its direct connection to Majorana states [9], and for its resilient nature, making it practically relevant in, e.g., superconducting spintronics [9].

Discovering new time-dependent physical phenomena in superconducting structures, and explaining existing experimental results, is clearly of substantial interest. Unfortunately, a solution of the quasiclassical Green's function equation is generally not attainable, even numerically, when the system evolves in time. This is because the relevant equations, presented below, are complicated partial differential equations (PDEs) of infinite order. So far, approximate solutions have been found for periodic [6,7,10–12] and slow [13,14] temporal evolutions. Although many situations are either slow or periodic, there is still a multitude of physical systems that are unsolvable with current techniques. For instance, the transient behavior of any sudden change that is not periodic, such as a sudden increase in the applied magnetic field or voltage,

would not be possible to study, even numerically, with these methods. Finding a way to solve the Usadel equation that is less restrictive on how it allows the system to evolve in time would therefore open the possibility to study a vast range of new physical phenomena.

Here we accomplish this goal and present a method solving the time-dependent Usadel equation in hybrid nanostructures that places no constraint on the time dependence. We apply this to a superconductor-normal metal-superconductor (SNS) Josephson junction with a time-dependent spin-splitting applied to the N part. Interestingly, we find that the transient behavior can involve a large increase in both the supercurrent and the superconducting order parameter. This is our main result, which stands in stark contrast to the equilibrium effect of an applied magnetic field, which is to exponentially dampen superconductivity [15].

In addition to the curious enhancement of superconductivity, which we suggest can be understood as the interplay between properties of Andreev reflection and the transient behavior of the distribution function, we show how the methodology developed herein can be used to uncover new physics in a wide range of systems. It only requires that the proximity effect is sufficiently weak. In particular, it could be used to study the mostly unexplored territory of explicit time dependence in odd-frequency superconducting condensates, both in the ballistic and diffusive limit.

Equations and notation. The quasiclassical theory is valid when the Fermi wavelength is much shorter than all other length scales. Here we shall focus on the dirty limit, which is valid when the mean free path is short. However, we note that the same derivation can be done with arbitrary impurity concentration, something that is further discussed in the Supplemental Material [16]. The relevant equation for the dirty limit is the Usadel equation [17,18],

$$D\vec{\nabla} \circ (\vec{g} \circ \vec{\nabla} \circ \vec{g}) + i(\vec{\sigma} \circ \vec{g} - \vec{g} \circ \vec{\sigma}) = 0. \quad (1)$$

Here, D is the diffusion coefficient, the 8×8 matrix

$$\check{g} = \begin{pmatrix} \hat{g}^R & \hat{g}^K \\ 0 & \hat{g}^A \end{pmatrix} \quad (2)$$

is the isotropic part of the impurity-averaged quasiclassical Green's function, $\check{\sigma}$ is a self-energy that depends on the specific system, and

$$\check{\nabla} \circ \check{g} = \nabla \check{g} - ie(\hat{a} \circ \check{g} - \check{g} \circ \hat{a}) \quad (3)$$

is the covariant derivative. The vector \hat{a} includes the effect of the vector potential, but it could also incorporate spin-orbit effects [19,20]. The electron charge is $e = -|e|$. Finally, the circle product is

$$a \circ b = \exp\left(\frac{i}{2}\partial_\varepsilon^a \partial_T^b - \frac{i}{2}\partial_T^a \partial_\varepsilon^b\right)ab, \quad (4)$$

which is what makes Eq. (1) difficult when the constituents depend on the center-of-mass time T . The superscripts in Eq. (4) denote which function the operators acts on and ε is energy. The superscripts R , K , and A are used to denote the upper-left, upper-right, and lower-right 4×4 blocks of 8×8 matrices, respectively.

Equation (1) can be made dimensionless by dividing every term by the Thouless energy, $\varepsilon_T := D/L^2$, where L is the length of the system. With this one can define dimensionless quantities, where lengths are given in multiples of L and energies are given in multiples of ε_T . Dimensionless quantities will be used in the rest of this paper. We also use natural units throughout, meaning that $c = \hbar = 1$.

Quasiclassical theory is invalid at interfaces between different materials. Consequently, one needs boundary conditions in order to connect the Green's functions in different materials. Here we use the Kupriyanov-Lukichev boundary condition [21],

$$\mathbf{e}_n \cdot (\check{g}_i \circ \check{\nabla} \circ \check{g}_i) = \frac{z}{2}(\check{g}_i \circ \check{g}_j - \check{g}_j \circ \check{g}_i), \quad (5)$$

which is valid for low-transparency tunneling interfaces. The subscripts i and j label the two different regions, the unit normal vector \mathbf{e}_n points out of region i , and z is the ratio between the bulk resistance of a part of the material that is of length L and the interface resistance. Although we use the Kupriyanov-Lukichev boundary condition here, the same method could also be used with other types of boundaries [22].

The quasiclassical Green's function satisfies the normalization condition $\check{g} \circ \check{g} = 1$ and the relations

$$\hat{g}^A = -\hat{\rho}_3(\hat{g}^R)^\dagger \hat{\rho}_3, \quad \hat{g}^K = \hat{g}^R \circ h - h \circ \hat{g}^A, \quad (6)$$

where $\hat{\rho}_3 = \text{diag}(1, 1, -1, -1)$. From Eq. (6) one can see that it is sufficient to solve for the retarded Green's function \hat{g}^R and the distribution function h . Equation (1) does not fully specify h , and we can use this freedom to make h block-diagonal [23].

Finally, we use capital letters to denote Fourier transforms,

$$F(t, T, \mathbf{r}) \equiv \mathcal{F}(f)(t, T, \mathbf{r}) = \frac{1}{2\pi} \int_{-\infty}^{\infty} d\varepsilon f(\varepsilon, T, \mathbf{r}) e^{-i\varepsilon t}, \quad (7)$$

and \bullet to denote the circle product between functions of the relative time t , that is, \bullet is the mathematical operation which satisfies $\mathcal{F}(f \circ g) = F \bullet G$.

The aim is to find the Green's function that solves Eq. (1) in a region that is connected through the boundary condition in Eq. (5) to a region with Green's function \check{g}_s . This region could, for instance, be a superconducting reservoir. We have developed a method which solves the Usadel equation with an arbitrary time dependence, allowing for the study of quantum quenches and ultrafast dynamics, and present this method below.

The first step is to write the retarded Green's function as $\hat{g}^R = \hat{\rho}_3 + \hat{g} + \hat{f}$, where \hat{g} and \hat{f} are block-diagonal and block-antidiagonal, respectively. Under the assumption that the proximity effect is small, the components of \hat{g} and \hat{f} are all much smaller than 1. One way to formalize this is to Taylor expand \hat{g} and \hat{f} in terms of the interface parameter z . When $\check{\sigma}^R$ is block-diagonal and $z = 0$, we find that $\hat{g}^R = \hat{\rho}_3$ solves the Usadel equation. Hence, assuming $\check{\sigma}^R$ is block-diagonal to lowest order in z , we can write

$$\hat{f} = \sum_{n=1}^{\infty} z^n \hat{f}_n \quad \text{and} \quad \hat{g} = \sum_{n=1}^{\infty} z^n \hat{g}_n. \quad (8)$$

From the normalization condition $\hat{g}^R \circ \hat{g}^R = 1$, we see that $2\hat{\rho}_3 \hat{g} + \hat{g} \circ \hat{g} = -\hat{f} \circ \hat{f}$ and $\hat{g} \circ \hat{f} = -\hat{f} \circ \hat{g}$. Hence, $\hat{g}_1 = 0$ and $\hat{g}_2 = -\frac{1}{2}\hat{\rho}_3 \hat{f}_1 \circ \hat{f}_1$.

To first order in z , the retarded part of the Usadel equation reads

$$\hat{\rho}_3 \check{\nabla} \circ (\check{\nabla} \circ \hat{f}_1) + 2i\varepsilon \hat{\rho}_3 \hat{f}_1 + i(\hat{\sigma}^R \circ \hat{f}_1 - \hat{f}_1 \circ \hat{\sigma}^R) = 0, \quad (9)$$

where $\varepsilon \hat{\rho}_3$ has been extracted from the self-energy and $\hat{\sigma}^R$ is the remaining part. The self-energy $\hat{\sigma}^R$ could also depend on \hat{g}^R , for instance, if the system included spin-orbit impurity scattering or spin-flip scattering [24]. In that case Eq. (9) would look slightly different, but the derivation would be similar. To first order in z , the boundary condition (5) reads

$$\mathbf{e}_n \cdot \check{\nabla} \circ \hat{f}_1 = \hat{f}_s. \quad (10)$$

Despite being linearized, Eqs. (9) and (10) are not much simpler than the original Usadel equation and Kupriyanov-Lukichev boundary condition. They still include the circle product, given in Eq. (4), meaning that they are still PDEs of infinite order. However, one observation can be made which will drastically simplify the equations. This is the fact that all the circle products are between \hat{f}_1 and functions that are independent of energy ε . It is this fact, not that the equations are linear, that is crucial for the solvability of Eqs. (9) and (10). As we shall see, this observation allows us to evaluate all the circle products if we first Fourier transform the equations.

When a function $(\varepsilon, T) \mapsto a(T)$ is independent of ε , the Fourier transform, as given by Eq. (7), is simply $A(t, T) = \delta(t)a(T)$, where δ is the Dirac δ distribution. Accordingly, the circle products of a function $(\varepsilon, T) \mapsto f(\varepsilon, T)$ with a function $(\varepsilon, T) \mapsto a(T)$ are, in Fourier space,

$$(A \bullet F)(t, T) = a(T + t/2)F(t, T), \quad (11a)$$

$$(F \bullet A)(t, T) = F(t, T)a(T - t/2). \quad (11b)$$

With this, all the circle products in Eq. (9) turn into normal matrix multiplications when evaluated in Fourier space. This is under the assumption that the self-energy $\hat{\sigma}^R$ does not

depend explicitly on ε . However, it can depend implicitly on energy through its dependence on \tilde{g} , as mentioned above.

Let the subscripts + and - denote $B_{\pm}(t, T) = b(T \pm t/2)$. Then the equations for the retarded Green's function become

$$2\frac{\partial \hat{F}_1}{\partial t} = \nabla^2 \hat{F}_1 + 2i(\nabla \hat{F}_1 \cdot \hat{A}_- - \hat{A}_+ \cdot \nabla \hat{F}_1) + i(\hat{F}_1 \nabla \cdot \hat{A}_- - \nabla \cdot \hat{A}_+ \hat{F}_1) - \hat{A}_+^2 \hat{F}_1 + \hat{A}_+ \hat{F}_1 \hat{A}_- - \hat{F}_1 \hat{A}_-^2 + i\hat{\rho}_3(\hat{\Sigma}_+^R \hat{F}_1 - \hat{F}_1 \hat{\Sigma}_+^R), \quad (12a)$$

$$e_n \cdot [\nabla \hat{F}_1 - i(\hat{A}_+ \hat{F}_1 - \hat{F}_1 \hat{A}_-)] = \hat{F}_s, \quad (12b)$$

Hence an approximate solution to the full time-dependent Usadel equation can be found by solving a normal PDE of matrices. The approximation is good as long as the proximity effect is weak and, crucially, no assumptions have been made with regard to the time dependence. This approach therefore works for systems that vary both fast and slow in time and regardless of whether or not the system is periodic. The equations for the distribution function h can be obtained in a similar way. This is shown in the Supplemental Material [16].

Application. We now use the above framework to show the counterintuitive result that the abrupt onset of a magnetic field can temporarily strongly increase superconducting order. Consider an SNS junction with no vector potential and a time-dependent, spatially uniform exchange field $m(T)$ that lifts the spin degeneracy of the bands. The geometry is shown in the inset of Fig. 1, where the nanowire geometry allows us to neglect the orbital effect of the magnetic field whereas the thick superconducting regions screen the effect of the magnetic field in the bulk. The self-energy associated with the exchange field is $\delta^R = m \text{diag}(1, -1, 1, -1)$. We also include the effect of inelastic scattering through the relaxation time approximation [6], which adds

$$\check{\sigma}_i = \begin{pmatrix} i\delta\hat{\rho}_3 & 2i\delta\hat{\rho}_3 h_{\text{eq}} \\ 0 & -i\delta\hat{\rho}_3 \end{pmatrix} \quad (13)$$

to the self-energy. Here δ is the inelastic scattering rate and $h_{\text{eq}}(\varepsilon) = \tanh(\beta\varepsilon/2)$, where β is the inverse temperature towards which the system relaxes.

If we write the upper-right block of \hat{F}_1 as $F_1 = \sigma_1 F_t + \sigma_2 F_s$, where σ_1 and σ_2 are Pauli matrices, the zeroth-order distribution function $H_0 = H_L I_4 + H_{\text{TS}} \text{diag}(1, -1, -1, 1)$, and let $m^{\pm}(t, T) := m(T + t/2) \pm m(T - t/2)$, we find that

$$\left(2\frac{\partial}{\partial t} - \nabla^2 + 2\delta\right) \begin{pmatrix} F_s \\ F_t \end{pmatrix} = \begin{pmatrix} -m^+ F_t \\ m^+ F_s \end{pmatrix}, \quad (14a)$$

$$e_n \cdot \nabla F_s|_{x=0,1} = F_{l,r}^{\text{BCS}}, \quad e_n \cdot \nabla F_t|_{x=0,1} = 0, \quad (14b)$$

$$\left(\frac{\partial}{\partial T} + 2\delta\right) \begin{pmatrix} H_L - H_{\text{eq}} \\ H_{\text{TS}} \end{pmatrix} = \begin{pmatrix} -m^- H_{\text{TS}} \\ m^- H_L \end{pmatrix}, \quad (14c)$$

where $F_l^{\text{BCS}} = \Delta e^{-\delta t} J_0(|\Delta|t)\theta(t)$ and $F_r^{\text{BCS}} = e^{i\phi} F_l^{\text{BCS}}$ are the anomalous Green's functions in the left and right superconductors, respectively. J_0 is the zeroth-order Bessel function of the first kind, Δ is the superconducting gap parameter, and ϕ is the phase difference between the two superconductors. Equation (14) can be solved analytically for arbitrary $m(T)$, and the solution is shown in the Supplemental Material [16].

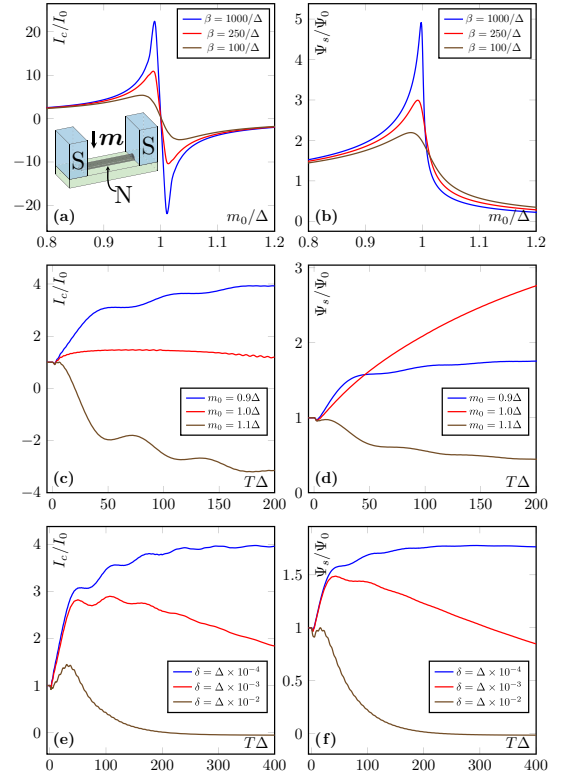


FIG. 1. Critical current I_c and singlet Cooper pair correlation function Ψ_s normalized by the values at zero exchange field, I_0 and Ψ_0 . The inset in (a) shows a sketch of the setup. Panels (a) and (b) show the steady-state values obtained with $\delta = 0$ for various values of exchange field m_0 . Panels (c) and (d) show the time evolution for different values of m_0 with $\delta/\Delta = 10^{-4}$ and $\beta\Delta = 1000$. Panels (e) and (f) show the time evolution for different values of δ with $m_0/\Delta = 0.9$ and $\beta\Delta = 1000$. In all cases $\Delta/\varepsilon_T = 10$. Ψ_s is computed for $\phi = 0$, which makes the enhancement predicted here applicable also to an SN junction.

The interface parameter z is assumed small enough to fulfill the criterion of a weak proximity effect for all relevant times t and T .

Consider an exchange field that abruptly changes value from 0 to m_0 at time $T = 0$, $m(T) = m_0\theta(T)$. The critical supercurrent

$$I_c = \max_{\phi \in (0, 2\pi]} \frac{\pi N_0 e D}{4} \text{Tr}[\hat{\rho}_3(\check{G} \bullet \check{\nabla} \bullet \check{G})^K]_{t=0} \quad (15)$$

and the singlet Cooper pair correlation function

$$\Psi_s = -i\pi N_0 (F_s \bullet H_L - F_t \bullet H_{\text{TS}})|_{t=0}, \quad (16)$$

following an abrupt change in the exchange field, are shown in Fig. 1. When the time becomes comparable to the inelastic scattering time, both I_c and Ψ_s are suppressed and the quantities reach their equilibrium values. However, before that, I_c and Ψ_s are significantly enhanced when the exchange field is

close to the superconducting gap Δ . When $m_0 \ll \Delta$ there is only a slight change to the current and Cooper pair correlation function.

We suggest that the behavior of I_c and Ψ_s can be understood from the interplay between the spin dependence of the nonequilibrium distribution function and the energy dependence of both the Andreev reflection probability and the degree of coherence between the participating electrons and holes. To see this, we note that in a time-independent situation both I_c and Ψ_s , jointly denoted A below, can be written as an integral over energy of the form

$$A = \int d\varepsilon (a_\uparrow h_\uparrow + a_\downarrow h_\downarrow), \quad (17)$$

as shown in the Supplemental Material [16]. Here h_\uparrow and h_\downarrow are the distribution functions for electrons with spin \uparrow and \downarrow . The explanation can be summarized as three key points.

First, $a_{\uparrow,\downarrow}$ is of largest amplitude at energies close to $\pm\Delta$ and $\pm m$, where a_\uparrow is large close to $\varepsilon = -m$ and a_\downarrow is large close to $\varepsilon = m$. These energies are special in the context of Andreev reflections, which is the process relevant for transferring superconductivity into the normal metal. At $\varepsilon = \pm\Delta$ there is a large peak in the Andreev reflection probability [25] which physically can be understood as resonant scattering produced by subsequent reflections by the interface and the superconducting order parameter [26]. At $\varepsilon = \mp m$ the wave vector of the incoming electrons, $k_{\uparrow,\downarrow}^e = \sqrt{2m(E_F + \varepsilon \pm m)}$, match that of the retroreflected holes, $k_{\uparrow,\downarrow}^h = \sqrt{2m(E_F - \varepsilon \mp m)}$. Hence, at energies close to $\pm m$ the superconducting correlations penetrate far into the normal metal.

Second, $a_{\uparrow,\downarrow}$ is antisymmetric close to $\mp m$, as long as $m < \Delta$. This is shown in the Supplemental Material [16]. That is, filled states with energy just above $\mp m$ contribute oppositely to filled states with energy just below $\mp m$. Hence, when $m > 0$ and the system is at equilibrium, such that $h_\uparrow(\varepsilon) = h_\downarrow(\varepsilon) = \tanh(\beta\varepsilon/2)$, the contributions to Ψ_s and I_c are suppressed because the coherent states are shifted away from the Fermi surface. However, before inelastic scattering relaxes the system, we find that the distribution functions evolve toward $h_{\uparrow,\downarrow}(\varepsilon) = \tanh[(\varepsilon \pm m)/\beta]$. This is physically reasonable, since an abrupt temporal change induced by the magnetic field not only shifts the energy levels but also preserves the occupation of these states before they have had time to relax. The energy shift in the antisymmetric contribution to $a_{\uparrow,\downarrow}$ coming from the coherent Andreev reflections are thus matched by a similar shift in the distribution function, so Ψ_s and I_c are not suppressed as m is increased.

Third, when $m \approx \Delta$ the enhanced probability of Andreev reflections amplifies the contribution from $\varepsilon \approx m$. In equilibrium, both the positive and negative contributions are amplified, so the overall effect is still a suppression of Ψ_s

and I_c when compared to $m = 0$. However, in the transient period with $h_{\uparrow,\downarrow}(\varepsilon) = \tanh[(\varepsilon \pm m)/\beta]$ the consequence is a manifold increase in Ψ_s and I_c . In other words, when $m \approx \Delta$ the Andreev reflections with the longest lifetimes are also the ones with the highest probability of occurring, and the nonequilibrium distribution functions that are present before the system has had time to relax allows this to manifest as a strong enhancement in superconductivity.

We find that the timescale for which the I_c and Ψ_s are able to reach their amplified states is given primarily by Δ . Hence, in order to experimentally detect the enhanced supercurrent it is necessary that δ/Δ is not too large. From Fig. 1 one can see that $\delta < 10^{-2}\Delta$ is sufficient to observe an increase in the supercurrent. Experimental values of the inelastic scattering rate, or Dynes parameter, are often found by parameter fitting, and values as low as $\delta/\Delta = 2.2 \times 10^{-5}$ have been reported in the millikelvin regime [27]. With $\Delta \approx 1$ meV and $\delta/\Delta = 2.2 \times 10^{-5}$, the relaxation time is about 10ns. A Zeeman splitting of 1 meV is achieved with a magnetic field strength of around 30 T/g, where g is the Landau factor. This could be either tens of T if $g = 2$ or tens of mT when $g \approx 10^3$. The latter can be found, for instance, in Dirac semimetals [28]. In the former case, an Ising-type superconductor such as NbSe₂ can be used to retain superconductivity at high in-plane fields.

The strong enhancement of the proximity-induced singlet order parameter Ψ_s suggests that the order parameter in the superconductor, if solved for self-consistently, could potentially also be enhanced by virtue of the inverse proximity effect. In turn, this would imply an increase in the critical temperature T_c of the superconducting transition. We leave this issue, which requires complicated time-dependent, self-consistent numerical calculations, for a future work.

Conclusion. We have presented a method for solving the time-dependent Usadel equation with arbitrary time dependence. This is made possible by two observations. First, the circle products simplify considerably in Fourier space when one of the arguments is independent of energy; second, by linearizing the equations, only such products remain.

We applied this method to analytically study SNS junctions with time-dependent Zeeman splitting m where a magnetic field is abruptly turned on. We demonstrated a strong enhancement of the supercurrent and Cooper pair correlation function when $m \approx \Delta$, where Δ is the superconducting gap. In particular, if the inelastic scattering rate δ is smaller than $\Delta \times 10^{-2}$ and the magnetic field changes value during a time frame shorter than $1/\delta$, our results show an up to twentyfold increase in the magnetic field that potentially lasts for tens of nanoseconds.

Acknowledgments. This work was supported by the Research Council of Norway through Grant No. 240806, and its Centres of Excellence funding scheme through Grant No. 262633 ‘‘QuSpin.’’ J.L. also acknowledges funding from the NV faculty at the Norwegian University of Science and Technology.

[1] M. Mitrano, A. Cantaluppi, D. Nicoletti, S. Kaiser, A. Perucchi, S. Lupi, P. Di Pietro, D. Pontiroli, M. Riccò, S. R. Clark *et al.*, *Nature (London)* **530**, 461 (2016).

[2] D. Nicoletti, E. Casandru, Y. Laplace, V. Khanna, C. R. Hunt, S. Kaiser, S. S. Dhesi, G. D. Gu, J. P. Hill, and A. Cavalleri, *Phys. Rev. B* **90**, 100503(R) (2014).

- [3] S. Kaiser, C. R. Hunt, D. Nicoletti, W. Hu, I. Gierz, H. Y. Liu, M. Le Tacon, T. Loew, D. Haug, B. Keimer, and A. Cavalleri, *Phys. Rev. B* **89**, 184516 (2014).
- [4] J. M. Warlaumont, J. C. Brown, T. Foxe, and R. A. Buhrman, *Phys. Rev. Lett.* **43**, 169 (1979).
- [5] H. A. Notarys, M. L. Yu, and J. E. Mercereau, *Phys. Rev. Lett.* **30**, 743 (1973).
- [6] P. Virtanen, T. T. Heikkilä, F. S. Bergeret, and J. C. Cuevas, *Phys. Rev. Lett.* **104**, 247003 (2010).
- [7] M. Houzet, *Phys. Rev. Lett.* **101**, 057009 (2008).
- [8] F. S. Bergeret, A. F. Volkov, and K. B. Efetov, *Phys. Rev. Lett.* **86**, 4096 (2001).
- [9] J. Linder and A. V. Balatsky, *Rev. Mod. Phys.* **91**, 045005 (2019).
- [10] J. C. Cuevas, J. Hammer, J. Kopu, J. K. Viljas, and M. Eschrig, *Phys. Rev. B* **73**, 184505 (2006).
- [11] A. V. Semenov, I. A. Devyatov, P. J. de Visser, and T. M. Klapwijk, *Phys. Rev. Lett.* **117**, 047002 (2016).
- [12] J. Linder, M. Amundsen, and J. A. Ouassou, *Sci. Rep.* **6**, 38739 (2016).
- [13] R. Watts-Tobin, Y. Krähenbühl, and L. Kramer, *J. Low Temp. Phys.* **42**, 459 (1981).
- [14] T. Kubo and A. Gurevich, *Phys. Rev. B* **100**, 064522 (2019).
- [15] A. I. Buzdin, *Rev. Mod. Phys.* **77**, 935 (2005).
- [16] See Supplemental Material at <http://link.aps.org/supplemental/10.1103/PhysRevB.103.L100502> for a derivation of the kinetic equations, analytical solutions, and a discussion on arbitrary impurity concentrations.
- [17] K. D. Usadel, *Phys. Rev. Lett.* **25**, 507 (1970).
- [18] J. Rammer and H. Smith, *Rev. Mod. Phys.* **58**, 323 (1986).
- [19] F. S. Bergeret and I. V. Tokatly, *Phys. Rev. Lett.* **110**, 117003 (2013).
- [20] M. Amundsen and J. Linder, *Phys. Rev. B* **96**, 064508 (2017).
- [21] M. Y. Kupriyanov and V. F. Lukichev, *Zh. Eksp. Teor. Fiz.* **94**, 139 (1988).
- [22] M. Eschrig, A. Cottet, W. Belzig, and J. Linder, *New J. Phys.* **17**, 083037 (2015).
- [23] A. Schmid and G. Schön, *J. Low Temp. Phys.* **20**, 207 (1975).
- [24] J. Linder, T. Yokoyama, and A. Sudbø, *Phys. Rev. B* **77**, 174514 (2008).
- [25] G. E. Blonder, M. Tinkham, and T. M. Klapwijk, *Phys. Rev. B* **25**, 4515 (1982).
- [26] Y. Asano, Y. Tanaka, and S. Kashiwaya, *Phys. Rev. B* **69**, 134501 (2004).
- [27] A. V. Feshchenko, L. Casparis, I. M. Khaymovich, D. Maradan, O.-P. Saira, M. Palma, M. Meschke, J. P. Pekola, and D. M. Zumbühl, *Phys. Rev. Appl.* **4**, 034001 (2015).
- [28] C. Li, B. de Ronde, J. de Boer, J. Ridderbos, F. Zwanenburg, Y. Huang, A. Golubov, and A. Brinkman, *Phys. Rev. Lett.* **123**, 026802 (2019).

Supplementary: Temporarily enhanced superconductivity from magnetic fields

Eirik Holm Fyhn¹ and Jacob Linder¹

¹Center for Quantum Spintronics, Department of Physics, Norwegian University of Science and Technology, NO-7491 Trondheim, Norway

(Dated: February 22, 2021)

I. KINETIC EQUATIONS

Finding the retarded Green's function is enough to calculate the local density of states, but for many other quantities, such as charge or spin currents, magnetization or Cooper-pair correlation functions, one needs the full Keldysh Green's function. Here we show the equations for the distribution function h , which can be used to find the Keldysh Green's function through the relations

$$\hat{g}^A = -\hat{\rho}_3 \left(\hat{g}^R \right)^\dagger \hat{\rho}_3, \quad \hat{g}^K = \hat{g}^R \circ h - h \circ \hat{g}^A. \quad (1)$$

We start by writing h as an expansion in the small parameter,

$$h = \sum_{n=0}^{\infty} z^n h_n. \quad (2)$$

In order to solve for the charge current in a way that consistently include the supercurrent contribution we need to solve for h to second order in z . This can be seen from the fact that charge and spin currents are given by the diagonal components of

$$\hat{j}^K = \hat{g}^R \circ \left(\tilde{\nabla} \circ \hat{g}^R \right) \circ h - h \circ \hat{g}^A \circ \left(\tilde{\nabla} \circ \hat{g}^A \right) + \tilde{\nabla} \circ h - \hat{g}^R \circ \left(\tilde{\nabla} \circ h \right) \circ \hat{g}^A, \quad (3)$$

where \hat{j}^K is the upper right block of $\check{j} := \check{g} \circ \tilde{\nabla} \circ \check{g}$. The supercurrent, which are given by the first two terms on the right hand side of Eq. (3), is at least second order in z . Hence, one must in general find h_0 , h_1 and h_2 .

The reason why the perturbation expansion in z works for \hat{g}^R , is that \hat{g}^R is independent of ε to zeroth order. This is not true for h . However, the equation for h is linear, so the perturbation expansion is nevertheless able to remove circle-products between functions that depend on ε . The equation for

h can be found by taking the covariant derivative of Eq. (3) and inserting the Usadel equation presented in the main text. We find that

$$\begin{aligned} \hat{\rho}_3 \frac{\partial h}{\partial T} \circ \hat{g}^A - \hat{g}^R \circ \frac{\partial h}{\partial T} \hat{\rho}_3 + \tilde{\nabla} \circ \tilde{\nabla} \circ h + \hat{j}^R \circ \tilde{\nabla} \circ h \\ - \left(\tilde{\nabla} \circ h \right) \circ \hat{j}^A - \hat{g}^R \circ \left[\tilde{\nabla} \circ \tilde{\nabla} \circ h \right] \circ \hat{g}^A \\ - \left(\tilde{\nabla} \circ \hat{g}^R \right) \circ \left(\tilde{\nabla} \circ h \right) \circ \hat{g}^A - \hat{g}^R \circ \left(\tilde{\nabla} \circ h \right) \circ \tilde{\nabla} \circ \hat{g}^A \\ = i[\check{\sigma}, \check{g}]_o^R \circ h - ih \circ [\check{\sigma}, \check{g}]_o^A - i[\check{\sigma}, \check{g}]_o^K, \quad (4) \end{aligned}$$

where \hat{j}^R and \hat{j}^A are the upper left and lower right blocks of \check{j} and $\varepsilon \text{diag}(\hat{\rho}_3, \hat{\rho}_3)$ has been extracted from the self-energy $\check{\sigma}$. The commutators are with respect to the circle-product and can be evaluated using

$$\begin{aligned} i[\check{\sigma}, \check{g}]_o^R \circ h - ih \circ [\check{\sigma}, \check{g}]_o^A - i[\check{\sigma}, \check{g}]_o^K \\ = i\hat{g}^R \circ \left[\hat{\sigma}^K - \left(\hat{\sigma}^R \circ h - h \circ \hat{\sigma}^A \right) \right] \\ - i \left[\hat{\sigma}^K - \left(\hat{\sigma}^R \circ h - h \circ \hat{\sigma}^A \right) \right] \circ \hat{g}^A. \quad (5) \end{aligned}$$

We will assume that $\hat{\sigma}^K$ is block-diagonal, just like $\hat{\sigma}^R$ and $\hat{\sigma}^A$. This assumption is valid in the system considered in the main manuscript. Unlike $\hat{\sigma}^R$ and $\hat{\sigma}^A$, however, there will be no restrictions on $\hat{\sigma}^K$ with regards to its energy-dependence. This is taken advantage of in the relaxation time approximation used in the main text. Note that the same derivation can be done when $\hat{\sigma}^K$, $\hat{\sigma}^R$ and $\hat{\sigma}^A$ are not block-diagonal. The only difference is which terms to include in the perturbation expansion of Eq. (4).

The Keldysh part of Kupriyanov-Lukichev boundary condition can be written

$$e_n \cdot \left[\tilde{\nabla} \circ h - \hat{g}^R \circ \left(\tilde{\nabla} \circ h \right) \circ \hat{g}^A \right] = \frac{z}{2} \left\{ \hat{g}^R \circ \left[\hat{g}_s^R \circ (h_s - h) - (h_s - h) \circ \hat{g}_s^A \right] - \left[\hat{g}_s^R \circ (h_s - h) - (h_s - h) \circ \hat{g}_s^A \right] \circ \hat{g}^A \right\}, \quad (6)$$

where h_s is the distribution function in the neighbouring region.

We find that to zeroth order in z ,

$$\frac{\partial h_0}{\partial T} = \tilde{\nabla} \circ \tilde{\nabla} \circ h_0 - i\hat{\rho}_3 \left(\hat{\sigma}^K - \hat{\sigma}^R \circ h_0 + h_0 \circ \hat{\sigma}^A \right), \quad (7a)$$

$$e_n \cdot \tilde{\nabla} \circ h_0 = 0, \quad (7b)$$

and to first order,

$$\frac{\partial h_1}{\partial T} = \tilde{\nabla} \circ \tilde{\nabla} \circ h_1 + i\hat{\rho}_3 \left(\hat{\sigma}^R \circ h_1 - h_1 \circ \hat{\sigma}^A \right), \quad (8a)$$

$$\begin{aligned} \mathbf{e}_n \cdot \tilde{\nabla} \circ h_1 = \frac{1}{4} \left\{ \hat{\rho}_3 \left[\hat{g}_s^R \circ (h_s - h_0) - (h_s - h_0) \circ \hat{g}_s^A \right] \right. \\ \left. + \left[\hat{g}_s^R \circ (h_s - h_0) - (h_s - h_0) \circ \hat{g}_s^A \right] \hat{\rho}_3 \right\}. \end{aligned} \quad (8b)$$

There is also a first order equation of off-diagonal matrices, but this is automatically satisfied from Eq. (7). Finally, h_2 satisfies

$$\begin{aligned} 2\frac{\partial h_2}{\partial T} = 2\tilde{\nabla} \circ \tilde{\nabla} \circ h_2 + 2i\hat{\rho}_3 \left(\hat{\sigma}^R \circ h_2 - h_2 \circ \hat{\sigma}^A \right) \\ + \hat{j}_2^R \circ (\tilde{\nabla} \circ h_0) - (\tilde{\nabla} \circ h_0) \circ \hat{j}_2^A + (\tilde{\nabla} \circ \hat{g}_2) \circ \tilde{\nabla} \circ h_0 \hat{\rho}_3 \\ + \hat{\rho}_3 (\tilde{\nabla} \circ h_0) \circ \tilde{\nabla} \circ \hat{g}_2^\dagger - (\tilde{\nabla} \circ \hat{f}_1) \circ (\tilde{\nabla} \circ h_0) \circ \hat{f}_1^\dagger \\ - \hat{f}_1 \circ (\tilde{\nabla} \circ h_0) \circ \tilde{\nabla} \circ \hat{f}_1^\dagger, \end{aligned} \quad (9a)$$

$$\begin{aligned} \mathbf{e}_n \cdot \tilde{\nabla} \circ h_2 = \frac{1}{4} \left\{ \hat{f}_1 \circ \left[\hat{g}_s^R \circ (h_s - h_0) - (h_s - h_0) \circ \hat{g}_s^A \right] \right. \\ \left. - \left[\hat{g}_s^R \circ (h_s - h_0) - (h_s - h_0) \circ \hat{g}_s^A \right] \circ \hat{f}_1^\dagger \right. \\ \left. - \hat{\rho}_3 \left[\hat{g}_s^R \circ h_1 - h_1 \circ \hat{g}_s^A \right] - \left[\hat{g}_s^R \circ h_1 - h_1 \circ \hat{g}_s^A \right] \hat{\rho}_3 \right\}. \end{aligned} \quad (9b)$$

where

$$\hat{j}_2^R = \hat{f}_1 \circ \tilde{\nabla} \circ \hat{f}_1 + \rho_3 \tilde{\nabla} \circ \hat{g}_2, \quad (10a)$$

$$\hat{j}_2^A = \hat{f}_1^\dagger \circ \tilde{\nabla} \circ \hat{f}_1^\dagger + \rho_3 \tilde{\nabla} \circ \hat{g}_2^\dagger. \quad (10b)$$

Equations (8b) and (9b) can be further simplified by noting that, since h_1 and h_2 are block-diagonal, so too must $[\hat{g}_s^R \circ (h_s - h_n) - (h_s - h_n) \circ \hat{g}_s^A]$ for $n = 1$ and $n = 2$. As a result they commute with $\hat{\rho}_3$. Additionally,

$$\begin{aligned} 0 = \hat{f}_1 \circ \left[\hat{g}_s^R \circ (h_s - h_0) - (h_s - h_0) \circ \hat{g}_s^A \right] \\ - \left[\hat{g}_s^R \circ (h_s - h_0) - (h_s - h_0) \circ \hat{g}_s^A \right] \circ \hat{f}_1^\dagger \end{aligned}$$

because h_2 would have off-diagonal components otherwise. Hence,

$$\mathbf{e}_n \cdot \tilde{\nabla} \circ h_1 = \frac{\hat{\rho}_3}{2} \left[\hat{g}_s^R \circ (h_s - h_0) - (h_s - h_0) \circ \hat{g}_s^A \right], \quad (11)$$

$$\mathbf{e}_n \cdot \tilde{\nabla} \circ h_2 = -\frac{\hat{\rho}_3}{2} \left[\hat{g}_s^R \circ h_1 - h_1 \circ \hat{g}_s^A \right]. \quad (12)$$

Unlike the equation for \hat{f}_1 , presented in the main text, the equations for the distribution functions has circle-products that do not reduce to ordinary matrix products in Fourier space. However, these are all circle-products of functions that can be evaluated prior to solving the equations. This suggests an order in which to solve the equations. One can find \hat{f}_1 and h_0 first, but in order to find h_1 one must first know h_0 and in order to find h_2 one must have solved \hat{f}_1 , h_0 and h_1 . To write Eqs. (7)–(9) in a way that does not require evaluation of circle-products between unknown functions is now only a matter of Fourier-transforming, writing at the covariant derivatives and using eq. (11) in the main text.

Note that the equation for \hat{f}_1 involve differentiation with respect to t , whereas the center of mass time T appear only as a parameter. The equations for the distribution functions h_0 , h_1 and h_2 are opposite in this regard, and involve differentiation with respect to T but not t .

II. ANALYTICAL SOLUTION TO EQ. (14)

The retarded and Keldysh self-energies for the SNS-junction with inelastic scattering and time-dependent and spatially homogeneous exchange field $m(T)$ are

$$\hat{\sigma}^R = i\delta\hat{\rho}_3 + m \text{diag}(1, -1, 1, -1), \quad (13a)$$

$$\hat{\sigma}^K = 2i\delta\hat{\rho}_3 h_{\text{eq}}, \quad (13b)$$

where δ is the inelastic scattering rate, $h_{\text{eq}}(\varepsilon) = \tanh(\beta\varepsilon/2)$ and β is the inverse temperature towards which the system relaxes.

From Eqs. (7)–(9) we see that h_0 , h_1 and h_2 only have non-zero components proportional to the identity matrix I_4 and $\text{diag}(1, -1, -1, 1)$. Hence, only the supercurrent contributes to the charge current $\propto \int d\varepsilon \text{Tr}(\hat{\rho}_3 \hat{j}^K)$. For this reason we need only find the retarded Green's function and h_0 . We repeat the relevant equations here for convenience. If we write the upper right block of \hat{F}_1 as $F_1 = \sigma_1 F_t + \sigma_2 F_s$, where σ_1 and σ_2 are Pauli matrices, the zeroth order distribution function $H_0 = H_L I_4 + H_{TS} \text{diag}(1, -1, -1, 1)$ and let $m^\pm(t, T) = m(T + t/2) \pm m(T - t/2)$, we find that

$$\left(2\frac{\partial}{\partial t} - \nabla^2 + 2\delta \right) \begin{pmatrix} F_s \\ F_t \end{pmatrix} = \begin{pmatrix} -m^+ F_t \\ m^+ F_s \end{pmatrix}, \quad (14a)$$

$$\mathbf{e}_n \cdot \nabla F_s|_{x=0,1} = F_{l,r}^{\text{BSC}}, \quad \mathbf{e}_n \cdot \nabla F_t|_{x=0,1} = 0 \quad (14b)$$

$$\left(\frac{\partial}{\partial T} + 2\delta \right) \begin{pmatrix} H_L - H_{\text{eq}} \\ H_{TS} \end{pmatrix} = \begin{pmatrix} -m^- H_{TS} \\ m^- H_L \end{pmatrix}, \quad (14c)$$

where $F_l^{\text{BSC}} = \Delta e^{-\delta t} J_0(|\Delta|t)\theta(t)$ and $F_r^{\text{BSC}} = e^{i\phi} F_l^{\text{BSC}}$ are the anomalous Green's functions in the left and right superconductors, respectively. J_0 is the zeroth order Bessel function of the first kind. The superconducting energy gap is Δ , and ϕ is the phase difference between the two superconductors. Finally, with the notation used in the main text $m^\pm(t, T) = m(T + t/2) \pm m(T - t/2)$.

Assuming that the system is at equilibrium at $T = -\infty$, we

find that the solution is

$$F_s = \frac{\Delta e^{-\delta t}}{2} \int_0^t d\tau J_0(|\Delta|\tau) \cos\left(\frac{1}{2} \int_\tau^t d\tilde{\tau} m^+(\tilde{\tau}, T)\right) \times \sum_{n=-\infty}^{\infty} [1 + (-1)^n e^{i\phi}] \cos(n\pi x) e^{-\frac{1}{2} n^2 \pi^2 (t-\tau)}, \quad (15a)$$

$$F_t = \frac{\Delta e^{-\delta t}}{2} \int_0^t d\tau J_0(|\Delta|\tau) \sin\left(\frac{1}{2} \int_\tau^t d\tilde{\tau} m^+(\tilde{\tau}, T)\right) \times \sum_{n=-\infty}^{\infty} [1 + (-1)^n e^{i\phi}] \cos(n\pi x) e^{-\frac{1}{2} n^2 \pi^2 (t-\tau)}, \quad (15b)$$

$$H_L = 2\delta H_{\text{eq}} \int_{-\infty}^T d\tau e^{-2\delta(T-\tau)} \cos\left(\int_\tau^T d\tilde{\tau} m^-(t, \tilde{\tau})\right), \quad (15c)$$

$$H_{TS} = 2\delta H_{\text{eq}} \int_{-\infty}^T d\tau e^{-2\delta(T-\tau)} \sin\left(\int_\tau^T d\tilde{\tau} m^-(t, \tilde{\tau})\right). \quad (15d)$$

III. OBSERVABLES

The singlet Cooper pair correlation function Ψ_s and electrical current I can be obtained from inserting the analytical solution given by Eq. (15) into the expressions

$$\Psi_s = -i\pi N_0 (F_s \bullet H_L - F_t \bullet H_{TS})|_{t=0}, \quad (16)$$

and

$$I = \frac{\pi e D}{4} \text{Tr} \left[\hat{\rho}_3 \left(\check{G} \bullet \check{\nabla} \bullet \check{G} \right)^K \right]_{t=0}, \quad (17)$$

After some algebra we find that

$$I = \pi N_0 e D \left[\text{Im} \{ F_s \bullet \nabla F_s^* + \nabla F_s^* \bullet F_s - F_t \bullet \nabla F_t^* - \nabla F_t^* \bullet F_t \} \bullet i H_L - \text{Im} \{ F_t \bullet \nabla F_s^* + \nabla F_s^* \bullet F_t + F_s \bullet \nabla F_t^* + \nabla F_t^* \bullet F_s \} \bullet i H_{TS} \right]_{t=0}. \quad (18)$$

To understand the non-equilibrium behaviour it is useful to use the distribution functions for spin-up, $H_+ = H_L + iH_{TS}$, and spin-down, $H_- = H_L - iH_{TS}$. If we write the upper right block of \hat{F} = antidiag(F_+ , F_-), then $F_\pm = F_t \mp iF_s$. With this we get that the singlet Cooper pair correlation function can be written

$$\Psi = \frac{\pi N_0}{2} (F_+ \bullet H_+ - F_- \bullet H_-)|_{t=0}, \quad (19)$$

and the current is

$$I = \frac{\pi N_0 e D}{4} (J_+ \bullet H_+ + J_- \bullet H_-)|_{t=0}, \quad (20)$$

where

$$J_+ = F_-^* \bullet \nabla F_+ + \nabla F_+ \bullet F_-^* - F_+ \bullet \nabla F_-^* - \nabla F_-^* \bullet F_+, \quad (21a)$$

$$J_- = F_+^* \bullet \nabla F_- + \nabla F_- \bullet F_+^* - F_- \bullet \nabla F_+^* - \nabla F_+^* \bullet F_-. \quad (21b)$$

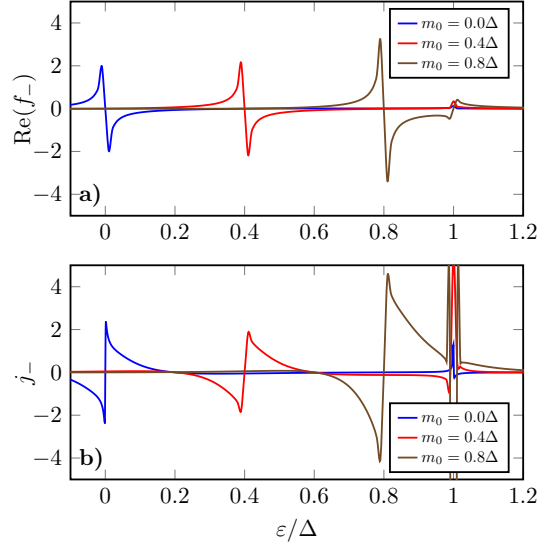


FIG. 1: a) The real part of the anomalous Green's function f_- with $\phi = 0$ and b) spectral current j_- with $\phi = \pi/2$ as a function of energy ε for various exchange fields m_0 . The energy gap in the superconductors is $\Delta = 50\varepsilon_T$, where ε_T is the Thouless energy, and the inelastic scattering rate is $\delta = \Delta \times 10^{-3}$.

We note in passing that both J_+ and J_- are proportional to $\sin \phi$, as can be seen most readily by evaluating them at $x = 1/2$. Hence, the critical current occurs when ϕ is a half-integral multiple of π . Also, when written as function of the exchange field m we have that $F_-(-m) = -F_+(m)$ and $J_-(-m) = J_+(m)$.

In order to study how the system evolves immediately after the exchange field is turned on, we can set the inelastic scattering rate to 0. In this case we find that

$$H_\pm(t, T) = H_{\text{eq}}(t) \exp\left(\pm i \int_{T-t/2}^{T+t/2} d\tau m(\tau)\right). \quad (22)$$

Assuming that $T > |t|/2$ for all the relevant relative times t , this is simply $H_\pm = H_{\text{eq}} e^{\pm i m_0 t}$. Hence, in energy space we have $h_\pm(\varepsilon) = h_{\text{eq}}(\varepsilon \pm m_0) = \tanh[\beta(\varepsilon \pm m_0)/2]$.

If $T > |t|/2$ for all the relevant relative times t we can also take advantage of the fact that the system is stationary, such that the circle-products in energy space reduces to normal multiplications. That is,

$$\Psi = \frac{N_0}{4} \int_{-\infty}^{\infty} d\varepsilon (f_+ h_+ - f_- h_-), \quad (23)$$

and

$$I = \frac{N_0 e D}{8} \int_{-\infty}^{\infty} d\varepsilon (j_+ h_+ + j_- h_-). \quad (24)$$

From Eq. (21) we can immediately see that the spectral current is antisymmetric in energy when $m_0 = 0$. In this

case $J_+ = J_- = -4i \text{Im}(F_s^* \bullet \nabla F_s)$ is purely imaginary, so the real part of its Fourier transform must be antisymmetric in ε . Because only the real part of the spectral current can give rise to a real electrical current, the spectral current is antisymmetric around $\varepsilon = 0$ when $m_0 = 0$. Similarly, F_\pm are purely imaginary when $\phi = 0$, $m_0 = 0$ and Δ is real, so the same arguments shows that the real parts of f_\pm are antisymmetric around $\varepsilon = 0$. It is the real part of f_\pm that is relevant for Ψ_s when $\phi = 0$, since Ψ_s is real.

When $m_0 \neq 0$ and $T > |t|/2$ we get that

$$F_\pm = \mp \frac{i\Delta e^{-\delta t} e^{\pm im_0 t}}{2} \int_0^t d\tau J_0(|\Delta|\tau) e^{\pm im_0 \tau} \times \sum_{n=-\infty}^{\infty} [1 + (-1)^n e^{i\phi}] \cos(n\pi x) e^{-\frac{1}{2}n^2 \pi^2 (t-\tau)}. \quad (25)$$

The factor $e^{\pm im_0 t}$ gives rise to a shift $\varepsilon \rightarrow \varepsilon \pm m$ in the Fourier transform. Hence, $f_\pm(\varepsilon) = p_\pm(\varepsilon \pm m_0 + i\delta)$, where p_\pm is the Fourier transform of the remaining integral. When $m_0 \ll \Delta$, the presence of $e^{\pm im_0 \tau}$ in the integrand works to shift oscillations with frequency Δ , but this does not affect the low frequency components. To see why, note that $J_0(x)$ is well approximated by $\cos(x - \pi/4)\sqrt{2/\pi x}$ for large x and

$$\cos(a)e^{ib} = \frac{e^{i(a+b)} + e^{-i(a-b)}}{2}. \quad (26)$$

Hence, the oscillatory part of the integrand is shifted to $\Delta \pm m_0$ while the low-frequency components in p_\pm are left unchanged. Because we know that p_\pm is antisymmetric for $m_0 = 0$, we see that f_\pm is antisymmetric close to $\varepsilon \pm m_0$ as long as $m_0 \ll \Delta$. When $m_0 \approx \Delta$, the oscillations in $J_0(|\Delta|\tau)$ are matched by those in $e^{\pm im_0 \tau}$, which affects the low-frequency components of p_\pm .

Figure 1 shows $\text{Re}(f_-)$ and j_- for various values of m_0 . From Fig. 1 one can see that the integrands are antisymmetric and large close to $\varepsilon = m_0$, which agrees with the discussion above. Moreover, we see that the values close to m_0 are enhanced as m_0 approaches $|\Delta|$. This can be understood as coming from the fact that Andreev reflections with long range occur at the energies where the probability of Andreev reflections is larger, as discussed in the main text. In equilibrium $h_\pm = \tanh(\beta\varepsilon/2)$, so the positive and negative contributions cancel when $m_0 > 0$. However, out of equilibrium the distribution function changes sign at $\varepsilon = m_0$, which allows for a significant contribution from the part close to $\varepsilon = m_0$.

IV. CONSISTENCY WITH MAXWELL'S EQUATIONS

Having solved the Usadel equation, the next step is to ensure that the solution is consistent with Maxwell's equation. There are no orbital effects in the one-dimensional wire, but there could in principle be an induced electric field coming from a nonuniform charge distribution. The charge density ρ can be calculated from

$$\rho(T) = -2eN_0 \left\{ \frac{\pi}{8} \text{Tr}[\hat{G}^K(0, T)] + 2e\phi(T) \right\}, \quad (27)$$

where ϕ is the electrochemical potential.

Since H_0 and H_1 has no component proportional to $\hat{\rho}_3$, we see that ρ is at least second order in z . Thus the induced electric field is also at least second order in z and thereby does not affect \hat{F}_1 , H_0 or H_1 . For this reason it follows that it does not affect the Cooper pair correlation function or the supercurrent. Nevertheless, it can in principle give rise to a resistive current contribution,

$$I_r = z^2 \frac{\pi e D}{2} \nabla \text{Tr}[\hat{\rho}_3 H_2(0, T)]. \quad (28)$$

By using the fact that the equilibrium distribution function at electrochemical potential ϕ is

$$H_{\text{eq}}(t, T) = \frac{-i}{\beta \sinh(\pi t/\beta)} \exp\left(-ie\hat{\rho}_3 \int_{T-t/2}^{T+t/2} d\tau \phi(\tau)\right), \quad (29)$$

we get from Eq. (9) that the resistive current solves

$$\frac{\partial I_r}{\partial(T\varepsilon_\tau)} - \frac{\partial^2 I_r}{\partial(x/L)^2} = 4z^2 \delta L^2 e^2 E, \quad (30)$$

where x , T and δ are now not dimensionless and $E = -\nabla\phi$ is the electric field. From Eq. (12) we get that the boundary condition is simply $I_r = 0$ at the interfaces. Thus, this resistive current does not contribute to the total current going through the wire and instead acts to redistribute charge.

By calculating $\text{Tr}[\hat{G}^K]$ from the analytical expression we find that the I_r is negligible and can be safely ignored.

V. BEYOND THE DIRTY LIMIT

The focus so far has been on the so-called dirty limit, where the elastic scattering time is small, such that the isotropic part of the Green's function dominates. However, the same framework as was presented here and in the main text can be applied also for systems outside the dirty limit. In fact, it works even better in the clean limit.

With arbitrary elastic scattering time τ_e , the quasiclassical Green's function solves the Eilenberger equation,

$$i\mathbf{v}_F \cdot \hat{\nabla} \circ \check{g} + \left[\varepsilon \hat{\rho}_3 + \check{\sigma} + \frac{i}{2\tau_e} \check{g}_s, \check{g} \right]_\circ = 0, \quad (31)$$

where \mathbf{v}_F is the Fermi velocity, the subscript \circ denotes that the commutator is taken with respect to the circle product and \check{g}_s is the isotropic part of the Green's function. Equation (31) gives the Usadel equation in the limit $\tau_e \rightarrow 0$.

The method presented in the main text works by writing the equations in the (t, T) -coordinates and eliminating circle products between functions that both depend on energy, except the term in the commutator that is linear in ε . This was done by linearizing the equations in the proximity effect. We see from Eq. (31) that the same is possible for arbitrary impurity concentrations. The difference is that in the Usadel equation it was the term $D\hat{\nabla} \circ (\check{g} \circ \hat{\nabla} \circ \check{g})$ that required linearization, whereas in the Eilenberger equation it is $i[\check{g}_s, \check{g}]/2\tau_e$. This term is absent in the clean limit since $\tau_e \rightarrow \infty$, so in this case

Eq. (31) is automatically free from the difficult kind of circle-products if δ does not depend on energy. This means that we do not need to linearize in the proximity effect. One consequence of this is that in the clean limit it could be possible to solve time-dependent transient situations even with retarded self-energies that are not block-diagonal to lowest order in z . In particular, this means that one could add superconducting pairing in the self-energy. Thus, one could potentially use this framework to find transient phenomena in clean superconductors.

Whether the full equations can be solved in time-dependent situations without additional simplifying assumption depends on the boundary conditions. One type of boundary condition which can be used in the clean limit is Zaitsev's linearized boundary condition [A. Zaitsev, *Zh. Eksp. Teor. Fiz.* **86**, 1742-1758], valid for a weak proximity effect. In that case, the antisymmetric part of the anomalous Green's function is continuous across the interfaces whereas the symmetric part has a drop proportional to the antisymmetric part of the anomalous Green function [N. Garcia and L.R. Tagirov, arXiv:cond-mat/0601212]. For such a boundary condition, the clean-limit equations can be solved even for an arbitrary time-dependence.

PAPER VI

Reference

Eirik Holm Fyhn and Jacob Linder,
Spin pumping in superconductor-antiferromagnetic insulator bi-layers.
Physical Review B **103**, 134508 (2021)
doi: 10.1103/physrevb.103.134508


CONTRIBUTIONS

EHF performed the analytical calculations and the numerical simulations, with support from JL. EHF drafted the manuscript. JL formulated the initial research goal. EHF and JL contributed to the physics discussions and the final manuscript revision. Specifically, in addition to participating in the discussion of the physics and the revision of the final manuscript, EHF wrote the initial draft, performed all the calculations, developed the code, performed the numerical simulations and produced all figures presented in the paper.

Spin pumping in superconductor-antiferromagnetic insulator bilayers

Eirik Holm Fyhn  and Jacob Linder

Center for Quantum Spintronics, Department of Physics, Norwegian, University of Science and Technology, NO-7491 Trondheim, Norway

 (Received 16 February 2021; revised 27 March 2021; accepted 30 March 2021; published 9 April 2021)

We study theoretically spin pumping in bilayers consisting of superconductors (SC) and antiferromagnetic insulators (AFI). We consider both compensated and uncompensated interfaces and include both the regular scattering channel and the Umklapp scattering channel. We find that at temperatures close to the critical temperatures and precession frequencies much lower than the gap, the spin current is enhanced in superconductors as compared to normal metals. Otherwise, the spin current is suppressed. The relevant precession frequencies, where the spin current in SC/AFI is enhanced compared to normal metals/AFI, is much lower than the typical resonance frequencies of antiferromagnets, which makes the detection of this effect experimentally challenging. A possible solution lies in the shifting of the resonance frequency by a static magnetic field.

DOI: [10.1103/PhysRevB.103.134508](https://doi.org/10.1103/PhysRevB.103.134508)

I. INTRODUCTION

Both superconductors (SC) and antiferromagnets (AF) are of particular interest in the context of spintronics. Antiferromagnets disturb neighboring components less than ferromagnetic or ferrimagnetic materials, because they produce no net stray field [1]. This means that antiferromagnetic components can be packed more tightly and are more robust against external magnetic fields than their ferromagnetic counterparts. Additionally, antiferromagnets operate at THz frequencies, which are much faster than the GHz frequencies of ferromagnets (F). This can allow for ultrafast information processing when working with antiferromagnets.

Superconductivity is a type of order that normally competes with magnetism. However, the discovery of spin-triplet superconductivity has shown that complete synergy between superconductivity and magnetism is possible [2–6], and superconductors are now an integral part of spintronics research. In addition to the potential for minimal Joule heating that comes with superconductivity, superconductors are interesting from a spintronics perspective because of spin-charge separation [7,8], which allows spin and charge imbalances to decay over different length scales. It has been observed that the spin relaxation time can be considerably longer than the charge relaxation time [9].

Since both superconductors and antiferromagnets are useful as building blocks in spintronic devices, it is of interest to study spin transport in hybrid superconductor-antiferromagnet devices. Despite this, SC/AF structures are largely unexplored compared to superconductor-ferromagnetic structures. Here, we study theoretically spin pumping in superconductor-antiferromagnetic insulator (SC/AFI) bilayers. This refers to the injection of a spin current in the superconductor, which we consider to be spin singlet and s wave, by the application of a precessing magnetic field in the AFI [10]. Spin pumping has been observed in F/SC structures [11–13] and investigated theoretically in F/SC structures by calculations based

on the local dynamic spin susceptibility in the SC [14,15] and quasiclassical theory [16,17]. The theoretical works found an enhanced spin current in superconductors compared to normal metals (NMs) below the transition temperatures [14,15].

While spin pumping in SC/AF structures has, to our knowledge, not been explored, some important work has been done with normal metal-antiferromagnetic systems. It has been found theoretically that spin pumping is of a similar magnitude as in the ferromagnetic case [18,19], and more recently measurements of the inverse spin-Hall voltage demonstrated the spin-pumping effect in MnF_2/Pt [20]. Combining the demonstration of AF/NM spin pumping with the above mentioned evidence of F/SC spin pumping, AF/SC spin pumping is feasible and merits further study.

We mainly follow the methodology presented in Ref. [15], but modified for a superconductor-antiferromagnetic insulator bilayer. In particular, the staggered magnetic order of the AFI gives rise to two different scattering channels [21–23], and the two different sublattices can be coupled to the superconductor in a symmetric or asymmetric way. To capture this we will not approximate the interaction Hamiltonian by a uniform scattering amplitude, as in Ref. [15], but instead model the interaction with an exchange coupling between itinerant electrons in the SC and the localized spins in the AFI. Using this coupling, it turns out that the relevant quantity is not the *local* dynamic spin susceptibility, as in Refs. [14,15], but instead the *planar* dynamic spin susceptibility. Using the planar dynamic spin susceptibility we find that the spin pumping into superconductors from antiferromagnets is enhanced as compared to spin pumping into normal metals when the temperature is close to the transition temperature and the precession frequency is small compared to the energy gap. Otherwise the spin current in the superconductor is suppressed. This is similar to the results obtained from ferromagnets. However, unlike in the case of ferromagnets, the resonance frequency in antiferromagnets is typically too large for spin pumping with

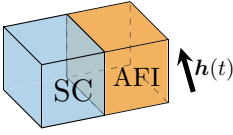


FIG. 1. Sketch of a superconductor (SC)-antiferromagnetic insulator (AFI) bilayer with a precessing external magnetic field $\mathbf{h}(t)$.

frequencies below the gap to be experimentally detectable. One possible solution is to apply a static magnetic field, which we discuss in Sec. VI.

II. MODEL

The system depicted in Fig. 1 is modeled by the Hamiltonian,

$$H = H_{\text{SC}} + H_{\text{AFI}} + H_{\text{int}}, \quad (1)$$

where the Bogoliubov–de Gennes Hamiltonian,

$$H_{\text{SC}} = \sum_{\mathbf{k} \in \square} \begin{pmatrix} c_{\mathbf{k},\uparrow}^\dagger & c_{-\mathbf{k},\downarrow} \end{pmatrix} \begin{pmatrix} \xi_{\mathbf{k}} & \Delta \\ \Delta^* & -\xi_{\mathbf{k}} \end{pmatrix} \begin{pmatrix} c_{\mathbf{k},\uparrow} \\ c_{-\mathbf{k},\downarrow}^\dagger \end{pmatrix}, \quad (2)$$

where \square is the first Brillouin zone (IBZ) in the superconductor, gives a mean-field description of superconductivity. The antiferromagnetic insulator Hamiltonian is given by

$$H_{\text{AFI}} = J \sum_{\langle i,j \rangle} \mathbf{S}_i \cdot \mathbf{S}_j - K \sum_i S_{i,z}^2 - \gamma \sum_i \mathbf{S}_i \cdot \mathbf{h}, \quad (3)$$

where $\langle i,j \rangle$ means that the sum goes over nearest neighbors and \sum_i goes over lattice points in the AFI. The exchange coupling at the interface is given by

$$H_{\text{int}} = -2 \sum_i J_i \begin{pmatrix} c_{i,\uparrow}^\dagger & c_{i,\downarrow}^\dagger \end{pmatrix} \boldsymbol{\sigma} \begin{pmatrix} c_{i,\uparrow} \\ c_{i,\downarrow} \end{pmatrix} \cdot \mathbf{S}_i, \quad (4)$$

where the sum goes over the lattice points in the interface. Here, $\xi_{\mathbf{k}}$ is the kinetic energy measured relative to the chemical potential μ , $c_{\mathbf{k},\sigma}$ is the annihilation operator for electrons with spin σ and wave vector \mathbf{k} , J is the antiferromagnetic exchange parameter, K is the easy-axis anisotropy, \mathbf{S}_i is the spin at lattice site i in the AFI, and γ gives the coupling strength to the external magnetic field \mathbf{h} . The vector of Pauli matrices is given by $\boldsymbol{\sigma}$, and $J_i = J_A$ ($J_i = J_B$) when i belongs to the A (B) sublattice. Also, Δ is the superconducting gap parameter, which we assume real and satisfies

$$1 = \lambda \int_0^{\omega_D} \frac{\tanh(\sqrt{\varepsilon^2 + \Delta^2}/2T)}{\sqrt{\varepsilon^2 + \Delta^2}}, \quad (5)$$

where T is the temperature, which we assume to be the same for the superconductor and AFI, and ω_D and λ are material-specific parameters that determine the critical temperature T_c and the zero-temperature gap $\Delta_0 := \Delta(0)$.

In order to diagonalize H_{AFI} we can do a Holstein-Primakoff transformation followed by a Fourier transform and a Bogoliubov transformation. This gives to second order in magnon operators the following antiferromagnetic

Hamiltonian:

$$H_{\text{AFI}} = \sum_{\mathbf{k} \in \diamond} (\omega_{\mathbf{k}}^{\alpha} \alpha_{\mathbf{k}}^\dagger \alpha_{\mathbf{k}} + \omega_{\mathbf{k}}^{\beta} \beta_{\mathbf{k}}^\dagger \beta_{\mathbf{k}}) + \sqrt{2N_A S} (u_0 + v_0) \gamma [h^- (\alpha_0 + \beta_0^\dagger) + h^+ (\alpha_0^\dagger + \beta_0)], \quad (6)$$

where \diamond is the first magnetic Brillouin zone, which is the IBZ corresponding to the A sublattice, N_A is the number of lattice points in the A sublattice, S is the spin at each lattice point, $\alpha_{\mathbf{k}} = u_{\mathbf{k}} a_{\mathbf{k}} - v_{\mathbf{k}} b_{-\mathbf{k}}^\dagger$ and $\beta_{\mathbf{k}} = u_{\mathbf{k}} b_{\mathbf{k}} - v_{\mathbf{k}} a_{-\mathbf{k}}^\dagger$, where $a_{\mathbf{k}}$ and $b_{\mathbf{k}}$ are the magnon annihilation operators for the A and B sublattices, and

$$u_{\mathbf{k}} = \frac{Jz + K}{\sqrt{(Jz + K)^2 - (J\gamma_{\mathbf{k}})^2}}, \quad (7a)$$

$$v_{\mathbf{k}} = -\frac{J\gamma_{\mathbf{k}}}{\sqrt{(Jz + K)^2 - (J\gamma_{\mathbf{k}})^2}}, \quad (7b)$$

$$\omega_{\mathbf{k}}^{\alpha} = S \sqrt{(Jz + K)^2 - (J\gamma_{\mathbf{k}})^2} + \gamma h_z, \quad (7c)$$

$$\omega_{\mathbf{k}}^{\beta} = S \sqrt{(Jz + K)^2 - (J\gamma_{\mathbf{k}})^2} - \gamma h_z. \quad (7d)$$

Here, h_z is the z component of the external magnetic field, which is the same as the magnetization direction in the antiferromagnet and the direction of the easy-axis anisotropy. Moreover, $h^\pm = h_x \pm i h_y$ and

$$\gamma_{\mathbf{k}} = \sum_{\langle \delta \rangle} \cos(\mathbf{k} \cdot \boldsymbol{\delta}) = \gamma_{-\mathbf{k}}, \quad (8)$$

where the sum goes over the nearest neighbor displacement vectors $\boldsymbol{\delta}$, and z is the number of nearest neighbors.

To write H_{int} in terms of Fourier components requires us to connect the reciprocal space in the superconductor with the reduced Brillouin zone of the magnetic lattice in the AFI. This gives rise to so-called Umklapp scattering, where the wave vector falls outside the IBZ in the AFI [23]. Whether this effect is present depends on the interface. Depending on how the interface slices the bipartite lattice of the AFI, the interface can have a different number of atoms belonging to the A and B lattices. If the interface has an equal number of atoms from each sublattice and the coupling strengths J_A and J_B are equal, we call it a compensated interface. Otherwise, it is uncompensated. We let $\mathbf{x} = \mathbf{0}$ be the location of a lattice point belonging to the A sublattice and \mathbf{x}_0 be such that all lattice points at the interface can be written $\mathbf{x}_0 + \tilde{\mathbf{x}}_i$, where $\mathbf{x}_0 \cdot \tilde{\mathbf{x}}_i = 0$.

To capture both compensated and uncompensated interfaces we will use the notation $\delta_{\mathbf{q}_i, \mathbf{k}_i}^A = 1$ to mean that $\mathbf{q} \cdot \tilde{\mathbf{x}}_i - \mathbf{k} \cdot \tilde{\mathbf{x}}_i = 2\pi n + d_1$ for all vectors $\tilde{\mathbf{x}}_i$ such that $\mathbf{x}_0 + \tilde{\mathbf{x}}_i$ is in the A sublattice at the interface and for some integer n and a constant d_1 that is independent of $\tilde{\mathbf{x}}_i$. Similarly, $\delta_{\mathbf{q}_i, \mathbf{k}_i}^B = 1$ means that $\mathbf{q} \cdot \tilde{\mathbf{x}}_i - \mathbf{k} \cdot \tilde{\mathbf{x}}_i = 2\pi n + d_2$ for all lattice vectors $\mathbf{x}_0 + \tilde{\mathbf{x}}_i$ in the B sublattice at the interface and for some integer n and a constant d_2 that is independent of $\tilde{\mathbf{x}}_i$. We can determine d_1 by noting that both $\tilde{\mathbf{x}}_i$ and $2\tilde{\mathbf{x}}_i$ is in the A sublattice, so $2d_1 = d_1 + 2\pi n \Rightarrow d_1 = 2\pi m$ for some integer m . Hence, we can set $d_1 = 0$. Similarly, if $\tilde{\mathbf{x}}_i$ is in the B sublattice, then $2\tilde{\mathbf{x}}_i$ is in the A sublattice, so $4\pi n + 2d_2 = 2\pi m \Rightarrow d_2 = l\pi$

for some integer l . The \mathbf{k} vectors that result in l being an odd number give rise to the Umklapp scattering channel. We can drop the superscripts because $\delta_{q_l, k_l}^A = 1 \iff \delta_{q_l, k_l}^B = 1$. This is because every lattice point in the B sublattice is midway between two lattice points in the A sublattice and vice versa. Finally, if the number of lattice points at the interface is equal on the superconductor and the antiferromagnet, then half of the possible \mathbf{k} vectors in the superconductor will give $l = 0$ and the other half will give $l = 1$. There is a vector \mathbf{G} connecting the region in \square with $l = 0$ to those with $l = 1$.

For a concrete example, consider the situation where the crystal lattices of the SC and AFI are equal and cubical. The 1BZ in the SC, \square , is therefore also cubical. Meanwhile, the sublattice in the AFI is face-centered cubic, so \diamond is the truncated octahedron inscribed in \square . A wave vector in the corner of \square will be in the center of the second Brillouin zone in the AFI. If we let \mathbf{G} be the vector in a corner of \square , then $\exp(i\mathbf{G} \cdot \mathbf{x}_i)$ is 1 when \mathbf{x}_i is in the A sublattice and -1 when \mathbf{x}_i is in the B sublattice. Thus \mathbf{G} is the vector that connects the region of \mathbf{k} vectors in \square with regular scattering and those with Umklapp-scattering.

Using this notation, H_{int} can, to first order in magnon operators, be written

$$H_{\text{int}} = \sum_{\mathbf{k} \in \square} \sum_{q \in \diamond} [T_{q\mathbf{k}}^\alpha \alpha_q s_{\mathbf{k}}^- + T_{q\mathbf{k}}^{\beta^\dagger} \beta_{q\mathbf{k}}^\dagger s_{\mathbf{k}}^- + \text{H.c.}] + H_{\text{int}}^Z, \quad (9)$$

where

$$H_{\text{int}}^Z = -\sqrt{2SN_A} \sum_{\mathbf{k} \in \square} \delta_{\mathbf{k}_1, 0} (\bar{J}_A - (-1)^l \bar{J}_B) s_{\mathbf{k}}^z e^{-i\mathbf{x}_0 \cdot \mathbf{k}} \quad (10)$$

is the Zeeman energy and

$$T_{q\mathbf{k}}^\alpha = -e^{i\mathbf{x}_0 \cdot (\mathbf{k} + \mathbf{q})} [\bar{J}_A u_q + (-1)^l \bar{J}_B v_q] \delta_{\mathbf{k}_1, -q_1}, \quad (11a)$$

$$T_{q\mathbf{k}}^{\beta^\dagger} = -e^{i\mathbf{x}_0 \cdot (\mathbf{k} - \mathbf{q})} [\bar{J}_A v_q + (-1)^l \bar{J}_B u_q] \delta_{\mathbf{k}_1, q_1}. \quad (11b)$$

Additionally,

$$\bar{J}_A = J_A \frac{2\sqrt{2SN_A^\parallel}}{N_S \sqrt{N_A}}, \quad (12a)$$

$$\bar{J}_B = J_B \frac{2\sqrt{2SN_B^\parallel}}{N_S \sqrt{N_A}}, \quad (12b)$$

where N_S is the number of lattice points in the superconductor and N_A^\parallel (N_B^\parallel) is the number of lattice points belonging to the A (B) sublattice at the interface, and

$$\bar{s}_{\mathbf{k}}^z = \frac{1}{2} \sum_{q \in \square} (c_{q\uparrow}^\dagger c_{q+\mathbf{k}\uparrow} - c_{q\downarrow}^\dagger c_{q+\mathbf{k}\downarrow}), \quad (13a)$$

$$\bar{s}_{\mathbf{k}}^- = \sum_{q \in \square} c_{q\downarrow}^\dagger c_{q+\mathbf{k}\uparrow}. \quad (13b)$$

The reason why the factor $(-1)^l$ is in front of the terms proportional to \bar{J}_B in Eqs. (10) and (11) is that the coordinate system is defined such that $\mathbf{x} = 0$ is the location of a lattice point belonging to the A sublattice.

III. GREEN'S FUNCTIONS

In order to calculate the spin current we will make use of Green's functions corresponding to three different types of operators. Let ψ be either α , β^\dagger , or s^+ , then the lesser, retarded, and advanced Green's functions are

$$G_\psi^<(t_1, t_2, \mathbf{k}) = -i \langle \psi_{\mathbf{k}}^\dagger(t_2) \psi_{\mathbf{k}}(t_1) \rangle_0, \quad (14a)$$

$$G_\psi^R(t_1, t_2, \mathbf{k}) = -i \theta(t_1 - t_2) \langle [\psi_{\mathbf{k}}(t_1), \psi_{\mathbf{k}}^\dagger(t_2)] \rangle_0, \quad (14b)$$

$$G_\psi^A(t_1, t_2, \mathbf{k}) = i \theta(t_2 - t_1) \langle [\psi_{\mathbf{k}}(t_1), \psi_{\mathbf{k}}^\dagger(t_2)] \rangle_0, \quad (14c)$$

respectively. The subscript 0 means that the expectation values are taken in the absence of H_{int} . This is done because we will treat H_{int} as a perturbation in the interaction picture. This is a good approximation as long as the transmission coefficients are small and has previously been shown to give good agreement with experiments [24–26]. We will also define the distribution function,

$$f^\psi(\varepsilon, \mathbf{k}) := \frac{G_\psi^<(\varepsilon, \mathbf{k})}{2i \text{Im} G_\psi^R(\varepsilon, \mathbf{k})}, \quad (15)$$

where the Green's functions in Eq. (14) are Fourier transformed with respect to the relative time $t_1 - t_2$. In thermal equilibrium, $f^\psi(\varepsilon, \mathbf{k})$ is equal to the Bose-Einstein distribution function $n_B(T, \varepsilon)$.

First consider the effect of spin pumping. We add spin pumping in the AFI by letting $h^\pm(t) = h_0 e^{\mp i\Omega t}$. The reader is referred to Appendix A for the detailed calculation, which shows that the retarded Green's functions are unaffected to second order in h_0 . Since the unperturbed Hamiltonian is diagonal in α and β^\dagger , this means that the retarded Green's functions for α and β^\dagger are

$$G_\alpha^R(\varepsilon, \mathbf{k}) = \frac{1}{\varepsilon - \omega_{\mathbf{k}}^\alpha + i\eta^\alpha}, \quad (16a)$$

$$G_{\beta^\dagger}^R(\varepsilon, \mathbf{k}) = -G_\beta^A(-\varepsilon, \mathbf{k}) = \frac{1}{\varepsilon + \omega_{\mathbf{k}}^\beta + i\eta^\beta}, \quad (16b)$$

where η^α and η^β are the lifetimes of the α and β magnons. The distribution functions are modified by the oscillating magnetic field, and to second order in h_0 ,

$$f^v(\varepsilon, \mathbf{k}) = n_B(\varepsilon, T) + \frac{2\pi N_A S [(u_0 + v_0) \gamma h_0]^2}{\eta^v} \delta_{\mathbf{k}, 0} \delta(\varepsilon - \Omega), \quad (17)$$

where $v \in \{\alpha, \beta^\dagger\}$.

The dynamic spin susceptibility $G_{s^+}^R$ is more complicated, but can be calculated from the imaginary time Green's function by use of analytical continuation and Matsubara summation techniques. This is shown in Appendix B, and the result is

$$G_{s^+}^R(\varepsilon, \mathbf{k}) = -\frac{1}{4} \sum_q \sum_{\omega=\pm E} \sum_{\tilde{\omega}=\pm\tilde{E}} \left(1 + \frac{\xi \tilde{\xi} + \Delta^2}{\omega \tilde{\omega}} \right) \times \frac{n_F(\tilde{\omega}, T) - n_F(\omega, T)}{\varepsilon + i\eta^{\text{SC}} - (\tilde{\omega} - \omega)}, \quad (18)$$

where $\xi = \xi_q$, $\tilde{\xi} = \xi_{q+\mathbf{k}}$, $E = \sqrt{\xi^2 + \Delta^2}$, and $\tilde{E} = \sqrt{\tilde{\xi}^2 + \Delta^2}$, n_F is the Fermi-Dirac distribution function.

Since the spin pumping in the AFI does not affect the Hamiltonian in the superconductor, the distribution function is $f^{s^\pm}(\varepsilon, \mathbf{k}) = n_B(\varepsilon, T)$.

IV. SPIN CURRENT

To find the spin current we follow Kato *et al.* [15] and use

$$I_s = -\frac{\partial}{\partial t} \langle s_0^z \rangle = -i \langle [H, s_0^z] \rangle. \quad (19)$$

From the fact that s_0^z commutes with $H_{\text{SC}} + H_{\text{AFI}}$, $[s_0^z, s_0^\pm] = s_0^\mp$, and $[A^\dagger, B] = -[A, B^\dagger]^\dagger$, we find that

$$[H, s_0^z] = \sum_{\mathbf{k} \in \square} \sum_{\mathbf{q} \in \diamond} [T_{\mathbf{qk}}^\alpha \alpha_{\mathbf{q}} s_{\mathbf{k}}^- + T_{\mathbf{qk}}^\beta \beta_{\mathbf{q}}^\dagger s_{\mathbf{k}}^- - \text{H.c.}]. \quad (20)$$

Thus, the spin current is

$$I_s(t) = 2 \sum_{\mathbf{k} \in \square} \sum_{\mathbf{q} \in \diamond} \sum_{v \in \{\alpha, \beta\}} \text{Im} \langle T_{\mathbf{qk}}^v s_{\mathbf{k}}^-(t) v_{\mathbf{q}}(t) \rangle. \quad (21)$$

We evaluate this expectation value in the interaction picture and treating the interfacial exchange interaction as a perturbation using the Keldysh formalism. First, let G_ψ with no superscript denote contour-ordered Green's functions,

$$G_\psi(\tau_1, \tau_2, \mathbf{k}) = -i \langle \mathcal{T}_c \psi_{\mathbf{k}}(\tau_1) \psi_{\mathbf{k}}^\dagger(\tau_2) \rangle_0, \quad (22)$$

where \mathcal{T}_c means that $\psi_{\mathbf{k}}$ and $\psi_{\mathbf{k}}^\dagger$ are ordered with respect to τ_1 and τ_2 along the complex Keldysh contour \mathcal{C} . Next, we define

$$C(\tau_1, \tau_2) := \langle \mathcal{T}_c T_{\mathbf{qk}}^v v_{\mathbf{q}}(\tau_1) s_{\mathbf{k}}^-(\tau_2) \rangle, \quad (23)$$

where v is either α or β^\dagger .

Going to the interaction picture with H_{int} as the interaction, we get

$$\begin{aligned} C(\tau_1, \tau_2) &= \left\langle \mathcal{T}_c T_{\mathbf{qk}}^v v_{\mathbf{q}}(\tau_1) s_{\mathbf{k}}^-(\tau_2) e^{-i \int_{\mathcal{C}} d\tau H_{\text{int}}(\tau)} \right\rangle_0 \\ &\approx \left\langle \mathcal{T}_c \int_{\mathcal{C}} d\tau |T_{\mathbf{qk}}^v|^2 v_{\mathbf{q}}(\tau) v_{\mathbf{q}}^\dagger(\tau) s_{\mathbf{k}}^+(\tau) s_{\mathbf{k}}^-(\tau_2) \right\rangle_0 \\ &= i |T_{\mathbf{qk}}^v|^2 [G_v(\mathbf{q}) \bullet G_{s^+}(\mathbf{k})](\tau_1, \tau_2), \end{aligned} \quad (24)$$

where we have used the bullet product \bullet to denote integration of the internal complex time parameter along the Keldysh contour. In the second equality it was used that

$$-i \langle \mathcal{T}_c s_{\mathbf{k}}^+(\tau) s_{\mathbf{k}}^-(\tau_2) \rangle_0 = \delta_{\mathbf{k}, \mathbf{k}'} G_{s^+}(\tau, \tau_2, \mathbf{k}), \quad (25)$$

as can be confirmed by using Wick's theorem. Next, if we choose τ_2 to be placed later in the contour we have

$$C(\tau_1, \tau_2) = C^<(\tau_1, \tau_2) = \langle T_{\mathbf{qk}}^v s_{\mathbf{k}}^-(\tau_2) v_{\mathbf{q}}(\tau_1) \rangle. \quad (26)$$

From the Langreth rules we have

$$C^<(t, t) = [G_v^R(\mathbf{q}) \circ G_{s^+}^<(\mathbf{k}) + G_v^<(\mathbf{q}) \circ G_{s^+}^A(\mathbf{k})](t, t), \quad (27)$$

where the circle product \circ means integration over the internal real time coordinate. The circle products are the same as normal convolution products, since $G_v^R(t_1, t_2)$ and $G_v^<(t_1, t_2)$ only depend on time through the relative time $t_1 - t_2$. Thus, by writing Eq. (27) in terms of Fourier transformed Green's functions, the circle products become normal products, so, by

inserting it into Eq. (21),

$$\begin{aligned} I_s &= 4 \int \frac{d\varepsilon}{2\pi} \sum_{\mathbf{k} \in \square} \sum_{\mathbf{q} \in \diamond} \sum_{v \in \{\alpha, \beta^\dagger\}} |T_{\mathbf{qk}}^v|^2 \text{Im} G_v^R(\varepsilon, \mathbf{q}) \\ &\quad \times \text{Im} G_{s^+}^R(\varepsilon, \mathbf{k}) [f^{v^+}(\varepsilon, \mathbf{q}) - f^{s^+}(\varepsilon, \mathbf{k})], \end{aligned} \quad (28)$$

where we used that $G_\psi^A(\varepsilon) = [G_\psi^R(\varepsilon)]^*$.

Inserting Eqs. (11), (16), and (17) into Eq. (28) and using Eq. (7) gives

$$I_s = I_r + I_U, \quad (29)$$

where

$$\begin{aligned} I_r &= -\bar{J}_A^2 \gamma^2 h_0^2 \left(\frac{1}{(\Omega - \omega_0^\alpha)^2 + (\eta^\alpha)^2} \left[\frac{U_K + (1-c)}{2 + U_K} \right]^2 \right. \\ &\quad \left. + \frac{1}{(\Omega + \omega_0^\beta)^2 + (\eta^\beta)^2} \left[\frac{cU_K + (c-1)}{2 + U_K} \right]^2 \right) \\ &\quad \times \sum_{\mathbf{k} \in \square, l=0} \text{Im} G_{s^+}^R(\Omega, \mathbf{k}) \delta_{\mathbf{k}_l, \mathbf{0}} \end{aligned} \quad (30)$$

and

$$\begin{aligned} I_U &= -\bar{J}_A^2 \gamma^2 h_0^2 \left(\frac{1}{(\Omega - \omega_0^\alpha)^2 + (\eta^\alpha)^2} \left[\frac{U_K + (1+c)}{2 + U_K} \right]^2 \right. \\ &\quad \left. + \frac{1}{(\Omega + \omega_0^\beta)^2 + (\eta^\beta)^2} \left[\frac{cU_K + (c+1)}{2 + U_K} \right]^2 \right) \\ &\quad \times \sum_{\mathbf{k} \in \square, l=0} \text{Im} G_{s^+}^R(\Omega, \mathbf{k} + \mathbf{G}) \delta_{\mathbf{k}_l, \mathbf{0}}. \end{aligned} \quad (31)$$

Here, $U_K = K/(Jz)$ and $c = \bar{J}_B/\bar{J}_A$ is the interface asymmetry parameter that gives the degree to which the interface is compensated. The sums are restricted to include only the \mathbf{k} vectors that satisfy $\delta_{\mathbf{k}_l, \mathbf{0}} = 1$ with $l = 0$ and \mathbf{G} is the vector that connects these to the \mathbf{k} vectors with $l = 1$. When both the SC and AFI are cubical with a lattice parameter a and a compensated interface, then $\mathbf{G} = \pi(\mathbf{e}_x + \mathbf{e}_y + \mathbf{e}_z)/a$. In order for the Umklapp scattering to produce a nonzero I_U , it is necessary that there exists $\mathbf{k}, \mathbf{q} \in \square$ such that both \mathbf{q} and $\mathbf{q} + \mathbf{k} + \mathbf{G}$ are close to the Fermi surface and $\delta_{\mathbf{k}_l, \mathbf{0}} = 1$. In a cubical lattice the minimal value of $\mathbf{k} + \mathbf{G}$ is $\sqrt{2}\pi/a$, so the maximal diameter of the Fermi surface must be at least $\sqrt{2}\pi/a$. The Umklapp current is also zero if the interface is fully uncompensated. In this case there is no Umklapp scattering and the current is simply $I_s = I_r$ with $c = 0$.

V. NUMERICAL RESULTS

Next we show numerical results for a cubical lattice with lattice constant a such that

$$\xi_{\mathbf{k}} = -2t \sum_{i \in \{x, y, z\}} \cos(ak_i) - \mu, \quad (32)$$

where t is the hopping parameter. In Fig. 2 we show the spin current into the superconductor I_s^{SC} for different temperatures T and precession frequencies Ω , normalized by the normal state value I_s^{NM} in Fig. 2(a) and a constant in Fig. 2(b). In

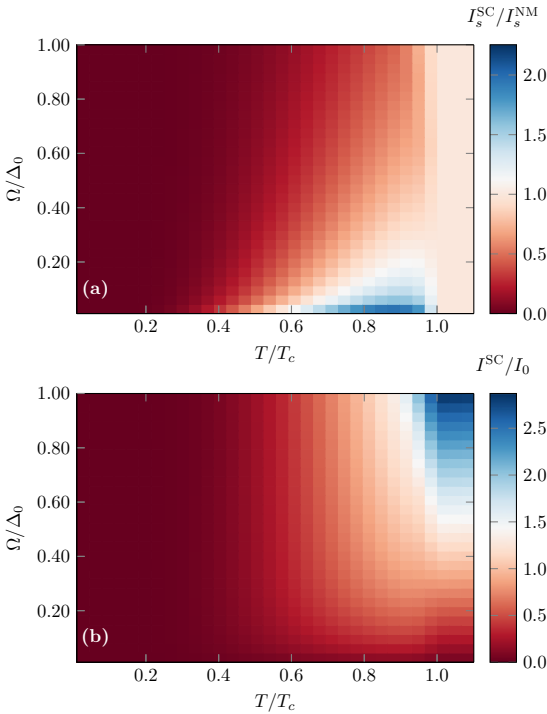


FIG. 2. The spin current into a superconductor with gap given by Eq. (5), I_s^{SC} , for different precession frequencies Ω and temperatures T and normalized by the normal state spin current, I_s^{NM} , found by setting $\Delta = 0$ in (a) and the constant $I_0 = \gamma^2 \hbar_0^2 \tilde{J}_A^2 N_S N_S^\perp / [(2\pi)^4 \Delta_0]$ in (b). N_S^\perp is the number of lattice points in the superconductor in the direction transverse to the interface, Δ_0 is the superconducting gap at $T = 0$, and T_c is the critical temperature.

this case we have used $\mu = -4t$, which means that $I_U = 0$. However, we find that both I_r and I_U scale in the same way as functions of Ω and T also for other values of μ . In Fig. 2 we have also used $U_k = 0.01$, which is close to the reported value for MnF_2 [27,28], $t = 1000\Delta_0$, $c = 0.5$, $\eta^\alpha = \eta^\beta = \Delta_0 \times 10^{-4}$, and $\omega_0^\alpha = \omega_0^\beta = 4\Delta_0$. This corresponds to a resonance frequency of 1 THz when $\Delta_0 = 1$ meV. From Fig. 2(b) we see that the normal state spin current at $T > T_c$ scales linearly with Ω as expected. In comparison, the spin current changes only very slowly with Ω in the superconducting state. This is consistent with the physical picture that it is the availability of quasiparticles rather than unoccupied states that limits the current in the superconducting state.

As one can see from Fig. 2(a), the spin current in the superconductor is peaked at small frequencies close to the critical temperature, where it can be more than twice as large as the normal-metal spin current. This is similar to the results for spin currents in superconductor-ferromagnetic bilayers [14,15]. Figure 3 shows the ratio $I_s^{\text{SC}}/I_s^{\text{NM}}$ as a function of Ω/Δ_0 for various T . It can be seen that at zero temperature the spin current in the superconducting case is zero for $\Omega < 2\Delta_0$. For $T > 0$ the ratio $I_s^{\text{SC}}/I_s^{\text{NM}}$ initially decreases as Ω increases and reaches a minimum at $\Omega = 2\Delta(T)$.

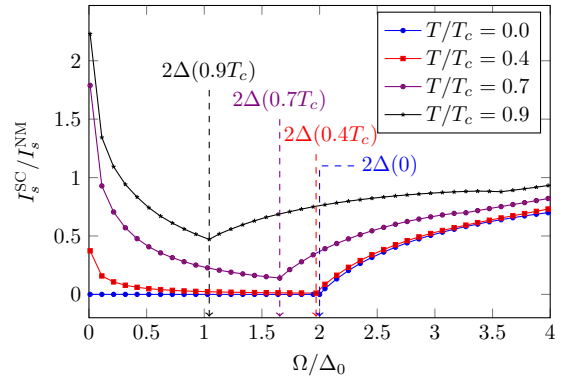


FIG. 3. The spin current into a superconductor I_s^{SC} , normalized by the normal state spin current I_s^{NM} , found by setting the gap $\Delta = 0$, as a function of the spin-pumping precession frequency Ω . Here, $\Delta(T)$ is the energy gap that solves Eq. (5) and T_c is the critical temperature.

This can be understood physically in the following way. The spin current is generated by spin-flip scatterings which excite particles by energy Ω and flip their spin. This can be seen from Eqs. (9), (18), (30), and (31) when $\eta^{\text{SC}} \ll 1$. In this case the sum in Eq. (18) only contributes to the imaginary part of $G_{s^+}^R(\Omega, \mathbf{k})$ when $\tilde{\omega} - \omega = \Omega$, and only when $n_F(\tilde{\omega}, T) - n_F(\omega, T) \neq 0$. In the normal metal case there are a number of electrons proportional to Ω around the Fermi surface which can be excited to an available state. Hence, the dynamic spin susceptibility is proportional to Ω .

In a superconductor the spin-flip scatterings can happen by breaking a Cooper pair or exciting a quasiparticle from above the gap to a higher energy. When $\Omega < 2\Delta(T)$ only the latter is possible. Thus, in order to get a nonzero spin current when $\Omega < 2\Delta(T)$ the temperature must be large enough for quasiparticle states above the gap to be occupied. This is why, in Fig. 3, the current is identically zero in the superconductor when $T = 0$ and $\Omega < 2\Delta_0$. On the other hand, when the temperature is close to the critical temperature there can be many available quasiparticles available because the density of states is peaked around the gap. This peak in the density of states is why the spin current in a superconductor can be larger than the spin current in a normal metal, but only when the temperature is close to the critical temperature. It is also only larger when $\Omega \ll \Delta(T)$, which is because the lack of states below the gap in the superconductor means that the spin susceptibility cannot increase as fast as in the normal state when Ω increases. In the normal state there is a range of energies $\propto \Omega$ around the Fermi surface that can be excited to an available state, but in the superconducting state the number of states that can be excited is limited by the number of quasiparticles present. Increasing Ω therefore decreases the ratio $I_s^{\text{SC}}/I_s^{\text{NM}}$ when $\Omega < 2\Delta(T)$, as can be seen in Figs. 2 and 3. At $\Omega = 2\Delta(T)$ the breaking of Cooper pairs becomes possible as a spin-transfer mechanism, which is why $I_s^{\text{SC}}/I_s^{\text{NM}}$ starts to increase. This can be seen most clearly in Fig. 3.

Figure 4 shows the ratio between regular spin current I_r and the Umklapp contribution I_U for $\mu = -2.2t$. The result is

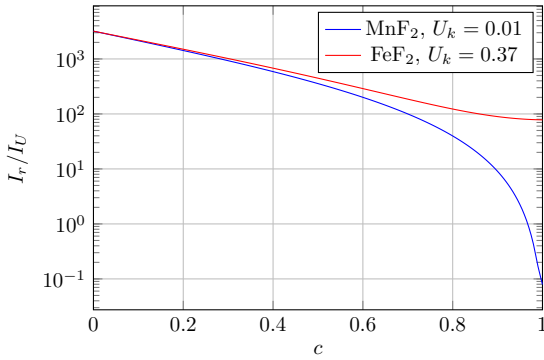


FIG. 4. The ratio of the spin-current contribution from the regular scattering channel I_r , and the Umklapp scattering channel I_U , as a function of the interface asymmetry parameter c for $\Omega/\Delta_0 = 0.1$, $T/T_c = 0.9$, $\mu = -2.2t$. The results are shown for easy axis anisotropy values $U_k = 0.01$ and $U_k = 0.37$, where the former is found in MnF_2 and the latter is found in FeF_2 [27–29].

shown for axis anisotropy $U_k = 0.01$, which corresponds to MnF_2 [27,28], and $U_k = 0.37$, corresponding to FeF_2 [29]. In both cases the regular current dominates when the interface asymmetry parameter c is small, meaning that the superconductor is coupled more strongly to one of the sublattices in the AFI. The Umklapp contribution becomes more important as c increases and when U_k is small the Umklapp contribution eventually becomes larger than the contribution from the regular scattering channel. This is consistent with the work by Kamra and Belzig showing that the in the absence of easy-axis anisotropy the cross-sublattice contribution quenches the spin-current from the regular scattering channel [19]. However, here we see that if we include the Umklapp scattering the spin current will not go all the way to zero, even in the absence of easy-axis anisotropy. Mathematically, this can be seen from Eqs. (30) and (31): When $U_k = 0$ we have $I_r \propto (1 - c)^2$ and $I_U \propto (1 + c)^2$. However, when $U_k = 0.37$ the regular contribution remains dominant for all values of c .

VI. EXPERIMENTAL DETECTION

Although the spin current can be enhanced in SC/AFI bilayers as compared to NM/AFI bilayers, it can be difficult to observe this enhancement experimentally. This is because the spin current is strongly peaked around the antiferromagnetic resonance frequencies $\omega_0^{\alpha/\beta}$. In antiferromagnets this resonance frequency is on the order of 1 THz, which is much larger than in ferromagnets [1]. This is an advantage for spintronics as it allows for ultrafast information processing, but in the context of this paper it means that observation of the enhancement produced by the superconducting order is hard to experimentally verify. A resonance frequency of 1 THz means that the spin current is most easily observed at $\Omega/\Delta_0 \approx 4$, assuming that $\Delta_0 = 1$ meV, but from Fig. 2 we see that the current is enhanced only for $\Omega/\Delta_0 < 0.2$.

In order to observe the strong suppression of spin current at low temperatures, it is necessary to probe frequencies below $2\Delta_0$. This is also below 1 THz, but not out of reach. The res-

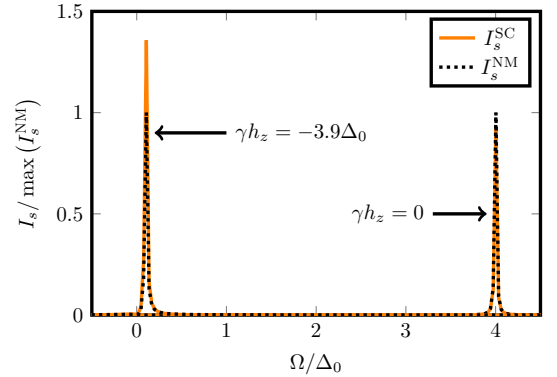


FIG. 5. The superconductor spin current I_s^{SC} and normal metal spin current I_s^{NM} normalized by the maximal value of I_s^{NM} as a function of the precession frequency Ω for two different values of constant external magnetic field h_z . Here, γ is the gyromagnetic ratio, $T/T_c = 0.9$, $\eta^{\alpha/\beta}/\Delta_0 = 0.01$, $c = 0.5$, $U_k = 0.01$, T_c is the critical temperature, and Δ_0 is the superconducting gap at zero temperature.

onance frequency of MnF_2 , which was used in the detection of spin pumping by Vaidya *et al.*, was reported to be around 250 GHz [20]. This corresponds to $\Omega \approx 1$ meV $\approx \Delta_0$, which makes the low-temperature suppression shown in Figs. 2 and 3 detectable.

One way to potentially detect the spin-current enhancement at low frequencies is to apply a constant magnetic field along the z axis. This was also done by Vaidya *et al.*, who reduced the frequency of MnF_2 to 120 GHz by applying a magnetic field of 4.7 T. From Eqs. (7), (30), (31) we see that the resonance frequencies are

$$\omega_{\text{res}} = \omega_0 \sqrt{U_k(2 + U_k)} \pm \gamma h_z, \quad (33)$$

where $\omega_0 = JzS$. Thus, by applying a magnetic field of $\omega_0 \sqrt{U_k(2 + U_k)}/\gamma$, the resonance frequency can be pushed well below Δ_0 , making the enhancement in spin current due to superconductivity detectable. This is illustrated in Fig. 5. At $\gamma h_z = 0$ the peak is at $\Omega = 4\Delta_0$, where the peak in I_s^{SC} is only slightly smaller than the peak in I_s^{NM} , in accordance with Fig. 3. However, when $\gamma h_z = -3.9\Delta_0$, the peak is shifted to $\Omega = 0.1\Delta_0$ and the peak in the superconducting case is taller. How large the applied magnetic field is required to be depends on the gyromagnetic ratio γ as well as ω_0 and U_k , but it will in general be several tesla. Experimental ingenuity is therefore required in order to make sure that the superconductivity is not completely suppressed by the magnetic field. This could, for instance, be done by shielding the superconductors or using superconductors that can withstand large magnetic field from a certain direction, such as Ising superconductors.

VII. CONCLUSION

We have derived an expression for the spin current in SC/AFI bilayers undergoing spin pumping, valid for both compensated and uncompensated interfaces and taking into consideration both the regular scattering channel and the Umklapp scattering channel. We found that for temperature

T well below the critical temperature T_c , the spin current is strongly suppressed as long as the precession frequency of the applied magnetic field is less than $2\Delta(T)$. This is because the energy gap in the superconductor inhibits spin-flip scatterings below the gap and there are few quasiparticles present that can be scattered to higher energies. However, at temperatures close to T_c there are quasiparticles present and because of their large density of states close to the gap, the spin current can be more than twice as large as for NM/AFI bilayers when the precession frequency is significantly less than the gap. The spin-current contribution from the Umklapp channel is typically much smaller than the contribution from the regular scattering channel, but it can be significant if the Fermi surface is large, the easy axis anisotropy is small, and the interface is compensated.

The relevant precession frequencies where the spin current in SC/AFI is enhanced compared to NM/AFI is much lower than the typical resonance frequencies of antiferromag-

nets, which makes the detection of this effect experimentally challenging. A possible solution lies in the shifting of the resonance frequency by a static magnetic field.

ACKNOWLEDGMENTS

This work was supported by the Research Council of Norway through Grant No. 240806, and its Centres of Excellence funding scheme Grant No. 262633 “*QuSpin*”. J.L. also acknowledges funding from the NV faculty at the Norwegian University of Science and Technology.

APPENDIX A: AFI GREEN'S FUNCTIONS

In this section we calculate the correction to the magnon Green's functions due to the precessing external magnetic field. The Hamiltonian for the antiferromagnetic insulator is given by Eq. (3), and we treat

$$V := \sqrt{2N_A S}(u_0 + v_0)\gamma[h^-(\alpha_0 + \beta_0^\dagger) + h^+(\alpha_0^\dagger + \beta_0)] \quad (\text{A1})$$

as a perturbation. In order to calculate G_v^R and $G_v^<$, where $v \in \{\alpha, \beta^\dagger\}$, we will first calculate the contour-ordered Green's function. This, in turn, is done by adding an infinitesimal imaginary part to the otherwise real time coordinates and integrating over the complex Keldysh contour.

To second order in V , the contour-ordered Green's function is

$$\begin{aligned} G_v(\tau_1, \tau_2, \mathbf{k}) &= -i\langle \mathcal{T}_c v_{\mathbf{k}}(\tau_1) v_{\mathbf{k}}^\dagger(\tau_2) e^{-i \int_{\mathcal{C}} d\tau V(\tau)} \rangle_0 \\ &= -i\langle \mathcal{T}_c v_{\mathbf{k}}(\tau_1) v_{\mathbf{k}}^\dagger(\tau_2) \rangle_0 - \left\langle \mathcal{T}_c \int_{\mathcal{C}} d\tau v_{\mathbf{k}}(\tau_1) v_{\mathbf{k}}^\dagger(\tau_2) V(\tau) \right\rangle_0 + i \left\langle \mathcal{T}_c \int_{\mathcal{C}} d\tau' d\tau v_{\mathbf{k}}(\tau_1) v_{\mathbf{k}}^\dagger(\tau_2) V(\tau) V(\tau') \right\rangle_0 + \mathcal{O}(V^3), \end{aligned} \quad (\text{A2})$$

where \mathcal{T}_c means ordering along the Keldysh contour \mathcal{C} and the subscript 0 means that the expectation values are evaluated in the absence of V . The first-order term is odd in magnon operators and is therefore zero. Inserting Eq. (A1), the correction to the equilibrium Green's function is

$$\Delta G_v(t_1, t_2, \mathbf{k}) := G_v(t_1, t_2, \mathbf{k}) - G_v^0(t_1, t_2, \mathbf{k}) = i\lambda^2 \left\langle \mathcal{T}_c \int_{\mathcal{C}} d\tau' d\tau v_{\mathbf{k}}(t_1) v_{\mathbf{0}}^\dagger(\tau) h^+(\tau) h^-(\tau') v_{\mathbf{0}}(\tau') v_{\mathbf{k}}^\dagger(t_2) \right\rangle_0, \quad (\text{A3})$$

where

$$\lambda = \sqrt{2N_A S}(u_0 + v_0)\gamma. \quad (\text{A4})$$

We can use Wick's theorem to evaluate the rewrite as

$$\begin{aligned} \left\langle \mathcal{T}_c \int_{\mathcal{C}} d\tau' d\tau v_{\mathbf{k}}(t_1) v_{\mathbf{0}}^\dagger(\tau) h^+(\tau) h^-(\tau') v_{\mathbf{0}}(\tau') v_{\mathbf{k}}^\dagger(t_2) \right\rangle_0 &= \int_{\mathcal{C}} d\tau' d\tau h^+(\tau) h^-(\tau') [\langle \mathcal{T}_c v_{\mathbf{k}}(t_1) v_{\mathbf{0}}^\dagger(\tau) \rangle_0 \langle \mathcal{T}_c v_{\mathbf{0}}(\tau') v_{\mathbf{k}}^\dagger(t_2) \rangle_0 \\ &\quad + \langle \mathcal{T}_c v_{\mathbf{k}}(t_1) v_{\mathbf{k}}^\dagger(t_2) \rangle_0 \langle \mathcal{T}_c v_{\mathbf{0}}(\tau') v_{\mathbf{0}}^\dagger(\tau) \rangle_0]. \end{aligned} \quad (\text{A5})$$

The second term is zero, which we show in the following. First, define

$$\Sigma(\tau_1, \tau_2) = h^+(\tau_1) h^-(\tau_2) = \langle \mathcal{T}_c h^+(\tau_1) h^-(\tau_2) \rangle_0. \quad (\text{A6})$$

Then,

$$\begin{aligned} \int_{\mathcal{C}} d\tau' d\tau h^+(\tau) h^-(\tau') \langle \mathcal{T}_c v_{\mathbf{k}}(\tau_1) v_{\mathbf{k}}^\dagger(\tau_2) \rangle_0 \langle \mathcal{T}_c v_{\mathbf{0}}(\tau') v_{\mathbf{0}}^\dagger(\tau) \rangle_0 &= -G_v^0(\tau_1, \tau_2, \mathbf{k}) \int_{\mathcal{C}} d\tau [\Sigma \bullet G_v^0]_{\mathbf{k}=\mathbf{0}}(\tau, \tau) \\ &= -G_v^0(\tau_1, \tau_2, \mathbf{k}) \left(\int_{-\infty}^{\infty} dt + \int_{\infty}^{-\infty} dt \right) [\Sigma \bullet G_v^0]_{\mathbf{k}=\mathbf{0}}(t, t) = 0, \end{aligned} \quad (\text{A7})$$

where it was used that \mathcal{C} goes from $-\infty - i\delta$ to $\infty - i\delta$ and then from $\infty + i\delta$ to $-\infty + i\delta$ with $\delta \in \mathbb{R}$ being an infinitesimal. The bullet product is

$$(A \bullet B)(\tau_1, \tau_2) = \int_{\mathcal{C}} d\tau A(\tau_1, \tau) B(\tau, \tau_2). \quad (\text{A8})$$

Hence, we are left with

$$\Delta G_v(\tau_1, \tau_2, \mathbf{k}) = -i\delta_{\mathbf{k},0}\lambda^2(G_v^0 \bullet \Sigma \bullet G_v^0)(\tau_1, \tau_2). \quad (\text{A9})$$

To get the real-time Green's functions we can use the Langreth rules. If

$$C(\tau_1, \tau_2) = (A \bullet B)(\tau_1, \tau_2), \quad (\text{A10a})$$

$$D(\tau_1, \tau_2) = (A \bullet B \bullet C)(\tau_1, \tau_2), \quad (\text{A10b})$$

where A and B are contour-ordered functions, then the corresponding advanced, retarded, and lesser Green's functions satisfy [30]

$$C^< = A^R \circ B^< + A^< \circ B^A, \quad (\text{A11a})$$

$$C^{R/A} = A^{R/A} \circ B^{R/A}, \quad (\text{A11b})$$

$$D^< = A^R \circ B^R \circ C^< + A^R \circ B^< \circ C^A + A^< \circ B^A \circ C^A, \quad (\text{A11c})$$

$$D^{R/A} = A^{R/A} \circ B^{R/A} \circ C^{R/A}, \quad (\text{A11d})$$

where the circle product is

$$(A \circ B)(t_1, t_2) = \int_{-\infty}^{\infty} dt A(t_1, t) B(t, t_2). \quad (\text{A12})$$

Using Eq. (A11c) as well as $\Sigma^< = \Sigma$ and $\Sigma^R = \Sigma^A = 0$ we see that $\Delta G_v^{R/A} = 0$ and

$$\Delta G_v^<(t_1, t_2, \mathbf{k}) = -i\delta_{\mathbf{k},0}\lambda^2(G_v^R \circ \Sigma \circ G_v^A)(t_1, t_2). \quad (\text{A13})$$

Next, if we let $h_x(t) = h_0 \cos(\Omega t)$ and $h_y(t) = -h_0 \sin(\Omega t)$ we get $h^\pm(t) = h_0 \exp(\mp i\Omega t)$, so

$$\Sigma(t_1, t_2) = h_0^2 e^{-i\Omega(t_1 - t_2)}. \quad (\text{A14})$$

The circle products in Eq. (A13) reduce to normal convolutions because G_v^0 and Σ only depend on the relative time. Thus, they further reduce to ordinary products in energy space. The Fourier transform of Σ is

$$\Sigma(\varepsilon) = \int_{-\infty}^{\infty} d(t_1 - t_2) \Sigma(t_1, t_2) e^{i\varepsilon(t_1 - t_2)} = 2\pi h_0^2 \delta(\varepsilon - \Omega). \quad (\text{A15})$$

We also have [30]

$$G_v^A(\varepsilon, \mathbf{k}) = [G_v^R(\varepsilon, \mathbf{k})]^*, \quad (\text{A16})$$

so, to second order in h ,

$$\Delta G_v^<(\varepsilon, \mathbf{k}) = -2i\pi h_0^2 \lambda^2 |G_v^R(\varepsilon, \mathbf{k})|^2 \delta_{\mathbf{k},0} \delta(\varepsilon - \Omega). \quad (\text{A17})$$

Inserting this into the definition of the distribution function and using Eq. (16) finally gives us Eq. (17).

APPENDIX B: BCS DYNAMIC SPIN SUSCEPTIBILITY

To calculate $\text{Im}G_{s^\pm}^R(\varepsilon, \mathbf{k})$ we will use the imaginary time Green's function [31],

$$\tilde{G}_{s^\pm}(\tau_1, \tau_2, \mathbf{k}) = -\langle \mathcal{T}_\tau s_{-\mathbf{k}}^+(\tau_1) s_{\mathbf{k}}^-(\tau_2) \rangle, \quad (\text{B1})$$

where \mathcal{T}_τ means time ordering in τ , together with the connection through analytical continuation,

$$G_{s^\pm}^R(\varepsilon, \mathbf{k}) = \tilde{G}_{s^\pm}(\varepsilon + i\eta^{\text{SC}}, \mathbf{k}), \quad (\text{B2})$$

where

$$\tilde{G}_{s^\pm}(i\omega_n, \mathbf{k}) = \int_0^\beta d(\tau_1 - \tau_2) \tilde{G}_{s^\pm}(\tau_1, \tau_2, \mathbf{k}) e^{i\omega_n(\tau_1 - \tau_2)} \quad (\text{B3})$$

and

$$\omega_n = \frac{2n\pi}{\beta} \quad (\text{B4})$$

are bosonic Matsubara frequencies. The inverse temperature is $\beta = 1/T$.

We will also make use of the Nambu spinors,

$$\phi_{\mathbf{k}}^\dagger = (c_{\mathbf{k},\uparrow}^\dagger \ c_{-\mathbf{k},\downarrow}). \quad (\text{B5})$$

With these spinors we can write

$$s_{\mathbf{k}}^- = \sum_{\mathbf{q}} \phi_{-\mathbf{q},2} \phi_{\mathbf{q}+\mathbf{k},1}, \quad s_{-\mathbf{k}}^+ = \sum_{\mathbf{q}} \phi_{\mathbf{q}+\mathbf{k},1}^\dagger \phi_{-\mathbf{q},2}^\dagger. \quad (\text{B6})$$

Thus,

$$\begin{aligned} \tilde{G}_{s^+}(\tau_1, \tau_2, \mathbf{k}) &= - \sum_{\mathbf{q}\mathbf{q}'} \langle \mathcal{T}_\tau \phi_{\mathbf{q}+\mathbf{k},1}^\dagger(\tau_1) \phi_{-\mathbf{q},2}^\dagger(\tau_1) \phi_{-\mathbf{q}',2}(\tau_2) \phi_{\mathbf{q}'+\mathbf{k},1}(\tau_2) \rangle \\ &= \sum_{\mathbf{q}\mathbf{q}'} \left(\langle \mathcal{T}_\tau \phi_{\mathbf{q}+\mathbf{k},1}^\dagger(\tau_1) \phi_{-\mathbf{q}',2}(\tau_2) \rangle \langle \mathcal{T}_\tau \phi_{-\mathbf{q},2}^\dagger(\tau_1) \phi_{\mathbf{q}'+\mathbf{k},1}(\tau_2) \rangle - \langle \mathcal{T}_\tau \phi_{\mathbf{q}+\mathbf{k},1}^\dagger(\tau_1) \phi_{\mathbf{q}'+\mathbf{k},1}(\tau_2) \rangle \langle \mathcal{T}_\tau \phi_{-\mathbf{q},2}^\dagger(\tau_1) \phi_{-\mathbf{q}',2}(\tau_2) \rangle \right) \\ &= \sum_{\mathbf{q}} [\mathcal{G}_{1,2}(\tau_2, \tau_1, \mathbf{q} + \mathbf{k}) \mathcal{G}_{2,1}(\tau_2, \tau_1, -\mathbf{q}) - \mathcal{G}_{1,1}(\tau_2, \tau_1, \mathbf{q} + \mathbf{k}) \mathcal{G}_{2,2}(\tau_2, \tau_1, -\mathbf{q})], \end{aligned} \quad (\text{B7})$$

where

$$\mathcal{G}(\tau_1, \tau_2, \mathbf{k}) = - \langle \mathcal{T}_\tau \phi_{\mathbf{k}}(\tau_1) \phi_{\mathbf{k}}^\dagger(\tau_2) \rangle = \frac{1}{\beta} \sum_n \frac{1}{(i\nu_n)^2 - \xi_{\mathbf{k}}^2 - |\Delta|^2} \begin{pmatrix} i\nu_n + \xi_{\mathbf{k}} & -\Delta \\ -\Delta^* & i\nu_n - \xi_{\mathbf{k}} \end{pmatrix} e^{-i\nu_n(\tau_1 - \tau_2)} \quad (\text{B8})$$

is the BCS single-particle Green's function. Here, $\nu_n = (2n + 1)\pi/\beta$ are fermionic Matsubara frequencies. Inserting this into Eq. (B3), we get

$$\begin{aligned} \tilde{G}_{s^+}(i\omega_n, \mathbf{k}) &= T \sum_{\mathbf{q},m} [\mathcal{G}_{1,2}(-i\nu_m - i\omega_n, \mathbf{q} + \mathbf{k}) \mathcal{G}_{2,1}(i\nu_m, -\mathbf{q}) - \mathcal{G}_{1,1}(-i\nu_m - i\omega_n, \mathbf{q} + \mathbf{k}) \mathcal{G}_{2,2}(i\nu_m, -\mathbf{q})] \\ &= T \sum_{\mathbf{q},m} [\mathcal{G}_{1,2}(i\nu_m + i\omega_n, \mathbf{q} + \mathbf{k}) \mathcal{G}_{2,1}(i\nu_m, -\mathbf{q}) + \mathcal{G}_{2,2}(i\nu_m + i\omega_n, \mathbf{q} + \mathbf{k}) \mathcal{G}_{2,2}(i\nu_m, -\mathbf{q})] \\ &= \frac{1}{2\beta} \sum_{\mathbf{q},m} \text{Tr}[\mathcal{G}(i\nu_m + i\omega_n, \mathbf{q} + \mathbf{k}) \mathcal{G}(i\nu_m, \mathbf{q})]. \end{aligned} \quad (\text{B9})$$

In the last equality we have used $\mathcal{G}(i\nu_m, -\mathbf{q}) = \mathcal{G}(i\nu_m, \mathbf{q})$, $\mathcal{G}_{1,2}(i\nu_n, \mathbf{k}) \mathcal{G}_{2,1}(i\nu_m, \mathbf{q}) = \mathcal{G}_{2,1}(i\nu_n, \mathbf{k}) \mathcal{G}_{1,2}(i\nu_m, \mathbf{q})$ and

$$\begin{aligned} \sum_{\mathbf{q},m} \mathcal{G}_{1,1}(i\nu_m + i\omega_n, \mathbf{q} + \mathbf{k}) \mathcal{G}_{1,1}(i\nu_m, \mathbf{q}) &= \sum_{\mathbf{q}',k} \mathcal{G}_{1,1}(-i\nu_k, \mathbf{q}') \mathcal{G}_{1,1}(-i\nu_k - i\omega_n, \mathbf{q}' + \mathbf{k}) \\ &= \sum_{\mathbf{q}',k} \mathcal{G}_{2,2}(i\nu_k, \mathbf{q}') \mathcal{G}_{2,2}(i\nu_k + i\omega_n, \mathbf{q}' + \mathbf{k}). \end{aligned} \quad (\text{B10})$$

In the first equality, we introduced $\mathbf{q}' = -\mathbf{q} - \mathbf{k}$ and $i\nu_k = -i\nu_m - i\omega_n$, and in the last equality we used $\mathcal{G}_{2,2}(i\nu_k, \mathbf{q}') = -\mathcal{G}_{1,1}(-i\nu_k, \mathbf{q}')$.

Next, we can use the spectral form,

$$\mathcal{G}(i\nu_m, \mathbf{q}) = \int_{-\infty}^{\infty} \frac{d\omega}{(-\pi)} \frac{\text{Im}\mathcal{G}(\omega + i\eta^{\text{SC}}, \mathbf{q})}{i\nu_m - \omega}, \quad (\text{B11})$$

and the Matsubara sum identity,

$$\frac{1}{\beta} \sum_m \frac{1}{i\nu_m + i\omega_n - \tilde{\omega}} \times \frac{1}{i\nu_m - \omega} = \frac{n_F(\omega, T) - n_F(\tilde{\omega}, T)}{i\omega_n - (\tilde{\omega} - \omega)}, \quad (\text{B12})$$

where we have used that ν_m are fermionic Matsubara frequencies, giving rise to the Fermi-Dirac distribution function n_F . We have also used that $n_F(\omega - i\omega_n) = n_F(\omega)$ since ω_n is a bosonic Matsubara frequency. Additionally, Eq. (B8) gives, assuming Δ real,

$$\text{Im}\mathcal{G}(\omega + i\eta^{\text{SC}}, \mathbf{k}) = - \frac{\pi}{2\sqrt{\xi_{\mathbf{k}}^2 + |\Delta|^2}} \begin{pmatrix} \omega + \xi_{\mathbf{k}} & -\Delta \\ -\Delta & \omega - \xi_{\mathbf{k}} \end{pmatrix} [\delta(\omega - \sqrt{\xi_{\mathbf{k}}^2 + |\Delta|^2}) - \delta(\omega + \sqrt{\xi_{\mathbf{k}}^2 + |\Delta|^2})], \quad (\text{B13})$$

in the limit $\eta^{\text{SC}} \rightarrow 0^+$. Hence, if we define $E_{\mathbf{k}} := \sqrt{\xi_{\mathbf{k}}^2 + |\Delta|^2}$,

$$\lim_{\eta^{\text{SC}} \rightarrow 0^+} \text{Tr}[\text{Im}\mathcal{G}(\tilde{\omega} + i\eta^{\text{SC}}, \mathbf{q} + \mathbf{k}) \text{Im}\mathcal{G}(\omega + i\eta^{\text{SC}}, \mathbf{q})] = \pi^2 \frac{\omega\tilde{\omega} + \xi_{\mathbf{k}}\tilde{\xi} + \Delta^2}{2E\tilde{E}} [\delta(\omega - E) - \delta(\omega + E)] [\delta(\tilde{\omega} - \tilde{E}) - \delta(\tilde{\omega} + \tilde{E})], \quad (\text{B14})$$

where $\xi = \xi_q$, $\tilde{\xi} = \xi_{q+k}$, $E = E_q$, and $\tilde{E} = E_{q+k}$. Inserting this into Eq. (B9) gives

$$\tilde{G}_{s^+}(i\omega_n, \mathbf{k}) = -\frac{1}{4} \sum_q \sum_{\omega=\pm E} \sum_{\tilde{\omega}=\pm\tilde{E}} \frac{\omega\tilde{\omega} + \xi\tilde{\xi} + \Delta^2}{\omega\tilde{\omega}} \frac{n_F(\tilde{\omega}, T_{\text{SC}}) - n_F(\omega, T_{\text{SC}})}{i\omega_n - (\tilde{\omega} - \omega)}. \quad (\text{B15})$$

From Eq. (B2) we then finally have Eq. (18).

-
- [1] V. Baltz, A. Manchon, M. Tsoi, T. Moriyama, T. Ono, and Y. Tserkovnyak, *Rev. Mod. Phys.* **90**, 015005 (2018).
- [2] F. S. Bergeret, A. F. Volkov, and K. B. Efetov, *Rev. Mod. Phys.* **77**, 1321 (2005).
- [3] A. I. Buzdin, *Rev. Mod. Phys.* **77**, 935 (2005).
- [4] J. Linder and J. Robinson, *Nat. Phys.* **11**, 307 (2015).
- [5] M. Eschrig, *Rep. Prog. Phys.* **78**, 104501 (2015).
- [6] J. Linder and A. V. Balatsky, *Rev. Mod. Phys.* **91**, 045005 (2019).
- [7] S. A. Kivelson and D. S. Rokhsar, *Phys. Rev. B* **41**, 11693 (1990).
- [8] H. L. Zhao and S. Hershfield, *Phys. Rev. B* **52**, 3632 (1995).
- [9] C. H. L. Quay, D. Chevallier, C. Bena, and M. Aprili, *Nat. Phys.* **9**, 84 (2013).
- [10] Y. Tserkovnyak, A. Brataas, and G. E. W. Bauer, *Phys. Rev. Lett.* **88**, 117601 (2002).
- [11] K.-R. Jeon, C. Ciccarelli, H. Kurebayashi, J. Wunderlich, L. F. Cohen, S. Komori, J. W. A. Robinson, and M. G. Blamire, *Phys. Rev. Applied* **10**, 014029 (2018).
- [12] K.-R. Jeon, C. Ciccarelli, A. J. Ferguson, H. Kurebayashi, L. F. Cohen, X. Montiel, M. Eschrig, J. W. A. Robinson, and M. G. Blamire, *Nature Mater.* **17**, 499 (2018).
- [13] Y. Yao, Q. Song, Y. Takamura, J. P. Cascales, W. Yuan, Y. Ma, Y. Yun, X. C. Xie, J. S. Moodera, and W. Han, *Phys. Rev. B* **97**, 224414 (2018).
- [14] M. Inoue, M. Ichioka, and H. Adachi, *Phys. Rev. B* **96**, 024414 (2017).
- [15] T. Kato, Y. Ohnuma, M. Matsuo, J. Rech, T. Jonckheere, and T. Martin, *Phys. Rev. B* **99**, 144411 (2019).
- [16] M. A. Silaev, *Phys. Rev. B* **102**, 144521 (2020).
- [17] M. A. Silaev, *Phys. Rev. B* **102**, 180502(R) (2020).
- [18] R. Cheng, J. Xiao, Q. Niu, and A. Brataas, *Phys. Rev. Lett.* **113**, 057601 (2014).
- [19] A. Kamra and W. Belzig, *Phys. Rev. Lett.* **119**, 197201 (2017).
- [20] P. Vaidya, S. A. Morley, J. van Tol, Y. Liu, R. Cheng, A. Brataas, D. Lederman, and E. del Barco, *Science* **368**, 160 (2020).
- [21] S. Takei, B. I. Halperin, A. Yacoby, and Y. Tserkovnyak, *Phys. Rev. B* **90**, 094408 (2014).
- [22] E. L. Fjærbu, N. Rohling, and A. Brataas, *Phys. Rev. B* **95**, 144408 (2017).
- [23] E. L. Fjærbu, N. Rohling, and A. Brataas, *Phys. Rev. B* **100**, 125432 (2019).
- [24] K. Oyanagi, S. Takahashi, L. J. Cornelissen, J. Shan, S. Daimon, T. Kikkawa, G. E. Bauer, B. J. van Wees, and E. Saitoh, *Nat. Commun.* **10**, 1 (2019).
- [25] T. Kato, Y. Ohnuma, and M. Matsuo, *Phys. Rev. B* **102**, 094437 (2020).
- [26] M. Umeda, Y. Shiomi, T. Kikkawa, T. Niizeki, J. Lustikova, S. Takahashi, and E. Saitoh, *Appl. Phys. Lett.* **112**, 232601 (2018).
- [27] M. Hagiwara, K. Katsumata, I. Yamada, and H. Suzuki, *J. Phys.: Condens. Matter* **8**, 7349 (1996).
- [28] F. M. Johnson and A. H. Nethercot, *Phys. Rev.* **114**, 705 (1959).
- [29] R. C. Ohlmann and M. Tinkham, *Phys. Rev.* **123**, 425 (1961).
- [30] J. Rammer, *Quantum Field Theory of Non-equilibrium States* (Cambridge University Press, Cambridge, 2007), Vol. 22.
- [31] H. Bruus and K. Flensberg, *Many-body Quantum Theory in Condensed Matter Physics: An Introduction* (Oxford University Press, Oxford, 2004).

PAPER VII

Reference

Eirik Holm Fyhn and Jacob Linder,

Spin-orbit pumping.

Physical Review B **105**, L020409 (2022)

doi: 10.1103/physrevb.105.l020409


CONTRIBUTIONS

EHF performed the analytical calculations and the numerical simulations, with support from JL. EHF drafted the manuscript. JL formulated the initial idea. EHF and JL contributed to the discussions of the physics, and the revision of the final manuscript. Specifically, in addition to participating in the discussion of the physics and the revision of the final manuscript, EHF wrote the initial draft, performed all the calculations, developed the code, performed the numerical simulations and produced all figures presented in the paper.

Spin-orbit pumping

Eirik Holm Fyhn  and Jacob Linder

Center for Quantum Spintronics, Department of Physics, Norwegian University of Science and Technology, NO-7491 Trondheim, Norway

 (Received 7 July 2021; revised 13 January 2022; accepted 15 January 2022; published 31 January 2022)

We study theoretically the effect of a rotating electric field on a diffusive nanowire and find an effect that is analogous to spin pumping, which refers to the generation of spin through a rotating magnetic field. The electron spin couples to the electric field because the particle motion induces an effective magnetic field in its rest frame. In a diffusive system the velocity of the particle, and therefore also its effective magnetic field, rapidly and randomly changes direction. Nevertheless, we demonstrate analytically and via a physical argument why the combination of the two effects described above produces a finite magnetization along the axis of rotation. This manifests as a measurable spin-voltage in the range of tens of microvolts.

DOI: [10.1103/PhysRevB.105.L020409](https://doi.org/10.1103/PhysRevB.105.L020409)

Introduction. As further miniaturization of transistors becomes ever more difficult [1], there is a pressing need for new technologies to aid or replace silicon-based information technology. Spintronics is a candidate which has as its underlying idea to use the electron spin as an information carrier [2,3]. This idea is promising because the spin degrees of freedom in solid-state systems can potentially be manipulated in a highly energy-efficient manner. This is important since the growing need for more computing power has significantly increased the energy consumption of information and communication technologies [4,5]. As a result, the study of spin transport and spin manipulation in low-dimensional and nanoscale devices is a growing field of research.

One important aspect of spin manipulation is the generation of spin, which can be done by so-called spin pumping [6,7]. This refers to the generation of spin through a precessing magnetic field. After its discovery in ferromagnets [6], spin pumping was studied for a wide range of systems, such as antiferromagnets [8–10], spin-glass systems [11], and superconducting hybrid structures [12–14]. Since the electron spin gives rise to a magnetic dipole moment, it is conceptually simplest to manipulate through magnetic fields. However, spin also couples to electric fields since, from the perspective of a moving electron, an electric field gives rise to an effective magnetic field. This interaction between spin and electric fields is known as spin-orbit coupling (SOC) and is the reason why electric fields play a central role in spintronics research [15,16]. In this Letter we investigate whether an effect analogous to spin pumping can be obtained from a time-dependent electric field through SOC.

Materials with SOC are most famously able to produce spin polarization through the spin Hall effect [17]. This refers to how spin accumulates when a charge current is passed through because the trajectories of electrons with opposite spins are bent in opposite directions. This can produce a measurable spin polarization [18–20], but unlike spin pumping it requires an applied electric current. The spin Hall effect is also widely used to detect the spin-currents produced by spin pumping [10,17,21].

The prospect of spin manipulation from external electric fields is especially interesting in the context of spin-based quantum bits. This is because magnetic fields are difficult to localize [22–24] compared to their electric counterparts [25,26], something which makes individual control of spin-based quantum bits more feasible with electric fields. Time-dependent SOC has, therefore, mostly been considered in quantum dots and quantum wells. In such structures, oscillating electric fields were studied experimentally [25,27] and theoretically [28–31] with a fixed direction in space. However, a harmonically oscillating electric field with fixed direction does not by itself break time reversal symmetry, which is necessary to produce magnetization. These systems, therefore, require an additional static magnetic field, but an entirely electric control of the spin motion can be obtained by a rotating electric field. This was pointed out by Serebrennikov [32] who considered an electron in a spherical potential under the influence of a rotating electric field. More recently, Entin-Wohlman *et al.* [33] showed that when a quantum dot subjected to a rotating electric field is placed in a junction with normal metals, the resulting time-dependent tunneling can induce a nonzero magnetization in the leads.

The prospect of spin-generation from purely electric fields from local gate electrodes is attractive also from a spintronics perspective since such devices could be placed in close proximity to other nanoscale devices without them being affected by undesirable stray fields. For this reason, and motivated by the success of the electrical control of spin dynamics in quantum dots, we present here a study of how magnetization can be induced in diffusive nanowires by purely electrical means. We consider an insulated wire subjected to a rotating electric field, as depicted in Fig. 1.

In diffusive systems the physical picture is complicated by the fact that the particles rapidly change momentum direction. This means that the effective magnetic fields also change direction frequently, as viewed from the rest frame of the particles. Nevertheless, we find using quasiclassical Keldysh theory that a finite, time-independent magnetization is induced along the axis of rotation. After presenting our results,

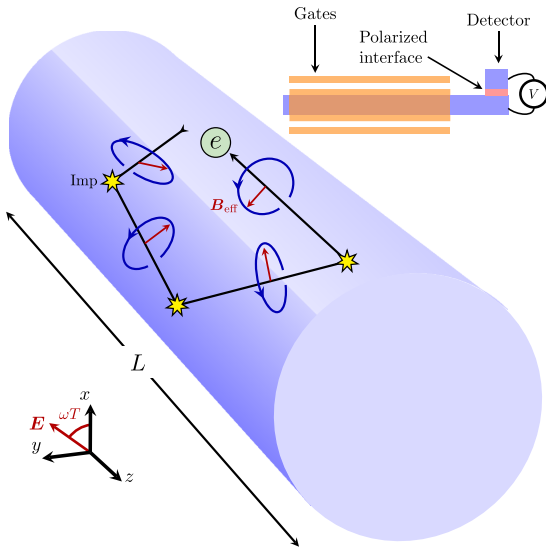


FIG. 1. Illustration of an insulated nanowire of length L subjected to an electric field E , which rotates in the xy -plane with angular frequency ω . The rotating field can be experimentally implemented using two pairs of gate voltage plates along the x and y axes with AC voltages and a phase-shift between the pairs, as illustrated in the top right part of the figure. The top right figure also illustrates a possible method of measuring the spin accumulation through the voltage difference across a spin-polarized interface. Additionally, the figure illustrates the physical mechanism behind the spin pumping effect induced by the electric field. The effective magnetic field B_{eff} in the rest frame of the electron is perpendicular to its motion in the laboratory frame and changes with each scattering event. Despite this, the projection of B_{eff} onto the plane (xy) perpendicular to the nanowire length (z) rotates in the same direction after any scattering event, as indicated by the blue ellipses. This causes the spin pumping effect.

we explain the physical origin of this effect. Hence, pumping spin by rotating electric fields, which we here refer to as spin-orbit pumping, or SO pumping, can be used as an alternative to conventional spin pumping. Systems with strong atomic SOC would be advantageous to realize spin-orbit pumping experimentally. The SOC in such a system can, depending on the lattice symmetry, have additional static terms. These terms will not induce spin-orbit pumping by themselves, but they can nevertheless affect the results. We do not include such terms here, but note that it would be interesting for future work to study how the inclusion of other types of SOC can affect spin-orbit pumping.

Equations. Under the assumption that the Fermi energy is the dominant energy scale and the mean free path is short, the system illustrated in Fig. 1 can be described by the quasiclassical Keldysh theory [34–36]. Moreover, if the mean free path is much shorter than the system length and the lengthscale associated with SOC, $1/m\alpha$, and the elastic scattering rate is much shorter than the angular frequency of the rotating electric field, the system can be classified as *diffusive*. In this

case the quasiclassical Green’s function \check{g}_s solves the Usadel equation [35,37]

$$\frac{\partial \check{g}_s}{\partial T} + D \check{\nabla} \circ (\check{g}_s \circ \check{\nabla} \circ \check{g}_s) + i[\check{\sigma}_{\text{inel}}, \check{g}_s]_{\circ} = 0, \quad (1)$$

Here T is time, D is the diffusion constant, $\check{\sigma}_{\text{inel}}$ is the self-energy matrix from inelastic relaxation processes [38], and $\check{\nabla}$ is the covariant derivative which includes the spin-orbit coupling. Moreover, the circle-product is

$$a \circ b = \exp\left(\frac{i}{2} \partial_T^a \partial_T^b - \frac{i}{2} \partial_T^a \partial_\varepsilon^b\right) ab, \quad (2)$$

where ε is energy. The time-varying electric field will generally also induce a magnetic field, but we find that this is negligible compared to the effective magnetic field felt by the moving particles due to the electric field.

The circle-product makes the Usadel equation difficult to solve in time-dependent situations, but in this case it can be simplified by a Fourier transform in energy [39]. From this we can find an equation for the magnetization,

$$\mathbf{m} = \frac{g\mu_B N_0}{16} \int_{-\infty}^{\infty} d\varepsilon \text{Tr}(\boldsymbol{\sigma} \check{g}_s^K), \quad (3)$$

where the superscript K denotes the Keldysh part, $\boldsymbol{\sigma}$ is the vector of Pauli matrices, g is the Landé g -factor, N_0 is the density of states at the Fermi energy, and μ_B is the Bohr magneton. We find that \mathbf{m} solves

$$\frac{\partial \mathbf{m}}{\partial T} - D \frac{\partial^2 \mathbf{m}}{\partial z^2} + 2\delta \mathbf{m} = 4DA \times \frac{\partial \mathbf{m}}{\partial z} + 4DA \times (\mathbf{A} \times \mathbf{m}) - g\mu_B N_0 DA \times \frac{\partial \mathbf{A}}{\partial T}, \quad (4)$$

as shown in the Supplementary Material [40,41]. Here, \mathbf{A} comes from the spin-orbit coupling and is given by

$$\mathbf{A} = m\alpha \mathbf{e}_E \times \mathbf{e}_z, \quad (5)$$

where α is the Rashba coupling, m is the effective mass, \mathbf{e}_z is the unit vector in the z -direction, and \mathbf{e}_E is the unit vector pointing in the direction of the electric field, which is assumed to be uniform in space. Finally, δ is an effective parameter describing the spin relaxation rate from sources other than spin-orbit coupling, such as inelastic phonon scattering. The spin relaxation rate described by δ is assumed independent of spin direction. Moreover, Eq. (5) already contains a relaxation term that depends on the spin direction due to \mathbf{A} , which we comment on below.

The left-hand side of Eq. (4) describes diffusion and the spin relaxation in the absence of SOC, while the right-hand side is the effect of the SOC. The first term on the right side describes spin precession of the diffusion current and the second term is spin relaxation due to the Dyakonov-Perel mechanism [42]. This relaxation comes from the randomization of spin precession angles caused by elastic scattering at nonmagnetic impurities. The third and final term is the source term coming from the time dependence of \mathbf{A} . It is this term which makes SOC capable of producing spin in diffusive systems. We can from this term immediately see that a time-varying electric field with fixed direction will not generate spin since $\mathbf{A} \times \partial \mathbf{A} / \partial T = 0$ in that case.

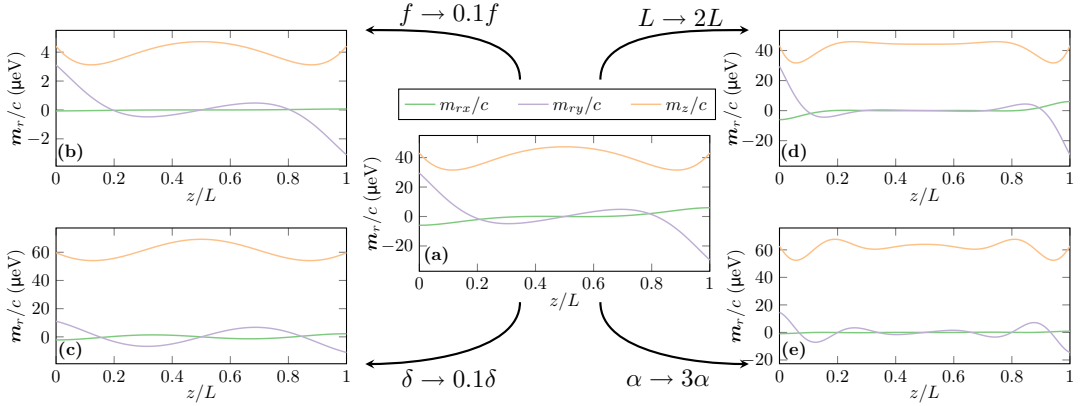


FIG. 2. Spatial distribution of the components of the magnetization \mathbf{m}_r for various system parameters. m_{rx} and m_{ry} are the x - and y -components of the magnetization as seen from the rotating frame of reference, while m_z is the z -component of the magnetization and therefore the same in the rotating frame and the laboratory frame. The normalization constant is $c = \frac{1}{2}g\mu_B N_0$. Panel (a) has Rashba coupling $\alpha = 3 \times 10^{-12}$ eVm, length $L = 1 \mu\text{m}$, frequency $f = 32$ GHz, and inelastic relaxation rate $\delta = 0.1$ meV. The remaining panels have the same parameters as (a), except for the quantity labeled at the corresponding arrow. Thus, the four side panels illustrate the effect of varying ω , L , δ , and α , respectively. (b) has $f = 3.2$ GHz, (c) has $\delta = 0.01$ meV, (d) has $L = 2 \mu\text{m}$, and (e) has $\alpha = 9 \times 10^{-12}$ eVm.

Equation (4) must be accompanied by boundary conditions. For simplicity we choose insulating boundaries, which means that the particle flux across the interfaces at $z = 0$ and $z = L$ must be zero. In the diffusive limit of the quasiclassical Green's function formalism, the relevant boundary condition is known as the Kupriyanov-Lukichev boundary condition [43]. From this we find that

$$\frac{\partial \mathbf{m}}{\partial z} + 2\mathbf{A} \times \mathbf{m} - \frac{1}{2}g\mu_B N_0 \frac{\partial \mathbf{A}}{\partial T} = 0 \quad (6)$$

at $z = 0$ and $z = L$, as shown in the Supplementary Material [40,44,45].

Equation (4) can be solved for times long after the rotating electric field has been turned on by looking for a stationary solution in the rotating reference frame. This is because all solutions converge to this unique stationary solution, as we prove in the Supplementary Material [40]. In the rotating reference frame, the electric field is time-independent and the magnetization along the z -direction is the same as in the laboratory frame. Converting the equations into the rotating frame can be done by inserting the rotation matrix $R(\omega T)$, which satisfies

$$\mathbf{A} = \begin{pmatrix} \cos(\omega T) & \sin(\omega T) & 0 \\ -\sin(\omega T) & \cos(\omega T) & 0 \\ 0 & 0 & 1 \end{pmatrix} \mathbf{A}_0 = R(\omega T)\mathbf{A}_0, \quad (7)$$

where \mathbf{A}_0 is constant in time. We choose $\mathbf{A}_0 = |\mathbf{A}_0|e_x$. To write Eq. (4) in the rotating system, we write $\mathbf{m} = R(\omega T)\mathbf{m}_r$ and use the relations $[R(\theta)\mathbf{u}] \times [R(\theta)\mathbf{v}] = R(\theta)\mathbf{u} \times \mathbf{v}$ and

$$\frac{\partial}{\partial T} R(\omega T)\mathbf{u} = R(\omega T) \frac{\partial \mathbf{u}}{\partial T} + R(\omega T)[\mathbf{u} \times \omega e_z]. \quad (8)$$

The equation for the magnetization in the rotating frame is therefore

$$D \frac{\partial^2 \mathbf{m}_r}{\partial z^2} - 2\delta \mathbf{m}_r + \boldsymbol{\Omega} \times \mathbf{m}_r + 4DA_0 \times \frac{\partial \mathbf{m}_r}{\partial z} + 4DA_0 \times \left[\mathbf{A}_0 \times \left(\mathbf{m}_r - \frac{g\mu_B N_0}{4} \boldsymbol{\Omega} \right) \right] = 0, \quad (9)$$

where we use that \mathbf{m}_r is independent of time and $\boldsymbol{\Omega} = \omega e_z$. The boundary condition in the rotating frame is

$$\frac{\partial \mathbf{m}_r}{\partial z} + 2\mathbf{A}_0 \times \left(\mathbf{m}_r - \frac{g\mu_B N_0}{4} \boldsymbol{\Omega} \right) = 0, \quad (10)$$

at $z = 0$ and $z = L$.

The magnetization is measurable through the so-called spin-voltage

$$\mu_z = \frac{m_z}{\frac{1}{2}g\mu_B N_0 |e|}. \quad (11)$$

If we connect the nanowire to a detector electrode through an interface with polarization P along the z -direction, as illustrated in Fig. 1, then $P\mu_z$ is the voltage difference between the nanowire and ferromagnet in the absence of electric current [46–51]. This is shown in the Supplementary Material [40,52–54].

Results. We solve Eqs. (9) and (10) numerically by using the finite element method. Figure 2 shows the resulting spatial distribution of \mathbf{m}_r for various system parameters and Fig. 3 shows the spatially averaged spin-voltage as a function of the Rashba coupling parameter and frequency, $f = \omega/2\pi$. We use $m = 0.1m_e$, where m_e is the electron mass and $D = 10^2 \text{ cm}^2 \text{ s}^{-1}$. Note that the z -component of the magnetization is equal in the rotating frame and laboratory-frame, so m_z in Fig. 2 is static and equal in both frames.

Figure 2 shows that the magnetization has nonzero components in the x - and y -directions that are antisymmetric around the middle of the wire. In the rotating frame, magnetization

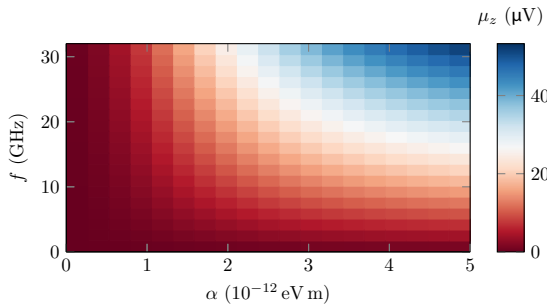


FIG. 3. Spatially averaged spin-voltage as a function of Rashba coupling parameter α and frequency f . The spin relaxation rate is set to $\delta = 0.1$ meV and the length of the wire is $L = 1$ μm .

along the y -direction is induced at the boundaries, as can be seen from Eq. (10). This magnetization is rotated around the z -axis from the term $\mathbf{\Omega} \times \mathbf{m}_r$ in Eq. (9), and it is rotated into the z -component because of $4DA_0 \times \partial \mathbf{m}_r / \partial z$. The first comes from the effective magnetic field present in the rotating frame and the second is the spin precession of the diffusion current from SOC. We can see the spin rotation effect of $\mathbf{\Omega}$ by comparing Figs. 2(a) and 2(b). From this we see that when f is decreased from 32 GHz to 3.2 GHz, m_z and m_{ry} are also scaled by a factor of 1/10. This is reasonable since the source term in the magnetization equation is proportional to f . The x -component m_{rx} , on the other hand, is reduced much more in Fig. 2(b), which is expected since the rotation from m_{ry} , coming from the term $\mathbf{\Omega} \times \mathbf{m}_r$, is much less.

Comparing Fig. 2(a) to Figs. 2(c) and 2(e) shows the effect of decreasing the inelastic relaxation and increasing the Rashba coupling, respectively. In both cases the ratio between the spin generation from SOC and the inelastic spin relaxation is increased. As a result, the magnetization along the z -axis is increased. From Eq. (10) we see $|\partial m_{ry} / \partial z|$ gets smaller at the boundaries when m_z is larger. This is reflected in the smaller y -component in Figs. 2(c) and 2(e). Finally, unlike Fig. 2(c), Fig. 2(e) has more rapid oscillations in m_z and m_{ry} . This is expected since increasing α not only increases the spin generation, but also the spin precession associated with SOC.

From Figs. 2 and 3 we see that the rotating electric field can produce a spin-voltage of tens of microvolt with the parameters used here. This is our main result and shows that spin-orbit pumping is capable of producing a measurable magnetization. We propose that the SO pumping effect can be understood in terms of normal spin pumping from the effective magnetic field in the reference frames of the moving charge carriers. Consider a particle with velocity $\mathbf{v} = (v_x, v_y, v_z)$ moving in the effective electric field $\mathbf{E} = E[\cos(\omega T), \sin(\omega T), 0]$. The effective magnetic field is obtained via a Lorentz transformation

$$\mathbf{B}_{\text{eff}} = \begin{pmatrix} v_z \sin(\omega T) \\ -v_z \cos(\omega T) \\ v_y \cos(\omega T) - v_x \sin(\omega T) \end{pmatrix} E. \quad (12)$$

This effective field rotates in an elliptical way around an axis. Although the direction of this axis changes with the particle

velocity, its component along the z -axis is always of the same sign. This is illustrated in Fig. 1 and can be most easily seen by noting that the projection of \mathbf{B}_{eff} onto the xy -plane always rotates counterclockwise when $\omega > 0$ and clockwise when $\omega < 0$. Since it is known from normal spin pumping that a rotating magnetic field induces a magnetization along the axis of rotation, this explains why a rotating electric field can generate a magnetization in the z -direction. Summarized, the physical picture of SO pumping in diffusive systems is as follows. With each elastic scattering, the spin precession axis jumps to a new direction. This randomizes the spin over time and gives rise to a spin relaxation. This is just the normal Dyakonov-Perel mechanism. However, since the electric field rotates, the spin precession axis also rotates between scatterings. Since this rotation is always in the same direction around the z -axis it gives rise to a net spin-accumulation polarized in the z -direction. The equivalence in the quasiclassical theory between SOC and the effective magnetic field \mathbf{B}_{eff} is shown explicitly in the Supplementary Material [40].

One difference from normal spin pumping is that a rotating electric field both generates and dissipates spin because of the Dyakonov-Perel mechanism. Thus, by increasing the electric field strength, both spin generation and spin relaxation is increased. When Dyakonov-Perel relaxation is the dominant spin relaxation mechanism, we can see from Eqs. (9) and (10) that the spin generation and spin relaxation mechanisms equalize when $\mathbf{m}_r = g\mu_B N_0 \mathbf{\Omega} / 4$. This can be seen from the fact that $\mathbf{m}_r = g\mu_B N_0 \mathbf{\Omega} / 4$ solves Eqs. (9) and (10) when $\delta = 0$. Thus, SO pumping in diffusive systems can at most produce a spin-voltage of $\mu_z = \omega / 2 |e| \approx 2 \times (f / \text{GHz}) \mu\text{V}$. However, in the presence of other spin relaxation mechanisms, the observed spin-voltage will be less, as is the case in Figs. 2 and 3.

Based on the physical picture of SO pumping as the cumulative effect of normal spin pumping from the rotating effective magnetic field observed between each scattering, it is clear that scattering processes work to reduce the SO pumping effect. It would therefore be of interest to study rotating electric fields in clean, ballistic systems to see if the SO pumping effect can be enhanced in such systems. We leave this for future work.

Conclusion. We found using quasiclassical Keldysh theory that a rotating electric field can induce a magnetization and a measurable spin-voltage of tens of μV . This spin-orbit pumping can be understood as a spin pumping from the effective magnetic field in the rest frame of the moving particles. This is because, despite the jumps occurring at each scattering event, the projection of the effective magnetic field onto the plane in which the electric field is applied always rotates in the same direction. Obtaining a spin-voltage above 10 μV with the material parameters used here requiring a Rashba coupling of 10^{-12} eV m. Rashba coupling strengths of this magnitude were obtained experimentally at temperatures below 15 K in nanowires with applied electric fields [26,55]. One reason for this requirement is that spin relaxation, both from inelastic relaxation and from SOC through Dyakonov-Perel relaxation, inhibits spin-orbit pumping. Thus, it would be of interest to study rotating electric fields in clean, ballistic nanowires to see whether the spin-orbit pumping effect is stronger in such systems. Nevertheless, the findings presented here shows that

spin-orbit pumping should be capable of producing an experimentally observable magnetization even in diffusive systems.

Acknowledgments. This work was supported by the Research Council of Norway through Grant No. 240806

and its Centres of Excellence funding scheme Grant No. 262633 “*QuSpin*.” J.L. also acknowledges funding from the NV faculty at the Norwegian University of Science and Technology.

- [1] A. Kaul, *Microelectronics to Nanoelectronics: Materials, Devices & Manufacturability* (CRC Press, Boca Raton, Florida, 2017).
- [2] S. Bader and S. Parkin, *Annu. Rev. Condens. Matter Phys.* **1**, 71 (2010).
- [3] A. Hirohata, K. Yamada, Y. Nakatani, I.-L. Prejbeanu, B. Diény, P. Pirro, and B. Hillebrands, *J. Magn. Magn. Mater.* **509**, 166711 (2020).
- [4] J. Puebla, J. Kim, K. Kondou, and Y. Otani, *Commun. Mater.* **1**, 24 (2020).
- [5] N. Jones, *Nature (London)* **561**, 163 (2018).
- [6] Y. Tserkovnyak, A. Brataas, and G. E. W. Bauer, *Phys. Rev. Lett.* **88**, 117601 (2002).
- [7] Y. Tserkovnyak, A. Brataas, G. E. W. Bauer, and B. I. Halperin, *Rev. Mod. Phys.* **77**, 1375 (2005).
- [8] R. Cheng, J. Xiao, Q. Niu, and A. Brataas, *Phys. Rev. Lett.* **113**, 057601 (2014).
- [9] O. Johansen and A. Brataas, *Phys. Rev. B* **95**, 220408(R) (2017).
- [10] P. Vaidya, S. A. Morley, J. van Tol, Y. Liu, R. Cheng, A. Brataas, D. Lederman, and E. del Barco, *Science* **368**, 160 (2020).
- [11] Y. Fujimoto, M. Ichioka, and H. Adachi, *Phys. Rev. B* **101**, 184412 (2020).
- [12] K.-R. Jeon, C. Ciccarelli, H. Kurebayashi, J. Wunderlich, L. F. Cohen, S. Komori, J. W. A. Robinson, and M. G. Blamire, *Phys. Rev. Applied* **10**, 014029 (2018).
- [13] T. Kato, Y. Ohnuma, M. Matsuo, J. Rech, T. Jonckheere, and T. Martin, *Phys. Rev. B* **99**, 144411 (2019).
- [14] E. H. Fyhn and J. Linder, *Phys. Rev. B* **103**, 134508 (2021).
- [15] A. Manchon, J. Zelezný, I. M. Miron, T. Jungwirth, J. Sinova, A. Thiaville, K. Garello, and P. Gambardella, *Rev. Mod. Phys.* **91**, 035004 (2019).
- [16] A. Manchon, H. C. Koo, J. Nitta, S. M. Frolov, and R. A. Duine, *Nat. Mater.* **14**, 871 (2015).
- [17] J. Sinova, S. O. Valenzuela, J. Wunderlich, C. H. Back, and T. Jungwirth, *Rev. Mod. Phys.* **87**, 1213 (2015).
- [18] Y. K. Kato, R. C. Myers, A. C. Gossard, and D. D. Awschalom, *Science* **306**, 1910 (2004).
- [19] S. O. Valenzuela and M. Tinkham, *Nature (London)* **442**, 176 (2006).
- [20] E. S. Garlid, Q. O. Hu, M. K. Chan, C. J. Palmstrøm, and P. A. Crowell, *Phys. Rev. Lett.* **105**, 156602 (2010).
- [21] O. Mosendz, J. E. Pearson, F. Y. Fradin, G. E. W. Bauer, S. D. Bader, and A. Hoffmann, *Phys. Rev. Lett.* **104**, 046601 (2010).
- [22] B. Simović, P. Studerus, S. Gustavsson, R. Leturcq, K. Ensslin, R. Schuhmann, J. Forrer, and A. Schweiger, *Rev. Sci. Instrum.* **77**, 064702 (2006).
- [23] A. C. Torrezan, T. P. Mayer Alegre, and G. Medeiros-Ribeiro, *Rev. Sci. Instrum.* **80**, 075111 (2009).
- [24] F. H. L. Koppens, C. Buizert, K. J. Tielrooij, I. T. Vink, K. C. Nowack, T. Meunier, L. P. Kouwenhoven, and L. M. K. Vandersypen, *Nature (London)* **442**, 766 (2006).
- [25] K. C. Nowack, F. H. L. Koppens, Y. V. Nazarov, and L. M. K. Vandersypen, *Science* **318**, 1430 (2007).
- [26] D. Liang and X. P. Gao, *Nano Lett.* **12**, 3263 (2012).
- [27] Y. Kato, R. C. Myers, D. C. Driscoll, A. C. Gossard, J. Levy, and D. D. Awschalom, *Science* **299**, 1201 (2003).
- [28] E. I. Rashba and A. L. Efros, *Phys. Rev. Lett.* **91**, 126405 (2003).
- [29] B. Venitucci, L. Bourdet, D. Pouzada, and Y.-M. Niquet, *Phys. Rev. B* **98**, 155319 (2018).
- [30] V. P. Michal, B. Venitucci, and Y.-M. Niquet, *Phys. Rev. B* **103**, 045305 (2021).
- [31] A. L. Efros and E. I. Rashba, *Phys. Rev. B* **73**, 165325 (2006).
- [32] Y. A. Serebrennikov, *Phys. Rev. B* **70**, 064422 (2004).
- [33] O. Entin-Wohlman, R. I. Shekhter, M. Jonson, and A. Aharony, *Phys. Rev. B* **102**, 075419 (2020).
- [34] W. Belzig, F. K. Wilhelm, C. Bruder, G. Schön, and A. D. Zaikin, *Superlattices Microstruct.* **25**, 1251 (1999).
- [35] J. Rammer and H. Smith, *Rev. Mod. Phys.* **58**, 323 (1986).
- [36] G. Eilenberger, *Z. Phys.* **214**, 195 (1968).
- [37] K. D. Usadel, *Phys. Rev. Lett.* **25**, 507 (1970).
- [38] P. Virtanen, T. T. Heikkilä, F. S. Bergeret, and J. C. Cuevas, *Phys. Rev. Lett.* **104**, 247003 (2010).
- [39] E. H. Fyhn and J. Linder, *Phys. Rev. B* **103**, L100502 (2021).
- [40] See Supplemental Material at <http://link.aps.org/supplemental/10.1103/PhysRevB.105.L020409> for a derivation of the equations.
- [41] M. Houzet, *Phys. Rev. Lett.* **101**, 057009 (2008).
- [42] M. Dyakonov and V. Perel, *Sov. Phys. Solid State* **13**, 3023 (1972).
- [43] M. Y. Kupriyanov and V. F. Lukichev, *Zh. Eksp. Teor. Fiz.* **94**, 139 (1988).
- [44] V. Chandrasekhar, in *Superconductivity: Conventional and Unconventional Superconductors* (Springer, Berlin, 2008), pp. 279–313.
- [45] J. A. Ouassou, T. D. Vethaak, and J. Linder, *Phys. Rev. B* **98**, 144509 (2018).
- [46] R. H. Silsbee, *Bull. Magn. Reson.* **2**, 284 (1980).
- [47] M. Johnson and R. H. Silsbee, *Phys. Rev. Lett.* **55**, 1790 (1985).
- [48] N. Tombros, C. Jozsa, M. Popinciuc, H. T. Jonkman, and B. J. van Wees, *Nature (London)* **448**, 571 (2007).
- [49] N. Poli, J. P. Morten, M. Urech, A. Brataas, D. B. Haviland, and V. Korenivski, *Phys. Rev. Lett.* **100**, 136601 (2008).
- [50] M. Silaev, P. Virtanen, T. T. Heikkilä, and F. S. Bergeret, *Phys. Rev. B* **91**, 024506 (2015).
- [51] T. T. Heikkilä, M. Silaev, P. Virtanen, and F. S. Bergeret, *Prog. Surf. Sci.* **94**, 100540 (2019).
- [52] F. S. Bergeret, A. Verso, and A. F. Volkov, *Phys. Rev. B* **86**, 214516 (2012).
- [53] J. A. Ouassou, A. Pal, M. Blamire, M. Eschrig, and J. Linder, *Sci. Rep.* **7**, 1932 (2017).
- [54] H. G. Hugdal, J. Linder, and S. H. Jacobsen, *Phys. Rev. B* **95**, 235403 (2017).
- [55] K. Takase, Y. Ashikawa, G. Zhang, K. Tateno, and S. Sasaki, *Sci. Rep.* **7**, 930 (2017).

Supplementary: Spin-orbit-pumping

Eirik Holm Fyhn¹ and Jacob Linder¹

¹Center for Quantum Spintronics, Department of Physics, Norwegian University of Science and Technology, NO-7491 Trondheim, Norway

(Dated: January 13, 2022)

I. DERIVATION OF MAGNETIZATION EQUATION

When a charged particle with mass m moves with momentum \mathbf{p} in an electric field $\mathbf{E} = E\mathbf{e}_E$, it will feel an effective magnetic field, $\mathbf{B}_{\text{eff}} = \mathbf{E} \times \mathbf{p}/m$ (in natural units), and therefore also an effective Zeeman energy

$$\mathcal{H}_{\text{SOC}} = \alpha (\boldsymbol{\sigma} \times \mathbf{p}) \cdot \mathbf{e}_E, \quad (1)$$

where $\boldsymbol{\sigma}$ is the vector of Pauli-matrices, such that $\boldsymbol{\sigma}/2$ is the spin operator, and $\alpha = g\mu_B E/2m$ is a parameter giving the strength of the spin-orbit coupling (SOC). Here, g is the Landé g -factor and μ_B is the Bohr magneton. In realistic system the SOC can be more complicated and depend on the crystal structure and atomic potential. Nevertheless, the spin-orbit effect can often be approximated by an Hamiltonian on the form of Eq. (1) where \mathbf{e}_E is the unit vector in the direction of the external electric field and α is an effective parameter called the Rashba coupling [1]. Here we use this Rashba form for the spin-orbit coupling and keep α as a free parameter.

The system under consideration can be treated quasiclassically if the material has a well-defined Fermi surface and the Fermi wavelength is much shorter than all other relevant length-scales, such as the mean free path, system length and the length scale associated with SOC, $1/m\alpha$. In this case, the system can be described by quasiclassical Green's functions, which can be collected in a 4×4 matrix as

$$\check{g} = \begin{pmatrix} g^R & g^K \\ 0 & g^A \end{pmatrix}, \quad (2)$$

where g^R , g^A and g^K are the retarded, advanced and Keldysh quasiclassical Green's functions, respectively. These are normalized such that $\check{g} \circ \check{g} = 1$ and solve the Eilenberger equation [2, 3],

$$\frac{\partial \check{g}}{\partial T} + \mathbf{v}_F \cdot \tilde{\nabla} \circ \check{g} - i \left[\check{\sigma}_{\text{inel}} - \frac{i}{2\tau} \check{g}_s, \check{g} \right]_{\circ} = 0, \quad (3)$$

where \mathbf{v}_F is the Fermi velocity, T is time, τ is the elastic impurity scattering time, \check{g}_s is the isotropic part of the quasiclassical Green's function and $\check{\sigma}_{\text{inel}}$ is the self-energy matrix from inelastic relaxation processes. Moreover, the circle-product is

$$a \circ b = \exp \left(\frac{i}{2} \partial_{\varepsilon}^a \partial_T^b - \frac{i}{2} \partial_T^a \partial_{\varepsilon}^b \right) ab, \quad (4)$$

where ε is energy and the covariant derivative is

$$\tilde{\nabla} \circ \check{g} = \nabla \check{g} - i (\mathbf{a} \circ \check{g} - \check{g} \circ \mathbf{a}), \quad (5)$$

where \mathbf{a} depend on the Rashba coupling through

$$\mathbf{a} = m\alpha \boldsymbol{\sigma} \times \mathbf{e}_E. \quad (6)$$

We include inelastic relaxation through the relaxation time approximation [4]. In this approximation the relaxation rate is given by δ and we assume that it is isotropic in spin-space. In this case, $\sigma_{\text{inel}}^R = -\sigma_{\text{inel}}^A = i\delta$ and $\sigma_{\text{inel}}^K = 2i\delta h_{\text{eq}}$, where h_{eq} is the equilibrium distribution function which the system relaxes towards. At inverse temperature β and electrochemical potential V , this is $h_{\text{eq}}(\varepsilon) = \tanh[\beta(\varepsilon - eV)/2]$, where e is the electron charge. Generally, SOC also gives rise to a term in the self-energy, which is $\sigma_{\text{SOC}}^R = \sigma_{\text{SOC}}^A = -m\alpha^2$. However, since we assume that α is constant in time, $\check{\sigma}_{\text{SOC}} \circ \check{g} = \check{g} \circ \check{\sigma}_{\text{SOC}}$, and $\check{\sigma}_{\text{SOC}}$ disappears from Eq. (3).

We can see how the effective magnetic field discussed in the main text enters the quasiclassical framework by noting that if $\mathbf{B}_{\text{eff}} = (2/g\mu_B)\alpha m\mathbf{e}_E \times \mathbf{v}_F$, we can rewrite Eq. (3) as

$$\frac{\partial \check{g}}{\partial T} + \mathbf{v}_F \cdot \nabla \check{g} - i \left[\frac{1}{2} g\mu_B \mathbf{B}_{\text{eff}} \cdot \boldsymbol{\sigma} - \frac{i}{2\tau} \check{g}_s + \check{\sigma}_{\text{inel}}, \check{g} \right]_{\circ} = 0, \quad (7)$$

where σ is the vector of Pauli matrices. The term $\frac{1}{2}g\mu_B\mathbf{B}_{\text{eff}} \cdot \sigma$ is exactly how the Zeeman energy from a magnetic field \mathbf{B}_{eff} would enter as a self-energy the Eilenberger equation. In other words, the spin-orbit coupling present in the covariant derivative is functionally equivalent to an external magnetic field \mathbf{B}_{eff} . This is in accordance with the physical picture of spin-orbit pumping as an effective spin-pumping from \mathbf{B}_{eff} , as discussed in the main text.

The isotropic part of \check{g} dominates when the impurity scattering time τ is small, such that the elastic impurity scattering term $-i\check{g}_s/2\tau$ is large. In particular, if the scattering time τ is much smaller than the inelastic scattering time, $1/\delta$, and the rate at which the Green's function changes, which in this case is given by the frequency of the rotating electric field, ω , and if the corresponding mean free path $l_{\text{mfp}} = v_F\tau$ is much smaller than the system length as well as the length scale associated with SOC, $1/m\alpha$, then the Eilenberger equation reduces to the Usadel equation [5, 6],

$$\frac{\partial \check{g}_s}{\partial T} + D\tilde{\nabla} \circ (\check{g}_s \circ \tilde{\nabla} \circ \check{g}_s) + i[\check{\sigma}_{\text{incl}}, \check{g}_s]_{\circ} = 0, \quad (8)$$

where D is the diffusion constant. In the non-superconducting case considered here, the equations are considerably simplified by the fact that the retarded and advanced are simply proportional to the unitary matrix. In this case we have $g_s^R = I_2$, $g_s^A = -I_2$, and $g_s^K = 2h$, where I_2 is the 2×2 identity matrix and h is the distribution function. From Eqs. (4) and (8) and the relaxation time approximation we get that the distribution function solves

$$\frac{\partial h}{\partial T} - D\tilde{\nabla} \circ \tilde{\nabla} \circ h + 2\delta(h - h_{\text{eq}}) = 0. \quad (9)$$

The circle-products can be removed either by a unitary transformation [7] or a Fourier transform in energy [8]. Here we choose the latter and use capital letters to denote Fourier transforms,

$$H(t, T, z) = \mathcal{F}\{h\}(t, T, z) = \frac{1}{2\pi} \int_{-\infty}^{\infty} d\varepsilon h(\varepsilon, T, z) e^{-i\varepsilon t}, \quad (10)$$

where $z \in (0, L)$ is the position along the wire. Next, we define the z -component of \mathbf{a} to be $a_z = \mathbf{A} \cdot \sigma$ and $H = H_0 + \mathbf{H} \cdot \sigma$. The Fourier transform is useful because

$$\mathcal{F}\{[\mathbf{A} \cdot \sigma, h]_{\circ}\}(t, T, z) = \mathbf{A}(T+t/2) \cdot \sigma H(t, T, z) - H(t, T, z) \mathbf{A}(T-t/2) \cdot \sigma. \quad (11)$$

We can use that for the Pauli matrices we have $\sigma_i \sigma_j = \delta_{ij} + i\varepsilon_{ijk} \sigma_k$, where ε_{ijk} is the Levi-Civita symbol, and define $\mathbf{A}_{\pm}(T, t) = \mathbf{A}(T+t/2) \pm \mathbf{A}(T-t/2)$ to get

$$\mathcal{F}\{[\mathbf{A} \cdot \sigma, h]_{\circ}\} = \mathbf{A}_- \cdot \mathbf{H} + (\mathbf{A}_- H_0 + i\mathbf{A}_+ \times \mathbf{H}) \cdot \sigma. \quad (12)$$

Using this we get that

$$\frac{1}{2} \text{Tr}[\sigma \mathcal{F}\{\tilde{\nabla} \circ \tilde{\nabla} \circ h\}] = \frac{\partial^2 \mathbf{H}}{\partial z^2} - 2i\mathbf{A}_- \frac{\partial H_0}{\partial z} + 2\mathbf{A}_+ \times \frac{\partial \mathbf{H}}{\partial z} - \mathbf{A}_- (\mathbf{A}_- \cdot \mathbf{H}) - i\mathbf{A}_+ \times \mathbf{A}_- H_0 + \mathbf{A}_+ \times (\mathbf{A}_+ \times \mathbf{H}). \quad (13)$$

Thus, by Fourier transforming Eq. (9), multiplying it with $\sigma/2$ and taking the trace, we get that

$$\frac{\partial \mathbf{H}}{\partial T} - D \frac{\partial^2 \mathbf{H}}{\partial z^2} + 2iD\mathbf{A}_- \frac{\partial H_0}{\partial z} - 2D\mathbf{A}_+ \times \frac{\partial \mathbf{H}}{\partial z} + D\mathbf{A}_- (\mathbf{A}_- \cdot \mathbf{H}) + iD\mathbf{A}_+ \times \mathbf{A}_- H_0 - D\mathbf{A}_+ \times (\mathbf{A}_+ \times \mathbf{H}) + 2\delta \mathbf{H} = 0. \quad (14)$$

In the quasiclassical framework, magnetization is given by $\mathbf{m} = \frac{1}{2}g\mu_B N_0 \pi \lim_{t \rightarrow 0} \text{Re}(\mathbf{H})$ in the absence of an exchange field. All we need to get an equation for \mathbf{m} is therefore to take the limit $t \rightarrow 0$ of Eq. (14). This requires some care, since H_0 is asymptotic to H_{eq} as $t \rightarrow 0$, and $H_{\text{eq}} = -i/[\beta \sinh(\pi t/\beta)]$ diverges as $t \rightarrow 0$. Nevertheless, the limit in Eq. (14) is well-defined since H_0 only occurs multiplied by \mathbf{A}_- , which goes to 0 as $t \rightarrow 0$.

First, we show that H_0 is asymptotic to H_{eq} . This is a consequence of the fact that the physics happens close to the Fermi-surface, meaning that for energies far away from the Fermi-surface the states are either fully occupied ($h_0(\varepsilon) = -1$) or entirely empty ($h_0(\varepsilon) = 1$). That is, $|\varepsilon| \gg 1 \implies h_0(\varepsilon) \approx h_{\text{eq}}(\varepsilon) \approx \varepsilon/|\varepsilon|$. Thus,

$$\lim_{t \rightarrow 0} i\pi t H_0 = \lim_{t \rightarrow 0} \frac{1}{2} i t \mathcal{F}\{h_0\} = \lim_{t \rightarrow 0} \frac{1}{2} \mathcal{F}\left\{\frac{\partial h_0}{\partial \varepsilon}\right\} = \frac{1}{2} \int_{-\infty}^{\infty} d\varepsilon \frac{\partial h_0}{\partial \varepsilon} = 1. \quad (15)$$

Hence, $H_0 \sim 1/i\pi t$ as $t \rightarrow 0$. Finally, using that $\lim_{t \rightarrow 0} \mathbf{A}_+(T, t) = 2\mathbf{A}(T)$, $\lim_{t \rightarrow 0} \mathbf{A}_-(T, t)/t = \partial \mathbf{A}(T)/\partial T$, we get the equation for the equation for the magnetization by taking the limit $t \rightarrow 0$ of Eq. (14) and multiplying it with $\frac{1}{2}g\mu_B N_0 \pi$. This yields

$$\frac{\partial \mathbf{m}}{\partial T} - D \frac{\partial^2 \mathbf{m}}{\partial z^2} + 2\delta \mathbf{m} = 4D\mathbf{A} \times \frac{\partial \mathbf{m}}{\partial z} + 4D\mathbf{A} \times (\mathbf{A} \times \mathbf{m}) - g\mu_B N_0 D\mathbf{A} \times \frac{\partial \mathbf{A}}{\partial T}, \quad (16)$$

which is the same as Eq. (1) in the main text.

II. BOUNDARY CONDITION

Quasiclassical theory is not valid across interfaces because the relevant length scale is short. Consequently, the quasiclassical Green's function is generally not continuous. Instead, the quasiclassical Green's functions in neighbouring materials are connected through boundary conditions. The boundary conditions express the so-called matrix current,

$$\check{\mathbf{I}}(\mathbf{R}, \varepsilon, T) = \int d\Omega v_F \check{g}(\mathbf{v}_F, \mathbf{R}, \varepsilon, T), \quad (17)$$

where the integral goes over all directions of the Fermi velocity, in terms of the propagators on both sides of the interface. Only the Keldysh-component is nonzero in our case. The matrix current contains in its Keldysh-component both the electrical current and the spin-current, as well as the heat-current and so-called spin-heat-current [9, 10]. There should be no current across insulating, spin-inactive interfaces, and so in this case

$$\mathbf{e}_n \cdot \check{\mathbf{I}}^K = -2D\mathbf{e}_n \cdot \check{\nabla} \circ h = 0, \quad (18)$$

where \mathbf{e}_n is the unit normal vector pointing out of the interface. Here, we have used that in the diffusive limit $\check{\mathbf{I}} = -D(\check{g}_s \circ \check{\nabla} \circ \check{g}_s)$.

More generally, one can use the Kupriyanov-Lukichev boundary condition [11],

$$N_{0i}D_i\mathbf{e}_n \cdot (\check{g}_{si} \circ \check{\nabla} \circ \check{g}_{si})^K = \frac{\zeta}{2} [\check{g}_{si}, \check{g}_{sj}]_o^K, \quad (19)$$

which is valid for low-transparency tunneling interfaces with no spin-active properties. Here, N_{0i} and D_i is the density of states at the Fermi surface and diffusion constant in material i , respectively, \mathbf{e}_n is the unit vector orthogonal to the interface and pointing from material i to material j , and ζ is the conductance across the interface. We can rewrite Eq. (19) to

$$\mathbf{e}_n \cdot \check{\nabla} \circ h_i = \frac{\zeta}{N_{0i}D_i} (h_j - h_i). \quad (20)$$

We assume that the nanowire is insulated, so we set $\zeta = 0$. Taking the Fourier transform, multiplying with $\sigma/2$, taking the trace and assuming that \mathbf{e}_n is in the z -direction, we get that

$$\frac{\partial \mathbf{H}}{\partial z} + \mathbf{A}_+ \times \mathbf{H} - iH_0\mathbf{A}_- = 0, \quad (21)$$

where we have dropped the subscript i . Again multiplying by $\frac{1}{2}g\mu_B N_0\pi$ and taking the limit $t \rightarrow 0$ we get

$$\frac{\partial \mathbf{m}}{\partial z} + 2\mathbf{A} \times \mathbf{m} - \frac{1}{2}g\mu_B N_0 \frac{\partial \mathbf{A}}{\partial T} = 0, \quad (22)$$

which is the boundary condition used in the main text.

III. CONVERGENCE TO THE STATIONARY SOLUTION AND ITS UNIQUENESS

In this section we show that regardless of initial condition, all solutions of Eq. (16) together with the boundary condition, Eq. (22), converge to the solution we present in the main manuscript for times long after the electric field has been turned on. In so doing, we also show that this solution is unique.

We start from the equation in the rotating frame, as derived in the main manuscript,

$$-\frac{\partial \mathbf{m}_r}{\partial T} + D \frac{\partial^2 \mathbf{m}_r}{\partial z^2} - 2\delta \mathbf{m}_r + \boldsymbol{\Omega} \times \mathbf{m}_r + 4DA_0 \times \frac{\partial \mathbf{m}_r}{\partial z} + 4DA_0 \times \left[A_0 \times \left(\mathbf{m}_r - \frac{g\mu_B N_0}{4} \boldsymbol{\Omega} \right) \right] = 0, \quad (23)$$

and the boundary condition,

$$\frac{\partial \mathbf{m}_r}{\partial z} + 2\mathbf{A}_0 \times \left(\mathbf{m}_r - \frac{g\mu_B N_0}{4} \boldsymbol{\Omega} \right) = \mathbf{0}. \quad (24)$$

Let the stationary solution found in the main text be \mathbf{u} . What we want to show is that all solutions converge to \mathbf{u} as time goes to infinity. Let \mathbf{v} be any other solution to Eqs. (23) and (24). Next, define $\mathbf{w} = \mathbf{u} - \mathbf{v}$. We want to show that \mathbf{w} must go to zero. Inserting \mathbf{w} in the equation above, we get

$$-\frac{\partial \mathbf{w}}{\partial T} + D \frac{\partial^2 \mathbf{w}}{\partial z^2} - 2\delta \mathbf{w} + \boldsymbol{\Omega} \times \mathbf{w} + 4DA_0 \times \frac{\partial \mathbf{w}}{\partial z} + 4DA_0 \times (\mathbf{A}_0 \times \mathbf{w}) = 0, \quad (25)$$

$$\frac{\partial \mathbf{w}}{\partial z} + 2\mathbf{A}_0 \times \mathbf{w} = 0 \quad \text{at } z = 0 \text{ and } z = L. \quad (26)$$

Next, we introduce the rotation matrix

$$R = \begin{pmatrix} 1 & & \\ & \cos(2A_0z) & -\sin(2A_0z) \\ & \sin(2A_0z) & \cos(2A_0z) \end{pmatrix}, \quad (27)$$

where $A_0 = |A_0|$, and define $\tilde{\mathbf{w}} = R\mathbf{w}$. Recall that A_0 points in the x -direction, so

$$-\frac{\partial \tilde{\mathbf{w}}}{\partial T} + D \frac{\partial^2 \tilde{\mathbf{w}}}{\partial z^2} - 2\delta \tilde{\mathbf{w}} + (R\boldsymbol{\Omega}) \times \tilde{\mathbf{w}} = 0, \quad (28)$$

$$\frac{\partial \tilde{\mathbf{w}}}{\partial z} = 0 \quad \text{at } z = 0 \text{ and } z = L, \quad (29)$$

where we used $R[\partial_z \mathbf{w} + 2A_0 \times \mathbf{w}] = \partial_z (R\mathbf{w})$ and $R(\mathbf{a} \times \mathbf{b}) = (R\mathbf{a}) \times (R\mathbf{b})$, for any vectors \mathbf{a} and \mathbf{b} . Next, take the dot product of these equations with $\tilde{\mathbf{w}}$ and use $(\mathbf{a} \times \mathbf{b}) \cdot \mathbf{b} = 0$ to obtain

$$-\frac{1}{2} \frac{\partial \tilde{w}^2}{\partial T} + \frac{D}{2} \frac{\partial^2 \tilde{w}^2}{\partial z^2} = D \left| \frac{\partial \tilde{\mathbf{w}}}{\partial z} \right|^2 + 2\delta \tilde{w}^2, \quad (30)$$

$$\frac{\partial \tilde{w}^2}{\partial z} = 0. \quad (31)$$

Finally, we define $W^2 = \int_0^L dz \tilde{w}^2$ and integrate Eq. (30) to obtain

$$\frac{\partial W^2}{\partial T} = -2 \int_0^L dz \left(D \left| \frac{\partial \tilde{\mathbf{w}}}{\partial z} \right|^2 + 2\delta \tilde{w}^2 \right). \quad (32)$$

The right hand side is negative as long as $W^2 \neq 0$. Moreover, since $W^2 \geq 0$, we see that $W^2 \rightarrow 0$ as $T \rightarrow \infty$. Hence, the stationary solution is unique and all solutions converge to the stationary solution independently of initial condition.

IV. DETECTOR SETUP

In order to detect the spin-voltage one can connect the nanowire to a detector electrode through a polarized tunneling boundary [12–17]. The detector can be a normal metal or ferromagnet. In the case of a normal metal, a spin-polarized interface can for instance be achieved by inserting a thin ferromagnetic insulator between the nanowire and detector electrode. In the following we show how the voltage difference between the nanowire and electrode can be used to determine the spin-voltage, as discussed in the main text.

Consider the detector setup illustrated in Fig. 1. The detector is connected to the nanowire through a polarized interface and forms an open circuit. Charge, unlike spin, is conserved inside the detector. Hence, the charge current into the electrode must be zero in the stationary state. Assuming that the interface is polarized in the z -direction, the charge current into the detector can generally be written

$$I_{\text{det}} = G_{\uparrow}(V^{\text{det}} - \mu_z) + G_{\downarrow}(V^{\text{det}} + \mu_z), \quad (33)$$

where G_{\uparrow} and G_{\downarrow} is the conductances for electrons with spin up and spin down, respectively. The spin-voltage inside the nanowire is μ_z and the voltage difference between the detector and nanowire is V^{det} . It is assumed that the spin-diffusion length inside the detector is short, such that the spin-voltage inside the detector is much smaller than V^{det} . The voltage inside the detector electrode will stabilize at the value satisfying $I_{\text{det}} = 0$, which we find from Eq. (33) happens at

$$V^{\text{det}} = \frac{G_{\uparrow} - G_{\downarrow}}{G_{\uparrow} + G_{\downarrow}} \mu_z = P \mu_z, \quad (34)$$

where we have inserted the polarization $P = (G_{\uparrow} - G_{\downarrow}) / (G_{\uparrow} + G_{\downarrow})$.

We can derive Eq. (33) more rigorously in the quasiclassical theory. In this way we can take into account the finite spin-voltage which will also be induced in the detector. In order to capture spin-active tunneling boundaries in the quasiclassical framework, we can use a generalization of the Kupriyanov-Lukichev condition [18, 19],

$$N_{0i} D_i \mathbf{e}_n \cdot (\check{g}_{si} \circ \tilde{\nabla} \circ \check{g}_{si})^K = \frac{\zeta}{2} [\check{g}_{si}, (t + u\sigma_z) \check{g}_{sj} (t + u\sigma_z)]_o^K - i \frac{G_{\phi}}{2} [g_{si}^K, \sigma_z]_o, \quad (35)$$

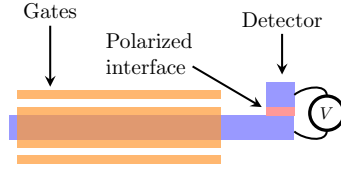


FIG. 1: Illustration of the system under consideration together with the proposed detection setup. The gates encapsulating the nanowire produce a magnetization inside the nanowire through spin-orbit pumping. The resulting spin-voltage can in turn be detected through the voltage difference V between the detector and the nanowire, given that the interface is polarized.

where we have assumed that the interface is polarized in the z -direction, $t = \sqrt{(1 + \sqrt{1 - P^2})/2}$, $u = \sqrt{(1 - \sqrt{1 - P^2})/2}$ and G_ϕ is the spin-mixing term originating from the reflected electrons [19]. To find the distribution function in the detector, we insert $h_j = h_0 + \mathbf{h} \cdot \boldsymbol{\sigma}$ and $h_i = h_0^{\text{det}} + \mathbf{h}^{\text{det}} \cdot \boldsymbol{\sigma}$, where the former is the distribution function in the nanowire and the latter is the distribution function in the detector. From this, we get

$$N_0^{\text{det}} D^{\text{det}} \mathbf{e}_n \cdot \tilde{\nabla} \circ h_0^{\text{det}} = \zeta (h_0 - h_0^{\text{det}}) + P\zeta (h_z - h_z^{\text{det}}), \quad (36a)$$

$$N_0^{\text{det}} D^{\text{det}} \mathbf{e}_n \cdot \tilde{\nabla} \circ h_z^{\text{det}} = \zeta (h_z - h_z^{\text{det}}) + P\zeta (h_0 - h_0^{\text{det}}), \quad (36b)$$

$$N_0^{\text{det}} D^{\text{det}} \mathbf{e}_n \cdot \tilde{\nabla} \circ h_x^{\text{det}} = \zeta (\sqrt{1 - P^2} h_x - h_x^{\text{det}}) - iP\zeta h_y^{\text{det}} + G_\phi h_y^{\text{det}}, \quad (36c)$$

$$N_0^{\text{det}} D^{\text{det}} \mathbf{e}_n \cdot \tilde{\nabla} \circ h_y^{\text{det}} = \zeta (\sqrt{1 - P^2} h_y - h_y^{\text{det}}) + iP\zeta h_x^{\text{det}} - G_\phi h_x^{\text{det}}. \quad (36d)$$

We can see that the boundary conditions couple h_0^{det} with h_z^{det} and h_x^{det} with h_y^{det} . We can rewrite the boundary condition in terms of current densities, voltages and spin-voltages by multiplying with $\pi/|e|$, where e is the electron charge, Fourier transforming and letting $t \rightarrow 0$, giving

$$-\mathbf{e}_n \cdot \mathbf{J}_e = \frac{\zeta}{N_0^{\text{det}}} (P [\mu_z - \mu_z^{\text{det}}] - V^{\text{det}}), \quad (37a)$$

$$-\mathbf{e}_n \cdot \mathbf{J}_z = \frac{\zeta}{N_0^{\text{det}}} (\mu_z - \mu_z^{\text{det}} - PV^{\text{det}}), \quad (37b)$$

where $J_e = -\lim_{t \rightarrow 0} (\pi D^{\text{det}} / |e|) \tilde{\nabla} \circ H_0^{\text{det}}$ and $J_z = -\lim_{t \rightarrow 0} (\pi D^{\text{det}} / |e|) \tilde{\nabla} \circ H_z^{\text{det}}$ is the normalized charge current density and spin current density in the z -direction, respectively. The electrochemical potential is

$$V^{\text{det}} = \frac{1}{2|e|} \int_{-\infty}^{\infty} d\varepsilon [h_0^{\text{det}} - \tanh(\beta\varepsilon/2)]. \quad (38)$$

We have set the electrochemical potential on the nanowire side to be 0.

To solve for μ_z^{det} and V^{det} we must solve Usadel equation. For concreteness we assume that the electrode is a normal metal, but the relevant equations will be the same if it was instead a ferromagnet that is weakly polarized in the z -direction. For the case of a normal metal, the Usadel equation is

$$\frac{\partial h^{\text{det}}}{\partial T} - D^{\text{det}} \tilde{\nabla} \circ \tilde{\nabla} \circ h^{\text{det}} + 2\delta(h^{\text{det}} - h_{\text{eq}}) + \frac{i}{2} [\check{\sigma}_{\text{sd}}, \check{g}_s^{\text{det}}]_{\circ}^K = 0, \quad (39)$$

where $\check{\sigma}_{\text{sp}}$ is a source of spin-diffusion. This could for instance come from scattering with magnetic impurities, in which case $\check{\sigma}_{\text{sd}} = -i\mathbf{n} \cdot \boldsymbol{\sigma} \check{g}_s^{\text{det}} \mathbf{n} \cdot \boldsymbol{\sigma} / 2\tau_{\text{sd}}$, where τ_{sd} is the scattering time and \mathbf{n} is the magnetization direction of the magnetic impurities [20]. Spin-diffusion could also come from spin-orbit coupling, as is the case in the nanowire. Here we assume that spin-diffusion come from magnetic impurities rather than SOC. Since the spin-accumulation in the z -direction is static in the nanowire and since there is no coupling between μ_z^{det} and μ_x^{det} or μ_y^{det} , we can look for static solutions to μ_z^{det} and V^{det} . From Eq. (39) we find that these solve

$$-D^{\text{det}} \nabla^2 V^{\text{det}} = 0 = \nabla \cdot \mathbf{J}_e, \quad (40a)$$

$$-D^{\text{det}} \nabla^2 \mu_z^{\text{det}} + 2 \left(\delta + \frac{1}{\tau_{\text{sd},x}} + \frac{1}{\tau_{\text{sd},y}} \right) \mu_z^{\text{det}} = 0, \quad (40b)$$

where $\tau_{sd,x}$ and $\tau_{sd,y}$ is the spin-diffusion times for magnetic impurities with magnetization in the x - and y -direction, respectively. Equation (40a) states that charge is conserved inside the detector, so the electrical current is constant. Since the detector is assumed to be an open circuit, $\mathbf{e}_n \cdot \mathbf{J}_e = 0$ on the far side of the detector, so from Eq. (37a) we get that

$$V^{\text{det}} = P [\mu_z - \mu_z^{\text{det}}]. \quad (41)$$

From Eq. (40b) we see that the spin-accumulation decay exponentially inside the detector over a length scale given by the spin-diffusion time. If we assume that the detector is thin we can approximate it as one-dimensional. Let the length of the detector be L^{det} and the axial coordinate be s , then

$$\mu_z^{\text{det}} = C \cosh(k_z [L^{\text{det}} - s]), \quad (42)$$

where $s = 0$ is at the interface with the nanowire, C is a constant and

$$k_z = \sqrt{2 \left(\delta + \frac{1}{\tau_{sd,x}} + \frac{1}{\tau_{sd,y}} \right) / D^{\text{det}}} \quad (43)$$

is the inverse spin-diffusion length. The coefficient C can be found from Eq. (37b). From this we find that the spin-voltage in the detector at the interface is

$$\mu_z^{\text{det}} = \frac{\zeta(1 - P^2)\mu_z}{N_0^{\text{det}} D^{\text{det}} k_z \tanh(k_z L^{\text{det}}) + \zeta(1 - P^2)}. \quad (44)$$

We see that $|\mu_z^{\text{det}}| \ll |\mu_z|$ if the spin-diffusion length, $1/k_z$, or interface conductance, ζ , is sufficiently small or the polarization, P , is sufficiently close to 1. In particular, $|\mu_z^{\text{det}}| \ll |\mu_z|$ if

$$\frac{1}{k_z} \ll \frac{N_0^{\text{det}} D^{\text{det}} \tanh(k_z L^{\text{det}})}{\zeta(1 - P^2)}. \quad (45)$$

In this case Eq. (41) reduces to

$$V^{\text{det}} = P\mu_z, \quad (46)$$

which is the same as Eq. (33). Since there is no current inside the detector, the electrochemical potential is constant and the voltage difference measured between the detector and nanowire will be $V = V^{\text{det}}$.

Finally, note that there is a finite spin-current into the detector if the polarization is different from 1. That is, the detector acts as a spin-sink. This can affect the magnetization in the nanowire where the spin-voltage is supposed to be measured. However, this effect can be neglected if the interface conductivity and contact area are small.

-
- [1] A. Manchon, H. C. Koo, J. Nitta, S. M. Frolov, and R. A. Duine, *Nat. Mater.* **14**, 871 (2015).
[2] G. Eilenberger, *Z. Physik* **214**, 195 (1968).
[3] W. Belzig, F. K. Wilhelm, C. Bruder, G. Schön, and A. D. Zaikin, *Superlattices Microstruct.* **25**, 1251 (1999).
[4] P. Virtanen, T. T. Heikkilä, F. S. Bergeret, and J. C. Cuevas, *Phys. Rev. Lett.* **104**, 247003 (2010).
[5] K. D. Usadel, *Phys. Rev. Lett.* **25**, 507 (1970).
[6] J. Rammer and H. Smith, *Rev. Mod. Phys.* **58**, 323 (1986).
[7] M. Houzet, *Phys. Rev. Lett.* **101**, 057009 (2008).
[8] E. H. Fyhn and J. Linder, *Phys. Rev. B* **103**, L100502 (2021).
[9] V. Chandrasekhar, in *Superconductivity: Conventional and Unconventional Superconductors* (Springer, Berlin, Heidelberg, 2008) pp. 279–313.
[10] J. A. Ouassou, T. D. Vethaak, and J. Linder, *Phys. Rev. B* **98**, 144509 (2018).
[11] M. Y. Kupriyanov and V. F. Lukichev, *Zh. Eksp. Teor. Fiz* **94** (1988).
[12] R. H. Silsbee, *Bull. Magn. Reson.* **2**, 284 (1980).
[13] M. Johnson and R. H. Silsbee, *Phys. Rev. Lett.* **55**, 1790 (1985).
[14] N. Tombros, C. Jozsa, M. Popinciuc, H. T. Jonkman, and B. J. van Wees, *Nature* **448**, 571 (2007).
[15] N. Poli, J. P. Morten, M. Urech, A. Brataas, D. B. Haviland, and V. Korenivski, *Phys. Rev. Lett.* **100**, 136601 (2008).
[16] M. Silaev, P. Virtanen, T. T. Heikkilä, and F. S. Bergeret, *Phys. Rev. B* **91**, 024506 (2015).
[17] T. T. Heikkilä, M. Silaev, P. Virtanen, and F. S. Bergeret, *Prog. Surf. Sci.* **94**, 100540 (2019).
[18] F. S. Bergeret, A. Verso, and A. F. Volkov, *Phys. Rev. B* **86**, 214516 (2012).
[19] J. A. Ouassou, A. Pal, M. Blamire, M. Eschrig, and J. Linder, *Sci. Rep.* **7**, 1932 (2017).
[20] H. G. Hugdal, J. Linder, and S. H. Jacobsen, *Phys. Rev. B* **95**, 235403 (2017).

PAPER VIII

Reference

Werner M. J. van Weerdenburg, Anand Kamlapure, Eirik Holm Fyhn, Xiaochun Huang, Niels P. E. van Mullekom, Manuel Steinbrecher, Peter Krogstrup, Jacob Linder, and Alexander Ako Khajetoorians,

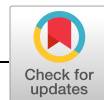
Extreme enhancement of superconductivity in epitaxial aluminum near the monolayer limit.

Science Advances 9, eadf5500 (2023)

DOI: 10.1126/sciadv.adf5500

CONTRIBUTIONS

WMJvW, AK, XH, MS, and NPEvM acquired the experimental data. The experimental analysis was designed by WMJvW, AK, and AAK, with WMJvW, AK, XH, and NPEvM implementing the experimental analysis. EHF performed the calculations based on the Usadel approach, with support from JL. AAK and PK designed the initial experimental concept, while WMJvW, AK, MS, PK and AAK together iterated changes to the experiments during implementation and subsequent analysis. All authors participated in the scientific discussion of the results, as well as participated in writing the manuscript. Specifically, in addition to participating in the discussion of the physics and the revision of the final manuscript, EHF developed the theoretical vortex model and developed and executed the code for solving the derived equations numerically. EHF also wrote the first draft of the part of the supplementary which explains the theoretical model for vortex simulations.



CONDENSED MATTER PHYSICS

Extreme enhancement of superconductivity in epitaxial aluminum near the monolayer limit

Werner M. J. van Weerdenburg^{1†}, Anand Kamlapure^{1†}, Eirik Holm Fyhn², Xiaochun Huang¹, Niels P. E. van Mullekom¹, Manuel Steinbrecher¹, Peter Krogstrup³, Jacob Linder², Alexander Ako Khajetoorians^{1*}

BCS theory has been widely successful at describing elemental bulk superconductors. Yet, as the length scales of such superconductors approach the atomic limit, dimensionality as well as the environment of the superconductor can lead to drastically different and unpredictable superconducting behavior. Here, we report a threefold enhancement of the superconducting critical temperature and gap size in ultrathin epitaxial Al films on Si(111), when approaching the 2D limit, based on high-resolution scanning tunneling microscopy/spectroscopy (STM/STS) measurements. Using spatially resolved spectroscopy, we characterize the vortex structure in the presence of a strong Zeeman field and find evidence of a paramagnetic Meissner effect originating from odd-frequency pairing contributions. These results illustrate two notable influences of reduced dimensionality on a BCS superconductor and present a platform to study BCS superconductivity in large magnetic fields.

INTRODUCTION

Bardeen-Cooper-Schrieffer (BCS) theory has been vastly successful at explaining the behavior of conventional superconductors (1). Yet, superconductors, both conventional and unconventional, can exhibit complex and unexpected behavior when one or more length scales approach a lower dimensional limit (2). While the superconducting critical temperature (T_c) of some materials reduces in the monolayer limit, compared to the bulk (3–5), it has also been shown that T_c can be greatly enhanced in this regime, as illustrated by FeSe/SrTiO₃ (6). Likewise, superconductivity can emerge at the interface of two insulating materials, as exemplified by the interface of LaAlO₃/SrTiO₃ (7). As many types of quantum technologies depend on the growth of superconductors integrated into heterostructures, including superconducting spintronic devices (8), high-precision magnetometers (9), and qubits based on superconducting nanostructures (10), it is imperative to understand what the role of dimensionality and the influence of the environment is on the superconductivity.

Elemental aluminum (Al) is exemplary of a type I BCS superconductor in the weak-coupling regime (1) and exhibits unexpected modifications to its superconducting behavior when scaled to the two-dimensional (2D) limit. It has been shown that the critical temperature of Al can be increased from its bulk value of $T_c = 1.2$ K by growing thin films, both epitaxial and granular. However, widely varying growth procedures resulting in oxidized films (11–18), granular Al (19–21), Al nanowires (22, 23), or doped Al films (24, 25) give dispersing values for T_c clouding ultimately what contributes to the aforementioned enhancement. In some of these studies, the cleanliness of the interface and the Al itself, as well as the relevant thickness, is ill-defined. Moreover, these studies are often

limited to a regime where the thickness is greater than six monolayers (MLs), mainly due to the challenges to synthesize monolayer scale epitaxial Al films. The dispersive findings question to what extent the enhancement of superconductivity is intrinsic to Al itself and to what extent the trend of increasing T_c persists as films are thinned down further. To this end, experimental approaches that combine high-purity growth methods in a controlled ultrahigh vacuum (UHV) environment with a concurrent *in situ* characterization are vital to identify the intrinsic superconducting behavior of Al films near the 2D limit. In addition to the observed enhancement of T_c , the upper critical field in the direction parallel to the film surface has been shown to increase substantially (16). Because of the low spin-orbit scattering rate in Al, these films characteristically show the Meservey-Tedrow-Fulde (MTF) effect, where the application of a magnetic field gives rise to a spin splitting of the quasiparticle excitations (26, 27). In addition, it has been proposed that this high-field regime can promote odd-frequency spin-triplet correlations (28–32), but it has been challenging to confirm their presence experimentally (28, 33, 34). The combination of thin film Al and large magnetic fields, as used in superconducting qubit devices, especially those aiming to induce topological superconductivity (10, 35, 36), puts forward questions about how superconductivity is affected by external magnetic fields and the role of unconventional pairing.

Here, we show that Al(111) films epitaxially grown on Si(111)–(7 × 7), approaching the monolayer limit, exhibit a greatly enhanced T_c up to about a factor of three, when compared to the bulk value. Using scanning tunneling microscopy/spectroscopy (STM/STS) at variable temperatures down to millikelvin, we first characterize the structural and large-scale electronic properties of epitaxial films of Al grown on Si(111) for various thicknesses (N). We subsequently characterize the associated superconducting gap (Δ) with each grown film. For the largest gap values, we corroborate these measurements with T_c by measuring $\Delta(T)$. Next, we probe the magnetic field-dependent properties of individual Al films for different thicknesses in magnetic fields with different field orientations. We confirm the expected type II behavior in out-of-plane magnetic

¹Institute for Molecules and Materials, Radboud University, 6525 AJ Nijmegen, Netherlands. ²Center for Quantum Spintronics, Department of Physics, Norwegian University of Science and Technology, NO-7491 Trondheim, Norway. ³NNF Quantum Computing Programme, Niels Bohr Institute, University of Copenhagen, 2100 Copenhagen, Denmark.

[†]These authors contributed equally to this work.

*Corresponding author. Email: a.khajetoorians@science.ru.nl

Copyright © 2023
The Authors, some
rights reserved;
exclusive licensee
American Association
for the Advancement
of Science. No claim to
original U.S. Government
Works. Distributed
under a Creative
Commons Attribution
License 4.0 (CC BY).

fields, including the observation of an Abrikosov lattice. For in-plane magnetic fields, we observe the MTF effect and use the spectral evolution in magnetic field to quantify the g -factor of the various films, which are all shown to exhibit $g \approx 2$. We finally characterize the vortex structure in the presence of the MTF effect, which shows a reshaping of the vortex structure when compared to zero in-plane field. Based on numerical simulations using the Usadel equation, we quantify the observed structure and relate it to the presence of both even and odd-frequency pairing correlations as well as their contribution to the screening currents.

RESULTS

Structural and spectroscopic properties of epitaxial Al films

Epitaxially grown Al films (see Materials and Methods) imaged with STM typically show a closed film of a given thickness, decorated with a density of islands a monolayer higher (Fig. 1A and fig. S2). Films with a given thickness exhibit two different periodicities (Fig. 1, B and C). A short-range threefold periodicity with $a \approx 0.25$ nm coincides with the expected atomic lattice constant of Al(111). In addition to the atomic periodicity, a long-range periodicity can be observed in films for thicknesses up to 26 MLs, which is also threefold symmetric and exhibits a periodicity $a_M \approx 2.6$ nm. This periodicity is commensurate with the underlying 7×7 reconstruction of Si(111) (37, 38), and it is reminiscent of the moiré-type structures seen for other thin superconducting films (39, 40). The appearance of both the moiré-type structure and the atomic periodicity is indicative that the interface is most likely pristine with negligible intermixing at the growth temperatures used. Epitaxial film growth is observed for Al films ≥ 4 MLs, as identified in (38). In attempts to measure even thinner Al films, our growth procedure resulted in broken and granular films.

The thickness of a given film can be corroborated with STS measured in a voltage range of ± 2 V. For a given N , layer-dependent broad peaks can be identified at given voltages, which vary depending on the given value of N (Fig. 1D). To better illustrate the measured peaks for both filled and empty states, dI/dV spectroscopy was

normalized to I/V . Moreover, different films with the same value of N reproducibly show the same spectroscopic features, enabling spectroscopic fingerprinting of the layer thickness, although the films are closed (see section S1 and fig. S3). The appearance of such peaks in STS is reminiscent of quantum well states (QWS) typically observed on other thin metallic films grown on Si(111) (41). For reference, the QWS energies extracted from (42, 43) are indicated in Fig. 1D by blue arrows underneath each measured spectrum. In this comparison, the QWS energies do not exactly match the measured peak positions, but there is a qualitative agreement between the energy difference between adjacent QWS, and the measured spectra, up to approximately 13 MLs. As seen from previous angle-resolved photoemission spectroscopy (ARPES) measurements (44) and the aforementioned calculations, the expected QWS have a smaller effective mass and are expected to disperse, when compared to the QWS of Pb/Si(111) (41). This inherently weakens the QWS intensity and makes a direct mapping of the exact QWS onset energies based solely on point-STs measurements imprecise. We note that a direct comparison to measured ARPES (44) is challenging, as we observe stronger features in the empty state region of the spectra, where there are no ARPES measurements. Likewise, ARPES spatially averages over regions of the film where we expect spectroscopic contributions from multiple thicknesses of the film.

Superconducting gap and critical temperature as a function of film coverage

We measured Δ as a function of coverage using high-energy resolution STS at variable temperature. Here, the coverage of a given film is defined as the cumulative Al material of its main layer and (vacancy) islands. Below, we first detail the spectral gap as measured at the lowest temperature, namely, $T = 30$ mK, for three coverages in Fig. 2A. A typical spectrum shows a BCS-like, hard gap structure symmetric around $V_s = 0$ mV and sharp coherence peaks at the gap energy Δ , which can be fitted and extracted with a broadened Maki function (see section S2 and fig. S5 for a discussion on the possible broadening contributions) (45). We find that the gap

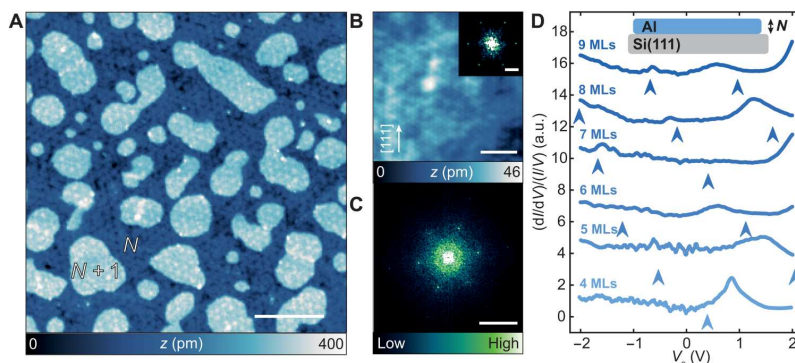


Fig. 1. Structural and spectroscopic properties of ultrathin epitaxial Al films. (A) Constant-current STM image of an Al/Si(111) sample with 8.5-ML coverage ($V_s = 100$ mV, $I_t = 20$ pA; scale bar, 20 nm). (B) Constant-current STM image with atomic resolution (coverage: 35.1 MLs, $V_s = 3$ mV, $I_t = 500$ pA; scale bar, 2 nm). Inset: fast Fourier transform (FFT) of the image in (B) (scale bar, 2 nm^{-1}). (C) FFT of the image in (A) (scale bar, 0.5 nm^{-1}). (D) Spectroscopy taken on 4- to 9-ML layers (stabilized at $V_s = 2$ V, $I_t = 200$ pA, $V_{\text{mod}} = 5$ mV, $T = 1.3$ K). The dI/dV signal (in arbitrary units; a.u.) is normalized by I/V to correct for the transmission factor of the tunneling barrier. Arrows indicate the calculated QWS energies from density functional theory in (42) (see section S1 and fig. S3). Inset sketch shows an Al film on Si(111) with a thickness of N MLs.

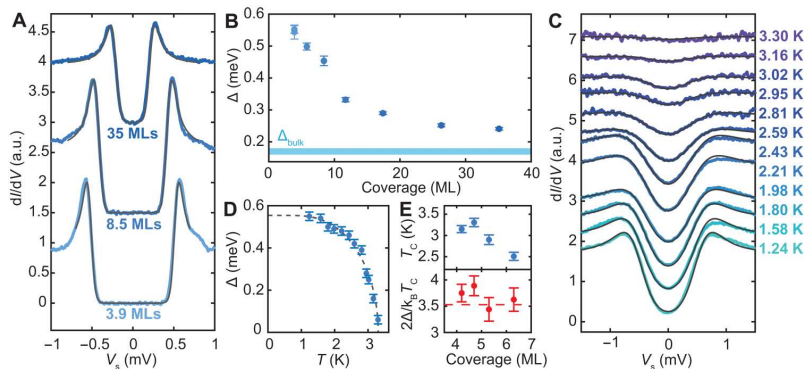


Fig. 2. Δ and T_c enhancement for ultrathin Al films. (A) Superconducting gap spectra taken at $T = 30$ mK for samples with varying Al coverage (artificially offset) with Maki fits (gray lines) (stabilized at $V_s = 3$ mV, $I_t = 200$ pA, $V_{mod} = 20$ μ V). (B) Extracted Δ at $T = 30$ mK for varying Al coverage, where the error bar represents the SD of Δ in an ensemble of 18 to 30 spectra. (C) Temperature-dependent superconducting gap spectra (artificially offset) for 4.5-ML coverage, manually matched with the Dynes equation (gray lines) (stabilized at $V_s = 5$ mV, $I_t = 300$ pA, $V_{mod} = 100$ μ V). (D) Extracted Δ as a function of temperature with the BCS fit with $T_c = 3.3 \pm 0.1$ K and $\Delta^{T=0} = 0.55 \pm 0.02$ meV. (E) Extracted T_c values and $2\Delta/k_B T_c$ ratios for four Al coverages (see fig. S7; error bars represent SD from the BCS fit). We note that the films in (C) to (E) were not measured at $T = 30$ mK and are therefore excluded from (B).

value shows the largest enhancement of $\Delta = 0.560 \pm 0.015$ meV for a coverage of 3.9 MLs (4 MLs with a distribution of vacancy islands), which is more than a threefold enhancement compared to the bulk value of $\Delta_{bulk} = 0.16$ to 0.18 meV (46, 47). We find that the spectra taken at various locations on the sample, including on (vacancy) islands and along the long-range periodicity, reveal a uniform superconducting gap with a constant Δ (± 0.02 meV) and small variations in coherence peak height (see fig. S4). Therefore, we assign Δ for each sample as the spatial average of all gap values extracted from ≥ 18 spectra, where the error bar represents the standard deviation of those values. The uniformity in the value of Δ is in contrast to the variations in the band structure on larger energy scales, where we see clear differences in STS for different layer heights. This observation suggests that the value of Δ is not significantly modulated due to the presence of different QWS stemming from variations in the film thickness, in contrast to reports on Pb/Si(111) (39, 48) and in line with observations for Pb/BP (49).

Measurements on films with different coverage yield a monotonously increasing trend in Δ as the film coverage is lowered, as shown in Fig. 2B for samples between 4 and 35 MLs. Here, each data point represents one grown sample. For the largest coverages we measured, namely, 35 MLs, we still observed a slight enhancement in Δ compared to the bulk value (blue bar), as was also seen in (18). The monotonous trend contrasts the observations for Pb/Si(111), where the critical temperature oscillates due to a modulation of the local density of states (LDOS) at E_F . Here, we see no clear correlation between the QWS energies and the corresponding gap size.

To quantify T_c in relation to the measured values of Δ at millikelvin temperature, we performed temperature-dependent measurements of $\Delta(T)$ for four different film coverages (see Materials and Methods for details and section S3 and fig. S6 for the temperature calibration). $\Delta(T)$ was measured for a given sample by incrementally raising the sample temperature between 1.3 and 4.0 K. With increasing T , $\Delta(T)$ shows the expected decrease until the gap is eventually fully quenched, coinciding with T_c (Fig. 2C). To

quantify the value to T_c , we first fitted each measured spectra with a BCS Dynes function (see section S2) (50). We subsequently fitted the numerically determined temperature dependence of the gap within BCS theory to the extracted $\Delta(T)$, as exemplified for an Al film with a 4.7-ML coverage in Fig. 2D, and find $T_c = 3.31 \pm 0.11$ K. In Fig. 2E, we illustrate the extracted T_c for four different films (see fig. S7). Based on BCS theory, the ratio between T_c and $\Delta(T=0)$ leads to an expected ratio of $2\Delta(T=0)/k_B T_c = 3.53$, which typically describes superconductors in the weak-coupling limit, such as bulk Al (46, 47). Based on the extracted values, we plot the ratio between Δ and T_c in Fig. 2E. The overall trend indicates that the ratio is in close agreement to the expected value 3.53 as seen for the bulk Al, suggesting that the thin Al films studied here may be in the weak-coupling limit. We note that the T_c was only measured for four films, and not for a given film multiple times. Therefore, the error bars coincide with the standard deviation given by the fits shown in Fig. 2D and fig. S7. To infer a coverage-dependent trend in the extracted ratio, further measurements are needed. Moreover, the effect of the sample morphology and defects on the gap value and the ratio requires further study.

The threefold enhancement of Δ and T_c is distinctly larger than reported epitaxial Al films in the literature, where capped films were studied ex situ only down to 6 MLs (18). Likewise, it exceeds most reported values for T_c of other studies on oxidized (single) Al films (12–18, 20, 21), likely due to the thinner films, the crystallinity, and the absence of the oxide layer. This observation directly refutes an early idea that the origin of the enhancement effect was due to the oxygen layer (12). In other reports (24, 25), enhanced values of T_c for Al films were obtained by doping with $\sim 2\%$ of Si impurities. However, potential intermixing of Si and Al with this quantity of impurities would likely obscure the moiré pattern and atomic-resolution images presented in Fig. 1. In addition, we can also exclude a considerable influence of Si intermixing on the enhancement of superconductivity, since we do not observe a considerable change in gap enhancement for films when the annealing time (and thus potential intermixing) is minimized (see section S4 and fig. S8).

These observations indicate that the enhanced superconductivity is an intrinsic property of ultrathin Al films, but it remains an open question if other weak-coupling superconductors present similar enhancement effects and what the role of the substrate/interface is (4).

Abrikosov lattice and out-of-plane magnetic field response

Subsequently, we characterize the magnetic field-dependent response of various Al films in two magnetic field orientations, i.e., perpendicular/parallel to the surface. First, we quantify the upper critical field for an Al film with an 11.7-ML coverage in a magnetic field perpendicular to the film plane (B_{c2}^{\perp}). By incrementally increasing B^{\perp} and measuring local point spectra (Fig. 3A), the coherence peaks flatten and the zero-bias conductance increases gradually until the gap has completely vanished at $B^{\perp} = 100$ mT. This upper limit for B_{c2}^{\perp} gives an estimate for the coherence length ξ of ~ 64 nm, as $\xi = \sqrt{\Phi_0/2\pi B_{c2}^{\perp}(T=0)}$, where Φ_0 is the magnetic flux quantum (51). The expected type II behavior can be observed by spatially imaging the zero-bias conductance for nonzero values of B^{\perp} . We measured a constant-contour dI/dV conductance map at $V_s = 0$ mV ($B^{\perp} = 50$ mT), which reveals an Abrikosov lattice, with a vortex radius on the order of the coherence length (Fig. 3B and fig. S9).

MTF effect and the Clogston-Chandrasekhar limit

After characterizing the out-of-plane response, we characterized the response of various films to an in-plane magnetic field (B^{\parallel}) for various coverages. Since screening currents cannot build up in the confined superconductor, orbital depairing is absent, and the magnetic field penetrates the superconductor, allowing us to study the superconducting state in combination with large magnetic fields compared to the typical out-of-plane critical values. In the absence of spin-orbit scattering, the quasi-particle excitations of the superconductor are sufficiently long-lived to observe the MTF effect in this regime (26, 27). This effect is exemplified by a spin-splitting of the coherence peaks, where each peak shifts by \pm

$g\mu_B SB^{\parallel}$, giving a total Zeeman splitting of $|E_z| = g\mu_B B^{\parallel}$ for $S = 1/2$. For a homogeneous superconductor in the absence of spin-orbit coupling, the superconducting state may only persist up to the Clogston-Chandrasekhar limit (52, 53), given by $h = \Delta/\sqrt{2}$, with $h = \mu_B B^{\parallel}$, where a first-order phase transition to the normal state occurs.

In Fig. 3C, we illustrate the measured MTF effect for two Al films with a coverage of 3.9 and 8.5 MLs, where the STS was measured for increasing values of B^{\parallel} , up to $B^{\parallel} = 4$ T. The manifestation of the MTF effect is the appearance of a spin-split gap structure. We quantify the splitting in Fig. 3C by subdividing the gap structure into two independent spin-polarized distributions and fitting two Maki functions with equal gaps, shifted with respect to each other by the Zeeman energy ΔE_z . As illustrated in Fig. 3D, we measured $\Delta E_z(B^{\parallel})$ for four film coverages (also see fig. S10) and quantified the splitting of the coherence peaks at each field increment. The resulting linear trend is used to extract the g -factors (see inset of Fig. 3D) with an average of $g = 1.98 \pm 0.02$ (where $g = \Delta E_z/\mu_B B^{\parallel}$ for $S = 1/2$). This measurement shows that the quasiparticles in the ultrathin regime remain free-electron like, and the linearity of the graph further illustrates that spin-orbit coupling is negligible in these films. In addition, we note that the expected Clogston-Chandrasekhar limit for the 8.5-ML film is at $B_{CC}^{\parallel} = \Delta/\sqrt{2}\mu_B \sim 5.5$ T, i.e., above our experimental limit of $B^{\parallel} = 4.0$ T. However, for films with a smaller gap size (with coverages of 11.7 and 17.4 MLs), we could observe a sudden quenching of superconductivity at in-plane fields near the theoretical limit.

Vortex structure in the presence of the MTF effect

The manifestation of the MTF effect in ultrathin Al films provides an opportunity to explore the atomic-scale variations in the conductance in response to variable magnetic field, for example, the resultant vortex behavior in the presence of the MTF effect. Moreover, the presence of large in-plane magnetic fields can induce pairing contributions in the form of odd-frequency spin-triplet correlations, which may act differently around a vortex and exhibit a paramagnetic Meissner response (33, 54, 55). Using a vector magnetic

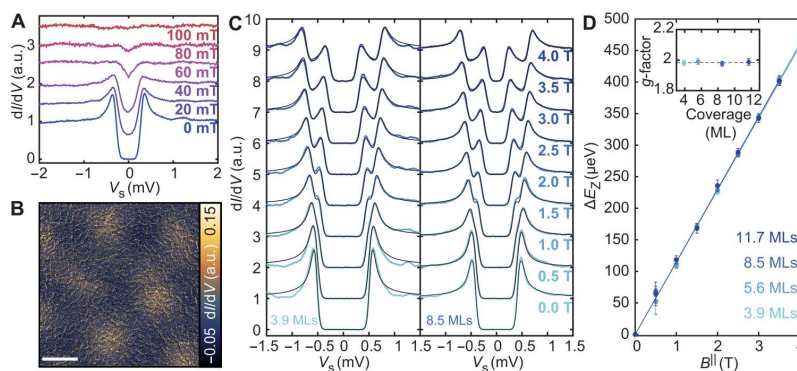


Fig. 3. Magnetic field response of Al films. (A) Evolution of the superconducting gap in out-of-plane magnetic field B^{\perp} for a 11.7-ML film, measured in between vortices in (B). (B) Constant-contour dI/dV map with $B^{\perp} = 50$ mT (height profile recorded at $V_s = 10$ mV, $I_t = 10$ pA; image taken with $V_s = 0$ mV, $V_{\text{mod}} = 20$ μ V; scale bar, 100 nm). (C) Evolution of the superconducting gap as a function of in-plane magnetic field B^{\parallel} for a 3.9- and 8.5-ML film. Black lines are fits using two Maki functions separated by Zeeman splitting ΔE_z (stabilized at $V_s = 3$ mV, $I_t = 200$ pA, $V_{\text{mod}} = 20$ μ V). (D) Extracted ΔE_z for four Al coverages (see fig. S10). The solid lines are weighted linear fits to extract the g -factor for each sample (inset).

field, we induced vortices in a given Al film with $B^\perp = 30$ mT and simultaneously applied $B^\parallel = 2.99$ T to enter the MTF regime. We subsequently spatially mapped the zero-bias conductance in constant-contour mode, as illustrated for an 8.5-ML Al film (Fig. 4A). The resulting image shows multiple round vortices with an expected flux density (see also section S5). Note that the vortices may occasionally move, likely due to interactions with the tip (also see figs. S9 and S11). This can yield vortices that appear noisy as well as obscure the symmetry of underlying vortex lattice. To further characterize the structure, we also performed STS along a horizontal and vertical line across a given vortex (Fig. 4, C and D). Both directions show a split gap structure with $\Delta = 0.45$ meV at ~ 150 nm from the vortex center and a gradual decrease of Δ toward the center with a constant Zeeman splitting. Closer to the vortex center, the spectral gap is rapidly quenched, resulting in an extended region of ~ 70 nm in diameter without any spectroscopic indications of superconductivity. In this regime, the apparent region with conductance associated with the normal state is radially larger than what is expected for a typical vortex in the absence of an in-plane magnetic field component (e.g., fig. S9). Besides this extended region where the quasiparticle gap is zero, the total radius of a vortex in the MTF regime is also larger compared to the typical vortex shape in the absence of an in-plane magnetic field, as illustrated by comparing the zero-bias conductance profiles in Fig. 4B (also see fig. S9).

To explain the observation of the vortex structure in the presence of the MTF effect, or the MTF vortex for short, we modeled the superconducting vortex structure using the quasiclassical Keldysh Green's function formalism (56, 57), assuming a single-phase winding in the superconducting gap parameter. We assume that the coherence length of the superconductor is large compared to the mean free path, dictated by the sample morphology (sample thickness, island size, and moiré periodicity), such that the

quasiclassical Green's function solves the Usadel equation (58). Therefore, we consider the diffusive limit, where only s -wave correlations can persist. This is in contrast to considerations in the ballistic limit (31). We fix Δ^∞ , the gap size at infinite distance from the vortex, and the spin-splitting field $h^\parallel = \mu_B B^\parallel$ to the experimental values ($h^\parallel/\Delta^\infty = 0.38$) and solve the Usadel equation self-consistently with both the superconducting gap equation and Maxwell's equations (see section S5 for more details). In Fig. 4E, we illustrate the calculated density of states and account for Dynes broadening as well as experimental broadening by convoluting with the Fermi-Dirac distribution with $T_{\text{eff}} = 250$ mK. The simulated distance-dependent spectra show an excellent agreement with the experimental data, reproducing the zero-bias conductance profiles (Fig. 4B), the evolution of the spin-split gap structure, and the extended region with a quenched quasiparticle gap (see fig. S9 for the calculated profile for $h^\parallel/\Delta^\infty = 0$). In addition, we can extract the coherence length of $\xi = 42$ nm.

The theoretical model provides a detailed understanding of the MTF vortex structure in a varying in-plane magnetic field. First, the solution to the gap equation consists of both even-frequency (ω_e) spin-singlet $\frac{1}{\sqrt{2}}(|\uparrow\downarrow\rangle - |\downarrow\uparrow\rangle)$ and odd-frequency (ω_o) spin-triplet $\frac{1}{\sqrt{2}}(|\uparrow\uparrow\rangle + |\downarrow\downarrow\rangle)$ pairing contributions. Therefore, there is always a coexistence of both types of pairing contributions in the presence of an in-plane magnetic field. To understand the vortex structure, it is important to identify the role of both types of pairing contributions. In Fig. 5 (A and B), we plot the contributions of ω_e and ω_o pairing correlations, Δ_{even} and Ψ_{odd} , respectively, as a function of distance across the MTF vortex structure, where $r = 0$ refers to the vortex center. Toward the vortex core, both order parameters decrease monotonically and gradually as the distance to the core is reduced. By evaluating the gap equation for increasing values of h^\parallel , we find an increasing contribution of ω_o pairs, as well as a

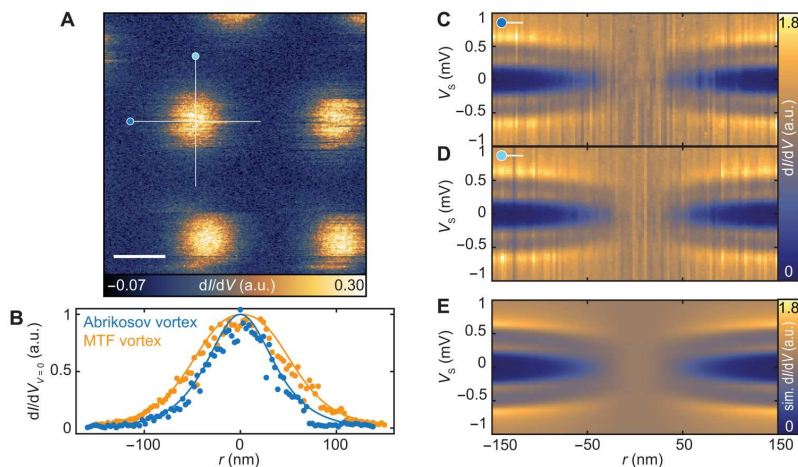


Fig. 4. MTF vortex in vector magnetic field. (A) Constant-contour dI/dV map in vector magnetic field with $B^\parallel = 2.99$ T and $B^\perp = 30$ mT for an 8.5-ML film (height recorded at $V_s = 10$ mV, $I_s = 10$ pA; image taken with $V_s = 0$ mV and z offset = 100 pm, $V_{\text{mod}} = 50$ μ V; scale bar, 100 nm). (B) Vortex profile at $V_s = 0$ mV, extracted from the line spectra across the Abrikosov vortex (blue; see fig. S9, B and C) and the MTF vortex (orange; C and E). Both the experimental (scatter points) and theoretical (lines) zero-bias conductance profiles are presented. (C and D) dI/dV spectra along a horizontal and vertical line across a vortex core (stabilized at $V_s = 3$ mV, $I_t = 200$ pA, $V_{\text{mod}} = 20$ μ V). (E) Simulated dI/dV signal by solving the self-consistent gap equation (see section S5) using $h^\parallel/\Delta^\infty = 0.38$, $\xi = 42$ nm, $\Gamma = 0.007 \Delta^\infty$, $\kappa = 5$ and broadened with $T_{\text{eff}} = 250$ mK.

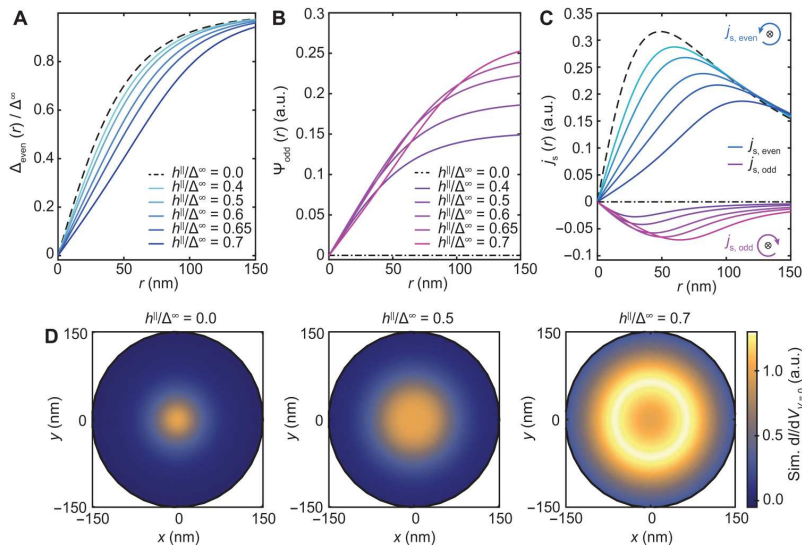


Fig. 5. Evolution of the MTF vortex structure with in-plane magnetic fields. Calculated gap function across a vortex for (A) ω_e spin-singlet pairs, (B) ω_o spin-triplet pairs, and (C) the calculated electric supercurrent density for various in-plane magnetic fields [color used consistently in (A) to (C)]. The supercurrent flow around the magnetic flux line (\otimes) is indicated schematically. (D) Simulated zero-bias conductance represented spatially for three $h^{\parallel}/\Delta^\infty$ ratios ($\xi = 42$ nm, $\Gamma = 0.001 \Delta^\infty$, $\kappa = 5$, as defined in section S5).

more extended and gradual vortex profile. The combination of the shallow vortex shape and the presence of ω_o correlations near the vortex core, which are more susceptible to single-particle excitations (54), explains the extended quenched gap region, despite a finite order parameter being present in this region. We also note that close to the vortex center, Δ_{even} is reduced beyond the Clogston-Chandrasekhar limit, which is only allowed for a local region in the superconductor.

Mesoscopically, the presence of vortices is driven by a circulating supercurrent that screens the penetrating magnetic flux. Therefore, we additionally calculated the ω_e and ω_o contributions to the supercurrent density and plot this as a function of distance in Fig. 5C for various values of $h^{\parallel}/\Delta^\infty$. In the absence of h^{\parallel} , we find the characteristic diamagnetic response of the screening current (59) (black dashed lines), consisting of purely ω_e pairs. At finite values for $h^{\parallel}/\Delta^\infty$, we find two contributions to the screening current with opposite signs, originating from the ω_e and ω_o pairing correlations. This demonstrates a paramagnetic Meissner contribution from the ω_o pair correlations. With increasing $h^{\parallel}/\Delta^\infty$, both screening current contributions extend further outward, and the paramagnetic component increases in amplitude, but the total screening current (i.e., the sum of both contributions) remains diamagnetic. In this way, the paramagnetic contribution to the supercurrent, originating from the odd-frequency correlations induced in the MTF regime, gives rise to an enhanced magnetic penetration depth and contributes to the enhanced vortex size.

In addition to the aforementioned details, we calculated how the measurable vortex structure evolves as a function of h^{\parallel} . Figure 5D provides a visual representation of the simulated spatial dI/dV signal at $V_s = 0$ mV, showing the evolution of the vortex structure. For $h^{\parallel}/\Delta^\infty = 0$, the vortex starts as the expected structure with a sharp rise

in conductance at the core (also see fig. S9). For a persistently rising field value, the high-conductance region broadens and flattens out near the core, as can be seen for $h^{\parallel}/\Delta^\infty = 0.5$, and finally develops a high-intensity ring around the vortex core at $h^{\parallel}/\Delta^\infty = 0.7$ due to the overlap of pronounced inner coherence peaks.

We propose that these MTF vortices can appear in any type II superconductor in the presence of a large magnetic field, given that spin-orbit scattering and orbital depairing are negligible. These reshaped vortices are likely to occur in experimental setups, even in the absence of an applied out-of-plane field, since a small misalignment between the sample plane and the in-plane magnetic field direction can induce an out-of-plane component (where $B_{c2}^{\parallel}/B_{c2}^{\perp} \ll 1$). In our case, we find a small tilt angle of 0.2° (see section S5 and fig. S11), estimated by the observed vortex density at $B^{\parallel} = 4.0$ T. Consequently, it is interesting to explore larger ratios of $h^{\parallel}/\Delta^\infty$, close to the Clogston-Chandrasekhar limit. In Fig. 6A, we show one instance of a vortex where $B^{\parallel} = 3.60$ T, while $B^{\perp} = 0.0$ T for an 11.7-ML Al film. Here, STS measurements along a horizontal line and the simulated dI/dV signal (Fig. 6, B and C) reveal the appearance of a zero-bias peak at finite distance from the vortex core, owing to the gradual merging of the two inner coherence peaks. We expect that for even larger $h^{\parallel}/\Delta^\infty$ ratios, this will give rise to a pronounced ring as seen in Fig. 5D. For these films, where $B_{c1}^{\perp}/B_{c2}^{\parallel}$ is very small, small angular offsets in the magnetic field can lead to vortex formation near the Clogston-Chandrasekhar limit. For experiments where large in-plane magnetic fields are needed to induce a topological superconducting phase, the appearance of the aforementioned in-gap states at zero energy may make it more complicated to assign a topological character in this field regime.

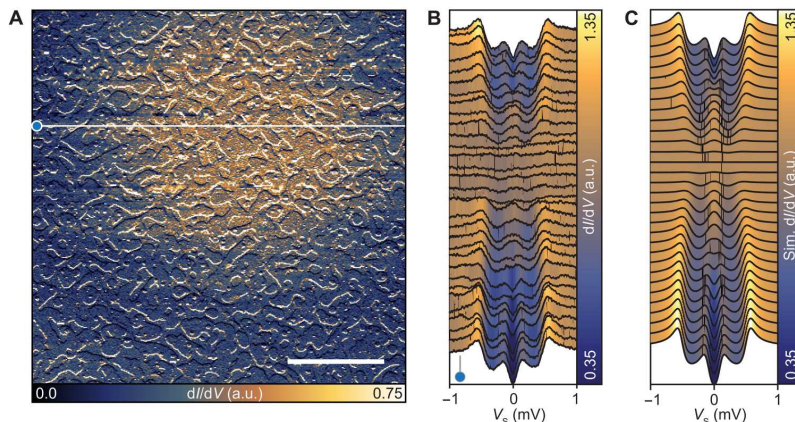


Fig. 6. Zero-bias peak in the MTF vortex profile for large $h^{\parallel}/\Delta^{\infty}$. (A) Constant-contour dI/dV map with $B^{\parallel} = 3.6$ T ($B^{\perp} = 0$ mT) for an 11.7-ML film (height recorded at $V_s = 10$ mV, $I_t = 10$ pA; image taken with $V_s = 0$ mV and z offset = 120 pm, $V_{\text{mod}} = 50$ μ V; scale bar, 100 nm). (B) Spectra measured along a line of 400 nm across a vortex structure [see white line in (A)]; stabilized at each point with $V_s = 3$ mV, $I_t = 200$ pA, $V_{\text{mod}} = 20$ μ V]. (C) Simulated dI/dV signal across a vortex core by solving the self-consistent gap equation using $h^{\parallel}/\Delta^{\infty} = 0.63$, $\Gamma = 0.1\Delta^{\infty}$, $\kappa = 5$, $\xi = 50$ nm and broadened with $T_{\text{eff}} = 250$ mK.

DISCUSSION

In conclusion, we have demonstrated that the superconducting gap size and critical temperature of Al can be enhanced up to threefold in the 2D limit, for films as thin as 4 MLs. Based on thickness-dependent measurements of the superconducting gap combined with variable temperature measurements, we establish that the ratio of Δ to T_c remains near the expected BCS ratio. While the enhancement of superconductivity can be seen gradually as films reach the 2D limit, it remains an open question how the enhanced superconductivity arises. More specifically, it remains to be explored if, besides electron-phonon coupling, other low-energy excitations become relevant in the lower dimensional limit, such as plasmons. It is also particularly interesting to explore if this enhancement is unique to Al, or if it can be generalized to other superconductors in the weak-coupling limit. In addition to the enhancement of the critical temperature, we quantify the type II behavior of these films, including a characterization of the vortex lattice in the presence of the MTF effect. Notably, we find that the shape of the vortex structure in the presence of the MTF effect is strongly modified, including an experimental observation of a gapless region. Our simulations confirm a connection between the extended vortex shape and the presence of odd-frequency pairing contributions, as exemplified by a paramagnetic contribution to the screening supercurrent. In addition, these results highlight that the presence of pairing correlations and the observation of a tunneling gap are not synonymous in a tunneling experiment (60). Therefore, further investigation with pair-sensitive tunneling techniques can provide more insight into the unconventional pairing contributions in the high-field regime of superconductivity (59, 61, 62).

MATERIALS AND METHODS

All presented STM/STS measurements were performed using two different homebuilt systems with base temperatures of 30 mK (63) and 1.3 K (system A and system B, respectively). All presented experimental data were measured at $T \approx 30$ mK, unless specified

otherwise. Since both systems have an identical UHV chamber design ($< 5 \times 10^{-10}$ mbar), the sample growth was performed using the same procedures. First, the Si(111) wafer (As doped, resistivity < 0.005 ohm-cm) is annealed at $\sim 750^\circ\text{C}$ for > 3 hours for degassing purposes by applying a direct current through the wafer. The temperature is measured by aligning a pyrometer onto the wafer surface. Afterward, the Si(111)- 7×7 reconstruction is prepared by repeated flash-annealing to $T = 1500$ to 1530°C . Second, the Si substrate is cooled on a liquid nitrogen cold stage (~ 110 K) for low-temperature Al growth. We deposited Al from a crucible with a cold-lip effusion cell (CLC-ST, CreaTec) at an evaporation temperature of $T = 1030^\circ\text{C}$, yielding a deposition rate of 0.39 MLs (A) or 1.06 MLs (B) per minute (see section S1 and fig. S1). Third, after depositing the desired amount of material, the sample is placed onto a manipulator arm and annealed at room temperature for 30 min for coverages of > 4 MLs and 10 to 20 min for coverages of < 4 MLs (A) and 15 min for coverages of 4 to 6 MLs (B). The anneal time is stopped by placing the sample into a flow cryostat-cooled manipulator arm (for system A) and transferring the sample into the STM body.

All samples were measured using an electrochemically etched W tip, which was prepared by dipping into an Au(111) crystal and subsequently characterized. STS measurements were done with a standard lock-in technique, where a sinusoidal modulation voltage ($f_{\text{mod}} = 877$ to 927 Hz and V_{mod} as indicated in the figure captions) was added to V_s . For variable temperature measurements on system B, we calibrated the used temperature sensor by measuring and fitting the temperature-dependent superconducting gaps of a film of Sn/Si(111) and bulk V(111) (see section S3 and fig. S6).

For vortex imaging, we spatially mapped the dI/dV signal in constant-contour mode, as done in (49). In this mode, we first recorded a constant-current line scan trace, measuring the values of z , with a closed feedback loop, at a bias voltage ($V_s = 3$ mV). Next, the recorded values of z (including a z offset) were used at the measuring bias ($V_s = 0$ mV). This method was repeated for every line of the image. Sharp topographic features, such as island edges, are likely to

contribute to the signal in this measurement mode. In all presented vortex maps, the orientation of the in-plane magnetic field is 10° off the vertical (y) axis of the images (64–73).

Supplementary Materials

This PDF file includes:

Sections S1 to S5

Figs. S1 to S11

REFERENCES AND NOTES

- J. Bardeen, L. N. Cooper, J. R. Schrieffer, Theory of superconductivity. *Phys. Rev.* **108**, 1175–1204 (1957).
- B. Sacépé, M. Feigel'man, T. M. Klapwijk, Quantum breakdown of superconductivity in low-dimensional materials. *Nat. Phys.* **16**, 734–746 (2020).
- S. Qin, J. Kim, Q. Niu, C.-K. Shih, Superconductivity at the two-dimensional limit. *Science* **324**, 1314–1317 (2009).
- T. Zhang, P. Cheng, W.-J. Li, Y.-J. Sun, G. Wang, X.-G. Zhu, K. He, L. Wang, X. Ma, X. Chen, Y. Wang, Y. Liu, H.-Q. Lin, J.-F. Jia, Q.-K. Xue, Superconductivity in one-atomic-layer metal films grown on Si(111). *Nat. Phys.* **6**, 104–108 (2010).
- M. M. Ugeda, A. J. Bradley, Y. Zhang, S. Onishi, Y. Chen, W. Ruan, C. Ojeda-Aristizabal, H. Ryu, M. T. Edmonds, H.-Z. Tsai, A. Riss, S.-K. Mo, D. Lee, A. Zettl, Z. Hussain, Z.-X. Shen, M. F. Crommie, Characterization of collective ground states in single-layer NbSe₂. *Nat. Phys.* **12**, 92–97 (2016).
- D. Huang, J. E. Hoffman, Monolayer FeSe on SrTiO₃. *Annu. Rev. Condens. Matter Phys.* **8**, 311–336 (2017).
- N. Reyren, S. Thiel, A. D. Caviglia, L. F. Kourkoutis, G. Hammerl, C. Richter, C. W. Schneider, T. Kopp, A. S. Rüetschi, D. Jaccard, M. Gabay, D. A. Muller, J. M. Triscone, J. Mannhart, Superconducting interfaces between insulating oxides. *Science* **317**, 1196–1199 (2007).
- J. Linder, J. W. A. Robinson, Superconducting spintronics. *Nat. Phys.* **11**, 307–315 (2015).
- J. P. Cleuziou, W. Wernsdorfer, V. Bouchiat, T. Ondarçuhu, M. Monthieux, Carbon nanotube superconducting quantum interference device. *Nat. Nanotechnol.* **1**, 53–59 (2006).
- N. P. de Leon, K. M. Itoh, D. Kim, K. K. Mehta, T. E. Northup, H. Paik, B. S. Palmer, N. Samarth, S. Sangtawesin, D. W. Steuerman, Materials challenges and opportunities for quantum computing hardware. *Science* **372**, eaabb2823 (2021).
- D. H. Douglass Jr., R. Meservey, Energy gap measurements by tunneling between superconducting films. I. Temperature dependence. *Phys. Rev.* **135**, A19–A23 (1964).
- M. Strongin, O. Kammerer, A. Paskin, Superconducting transition temperature of thin films. *Phys. Rev. Lett.* **14**, 949–951 (1965).
- D. G. Walmisley, C. K. Campbell, R. C. Dynes, Superconductivity of very thin aluminum films. *Can. J. Phys.* **46**, 1129–1132 (1968).
- O. A. E. Cherney, J. Shewchun, Enhancement of superconductivity in thin aluminum films. *Can. J. Phys.* **47**, 1101–1106 (1969).
- P. N. Chubov, V. Eremenko, Y. A. Filipenko, Dependence of the critical temperature and energy gap on the thickness of superconducting aluminum films. *J. Exp. Theor. Phys.* **28**, 389–395 (1969).
- R. Meservey, P. M. Tedrow, Properties of very thin aluminum films. *J. Appl. Phys.* **42**, 51–53 (1971).
- N. A. Court, A. J. Ferguson, R. G. Clark, Energy gap measurement of nanostructured aluminum thin films for single Cooper-pair devices. *Supercond. Sci. Technol.* **21**, 015013 (2008).
- P. W. Adams, H. Nam, C. K. Shih, G. Catelani, Zeeman-limited superconductivity in crystalline Al films. *Phys. Rev. B* **95**, 094520 (2017).
- R. W. Cohen, B. Abeles, Superconductivity in granular aluminum films. *Phys. Rev.* **168**, 444–450 (1968).
- P. Townsend, S. Gregory, R. G. Taylor, Superconducting behavior of thin films and small particles of aluminum. *Phys. Rev. B* **5**, 54–66 (1972).
- R. B. Pettit, J. Silcox, Film structure and enhanced superconductivity in evaporated aluminum films. *Phys. Rev. B* **13**, 2865–2872 (1976).
- M. Savolainen, V. Touboltsev, P. Koppinen, K. P. Riikonen, K. Arutyunov, Ion beam sputtering for progressive reduction of nanostructures dimensions. *Appl. Phys. A* **79**, 1769–1773 (2004).
- M. Zgirski, K. P. Riikonen, V. Touboltsev, K. Arutyunov, Size dependent breakdown of superconductivity in ultranarrow nanowires. *Nano Lett.* **5**, 1029–1033 (2005).
- D. J. Monsma, S. S. P. Parkin, Spin polarization of tunneling current from ferromagnet/Al₂O₃ interfaces using copper-doped aluminum superconducting films. *Appl. Phys. Lett.* **77**, 720–722 (2000).
- C. Kaiser, S. S. P. Parkin, Spin polarization in ferromagnet/insulator/superconductor structures with the superconductor on top of the barrier. *Appl. Phys. Lett.* **84**, 3582–3584 (2004).
- R. Meservey, P. M. Tedrow, P. Fulde, Magnetic field splitting of the quasiparticle states in superconducting aluminum films. *Phys. Rev. Lett.* **25**, 1270–1272 (1970).
- R. Meservey, P. M. Tedrow, Spin-polarized electron tunneling. *Phys. Rep.* **238**, 173–243 (1994).
- J. Linder, J. W. A. Robinson, Strong odd-frequency correlations in fully gapped Zeeman-split superconductors. *Sci. Rep.* **5**, 15483 (2015).
- M. Matsumoto, M. Koga, H. Kusunose, Coexistence of even- and odd-frequency superconductivities under broken time-reversal symmetry. *J. Phys. Soc. Japan* **81**, 033702 (2012).
- V. Berezinskii, New model of the anisotropic phase of superfluid He₃. *Jetp Lett.* **20**, 287–289 (1974).
- Y. Tanaka, M. Sato, N. Nagaosa, Symmetry and topology in superconductors—Odd-frequency pairing and edge states. *J. Phys. Soc. Japan* **81**, 011013 (2012).
- F. S. Bergeret, A. F. Volkov, K. B. Efetov, Odd triplet superconductivity and related phenomena in superconductor-ferromagnet structures. *Rev. Mod. Phys.* **77**, 1321–1373 (2005).
- A. Di Bernardo, Z. Salman, X. L. Wang, M. Amado, M. Egilmez, M. G. Flokstra, A. Suter, S. L. Lee, J. H. Zhao, T. Prokscha, E. Morenzoni, M. G. Blamire, J. Linder, J. W. A. Robinson, Intrinsic paramagnetic meissner effect due to *s*-wave odd-frequency superconductivity. *Phys. Rev. X* **5**, 041021 (2015).
- V. Perrin, F. L. N. Santos, G. C. Ménard, C. Brun, T. Cren, M. Civelli, P. Simon, Unveiling odd-frequency pairing around a magnetic impurity in a superconductor. *Phys. Rev. Lett.* **125**, 117003 (2020).
- P. Krogstrup, N. L. B. Ziino, W. Chang, S. M. Albrecht, M. H. Madsen, E. Johnson, J. Nygård, C. M. Marcus, T. S. Jespersen, Epitaxy of semiconductor–superconductor nanowires. *Nat. Mater.* **14**, 400–406 (2015).
- M. T. Deng, S. Vaitiekėnas, E. B. Hansen, J. Danon, M. Leijnse, K. Flensberg, J. Nygård, P. Krogstrup, C. M. Marcus, Majorana bound state in a coupled quantum-dot hybrid-nanowire system. *Science* **354**, 1557–1562 (2016).
- G. Binnig, H. Rohrer, C. Gerber, E. Weibel, 7×7 reconstruction on Si(111) resolved in real space. *Phys. Rev. Lett.* **50**, 120–123 (1983).
- H. Liu, Y. F. Zhang, D. Y. Wang, M. H. Pan, J. F. Jia, Q. K. Xue, Two-dimensional growth of Al films on Si(111)- 7×7 at low temperature. *Surf. Sci.* **571**, 5–11 (2004).
- D. Eom, S. Qin, M. Y. Chou, C. K. Shih, Persistent superconductivity in ultrathin Pb Films: A scanning tunneling spectroscopy study. *Phys. Rev. Lett.* **96**, 027005 (2006).
- I. B. Altfeder, D. M. Chen, K. A. Matveev, Imaging buried interfacial lattices with quantized electrons. *Phys. Rev. Lett.* **80**, 4895–4898 (1998).
- A. Mans, J. H. Dil, A. R. H. F. Ettema, H. H. Weitering, Quantum electronic stability and spectroscopy of ultrathin Pb films on Si(111) 7×7 . *Phys. Rev. B* **66**, 195410 (2002).
- D.-L. Nguyen, C.-M. Wei, M.-Y. Chou, Theoretical study of quantum size effects in thin Al(100), Al(110), and Al(111) films. *Phys. Rev. B* **99**, 205401 (2019).
- G. Q. Huang, Electronic structures, surface phonons, and electron-phonon interactions of Al(100) and Al(111) thin films from density functional perturbation theory. *Phys. Rev. B* **78**, 214514 (2008).
- L. Aballe, C. Rogero, P. Kratzer, S. Gokhale, K. Horn, Probing Interface electronic structure with overlayers quantum-well resonances: Al/Si(111). *Phys. Rev. Lett.* **87**, 156801 (2001).
- K. Maki, Pauli paramagnetism and superconducting state. II. *Prog. Theor. Phys.* **32**, 29–36 (1964).
- J. F. Cochran, D. E. Mapother, Superconducting transition in aluminum. *Phys. Rev.* **111**, 132–142 (1958).
- G. L. Wells, J. E. Jackson, E. N. Mitchell, Superconducting tunneling in single-crystal and polycrystalline films of aluminum. *Phys. Rev. B* **1**, 3636–3644 (1970).
- Y. Guo, Y.-F. Zhang, X.-Y. Bao, T.-Z. Han, Z. Tang, L.-X. Zhang, W.-G. Zhu, E. G. Wang, Q. Niu, Z. Q. Qiu, J.-F. Jia, Z.-X. Zhao, Q.-K. Xue, Superconductivity modulated by quantum size effects. *Science* **306**, 1915–1917 (2004).
- A. Kamlapure, M. Simonato, E. Sierda, M. Steinbrecher, U. Kamber, E. J. Knol, P. Krogstrup, M. I. Katsnelson, M. Rösner, A. A. Khajetoorians, Tuning lower dimensional superconductivity with hybridization at a superconducting-semiconducting interface. *Nat. Commun.* **13**, 4452 (2022).
- R. C. Dynes, V. Narayananmurti, J. P. Garno, Direct measurement of quasiparticle-lifetime broadening in a strong-coupled superconductor. *Phys. Rev. Lett.* **41**, 1509–1512 (1978).
- M. Tinkham, *Introduction to Superconductivity* (Knovel Library, Dover Publications, ed. 2, 2004).
- A. M. Clogston, Upper limit for the critical field in hard superconductors. *Phys. Rev. Lett.* **9**, 266–267 (1962).

53. B. Chandrasekhar, A note on the maximum critical field of high-field superconductors. *Appl. Phys. Lett.* **1**, 7–8 (1962).
54. J. Linder, A. V. Balatsky, Odd-frequency superconductivity. *Rev. Mod. Phys.* **91**, 045005 (2019).
55. F. S. Bergeret, A. F. Volkov, K. B. Efetov, Josephson current in superconductor-ferromagnet structures with a nonhomogeneous magnetization. *Phys. Rev. B* **64**, 134506 (2001).
56. J. Rammer, H. Smith, Quantum field-theoretical methods in transport theory of metals. *Rev. Mod. Phys.* **58**, 323–359 (1986).
57. W. Belzig, F. K. Wilhelm, C. Bruder, G. Schön, A. D. Zaikin, Quasiclassical Green's function approach to mesoscopic superconductivity. *Superlattices Microstruct.* **25**, 1251–1288 (1999).
58. K. D. Usadel, Generalized diffusion equation for superconducting alloys. *Phys. Rev. Lett.* **25**, 507–509 (1970).
59. X. Liu, Y. X. Chong, R. Sharma, J. C. S. Davis, Atomic-scale visualization of electronic fluid flow. *Nat. Mater.* **20**, 1480–1484 (2021).
60. K. M. Bastiaans, D. Chatzopoulos, J.-F. Ge, D. Cho, W. O. Tromp, J. M. van Ruitenbeek, M. H. Fischer, P. J. de Visser, D. J. Thoen, E. F. C. Driessen, T. M. Klapwijk, M. P. Allan, Direct evidence for Cooper pairing without a spectral gap in a disordered superconductor above T_c . *Science* **374**, 608–611 (2021).
61. G. Deutscher, Andreev–Saint-James reflections: A probe of cuprate superconductors. *Rev. Mod. Phys.* **77**, 109–135 (2005).
62. O. Peters, N. Bogdanoff, S. Acero González, L. Melischek, J. R. Simon, G. Reecht, C. B. Winkelmann, F. von Oppen, K. J. Franke, Resonant Andreev reflections probed by photon-assisted tunnelling at the atomic scale. *Nat. Phys.* **16**, 1222–1226 (2020).
63. H. von Allwörden, A. Eich, E. J. Knol, J. Hermenau, A. Sonntag, J. W. Gerritsen, D. Wegner, A. A. Khajetoorians, Design and performance of an ultra-high vacuum spin-polarized scanning tunneling microscope operating at 30 mK and in a vector magnetic field. *Rev. Sci. Instrum.* **89**, 033902 (2018).
64. M. Assig, M. Etzkorn, A. Enders, W. Stiepany, C. R. Ast, K. Kern, A 10 mK scanning tunneling microscope operating in ultra high vacuum and high magnetic fields. *Rev. Sci. Instrum.* **84**, 033903 (2013).
65. W. M. J. van Weerdenburg, M. Steinbrecher, N. P. E. van Mullekom, J. W. Gerritsen, H. von Allwörden, F. D. Natterer, A. A. Khajetoorians, A scanning tunneling microscope capable of electron spin resonance and pump–probe spectroscopy at mK temperature and in vector magnetic field. *Rev. Sci. Instrum.* **92**, 033906 (2021).
66. C. R. Ast, B. Jäck, J. Senkpiel, M. Eltschka, M. Etkorn, J. Ankerhold, K. Kern, Sensing the quantum limit in scanning tunnelling spectroscopy. *Nat. Commun.* **7**, 13009 (2016).
67. A. Wexler, W. S. Corak, Superconductivity of vanadium. *Phys. Rev.* **85**, 85–90 (1952).
68. I. Giaever, K. Megerle, Study of superconductors by electron tunneling. *Phys. Rev.* **122**, 1101–1111 (1961).
69. P. Townsend, J. Sutton, Investigation by electron tunneling of the superconducting energy gaps in Nb, Ta, Sn, and Pb. *Phys. Rev.* **128**, 591–595 (1962).
70. J. L. Brewster, M. Levy, I. Rudnick, Ultrasonic determination of the superconducting energy gap in vanadium. *Phys. Rev.* **132**, 1062–1072 (1963).
71. H. Huang, C. Padurariu, J. Senkpiel, R. Drost, A. L. Yeyati, J. C. Cuevas, B. Kubala, J. Ankerhold, K. Kern, C. R. Ast, Tunnelling dynamics between superconducting bound states at the atomic limit. *Nat. Phys.* **16**, 1227–1231 (2020).
72. J. Mayoh, A. M. Garcia-Garcia, Global critical temperature in disordered superconductors with weak multifractality. *Phys. Rev. B* **92**, 174526 (2015).
73. E. H. Fyhn, J. Linder, Superconducting vortices in half-metals. *Phys. Rev. B* **100**, 224508 (2019).

Acknowledgments: We thank M. Rösner and M. I. Katsnelson for valuable scientific discussions and input. **Funding:** This project has received funding from the European Research Council (ERC) under the European Union's Horizon 2020 Research and Innovation Programme (grant agreement no. 818399). A.A.K. acknowledges the NWO-VIDI project "Manipulating the interplay between superconductivity and chiral magnetism at the single-atom level" with project number 680-47-534. This publication is part of the project TOPCORE (with project number OCENWGROOT.2019.048) of the research program Open Competition ENW Groot, which is (partly) financed by the Dutch Research Council (NWO). We also acknowledge funding from Microsoft Quantum. E.H.F. and J.L. acknowledge funding by the Research Council of Norway through grant 323766, and its Centres of Excellence funding scheme grant 262633 "QuSpin." J.L. also acknowledges funding from the NV-faculty at the Norwegian University of Science and Technology. **Author contributions:** W.M.J.v.W., A.K., X.H., M.S., and N.P.E.v.M. acquired the experimental data. The experimental analysis was designed by W.M.J.v.W., A.K., and A.A.K., with W.M.J.v.W., A.K., X.H., and N.P.E.v.M. implementing the experimental analysis. E.H.F. and J.L. performed the calculations based on the Usadel approach. A.A.K. and P.K. designed the initial experimental concept, while W.M.J.v.W., A.K., M.S., P.K., and A.A.K. together iterated changes to the experiments during implementation and subsequent analysis. All authors participated in the scientific discussion of the results, as well as participated in writing the manuscript. **Competing interests:** The authors declare that they have no competing interests. **Data and materials availability:** All data needed to evaluate the conclusions in the paper are present in the paper and/or the Supplementary Materials.

Submitted 28 October 2022

Accepted 31 January 2023

Published 1 March 2023

10.1126/sciadv.adf5500

Extreme enhancement of superconductivity in epitaxial aluminum near the monolayer limit

Werner M.J. van Weerdenburg, Anand Kamlapure, Eirik Holm Fyhn, Xiaochun Huang, Niels P.E. van Mullekom, Manuel Steinbrecher, Peter Krogstrup, Jacob Linder, and Alexander Ako Khajetoorians

Sci. Adv., **9** (9), eadf5500.
DOI: 10.1126/sciadv.adf5500

View the article online

<https://www.science.org/doi/10.1126/sciadv.adf5500>

Permissions

<https://www.science.org/help/reprints-and-permissions>

Use of this article is subject to the [Terms of service](#)

Science Advances (ISSN) is published by the American Association for the Advancement of Science, 1200 New York Avenue NW, Washington, DC 20005. The title *Science Advances* is a registered trademark of AAAS.
Copyright © 2023 The Authors, some rights reserved; exclusive licensee American Association for the Advancement of Science. No claim to original U.S. Government Works. Distributed under a Creative Commons Attribution License 4.0 (CC BY).

Supplementary Materials for

Extreme enhancement of superconductivity in epitaxial aluminum near the monolayer limit

Werner M.J. van Weerdenburg *et al.*

Corresponding author: Alexander Ako Khajetoorians, a.khajetoorians@science.ru.nl

Sci. Adv. **9**, eadf5500 (2023)
DOI: 10.1126/sciadv.adf5500

This PDF file includes:

Sections S1 to S5
Figs. S1 to S11

S1 Film morphology and characterization

Calibration of the coverage

Prior to sample growth on Si(111), the deposition rate at $T = 1030$ °C is characterized by depositing Al onto a quartz microbalance (QMB). We repeat this calibration between multiple sample preparations to ensure that the deposition rate does not substantially change over time. We also calibrated the Al deposition by evaporating Al onto a clean Si(111)-7x7 surface at room temperature, for both STMs used in this study. This growth method yields small islands of thickness ≥ 4 ML, which enable calibration as also seen in ref. (38). Fig. S1A shows a constant-current STM image illustrating this calibration, after depositing Al for 12 minutes, followed by an additional 10 minutes waiting time before low temperature characterization. The corresponding apparent height histogram in Fig. S1B shows the density for each specified thickness. Based on this analysis, we extracted a deposition rate of 0.39 ML/min for system A. This rate is used to estimate the coverage of each sample in combination with morphology analysis on large-scale images to precisely determine the amount of main layer and (vacancy) islands.

Film morphology for different coverages

The morphology of the Al films measured in this work vary as a function of coverage and annealing conditions. In Fig. S2, we present the morphology of three different Al films with different coverage, grown with the described sample preparation (see Materials and Methods) and with a room-temperature anneal time of (A) 10 minutes, and (B,C) 30 minutes. The key differences are: (i) the roughness of the film increases as we approach the 4 ML coverage limit, where we still observe a closed, metallic film (ii) the apparent height variation changes for thicker films, e.g. as shown for 35 ML, where samples can show $N-2/ N+2$ variations in addition to the $N-1/N+1$ variations observed in thinner films. We note that the morphology is extremely sensitive to the annealing time (also see Fig. S7A). However, the length scale related to the mean surface roughness typically remains smaller than the coherence length of the superconductor (i.e. < 50 nm).

Large-scale scanning tunneling spectroscopy and comparison to DFT and ARPES

We measured dI/dV in a large bias voltage range between $V_s = \pm 2$ V on various thicknesses for a given sample. To compare to previous results, we plotted the calculated quantum well state (QWS) energies for Al(111) from DFT calculations derived from refs. (42, 43) in the upper panel of Fig. S3A, as well as the extracted QWS energies from ARPES measurements on various Al(111) films derived from ref. (44). We note that ARPES macroscopically averages over large areas of the film, compared to STS, and therefore the measured spectra will presumably convolute all layer thicknesses present on the film. Furthermore, we compare the QWS energies from DFT with the peak positions observed in the large-scale STS measurements in the lower panel of Fig. S3A. The spectra for layer thicknesses between 11 ML and 37 ML are shown in Fig. S3B-E.

Spatial measurement of superconductivity

To check the effect of the film morphology (i.e. islands, moiré-type pattern) on the superconductivity, we measured dI/dV spectra along a line across an Al film with 8.5 ML coverage. Fig. S4A shows the main layer (8 ML) and an island (9 ML), as well as the long-range periodicity, with the measured line running across all these morphological features. The spectra along this line (Fig. S4B) show a constant gap size with small variations in the coherence peak height. Similarly, we measured spectra on arbitrary locations on all samples and find negligible variations in the gap size, as indicated by the error bars in Fig. 2B.

S2 Fitting superconducting spectra and the influence of broadening

For fitting superconducting gap spectra and extracting Δ , we used two different BCS-based fitting models.

1) The Maki equation for the density of states (45), based on Pauli paramagnetism in small superconductors:

$$\rho(E) = \Re \left(\frac{u}{\sqrt{u^2 - 1}} \right),$$

where $u = \frac{E}{\Delta} + \zeta \frac{u}{\sqrt{1-u^2}}$ (see ref. (64) for the analytical solution) and ζ describes the pair-breaking parameter. Note that this description is valid in absence of magnetic field, i.e. no spin-splitting.

2) The Dynes equation (50), a phenomenological equation to capture the broadening due to finite quasiparticle recombination times:

$$\rho(E) = \frac{E - i\Gamma}{\sqrt{(E - i\Gamma)^2 - \Delta^2}}.$$

The Maki equation renormalizes the coherence peak height, while the Dynes equation induces a Gaussian type of broadening which may induce in-gap conductance.

In Fig. S5, we plot a typical superconducting gap of a film with coverage 8.5 ML (blue circles), and in Fig. S5A fitted with the Maki equation (red line), with a magnified focus of the fit on the left coherence peak. We find an excellent agreement between data and fit for $\Delta = 0.46$ meV, $\zeta = 0.02$ meV if we include a Fermi-Dirac broadening with an effective temperature $T_{\text{eff}} = 250$ mK. Noteworthy, this approach does not specify the origin of the broadening effects and can include broadening contributions that are unrelated to temperature. Moreover, this effective temperature is considerably larger than the measurement temperature of $T = 30$ mK, which suggests additional non-thermal broadening. Previously, we calibrated the energy resolution of our experimental setup at ~ 65 μeV in ref. (65). Here, we consider three potential broadening contributions.

Firstly, tunneling spectroscopy at mK temperature suffers from an intrinsic broadening mechanism, based on the quantization of the tunneling current and its interaction with the electromagnetic environment (66). The capacitive noise can be described by the $P(E)$ theory and in practice adds a

Gaussian broadening $P_N(E) = \frac{1}{\sqrt{4\pi E_C k_B T}} \exp\left[-\frac{E^2}{4E_C k_B T}\right]$, where $E_C = Q^2/2C_J$ is the charging energy of the Cooper pairs with $Q = 2e$ and C_J the capacitance of the tunnel junction. In Fig. S5B, we fitted the same spectrum with the Maki equation, extended by the $P_N(E)$ contribution and find that we require a capacitance of $C_J = 0.25$ fF to account for the broadening, if T_{eff} equals the measurement temperature. However, assuming the proposed model in ref. (66) for a tip with diameter $d = 0.3$ nm and an opening angle of $\alpha = 60^\circ$, we find a capacitance of 12.7 fF instead, suggesting that the $P_N(E)$ broadening is not the main broadening contribution.

Secondly, we considered a sample with a convolution of two-layer thicknesses, where each layer has a distinct value of Δ , namely Δ_N and Δ_{N+1} . We model this by combining two Maki equations for each value of Δ , considering a 50% contribution of each Δ . In Fig. S5C, we illustrate the resultant convolution as well as a decomposition of each of gap contributions (dashed lines). The result shows a good match with the data, using $T_{\text{eff}} = 150$ mK and a difference $|\Delta_N - \Delta_{N+1}| = 70$ μeV . Based on the data shown in Fig. 2B it is reasonable to consider such differences in the limit where $N < 10$ ML. However, we also observed that the inherent broadening remained for higher coverages, and therefore we cannot conclude that this is solely responsible for the observed gap broadening. Ultimately, a gap difference larger than the energy resolution is required to confirm the existence of such a double-gap proximity effect, as this would result in a kink in the spectral shape.

Lastly, we considered the hybridization model proposed in ref. (49). For Pb films on black phosphorus (BP), weak hybridization between the bands of BP and the quantum well states of Pb leads to a non-thermal broadening of the superconducting gap and anisotropic vortices. However, for Al films on Si, no renormalization of the superconducting gap is not expected, as indicated by the observed isotropic vortices. A good agreement between the model and the data (Fig. S5D) is only found by taking a large amount of anisotropy (e.g. $m_x/m_y = 8$, where m_x and m_y describe the effective mass of the Al band in x - and y -direction respectively) and a weighting function (using $T_{\text{eff}} = 150$ mK). However, such large anisotropy values are expected to influence the vortex shape, as seen for vortices in Pb on black phosphorus, but the vortices in Al are isotropic (Fig. 3B, Fig. S9). Therefore, we expect that the broadening mechanism in Al films does not stem from anisotropic hybridization effects.

S3 Temperature calibration for temperature dependent measurements above 1 K

To perform temperature dependent measurements, we heated the sample with a Zener diode. To calibrate the temperature sensor, we measured the temperature dependence of V(111) bulk, and a thick Sn film epitaxially grown on Si(111)-(7x7) (67-71). We prepared the V(111) sample with repeated

sputter and anneal cycles ($T_{\text{anneal}} = 850$ °C). For the second study, we deposited Sn on a clean Si(111)-(7×7) substrate held at $T \sim 110$ K. Based on a previous calibration, we expected a coverage between 120-150 ML, i.e. in the bulk regime.

In Fig. S6, we plot the dI/dV spectroscopy measured as a function of temperature, where the temperature value refers to the sensor reading, for the two aforementioned samples. We extracted $\Delta(T)$ by fitting a Dynes equation (black lines). The resultant $\Delta(T)$ is plotted below each subfigure. Both material systems show an excellent agreement with the BCS equation and the measured $\Delta(T)$. Using the extracted values for Δ and T_c ($\Delta_{\text{Sn}}^{T=0} = 0.67 \pm 0.03$ meV, $T_{c,\text{Sn}} = 3.9 \pm 0.2$ K, $\Delta_{\text{V}}^{T=0} = 0.79 \pm 0.04$ meV, $T_{c,\text{V}} = 5.1 \pm 0.2$ K), we find that the BCS ratio $2\Delta/k_B T_c = 3.99 \pm 0.27$ for Sn/Si(111) and $2\Delta/k_B T_c = 3.60 \pm 0.23$ for V(111). Since these values, in particular those for V, match with literature (67, 70, 71), we conclude that the temperature of the STM sensor gives a reliable measurement of the sample temperature in the range between 1.2 K and 5.1 K.

Temperature dependence of three thin Al films

Temperature dependent measurements as described in the main manuscript were performed for three other Al films with coverages of 6.3 ML, 5.3 ML and 4.2 ML, as shown in Fig. S7A-C. We apply the same analysis and extract $\Delta_{6.3\text{ ML}}^{T=0} = 0.39 \pm 0.02$ meV, $\Delta_{5.3\text{ ML}}^{T=0} = 0.43 \pm 0.02$ meV and $\Delta_{4.2\text{ ML}}^{T=0} = 0.51 \pm 0.02$ meV, as well as $T_{c,6.3\text{ ML}} = 2.51 \pm 0.10$ K, $T_{c,5.3\text{ ML}} = 2.90 \pm 0.11$ K and $T_{c,4.2\text{ ML}} = 3.15 \pm 0.08$ K. Here, the error bars represent the standard deviation given by the BCS fit.

S4 Effect of minimal annealing on the film morphology and resultant superconductivity

In order to explore the role of room temperature annealing on the morphology and resultant superconducting gap, we prepared an additional sample with a coverage of 8.5 ML. After cold deposition, the sample was minimally annealed at room temperature (~ 1 min). The resulting sample shows small islands on top of a closed layer with atomic resolution visible, as shown in Fig. S8A. The moiré-like periodicity was not visible, likely obstructed by the abundance of small islands. Still, we find a spatially homogeneous gap with a gap size of ~ 0.5 meV, shown in Fig. S8B, which is similarly enhanced compared to the annealed sample with 8.5 ML coverage (see Fig. 2A).

S5 Al films in (high) magnetic fields

Theoretical model for vortex simulations

To model the superconducting vortices, we use quasiclassical Keldysh theory, which is valid when the Fermi energy is much larger than all other energy scales. Assuming that the mean free path is also much less than the coherence length, the system can be fully described by the momentum-averaged quasiclassical Green's function,

$$\check{g} = \begin{pmatrix} \hat{g}^R & \hat{g}^K \\ 0 & \hat{g}^A \end{pmatrix}, \quad (1)$$

where \hat{g}^R , \hat{g}^A and \hat{g}^K are the retarded, advanced and Keldysh components of the Green's function, respectively. In thermal equilibrium it is sufficient to find the retarded Green's function, since $\hat{g}^A = -\hat{\tau}_z (\hat{g}^R)^\dagger \hat{\tau}_z$ and $\hat{g}^K = (\hat{g}^R - \hat{g}^A) \tanh(\beta\epsilon/2)$, where $\hat{\tau}_z = \text{diag}(1, 1, -1, -1)$, β is the inverse temperature and ϵ is the energy.

The retarded quasiclassical Green's function solves the Usadel equation (58),

$$D\vec{\nabla} \cdot (\hat{g}^R \vec{\nabla} \hat{g}^R) + i[\hat{\tau}_z(\epsilon + i\Gamma) + h^\parallel \hat{\sigma}_z + \hat{\Delta}, \hat{g}^R] = 0, \quad (2)$$

Here, D is the diffusion constant, Γ is the Dynes parameter, h^{\parallel} is the spin-splitting field, $\hat{\Delta} = \text{antiadiag}(\Delta, -\Delta, \Delta^*, -\Delta^*)$ and the covariant derivative is

$$\tilde{\nabla} \hat{g}^R = \nabla \hat{g}^R - ie[\hat{\tau}_z \mathbf{A}, \hat{g}^R], \quad (3)$$

where $e = -|e|$ is the electron charge and \mathbf{A} is the vector potential. The superconducting gap parameter, Δ , must solve the gap equation (72).

$$\Delta = \frac{1}{16 \log(2\omega_D/\Delta_0)} \int_{-\omega_D}^{\omega_D} d\varepsilon \text{Tr}[-i\hat{\sigma}_y(\hat{\tau}_x - i\hat{\tau}_y)\hat{g}^K], \quad (4)$$

where ω_D is the Debye frequency and Δ_0 is the zero-temperature BCS bulk solution. Additionally, the vector potential must solve Maxwell's equation. Assuming $\nabla \cdot \mathbf{A} = 0$, Maxwell's equation reads (57)

$$\nabla^2 \mathbf{A} = -\frac{\mu N_0 e D}{4} \int_{-E_c}^{E_c} d\varepsilon \text{Tr}[\hat{\tau}_z (\hat{g} \tilde{\nabla} \hat{g})^K], \quad (5)$$

where ∇^2 is the vector Laplacian, E_c is a cut-off energy, μ is the magnetic permeability and N_0 is the normal state density of states at the Fermi level. For a self-consistent solution, we must solve eqs. (2), (4) and (5) simultaneously.

To model the vortex, we solve eqs. (2), (4) and (5) on an infinite plane with a single phase winding in the gap parameter around the origin and assume that the vector potential points in the azimuthal direction. That is, using polar coordinates, $\Delta(\mathbf{r}) = \Delta(r)e^{i\theta}$ and $\mathbf{A} = A\mathbf{e}_\theta$, where \mathbf{e}_θ is the unit vector in the θ -direction. The latter means that $\nabla^2 \mathbf{A} = (\nabla^2 A - A/r^2)\mathbf{e}_\theta$. We solve the equations numerically by using the Ricatti parametrization,

$$\hat{g}^R = \begin{pmatrix} N & 0 \\ 0 & -\tilde{N} \end{pmatrix} \begin{pmatrix} 1 + \gamma\tilde{\gamma} & 2\gamma \\ 2\tilde{\gamma} & 1 + \tilde{\gamma}\gamma \end{pmatrix}, \quad (6)$$

where $\tilde{\gamma}(\epsilon) = \gamma^*(-\epsilon)$ and $N = (1 - \gamma\tilde{\gamma})^{-1}$. If we choose the spin-quantization axis to be along the in-plane magnetic field, we need only solve for two components of γ , and we may write

$$\gamma(\mathbf{r}, \theta) = \begin{pmatrix} 0 & \gamma_1(r) \\ -\gamma_2(r) & 0 \end{pmatrix} e^{i\theta}. \quad (7)$$

Next, we make all quantities dimensionless by dividing eqs. (2) and (4) by the superconducting gap at $r \rightarrow \infty$, Δ^∞ , and multiplying eq. (5) by $2e\xi$, where $\xi = \sqrt{D/\Delta^\infty}$ is the diffusive superconducting coherence length. We define the dimensionless quantities $\bar{\varepsilon} = \varepsilon/\Delta^\infty$, $\bar{h}^{\parallel} = h^{\parallel}/\Delta^\infty$, $\bar{\Gamma} = \Gamma/\Delta^\infty$, $\bar{\Delta} = \Delta/\Delta^\infty$, $\bar{r} = r/\xi$, and $\bar{A} = 2e\xi A$. To solve the equations numerically on an infinite domain, we also define $z = \bar{r}/(1 + \bar{r})$.

From eq. (2) we find that

$$\begin{aligned}
(1-z)^4 \frac{\partial^2 \gamma_{1/2}}{\partial z^2} + \frac{(1-2z)(1-z)^3}{z} \frac{\partial \gamma_{1/2}}{\partial z} - \frac{(1-z)^2}{z^2} \gamma_{1/2} + 2i(\bar{\varepsilon} + i\bar{\Gamma} \pm \bar{h}^{\parallel}) \gamma_{1/2} - i\bar{\Delta} - i\bar{\Delta}^* \gamma_{1/2}^2 \\
+ \frac{2\tilde{\gamma}_{1/2}}{1 + \gamma_{1/2}\tilde{\gamma}_{2/1}} \left[\frac{(1-z)^2 \gamma_{1/2}^2}{z^2} - (1-z^4) \left(\frac{\partial \gamma_{1/2}}{\partial z} \right)^2 \right] \\
- \bar{A} \gamma_{1/2} \frac{1 - \gamma_{1/2}\tilde{\gamma}_{2/1}}{1 + \gamma_{1/2}\tilde{\gamma}_{2/1}} \left(\bar{A} - \frac{2(1-z)}{z} \right) = 0,
\end{aligned} \tag{8}$$

from eq. (4), we get

$$\bar{\Delta} = \frac{1}{2 \log(2\omega_D/\Delta_0)} \int_{-\omega_D/\Delta^\infty}^{\omega_D/\Delta^\infty} d\bar{\varepsilon} \Re \left(\frac{\gamma_1}{1 + \gamma_1 \tilde{\gamma}_2} + \frac{\gamma_2}{1 + \gamma_2 \tilde{\gamma}_1} \right) \tanh \left(\frac{\beta \bar{\varepsilon}}{2} \right), \tag{9}$$

and from eq. (5), we get that

$$\begin{aligned}
(1-z)^4 \frac{\partial^2 \bar{A}}{\partial z^2} - \frac{(1-z)^2}{z^2} \bar{A} + \frac{(1-2z)(1-z)^3}{z} \frac{\partial \bar{A}}{\partial z} \\
= \frac{1}{\kappa^2} \left(\bar{A} - \frac{1-z}{z} \right) \int_0^{E_c/\Delta^\infty} d\bar{\varepsilon} \Im \left(\frac{\gamma_1 \tilde{\gamma}_2}{(1 + \gamma_1 \tilde{\gamma}_2)^2} + \frac{\gamma_2 \tilde{\gamma}_1}{(1 + \gamma_2 \tilde{\gamma}_1)^2} \right) \tanh \left(\frac{\beta \bar{\varepsilon}}{2} \right),
\end{aligned} \tag{10}$$

where κ is a dimensionless parameter which we set equal to 5 in all calculations.

Having found the quasiclassical Green's function, one can calculate the local density of states, and thereby the theoretical prediction for the current as measured by the STM. In terms of the Riccati parameters, the local density of states reads

$$\rho(E) = \frac{N_0}{2} \Re \left(\frac{1 - \gamma_1 \tilde{\gamma}_2}{1 + \gamma_1 \tilde{\gamma}_2} + \frac{1 - \gamma_2 \tilde{\gamma}_1}{1 + \gamma_2 \tilde{\gamma}_1} \right). \tag{11}$$

Assuming a constant tunnelling transmission, we get that the differential conductance is

$$\frac{dI}{dV} = C \int_{-\infty}^{\infty} d\bar{\varepsilon} \Re \left(\frac{1 - \gamma_1 \tilde{\gamma}_2}{1 + \gamma_1 \tilde{\gamma}_2} + \frac{1 - \gamma_2 \tilde{\gamma}_1}{1 + \gamma_2 \tilde{\gamma}_1} \right) \frac{\exp(\varepsilon - eV/k_B T_{\text{eff}})}{(1 + \exp(\varepsilon - eV/k_B T_{\text{eff}}))^2}, \tag{12}$$

where V is the applied bias voltage, k_B is the Boltzmann constant and T_{eff} is an experimental broadening parameter and C is a proportionality constant.

The presence of the spin-splitting field h^{\parallel} induces odd-frequency superconducting correlations. These correlations are characterized by $|\text{Tr}[\hat{\sigma}_x(\hat{\tau}_x - i\hat{\tau}_y)\hat{g}^K]| > 0$. However, unlike the even frequency correlations, the odd-frequency correlations vanish upon integration over $\bar{\varepsilon}$ and therefore require another correlation function compared to eq. (4). Here we use the correlation function obtained by multiplying the integrand with $\bar{\varepsilon}$,

$$\Psi_{\text{odd}} = \frac{-i}{16} \int_{-\omega_D/\Delta^\infty}^{\omega_D/\Delta^\infty} d\bar{\varepsilon} \text{Tr}[\hat{\sigma}_x(\hat{\tau}_x - i\hat{\tau}_y)\hat{g}^K] \bar{\varepsilon} = \int_{-\omega_D/\Delta^\infty}^{\omega_D/\Delta^\infty} d\bar{\varepsilon} \Im \left(\frac{\gamma_1}{1 + \gamma_1 \tilde{\gamma}_2} - \frac{\gamma_2}{1 + \gamma_2 \tilde{\gamma}_1} \right) \tanh \left(\frac{\beta \bar{\varepsilon}}{2} \right) \bar{\varepsilon}. \tag{13}$$

This is equivalent to differentiating the anomalous Green's function with respect to relative time (73).

When calculating the electric current density, we can separate the contributions from the even-frequency correlations and the odd-frequency correlations. In terms of the even-frequency retarded anomalous Green's function,

$$f_{\text{even}} = \frac{\gamma_1}{1 + \gamma_1 \tilde{\gamma}_2} + \frac{\gamma_2}{1 + \gamma_2 \tilde{\gamma}_1}, \quad (14)$$

and the odd-frequency retarded anomalous Green's function,

$$f_{\text{odd}} = \frac{\gamma_1}{1 + \gamma_1 \tilde{\gamma}_2} - \frac{\gamma_2}{1 + \gamma_2 \tilde{\gamma}_1}, \quad (15)$$

the electric supercurrent density can be written

$$j_s = j_{s,\text{even}} + j_{s,\text{odd}}, \quad (16)$$

where

$$j_{s,\text{even}} = -N_0 e D \left(2eA - \frac{1}{r} \right) \int_{-E_c}^{E_c} d\varepsilon \Im (f_{\text{even}} \tilde{f}_{\text{even}}) \tanh \left(\frac{\beta \varepsilon}{2} \right), \quad (17)$$

is the electric current density associated with the even-frequency correlations and

$$j_{s,\text{odd}} = N_0 e D \left(2eA - \frac{1}{r} \right) \int_{-E_c}^{E_c} d\varepsilon \Im (f_{\text{odd}} \tilde{f}_{\text{odd}}) \tanh \left(\frac{\beta \varepsilon}{2} \right), \quad (18)$$

is the electric current density associated with the odd-frequency correlations.

Abrikosov vortex lattice of thin film Al

In order to compare the typical Abrikosov vortex with the MTF vortex structure, we measured a zero-bias conductance map in the same area as the map shown in Fig. 4A, but now with an applied magnetic field of $B^\perp = 30$ mT and $B^\parallel = 0$ T (Fig. S9A). The map shows several round vortices, which are likely influenced by the tip during scanning (fast scan direction: horizontal). We characterize the Abrikosov vortex structure by taking spectra along a horizontal line, plotted in Fig. S9B. We observe that the spectral gap reduces gradually towards the vortex core and can reproduce this trend by solving the self-consistent gap equation in the absence of in-plane fields (Fig. S9C), while keeping the other parameters the same as in Fig. 4E. The zero-bias conductance profile, as plotted in Fig. 4B, shows a much sharper peak, compared to the MTF vortex.

In-plane magnetic field dependence on three thin Al films

The measurement in Fig. 3C is repeated on two additional films with coverages of 11.7 ML, and 5.6 ML, as shown in Fig. S10A-B. Additionally, we plot the extracted gap values as a function of B^\parallel in Fig. S10C, for each of the four film coverages presented in Fig. 3C and Fig. S10A-B. We find that the gap values are robust against B^\parallel fields, demonstrating that the MTF effect can be understood as the Zeeman shifting of two spin-polarized gap functions, without a modification of the gap value. We note that the presented spectrum at $B^\parallel = 4.0$ T in Fig. S10B is likely influenced by a nearby MTF vortex.

Zero-bias conductance maps in in-plane and vector magnetic fields

To ascertain the origin of the vortex structure in Fig. 6, we imaged the zero-bias conductance in large in-plane magnetic field ($B^{\parallel} = 4$ T) for a 5.6 ML Al film in an 800 nm x 500 nm image (Fig. S11A/B). By measuring the density of vortices, we can estimate the number of flux lines that penetrate the film due to an out-of-plane component. While the sparsity of objects is low in Fig. S11B, we estimate that the intervortex distance d is between 400 – 450 nm. Using $B^{\text{tilt}} = \sqrt{4/3} \Phi_0 / d^2$, we find that the corresponding out-of-plane component is $B^{\text{tilt}} \sim 12$ to 15 mT. The angle between the applied field ($B^{\parallel} = 4$ T) and the sample is therefore $\alpha_{\text{tilt}} \sim 0.2^\circ$. We suspect that the placement of the Si wafer on the sample plate is the main contribution to this angle, for this particular sample. By measuring the zero-bias conductance for the same area in a vector magnetic field of $B^{\parallel} = 3$ T and $B^{\perp} = 30$ mT, we expect a total out-of-plane component of either ~ 40 mT ($B^{\perp} + B^{\text{tilt}}$) or ~ 20 mT ($B^{\perp} - B^{\text{tilt}}$), depending on the orientation of the tilt. From the flux density in Fig. S11C, we conclude that B^{\perp} and B^{tilt} align, resulting in a higher vortex density. Comparable tilt angles are expected for all samples in this study.

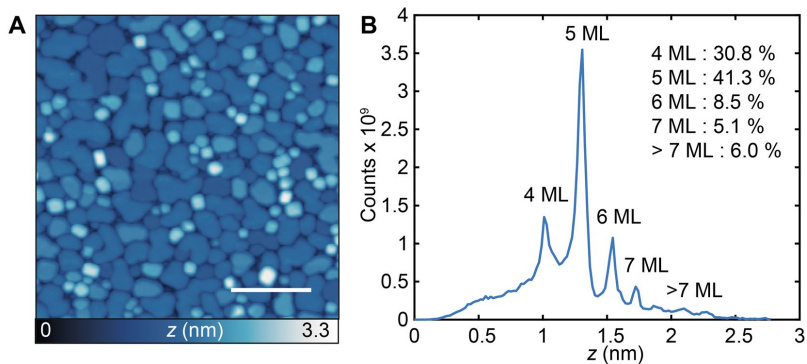


Fig. S1. Coverage calibration with room-temperature growth. (A) Constant-current image of Al islands grown on Si(111)-(7x7) after depositing Al for 12 minutes ($V_s = 1$ V, $I_t = 10$ pA, scale bar = 50 nm, $T \approx 7$ K). (B) Apparent height histogram of (A) with layer numbers assigned. Inset numbers: percentages for each layer thickness as extracted by flooding analysis.

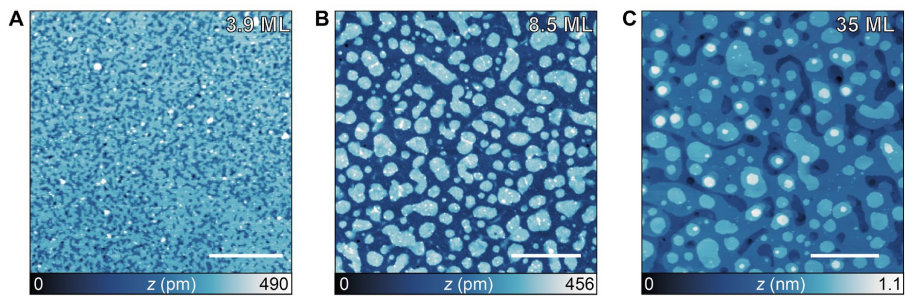


Fig. S2. Morphology of various coverages. Constant-current STM images of Al films with (A) 3.9 ML, (B) 8.5 ML, and (C) 35.1 ML coverages ($V_s = 1 \text{ V}$, $I_t = 10 \text{ pA}$, scale bar = 50 nm, (A,B) $T \approx 30 \text{ mK}$ and (C) $T \approx 7 \text{ K}$).

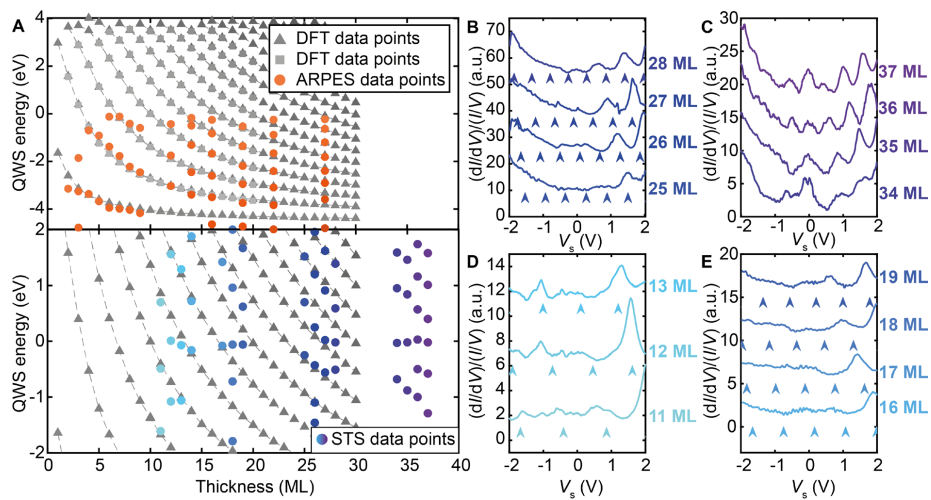


Fig. S3. dI/dV comparison to QWS derived from DFT and ARPES. (A) Calculated QWS energies from DFT (gray), extracted from ref. (42, 43), and ARPES peak positions (orange), extracted by eye from ref. (44), for Al(111) films on Si(111) as a function of film thickness. (B-E) dI/dV spectra normalized by the total conductance I/V , obtained for four Al films with coverages of (B) 26.3 ML, (C) 35.1 ML, (D) 11.7 ML and (E) 17.4 ML, where the arrows indicate the DFT energies in (A) (stabilized $V_s = 2$ V, $I_t = 200$ pA or 500 pA, $V_{mod} = 5$ mV, (B,C,E) $T \approx 30$ mK and (D) $T \approx 7$ K).

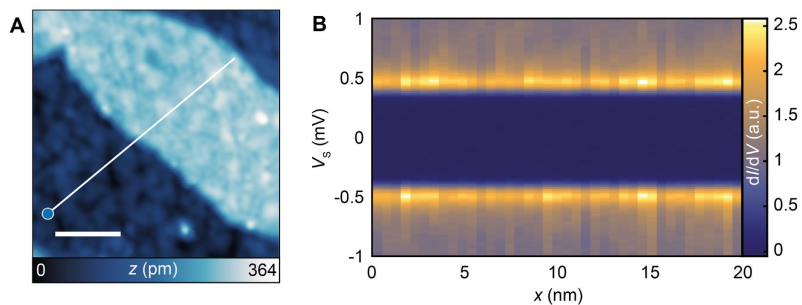


Fig. S4. Spatial measurement of superconductivity. (A) Constant-current STM image of an Al film with 8.5 ML coverage ($V_s = 100$ mV, $I_t = 10$ pA, scale bar = 5 nm). (B) dI/dV spectra along a line across 8 ML and 9 ML regions and across the long-range periodicity (line indicated in (A)); each spectrum is stabilized at $V_s = 3$ mV, $I_t = 200$ pA, $V_{\text{mod}} = 20$ μ V).

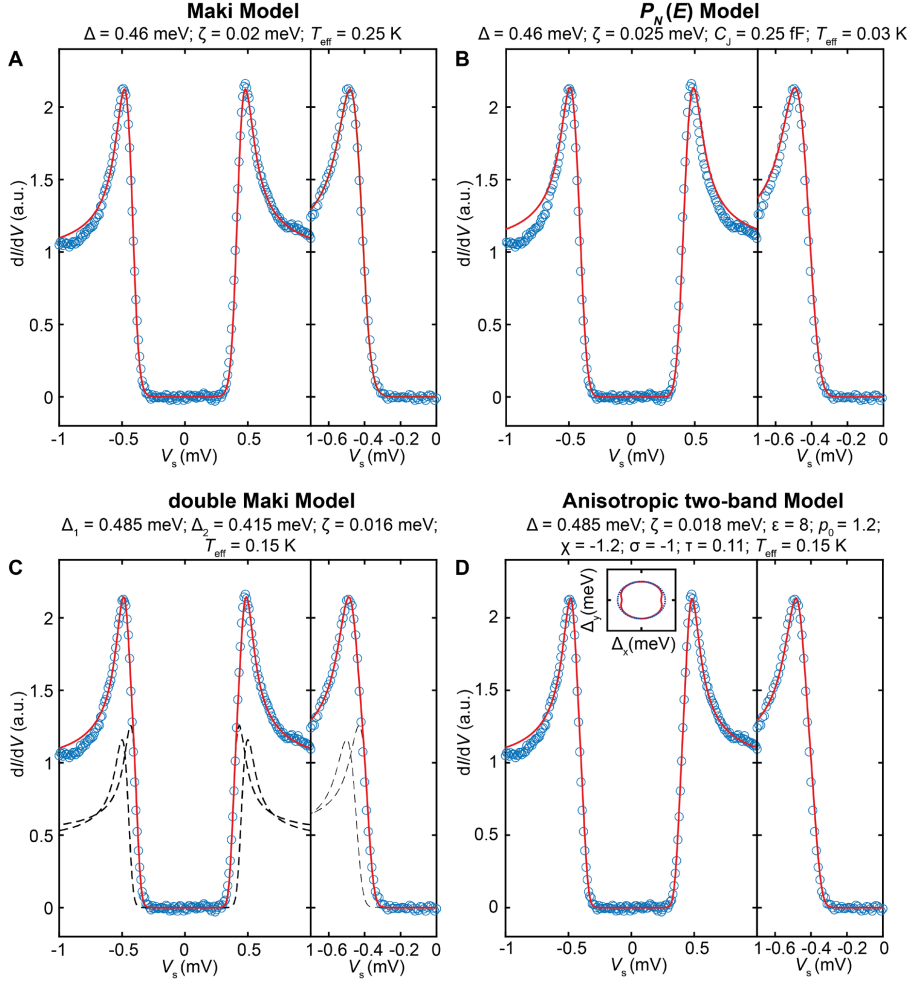


Fig. S5. Comparison of different fitting methods and broadening contributions. Example of a typical superconducting gap spectrum (blue dots) measured on an Al film with 8.5 ML coverage, compared to different models (red lines) (stabilized at $V_s = 3$ mV, $I_t = 200$ pA, $V_{\text{mod}} = 20$ μ V). (A) Fit with the Maki equation, (B) a $P_N(E)$ broadening Maki equation, (C) a double Maki equation using two different gap sizes Δ_1 and Δ_2 (individual contributions in black dashed lines), and (D) a Maki-based anisotropic two-band model. The fitting parameters, indicated above each plot, are the gap size Δ , the Maki broadening ζ , the effective temperature T_{eff} , the junction capacitance C_j , the degree of anisotropy $\varepsilon = \frac{m_x^*}{m_y^*} - 1$ and the effective mass m_i^* of the Al band in direction i , $p_0 = \tau/\mu$, $\sigma = \delta/\mu$, $\chi = m^*/m_x^*$, τ is the coupling between bands, μ is the chemical potential, and δ is the energy offset between bands. The inset of (D) shows the resulting anisotropic gap structure.

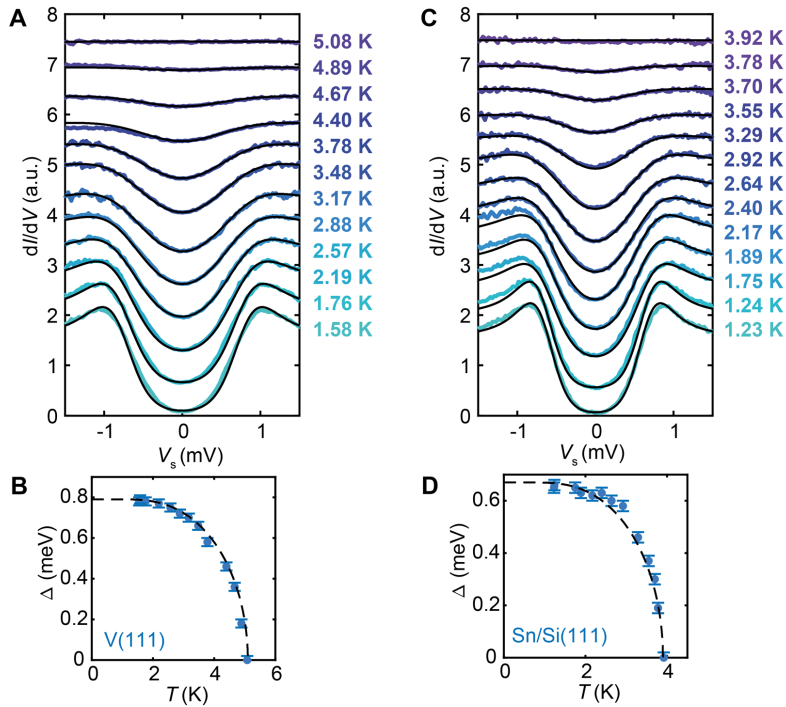


Fig. S6. Temperature calibration of the temperature dependent measurements made above 1 K.

(A) Superconducting gap measurements as a function of STM temperature (see legend; artificially offset) on bulk V(111) (stabilized at $V_s = 5$ mV, $I_t = 300$ pA, $V_{\text{mod}} = 100$ μ V). (B) Extracted $\Delta(T)$ fitted with the BCS equation (dashed line). (C) Superconducting gap measurements as a function of STM temperature (artificially offset) for a Sn film with an estimated coverage of 120-150 ML, grown on Si(111) (stabilized at $V_s = 5$ mV, $I_t = 300$ pA, $V_{\text{mod}} = 100$ μ V). (D) Extracted $\Delta(T)$ fitted with the BCS equation (dashed line).

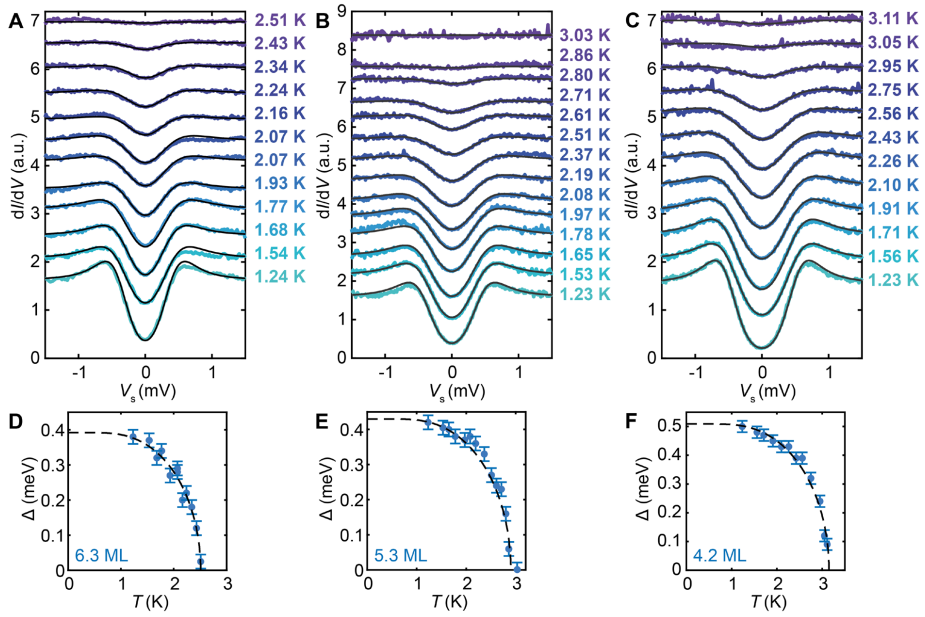


Fig. S7. Temperature dependence of three Al films. (A-C) Temperature dependent spectra (artificially offset) fitted with the Dynes equation (stabilized at $V_s = 5$ mV, $I_t = 300$ pA, $V_{\text{mod}} = 100$ μ V). (D-F) Extracted $\Delta(T)$ fitted with the BCS equation (dashed lines). The film coverages of (A,D) 6.3 ML, (B,E) 5.3 ML and (C,F) 4.2 ML yield a BCS ratio of 3.63 ± 0.02 , 3.44 ± 0.02 and 3.75 ± 0.01 respectively (see Fig. 2E).

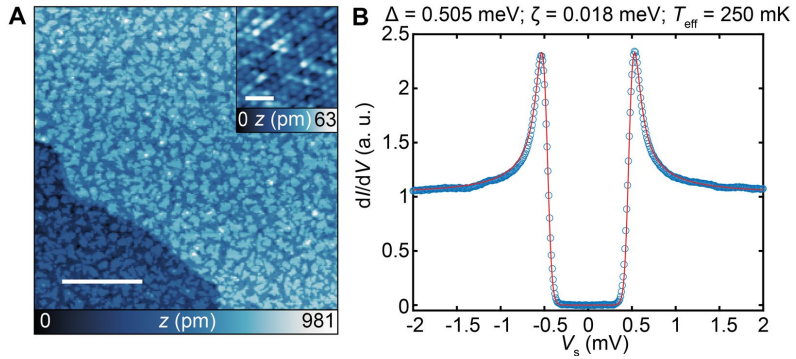


Fig. S8. Morphology and superconductivity after minimal annealing. (A) Constant-current image of the morphology of an 8.5 ML Al film after cold-growth and minimal annealing (transfer time of ~ 1 minute; $V_s = 2$ V, $I_t = 10$ pA, scale bar = 50 nm, $T \approx 7$ K). Inset: Constant-current STM image showing atomic resolution in a flat region ($V_s = 3$ mV, $I_t = 500$ pA, scale bar = 1 nm). (B) Spatially averaged superconducting gap fitted with the Maki equation (red line; parameters indicated above graph; stabilized at $V_s = 3$ mV, $I_t = 200$ pA, $V_{\text{mod}} = 20$ μ V).

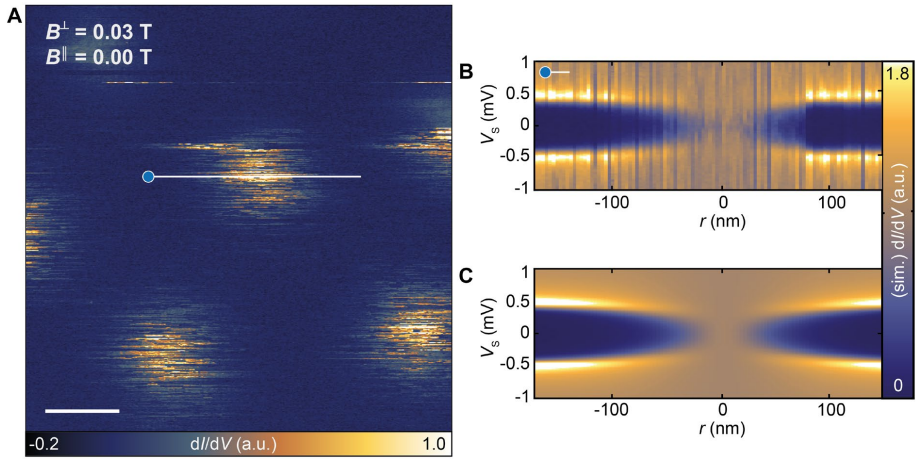


Fig. S9. Abrikosov vortices. (A) Constant-contour dI/dV map with $B^\perp = 30$ mT ($B^\parallel = 0.0$ T) for an 8.5 ML film (height recorded at $V_s = 10$ mV, $I_t = 10$ pA; image taken with $V_s = 0$ mV and z-offset = 100 pm, $V_{\text{mod}} = 50$ μ V, scale bar = 100 nm). (B) dI/dV spectra along a horizontal line across a vortex core (stabilized at $V_s = 3$ mV, $I_t = 200$ pA, $V_{\text{mod}} = 20$ μ V). (C) Simulated dI/dV signal by solving the self-consistent gap equation using $h^\parallel/\Delta^\infty = 0$, $\xi = 42$ nm, $\Gamma = 0.001 \Delta^\infty$, $\kappa = 5$, and broadened with $T_{\text{eff}} = 250$ mK.

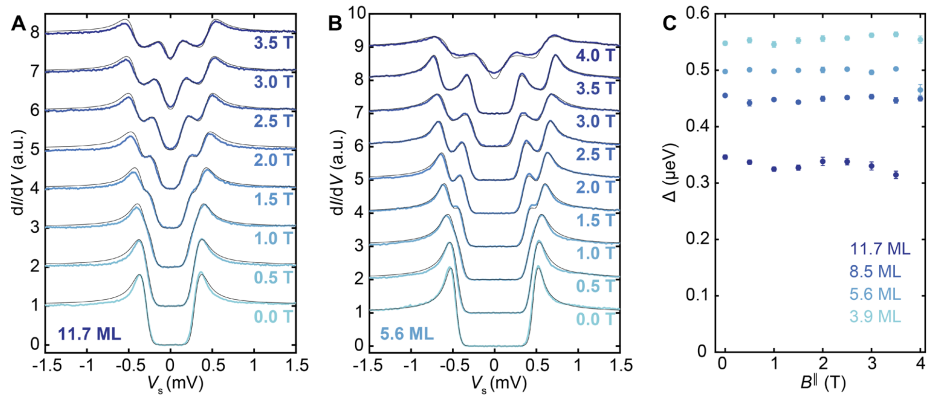


Fig. S10. In-plane magnetic field dependence for two additional Al films. Evolution of the SC gap in in-plane magnetic field B^{\parallel} for film coverages of (A) 11.7 ML, and (B) 5.6 ML. Black lines are fits using a double-Maki fit with Zeeman splitting (stabilized at $V_s = 3$ mV, $I_t = 200$ pA, $V_{\text{mod}} = 20$ μ V) (C) Extracted Δ for four Al coverages (also see Fig. 3C) as a function of B^{\parallel} . Note that Δ stays approximately constant while the two spin-polarized gaps shift with respect to each other by ΔE_z (see Fig. 3D)

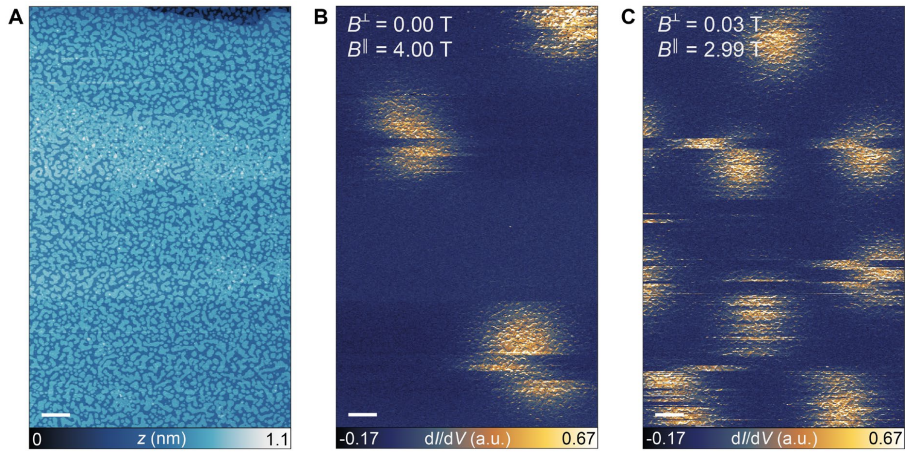


Fig. S11. Zero-bias conductance in large in-plane and vector fields. (A) Constant-current STM image of a 5.6 ML Al film and (B) simultaneously recorded constant-contour dI/dV map with $B^{\parallel} = 4$ T ($B^{\perp} = 0$ mT). (C) Constant-contour dI/dV map with $B^{\perp} = 30$ mT and $B^{\parallel} = 2.99$ T (height profiles recorded at $V_s = 10$ mV, $I_t = 10$ pA; dI/dV maps taken with $V_s = 0$ mV and z -offset = 100 pm, $V_{\text{mod}} = 50$ μ V, scale bar = 50 nm).

PAPER IX

Reference

Eirik Holm Fyhn, Arne Brataas, Alireza Qaiumzadeh, and Jacob Linder,

Quasiclassical theory for antiferromagnetic metals.

Physical Review B **107**, 174503 (2023)

doi: 10.1103/physrevb.107.174503

CONTRIBUTIONS

EHF determined the methodology for the derivation of all the equations presented in the manuscript and performed all the analytical work. EHF also wrote the first draft and made all the figures presented in the paper. All authors contributed to the physics discussions and the final manuscript.

Quasiclassical theory for antiferromagnetic metals

Eirik Holm Fyhn , Arne Brataas , Alireza Qaiumzadeh , and Jacob Linder

Center for Quantum Spintronics, Department of Physics, Norwegian University of Science and Technology, NO-7491 Trondheim, Norway



(Received 25 October 2022; revised 18 April 2023; accepted 24 April 2023; published 2 May 2023)

Unlike ferromagnetism, antiferromagnetism cannot readily be included in the quasiclassical Keldysh theory because of the rapid spatial variation in the directions of the magnetic moments. The quasiclassical framework is useful because it separates the quantum effects occurring at length scales comparable to the Fermi wavelength from other length scales, and has successfully been used to study a wide range of phenomena involving both superconductivity and ferromagnetism. Starting from a tight-binding Hamiltonian, we develop general quasiclassical equations of motion and boundary conditions, which can be used to describe two-sublattice metallic antiferromagnets in the dirty limit. The boundary conditions are applicable also for spin-active boundaries that can be either compensated or uncompensated. Additionally, we show how nonuniform or dynamic magnetic textures influence the equations and we derive a general expression for observables within this framework.

DOI: [10.1103/PhysRevB.107.174503](https://doi.org/10.1103/PhysRevB.107.174503)

I. INTRODUCTION

The quasiclassical Keldysh Green's function technique [1–5] is a powerful tool to study mesoscopic structures [5–24]. It is applicable to systems where the Fermi wavelength is much smaller than all other length scales and can be used to study a wide range of systems, including heterostructure with multiple competing types of order, such as superconductivity and ferromagnetism [6–12], both in and out of equilibrium. In addition, the quasiclassical framework is versatile in regards to sample geometry [18–20] and the details of external or intrinsic fields, such as applied magnetic fields [22,23] or spin-orbit coupling [15,21], whether they are time dependent [9,13–15] or spatially inhomogeneous [11,20,24]. This makes the quasiclassical framework especially useful to the field of superconducting spintronics [25], which aims to utilize superconductivity in the field of spintronics. In spintronics, spin is used as an information carrier rather than the electric charge used in conventional electronics [26,27]. The combination of superconductivity and magnetism is therefore at the core of superconducting spintronics.

While the presence of a magnetic field typically suppresses superconductivity, the relationship between ferromagnets and superconductors (SC) can be synergistic [8,25]. The interplay between magnetic and superconducting orders may give rise to spin-polarized superconductivity, which can transport spin angular momentum with zero resistance [8,28], and the presence of superconductivity has also been shown to be beneficial for other central effects in spintronics, such as giving rise to infinite magnetoresistance [29].

Antiferromagnets (AFs) have many important advantages over ferromagnets in the context of spintronics [30]. The alternating magnetic moments mean that they are more robust and impervious to external magnetic fields while creating negligible magnetic stray fields of their own. As a result, they are less intrusive to neighboring components. Moreover, the resonance frequencies in AFs are on the order of terahertz [31,32], which allows for very fast information processing.

The fact that spin transport has been shown to be long ranged in AFs [33] also makes them promising and an active research topic in spintronics.

Superconductivity may coexist with antiferromagnetism [34–36], and AFs have a prominent role in the context of high- T_c superconductivity [36–38]. Despite this, AFs are much less studied in the field of superconducting spintronics compared to ferromagnets. Heterostructures composed of superconductors and ferromagnets, including strongly polarized ferromagnets [6], has been studied theoretically in a wide range of systems [6–12], including in systems with complex geometries [19,20]. On the other hand, while antiferromagnetic-superconductor junctions have been studied theoretically [39–44], such studies are typically limited to simple geometries and clean systems. This is because the rapid variation of the magnetic moments in AFs means that they, unlike ferromagnets, cannot readily be incorporated into the quasiclassical framework used for normal metals. The quasiclassical Keldysh theory separates the short-range quantum effects from the long-range semiclassical dynamics, thereby allowing the inclusion of long-range spatial and temporal gradients. As such, it is desirable with a quasiclassical framework that is applicable to systems with both superconductivity and AFs.

One approach, which has been used previously when studying the superconducting proximity effect in antiferromagnetic metals (AFMs) [45–47], is to treat the AFM as a normal metal. The reasoning is that the magnetic order is compensated on the length scale of the superconducting correlation length. Using this framework, Hübener *et al.* [45] studied AFM/SC/AFM structures and found an anomalous strong suppression of the proximity effect happening when the thickness of the AFM exceeded around 6 nm. They argued that the drop in superconducting critical temperature could possibly be associated with the onset of an incommensurate spin-density wave (SDW) state. However, based on the theory presented in the present paper, the observed suppression is expected even without the SDW state. This is because Hübener

et al. [45] also reported a mean free path of 5.3 nm for their samples, and the theory presented here shows that even non-magnetic impurities behave magnetically in the presence of antiferromagnetic order. As such, conventional, spin-singlet superconductivity can be expected to be suppressed in antiferromagnetic systems when they enter the diffusive regime, and in particular more so than in diffusive normal metals. This happens when the system size exceeds the mean free path, which was exactly the case in Ref. [45].

Quasiclassical equations of motion for AFMs, but without superconductivity, have been derived by Manchon [48]. This was done by defining sublattice-resolved Green's function. Such Green's functions can be treated quasiclassically because, while the magnetic order varies rapidly in the antiferromagnet, the Néel order varies slowly. More recently, Bobkov *et al.* [49] derived a sublattice-resolved quasiclassical theory for antiferromagnetic insulators with superconductivity. Other related types of magnetically ordered systems that have been studied within quasiclassical theory are spiral ferromagnets [50,51] and SDW AFs [52,53]. Spiral ferromagnets have compensated magnetic order similar to AFs. However, in order for these to be treated quasiclassically, the spatial modulation of the magnetic order must be slow compared to the Fermi wavelength. SDW is also a state of matter with spatial modulation of the magnetic order, typically formed by itinerant particles with Fermi-surface nesting [54,55]. SDW can also coexist with SC [54,56], and quasiclassical theory has been developed to model systems with both SDW and SC [52,53]. This is possible because the SDW state can be modeled using a mean-field approach with a slowly varying SDW order parameter.

Here, we develop quasiclassical equations of motion for two-sublattice AFMs with superconductivity and impurities, as well as external fields and spin-orbit coupling, and where all the parameters, including the direction of the Néel vector, may be inhomogeneous in time and space, as long as it is not rapidly varying on the atomic length scale. We also develop boundary conditions for the diffusive regime, which work also for spin-active interfaces that can be either uncompensated or compensated. Because we consider antiferromagnetic metals, we assume that the Fermi level is deep within the conduction band compared to other energy scales except for the exchange energy between localized spins and itinerant electrons, as illustrated in Fig. 1. This exchange energy may be either large or small compared to the distance between the Fermi level and the edges of the conduction band. The quasiclassical theory can therefore not be used to model heavy-fermion antiferromagnetic superconductors, where the Fermi energy is comparable to the superconducting gap [57]. On the other hand, it is well suited to study heterostructures or other systems in which the Fermi level can be assumed to lie deep within the conduction band.

Although our starting point is similar to that presented in Refs. [48,49], except that we additionally consider the other effects mentioned above, there are a few important differences. Instead of equations for sublattice-resolved Green's functions, we derive equations for the conduction band Green's functions. This is possible because there is no rapidly varying magnetic order for these Green's functions, just as there is no rapidly varying magnetic order for

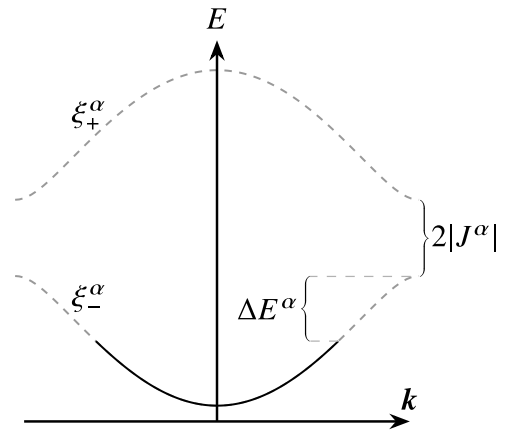


FIG. 1. A sketch of the energy bands in an antiferromagnet, where $\xi_{\pm}^{\alpha} = -\mu^{\alpha} \pm \sqrt{(J^{\alpha})^2 + (K^{\alpha})^2}$. Here, α labels different materials, μ^{α} is the chemical potential, J^{α} is the exchange coupling between itinerant electrons and localized magnetic moments and K^{α} is the kinetic energy and ΔE^{α} is the smallest difference between the Fermi level and the edges of the conduction band. The gap between the energy bands is $2|J^{\alpha}|$. This gap can be arbitrary within the quasiclassical theory developed here, but ΔE^{α} must be large compared to other energies in the system, not including the gap.

sublattice-resolved Green's functions. The reason why we project onto the conduction band is that only states close to the Fermi level contribute to the quasiclassical Green's function, and the Fermi level lies deep inside the conduction band. As a result, we end up with fewer Green's functions to solve for. More importantly, however, it means that the chemical potential drops out of the equations, similar to how it drops out in Keldysh theory for normal metals. Therefore, we can consistently let it be much larger than other energies. This procedure, leaving only the conduction band, means that the spin- and sublattice degrees of freedom are not independent. An important consequence of this fact is that the effect of nonmagnetic impurities in AFMs is similar to the effect of magnetic impurities in normal metals.

We summarize the main results, outline how they are derived, and describe the necessary assumptions in Sec. II. The derivations are presented in Secs. III–XIV. This includes the derivation of quasiclassical equations of motion, boundary conditions for the diffusive regime and a general expression for computing observables. Concluding remarks are given in Sec. XV.

II. OUTLINE

The main results are equations for the isotropic part of the quasiclassical Green's function $\check{g}_{\alpha}^{\check{\nu}}$ and the matrix current $\check{j}_{\alpha}^{\check{\nu}}$, where α labels the materials in the junction. Under the assumptions that the quasiclassical Green's function is approximately spherically symmetric and that the energy difference between the Fermi level and the edges of the conduction band is larger than all other energy scales, except

possibly the exchange energy J^α , we find in Sec. XI that \check{g}_s^α and \check{j}^α solve

$$i\tilde{\nabla} \circ \check{j}^\alpha + \left[\tau_z \varepsilon - \check{V}_s^\alpha + \frac{i(J^\alpha)^2}{2\tau_{\text{imp}}^\alpha (\eta^\alpha)^2} \sigma_z \tau_z \check{g}_s^\alpha \sigma_z \tau_z, \check{g}_s^\alpha \right] = 0, \quad (1a)$$

$$\check{j}^\alpha = -\check{g}_s^\alpha \circ \tilde{\nabla} \circ (D^\alpha \check{g}_s^\alpha) - \check{g}_s^\alpha \circ \left[\frac{(J^\alpha)^2}{2(\eta^\alpha)^2} \sigma_z \tau_z \check{g}_s^\alpha \sigma_z \tau_z, \check{j}^\alpha \right], \quad (1b)$$

where all the symbols are explained below. In the absence of antiferromagnetism, $J^\alpha \rightarrow 0$, Eq. (1) reduces to the well-known Usadel equation for normal metals [4]. In the limit of very strong exchange coupling, such that $(J^\alpha/\eta^\alpha)^2 \rightarrow 1$, the short-range correlations become negligible in the diffusive limit, as we show in Sec. XI.

The itinerant electrons in an AFM are described by a Hamiltonian including kinetic energy K^α , exchange energy to the magnetic lattice J^α , chemical potential μ^α , as well as other additional terms coming from superconductivity, impurity scattering, external fields, or spin-orbit coupling. Equation (1) is valid under the assumption that K^α at the Fermi level is large compared to all additional energies such as the impurity scattering rate and the superconducting gap. Note that K^α need not be large compared to J^α . As a result, the fraction $(J^\alpha)^2/(\eta^\alpha)^2$, where $\eta^\alpha = \sqrt{(J^\alpha)^2 + (K^\alpha)^2}$, can take any value between 0 and 1.

The second assumption behind Eq. (1) is that the system is in the dirty regime. This means two things. First, it means that the elastic impurity scattering rate $1/\tau_{\text{imp}}$ is dominant out of all the additional energies in the system, not including K^α , J^α , and μ^α . Second, it means that the matrix current \check{j}^α is small compared to the Fermi velocity. As we show in Sec. XI, this is the case if the variation in \check{g}_s^α is small compared to 1 over the length of the mean free path, either because the mean free path is short or because the proximity effect is weak.

To complete the theory for use in systems involving more than one material, we derive the boundary condition

$$e_n \cdot \check{j}^\alpha = [\hat{j}_l^{\alpha\beta} \circ \check{g}_s^\beta(\mathbf{x}_l^\beta) \circ \hat{j}_l^{\beta\alpha} + i(S_c^\alpha)^T \hat{R}_l S_c^\alpha \cdot \check{g}_s^\alpha]_\circ, \quad (2)$$

which are valid when the quasiclassical Green's function is isotropic also close to the interface. This is the case for instance when the tunneling is weak. Equation (2) can be used to model interfaces that are compensated or uncompensated, magnetic or nonmagnetic, and conducting or isolating. In the absence of antiferromagnetism, Eq. (2) reduces to the generalized Kupriyanov-Lukichev boundary condition for spin-active boundaries [58,59].

In Sec. XIV, we derive a general expression for computing observables, which can be used to compute quantities such as densities and currents once \check{g}_s^α and \check{j}^α have been found. The expression, Eq. (198), contains not only the contribution from states captured by the quasiclassical Green's function but also a general expression for the contribution from states further away from the Fermi level.

We present a detailed, self-contained derivation of Eqs. (1) and (2), starting from a general tight-binding Hamiltonian with a tunneling contact, introduced in Sec. III. The full Green's functions and their equations of motion are presented in Sec. IV. Impurity averaging is performed in Sec. V, where

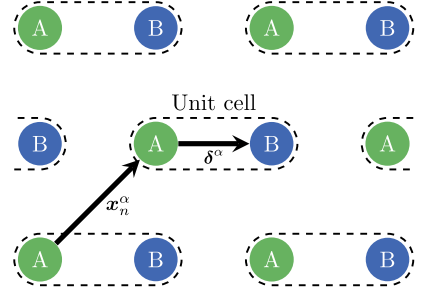


FIG. 2. Sketch of a plane in material α for the case of a square lattice. Each unit cell contains two orbitals. One is located at sublattice A, \mathbf{x}_n^α , and one is located at sublattice B, $\mathbf{x}_n^\alpha + \delta^\alpha$.

we derive the impurity self-energy to second order in the impurity potential. This is valid as long as the impurity potential is weak, but since the self-energy depends only on the isotropic part of the Green's function, effects such as skew scattering [60] would require going to third order. In Sec. VI, we use the tunneling Hamiltonian to remove the intermaterial Green's functions from the equations of motion. In Sec. VII we Fourier transform in relative coordinates, and it is taken into consideration both that the system is defined on a discrete lattice and, more importantly, different matrix elements correspond to different relative spatial positions because of the relative displacement between the two sublattices. In Sec. VIII we transform the Green's functions into the basis of the antiferromagnetic energy bands, and thereby extract the conduction band. From this, we carefully define the quasiclassical Green's functions in Sec. IX and use them to remove higher-order spatial derivatives from the gradient expansion. Next, in Sec. X, we derive the quasiclassical expression for the impurity scattering and show how it is modified by the antiferromagnetic order. The main results are then derived in Sec. XI and Sec. XII. Finally, in Sec. XIII we show how the equations are influenced by nonuniform magnetic textures.

III. HAMILTONIAN

We consider a system composed of two materials, which we label material L and material R , connected through a tunneling contact. The Hamiltonian is

$$\mathcal{H}(t) = \mathcal{H}_L(t) + \mathcal{H}_R(t) + \mathcal{H}_T. \quad (3)$$

Here,

$$\mathcal{H}_\alpha(t) = \sum_{n,m \in A_\alpha} c_n^{\alpha\dagger} [H_0^\alpha(t) + V^\alpha(t)]_{nm} c_m^\alpha, \quad (4)$$

where $\alpha \in \{L, R\}$ denotes material, A_α is the set of unit cells in material α . As sketched in Fig. 2, each unit cell, labeled by a 3-tuple n , contains one orbital associated with the A -sublattice at position \mathbf{x}_n^α , and one orbital associated with the B -sublattice at position $\mathbf{x}_n^\alpha + \delta^\alpha$. We let the annihilation operators for the orbitals with spin σ at unit cell n in material

α at the A - and B -sublattice be $c_{nA\sigma}^\alpha$ and $c_{nB\sigma}^\alpha$, respectively, and define

$$c_n^{\alpha\uparrow} = (c_{nA\uparrow}^{\alpha\uparrow} c_{nA\downarrow}^{\alpha\uparrow} c_{nB\uparrow}^{\alpha\uparrow} c_{nB\downarrow}^{\alpha\uparrow} c_{nA\downarrow}^\alpha - c_{nA\uparrow}^\alpha c_{nB\downarrow}^\alpha - c_{nB\uparrow}^\alpha). \quad (5)$$

We include only nearest-neighbor hopping and assume that this hopping is only between the two different sublattices. The hopping parameter t^α , chemical potential μ^α , and the exchange energy J^α between localized spins and conducting electrons are collected in H_0^α . The full electrochemical potential need not be constant. However, we take μ^α to be constant. Any deviation in the electrochemical potential away from μ^α is included in V^α . If σ is the vector of Pauli matrices in spin-space, τ are the Pauli matrices in Nambu-space, and ρ are the Pauli matrices in sublattice space, then

$$\begin{aligned} (H_0^\alpha)_{nm}(t) &= -\frac{1}{4}t^\alpha(\rho_x + i\rho_y)\tau_z\chi_{\text{N.N.}}(\mathbf{x}_n^\alpha - \delta^\alpha - \mathbf{x}_m^\alpha) \\ &\quad -\frac{1}{4}t^\alpha(\rho_x - i\rho_y)\tau_z\chi_{\text{N.N.}}(\mathbf{x}_n^\alpha + \delta^\alpha - \mathbf{x}_m^\alpha) - \frac{1}{2}\delta_{nm}\mu^\alpha\tau_z \\ &\quad -\frac{1}{2}\delta_{nm}J^\alpha\rho_z\sigma \cdot \left[\frac{1+\rho_z}{2}\mathbf{n}(\mathbf{x}_n^\alpha, t) + \frac{1-\rho_z}{2}\mathbf{n}(\mathbf{x}_n^\alpha + \delta^\alpha, t) \right], \end{aligned} \quad (6)$$

where $\mathbf{n} = (\sin\theta\cos\phi, \sin\theta\sin\phi, \cos\theta)$ is the direction of the Néel vector, and $\chi_{\text{N.N.}}(\mathbf{x})$ is a nearest neighbor characteristic function, which is 1 if \mathbf{x} is a nearest neighbor vector between a A -lattice point and a B -lattice point and 0 otherwise. Because the direction Néel vector generally is influenced by the dynamics of the itinerant electron, it should be solved for self-consistently. This can be done with the Landau-Lifshitz-Gilbert equation [30].

The term proportional to V^α in Eq. (4) contains all additional effects that may be present in the model, such as superconductivity, external spin-splitting fields and corrections to the hopping term from the vector potential or spin-orbit coupling. Additionally, V^α importantly also determines the spatial geometry of material α by a potential that is zero inside the material and very large outside the material. We can therefore let the lattice A_α run to infinity in all spatial directions, meaning that $A_\alpha = \mathbb{Z}^3$, where \mathbb{Z} is the set of integers, while still having the system be confined to a finite region of space. Note that the potential can also be spin dependent, for instance if there is a spin-splitting field in the neighboring region. This will influence the boundary condition we derive in Sec. XII.

Finally, the tunneling Hamiltonian is

$$\mathcal{H}_T = \sum_{n,m \in \mathbb{Z}^3} c_n^{L\dagger} T_{nm}^{LR} c_m^R = \sum_{i,j \in \mathbb{Z}^3} c_n^{R\dagger} T_{nm}^{RL} c_m^L, \quad (7)$$

where T^{RL} and $T^{LR} = (T^{RL})^\dagger$ are matrices satisfying $T^{LR} = \text{diag}(T, i\sigma_y T^* i\sigma_y)$ for some 4×4 matrix T .

We rotate spin space such that the Néel vector is always parallel to the z axis. To do this we define the rotation matrix

$$R(\mathbf{x}, t) = \exp \left\{ -i \frac{\theta[\mathbf{n}(\mathbf{x}, t) \cdot \mathbf{e}_z] \cdot \boldsymbol{\sigma}}{2 \sin \theta} \right\}, \quad (8)$$

and

$$\tilde{c}_n^\alpha(t) = \left[\frac{1+\rho_z}{2} R^\dagger(\mathbf{x}_n^\alpha, t) + \frac{1-\rho_z}{2} R^\dagger(\mathbf{x}_n^\alpha + \delta^\alpha, t) \right] c_n^\alpha, \quad (9)$$

such that

$$\mathcal{H}_\alpha(t) = \sum_{n,m \in \mathbb{Z}^3} \tilde{c}_n^{\alpha\dagger}(t) [\tilde{H}_0^\alpha(t) + \tilde{V}^\alpha(t)]_{nm} \tilde{c}_m^\alpha(t), \quad (10)$$

where, if we assume that \mathbf{n} varies slowly in space over the distance of neighboring lattice points,

$$\begin{aligned} (\tilde{H}_0^\alpha)_{nm}(t) &= -\frac{1}{2}\delta_{nm}[J^\alpha\rho_z\sigma_z + \mu\tau_z] + \frac{1}{2}K_{nm}^\alpha\tau_z \\ &\quad -\frac{\tau_z}{2}(K_{nm}^\alpha[\mathbf{x}_n^\alpha - \mathbf{x}_m^\alpha] + [\delta^\alpha\rho_B, K_{nm}^\alpha]) \\ &\quad \cdot (R^\dagger\nabla R)(\mathbf{x}_n^\alpha, t). \end{aligned} \quad (11)$$

where the kinetic term is

$$\begin{aligned} K_{nm}^\alpha &= -\frac{t^\alpha}{2}[(\rho_x + i\rho_y)\chi_{\text{N.N.}}(\mathbf{x}_n^\alpha - \delta^\alpha - \mathbf{x}_m^\alpha) \\ &\quad + (\rho_x - i\rho_y)\chi_{\text{N.N.}}(\mathbf{x}_n^\alpha + \delta^\alpha - \mathbf{x}_m^\alpha)] \end{aligned} \quad (12)$$

Finally, we also define the projection operators in sublattice space,

$$\rho_A = \frac{1+\rho_z}{2} \quad \text{and} \quad \rho_B = \frac{1-\rho_z}{2}, \quad (13)$$

for ease of notation.

IV. GREEN'S FUNCTIONS AND EQUATIONS OF MOTION

In this section, we define the full Green's functions. These are the starting point of our derivation and will later be used to define the quasiclassical, impurity-averaged conduction band Green's functions, which are the objects of the final equations. To obtain the final equations we must first derive the equation of motion for the full Green's function. These are called the Gor'kov equations and are derived in this section.

The retarded, advanced, and Keldysh Green's functions are defined respectively as

$$\hat{G}_{nm}^{R,\alpha\beta}(t_1, t_2) = -i\tau_z \{ \tilde{c}_n^\alpha(t_1), \tilde{c}_m^{\beta\dagger}(t_2) \} \theta(t_1 - t_2), \quad (14a)$$

$$\hat{G}_{nm}^{A,\alpha\beta}(t_1, t_2) = +i\tau_z \{ \tilde{c}_n^\alpha(t_1), \tilde{c}_m^{\beta\dagger}(t_2) \} \theta(t_2 - t_1), \quad (14b)$$

$$\hat{G}_{nm}^{K,\alpha\beta}(t_1, t_2) = -i\tau_z \{ [\tilde{c}_n^\alpha(t_1), \tilde{c}_m^{\beta\dagger}(t_2)] \}. \quad (14c)$$

These are 8×8 matrices, and are collected in larger 16×16 matrices,

$$\check{G}_{nm}^{\alpha\beta} = \begin{pmatrix} \hat{G}_{nm}^{R,\alpha\beta} & \hat{G}_{nm}^{K,\alpha\beta} \\ \hat{G}_{nm}^{A,\alpha\beta} & \hat{G}_{nm}^{A,\alpha\beta} \end{pmatrix}, \quad (15)$$

and even larger 32×32 matrices,

$$\check{G}_{nm} = \begin{pmatrix} \check{G}_{nm}^{LL} & \check{G}_{nm}^{LR} \\ \check{G}_{nm}^{RL} & \check{G}_{nm}^{RR} \end{pmatrix}. \quad (16)$$

We use the notation that $\hat{\cdot}$ indicates a nontrivial matrix structure in Nambu-space, $\check{\cdot}$ indicates a nontrivial structure in Keldysh-space, and $\check{\cdot}$ indicates a nontrivial structure in material-space.

In order to derive the equations of motion, we use that any operator A evolves in time according to

$$\frac{\partial A}{\partial t} = i[\mathcal{H}, A] + \left(\frac{\partial A}{\partial t} \right)_{\mathcal{H}\mathcal{C}}. \quad (17)$$

From this, together with the relation $[AB, C] = A\{B, C\} - \{A, C\}B$, we find

$$\begin{aligned} \frac{\partial \tilde{c}_n^\alpha}{\partial t} = & -2i \sum_{m \in \mathbb{Z}^3} [\tilde{H}_0^\alpha(t) + \tilde{V}^\alpha(t)]_{nm} \tilde{c}_m^\alpha - i \sum_{m \in \mathbb{Z}^3} \tilde{T}_{nm}^{\alpha\beta} \tilde{c}_m^\beta \\ & - [\rho_A(R^\dagger \dot{R})(\mathbf{x}_n, t) + \rho_B(R^\dagger \dot{R})(\mathbf{x}_n + \delta, t)] \tilde{c}_n^\alpha, \end{aligned} \quad (18)$$

where $\beta \neq \alpha$, and

$$\begin{aligned} \frac{\partial \tilde{c}_n^{\alpha\dagger}}{\partial t} = & 2i \sum_{m \in \mathbb{Z}^3} \tilde{c}_m^{\alpha\dagger} [\tilde{H}_0^\alpha(t) + \tilde{V}^\alpha(t)]_{mn} + i \sum_{m \in \mathbb{Z}^3} \tilde{T}_{nm}^{\alpha\beta} \tilde{c}_m^\beta \\ & + \tilde{c}_n^{\alpha\dagger} [\rho_A(R^\dagger \dot{R})(\mathbf{x}_n, t) + \rho_B(R^\dagger \dot{R})(\mathbf{x}_n + \delta, t)]. \end{aligned} \quad (19)$$

From this, we derive the Gor'kov equations,

$$i\tau_z \frac{\partial \check{G}}{\partial t} - \check{\Sigma} \bullet \check{G} = \delta(t_1 - t_2) \delta_{nm}, \quad (20a)$$

$$\frac{\partial \check{G}}{\partial t'} i\tau_z + \check{G} \bullet \check{\Sigma} = -\delta(t_1 - t_2) \delta_{nm}, \quad (20b)$$

where

$$\check{\Sigma} = \begin{pmatrix} \hat{H}_0^L + \check{V}^L & \hat{T}^{LR} \\ \hat{T}^{RL} & \hat{H}_0^R + \check{V}^R \end{pmatrix}, \quad (21)$$

and

$$(\hat{H}_0^\alpha)_{nm}(t_1, t_2) = (K_{nm}^\alpha - \delta_{nm}[J^\alpha \rho_z \sigma_z \tau_z + \mu]) \delta(t_1 - t_2), \quad (22a)$$

$$(\hat{T}^{\alpha\beta})_{nm}(t_1, t_2) = \tilde{T}_{nm}^{\alpha\beta} \tau_z \delta(t_1 - t_2), \quad (22b)$$

$$\begin{aligned} \check{V}_{nm}^\alpha(t_1, t_2) = & (\check{\Sigma}_{\text{inel}}^\alpha)_{nm}(t_1, t_2) + \{2\tilde{V}_{nm}^\alpha(t) \\ & - \tau_z [K_{nm}^\alpha [\mathbf{x}_n^\alpha - \mathbf{x}_m^\alpha] + [\delta^\alpha \rho_B, K_{nm}^\alpha]] \\ & \cdot (R^\dagger \nabla R)(\mathbf{x}_n^\alpha, t_1) \\ & - i[\rho_A(R^\dagger \dot{R})(\mathbf{x}_n, t_1) + \rho_B(R^\dagger \dot{R})(\mathbf{x}_n + \delta, t)] \\ & \times \delta_{nm}\} \tau_z \delta(t_1 - t_2). \end{aligned} \quad (22c)$$

We have added in \check{V}_{nm}^α a term, which models inelastic processes $\check{\Sigma}_{\text{inel}}^\alpha$. The bullet product between two matrix-valued functions, A and B , is defined as

$$(A \bullet B)_{nm}(t_1, t_2) = \int_{-\infty}^{\infty} dt \sum_{l \in \mathbb{Z}^3} A_{nl}(t_1, t) B_{lm}(t, t_2). \quad (23)$$

We also define the circle-product to be the integral over time,

$$(A \circ B)(t_1, t_2) = \int_{-\infty}^{\infty} dt A(t_1, t) B(t, t_2). \quad (24)$$

From Eq. (20) we also get the Dyson equations,

$$\check{G} = \check{G}_0 + \check{G}_0 \bullet \delta \check{\Sigma} \bullet \check{G}, \quad (25a)$$

$$\check{G} = \check{G}_0 + \check{G} \bullet \delta \check{\Sigma} \bullet \check{G}_0, \quad (25b)$$

if $\check{\Sigma} = \check{\Sigma}_0 + \delta \check{\Sigma}$ and \check{G}_0 solves

$$i\tau_z \frac{\partial \check{G}_0}{\partial t_1} - \check{\Sigma}_0 \bullet \check{G}_0 = \delta(t_1 - t_2) \delta_{nm}, \quad (26a)$$

$$\frac{\partial \check{G}_0}{\partial t_2} i\tau_z + \check{G}_0 \bullet \check{\Sigma}_0 = -\delta(t_1 - t_2) \delta_{nm}. \quad (26b)$$

Equation (25) can be derived by taking bullet products of Eqs. (26a) and (26b) with \check{G} from the left and right, respectively, and using that $A \bullet (\partial B / \partial t_1) = -(\partial A / \partial t_2) \bullet B$ when $\lim_{t \rightarrow \pm\infty} A(t_1, t) B(t, t_2) = 0$.

V. IMPURITY AVERAGING

In this section, we average over impurities and identify the self-energy, which relates the impurity-averaged Green's function to the Green's function in the absence of impurities. The impurity-averaged Green's function can then be found by replacing the impurity potential in the Gor'kov equations with this self-energy. We determine this self-energy to second order in the impurity potential. This is valid under the assumption that the impurity potentials are weak, although the number of impurities may be large. By not going to third order, the self-energy depends only on the isotropic part of the Green's function and therefore does not capture effects such as skew scattering [60].

Let $m^{\alpha X}$ be the number of impurities in material α on sublattice $X \in \{A, B\}$. Next, we assume that the impurity potentials are local and that the potential strength and position of the i th impurity in material α on sublattice X are $U_i^{\alpha X}$ and $r_i^{\alpha X}$, respectively. The self-energy term from the impurity potential is then

$$\begin{aligned} \check{V}_{nm}^{\text{imp}} = & \delta_{nm} \delta(t_1 - t_2) \\ & \times \sum_{X \in \{A, B\}} \left(\sum_{i=1}^{m^{LX}} \rho_X U_i^{LX} \delta_{nr_i^{LX}} \quad \sum_{i=1}^{m^{RX}} \rho_X U_i^{RX} \delta_{nr_i^{RX}} \right). \end{aligned} \quad (27)$$

Next, we define the impurity average as the sum over all possible impurity locations and impurity potential strengths, weighted by some normalized distribution function $p_{\text{imp}} : \{U_i\}, \{r_i\} \mapsto \mathbb{R}$, where $\{U_i\}$ and $\{r_i\}$ denote the set of potential strengths and locations, respectively. That is,

$$\begin{aligned} \langle A \rangle_{\text{imp}} = & \prod_{\alpha \in \{L, R\}} \prod_{X \in \{A, B\}} \prod_{i=1}^{m^{\alpha X}} \int_{-\infty}^{\infty} dU_i^{\alpha X} \\ & \times \sum_{r_i^{\alpha X} \in \mathbb{Z}^3} p_{\text{imp}}(\{U_i\}, \{r_i\}) A(\{U_i\}, \{r_i\}). \end{aligned} \quad (28)$$

We do not specify p_{imp} , but we assume it is such that impurities are independently and uniformly distributed. By assuming that they are uniformly distributed in space, we have that $\langle \delta_{nr_i^{\alpha X}} \rangle_{\text{imp}} = 1/N^\alpha = n_{\text{imp}}^{\alpha X} / m^{\alpha X}$, where N^α is the number of unit cells in material α and $n_{\text{imp}}^{\alpha X} = m^{\alpha X} / N^\alpha$ is the impurity density on sublattice X in material α . The assumption that impurities are independent means that $\langle U_i^{\alpha X} \delta_{nr_i^{\alpha X}} U_j^{\beta Y} \delta_{mr_j^{\beta Y}} \rangle_{\text{imp}} = \langle U_i^{\alpha X} \delta_{nr_i^{\alpha X}} \rangle_{\text{imp}} \langle U_j^{\beta Y} \delta_{mr_j^{\beta Y}} \rangle_{\text{imp}}$ if $i \neq j$, $\alpha \neq \beta$ or $X \neq Y$. Finally, we also assume that the strengths and locations

of impurities are uncorrelated, such that $\langle U_i^{\alpha X} \delta_{nr_i^{\alpha X}} \rangle_{\text{imp}} = \langle U_i^{\alpha X} \rangle_{\text{imp}} \langle \delta_{nr_i^{\alpha X}} \rangle_{\text{imp}}$, and that the impurities on each sublattice and material are identically distributed, such that $\langle U_i^{\alpha X} \rangle_{\text{imp}} = \langle U_j^{\alpha X} \rangle_{\text{imp}} =: \langle U^{\alpha X} \rangle_{\text{imp}}$ for all i and j .

To find how the impurity-averaged Green's function, $\check{G}_{\text{imp}} := \langle \check{G} \rangle_{\text{imp}}$ is related to the Green's function in the absence of impurities, \check{G}_0 , we take the impurity average of Eq. (25a) with $\delta \check{\Sigma} = \check{V}^{\text{imp}}$ to obtain

$$\check{G}_{\text{imp}} = \check{G}_0 + \check{G}_0 \bullet \langle \check{V}^{\text{imp}} \bullet \check{G} \rangle_{\text{imp}}. \quad (29)$$

We want an equation on the form

$$\check{G}_{\text{imp}} = \check{G}_0 + \check{G}_0 \bullet \check{\Sigma}_{\text{imp}} \bullet \check{G}_{\text{imp}}. \quad (30)$$

That is, we want to remove \check{G} , which depends on the specific realizations of the impurity configuration. To find $\check{\Sigma}_{\text{imp}}$ to second order in \check{V}^{imp} , we again set $\delta \check{\Sigma} = \check{V}^{\text{imp}}$ and insert Eq. (25a) twice into Eq. (29) to obtain

$$\begin{aligned} \check{G}_{\text{imp}} &= \check{G}_0 + \check{G}_0 \bullet \langle \check{V}^{\text{imp}} \rangle_{\text{imp}} \bullet \check{G}_0 \\ &+ \check{G}_0 \bullet \langle \check{V}^{\text{imp}} \bullet \check{G}_0 \bullet \check{V}^{\text{imp}} \rangle_{\text{imp}} \bullet \check{G}_0 \\ &+ \check{G}_0 \bullet \langle \check{V}^{\text{imp}} \bullet \check{G}_0 \bullet \check{V}^{\text{imp}} \bullet \check{G}_0 \bullet \check{V}^{\text{imp}} \bullet \check{G} \rangle_{\text{imp}}. \end{aligned} \quad (31)$$

We need \check{G}_0 as a function of \check{G}_{imp} to get Eq. (30). This can be found to the appropriate order in \check{V}^{imp} in inserting Eq. (25a) with $\delta \check{\Sigma} = \check{V}^{\text{imp}}$ once into Eq. (29) and solving for \check{G}_0 , giving

$$\begin{aligned} \check{G}_0 &= \check{G}_{\text{imp}} - \check{G}_0 \bullet \langle \check{V}^{\text{imp}} \rangle_{\text{imp}} \bullet \check{G}_0 \\ &- \check{G}_0 \bullet \langle \check{V}^{\text{imp}} \bullet \check{G}_0 \bullet \check{V}^{\text{imp}} \bullet \check{G} \rangle_{\text{imp}}. \end{aligned} \quad (32)$$

In order to find a self-consistent expression for the impurity self-energy $\check{\Sigma}_{\text{imp}}$ as a function of \check{V}^{imp} and \check{G}_{imp} , we insert the

expression for \check{G}_0 iteratively into Eq. (31). By comparing the result to Eq. (30), this gives that, to second order in \check{V}^{imp} ,

$$\begin{aligned} \check{\Sigma}_{\text{imp}} &= \langle \check{V}^{\text{imp}} \rangle_{\text{imp}} + \langle \check{V}^{\text{imp}} \bullet \check{G}_{\text{imp}} \bullet \check{V}^{\text{imp}} \rangle_{\text{imp}} \\ &- \langle \check{V}^{\text{imp}} \rangle_{\text{imp}} \bullet \check{G}_{\text{imp}} \bullet \langle \check{V}^{\text{imp}} \rangle_{\text{imp}}. \end{aligned} \quad (33)$$

Using the properties of ρ_{imp} , we see that the first-order term

$$\begin{aligned} [\check{\Sigma}_{\text{imp}}^{(1)}(t_1, t_2)]_{nm} &= [(\check{V}^{\text{imp}})_{\text{imp}}(t_1, t_2)]_{nm} = \delta_{nm} \delta(t_1 - t_2) \\ &\times \sum_{X \in \{A, B\}} \left(n_{\text{imp}}^{LX} \rho_X \langle U^{LX} \rangle_{\text{imp}} n_{\text{imp}}^{RX} \rho_X \langle U^{RX} \rangle_{\text{imp}} \right) \end{aligned} \quad (34)$$

is an energy shift that may be sublattice dependent if the number or strength of impurities is different on the two sublattices. It may in general also be spin dependent if the impurities are magnetic, meaning that $U_i^{\alpha X}$ has a nontrivial structure in spin space. Here we assume that the impurities are not magnetic. Nevertheless, we shall see in Sec. X that they will have an effective magnetic component in the final equations.

To evaluate the second-order term,

$$\begin{aligned} \check{\Sigma}_{\text{imp}}^{(2)} &= \langle \check{V}^{\text{imp}} \bullet \check{G}_{\text{imp}} \bullet \check{V}^{\text{imp}} \rangle_{\text{imp}} \\ &- \langle \check{V}^{\text{imp}} \rangle_{\text{imp}} \bullet \check{G}_{\text{imp}} \bullet \langle \check{V}^{\text{imp}} \rangle_{\text{imp}}. \end{aligned} \quad (35)$$

Note that the assumption that the impurities are independent means that the contributions with different impurities to the left and right of the Green's function cancel. Hence,

$$\begin{aligned} [\check{\Sigma}_{\text{imp}}^{(2)}(t_1, t_2)]_{nm}^{\alpha\beta} &= \delta_{\alpha\beta} \sum_{X \in \{A, B\}} \sum_{i=1}^{m^{\alpha X}} [\rho_X \langle \check{G}_{\text{imp}}^{\alpha\alpha} \rangle_{nm} \rho_X \langle U_i^{\alpha X} \delta_{nr_i^{\alpha X}} U_i^{\alpha X} \delta_{nr_i^{\alpha X}} \rangle_{\text{imp}} - \rho_X \langle \check{G}_{\text{imp}}^{\alpha\alpha} \rangle_{nm} \rho_X \langle U_i^{\alpha X} \delta_{nr_i^{\alpha X}} \rangle_{\text{imp}} \langle U_i^{\alpha X} \delta_{nr_i^{\alpha X}} \rangle_{\text{imp}}] \\ &= \delta_{\alpha\beta} \sum_{X \in \{A, B\}} \delta_{nm} n_{\text{imp}}^{\alpha X} \langle U^{X\alpha} U^{X\alpha} \rangle_{\text{imp}} \rho_X \langle \check{G}_{\text{imp}}^{\alpha\alpha} \rangle_{nm} \rho_X - \delta_{\alpha\beta} \sum_{X \in \{A, B\}} \frac{n_{\text{imp}}^{\alpha X}}{N^{\alpha}} \langle U^{X\alpha} \rangle_{\text{imp}}^2 \rho_X \langle \check{G}_{\text{imp}}^{\alpha\alpha} \rangle_{nm} \rho_X. \end{aligned} \quad (36)$$

We can neglect the second term because N^{α} is large and the amplitude of the Green's function decreases as a function of relative distance in the presence of impurities, as will be shown later. Thus, to second order the impurity self-energy is

$$\begin{aligned} [\check{\Sigma}_{\text{imp}}(t_1, t_2)]_{nm}^{\alpha\beta} &= \delta_{\alpha\beta} \delta_{nm} \sum_{X \in \{A, B\}} n_{\text{imp}}^{\alpha X} \rho_X \langle U^{X\alpha} \rangle_{\text{imp}} \\ &+ \langle U^{X\alpha} U^{X\alpha} \rangle_{\text{imp}} \rho_X \langle \check{G}_{\text{imp}}^{\alpha\alpha} \rangle_{nm}(t_1, t_2) \rho_X. \end{aligned} \quad (37)$$

From here on we drop the subscript on the impurity averaged Green's function, such that $\check{G}_{\text{imp}} \rightarrow \check{G}$.

VI. TUNNELING

In order to get closed equations for \check{G}^{LL} and \check{G}^{RR} , we must first remove \check{G}^{LR} and \check{G}^{RL} . In this section, we do this by treating the tunneling self-energy as the perturbation in the

Dyson equation. However, we note that the derived effective tunneling self-energy is still of infinite order in the tunneling amplitudes \hat{T}^{LR} .

Let

$$\check{T} = \begin{pmatrix} & \hat{T}^{LR} \\ \hat{T}^{RL} & \end{pmatrix}, \quad (38)$$

and let \check{G}_0 be the Green's function with $\hat{T}^{RL} = \hat{T}^{LR} = 0$, meaning that it solves Eq. (26) with $\delta \check{\Sigma} = \check{\Sigma} - \check{T} = \text{diag}(\check{\Sigma}^{LL}, \check{\Sigma}^{RR})$. Here $\delta \check{\Sigma}$ includes the impurity self-energy term obtained from the impurity average above. Note that this means that \check{G}_0^{RR} still depends on \check{G}^{LL} . This is because \check{G}_0^{RR} depend on \check{G}^{RR} through the impurity self-energy found in Sec. V, and \check{G}^{RR} depend on \check{G}^{LL} . For the same reason \check{G}_0^{LL} depends on \check{G}^{RR} .

From the Dyson equation, (25), we have that

$$\check{G} = \check{G}_0 + \check{G}_0 \bullet \check{T} \bullet \check{G}, \quad (39a)$$

$$\check{G} = \check{G}_0 + \check{G} \bullet \check{T} \bullet \check{G}_0. \quad (39b)$$

From the upper-right block of Eq. (39a) we have that

$$\begin{aligned}
 \check{G}^{LR} &= \check{G}_0^{LR} + \check{G}_0^{LR} \bullet \hat{T}^{RL} \bullet \check{G}^{LR} + \check{G}_0^{LL} \bullet \hat{T}^{LR} \bullet \check{G}^{RR} \\
 &= \check{G}_0^{LR} \bullet \left(i\tau_z \frac{\partial \check{G}^{RR}}{\partial t} - \check{\Sigma}^{RR} \bullet \check{G}^{RR} - \hat{T}^{RL} \bullet \check{G}^{LR} \right) \\
 &\quad + \check{G}_0^{LR} \bullet \hat{T}^{RL} \bullet \check{G}^{LR} + \check{G}_0^{LL} \bullet \hat{T}^{LR} \bullet \check{G}^{RR} \\
 &= - \left(\frac{\partial \check{G}_0^{LR}}{\partial t'} i\tau_z + \check{G}_0^{LR} \bullet \check{\Sigma}^{RR} \right) \bullet \check{G}^{RR} + \check{G}_0^{LL} \bullet \hat{T}^{LR} \bullet \check{G}^{RR} \\
 &= \check{G}_0^{LL} \bullet \hat{T}^{LR} \bullet \check{G}^{RR}, \tag{40}
 \end{aligned}$$

where we used Eq. (26) in the last equality.

Doing the same for \check{G}^{LR} , and from similar calculations using Eq. (39b) we find that

$$\check{G}^{LR} = \check{G}_0^{LL} \bullet \hat{T}^{LR} \bullet \check{G}^{RR} = \check{G}^{LL} \bullet \hat{T}^{LR} \bullet \check{G}_0^{RR}, \tag{41a}$$

$$\check{G}^{RL} = \check{G}_0^{RR} \bullet \hat{T}^{RL} \bullet \check{G}^{LL} = \check{G}^{RR} \bullet \hat{T}^{RL} \bullet \check{G}_0^{LL}. \tag{41b}$$

Inserting this into the Gor'kov equation, we can remove \check{G}^{RL} and \check{G}^{LR} and get a block-diagonal self-energy,

$$\check{\Sigma} = \check{H}_0 + \check{V} + \check{\Sigma}_{\text{imp}} + \check{\Sigma}_T, \tag{42}$$

where

$$\check{H}_0 = \begin{pmatrix} \hat{H}_0^L & \\ & \hat{H}_0^R \end{pmatrix}, \tag{43a}$$

$$\check{V} = \begin{pmatrix} \check{V}^L & \\ & \check{V}^R \end{pmatrix}, \tag{43b}$$

$$\check{\Sigma}_T = \begin{pmatrix} \hat{T}^{LR} \bullet \check{G}_0^{RR} \bullet \hat{T}^{RL} & \\ & \hat{T}^{RL} \bullet \check{G}_0^{LL} \bullet \hat{T}^{LR} \end{pmatrix}. \tag{43c}$$

VII. FOURIER TRANSFORM AND WIGNER COORDINATES

In the quasiclassical framework, functions vary slowly with the center-of-mass (COM) coordinates, and quickly with the relative coordinates. It is therefore useful to Fourier transform in the relative coordinates to obtain functions of momentum, energy, COM time, and COM position, also known as Wigner coordinates. The Fourier transform in relative time reads

$$\mathcal{F}_t(A)(T, \varepsilon) = \int_{-\infty}^{\infty} dt A(T + t/2, T - t/2) e^{i\varepsilon t}, \tag{44}$$

and for the Fourier transform in relative position we use

$$\mathcal{F}_r(A)s(\mathbf{k}, \mathbf{x}_n^\alpha s) = \sum_{m \in \mathbb{Z}^3} e^{-i\rho_B \mathbf{k} \cdot \delta^\alpha} A_{(n+m)n} e^{i\rho_B \mathbf{k} \cdot \delta^\alpha} e^{-i\mathbf{k} \cdot \mathbf{x}_m^\alpha}. \tag{45}$$

This is a three-dimensional discrete-time Fourier transform (DTFT), and the inverse transform is given by

$$\mathcal{F}_r^{-1}(A)_{(n+m)n} = V_e^\alpha \int_{\diamond_\alpha} \frac{d[3]k}{(2\pi)^3} e^{i\rho_B \mathbf{k} \cdot \delta^\alpha} A(\mathbf{k}, \mathbf{x}_n^\alpha) e^{-i\rho_B \mathbf{k} \cdot \delta^\alpha} e^{i\mathbf{k} \cdot \mathbf{x}_m^\alpha}, \tag{46}$$

where V_e^α is the volume of the unit cell and \diamond_α is the first Brillouin zone in material α . Note that \mathbf{x}_n^α in Eq. (45) is not exactly the COM position, since the COM position for term m on the right is $(\mathbf{x}_n^\alpha + \mathbf{x}_m^\alpha)/2$.

We use the same symbols as before to denote the bullet and circle products in the Wigner coordinates, meaning that they

satisfy

$$\mathcal{F}_r[\mathcal{F}_t(A)] \bullet \mathcal{F}_r[\mathcal{F}_t(B)] = \mathcal{F}_r[\mathcal{F}_t(A \bullet B)] \tag{47}$$

and

$$\mathcal{F}_t(A) \circ \mathcal{F}_t(B) = \mathcal{F}_t(A \circ B). \tag{48}$$

Thus, the Gor'kov equations in the Wigner coordinates read

$$\tau_z \varepsilon \circ \check{G} - \check{\Sigma} \bullet \check{G} = 1, \tag{49a}$$

$$\check{G} \circ \tau_z \varepsilon - \check{G} \bullet \check{\Sigma} = 1. \tag{49b}$$

The circle product in the Wigner product is the same as in continuous models for normal metals [5,61],

$$A \circ B = \exp\left(\frac{i}{2} \partial_\varepsilon^A \partial_T^B - \frac{i}{2} \partial_T^A \partial_\varepsilon^B\right) AB, \tag{50}$$

where the superscripts on the differential operators denote which function they act on. The spatial part of the bullet product, on the other hand, is different, and there are three reasons for this. First, since we are working on a discrete lattice, we cannot Taylor expand, which is how the series expansion in differential operators is achieved in Eq. (50). Second, since we are working with two sublattices that are located differently in space, the COM positions and relative positions are different for different matrix elements. Third, the COM position is not set constant in the way we have defined the Fourier transform in Eq. (45). Nevertheless, the bullet product can still be written as a series of differential operators of increasing order. To derive the explicit series expansion, one can use the Newton forward difference equation, which is the discrete analog to the Taylor series expansion. The zeroth-order term is the same, namely just the normal matrix product, and we will end up keeping only the zeroth-order terms, except for the kinetic energy term, the tunneling term, and the potential, which is large outside the material. We will evaluate these terms explicitly when considering the boundary condition. Note, however, that we cannot neglect the higher-order terms at this stage because the Green's function is strongly peaked in momentum space.

To evaluate $\hat{H}_0^\alpha \bullet \check{G}^{\alpha\alpha}$ and $\check{G}^{\alpha\alpha} \bullet \hat{H}_0^\alpha$ in Wigner coordinates, note that

$$\begin{aligned}
 \mathcal{F}_r[A \bullet B](\mathbf{k}, \mathbf{x}_n^\alpha) &= \sum_{m \in \mathbb{Z}^3} \mathcal{F}[A](\mathbf{k}, \mathbf{x}_m^\alpha + \mathbf{x}_n^\alpha) \\
 &\quad \circ e^{-i\rho_B \mathbf{k} \cdot \delta^\alpha} B_{(n+m)n} e^{i\rho_B \mathbf{k} \cdot \delta^\alpha} e^{-i\mathbf{k} \cdot \mathbf{x}_m^\alpha}. \tag{51}
 \end{aligned}$$

Hence, as \hat{H}_0^α does not depend on COM-position,

$$\mathcal{F}_t\{\mathcal{F}_r[\hat{H}_0^\alpha \bullet \check{G}^{\alpha\alpha}]\}(\mathbf{k}, \mathbf{x}_n^\alpha) = \hat{H}_0^\alpha(\mathbf{k}) \check{G}^{\alpha\alpha}(\mathbf{k}, \mathbf{x}_n^\alpha). \tag{52}$$

Here,

$$\hat{H}_0^\alpha(\mathbf{k}) = \rho_\alpha K^\alpha(\mathbf{k}) - (J^\alpha \rho_z \sigma_z \tau_z + \mu), \tag{53}$$

and

$$K^\alpha(\mathbf{k}) = - \sum_{\delta_i \in \text{N.N.}} t^\alpha \cos(\mathbf{k} \cdot \delta_i) \tag{54}$$

where the sum goes over all the six nearest-neighbor-displacement vectors.

Interchanging the order, we find that

$$\begin{aligned} \mathcal{F}_i \{ \mathcal{F}_r [\check{G}^{\alpha\alpha} \bullet \hat{H}_0^\alpha] \} \\ = \check{G}^{\alpha\alpha} \hat{H}_0^\alpha \\ - \frac{1}{2} \sum_{\delta_i \in \text{N.N.}} (\Delta_R \check{G}^{\alpha\alpha}) \cdot (\delta_i + \delta^\alpha) (\rho_x + i \rho_y) t^\alpha e^{-ik \cdot \delta_i} \\ - \frac{1}{2} \sum_{\delta_i \in \text{N.N.}} (\Delta_R \check{G}^{\alpha\alpha}) \cdot (\delta_i - \delta^\alpha) (\rho_x - i \rho_y) t^\alpha e^{-ik \cdot \delta_i} \end{aligned} \quad (55)$$

where the symbols on the right-hand side denote functions of Wigner coordinates and the discrete finite difference operator is defined as

$$\mathbf{x}_m^\alpha \cdot \Delta_R \check{G}^{\alpha\alpha}(\mathbf{k}, \mathbf{x}_n^\alpha) = \check{G}^{\alpha\alpha}(\mathbf{k}, \mathbf{x}_n^\alpha + \mathbf{x}_m^\alpha) - \check{G}^{\alpha\alpha}(\mathbf{k}, \mathbf{x}_n^\alpha). \quad (56)$$

The finite difference is only well defined when \mathbf{x}_m^α is a lattice vector, meaning that \mathbf{x}_m^α is a displacement vector from one unit cell to another. However, we can define

$$\delta_i \cdot \Delta_R \check{G}^{\alpha\alpha}(\mathbf{k}, \mathbf{x}_n^\alpha) = [\check{G}^{\alpha\alpha}(\mathbf{k}, \mathbf{x}_n^\alpha + 2\delta_i) - \check{G}^{\alpha\alpha}(\mathbf{k}, \mathbf{x}_n^\alpha)]/2. \quad (57)$$

This is possible because we assume that $2\delta_i$ is a lattice vector when δ_i is a nearest-neighbor-displacement vector. With this,

$$\begin{aligned} \delta_i \cdot \Delta_R \check{G}^{\alpha\alpha}(\mathbf{k}, \mathbf{x}_n^\alpha) + \delta^\alpha \cdot \Delta_R \check{G}^{\alpha\alpha}(\mathbf{k}, \mathbf{x}_n^\alpha) \\ = (\delta_i + \delta^\alpha) \cdot \Delta_R \check{G}^{\alpha\alpha}(\mathbf{k}, \mathbf{x}_n^\alpha) + \frac{1}{2} \check{G}^{\alpha\alpha}(\mathbf{k}, \mathbf{x}_n^\alpha + 2\delta_i) \\ + \frac{1}{2} \check{G}^{\alpha\alpha}(\mathbf{k}, \mathbf{x}_n^\alpha + 2\delta^\alpha) - \check{G}^{\alpha\alpha}(\mathbf{k}, \mathbf{x}_n^\alpha + \delta_i + \delta^\alpha). \end{aligned} \quad (58)$$

The last three terms are equal to $|\delta_i - \delta^\alpha|^2/2$ times the second-order central difference of $\check{G}^{\alpha\alpha}$, so they are negligible under the assumption that the Green's function changes slowly as a function COM position compared to the interlattice spacing. By the same reasoning we also approximate $(-\mathbf{x}_m^\alpha) \cdot \Delta_R \check{G}^{\alpha\alpha} = -\mathbf{x}_m^\alpha \cdot \Delta_R \check{G}^{\alpha\alpha}$, since the difference is equal to the $|\mathbf{x}_m^\alpha|^2$ multiplied by the second-order derivative of $\check{G}^{\alpha\alpha}$. With this we have

$$\begin{aligned} \mathcal{F}_i \{ \mathcal{F}_r [\check{G}^{\alpha\alpha} \bullet \hat{H}_0^\alpha] \} = \check{G}^{\alpha\alpha} \hat{H}_0^\alpha \\ + i (\Delta_R \check{G}^{\alpha\alpha}) \cdot (\rho_x \nabla_k K^\alpha + \delta^\alpha \rho_y K^\alpha). \end{aligned} \quad (59)$$

The dot product in the last term must be interpreted in the following sense: If $\nabla_k K^\alpha = A_1 \delta_1 + A_2 \delta_2 + A_3 \delta_3$, where δ_1 , δ_2 and δ_3 are three different, linearly independent, nearest-neighbor-displacement vectors, then

$$(\Delta_R \check{G}^{\alpha\alpha}) \cdot \nabla_k K^\alpha = \sum_{i=1}^3 \delta_i \cdot (\Delta_R \check{G}^{\alpha\alpha}) A_i. \quad (60)$$

VIII. EXTRACTING THE CONDUCTION BAND

The main idea behind the quasiclassical theory is that most of the interesting physics happens close to the Fermi surface. Therefore, it is of interest to isolate the contribution from states close to the Fermi surface. In our model there are two energy bands that are not overlapping, so only one of these can pass through the Fermi surface. In real materials, it is not always the case that the energy bands are not overlapping. It is sufficient that the energy bands are not overlapping near the Fermi surface.

To separate the two bands, we must diagonalize \hat{H}_0^α . We find that

$$\hat{H}_0^\alpha = S^\alpha D^\alpha (S^\alpha)^T, \quad (61)$$

where

$$D^\alpha = \text{diag}(\xi_-^\alpha, \xi_-^\alpha, \xi_-^\alpha, \xi_-^\alpha, \xi_+^\alpha, \xi_+^\alpha, \xi_+^\alpha, \xi_+^\alpha) \quad (62)$$

and $(S^\alpha)^T$ denotes the transpose of

$$\begin{aligned} S^\alpha = \frac{1}{\sqrt{2\eta^\alpha}} \left[\begin{pmatrix} -\sigma_0 & 0 & \sigma_0 & 0 \\ \sigma_0 & 0 & \sigma_0 & 0 \\ 0 & -\sigma_0 & 0 & \sigma_0 \\ 0 & \sigma_0 & 0 & \sigma_0 \end{pmatrix} \bar{S}^\alpha \right. \\ \left. - \begin{pmatrix} \sigma_z & 0 & \sigma_z & 0 \\ \sigma_z & 0 & -\sigma_z & 0 \\ 0 & -\sigma_z & 0 & -\sigma_z \\ 0 & -\sigma_z & 0 & \sigma_z \end{pmatrix} \Delta S^\alpha \right], \end{aligned} \quad (63)$$

where σ_0 is the 2×2 identity matrix, $\eta^\alpha = \sqrt{(J^\alpha)^2 + (K^\alpha)^2}$, $\xi_\pm^\alpha = -\mu^\alpha \pm \eta^\alpha$, $s^\alpha = (s_+^\alpha + s_-^\alpha)/2$, and $\Delta S^\alpha = (s_+^\alpha - s_-^\alpha)/2$, with $s_\pm^\alpha = \sqrt{\eta^\alpha} \pm J^\alpha$.

Next, we define

$$\begin{pmatrix} \check{G}_{--}^{\alpha\alpha} & \check{G}_{-+}^{\alpha\alpha} \\ \check{G}_{+-}^{\alpha\alpha} & \check{G}_{++}^{\alpha\alpha} \end{pmatrix} = (S^\alpha)^T \check{G}^{\alpha\alpha} S^\alpha. \quad (64)$$

We want an equation for the Green's function associated with the energy band, which crosses the Fermi surface. This can be either $\check{G}_{--}^{\alpha\alpha}$ or $\check{G}_{++}^{\alpha\alpha}$. Here we choose $\check{G}_{--}^{\alpha\alpha}$. To derive this equation, we first find that

$$(S^\alpha)^T \rho_x \nabla_k K^\alpha S^\alpha = \nabla_k D + \frac{J^\alpha \nabla_k \eta^\alpha}{K^\alpha} \begin{pmatrix} 0 & 0 & \sigma_z & 0 \\ 0 & 0 & 0 & -\sigma_z \\ \sigma_z & 0 & 0 & 0 \\ 0 & -\sigma_z & 0 & 0 \end{pmatrix} \quad (65)$$

and

$$(S^\alpha)^T i \rho_y S^\alpha = \begin{pmatrix} 0 & 0 & -\sigma_0 & 0 \\ 0 & 0 & 0 & -\sigma_0 \\ \sigma_0 & 0 & 0 & 0 \\ 0 & \sigma_0 & 0 & 0 \end{pmatrix}. \quad (66)$$

Additionally, we continue to use τ_z to denote the third Pauli matrix in Nambu space after transforming to the band basis, which means that

$$(S^\alpha)^T \tau_z S^\alpha = \begin{pmatrix} \sigma_0 & 0 & 0 & 0 \\ 0 & -\sigma_0 & 0 & 0 \\ 0 & 0 & \sigma_0 & 0 \\ 0 & 0 & 0 & -\sigma_0 \end{pmatrix} = \begin{pmatrix} \tau_z & 0 \\ 0 & \tau_z \end{pmatrix}. \quad (67)$$

Transforming the first Gor'kov equation to the AFM energy band basis and extracting the block corresponding to the conduction band, we get

$$\tau_z \varepsilon \circ \check{G}_{--}^{\alpha\alpha} - \xi_-^\alpha \check{G}_{--}^{\alpha\alpha} - [(\check{\Sigma}^\alpha - \hat{H}_0^\alpha) \bullet \check{G}^{\alpha\alpha}]_{--} = 1, \quad (68)$$

where $\check{\Sigma}^\alpha$ is the block of $\check{\Sigma}$, given by Eq. (42), corresponding to material α and the subscript on the last term on the left-hand side means that one should take the upper left block in the

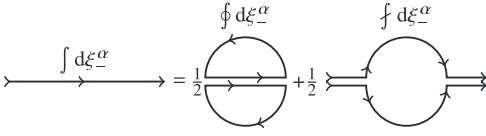


FIG. 3. A sketch of the integration decomposition introduced by Eilenberger [3].

conduction band basis. That is, for a general matrix A in the sublattice basis,

$$\begin{pmatrix} A_{--} & A_{-+} \\ A_{+-} & A_{++} \end{pmatrix} = (S^\alpha)^T A S^\alpha. \quad (69)$$

The second Gor'kov equation becomes

$$\begin{aligned} \check{G}_{--}^{\alpha\alpha} \circ \tau_z \varepsilon - \xi_-^\alpha \check{G}_{--}^{\alpha\alpha} - i \nabla_k \xi_-^\alpha \cdot \Delta_R \check{G}_{--}^{\alpha\alpha} \\ - \frac{i J^\alpha \nabla_k \eta^\alpha}{K^\alpha} \cdot \Delta_R \check{G}_{-+}^{\alpha\alpha} \tau_z \sigma_z - K^\alpha \delta^\alpha \cdot \Delta_R \check{G}_{-+}^{\alpha\alpha} \\ - [\check{G}_{--}^{\alpha\alpha} \bullet (\check{\Sigma}^\alpha - \hat{H}_0^\alpha)]_{--} = 1. \end{aligned} \quad (70)$$

IX. QUASICLASSICAL GREEN'S FUNCTIONS

In this section, we derive the quasiclassical equations of motion. To do so, we must integrate the Green's function over momenta. Note that since we only want the contribution from states close to the Fermi surface, we cannot integrate over all momenta, but must instead integrate over a contour close to the Fermi surface. While it is true that the Green's function will be strongly peaked around the Fermi surface, the contribution from far away from the Fermi surface is not negligible. This is because the retarded and advanced Green's function goes as $1/\xi_-^\alpha$ far away from the Fermi surface.

Observables are given as integrals over all momenta. To extract the quasiclassical contribution, one must decompose this integral into one part, which includes the contribution close to the Fermi surface and one part, which includes the rest. By using the Eilenberger decomposition [3], as illustrated in Fig. 3, the contribution from the Fermi surface is included as two closed contours in the complex plane, which simplifies the calculations. We show how observables can be expressed as a quasiclassical contribution and a rest term in Sec. XIV.

To get the quasiclassical equations of motion, we must integrate the Gor'kov equations over the closed contours. This allows us to simplify many of the bullet products when the self-energy varies slowly as a function of COM position, as we show in this section. Note that the tunneling term and the potential, which is large outside of the material change rapidly as a function of COM position. These can therefore not be simplified in the same way. However, these terms are only nonzero at the interface. In this section, we consider only positions inside the material and therefore ignore these terms. We will return to them when deriving the boundary conditions. Hence, as long as we consider COM positions away from the boundaries,

$$\check{\Sigma}^\alpha - \hat{H}_0^\alpha = \check{V}^\alpha + \check{\Sigma}_{\text{imp}}^\alpha. \quad (71)$$

To simplify the bullet product, we can use the gradient expansion. However, the gradient expansion is more com-

plified in our case compared to the continuous case. This is because we are working with two discrete sublattices. To derive the gradient expansion for discrete lattices, we can use the Newton forward difference equation. If the basis vectors are $\{\mathbf{v}_1^\alpha, \mathbf{v}_2^\alpha, \mathbf{v}_3^\alpha\}$, such that $\mathbf{x}_m^\alpha = a_1^m \mathbf{v}_1^\alpha + a_2^m \mathbf{v}_2^\alpha + a_3^m \mathbf{v}_3^\alpha$, with integers a_1^m, a_2^m , and a_3^m , then

$$A(\mathbf{x}_n^\alpha + \mathbf{x}_m^\alpha) = \sum_{j \in \mathbb{N}_0^3} \frac{(\mathbf{x}_m^\alpha)_j}{j!} \prod_{i=1}^3 \left(\frac{[\text{sgn}(a_i^m) \mathbf{v}_i^\alpha] \cdot \Delta_R}{|\mathbf{v}_i^\alpha|} \right)^{j_i} A(\mathbf{x}_n^\alpha), \quad (72)$$

where $j = (j_1, j_2, j_3)$ is a multi-index, $j! = j_1! j_2! j_3!$ and

$$(\mathbf{x}_m^\alpha)_j = (a_1^m \mathbf{v}_1^\alpha)_{j_1} (a_2^m \mathbf{v}_2^\alpha)_{j_2} (a_3^m \mathbf{v}_3^\alpha)_{j_3}, \quad (73a)$$

$$(a_i^m \mathbf{v}_i^\alpha)_{j_i} = \text{sgn}(a_i^m)^{j_i} |a_i^m|^{j_i} [|a_i^m| - (j_i - 1)] (|a_i^m \mathbf{v}_i^\alpha|)_{j_i - 1}. \quad (73b)$$

Hence, we see from Eq. (51) that the bullet product can be written as a series expansion in derivative operators,

$$A \bullet B = A \circ B + [\Delta_R A] \circ (i \nabla_k B - [\delta^\alpha \rho_B, B]) + \dots, \quad (74)$$

where the circle product in the second term on the right-hand side includes a dot product, which must be interpreted according to Eq. (60). Equation (74) is the gradient expansion. The gradient expansion is useful because the higher-order terms can be neglected after a proper integral over momenta.

We define the quasiclassical Green's function

$$\check{g}^\alpha = \frac{i}{\pi} \oint d\xi_-^\alpha \check{G}_{--}^{\alpha\alpha}, \quad (75)$$

where the closed paths are illustrated in Fig. 3. They follow the real line from $\xi_-^\alpha = -E_c^\alpha$ to $\xi_-^\alpha = E_c^\alpha$ and then split into two semicircular paths to close the contours. Here, E_c^α is some cutoff that is far larger than the other energies in the system, but smaller than $|\mu^\alpha|$. Since the interval $(-E_c^\alpha, E_c^\alpha)$ must be inside the conduction band, E_c^α must also be smaller than ΔE^α , which is the smallest energy difference between the Fermi level and the edges of the conduction band.

We can relate the kinetic energy K^α at the Fermi level to ΔE^α . To do so, note that $\xi_-^\alpha + \Delta E^\alpha = -\mu^\alpha - \sqrt{(J^\alpha)^2 + (K^\alpha)^2} + \Delta E^\alpha \leq -\mu^\alpha - |J^\alpha|$ means that

$$\left(\frac{J^\alpha}{K^\alpha} \right)^2 \leq \frac{(J^\alpha)^2}{2|J^\alpha| \Delta E^\alpha + (\Delta E^\alpha)^2}. \quad (76)$$

It is possible that $\Delta E^\alpha \ll J^\alpha$. For this reason, one can still consider $J^\alpha \gg K^\alpha$ within this framework, meaning that $J^\alpha/\eta^\alpha = J^\alpha/\sqrt{(J^\alpha)^2 + (K^\alpha)^2} \rightarrow 1$. The only requirement for the quasiclassical theory presented here to be valid is that ΔE^α is large compared to all other energies except possibly the exchange energy J^α . We can have any ratio J^α/K^α , and the limit $J^\alpha/K^\alpha \rightarrow 0$ should reproduce the quasiclassical theory for normal metals.

Since the contours are closed in the complex plane and we assume that the functions are analytic in ξ_-^α , we can use the residue theorem to evaluate

$$\check{g}^\alpha = - \sum_{\xi_i} \text{sgn}(\text{Im}[\xi_i]) \text{Res}(\check{G}_{--}^{\alpha\alpha}, \xi_i), \quad (77)$$

where the sum goes over all poles of $\check{G}_{--}^{\alpha\alpha}$, which are inside the contours and $\text{Res}(\check{G}_{--}^{\alpha\alpha}, \xi_i)$ denote the corresponding residues. To obtain an equation for the quasiclassical Green's function, we integrate the Gor'kov equations, Eqs. (68) and (70), over momenta and use Eqs. (74) and (75).

Consider first terms on the form $\check{G}_{--}^{\alpha\alpha} \bullet A$, for some A . The zeroth-order term in gradients is $\check{G}_{--}^{\alpha\alpha} \circ A$. If $A(\xi_-^\alpha)$ has no poles inside the contour, we see that

$$\begin{aligned} \frac{i}{\pi} \oint d\xi_-^\alpha \check{G}_{--}^{\alpha\alpha} \circ A &= - \sum_{\xi_i} \text{sgn}(\text{Im}[\xi_i]) \text{Res}(\check{G}_{--}^{\alpha\alpha}, \xi_i) \circ A(\xi_-^\alpha) \\ &= \check{g}^\alpha \circ A(0) + \mathcal{O}(\check{g}^\alpha \circ a \partial_{\xi_-^\alpha} A), \end{aligned} \quad (78)$$

where a is the maximal distance from the poles of $\check{G}_{--}^{\alpha\alpha}$ to $\xi_-^\alpha = 0$. It is therefore much smaller than E_F^α . We can neglect the second term when A varies slowly as a function of ξ_-^α , such that $|a \partial_{\xi_-^\alpha} A| \ll |A|$. Note that this is not true when $A = \xi_-^\alpha$, which is the case for the second terms on the left-hand sides of Eqs. (68) and (70). We can therefore not evaluate $\oint d\xi_-^\alpha \xi_-^\alpha \check{G}_{--}^{\alpha\alpha}$ in terms of the quasiclassical Green's function.

$$\left| \frac{a \partial_{\xi_-^\alpha} \nabla_k K^\alpha}{\nabla_k K^\alpha} \right| = \left| \frac{a \sum_{\delta_i} \delta_i (\delta_i \cdot \hat{\mathbf{k}}_F) \cos(\mathbf{k}_F \cdot \delta_i)}{v_F^\alpha \cdot \hat{\mathbf{k}}_F \sum_{\delta_i} (\delta_i \cdot \hat{\mathbf{k}}_F) \sin(\mathbf{k}_F \cdot \delta_i)} \right| < \left| \frac{a \sum_{\delta_i} \delta_i (\delta_i \cdot \hat{\mathbf{k}}_F) \cos(\mathbf{k}_F \cdot \delta_i)}{v_F^\alpha \cdot \hat{\mathbf{k}}_F \sum_{\delta_i} (\delta_i \cdot \hat{\mathbf{k}}_F) (\mathbf{k}_F \cdot \delta_i)} \right| \lesssim \frac{a \lambda_F}{|v_F^\alpha \cdot \hat{\mathbf{k}}_F|}, \quad (80)$$

where $v_F^\alpha = \nabla_k \xi_-^\alpha$ is the Fermi velocity, $\lambda_F = 1/|\mathbf{k}_F|$ is the Fermi wavelength, and $\hat{\mathbf{k}}_F$ is the unit vector in the direction of \mathbf{k}_F . Hence, the variation in $\nabla_k K^\alpha$ is negligible provided that $\lambda_F \ll |v_F^\alpha|/a$.

Physically, the condition can be understood in the following sense. The inverse energy $1/a$ defines a time, so $|v_F^\alpha|/a$ is the distance an electron with speed $|v_F^\alpha|$ travels in this time. For instance, when the dominant energy scale, other than J^α and K^α , comes from the impurity scattering, then a is at most the impurity scattering rate. In this case, the condition $\lambda_F \ll |v_F^\alpha|/a$ implies that the mean free path should be much greater than the Fermi wavelength. This condition holds provided that the energy difference between the Fermi level and the bottom of the conduction band is sufficiently large. Under this assumption, we can approximate

$$\frac{i}{\pi} \oint d\xi_-^\alpha \check{G}_{--}^{\alpha\alpha} \circ (\check{V}^\alpha + \check{\Sigma}_{\text{imp}}^\alpha)_{--} = \check{g}^\alpha \circ (\check{V}^\alpha + \check{\Sigma}_{\text{imp}}^\alpha)_{--} \quad (81)$$

in the presence of an inhomogeneous magnetic texture. A similar argument can be used to show that the same assumptions also imply that the condition $|a \partial_{\xi_-^\alpha} A| \ll |A|$ holds in the presence of corrections to the hopping amplitude, which can come from an external vector potential or spin-orbit coupling. With these assumptions,

$$\begin{aligned} \frac{i}{\pi} \oint d\xi_-^\alpha [(\check{V}^\alpha + \check{\Sigma}_{\text{imp}}^\alpha) \circ \check{G}^{\alpha\alpha}]_{--} \\ \approx (\check{V}^\alpha + \check{\Sigma}_{\text{imp}}^\alpha)_{--} \circ \check{g}^\alpha + \frac{i}{\pi} \oint d\xi_-^\alpha (\check{V}^\alpha + \check{\Sigma}_{\text{imp}}^\alpha)_{-+} \circ \check{G}_{+-}^{\alpha\alpha}. \end{aligned} \quad (82)$$

From Eq. (37) we see that $(\check{\Sigma}_{\text{imp}}^\alpha)_{--}$ only depend on momentum through S . Equation (22c) shows that \check{V}_{nm}^α depend on relative coordinates if there are magnetic textures or if the Hamiltonian includes terms other than the kinetic term, which depend on relative position. Corrections to the hopping term from the vector potential or spin-orbit coupling are included in \check{V}_{nm}^α , and these terms will depend on relative position. As a result, $(\check{V}^\alpha)_{--}$ depends on momentum, and therefore also on ξ_-^α . However, we assume that the dependence on momentum and ξ_-^α is sufficiently slow, such that the condition $|a \partial_{\xi_-^\alpha} A| \ll |A|$ is valid when $A = (\check{V}^\alpha + \check{\Sigma}_{\text{imp}}^\alpha)_{--}$. As we now show, this assumption is reasonable as long as the Fermi level is far away from the bottom of the conduction band.

Fourier transforming the term in Eq. (22c) coming from the magnetic texture, we get that

$$\begin{aligned} \mathcal{F}_r \{ (K_{nm}^\alpha [\mathbf{x}_n^\alpha - \mathbf{x}_m^\alpha] + [\delta^\alpha \rho_B, K_{nm}^\alpha]) \cdot (R^\dagger \nabla R) (\mathbf{x}_n^\alpha, t_1) \} \\ = i \nabla_k \mathcal{F}_r \{ K_{nm}^\alpha \} (\mathbf{k}, \mathbf{x}_n^\alpha) \cdot (R^\dagger \nabla R) (\mathbf{x}_n^\alpha, t_1). \end{aligned} \quad (79)$$

As long as the Fermi level is sufficiently far away from the bottom of the conduction band, the gradient $\nabla_k \mathcal{F}_r \{ K_{nm}^\alpha \} = \nabla_k K^\alpha$ will be approximately constant near the Fermi surface. This can be seen from Eq. (54), since

Equation (78) works the same when reversing the order of A and $\check{G}_{--}^{\alpha\alpha}$, so it is also true that

$$\begin{aligned} \frac{i}{\pi} \oint d\xi_-^\alpha [\check{G}^{\alpha\alpha} \circ (\check{V}^\alpha + \check{\Sigma}_{\text{imp}}^\alpha)]_{--} \approx \check{g}^\alpha \circ (\check{V}^\alpha + \check{\Sigma}_{\text{imp}}^\alpha)_{--} \\ + \frac{i}{\pi} \oint d\xi_-^\alpha \check{G}_{-+}^{\alpha\alpha} \circ (\check{V}^\alpha + \check{\Sigma}_{\text{imp}}^\alpha)_{+-}. \end{aligned} \quad (83)$$

If we are also sufficiently far away from the top of the conduction band, then the velocity $v_F^\alpha = \nabla_k \xi_-^\alpha$ is also approximately constant at all the poles of the Green's function. By approximately constant, we mean that the variation is small compared to v_F^α . To see why, note that

$$\nabla_k \xi_-^\alpha = \frac{\sqrt{(\mu^\alpha - \xi_-^\alpha)^2 - (J^\alpha)^2} \nabla_k K^\alpha}{(\mu^\alpha - \xi_-^\alpha)}. \quad (84)$$

Differentiating with respect to ξ_-^α gives

$$\frac{|a \partial_{\xi_-^\alpha} \nabla_k \xi_-^\alpha|}{|\nabla_k \mathcal{F}_r \{ K_{nm}^\alpha \}|} = \left| \frac{a (J^\alpha)^2}{(\xi_-^\alpha - \mu^\alpha) (K^\alpha)^2} + \frac{a \partial_{\xi_-^\alpha} \nabla_k K^\alpha}{\nabla_k K^\alpha} \right|. \quad (85)$$

From Eq. (76), we know that $(J^\alpha/K^\alpha)^2 < |J^\alpha|/2\Delta E^\alpha$. Since $|J^\alpha/(\xi_-^\alpha - \mu^\alpha)| \approx |J^\alpha/\mu^\alpha| < 1$ and $a/\Delta E^\alpha \ll 1$, the first term on the right-hand side of Eq. (85) is small. We have shown that the second term on the right-hand side of Eq. (85) is also negligible. As a result, integrating the third term on the left-hand side of Eq. (70) gives

$$-\frac{i}{\pi} \oint d\xi_-^\alpha i \nabla_k \xi_-^\alpha \cdot \Delta_R \check{G}_{--}^{\alpha\alpha} = -i v_F^\alpha \cdot \Delta_R \check{g}^\alpha. \quad (86)$$

Next, consider the higher-order terms in the gradient expansion. We will show that we can ignore these terms when the Hamiltonian, and therefore the Green's function, vary slowly in the center-of-mass (COM) spatial coordinate. Assuming $|a\partial_{\xi^\alpha}A| \ll |A|$,

$$\begin{aligned} & \frac{i}{\pi} \oint d\xi^\alpha [\Delta_R \check{G}_{--}^{\alpha\alpha}] \circ (i\nabla_k A - [\delta^\alpha \rho_B, A]) \\ & \approx [\Delta_R \check{g}^\alpha] \circ (i\nabla_k A - [\delta^\alpha \rho_B, A]), \end{aligned} \quad (87)$$

where we used Eq. (78). The gradient $\nabla_k A$ is evaluated at the Fermi surface. We define the characteristic COM length scale L to be the smallest number satisfying

$$|\Delta_R \check{g}^\alpha| < \frac{|\check{g}^\alpha|}{L}, \quad (88)$$

everywhere and for all momentum directions, where the norms can be understood using an appropriate matrix norm such as the Frobenius norm. In the quasiclassical framework, L is assumed to be much larger than the length of the nearest-neighbor-displacement vectors and the Fermi wavelength. As a result,

$$|\Delta_R \check{g}^\alpha \circ [\delta^\alpha \rho_B, A]| < \frac{|\delta^\alpha|}{L} |\check{g}^\alpha| \circ |A| \ll |\check{g}^\alpha| \circ |A|, \quad (89)$$

meaning that the second term in Eq. (87) is negligible compared to the zeroth-order term, $\check{g}^\alpha \circ A$. The magnitude of the first term is

$$|[\Delta_R \check{g}^\alpha] \circ (i\nabla_k A)| < \frac{|v_F^\alpha|}{L} |\check{g}^\alpha| \circ |\partial_{\xi^\alpha} A|. \quad (90)$$

Therefore, this term is negligible compared to the zeroth-order term if $||v_F^\alpha| \partial_{\xi^\alpha} A / L| \ll |A|$. This is guaranteed to be the case if $L > |v_F^\alpha| / a$, since $|a\partial_{\xi^\alpha} A| \ll |A|$. Physically, this criterion can again be understood by considering the time scale defined by $1/a$. For instance, $1/a$ can be on the order of the elastic impurity scattering time. The condition $L > |v_F^\alpha| / a$ then states that the variation is small over a distance equal to the mean free path. However, we note that this condition is too strict. It assumes only that $|\partial_{\xi^\alpha} A| / |A| \ll 1/a$, but if one can replace $1/a$ with a smaller number, then one can also loosen the condition on L .

With these assumptions, we neglect the first-order terms in the gradient expansion of $\check{G}_{--}^{\alpha\alpha} \bullet A$ after integration over ξ^α . Since L is large, higher-order terms will be even smaller than the first-order terms, so we neglect all terms except the zeroth-order term in the gradient expansion of $\check{G}_{--}^{\alpha\alpha} \bullet A$. Next, we must consider

$$\frac{i}{\pi} \oint d\xi^\alpha [\Delta_R A] \circ (i\nabla_k \check{G}_{--}^{\alpha\alpha} - [\delta^\alpha \rho_B, \check{G}_{--}^{\alpha\alpha}]). \quad (91)$$

We can use Eq. (78) one the second term on the right-hand side, which we see can be neglected since $|\Delta_R A| < |A|/L$ and $|\delta^\alpha|/L \ll 1$. However, we cannot use Eq. (78) to evaluate the first term on the right-hand side of Eq. (91). This is because $\check{G}_{--}^{\alpha\alpha}$ varies rapidly as a function of \mathbf{k} near its poles. To proceed, we can use the contour integral of a total derivative is

zero. This implies that

$$\oint d\xi^\alpha A \frac{\partial B}{\partial k} = \oint d\xi^\alpha A \frac{\partial \xi^\alpha}{\partial k} \frac{\partial B}{\partial \xi^\alpha} = - \oint d\xi^\alpha \frac{\partial}{\partial \xi^\alpha} \left(A \frac{\partial \xi^\alpha}{\partial k} \right) B, \quad (92)$$

for any A and B , where $\partial/\partial k$ is differentiation with respect to the amplitude of \mathbf{k} in spherical coordinates. This is not to be confused with the gradient operator ∇_k . We already assume that $\nabla_k \xi^\alpha$ is approximately constant on all the poles of $\check{G}_{--}^{\alpha\alpha}$. Using this we find that

$$\begin{aligned} \frac{i}{\pi} \oint d\xi^\alpha \Delta_R A \circ \nabla_k \check{G}_{--}^{\alpha\alpha} &= \frac{\Delta_R A}{k_F} \circ \left[e_\theta \frac{\partial}{\partial \theta} + e_\phi \frac{1}{\sin \theta} \frac{\partial}{\partial \phi} \right] \check{g}^\alpha \\ &\quad - e_k \cdot (\partial_k \Delta_R A) \circ \check{g}^\alpha, \end{aligned} \quad (93)$$

where k_F^α is the Fermi momentum, satisfying $\xi^\alpha(k_F^\alpha) = 0$ and θ and ϕ are the azimuthal and polar angles in momentum space, respectively. As long as \check{g}^α does not vary rapidly as a function of θ and ϕ , the right-hand side of Eq. (93) is negligible under the same assumptions as Eq. (87). Hence, we can also neglect the higher-order terms in the gradient expansion of $A \bullet \check{G}_{--}^{\alpha\alpha}$. Combining the above results,

$$\begin{aligned} & \frac{i}{\pi} \oint d\xi^\alpha [(\check{\Sigma}^\alpha - \hat{H}_0^\alpha) \bullet \check{G}_{--}^{\alpha\alpha}]_{--} \\ &= (\check{\Sigma}^\alpha - \hat{H}_0^\alpha)_{--} \circ \check{g}^\alpha + \frac{i}{\pi} \oint d\xi^\alpha (\check{\Sigma}^\alpha - \hat{H}_0^\alpha)_{-+} \circ \check{G}_{++}^{\alpha\alpha}, \end{aligned} \quad (94)$$

and

$$\begin{aligned} & \frac{i}{\pi} \oint d\xi^\alpha [\check{G}_{--}^{\alpha\alpha} \bullet (\check{\Sigma}^\alpha - \hat{H}_0^\alpha)]_{--} \\ &= \check{g}^\alpha \circ (\check{\Sigma}^\alpha - \hat{H}_0^\alpha)_{--} + \frac{i}{\pi} \oint d\xi^\alpha \check{G}_{-+}^{\alpha\alpha} \circ (\check{\Sigma}^\alpha - \hat{H}_0^\alpha)_{+-}. \end{aligned} \quad (95)$$

The circle-products in the last terms on the right-hand side of Eqs. (94) and (95) comes from a truncation in the gradient expansion, which is valid for the same reasons as the truncation in the gradient expansions involving $\check{G}_{--}^{\alpha\alpha}$.

To complete the derivation of the quasiclassical equations, we must remove the terms involving $\check{G}_{-+}^{\alpha\alpha}$ and $\check{G}_{+-}^{\alpha\alpha}$. Physically, this can be done because the energy difference between the two bands is large for momenta close to the Fermi surface. This means that there is negligible coupling between the electrons near the Fermi surface and the electrons in the other band. In order to show

$$\left| \frac{i}{\pi} \oint d\xi^\alpha \check{G}_{-+}^{\alpha\alpha} \right| \ll |\check{g}^\alpha| \quad \text{and} \quad \left| \frac{i}{\pi} \oint d\xi^\alpha \check{G}_{+-}^{\alpha\alpha} \right| \ll |\check{g}^\alpha|, \quad (96)$$

we define

$$\check{g}_{\pm\mp}^\alpha = \frac{i}{\pi} \oint d\xi^\alpha \check{G}_{\pm\mp}^{\alpha\alpha}. \quad (97)$$

We get from the first Gor'kov equation that

$$\begin{aligned} \tau_z \varepsilon \circ \check{g}_{+-}^\alpha - \xi_+^\alpha \check{g}_{+-}^\alpha - (\check{\Sigma}^\alpha - \hat{H}_0^\alpha)_{++} \circ \check{g}_{+-}^\alpha \\ - (\check{\Sigma}^\alpha - \hat{H}_0^\alpha)_{+-} \circ \check{g}^\alpha = 0, \end{aligned} \quad (98)$$

where $\xi_+^\alpha(\mathbf{k}_F) = -\mu^\alpha + \eta^\alpha(\mathbf{k}_F^\alpha)$ is evaluated at the Fermi surface defined by $\xi_-^\alpha(\mathbf{k}_F) = -\mu^\alpha - \eta^\alpha(\mathbf{k}_F^\alpha) = 0$. As a result, $|\xi_+^\alpha| = 2|\mu^\alpha|$, which is much larger than $|(\check{\Sigma}^\alpha - \hat{H}_0^\alpha)_{+-}|$ by assumption. We will also assume $|\varepsilon| \ll E_c^\alpha$, and consider larger $|\varepsilon|$ separately when computing observables in Sec. XIV. Therefore, $\check{g}_{+-}^\alpha \approx (\check{\Sigma}^\alpha - \hat{H}_0^\alpha)_{+-} \circ \check{g}^\alpha / \xi_+^\alpha$ is negligible. The

same argument from the second Gor'kov equation shows that \check{g}_{-+}^α is negligible as well.

Finally, integrating the Gor'kov equations, Eqs. (68) and (70), over the contours in ξ_-^α space and using Eqs. (94)–(96) we get

$$\tau_{z\varepsilon} \circ \check{g}^\alpha - (\check{\Sigma}^\alpha - \hat{H}_0^\alpha)_{--} \circ \check{g}^\alpha = \frac{i}{\pi} \oint d\xi_-^\alpha \xi_-^\alpha \check{C}_{\xi_-}^{\alpha\alpha}, \quad (99a)$$

$$\check{g}^\alpha \circ \tau_{z\varepsilon} - i\mathbf{v}_F^\alpha \cdot \Delta_R \check{g}^\alpha - \check{g}^\alpha \circ (\check{\Sigma}^\alpha - \hat{H}_0^\alpha)_{--} = \frac{i}{\pi} \oint d\xi_-^\alpha \xi_-^\alpha \check{C}_{\xi_-}^{\alpha\alpha}. \quad (99b)$$

We have no way to evaluate the right-hand sides because it would require first finding the poles of $\check{G}_{--}^{\alpha\alpha}$. Instead, we can subtract Eq. (99b) from Eq. (99a) to obtain the Eilenberger equation,

$$i\mathbf{v}_F^\alpha \cdot \Delta_R \check{g}^\alpha + [\tau_{z\varepsilon} - (\check{\Sigma}^\alpha - \hat{H}_0^\alpha)_{--}, \check{g}^\alpha]_0 = 0. \quad (100)$$

The distances between neighboring points are short compared to the characteristic COM length scale L , defined in Eq. (88), so we can approximate \check{g}^α by a continuous function in COM position and replace Δ_R by the gradient operator, ∇_R . One way to do this rigorously is to define the continuous function as a weighted average,

$$\check{g}_c^\alpha(\mathbf{R}) = \sum_{n \in \mathbb{Z}^3} \check{g}^\alpha(\mathbf{x}_n^\alpha) \frac{1}{C(\mathbf{R})} e^{-(\mathbf{R} - \mathbf{x}_n^\alpha)^2 / l^2}, \quad (101)$$

where $l \ll L$ and $C(\mathbf{R}) = \sum_{n \in \mathbb{Z}^3} e^{-(\mathbf{R} - \mathbf{x}_n^\alpha)^2 / l^2}$. From the fact that $l \ll L$, it is clear that $\check{g}^\alpha(\mathbf{x}_n^\alpha) \approx \check{g}_c^\alpha(\mathbf{x}_n^\alpha)$. Moreover, if $|\mathbf{x}_m^\alpha| \ll L$,

$$\begin{aligned} (\mathbf{x}_m^\alpha \cdot \Delta_R \check{g}^\alpha)(\mathbf{x}_n^\alpha) &\approx \sum_{n \in \mathbb{Z}^3} (\mathbf{x}_m^\alpha \cdot \Delta_R \check{g}^\alpha)(\mathbf{x}_n^\alpha) \frac{1}{C(\mathbf{R})} e^{-(\mathbf{R} - \mathbf{x}_n^\alpha)^2 / (2l)} = \sum_{n \in \mathbb{Z}^3} [\check{g}^\alpha(\mathbf{x}_n^\alpha + \mathbf{x}_m^\alpha) - \check{g}^\alpha(\mathbf{x}_n^\alpha)] \frac{1}{C(\mathbf{R})} e^{-(\mathbf{R} - \mathbf{x}_n^\alpha)^2 / (2l)} \\ &= \sum_{n \in \mathbb{Z}^3} \check{g}^\alpha(\mathbf{x}_n^\alpha) \left[\frac{e^{-(\mathbf{R} + \mathbf{x}_m^\alpha - \mathbf{x}_n^\alpha)^2 / (2l)}}{C(\mathbf{R} + \mathbf{x}_m^\alpha)} - \frac{e^{-(\mathbf{R} - \mathbf{x}_n^\alpha)^2 / (2l)}}{C(\mathbf{R})} \right] \approx \mathbf{x}_m^\alpha \cdot \nabla_R \check{g}_c^\alpha(\mathbf{x}_n^\alpha). \end{aligned} \quad (102)$$

Inserting this into Eq. (100) and relabeling $\check{g}_c^\alpha \rightarrow \check{g}^\alpha$, the Eilenberger equation now becomes, in terms of continuous COM coordinates,

$$i\mathbf{v}_F^\alpha \cdot \nabla_R \check{g}^\alpha + [\tau_{z\varepsilon} - (\check{\Sigma}^\alpha - \hat{H}_0^\alpha)_{--}, \check{g}^\alpha]_0 = 0. \quad (103)$$

The Eilenberger equation does not have a unique steady-state solution. This can be seen from the fact that any constant multiple of the identity matrix is a solution. To compensate for this, one typically assumes a normalization condition. In a spatially and temporally uniform system, we see from Eq. (70) that

$$\check{G}_{--}^{\alpha\alpha} = (\tau_{z\varepsilon} - \check{\xi}_-^\alpha - \check{V}^\alpha - \check{\Sigma}_{\text{imp}}^\alpha)^{-1} = P(-\check{\xi}_-^\alpha + D)^{-1} P^{-1}, \quad (104)$$

where $\tau_{z\varepsilon} - \check{V}^\alpha - \check{\Sigma}_{\text{imp}}^\alpha = PDP^{-1}$ and D is diagonal. Since D varies slowly as a function of $\check{\xi}_-^\alpha$ within the contour, we see that

$$\frac{i}{\pi} \oint d\xi_-^\alpha (-\check{\xi}_-^\alpha + D)_{ll}^{-1} = -\text{sgn}[\text{Im}(D_{ll})], \quad (105)$$

which implies that $\check{g}^\alpha \check{g}^\alpha = 1$. More generally, we assume that $\check{g}^\alpha \circ \check{g}^\alpha = 1$. This is consistent with the fact that $\check{g}^\alpha \circ \check{g}^\alpha = 1$ must also solve the Eilenberger equation, as can be seen by taking the circle product of the Eilenberger equation by \check{g}^α from the left and from the right, as well as the fact that the initial condition, if taken at $T \rightarrow -\infty$, should be a time-invariant

state, such that $\check{g}^\alpha \circ \check{g}^\alpha = \check{g}^\alpha \check{g}^\alpha = 1$. Moreover, it is possible to derive $\check{g}^\alpha \circ \check{g}^\alpha = 1$ if one defines the quasiclassical Green's function in terms of trajectory Green's function, as shown by Shelankov [62].

X. QUASICLASSICAL IMPURITY SELF-ENERGY

Before deriving the dirty limit equation of motion for the quasiclassical Green's function, we must express the impurity self-energy in terms of the quasiclassical Green's function. From Sec. V we have that

$$\begin{aligned} \check{\Sigma}_{\text{imp}}^\alpha(\varepsilon, T, \mathbf{k}, \mathbf{x}_n^\alpha) &= \sum_{X \in \{A, B\}} n_{\text{imp}}^{\alpha X} (\rho_X \langle U^{X\alpha} \rangle_{\text{imp}} \\ &\quad + \langle U^{X\alpha} U^{X\alpha} \rangle_{\text{imp}} \rho_X \langle \check{G}^{\alpha\alpha} \rangle_{nm}(\varepsilon, T) \rho_X). \end{aligned} \quad (106)$$

If on average there are an equal amount of impurities of equal average strength on both sublattices, and the impurities are not magnetic, then the first term is simply equivalent to a shift in the electrochemical potential. It can therefore be absorbed into μ^α .

To evaluate the second term in Eq. (106) we use the Eilenberger contour,

$$\begin{aligned} (\check{G}^{\alpha\alpha})_{nm} &= V_e^\alpha \int_{\diamond_\alpha} \frac{d[3]k}{(2\pi)^3} e^{i\rho_{\mathbf{b}k}\cdot\delta^\alpha} \check{G}^{\alpha\alpha}(\mathbf{k}, \mathbf{x}_n^\alpha) e^{-i\rho_{\mathbf{b}k}\cdot\delta^\alpha} = V_e^\alpha \int \frac{d\Omega}{4\pi} \int_{\xi_{\min}}^{\xi_{\max}} \frac{p^2 d\xi_{-\alpha}}{2\pi^2 (\xi_{-\alpha})'} e^{i\rho_{\mathbf{b}k}\cdot\delta^\alpha} \check{G}^{\alpha\alpha}(\mathbf{k}, \mathbf{x}_n^\alpha) e^{-i\rho_{\mathbf{b}k}\cdot\delta^\alpha} \\ &= V_e^\alpha \int \frac{d\Omega}{4\pi} \oint \frac{k^2 d\xi_{-\alpha}}{2\pi^2 v_F^\alpha} e^{i\rho_{\mathbf{b}k}\cdot\delta^\alpha} \check{G}^{\alpha\alpha}(\mathbf{k}, \mathbf{x}_n^\alpha) e^{-i\rho_{\mathbf{b}k}\cdot\delta^\alpha} + V_e^\alpha \int \frac{d\Omega}{4\pi} \oint \frac{k^2 d\xi_{-\alpha}}{2\pi^2 (\xi_{-\alpha})'} e^{i\rho_{\mathbf{b}k}\cdot\delta^\alpha} \check{G}^{\alpha\alpha}(\mathbf{k}, \mathbf{x}_n^\alpha) e^{-i\rho_{\mathbf{b}k}\cdot\delta^\alpha}. \end{aligned} \quad (107)$$

Using that

$$\rho_X e^{i\rho_{\mathbf{b}k}\cdot\delta^\alpha} \check{G}^{\alpha\alpha}(\mathbf{k}, \mathbf{x}_n^\alpha) e^{-i\rho_{\mathbf{b}k}\cdot\delta^\alpha} \rho_X = \rho_X \check{G}^{\alpha\alpha}(\mathbf{k}, \mathbf{x}_n^\alpha) \rho_X, \quad (108)$$

where $X \in \{A, B\}$, we see that we can remove the exponentials in Eq. (107). The first term on the right-hand side of Eq. (107) is what gives us the quasiclassical Green's function. To evaluate the second term, we can use the fact that we are far away from the Fermi surface, so, if we neglect spatial and temporal derivatives in the Gor'kov equations,

$$\begin{aligned} \check{G}^{\alpha\alpha} &\approx (\varepsilon\tau_z - \hat{H}_0^\alpha - \check{V}^\alpha - \check{\Sigma}_{\text{imp}}^\alpha)^{-1} \\ &= (-\hat{H}_0^\alpha)^{-1} - (\hat{H}_0^\alpha)^{-1} (\varepsilon\tau_z - \check{V}^\alpha - \check{\Sigma}_{\text{imp}}^\alpha) (\hat{H}_0^\alpha)^{-1} \\ &\quad + \mathcal{O}([\xi_{-\alpha}]^{-3}). \end{aligned} \quad (109)$$

We can neglect the second term after integration for the following reason. We can complete the contour in $\int d\xi_{-\alpha}$ with a semicircle of radius $(|\xi_{\min}| + |\xi_{\max}|)/2$. Since there are no poles inside the closed contour, the integral $\int d\xi_{-\alpha}$ must be equal to minus the integral over the semicircle arc. The integral over this arc is negligible because it is less than $\pi(|\xi_{\min}| + |\xi_{\max}|)/2 \times a \max(N_0^\alpha)/\min(|\xi_{\min}|, |\xi_{\max}|)^2$, which is $\mathcal{O}(N_0^\alpha(0)a/\Delta E^\alpha)$, where a is again an order of magnitude estimate of the elements of $(\varepsilon\tau_z - \check{V}^\alpha - \check{\Sigma}_{\text{imp}}^\alpha)$, and therefore much smaller than ΔE^α , and

$$\begin{aligned} N_0^\alpha(\varepsilon) &= \int \frac{d[3]k}{(2\pi)^3} \delta(\xi(\mathbf{k}) - \varepsilon) \\ &= \int \frac{d\Omega}{4\pi} \int \frac{k^2 d\xi}{2\pi^2 \xi'} \delta(\xi(\mathbf{k}) - \varepsilon) \end{aligned} \quad (110)$$

is the normal state density of states per spin. For the same reason, the terms of higher order in $(\xi^\alpha)^{-1}$ are also negligible. The first term, however, is not negligible, as the same argument shows that this integral is $\mathcal{O}(N_0(0))$, which is the same as the quasiclassical term.

Evaluating the $(-\hat{H}_0^\alpha)^{-1}$ and applying the projection operators, we get

$$\sum_{X \in A, B} \rho_X (-\hat{H}_0^\alpha)^{-1} \rho_X = \frac{\mu^\alpha - J^\alpha \rho_z \sigma_z \tau_z}{\xi_{-}^\alpha \xi_{+}^\alpha}. \quad (111)$$

Integrating out the momentum dependence, we see that we get constant matrices with the same matrix structure as a chemical potential and an antiferromagnetic spin-splitting. We can therefore include this by renormalizing μ^α and J^α .

In order to evaluate the quasiclassical contribution, we define

$$S_c^\alpha \begin{pmatrix} 1 \\ 0 \end{pmatrix} = S_c^\alpha, \quad (112)$$

where 1 and 0 are 4×4 matrices, such that

$$A_{--} = (S_c^\alpha)^T A S_c^\alpha. \quad (113)$$

Since only the contribution from the conduction band is non-negligible close to the Fermi surface, we have that

$$\oint \frac{k^2 d\xi_{-\alpha}}{2\pi^2 v_F^\alpha} \check{G}^{\alpha\alpha}(\mathbf{k}, \mathbf{x}_n^\alpha) = -i\pi N_0^\alpha(0) S_c^\alpha \check{g}^\alpha (S_c^\alpha)^T, \quad (114)$$

where S_c^α is evaluated at the Fermi surface.

Hence, if we define

$$\check{g}_s^\alpha := \int \frac{d\Omega}{4\pi} \check{g}^\alpha = \langle \check{g}^\alpha \rangle, \quad (115)$$

where in the last equality we also defined the angular average in momentum space as $\langle \cdot \rangle$, then

$$(\check{\Sigma}_{\text{imp}}^\alpha)_{--} = -\frac{i}{\tau_{\text{imp}}} \sum_{X \in \{A, B\}} (S_c^\alpha)^T \rho_X S_c^\alpha \check{g}_s^\alpha (S_c^\alpha)^T \rho_X S_c^\alpha, \quad (116)$$

where

$$\tau_{\text{imp}}^\alpha = (\pi N_0^\alpha(0) V_e^\alpha n_{\text{imp}}^{\alpha A} (U^{A\alpha} U^{A\alpha})_{\text{imp}})^{-1} \quad (117)$$

is the impurity scattering time.

Next, we find that

$$(S_c^\alpha)^T \rho_{A/B} S_c^\alpha = \frac{1}{2} \left(1 \pm \frac{J^\alpha}{\eta^\alpha} \sigma_z \tau_z \right), \quad (118)$$

such that

$$(\check{\Sigma}_{\text{imp}}^\alpha)_{--} = -\frac{i}{2\tau_{\text{imp}}^\alpha} \left(\check{g}_s^\alpha + \frac{(J^\alpha)^2}{(\eta^\alpha)^2} \sigma_z \tau_z \check{g}_s^\alpha \sigma_z \tau_z \right). \quad (119)$$

This reduces to the normal state impurity self-energy in the absence of antiferromagnetism when $J^\alpha = 0$. However, when $J^\alpha \neq 0$ we get an additional term, which is the same as one gets when adding magnetic impurities in the quasiclassical theory for normal metals. This is an important result, which means that impurities in the antiferromagnet behave as if they were magnetic. This effect becomes important when the system size becomes larger than the mean free path, and this is why one should expect the critical temperature to decrease in superconducting proximity structures when the antiferromagnet becomes larger than its mean free path, which explains the findings of Hübener *et al.* [45], as alluded to in Sec. I. Physical consequences of well Eq. (119), as well as a physical explanation for its existence is further discussed in Ref. [63].

The effective magnetic component of nonmagnetic impurities is similar to how interfacial disorder in antiferromagnetic insulators has been shown to give rise to magnetic effects when the interface is uncompensated [64], except that here it is a bulk effect. As a result, it is present even though the

magnetization is fully compensated. Another type of material in which one can find effective “magnetic” coupling from nonmagnetic impurities is in Rashba superconductors [65,66]. The strong coupling between spin and momentum degrees of freedom in Rashba superconductors means that nonmagnetic impurities get a nontrivial matrix structure in the helical basis [65]. However, the effective “magnetic” impurities in Rashba superconductors are different from what we see here. They couple to the p -wave part of the Green’s function and not the s -wave part. They are “magnetic” in the sense that they couple different components in the helical basis, but not in the sense that it is *as if* the system has magnetic impurities. Here we find that nonmagnetic impurities in AFMs are mathematically equivalent to having magnetic impurities in the original model.

XI. THE DIRTY LIMIT

In this section, we derive the equations of motion in the dirty limit, which are valid for diffusive systems. There are two central assumptions in the dirty limit. First, it is assumed that the quasiclassical Green’s function is dominated by the s -wave and p -wave components. Second, it is assumed that the elastic impurity scattering rate is large compared to the other energies in the system, except for the minimal distance between the Fermi level and the edges of the conduction band ΔE^α , and possibly J^α . We show that the resulting equations are valid if the variation in \check{g}^α over the length scale of the mean free path is small compared to 1. This is the case for instance if the system varies slowly in space or the proximity effect is small. In the limit of very strong exchange coupling, such that $(J^\alpha)^2/(\eta^\alpha)^2 = \mathcal{O}(1)$, we show that the quasiclassical Green’s function can be separated into short-range correlations and long-range components, where the former vanish in the diffusive limit. Therefore, this regime can be solved by projecting the Green’s function onto the set of long-range components. The derivation is done by averaging the Eilenberger equation,

$$i\mathbf{v}_F^\alpha \cdot \nabla_R \check{g}^\alpha + [\tau_z \varepsilon - \check{V}_{s-}^\alpha - (\check{\Sigma}_{\text{imp}}^\alpha)_{--}, \check{g}^\alpha]_\circ = 0, \quad (120)$$

over momentum directions. This will reduce the problem from having infinitely many coupled Green’s functions, one for each momentum direction, to having only two coupled Green’s functions.

Before proceeding, we first replace the gradient term with the covariant derivative. This is done by extracting the p -wave part of \check{V}_{s-}^α , meaning that we write

$$\check{V}_{s-}^\alpha = -\mathbf{v}_F^\alpha \cdot \hat{\mathbf{A}} + \check{V}_s^\alpha + \Delta \check{V}^\alpha, \quad (121)$$

where $\check{V}_s^\alpha = \langle \check{V}_{s-}^\alpha \rangle$ is the s -wave part and $-\mathbf{v}_F^\alpha \cdot \hat{\mathbf{A}}$ is the p -wave part of \check{V}_{s-}^α . The p -wave contribution includes the vector gauge potential from the electromagnetic field as well as spin-orbit coupling and the spatial variation in the Néel vector. The covariant derivative is then defined as

$$\tilde{\nabla} \circ \check{g} = \nabla_R \check{g} - i[\hat{\mathbf{A}}, \check{g}]_\circ, \quad (122)$$

such that

$$i\mathbf{v}_F^\alpha \cdot \tilde{\nabla} \circ \check{g}^\alpha + [\tau_z \varepsilon - \check{V}_s^\alpha - \Delta \check{V}^\alpha - (\check{\Sigma}_{\text{imp}}^\alpha)_{--}, \check{g}^\alpha]_\circ = 0. \quad (123)$$

Doing an angular average of Eq. (123), we get

$$i\tilde{\nabla} \circ \langle \mathbf{v}_F^\alpha \check{g}^\alpha \rangle + \left[\tau_z \varepsilon - \check{V}_s^\alpha + \frac{i(J^\alpha)^2}{2\tau_{\text{imp}}^\alpha (\eta^\alpha)^2} \sigma_z \tau_z \check{g}_s^\alpha \sigma_z \tau_z, \check{g}^\alpha \right]_\circ - \langle [\Delta \check{V}^\alpha, \check{g}^\alpha]_\circ \rangle = 0. \quad (124)$$

If we take the product with \mathbf{v}_F^α before averaging, we get

$$i\tilde{\nabla} \circ \langle \mathbf{v}_F^\alpha \otimes \mathbf{v}_F^\alpha \check{g}^\alpha \rangle + \left[\tau_z \varepsilon - \check{V}_s^\alpha + \frac{i}{2\tau_{\text{imp}}^\alpha} \check{g}_s^\alpha, \langle \mathbf{v}_F^\alpha \check{g}^\alpha \rangle \right]_\circ + \left[\frac{i(J^\alpha)^2}{2\tau_{\text{imp}}^\alpha (\eta^\alpha)^2} \sigma_z \tau_z \check{g}_s^\alpha \sigma_z \tau_z, \langle \mathbf{v}_F^\alpha \check{g}^\alpha \rangle \right]_\circ - \langle [\Delta \check{V}^\alpha, \mathbf{v}_F^\alpha \check{g}^\alpha]_\circ \rangle = 0, \quad (125)$$

where \otimes denotes the tensor product. Next, we define the matrix current

$$\check{\mathbf{j}}^\alpha := \langle \mathbf{v}_F^\alpha \check{g}^\alpha \rangle. \quad (126)$$

The aim is a set of equations for $\check{\mathbf{j}}^\alpha$ and $\check{g}_s^\alpha = \langle \check{g}^\alpha \rangle$. This can be obtained from Eqs. (124) and (125) if we assume that $\Delta \check{V}^\alpha$ is negligible. Neglecting the terms proportional to $\Delta \check{V}^\alpha$, multiplying Eq. (125) by τ_{imp}^α , and defining the diffusion tensor,

$$D^\alpha := \tau_{\text{imp}}^\alpha \langle \mathbf{v}_F^\alpha \otimes \mathbf{v}_F^\alpha \rangle, \quad (127)$$

Eqs. (124) and (125) become

$$i\tilde{\nabla} \circ \check{\mathbf{j}}^\alpha + \left[\tau_z \varepsilon - \check{V}_s^\alpha + \frac{i(J^\alpha)^2}{2\tau_{\text{imp}}^\alpha (\eta^\alpha)^2} \sigma_z \tau_z \check{g}_s^\alpha \sigma_z \tau_z, \check{g}_s^\alpha \right]_\circ = 0, \quad (128)$$

and

$$\check{g}_s^\alpha \circ \check{\mathbf{j}}^\alpha = -\tilde{\nabla} \circ (D^\alpha \check{g}_s^\alpha) + i\tau_{\text{imp}}^\alpha [\tau_z \varepsilon - \check{V}_s^\alpha, \check{\mathbf{j}}^\alpha]_\circ - \left[\frac{(J^\alpha)^2}{2(\eta^\alpha)^2} \sigma_z \tau_z \check{g}_s^\alpha \sigma_z \tau_z, \check{\mathbf{j}}^\alpha \right]_\circ, \quad (129)$$

respectively. In Eq. (129) we assumed that the higher-order spherical harmonics in \check{g}^α are small, and used that $\{\check{\mathbf{j}}^\alpha, \check{g}_s^\alpha\} = 0$. The latter follows from the former together with the p -wave component of the normalization condition, $\langle \mathbf{v}_F^\alpha \check{g}^\alpha \circ \check{g}^\alpha \rangle = \langle \check{\mathbf{j}}^\alpha, \check{g}_s^\alpha \rangle = 0$. The assumption that the d -wave component is negligible compared to 1 is consistent as long as $\check{\mathbf{j}}^\alpha$ is small compared to the Fermi velocity. To see why, note that the normalization condition

$$\check{g}^\alpha \circ \check{g}^\alpha = \check{g}_s^\alpha \circ \check{g}_s^\alpha + \{\check{g}_s^\alpha, \Delta \check{g}^\alpha\}_\circ + \Delta \check{g}^\alpha \circ \Delta \check{g}^\alpha = 1 \quad (130)$$

must be satisfied for all momenta. Hence, if $\Delta \check{g}^\alpha = \check{g}_p^\alpha + \check{g}_d^\alpha + \dots$, where \check{g}_p^α is the p -wave component and \check{g}_d^α is the d -wave component, the d -wave component resulting from $\check{g}_p^\alpha \circ \check{g}_p^\alpha$ must be canceled by the d -wave term in $\{\check{g}_s^\alpha, \check{g}_d^\alpha\}_\circ$. If $\check{g}_s = \mathcal{O}(1)$, then \check{g}_d^α will be $\mathcal{O}[(\check{\mathbf{j}}^\alpha \cdot \mathbf{v}_F^\alpha / (v_F^\alpha)^2)^2]$, which we assume is negligible compared to 1. Hence,

$$\tau_{\text{imp}}^\alpha \langle \mathbf{v}_F^\alpha \otimes \mathbf{v}_F^\alpha \check{g}^\alpha \rangle \approx D^\alpha \check{g}_s^\alpha + \tau_{\text{imp}}^\alpha \left\langle \frac{\mathbf{v}_F^\alpha \otimes \mathbf{v}_F^\alpha (\check{\mathbf{j}}^\alpha \cdot \mathbf{v}_F^\alpha)}{(v_F^\alpha)^2} \right\rangle \approx D^\alpha \check{g}_s^\alpha. \quad (131)$$

If the Fermi surface is spherically symmetric, then $D_{ij}^\alpha = \delta_{ij} \tau_{\text{imp}}^\alpha (v_F^\alpha)^2 / 3$.

For a complete description in terms of $\check{\mathbf{j}}^\alpha$ and \check{g}_s^α , we must also express the normalization condition, $\check{g}_s^\alpha \circ \check{g}_s^\alpha = 1$ in terms of \check{g}_s^α and $\check{\mathbf{j}}^\alpha$. Taking the angular average of the normalization condition and using that $\langle \mathbf{v}_F^\alpha / (v_F^\alpha)^2 \rangle = 0$, we get that

$$\check{g}_s^\alpha \circ \check{g}_s^\alpha = 1 + \mathcal{O}(|\check{\mathbf{j}}^\alpha / v_F^\alpha|^2). \quad (132)$$

We have already assumed that $(\check{\mathbf{j}}^\alpha \cdot \mathbf{v}_F^\alpha / (v_F^\alpha)^2)^2$ is negligible compared to 1, so

$$\check{g}_s^\alpha \circ \check{g}_s^\alpha = 1. \quad (133)$$

Using Eq. (133), we can rewrite Eq. (129) to

$$\check{\mathbf{j}}^\alpha = -\check{g}_s^\alpha \circ \check{\nabla} \circ (D^\alpha \check{g}_s^\alpha) + i\tau_{\text{imp}}^\alpha \check{g}_s^\alpha \circ [\tau_z \varepsilon - \check{V}_s^\alpha, \check{\mathbf{j}}^\alpha]_o - \check{g}_s^\alpha \circ \left[\frac{(J^\alpha)^2}{2(\eta^\alpha)^2} \sigma_z \tau_z \check{g}_s^\alpha \sigma_z \tau_z, \check{\mathbf{j}}^\alpha \right]. \quad (134)$$

Eqs. (133), (128), and (134) can be used to study systems with an arbitrary amount of disorder, provided that the matrix current squared $|\check{\mathbf{j}}^\alpha|^2$ is small compared to the Fermi velocity squared $|v_F^\alpha|^2$. To say that $|\check{\mathbf{j}}^\alpha|^2 \ll |v_F^\alpha|^2$ is the same as saying that the quasiclassical Green's function is approximately isotropic in momentum space. Physically, this is expected to be the case when the elastic scattering time τ_{imp}^α is small, but this can also happen, for example, if the tunneling is weak. In Sec. XII we show that the matrix current at the boundary is proportional to the square amplitude of the tunneling in the absence of spin-active boundaries.

We can also simplify Eq. (134) a bit further if we assume that $|\tau_{\text{imp}}^\alpha \check{V}_s^\alpha| \ll 1$ and only consider energies $|\varepsilon| \ll 1/\tau_{\text{imp}}^\alpha$. In this case, we can neglect the second term on the right-hand side of Eq. (134), since this term must be much smaller in magnitude than $\check{\mathbf{j}}^\alpha$. Hence,

$$\check{\mathbf{j}}^\alpha = -\check{g}_s^\alpha \circ \check{\nabla} \circ (D^\alpha \check{g}_s^\alpha) - \check{g}_s^\alpha \circ \left[\frac{(J^\alpha)^2}{2(\eta^\alpha)^2} \sigma_z \tau_z \check{g}_s^\alpha \sigma_z \tau_z, \check{\mathbf{j}}^\alpha \right]_o. \quad (135)$$

At this point, it might be tempting to also assume that the last term in the commutator in Eq. (128) is dominant, but this is *not* generally true. Although $1/\tau_{\text{imp}}^\alpha \gg |\check{V}_s^\alpha|$, one can not say in general that

$$\left[\frac{i(J^\alpha)^2}{2\tau_{\text{imp}}^\alpha (\eta^\alpha)^2} \sigma_z \tau_z \check{g}_s^\alpha \sigma_z \tau_z, \check{g}_s^\alpha \right]_o \gg [|\check{V}_s^\alpha, \check{g}_s^\alpha]_o. \quad (136)$$

This can be because the prefactor $(J^\alpha)^2/(\eta^\alpha)^2$ is small, or it can be because the matrices on the right-hand side commute, even for very strong antiferromagnets with $(J^\alpha)^2/(\eta^\alpha)^2 = \mathcal{O}(1)$. This is because, even though the prefactor can be large, the commutator can still be small. Thus, one must in general keep all terms in Eq. (128).

Next, consider the case of very strong exchange coupling, such that $(J^\alpha)^2/(\eta^\alpha)^2 = \mathcal{O}(1)$. In this case the prefactor $(J^\alpha)^2/[2\tau_{\text{imp}}^\alpha (\eta^\alpha)^2]$ is large in the diffusive limit. This will strongly suppress some components of the quasiclassical Green's function, making them negligible in the diffusive limit. We can write the quasiclassical Green's functions in

terms of Pauli matrices in spin space and Nambu space as

$$\check{g}^\alpha = \sum_{i=0}^3 \sum_{j=0}^3 c_{ij} \tau_i \sigma_j, \quad (137)$$

where σ_0 and τ_0 are identity matrices and $\{c_{ij}\}$ is a set of scalar functions. We can separate these components into *long-range* components, satisfying

$$\sigma_z \tau_z c_{ij} \tau_i \sigma_j \sigma_z \tau_z = c_{ij} \tau_i \sigma_j, \quad (138)$$

and *short-range* components, satisfying

$$\sigma_z \tau_z c_{ij} \tau_i \sigma_j \sigma_z \tau_z = -c_{ij} \tau_i \sigma_j. \quad (139)$$

That is, long-range components have either $i \in \{0, 3\}$ and $j \in \{0, 3\}$ or $i \in \{1, 2\}$ and $j \in \{1, 2\}$, while the short-range components are the remaining components. Note that the product of two long-ranged components or two short-ranged components is a long-range component, while the product of one long-range component and one short-range component is a short-range component.

Let the subscripts SR and LR denote the short-range and long-range components, respectively, such that $\check{g}^\alpha = \check{g}_{\text{SR}}^\alpha + \check{g}_{\text{LR}}^\alpha$. Using the product properties of long-range and short-range components, the long-range component of Eq. (128) becomes

$$i\check{\nabla}_{\text{LR}} \circ \check{\mathbf{j}}_{\text{LR}}^\alpha + [\tau_z \varepsilon - \check{V}_{\text{LR},s}^\alpha, \check{g}_{\text{LR},s}^\alpha]_o + [\hat{\mathbf{A}}_{\text{SR}}, \check{\mathbf{j}}_{\text{SR}}^\alpha]_o - [\check{V}_{\text{SR},s}^\alpha, \check{g}_{\text{SR},s}^\alpha]_o = 0, \quad (140)$$

where $\check{\nabla}_{\text{LR}} \circ \check{\mathbf{j}}_{\text{LR}}^\alpha = \nabla_R \cdot \check{\mathbf{j}}_{\text{LR}}^\alpha - i[\hat{\mathbf{A}}_{\text{LR}}, \check{\mathbf{j}}_{\text{LR}}^\alpha]_o$. We want to show that the short-range components vanish from the equations in the diffusive limit when $(J^\alpha)^2/(\eta^\alpha)^2 \rightarrow 1$. This means that in this limit one can solve quasiclassical equations by simply setting the short-ranged components to zero.

Assuming that $(J^\alpha)^2/(\eta^\alpha)^2 \approx 1$, $|\tau_{\text{imp}}^\alpha \check{V}_s^\alpha| \ll 1$ and only considering energies $|\varepsilon| \ll 1/\tau_{\text{imp}}^\alpha$, the Eilenberger equation for the short-range components becomes

$$\check{\nabla} \circ (v_F^\alpha \check{g}_{\text{SR}}^\alpha) + \frac{1}{\tau_{\text{imp}}^\alpha} [(\check{g}_{\text{LR}}^\alpha), \check{g}_{\text{SR}}^\alpha]_o = 0. \quad (141)$$

The short-range correlations and the long-range correlations will generally not commute. As a result, we see that the short-range correlations decay exponentially over a distance equal to the mean free path in this case.

Making no assumptions other than assuming that τ_{imp}^α is small and $\check{g}_s^\alpha \circ \check{g}_s^\alpha = 1$, which is valid even if the short-range components are not isotropic, provided they are small in magnitude, the short-range component of Eq. (125) becomes

$$\check{\mathbf{j}}_{\text{SR}}^\alpha = -\tau_{\text{imp}}^\alpha (\check{g}_s^\alpha \circ \check{\nabla} \circ (v_F^\alpha \otimes v_F^\alpha \check{g}_s^\alpha))_{\text{SR}} - \left(\frac{\check{g}_s^\alpha}{2} \circ [(\check{g}_{\text{LR}}^\alpha) - \check{g}_{\text{SR}}^\alpha, \check{\mathbf{j}}^\alpha]_o \right)_{\text{SR}}. \quad (142)$$

Using that $\check{g}_{\text{SR}}^\alpha$ decays exponentially away from the interface with over a length-scale equal to the mean free path, Eq. (142) implies that, since $\check{g}_{\text{LR}}^\alpha = \mathcal{O}(1)$,

$$\check{g}_{\text{SR}}^\alpha = \mathcal{O} \left(\frac{J^\alpha \check{\mathbf{j}}_{\text{SR}}^\alpha}{|D^\alpha|} \right), \quad (143)$$

where $J_{\text{imp}}^\alpha = v_F^\alpha \tau_{\text{imp}}^\alpha$ is the mean free path. The short-range component of the matrix current will be largest closest to the interface, where it will be determined by the boundary conditions. Moreover, in the diffusive regime, the matrix current is small at the interface, as discussed in Sec. XII. Hence, in the diffusive regime we see that $\check{g}_{\text{SR}}^\alpha = \mathcal{O}(\tau_{\text{imp}}^\alpha)$. Hence, to zeroth order in τ_{imp}^α the long-ranged components can be solved for consistently in the limit $(J^\alpha)^2/(\eta^\alpha)^2 \rightarrow 1$ by setting the short-ranged components to zero, effectively projecting out these components from the Green's function.

Very close to the interface the term $[\hat{A}_{\text{SR}}, \check{J}_{\text{SR}}]_\circ$ can give a contribution to Eq. (140). This is not a problem if $\hat{A}_{\text{SR}} = 0$, but in Sec. XIII we show that, similar to spin-orbit coupling, nonuniform magnetic textures can induce a nonzero \hat{A}_{SR} . This means that if there are domain walls very close to the interface to a spin-singlet superconductor, it can induce long-ranged superconducting correlations in the antiferromagnetic metal. As long as $\hat{A}_{\text{SR}} = 0$, the limit of very strong exchange coupling, $(J^\alpha)^2/(\eta^\alpha)^2 \rightarrow 1$, can be consistently captured by setting the short-range components to zero and solving

$$i\check{\nabla}_{\text{LR}} \circ \check{J}_{\text{LR}}^\alpha + [\tau_z \varepsilon - \check{J}_{\text{LR},s}^\alpha, \check{g}_{\text{LR},s}^\alpha]_\circ = 0. \quad (144)$$

The matrix current can be found by doing the same projection in Eq. (125), which in the limit $(J^\alpha)^2/(\eta^\alpha)^2 \rightarrow 1$ simply becomes

$$\check{J}_{\text{LR}}^\alpha = -\frac{\check{g}_{\text{LR},s}^\alpha \circ \check{\nabla} \circ (D^\alpha \check{g}_{\text{LR},s}^\alpha)}{2}. \quad (145)$$

From Eq. (135) we see that $\check{J}^\alpha \cdot \mathbf{v}_F / (v_F^\alpha)^2 = \mathcal{O}(J_{\text{imp}}^\alpha \check{\nabla} \circ \check{g}_s^\alpha)$, where $J_{\text{imp}}^\alpha = v_F^\alpha \tau_{\text{imp}}^\alpha$ is the mean free path. As a result, the assumption that $\check{g}_s^\alpha \circ \check{g}_s^\alpha = 1$ is consistent as long as the change in \check{g}_s^α over the length of the mean free path is small compared to 1. In the limit of strong exchange coupling, the short-ranged components can decay over a length scale equal to the mean free path, but these components also become negligible, as shown above. Therefore, although the short-ranged components are not necessarily isotropic in the limit $J^\alpha \rightarrow \infty$, one can still solve the diffusive equations as long as there is no strong spin-orbit coupling or sudden change in the Néel vector close to the interface. To simplify the equations in this limit, one can project out the long-range components. Spin-orbit coupling or nonuniform Néel vector close to the boundary can induce long-range components from the short-range components of the matrix current. In this case, it is therefore not always consistent to simply set the short-range components to zero. Instead, if the limit of very strong exchange coupling is necessary, one should solve the full Eilenberger equation for the short-ranged components.

Equations (135) and (128) are our main results, together with the boundary condition derived in Sec. XII. They provide general equations of motion, which can be solved to obtain information about currents, densities, the local density of states, and superconducting correlations in systems with antiferromagnetism and arbitrary geometry both in and out of equilibrium. In the absence of antiferromagnetism, meaning that $J^\alpha \rightarrow 0$, Eqs. (135) and (128) reduce to the well-known Usadel equation for normal dirty metals [4]. In the presence of antiferromagnetism, there are three important differences. First, all self-energies must be projected onto the conduction

band, which means that they must be transformed according to the S_c^α matrix. Second, the coupling between spin and sublattice gives rise to effective magnetic impurities with scattering time $\tau_{\text{imp}}^\alpha (\eta^\alpha)^2 / (J^\alpha)^2$. Third, the magnetic impurities also modify the equation for the matrix current, which in the normal metal case is simply $\check{J}^\alpha = -\check{g}_s^\alpha \circ \check{\nabla} \circ (D^\alpha \check{g}_s^\alpha)$.

One can solve Eq. (135) for \check{J}^α in time-independent situations. If we can diagonalize $(\check{g}_s^\alpha \sigma_z \tau_z \check{g}_s^\alpha \sigma_z \tau_z)_{ij} = \check{U}_{ik}^{-1} \lambda_k \check{U}_{kj}$, we find that

$$\check{J}_{ij}^\alpha = -\check{U}_{ik}^{-1} \frac{\check{U}_{km} [\check{g}_s^\alpha \check{\nabla} \cdot (D^\alpha \check{g}_s^\alpha)]_{mn} \check{U}_{ml}^{-1}}{1 + (J^\alpha)^2 (\lambda_k + \lambda_l) / [2(\eta^\alpha)^2]} \check{U}_{lj}, \quad (146)$$

with summation over repeated indices. Alternatively, since $(J^\alpha/\eta^\alpha)^2$ is smaller by 1 by definition, one can solve for \check{J}^α by iteratively inserting into the right-hand side of Eq. (135). To get a series expansion with a faster convergence rate it can be beneficial to rewrite Eq. (135) as

$$\check{J}^\alpha = -[1 + (J^\alpha/\eta^\alpha)^2]^{-1} \left\{ \check{g}_s^\alpha \circ \check{\nabla} \circ (D^\alpha \check{g}_s^\alpha) + \check{g}_s^\alpha \circ \left[\frac{(J^\alpha)^2}{2(\eta^\alpha)^2} \sigma_z \tau_z [\check{g}_s^\alpha, \sigma_z \tau_z], \check{J}^\alpha \right]_\circ \right\}. \quad (147)$$

This is because the effective magnetic impurities in Eq. (128) will tend to suppress $[\check{g}_s^\alpha, \sigma_z \tau_z]$. In the limit of small J^α/η^α or vanishing $[\check{g}_s^\alpha, \sigma_z \tau_z]$, one can solve Eqs. (128) and (135) in the same way as the Usadel equation for normal metals, but with a renormalized diffusion coefficient, $D^\alpha \rightarrow D^\alpha / [1 + (J^\alpha/\eta^\alpha)^2]$, additional magnetic impurities and self-energies, which are projected onto the conduction band of the antiferromagnet. Otherwise, in the more general case, one can for instance solve Eqs. (128) and (135) numerically using the algorithm presented in Appendix.

XII. BOUNDARY CONDITION

Next, we derive the boundary condition, which is valid in the diffusive regime. To do so, we must evaluate the two terms, which we could neglect in the equation of motion inside the materials. These are the tunneling terms and the potentials, which are large only outside the materials. Here we consider the interface between material L and R . To get the boundary condition at the interface to a vacuum or an insulator, one need only set the tunneling to zero. As before, let (α, β) be either (L, R) or (R, L) . We assume that the Green's functions are approximately spherically symmetric also close to the interface. This is the case as long as the matrix current at the interface is small compared to the Fermi velocity, which happens for instance when the tunneling amplitudes are small.

The way the boundary condition is derived here is that we sum the Gor'kov equations over a small set of unit cells, which includes the interface. We take this set to be the shape of a wide cylinder. The width of this cylinder is much larger than its length but much smaller than the characteristic length scale L of the bulk as defined in Sec. IX. Then we integrate over all momentum directions and integrate over the Eilenberger contour. First, we consider the potential, which is large only outside material α ,

$$(\hat{\Sigma}_R^\alpha)_{nm}(t_1, t_2) = \hat{K}_n^\alpha(t_1) \delta_{nm} \delta(t_1 - t_2), \quad (148)$$

where \hat{R}_n^α is nonzero only at the boundary and outside of material α . Taking the bullet product with $\check{G}^{\alpha\alpha}$, we have

$$\left(\check{G}^{\alpha\alpha} \bullet \hat{\Sigma}_R^\alpha\right)_{nm}(t_1, t_2) = \check{G}_{nm}^\alpha(t_1, t_2) \hat{R}_m^\alpha(t_2). \quad (149)$$

Next, we sum this over a set of unit cells V and define $I \subset V$ to be the subset of V , which is at the interface. We get

$$\left\langle \frac{i}{\pi} \oint d\xi_-^\alpha \sum_{n \in V} \check{G}^{\alpha\alpha} \bullet \hat{\Sigma}_R^\alpha \right\rangle = \sum_{n \in I} S_c^\alpha \check{g}_s^\alpha(\mathbf{x}_n^\alpha) (S_c^\alpha)^T \circ \hat{R}_n^\alpha. \quad (150)$$

Note that in our model $\hat{\Sigma}_R^\alpha$ is very large outside material α , such that $\check{G}^{\alpha\alpha}(\mathbf{k}, \mathbf{x}) \hat{\Sigma}_R^\alpha(\mathbf{x}) \sim 1$ when \mathbf{x} is outside material α . Nevertheless, only the points in I contribute in Eq. (150). This is because the poles of $\check{G}^{\alpha\alpha}$ are shifted outside of the Eilenberger contour when \mathbf{x} is outside of material α , rendering the quasiclassical Green's function exactly equal to zero. The points at, or very close to, the interface are therefore the only points where both \check{g}^α and \hat{R}_n^α are different from 0.

Since the width of the cylinder is small compared to L , \check{g}_s^α is approximately constant on the points in I . We further assume that \hat{R}_n^α is also approximately constant on the points in I . This means that if $l \in I$ and Γ is the number of unit cells in I , then

$$\left\langle \frac{i}{\pi} \oint d\xi_-^\alpha \sum_{n \in V} \check{G}^{\alpha\alpha} \bullet \hat{\Sigma}_R^\alpha \right\rangle = \Gamma S_c^\alpha \check{g}_s^\alpha(\mathbf{x}_l^\alpha) (S_c^\alpha)^T \circ \hat{R}_l^\alpha. \quad (151)$$

Next, we must evaluate

$$\begin{aligned} & \left(\hat{\Sigma}_R^\alpha \bullet \check{G}^{\alpha\alpha}\right)(\mathbf{k}, \mathbf{x}_n^\alpha) \\ &= V_e^\alpha \sum_{m \in \mathbb{Z}^3} \int_{\diamond_\alpha} \frac{d[3]q}{(2\pi)^3} \hat{R}_m^\alpha \circ e^{-i\rho_B(\mathbf{k}-\mathbf{q}) \cdot \delta^\alpha} \\ & \quad \times \check{G}^{\alpha\alpha}(\mathbf{q}, \mathbf{x}_n) e^{i\rho_B(\mathbf{k}-\mathbf{q}) \cdot \delta^\alpha} e^{-i(\mathbf{k}-\mathbf{q}) \cdot (\mathbf{x}_m^\alpha - \mathbf{x}_n^\alpha)}. \end{aligned} \quad (152)$$

First, we evaluate the sum over m . We use that $\hat{R}_m^\alpha = \hat{R}_l^\alpha$, where \mathbf{x}_l^α is a point on the interface close to \mathbf{x}_n^α , whenever \mathbf{x}_m^α is on the interface. Otherwise, $\hat{R}_m^\alpha = 0$. We find that

$$\left(\hat{\Sigma}_R^\alpha \bullet \check{G}^{\alpha\alpha}\right)_{ij}(\mathbf{k}, \mathbf{x}_n^\alpha) = \hat{R}_l^\alpha \circ \int_{\diamond_\alpha} \frac{d[3]q}{(2\pi)^3} f_{ij}(\mathbf{q}) \check{G}_{ij}^{\alpha\alpha}(\mathbf{k} + \mathbf{q}, \mathbf{x}_n), \quad (153)$$

where f_{ij} is a normalized function, which is peaked at $\mathbf{q} = 0$. Next, integrating over the Eilenberger contour and averaging over momentum directions, we find that

$$\left\langle \frac{i}{\pi} \oint d\xi_-^\alpha \sum_{n \in V} \hat{\Sigma}_R^\alpha \bullet \check{G}^{\alpha\alpha} \right\rangle = \Gamma \hat{R}_l^\alpha \circ S_c^\alpha \check{g}_s^\alpha(\mathbf{x}_l^\alpha) (S_c^\alpha)^T. \quad (154)$$

Next, we must evaluate the tunneling self-energy,

$$\check{\Sigma}_T^\alpha = \hat{T}^{\alpha\beta} \bullet \check{G}_0^{\beta\beta} \bullet \hat{T}^{\beta\alpha}. \quad (155)$$

To proceed, we must assume some properties of the tunneling term. The tunneling should be short ranged and only at lattice points at the interface between the two materials. For each unit cell in material α at the interface we assume that there is exactly one connected unit cell in material β . For simplicity, we label the connected unit cells the same. This means that if \mathbf{x}_n^α is at the interface, then the connected unit cell in material

β is \mathbf{x}_n^β . With this we have

$$\hat{T}_{nm}^{\alpha\beta} = \sum_{l \in \text{int}} \hat{T}_l^{\alpha\beta} \delta_{ln} \delta_{lm}, \quad (156)$$

where the sum goes over all the points at the interface. Hence, if χ_{int} is the characteristic function, which is 1 if the argument is at the interface and 0 otherwise, then

$$\left(\check{\Sigma}_T^\alpha\right)_{nm}(t_1, t_2) = \hat{T}_n^{\alpha\beta}(t_1) (\check{G}_0^{\beta\beta})_{nm}(t_1, t_2) \hat{T}_m^{\beta\alpha}(t_2) \chi_{\text{int}}(n) \chi_{\text{int}}(m), \quad (157)$$

In order to evaluate the bullet product

$$\begin{aligned} \left(\check{G}^{\alpha\alpha} \bullet \check{\Sigma}_T^\alpha\right)(\mathbf{k}, \mathbf{x}_n^\alpha) &= \chi_{\text{int}}(n) \sum_{m \in \text{int}} \check{G}^{\alpha\alpha}(\mathbf{k}, \mathbf{x}_m^\alpha) \\ & \quad \circ e^{-i\rho_B \mathbf{k} \cdot \delta^\alpha} \hat{T}_m^{\alpha\beta} \circ (\check{G}_0^{\beta\beta})_{mn} \circ \hat{T}_n^{\beta\alpha} e^{i\rho_B \mathbf{k} \cdot \delta^\alpha} \\ & \quad \times e^{-i\mathbf{k} \cdot (\mathbf{x}_m^\alpha - \mathbf{x}_n^\alpha)}, \end{aligned} \quad (158)$$

we write

$$\begin{aligned} (\check{G}_0^{\beta\beta})_{mn} &= V_e^\beta \int_{\diamond_\beta} \frac{d[3]p}{(2\pi)^3} e^{i\rho_B \mathbf{p} \cdot \delta^\beta} \check{G}_0^{\beta\beta}(\mathbf{x}^\beta, \mathbf{p}) e^{-i\rho_B \mathbf{p} \cdot \delta^\beta} \\ & \quad \times e^{i\mathbf{p} \cdot (\mathbf{x}_m^\beta - \mathbf{x}_n^\beta)}. \end{aligned} \quad (159)$$

We can separate this integral into the quasiclassical contribution and a rest term, or high-energy contribution, according to the Eilenberger contour. The high-energy contribution was not negligible when we calculated the impurity self-energy. This was because we evaluated the Green's function at $m = n$. The high-energy contribution to the term in Eq. (158) with $m = n$ will only renormalize \hat{R}_n , because it only depends on \hat{H}_0^β , as we showed earlier. When evaluated at $m \neq n$ the oscillating exponential suppresses the integral for the high-energy contribution. For this reason, we neglect the high-energy contribution.

Next, we must evaluate the quasiclassical part. Close to the Fermi surface we have $\xi_-^\beta(p) = 0 + (p - p_F^\beta)(\xi_-^\beta)/(p_F^\beta) = v_F^\beta(p - p_F^\beta)$. Hence, if the poles are located at $\{\xi_i\}_i$,

$$\begin{aligned} \frac{i}{\pi} \oint d\xi \check{G}_0^{\beta\beta} e^{ipr} &= - \sum_{\xi_i} \text{sgn}(\text{Im}[\xi_i]) \text{Res}(\check{G}_0^{\beta\beta}, \xi_i) \\ & \quad \times \exp(i\mathbf{r} \cdot \mathbf{e}_p [p_F + \xi_i/v_F^\beta]) \end{aligned} \quad (160)$$

From Eq. (119) we know that impurity scattering gives rise to an imaginary shift in the pole location, such that $|\text{Im}(\xi_i)| \geq 1/2\tau_{\text{imp}}^\beta$. Therefore,

$$|e^{ir\xi_i/v_F^\beta}| < e^{-r/2l_{\text{mfp}}^\beta}, \quad (161)$$

where $l_{\text{mfp}}^\beta = \tau_{\text{imp}}^\beta v_F^\beta$ is the mean free path. The effective mean free path very close to the interface may additionally be lowered by interfacial disorder.

The exponential decay means that we need only consider relative distances up to around the mean free path in the sum over $m \in \text{int}$. In the dirty limit, which is what we consider here, it is assumed that $1/2\tau_{\text{imp}}^\beta$ is much larger than all the other self-energy contributions, and therefore $|\text{Im}(\xi_i)|$ is much larger than the real part of ξ_i . As a result, when $r < 2l_{\text{mfp}}^\beta$, $r \text{Re}(\xi_i)/v_F^\beta < 2\tau_{\text{imp}}^\beta \text{Re}(\xi_i) \ll 1$, which means that we can

neglect $\text{Re}\xi_i/v_F^\beta$ in the exponential function when $r < 2l_{\text{mfp}}^\beta$. Hence,

$$\frac{i}{\pi} \oint d\xi_{-}^{\beta} \check{G}_0^{\beta\beta} e^{i\mathbf{p}\cdot\mathbf{r}} = S_c^\beta \check{g}_0^\beta (S_c^\beta)^T e^{i\mathbf{r}\cdot\mathbf{p}_F^\beta} f^\beta(\mathbf{r}). \quad (162)$$

where $f^\beta(\mathbf{r})$ is an exponentially decaying function that gives rise to a soft cutoff as a function of relative distance at $|\mathbf{r}| \approx 2l_{\text{mfp}}^\beta$. Hence, we find that

$$\left\langle \frac{i}{\pi} \oint d\xi_{-}^{\alpha} \sum_{n \in V} \check{G}^{\alpha\alpha} \bullet \hat{\Sigma}_T \right\rangle = -i\pi V_e^\beta \sum_{n \in I} \sum_{m \in \text{int}} \int \frac{d\Omega_p}{4\pi} \int \frac{d\Omega_k}{4\pi} \frac{f^\beta(\mathbf{x}_m^\beta - \mathbf{x}_n^\beta) (\mathbf{p}_F^\beta)^2}{2\pi v_F^\beta} S_c^\alpha \check{g}_s^\alpha(\mathbf{k}_F^\alpha, \mathbf{x}_m^\alpha) (S_c^\alpha)^T \circ e^{-i\rho_B \mathbf{k}_F^\alpha \cdot \delta^\alpha} \hat{\Gamma}_n^{\alpha\beta} e^{i\rho_B \mathbf{p}_F^\beta \cdot \delta^\beta} S_c^\beta \check{g}_0^\beta(\mathbf{p}_F^\beta, \mathbf{x}_n^\beta) (S_c^\beta)^T \circ e^{-i\rho_B \mathbf{p}_F^\beta \cdot \delta^\beta} \hat{\Gamma}_m^{\beta\alpha} e^{i\rho_B \mathbf{k}_F^\alpha \cdot \delta^\alpha} e^{-i\mathbf{k}_F^\alpha \cdot (\mathbf{x}_m^\alpha - \mathbf{x}_n^\alpha)} e^{i\mathbf{p}_F^\beta \cdot (\mathbf{x}_m^\beta - \mathbf{x}_n^\beta)}. \quad (163)$$

Next, we assume that the averaging over all momentum directions for both \mathbf{p}_F^β and \mathbf{k}_F^α gives the s -wave contribution from the Green's function together with a renormalization of the tunneling amplitudes. This is the case because we assume that the Green's functions are approximately spherically symmetric also close to the interface. As a result, we finally have

$$\left\langle \frac{i}{\pi} \oint d\xi_{-}^{\alpha} \sum_{n \in V} \check{G}^{\alpha\alpha} \bullet \hat{\Sigma}_T \right\rangle_{--} = -i \sum_{n \in I} \check{g}_s^\alpha(\mathbf{x}_n^\alpha) \circ \hat{\mathcal{T}}_n^{\alpha\beta} \circ \check{g}_{0,s}^\beta(\mathbf{x}_n^\beta) \circ \hat{\mathcal{T}}_n^{\beta\alpha}, \quad (164)$$

where

$$\hat{\mathcal{T}}_n^{\alpha\beta} = (S_c^\alpha)^T \hat{\Gamma}_n^{\alpha\beta} S_c^\beta, \quad (165)$$

and where $\hat{\Gamma}_n^{\alpha\beta}$ are the renormalized versions of $\hat{\Gamma}_n^{\alpha\beta}$ resulting from the average over momentum directions. Similarly, $\hat{\mathcal{T}}_n^{\beta\alpha} = (S_c^\beta)^T \hat{\Gamma}_n^{\beta\alpha} S_c^\alpha$. In a similar way, we find that

$$\left\langle \frac{i}{\pi} \oint d\xi_{-}^{\alpha} \sum_{n \in V} \hat{\Sigma}_T \bullet \check{G}^{\alpha\alpha} \right\rangle_{--} = -i \sum_{n \in I} \hat{\mathcal{T}}_n^{\alpha\beta} \circ \check{g}_{0,s}^\beta(\mathbf{x}_n^\beta) \circ \hat{\mathcal{T}}_n^{\beta\alpha} \circ \check{g}_s^\alpha(\mathbf{x}_n^\alpha). \quad (166)$$

We choose the volume defined by the unit cells in V to be approximately the shape of a wide cylinder, which includes the interface. Let the discs at the ends of this cylinder have Γ_2 points and define a plane. Let \mathbf{e}_n be the unit vector that is orthogonal to this plane and points out of material α . We assume that the width of the cylinder is much larger than the length. Inserting Eqs. (164) and (151) into Eq. (70), integrating over the Eilenberger contour and momentum directions and summing over the unit cells in V , we get that

$$i\Gamma_2 \mathbf{e}_n \cdot \check{\mathbf{j}}^\alpha(\mathbf{x}_l^\alpha) / |\delta| + \sum_{n \in V} \check{g}_s^\alpha \circ \varepsilon \tau_z - \left\langle \frac{i}{\pi} \oint d\xi_{-}^{\alpha} \sum_{n \in V} \check{G}^{\alpha\alpha} \bullet (\check{\Sigma}_{\text{imp}}^\alpha + \check{V}^\alpha) \right\rangle_{--} + i\Gamma \check{g}_s^\alpha(\mathbf{x}_l^\alpha) \circ \hat{\mathcal{T}}_l^{\alpha\beta} \circ \check{g}_{0,s}^\beta(\mathbf{x}_l^\beta) \circ \hat{\mathcal{T}}_l^{\beta\alpha} - \Gamma \check{g}_s^\alpha(\mathbf{x}_l^\alpha) \circ (S_c^\alpha)^T \hat{\mathcal{R}}_l S_c^\alpha = \left\langle \frac{i}{\pi} \oint d\xi_{-}^{\alpha} \sum_{n \in V} \check{G}^{\alpha\alpha} \xi_{-}^{\alpha} \right\rangle, \quad (167)$$

where l is again a unit cell in I and $|\delta|$ is the distance between nearest neighbors in the direction of \mathbf{e}_n . We note that Γ/Γ_2 can in general be different from 1 because the interface need not lie in a perfect plane parallel to the ends of the cylinder. We assume that the second and third terms on the left-hand side of Eq. (167) are negligible compared to the fourth and fifth terms because the width of the cylinder is much larger than its length and $\hat{\mathcal{R}}_l$ and $\hat{\mathcal{T}}_l^{\alpha\beta} \hat{\mathcal{T}}_l^{\beta\alpha}$ are large compared to ε and $(\check{\Sigma}_{\text{imp}}^\alpha + \check{V}^\alpha)$. However, we cannot neglect the term on the right-hand side. The way to remove this term is again to use the other Gor'kov equation. From the other Gor'kov equation, Eq. (68), we get, using Eqs. (166) and (154), that

$$\sum_{n \in V} \varepsilon \tau_z \circ \check{g}_s^\alpha - \left\langle \frac{i}{\pi} \oint d\xi_{-}^{\alpha} \sum_{n \in V} (\check{\Sigma}_{\text{imp}}^\alpha + \check{V}^\alpha) \bullet \check{G}^{\alpha\alpha} \right\rangle_{--} + i\Gamma \hat{\mathcal{T}}_l^{\alpha\beta} \circ \check{g}_{0,s}^\beta(\mathbf{x}_l^\beta) \circ \hat{\mathcal{T}}_l^{\beta\alpha} \circ \check{g}_s^\alpha(\mathbf{x}_l^\alpha) - \Gamma (S_c^\alpha)^T \hat{\mathcal{R}}_l S_c^\alpha \circ \check{g}_s^\alpha(\mathbf{x}_l^\alpha) = \left\langle \frac{i}{\pi} \oint d\xi_{-}^{\alpha} \sum_{n \in V} \check{G}^{\alpha\alpha} \xi_{-}^{\alpha} \right\rangle. \quad (168)$$

Here, we neglect the first two terms for the same reason as above. Combining Eqs. (167) and (168) and absorbing the factor $|\delta|\Gamma/\Gamma_2$ into the reflection and tunneling matrices, we finally get the boundary condition,

$$\mathbf{e}_n \cdot \check{\mathbf{j}}^\alpha = [\hat{\mathcal{T}}_l^{\alpha\beta} \circ \check{g}_{0,s}^\beta(\mathbf{x}_l^\beta) \circ \hat{\mathcal{T}}_l^{\beta\alpha} + i(S_c^\alpha)^T \hat{\mathcal{R}}_l S_c^\alpha \circ \check{g}_s^\alpha]_o. \quad (169)$$

One can use the Dyson equation to write $\check{g}_{0,s}^\beta$ as a series expansion in \check{g}_s^β and the tunneling matrix. In principle, this should produce a generalization of the Nazarov boundary condition [67,68]. However, we are here interested in the diffusive regime, meaning that the matrix current is small compared to the Fermi velocity. This is the case when the tunneling and reflection amplitudes are small. For this reason, we need only consider Eq. (169) to the lowest order in the tunneling matrices, which are obtained by setting $\check{g}_{0,s}^\beta = \check{g}_s^\beta$, yielding

$$\mathbf{e}_n \cdot \check{\mathbf{j}}^\alpha = [\hat{\mathcal{T}}_l^{\alpha\beta} \circ \check{g}_s^\beta(\mathbf{x}_l^\beta) \circ \hat{\mathcal{T}}_l^{\beta\alpha} + i(S_c^\alpha)^T \hat{R}_l S_c^\alpha \cdot \check{g}_s^\alpha]_o. \quad (170)$$

We note that in the absence of antiferromagnetism, this exactly reproduces the generalized Kupriyanov-Lukichev boundary condition for spin-active boundaries in the quasiclassical theory for normal metals [58,59].

XIII. NONUNIFORM MAGNETIC TEXTURES

In this section, we derive the self-energy terms associated with nonuniform magnetic textures in antiferromagnets. We find that a spatial gradient in the magnetic texture gives rise to a term in the covariant gradient, similar to spin-orbit coupling, and a temporal gradient gives rise to an effective magnetic field.

In both cases, we must evaluate $R^\dagger \partial R$, where ∂ can be either the time derivative or gradient operator and R is given by Eq. (8). We find that

$$R^\dagger \partial R = -\frac{i}{2} \partial(\theta \sin \phi \sigma_x - \theta \cos \phi \sigma_y), \quad (171)$$

where the direction of the Néel vector is $\mathbf{n} = (\sin \theta \cos \phi, \sin \theta \sin \phi, \cos \theta)$. From Eq. (22c) we see that the spatial gradient of the Néel vector gives rise to a self-energy term equal to

$$(\Sigma_s^\alpha)_{nm}(t_1, t_2) = -(K_{nm}^\alpha [\mathbf{x}_n^\alpha - \mathbf{x}_m^\alpha] + [\delta^\alpha \rho_B, K_{nm}^\alpha]) \cdot (R^\dagger \nabla R)(\mathbf{x}_n^\alpha, t_1) \delta(t_1 - t_2). \quad (172)$$

To get how it looks in the final equation, we must Fourier transform and project onto the conduction band by use of S_c^α . By doing this, we get

$$(S_c^\alpha)^T \Sigma_s^\alpha(\mathbf{k}, \mathbf{x}_n^\alpha, T) S_c^\alpha = -\frac{\mathbf{v}_F^\alpha}{2} \cdot \nabla(\theta \sin \phi \sigma_x - \theta \cos \phi \sigma_y). \quad (173)$$

Since this is a momentum-dependent self-energy, we see that this is supposed to go into the covariant derivative. As a result, the covariant derivative looks like

$$\check{\nabla} \circ \check{g}^\alpha = \nabla \check{g}^\alpha - i \left[\frac{1}{2} \nabla(\theta \sin \phi \sigma_x - \theta \cos \phi \sigma_y), \check{g}^\alpha \right] - i[\check{A}_{\text{rest}}, \check{g}^\alpha], \quad (174)$$

where \check{A}_{rest} is the remaining p -wave contribution, which may come from the vector gauge field or spin-orbit coupling.

The temporal gradient gives rise to a term similar to a magnetic field. From Eq. (22c) we see that the temporal gradient of the Néel vector gives rise to a self-energy term equal to

$$(\Sigma_t^\alpha)_{nm}(t_1, t_2) = -i\tau_z (R^\dagger \dot{R})(\mathbf{x}_n^\alpha, t_1) \delta_{nm} \delta(t_1 - t_2), \quad (175)$$

since

$$\rho_A (R^\dagger \dot{R})(\mathbf{x}_n^\alpha, t_1) + \rho_B (R^\dagger \dot{R})(\mathbf{x}_n^\alpha + \delta^\alpha, t_1) \approx (R^\dagger \dot{R})(\mathbf{x}_n^\alpha, t_1). \quad (176)$$

If we again Fourier transform in relative coordinates and transform using S_c^α , we get

$$(S_c^\alpha)^T \Sigma_t^\alpha(\mathbf{k}, \mathbf{x}_n^\alpha, T) S_c^\alpha = -\frac{1}{2} \sqrt{1 - (J^\alpha/\eta^\alpha)^2} \times \tau_z \partial_T (\theta \sin \phi \sigma_x - \theta \cos \phi \sigma_y). \quad (177)$$

The factor $\sqrt{1 - (J^\alpha/\eta^\alpha)^2}$ comes from the projection of σ_x and σ_y onto the conduction band. To understand the physical reason for this factor, consider a general electron state near the Fermi level. An electron near the Fermi level will in general be in a superposition of spin-up and spin-down, but the spin-up component and the spin-down component will have different spatial distributions. For the spin of this electron at a given lattice site to have a nonzero projection in a direction orthogonal to the Néel vector, it will need to be in a superposition of spin-up and spin-down. At $J^\alpha/\eta^\alpha = 0$, an electron state near the Fermi level, which is in an equal superposition of spin-up and spin-down will have spin everywhere orthogonal to the Néel vector. However, as J^α/η^α increases, the spin-up and spin-down component starts to separate in space, and in the limit $J^\alpha/\eta^\alpha \rightarrow 1$, any superposition of spin-up and spin-down has all of its spin-up component localized on one sublattice and all of its spin-down component localized on the other sublattice. This means that it has spin along the Néel vector everywhere in space. As a result, the effect of spin-splitting fields orthogonal to the Néel vector is suppressed as J^α/η^α increases.

XIV. OBSERVABLES

Generally, observables such as densities or currents may be written

$$Q(\mathbf{x}_n^\alpha, T) = \langle c_n^{\alpha\dagger}(T) M(\mathbf{x}_n^\alpha, -i\Delta_R) c_n^\alpha(T) - (c_n^\alpha)^T(T) M^T(\mathbf{x}_n^\alpha, -i\Delta_R) (c_n^{\alpha\dagger})^T(T) \rangle + C, \quad (178)$$

where C is a constant and M is a matrix that depends on the observable. We can relate this to our Green's functions, which are defined by the spin-rotated creation and annihilation operators \check{c}_n^α , as defined by Eq. (9), if we define

$$\check{M} = [\rho_A R^\dagger(\mathbf{x}_n^\alpha, t) + \rho_B R^\dagger(\mathbf{x}_n^\alpha + \delta^\alpha, t)] M \times [\rho_A R(\mathbf{x}_n^\alpha, t) + \rho_B R(\mathbf{x}_n^\alpha + \delta^\alpha, t)]. \quad (179)$$

With this

$$Q(\mathbf{x}_n^\alpha, T) = C + i \int_{\diamond^\alpha} \frac{d[3k]}{(2\pi)^3} \int_{-\infty}^{\infty} \frac{d\varepsilon}{2\pi} \times \text{Tr}[\check{M}(\mathbf{x}_n^\alpha, \mathbf{k}) \tau_z \hat{G}^{K,\alpha\alpha}(\mathbf{k}, \mathbf{x}_n^\alpha, T, \varepsilon)]. \quad (180)$$

The quasiclassical treatment is only valid for $\varepsilon \ll E_c^\alpha$. As a result, we should split the energy integral,

$$\int_{\diamond^\alpha} \frac{d[3]k}{(2\pi)^3} \int_{-\infty}^{\infty} \frac{d\varepsilon}{2\pi} \text{Tr}[\tilde{M}(\mathbf{x}_n^\alpha, \mathbf{k}) \tau_z \hat{G}^{K,\alpha\alpha}(\mathbf{k}, \mathbf{x}_n^\alpha, T, \varepsilon)] = \int_{-a}^a \frac{d\varepsilon}{2\pi} \int_{\diamond^\alpha} \frac{d[3]k}{(2\pi)^3} \text{Tr}[\tilde{M}(\mathbf{x}_n^\alpha, \mathbf{k}) \tau_z \hat{G}^{K,\alpha\alpha}(\mathbf{k}, \mathbf{x}_n^\alpha, T, \varepsilon)] \\ + \left(\int_{-\infty}^{-a} \frac{d\varepsilon}{2\pi} + \int_a^{\infty} \frac{d\varepsilon}{2\pi} \right) \int_{\diamond^\alpha} \frac{d[3]k}{(2\pi)^3} \text{Tr}[\tilde{M}(\mathbf{x}_n^\alpha, \mathbf{k}) \tau_z \hat{G}^{K,\alpha\alpha}(\mathbf{k}, \mathbf{x}_n^\alpha, T, \varepsilon)], \quad (181)$$

where a is much smaller than E_c^α . In the diffusive regime, a should also be much smaller than the elastic impurity scattering rate. We can rewrite the first term on the right-hand side by again using the Eilenberger contour. The Keldysh Green's function is $\sim 1/(\xi_-^\alpha)^2$ for large $(\xi_-^\alpha)^2$, so we can neglect the high energy contribution, $\int d\xi_-^\alpha$. Hence,

$$\int_{-a}^a \frac{d\varepsilon}{2\pi} \int_{\diamond^\alpha} \frac{d[3]k}{(2\pi)^3} \text{Tr}[\tilde{M}(\mathbf{x}_n^\alpha, \mathbf{k}) \tau_z \hat{G}^{K,\alpha\alpha}(\mathbf{k}, \mathbf{x}_n^\alpha, T, \varepsilon)] = -i\pi N_0 \left\langle \int_{-a}^a \frac{d\varepsilon}{2\pi} \text{Tr}[(S_c^\alpha)^T \tilde{M}(\mathbf{x}_n^\alpha, \mathbf{k}_F) S_c^\alpha \tau_z \hat{g}^{K,\alpha}(\mathbf{k}_F, \mathbf{x}_n^\alpha, T, \varepsilon)] \right\rangle. \quad (182)$$

Next, we must evaluate the second term on the right-hand side of Eq. (181). Generally, we can write

$$\hat{G}^{R,\alpha\alpha} = (\tau_z \varepsilon - \hat{H}_0^\alpha - \hat{\Sigma}^{R,\alpha})^{-1} + \delta \hat{G}^{R,\alpha\alpha}. \quad (183)$$

Inserting this into the equation

$$\tau_z \varepsilon \circ \hat{G}^{R,\alpha\alpha} - \hat{H}_0^\alpha \hat{G}^{R,\alpha\alpha} - \hat{\Sigma}^{R,\alpha} \bullet \hat{G}^{R,\alpha\alpha} = 1, \quad (184)$$

one gets an equation for $\delta \hat{G}^{R,\alpha\alpha}$. We find that the contribution to the expression for the observable from $\delta \hat{G}^{R,\alpha\alpha}$ is negligible, so we neglect it in the following. We assume that a is sufficiently large such that states at $|\varepsilon| \geq a$ are either completely occupied or completely unoccupied. Moreover, a is much larger than the superconducting gap, so the density of states at energies above a should not be affected by superconductivity. For this reason, we assume that we can neglect superconductivity when considering the high-energy contribution. When this is the case,

$$\hat{G}^{K,\alpha\alpha} = \text{sgn}(\varepsilon)[\hat{G}^{R,\alpha\alpha} - (\hat{G}^{R,\alpha\alpha})^\dagger]. \quad (185)$$

By neglecting $\delta \hat{G}^{R,\alpha\alpha}$, we find that

$$\hat{G}^{R,\alpha\alpha} = S^\alpha \left[\tau_z \varepsilon - \begin{pmatrix} \xi_-^\alpha & \\ & \xi_+^\alpha \end{pmatrix} - (S^\alpha)^T \hat{\Sigma}^{R,\alpha} S^\alpha \right]^{-1} (S^\alpha)^T. \quad (186)$$

Let $(S^\alpha)^T \hat{\Sigma}^{R,\alpha} S^\alpha = A$, then

$$[(S^\alpha)^T \hat{G}^{R,\alpha\alpha} S^\alpha]_{--} = [\tau_z \varepsilon - \xi_-^\alpha - A_{--} - A_{-+}(\tau_z \varepsilon - \xi_+^\alpha - A_{++})^{-1} A_{+-}]^{-1}, \quad (187a)$$

$$[(S^\alpha)^T \hat{G}^{R,\alpha\alpha} S^\alpha]_{++} = [\tau_z \varepsilon - \xi_+^\alpha - A_{++} - A_{+-}(\tau_z \varepsilon - \xi_-^\alpha - A_{--})^{-1} A_{-+}]^{-1}, \quad (187b)$$

$$[(S^\alpha)^T \hat{G}^{R,\alpha\alpha} S^\alpha]_{-+} = -[(S^\alpha)^T \hat{G}^{R,\alpha\alpha} S^\alpha]_{-+} A_{-+} (\tau_z \varepsilon - \xi_+^\alpha - A_{++})^{-1}, \quad (187c)$$

$$[(S^\alpha)^T \hat{G}^{R,\alpha\alpha} S^\alpha]_{+-} = -[(S^\alpha)^T \hat{G}^{R,\alpha\alpha} S^\alpha]_{+-} A_{+-} (\tau_z \varepsilon - \xi_-^\alpha - A_{--})^{-1}. \quad (187d)$$

If

$$A_{--} - A_{-+}(\tau_z \varepsilon - \xi_+^\alpha - A_{++})^{-1} A_{+-} = P_- J_- P_-^\dagger, \quad (188a)$$

$$A_{++} - A_{+-}(\tau_z \varepsilon - \xi_-^\alpha - A_{--})^{-1} A_{-+} = P_+ J_+ P_+^\dagger, \quad (188b)$$

where J_- and J_+ are diagonal, we find that

$$[(S^\alpha)^T \hat{G}^{K,\alpha\alpha} S^\alpha]_{\pm\pm,ij} = 2\pi i \text{sgn}(\varepsilon) \sum_l P_{\pm,il} \frac{\text{Im}(J_{\pm,ll})/\pi}{[\varepsilon \tau_{z,ll} - \xi_{\pm}^\alpha - \text{Re}(J_{\pm,ll})]^2 + [\text{Im}(J_{\pm,ll})]^2} P_{\pm,ij}^\dagger. \quad (189)$$

If not for the fact that J_{\pm} depends on ε , this would be a sum of Lorentz distribution as functions of ε . However, the dependence of J_{\pm} on ε is very weak close to the peak of the distribution. For this reason, we neglect the dependence of both P_{\pm} and J_{\pm} on ε . From Eq. (187) we can see that $[(S^\alpha)^T \hat{G}^{R,\alpha\alpha} S^\alpha]_{\pm\pm}$ are products of two functions with peaks at distantly separated values of ε . One peak is close to ξ_-^α and the other is close to ξ_+^α . As a result, we neglect these terms.

To proceed, we must evaluate terms that look like

$$I_{\pm} := \left(\int_{-\infty}^{-a} \frac{d\varepsilon}{2\pi} + \int_a^{\infty} \frac{d\varepsilon}{2\pi} \right) \int_{\xi_{\min}}^{\xi_{\max}} d\xi_-^\alpha 2\pi \text{sgn}(\varepsilon) g(\xi_-^\alpha) \frac{\text{Im}(J_{\pm,ll})/\pi}{[\varepsilon \tau_{z,ll} - \xi_{\pm}^\alpha - \text{Re}(J_{\pm,ll})]^2 + [\text{Im}(J_{\pm,ll})]^2}, \quad (190)$$

where the function g can be identified from Eqs. (181) and (189).

From the fact that the retarded Green's function should be nonzero only for positive relative times, we have that $\text{Im}(J_{-,ll}) = \tau_{z,ll} |\text{Im}(J_{-,ll})|$. If we define

$$f(y) = \int_{-\infty}^y dx \frac{|\text{Im}(J_{\pm,ll})|/\pi}{x^2 + [\text{Im}(J_{\pm,ll})]^2}, \quad (191)$$

we find that

$$I_- = \int_{a-\text{Re}(J_{\pm,ll})+C}^{\xi_{\max}} d\xi_{-}^{-\alpha} g(\xi_{-}^{-\alpha}) - \int_{\xi_{\min}}^{-a-\text{Re}(J_{\pm,ll})-C} d\xi_{-}^{-\alpha} g(\xi_{-}^{-\alpha}) + \int_{-C}^C d\xi_{-}^{-\alpha} f(\xi_{-}^{-\alpha}) \{g[\xi_{-}^{-\alpha} + a - \text{Re}(J_{\pm,ll})] - g[-\xi_{-}^{-\alpha} - a - \text{Re}(J_{\pm,ll})]\}, \quad (192)$$

where C is a number, which is on the order of $\text{Im}(J_{\pm,ll})$, and sufficiently large such that $f(y) \approx 0$ for $y \leq -C$ and $f(y) = 1$ for $y \geq C$. From Eqs. (181) and (189), one can see that g is a slowly varying function. For this reason, we can neglect the last integral in Eq. (192). Next, we rewrite I_- as one term, which depends on $J_{\pm,ll}$ and one, which does not, as

$$I_- \approx \int_{a+C}^{\xi_{\max}} d\xi_{-}^{-\alpha} g(\xi_{-}^{-\alpha}) - \int_{\xi_{\min}}^{-a-C} d\xi_{-}^{-\alpha} g(\xi_{-}^{-\alpha}) + \text{Re}(J_{\pm,ll}) [g(a) + g(-a)], \quad (193)$$

so that, since $g(\pm a) \approx g(0)$,

$$\left(\int_{-\infty}^{-a} \frac{d\varepsilon}{2\pi} + \int_a^{\infty} \frac{d\varepsilon}{2\pi} \right) \int_{\xi_{\min}}^{\xi_{\max}} d\xi_{-}^{-\alpha} g(\xi_{-}^{-\alpha}) [(S^\alpha)^T \hat{G}^{k,\alpha\alpha} S^\alpha]_{--ij} = i\delta_{ij} \int_{a+C}^{\xi_{\max}} d\xi_{-}^{-\alpha} g(\xi_{-}^{-\alpha}) - i\delta_{ij} \int_{\xi_{\min}}^{-a-C} d\xi_{-}^{-\alpha} g(\xi_{-}^{-\alpha}) + ig(0)[A_{--} + A_{--}^\dagger]_{ij}, \quad (194)$$

where we have used that for $\xi_{-}^{-\alpha} \approx 0$,

$$2P_- \text{Re}(J_-) P_-^\dagger = P_- J_- P_-^\dagger + (P_- J_- P_-^\dagger)^\dagger \approx A_{--} + A_{--}^\dagger. \quad (195)$$

Evaluating I_+ is less difficult because $\xi_+^\alpha \gg a$ for all k . Hence,

$$I_+ = \int_{\xi_{\min}}^{\xi_{\max}} d\xi_{-}^{-\alpha} g(\xi_{-}^{-\alpha}). \quad (196)$$

Inserting this into the expression for the high- ε contribution to the observable, we find

$$\left(\int_{-\infty}^{-a} \frac{d\varepsilon}{2\pi} + \int_a^{\infty} \frac{d\varepsilon}{2\pi} \right) \int \frac{d[3]k}{(2\pi)^3} \text{Tr}[\tilde{M} \tau_z \hat{G}^{K,\alpha\alpha}] = i \left\langle \int_{\xi_{\min}}^{\xi_{\max}} d\xi_{-}^{-\alpha} N_0^\alpha(\xi_{-}^{-\alpha}) \text{Tr}\{[(S^\alpha)^T \tilde{M} S^\alpha]_{++\tau_z}\} \right\rangle + i \left\langle \int_{a+C}^{\xi_{\max}} d\xi_{-}^{-\alpha} N_0^\alpha(\xi_{-}^{-\alpha}) \text{Tr}\{[(S^\alpha)^T \tilde{M} S^\alpha]_{--\tau_z}\} \right\rangle - i \left\langle \int_{\xi_{\min}}^{-a-C} d\xi_{-}^{-\alpha} N_0^\alpha(\xi_{-}^{-\alpha}) \text{Tr}\{[(S^\alpha)^T \tilde{M} S^\alpha]_{--\tau_z}\} \right\rangle + i \langle N_0^\alpha \text{Tr}\{[(S^\alpha)^T \tilde{M} S^\alpha]_{--\tau_z} [A_{--} + A_{--}^\dagger]\} \rangle. \quad (197)$$

The first three terms on the right-hand side are just constants and can be absorbed into the constant C in the expression for the observable. By doing this, we get that the observable can finally be written

$$Q = C + \frac{N_0^\alpha}{2} \left\langle \int_{-a}^a d\varepsilon \text{Tr}[(S_c^\alpha)^T \tilde{M} S_c^\alpha \tau_z \hat{g}^{K,\alpha\alpha}] \right\rangle - N_0^\alpha \langle \text{Tr}\{[(S_c^\alpha)^T \tilde{M} S_c^\alpha \tau_z (S_c^\alpha)^T [\hat{\Sigma}^{R,\alpha} + (\hat{\Sigma}^{R,\alpha})^\dagger] S_c^\alpha]\} \rangle. \quad (198)$$

To compute observables from the quasiclassical Green's functions, one therefore generally also need to take into account the contribution from the self-energy term. Note that since the quasiclassical Green's function is not gauge-invariant, the second term in Eq. (198) is required to make the observables gauge-invariant.

For concrete examples of observables, consider the electric charge density in material α , n_e^α , and the spin densities in material α , $s^\alpha = (s_x^\alpha, s_y^\alpha, s_z^\alpha)$. For the electric charge density $\tilde{M} = e\tau_z/4$, which can be confirmed by inserting this into Eq. (178). The denominator 4 comes from the fact that we count each electron 4 times in Eq. (178). To derive the formula for electric charge density, we can insert this into Eq. (198), giving

$$n_e^\alpha = \frac{N_0^\alpha e}{8} \int_{-a}^a d\varepsilon \text{Tr}(\hat{g}_s^{K,\alpha}) - 2N_0^\alpha e \phi_e^\alpha, \quad (199)$$

where we dropped the constant and ϕ_e^α is the deviation in the electrochemical potential away from μ^α , and may therefore vary in both time and space. In other words, ϕ_e^α is the real, diagonal part of the self-energy. Equation 199 reproduces earlier

results for charge density in the quasiclassical regime [1,69]. We can see that the second term in Eq. (199) is necessary to retain gauge invariance. Take for example, a nonsuperconducting stationary system in equilibrium with an electrochemical potential ϕ_e^α . The symmetric part of the quasiclassical Keldysh function is then $\hat{g}_s^{K,\alpha} = 2\text{diag}[\tanh[\beta(\varepsilon + \phi_e^\alpha)/2], \tanh[\beta(\varepsilon + \phi_e^\alpha)/2], -\tanh[\beta(\varepsilon - \phi_e^\alpha)/2], -\tanh[\beta(\varepsilon - \phi_e^\alpha)/2]]$, where β is inverse temperature. Taking the trace and integrating over energies, we get

$$\frac{N_0^\alpha e}{8} \int_{-a}^a d\varepsilon \text{Tr}(\hat{g}_s^{K,\alpha}) = \frac{N_0^\alpha e}{8} 16\phi_e^\alpha = 2N_0^\alpha e\phi_e^\alpha. \quad (200)$$

The electrochemical potential is gauge dependent, so the second term in Eq. (199) is required to cancel the gauge-dependent contribution from $\hat{g}_s^{K,\alpha}$ in this case.

For the spin density in direction i , $\tilde{M} = \sigma_i/8$. The projection of spin Pauli matrices onto the conduction band is trivial for the z direction since it commutes with the S^α matrix. That is, $(S_c^\alpha)^T \sigma_z S_c^\alpha = \sigma_z$. However, $(S_c^\alpha)^T \sigma_{x/y} S_c^\alpha = \sqrt{1 - (J^\alpha/\eta^\alpha)^2} \sigma_{x/y}$, so for the directions orthogonal to the Néel vector we get an additional factor $\sqrt{1 - (J^\alpha/\eta^\alpha)^2}$. If the initial Hamiltonian in material α , given by Eq. (4), has a Zeeman spin-splitting field \mathbf{h}^α , this gives rise to a self-energy term equal to $\hat{\Sigma}_Z^{K,\alpha} = \mathbf{h}^\alpha \cdot \boldsymbol{\sigma} \tau_z$ before projection onto the conduction band. Inserting this into Eq. (198), we get that the spin densities are given by

$$s_x^\alpha = \sqrt{1 - \left(\frac{J^\alpha}{\eta^\alpha}\right)^2} \frac{N_0^\alpha}{16} \int_{-a}^a d\varepsilon \text{Tr}(\sigma_x \tau_z \hat{g}_s^{K,\alpha}) - \left[1 - \left(\frac{J^\alpha}{\eta^\alpha}\right)^2\right] N_0^\alpha h_x^\alpha, \quad (201a)$$

$$s_y^\alpha = \sqrt{1 - \left(\frac{J^\alpha}{\eta^\alpha}\right)^2} \frac{N_0^\alpha}{16} \int_{-a}^a d\varepsilon \text{Tr}(\sigma_y \tau_z \hat{g}_s^{K,\alpha}) - \left[1 - \left(\frac{J^\alpha}{\eta^\alpha}\right)^2\right] N_0^\alpha h_y^\alpha, \quad (201b)$$

$$s_z^\alpha = \frac{N_0^\alpha}{16} \int_{-a}^a d\varepsilon \text{Tr}(\sigma_y \tau_z \hat{g}_s^{K,\alpha}) - N_0^\alpha h_y^\alpha, \quad (201c)$$

where we again dropped the constant. The extra factor of $\sqrt{1 - (J^\alpha/\eta^\alpha)^2}$ comes from the fact itinerant electrons become more polarized in the direction of the Néel vector as J^α/η^α increases, as discussed above. This polarization comes in through two different aspects. First, the Zeeman spin-splitting felt by the itinerant electrons is reduced by a factor $\sqrt{1 - (J^\alpha/\eta^\alpha)^2}$. Second, the σ_x and σ_y components of the Green's function do not correspond to spin in the same sense as in a normal metal. In the limit of very strong exchange coupling J^α , the itinerant electrons become fully polarized, and $s_x^\alpha = s_y^\alpha = 0$.

To compute the sublattice-resolved charge densities, one can use Eq. (118) together with $\tilde{M} = e\tau_z \rho_{A/B}/4$, which gives

$$n_{A/B}^\alpha = \frac{1}{2} n_e^\alpha \pm \frac{eJ^\alpha}{\eta^\alpha} s_z^\alpha. \quad (202)$$

One can similarly use Eq. (198) to compute energy and spin-energy densities [70] and all associated current. Another way to derive expressions for currents is to use the expressions for densities together with Eq. (128) to obtain conservation laws of the form $\partial n/\partial t + \nabla \cdot \mathbf{j} = S$, where n is the density, \mathbf{j} can be identified as the current and S is a source term. For instance, multiplying Eq. (128) with $-ieN_0\tau_z/8$, taking the trace, integrating over energy and adding $-2N_0e\partial\phi_e^\alpha/\partial t$ to both sides of the equality sign, one obtains $\partial n_e^\alpha/\partial t + \nabla \cdot \mathbf{j}_e^\alpha = S_e^\alpha$, where the electric current density can be identified as

$$\mathbf{j}_e^\alpha = \frac{N_0^\alpha e}{8} \int_{-a}^a d\varepsilon \text{Tr}(\tau_z \hat{\mathbf{j}}^{K,\alpha}). \quad (203)$$

XV. CONCLUSION

We have derived quasiclassical equations of motion, which are valid for mesoscopic heterostructures with antiferromagnetic order, superconductivity, impurity scattering, external electric or magnetic fields, spin-orbit coupling, temporally or spatially inhomogeneous Néel vector, or, in principle any other effect that can be modeled using a quadratic Hamiltonian. These are valid when the distance between the Fermi level and the edges of the conduction band ΔE^α is larger than all other energy scales except possibly the exchange energy, which couples the itinerant electrons to the localized, antiferromagnetically ordered spins. The ratio between the exchange energy and the chemical potential relative to the center of the two energy bands J^α/η^α can take any value between 0

and 1. Our main results are the quasiclassical equation in the dirty regime, which are valid when the elastic impurity scattering rate is high compared to other energies, except for ΔE^α and possibly J^α , and when the isotropic part of the quasiclassical Green's function dominates. The latter is true when the matrix current is small, which happens for instance when the system varies slowly on the scale of the mean free path, or when the proximity effect is small. In the limit of very strong exchange coupling, such that $(J^\alpha/\eta^\alpha)^2 \rightarrow 1$, the short-ranged correlations can vary on the scale of the mean free path. However, these correlations become vanishingly small in the diffusive limit. Therefore, one can solve the equations by projecting the Green's functions onto the set of long-range components. Being based on Keldysh theory, the equations can be used to study nonequilibrium situations, such

as externally driven currents or spin injection. Additionally, they can also be solved to study time-dependent phenomena, as there are ways to evaluate the circle products [9,13–15]. In the absence of antiferromagnetism, the equations reduce to the Eilenberger equation [3] and Usadel equation [4] for normal metals, as expected. However, with antiferromagnetism, there are a few important differences. First, all self-energy terms must be projected onto the conduction band. Second, even nonmagnetic impurities behave magnetically because of the coupling between spin and sublattice. Finally, this also changes the equation for the matrix current in the dirty regime. We discuss the physical origin and implications of these effects in Ref. [63].

We have also derived boundary conditions that are valid in the diffusive regime. These are valid as long as the tunneling amplitudes are small, such that the matrix current is small compared to the Fermi velocity. They take into account both tunneling and reflection and allow for both compensated and uncompensated interfaces, meaning that the coupling can be asymmetric in sublattice. Additionally, the boundary conditions allow for spin-active boundaries and isolating, spin-active boundaries can be obtained by setting the tunneling matrices to zero. In the absence of antiferromagnetism, the boundary conditions reduce to the generalized Kupriyanov-Lukichev boundary conditions for spin-active boundaries [58,59].

Finally, we have derived an expression that can be used to compute observables from the quasiclassical Green's function. This expression also includes the contribution from energies, which are not captured by the quasiclassical Green's function. As we saw in the example of charge density, the high-energy contribution is needed to make the observables gauge invariant.

ACKNOWLEDGMENTS

This work was supported by the Research Council of Norway through Grant No. 323766, and its Centres of Excellence funding scheme Grant No. 262633 “*QuSpin*”. J.L. also acknowledges computational resources provided by Sigma2 - the National Infrastructure for High-Performance Computing and Data Storage in Norway from Project No. NN9577K.

APPENDIX: NUMERICAL SOLUTION ALGORITHM

As an example, we illustrate how one can solve Eqs. (128), (135), and (170) in a time-independent one-dimensional system at thermal equilibrium. The components of the Green's function are not independent because of the normalization condition, so it is necessary to use a parametrization scheme. For instance, one can use the Ricatti parametrization [71,72] or the θ parametrization [73]. In order to solve Eqs. (128), (135), and (170) numerically, one must first define a set of algebraic equations. These equations can then be solved for the unknown parameters. For simplicity, assume we need only solve Eqs. (128), (135), and (170) in one material because the solution is known in all neighboring materials. For this reason, we remove the superscript α . Let there be N discretization points, and denote by u_n^j the j th parameter at discretization point $n \in \{1, \dots, N\}$. The spherically symmetric part of the

quasiclassical Green's function at point n is a function of the M parameters. Depending on the problem, the number of different parameters needed to characterize the system will vary. At most, $M = 8$ in thermal equilibrium since it is only necessary to compute the retarded Green's function. Let $\hat{g}_{s,n}^R$ be the spherically symmetric part of the retarded Green's function in position $x = (n - 1)\Delta x$, where Δx is the distance between discretization points. Then,

$$\hat{g}_{s,n}^R = \hat{g}_{s,n}^R(u_n^1, u_n^2, \dots, u_n^M) \quad (\text{A1})$$

is a function of only the local parameters $(u_n^1, u_n^2, \dots, u_n^M)$.

In order to solve Eqs. (135) and (128), we need not only the Green's function but also its spatial derivative. Let the derivative at point n be $(\partial_x \hat{g}_{s,n}^R)$. This can be obtained from the gradients of the parameters,

$$(\partial_x \hat{g}_{s,n}^R) = \sum_{j=1}^M \frac{\partial \hat{g}_{s,n}^R}{\partial u_n^j} \frac{\partial u_n^j}{\partial x}. \quad (\text{A2})$$

Thus, we have $2M$ unknown parameters at each point: $(u_n^1, \dots, u_n^M, \partial_x u_n^1, \dots, \partial_x u_n^M)$. The circle products reduce to normal matrix products in a static system, so, if \hat{j}_n^R is the retarded matrix current at point n , we get from Eq. (135) that

$$\begin{aligned} \hat{j}_n^R = & -D \hat{g}_{s,n}^R (\partial_x \hat{g}_{s,n}^R)_n + i D \hat{g}_{s,n}^R [A_x^R, \hat{g}_{s,n}^R] \\ & - \hat{g}_{s,n}^R \left[\frac{J^2}{2\eta^2} \sigma_z \tau_z \hat{g}_{s,n}^R \sigma_z \tau_z, \hat{j}_n^R \right]. \end{aligned} \quad (\text{A3})$$

The boundary conditions, given by Eq. (170), is in this case

$$\hat{j}_1^R = -[\hat{T}_L \hat{g}_{s,L}^R \hat{T}_L^\dagger + i \hat{R}_L, \hat{g}_{s,1}^R], \quad (\text{A4a})$$

$$\hat{j}_N^R = [\hat{T}_R \hat{g}_{s,R}^R \hat{T}_R^\dagger + i \hat{R}_R, \hat{g}_{s,N}^R], \quad (\text{A4b})$$

where \hat{T}_L and \hat{T}_R are the tunneling matrices, \hat{R}_L and \hat{R}_R are the reflection matrices, and $\hat{g}_{s,L}^R$ and $\hat{g}_{s,R}^R$ are the quasiclassical Green's functions on the left ($x = 0$) and right ($x = [N - 1]\Delta x$) side, respectively. If a boundary is insulating, then the corresponding tunneling matrix is zero. A magnetic insulator will have nonzero magnetic components in the reflection matrix, so that $\hat{R} = r_0 + \mathbf{m} \cdot \boldsymbol{\sigma}$ for some scalar r_0 and some vector \mathbf{m} .

We have $2NM$ unknown parameters, so we need $2NM$ algebraic equations. These can be obtained by integrating Eq. (128) in space. Equation (128) can in this case be written

$$\frac{\partial \hat{j}^R}{\partial x} + F = 0, \quad (\text{A5})$$

where

$$F = -i \left[\tau_z \varepsilon - \hat{V}_s^R + \frac{iJ^2}{2\tau_{\text{imp}}\eta^2} \sigma_z \tau_z \hat{g}_s^R \sigma_z \tau_z, \hat{g}_s^R \right] - i [A_x^R, \hat{j}^R]. \quad (\text{A6})$$

To obtain algebraic equations, we can integrate Eq. (A5) between two discretization points and use a numerical integration scheme to approximate the integral of F . Integrating between $(i - 1)\Delta x$ and $(i + j - 1)\Delta x$, we get

$$\hat{j}_{i+j}^R - \hat{j}_i^R + \sum_{k=1}^j w_k F_{i+k} = 0, \quad (\text{A7})$$

where (w_1, \dots, w_j) is the set of weights defined by the numerical integration scheme and F_n is Eq. (A6) evaluated with $\hat{g}_s^R = \hat{g}_{s,n}^R$ and $\hat{j}_s^R = \hat{j}_{s,n}^R$. Equation (A7) is a matrix-valued equation from which one can take M independent scalar equations. For instance, in the most general case with $M = 8$, one can take the upper right and lower left 2×2 blocks of Eq. (A7). Another M algebraic equations can be found from the same interval by integrating $\partial_x u^p$ for $p \in 1, \dots, M$,

$$u_{i+j}^p - u_i^p - \sum_{k=1}^j w_k \partial_x u_{i+k}^p = 0. \quad (\text{A8})$$

To obtain $2NM$ algebraic equations, one can choose N different subintervals, each of which defines $2M$ algebraic equations through Eqs. (A7) and (A8). These can be solved using Newton's method, and one can use for instance forward-mode automatic differentiation or finite differences to determine the Jacobian. The algorithm for solving Eqs. (128), (135), and (170) for arbitrary values of J/η in one dimension is summarized in Algorithm 1. Having found the retarded Green's function, one can determine the advanced and Keldysh Green's functions, and thereby compute observables, through

$$\hat{g}_s^A = -\tau_z (\hat{g}_s^R)^\dagger \tau_z, \quad (\text{A9a})$$

$$\hat{g}_s^K = (\hat{g}_s^R - \hat{g}_s^A) \tanh(\beta\varepsilon/2), \quad (\text{A9b})$$

where β is inverse temperature. Equation (A9a) follows from the definition of the advanced and retarded Green's function

Algorithm 1. Numerical scheme for solving Eqs. (128), (135), and (170).

Require (n_i, m_i) for $i \in \{1, \dots, N\}$ are N different intervals and $(w_1^i, \dots, w_{m_i-n_i}^i)$ are corresponding numerical weights.

```

1: function (R){ $u_n^i$ }, { $\partial_x u_n^i$ }
2:   for  $i \leftarrow 1$  to  $N$  do
3:      $\hat{g}_{s,i}^R \leftarrow \hat{g}_{s,i}^R(u_1^i, \dots, u_{m_i}^i)$ 
4:      $(\partial_x \hat{g}_s^R)_i \leftarrow (\partial_x \hat{g}_s^R)(u_1^i, \dots, u_{m_i}^i, \partial_x u_1^i, \dots, \partial_x u_{m_i}^i)$ 
5:     if  $i = 1$  or  $i = N$  then
6:        $\hat{j}_i^R \leftarrow \hat{j}_i^R(\hat{g}_{s,i}^R, (\partial_x \hat{g}_s^R)_i)$   $\triangleright$  Eq. (A4)
7:     else
8:        $\hat{j}_{i,0}^R \leftarrow 0$ 
9:        $\hat{j}_i^R \leftarrow \hat{j}_i^R(\hat{g}_{s,i}^R, (\partial_x \hat{g}_s^R)_i, \hat{j}_{i,0}^R)$   $\triangleright$  Eq. (A3)
10:      while  $|\hat{j}_i^R - \hat{j}_{i,0}^R| >$  tolerance do
11:         $\hat{j}_{i,0}^R \leftarrow \hat{j}_i^R$ 
12:         $\hat{j}_i^R \leftarrow \hat{j}_i^R(\hat{g}_{s,i}^R, (\partial_x \hat{g}_s^R)_i, \hat{j}_{i,0}^R)$   $\triangleright$  Eq. (A3)
13:      end while
14:    end if
15:  end for
16:  for  $i \leftarrow 1$  to  $N$  do
17:     $r_1^i \leftarrow \hat{j}_{m_i}^R - \hat{j}_{n_i}^R + \sum_{k=1}^{m_i-n_i} w_k^i F_{n_i+k}$   $\triangleright$  Eq. (A7)
18:     $r_2^i \leftarrow \{u_{m_i}^p - u_{n_i}^p - \sum_{k=1}^{m_i-n_i} w_k^i \partial_x u_{n_i+k}^p\}$ 
19:  end for
20:  return  $\{r_1^i\}, \{r_2^i\}$ 
21: end function
22: Solve  $R(\{u_n^i\}, \{\partial_x u_n^i\}) = 0$ 

```

while Eq. (A9b) follows from the fluctuation-dissipation theorem.

-
- [1] J. Rammer and H. Smith, *Rev. Mod. Phys.* **58**, 323 (1986).
[2] V. Chandrasekhar, in *Superconductivity: Conventional and Unconventional Superconductors* (Springer, Berlin, 2008), pp. 279–313
[3] G. Eilenberger, *Z. Phys.* **214**, 195 (1968).
[4] K. D. Usadel, *Phys. Rev. Lett.* **25**, 507 (1970).
[5] W. Belzig, F. K. Wilhelm, C. Bruder, G. Schön, and A. D. Zaikin, *Superlattices Microstruct.* **25**, 1251 (1999).
[6] M. Eschrig, J. Kopu, J. C. Cuevas, and G. Schön, *Phys. Rev. Lett.* **90**, 137003 (2003).
[7] A. I. Buzdin, *Rev. Mod. Phys.* **77**, 935 (2005).
[8] F. S. Bergeret, A. F. Volkov, and K. B. Efetov, *Rev. Mod. Phys.* **77**, 1321 (2005).
[9] M. Houzet, *Phys. Rev. Lett.* **101**, 057009 (2008).
[10] T. T. Heikkilä, M. Silaev, P. Virtanen, and F. S. Bergeret, *Prog. Surf. Sci.* **94**, 100540 (2019).
[11] R. Fermin, D. van Dinter, M. Hubert, B. Woltjes, M. Silaev, J. Aarts, and K. Lahabi, *Nano Lett.* **22**, 2209 (2022).
[12] R. Ojajarvi, F. S. Bergeret, M. A. Silaev, and T. T. Heikkilä, *Phys. Rev. Lett.* **128**, 167701 (2022).
[13] E. H. Fyhn and J. Linder, *Phys. Rev. B* **103**, L100502 (2021).
[14] P. Virtanen, T. T. Heikkilä, F. S. Bergeret, and J. C. Cuevas, *Phys. Rev. Lett.* **104**, 247003 (2010).
[15] E. H. Fyhn and J. Linder, *Phys. Rev. B* **105**, L020409 (2022).
[16] J. A. Ouassou, A. Pal, M. Blamire, M. Eschrig, and J. Linder, *Sci. Rep.* **7**, 1932 (2017).
[17] H. G. Hugdal, J. Linder, and S. H. Jacobsen, *Phys. Rev. B* **95**, 235403 (2017).
[18] M. Amundsen, J. A. Ouassou, and J. Linder, *Phys. Rev. Lett.* **120**, 207001 (2018).
[19] M. Amundsen and J. Linder, *Sci. Rep.* **6**, 22765 (2016).
[20] T. Salamone, H. G. Hugdal, M. Amundsen, and S. H. Jacobsen, *Phys. Rev. B* **105**, 134511 (2022).
[21] T. Wakamura, N. Hasegawa, K. Ohnishi, Y. Niimi, and Y. C. Otani, *Phys. Rev. Lett.* **112**, 036602 (2014).
[22] E. H. Fyhn, M. Amundsen, A. Zalic, T. Dvir, H. Steinberg, and J. Linder, *Phys. Rev. B* **102**, 024510 (2020).
[23] J. A. Ouassou, T. D. Vethaak, and J. Linder, *Phys. Rev. B* **98**, 144509 (2018).
[24] E. H. Fyhn and J. Linder, *Phys. Rev. B* **100**, 214503 (2019).
[25] J. Linder and J. W. A. Robinson, *Nat. Phys.* **11**, 307 (2015).
[26] I. Žutić, J. Fabian, and S. Das Sarma, *Rev. Mod. Phys.* **76**, 323 (2004).
[27] H. Zabel, *Superlattices Microstruct.* **46**, 541 (2009).
[28] R. S. Keizer, S. T. B. Goennenwein, T. M. Klapwijk, G. Miao, G. Xiao, and A. Gupta, *Nature (London)* **439**, 825 (2006).
[29] B. Li, N. Roschewsky, B. A. Assaf, M. Eich, M. Epstein-Martin, D. Heiman, M. Münzenberg, and J. S. Moodera, *Phys. Rev. Lett.* **110**, 097001 (2013).

- [30] V. Baltz, A. Manchon, M. Tsoi, T. Moriyama, T. Ono, and Y. Tserkovnyak, *Rev. Mod. Phys.* **90**, 015005 (2018).
- [31] A. Pimenov, A. Shuvaev, A. Loidl, F. Schrettle, A. A. Mukhin, V. D. Travkin, V. Y. Ivanov, and A. M. Balbashov, *Phys. Rev. Lett.* **102**, 107203 (2009).
- [32] S. Baiertl, J. H. Mentink, M. Hohenleutner, L. Braun, T.-M. Do, C. Lange, A. Sell, M. Fiebig, G. Woltersdorf, T. Kampfrath, and R. Huber, *Phys. Rev. Lett.* **117**, 197201 (2016).
- [33] R. Lebrun, A. Ross, S. A. Bender, A. Qaiumzadeh, L. Baldrati, J. Cramer, A. Brataas, R. A. Duine, and M. Kläui, *Nature (London)* **561**, 222 (2018).
- [34] L. Bulaevskii, A. Buzdin, M. Kulić, and S. Panjukov, *Adv. Phys.* **34**, 175 (1985).
- [35] X. F. Lu, N. Z. Wang, H. Wu, Y. P. Wu, D. Zhao, X. Z. Zeng, X. G. Luo, T. Wu, W. Bao, G. H. Zhang *et al.*, *Nat. Mater.* **14**, 325 (2015).
- [36] H. Mukuda, S. Shimizu, A. Iyo, and Y. Kitaoka, *J. Phys. Soc. Jpn.* **81**, 011008 (2012).
- [37] S.-C. Zhang, *Science* **275**, 1089 (1997).
- [38] J. Orenstein and A. J. Millis, *Science* **288**, 468 (2000).
- [39] M. F. Jakobsen, K. B. Naess, P. Dutta, A. Brataas, and A. Qaiumzadeh, *Phys. Rev. B* **102**, 140504(R) (2020).
- [40] X. Zhou, M. Lan, Y. Ye, Y. Feng, X. Zhai, L. Gong, H. Wang, J. Zhao, and Y. Xu, *Europhys. Lett.* **125**, 37001 (2019).
- [41] L. Bulaevskii, R. Eneias, and A. Ferraz, *Phys. Rev. B* **95**, 104513 (2017).
- [42] M. F. Jakobsen, A. Brataas, and A. Qaiumzadeh, *Phys. Rev. Lett.* **127**, 017701 (2021).
- [43] L. G. Johnsen, S. H. Jacobsen, and J. Linder, *Phys. Rev. B* **103**, L060505 (2021).
- [44] S. Zhen, H. Zhang, Q. Zhang, and Z. Dong, *J. Supercond. Nov. Magn.* **32**, 1945 (2019).
- [45] M. Hübener, D. Tikhonov, I. A. Garifullin, K. Westerholt, and H. Zabel, *J. Phys.: Condens. Matter* **14**, 8687 (2002).
- [46] J. J. Hauser, H. C. Theuerer, and N. R. Werthamer, *Phys. Rev.* **142**, 118 (1966).
- [47] Y. Cheng and M. B. Stearns, *J. Appl. Phys.* **67**, 5038 (1990).
- [48] A. Manchon, *J. Phys.: Condens. Matter* **29**, 104002 (2017).
- [49] G. A. Bobkov, I. V. Bobkova, A. M. Bobkov, and A. Kamra, *Phys. Rev. B* **106**, 144512 (2022).
- [50] A. F. Volkov, A. Anishchanka, and K. B. Efetov, *Phys. Rev. B* **73**, 104412 (2006).
- [51] G. B. Halász, J. W. A. Robinson, J. F. Annett, and M. G. Blamire, *Phys. Rev. B* **79**, 224505 (2009).
- [52] A. Moor, A. F. Volkov, and K. B. Efetov, *Phys. Rev. B* **83**, 134524 (2011).
- [53] M. Dzero, M. Khodas, A. D. Klironomos, M. G. Vavilov, and A. Levchenko, *Phys. Rev. B* **92**, 144501 (2015).
- [54] A. M. Gabovich, A. I. Voitenko, J. F. Annett, and M. Ausloos, *Supercond. Sci. Technol.* **14**, R1 (2001).
- [55] Y. Hu, T. Zhang, D. Zhao, C. Chen, S. Ding, W. Yang, X. Wang, C. Li, H. Wang, D. Feng, and T. Zhang, *Nat. Commun.* **13**, 445 (2022).
- [56] M. G. Vavilov and A. V. Chubukov, *Phys. Rev. B* **84**, 214521 (2011).
- [57] C. Petrovic, P. G. Pagliuso, M. F. Hundley, R. Movshovich, J. L. Sarrao, J. D. Thompson, Z. Fisk, and P. Monthoux, *J. Phys.: Condens. Matter* **13**, L337 (2001).
- [58] M. Yu. Kuprianov and V. F. Lukichev, *Zh. Eksp. Teor. Fiz.* **94**, 139 (1988).
- [59] M. Eschrig, A. Cottet, W. Belzig, and J. Linder, *New J. Phys.* **17**, 083037 (2015).
- [60] N. A. Sinitsyn, A. H. MacDonald, T. Jungwirth, V. K. Dugaev, and J. Sinova, *Phys. Rev. B* **75**, 045315 (2007).
- [61] A. Larkin and Y. Ovchinnikov, Vortex motion in superconductors, in *Nonequilibrium Superconductivity*, edited by D. Langenberg and A. I. Larkin (Elsevier, Amsterdam, 1986), pp. 493–542.
- [62] A. L. Shelankov, *J. Low Temp. Phys.* **60**, 29 (1985).
- [63] E. H. Fyhn, A. Brataas, A. Qaiumzadeh, and J. Linder, [arXiv:2210.09325](https://arxiv.org/abs/2210.09325) (accompanying submission).
- [64] A. Kamra, A. Rezaei, and W. Belzig, *Phys. Rev. Lett.* **121**, 247702 (2018).
- [65] M. Houzet and J. S. Meyer, *Phys. Rev. B* **92**, 014509 (2015).
- [66] S. Ilić and F. S. Bergeret, *Phys. Rev. Lett.* **128**, 177001 (2022).
- [67] Y. V. Nazarov, *Superlattices Microstruct.* **25**, 1221 (1999).
- [68] Y. V. Nazarov and Y. M. Blanter, *Quantum Transport: Introduction to Nanoscience* (Cambridge University Press, Cambridge, 2009).
- [69] G. M. Eliashberg, *Sov. Phys. JETP* **34**, 668 (1972).
- [70] F. S. Bergeret, M. Silaev, P. Virtanen, and T. T. Heikkilä, *Rev. Mod. Phys.* **90**, 041001 (2018).
- [71] M. Eschrig, *Phys. Rev. B* **61**, 9061 (2000).
- [72] A. Konstandin, J. Kopu, and M. Eschrig, *Phys. Rev. B* **72**, 140501(R) (2005).
- [73] D. A. Ivanov and Y. V. Fominov, *Phys. Rev. B* **73**, 214524 (2006).

PAPER X

Reference

Eirik Holm Fyhn, Arne Brataas, Alireza Qaiumzadeh, and Jacob Linder,

Superconducting proximity effect and long-ranged triplets in dirty metallic antiferromagnets.

arXiv:2210.09325

DOI: 10.48550/arxiv.2210.09325

CONTRIBUTIONS

EHF performed the analytical calculations and the numerical simulations. EHF developed the code, drafted the manuscript and produced all the figures presented in the paper. All authors contributed to the physics discussions and the final manuscript.

Superconducting proximity effect and long-ranged triplets in dirty metallic antiferromagnets

Eirik Holm Fyhn,¹ Arne Brataas,¹ Alireza Qaiumzadeh,¹ and Jacob Linder¹

¹*Center for Quantum Spintronics, Department of Physics, Norwegian University of Science and Technology, NO-7491 Trondheim, Norway*

(Dated: May 30, 2023)

Antiferromagnets have no net spin-splitting on the scale of the superconducting coherence length. Despite this, antiferromagnets have been observed to suppress superconductivity in a similar way as ferromagnets, a phenomenon that still lacks a clear understanding. We find that this effect can be explained by the role of impurities in antiferromagnets. Using quasiclassical Green's functions, we study the proximity effect and critical temperature in diffusive superconductor-metallic antiferromagnet bilayers. The non-magnetic impurities acquire an effective magnetic component in the antiferromagnet. This not only reduces the critical temperature but also separates the superconducting correlations into short-ranged and long-ranged components, similar to ferromagnetic proximity systems.

Introduction: Antiferromagnets and superconductors both have prominent roles in condensed matter physics [1–9]. Separately, they are both theoretically interesting due to their different types of quantum order [10–13]. They are also technologically useful: superconductors in part because of their perfect diamagnetism and dissipationless current [14, 15], and antiferromagnets because of their ultrafast dynamics [16, 17], negligible stray-field and considerable magnetotransport effects [1]. However, while materials with superconducting or magnetic properties can be interesting on their own, new physics and applications can be found in systems that combine both. For instance, combining superconductivity and ferromagnetism in mesoscopic heterostructures is now a well-established method to produce odd-frequency superconductivity and long-range spin-triplet superconductivity [13, 18]. The latter can carry dissipationless spin-currents, giving superconductors a unique role in the field of spintronics [2].

Superconductor-antiferromagnet (SC-AF) heterostructures have been studied both theoretically and experimentally [19–30], but much less than their ferromagnetic counterparts. As a result, much remains to be fully understood about SC-AF heterostructures. For instance, experiments show that proximity to antiferromagnets can severely suppress the superconducting critical temperature [28–30]. This suppression is much stronger than the prediction by the theoretical models which considered the AFs to be similar to normal metals due to their lack of uncompensated magnetic moments [29–31]. In fact, the suppression has been reported to be even larger than the suppression seen in ferromagnetic junctions [28]. Various proposals have been suggested to explain this suppression, such as finite spin-splitting coming from uncompensated interfaces [30], the possibility of magnetic impurities having been infused into the superconductor during sample preparation [28], or the complex spin structure of the specific antiferromagnetic materials used in the experiments [29].

More recently, in a theoretical study of superconductor-antiferromagnetic insulator bilayers with compensated interfaces, Bobkov *et al.* [32] suggested that a band-gap opening mechanism together with the induction of spin-triplet Cooper pairs could explain the suppression. As these effects are smaller when the mean free path is shorter, they argued that the suppression would be larger for cleaner systems, but noted that a

fully detailed analysis of the roles of impurities and AF length should consider a metallic AF.

Here, we study the proximity effect in diffusive superconductor (SC)-antiferromagnetic metal (AFM) bilayers using our newly derived quasiclassical framework [33]. Interestingly, our results show that the suppression of superconductivity is not larger for clean systems, but that impurity scattering is in fact the dominant mechanism for superconductivity suppression in metallic AFs. The reason is that the sublattice-spin coupling in the antiferromagnet gives the non-magnetic impurities an effective magnetic component. These effective magnetic impurities are detrimental to superconductivity, except for spin-triplet superconductivity with spin aligned orthogonal to the Néel vector. As a result, dirty AFMs work as superconductivity filters letting only spin-triplet superconductivity with orthogonal spin-projection to the Néel vector pass through. After studying the critical temperature in SC/AFM bilayers, we show how the superconducting correlations penetrate into the antiferromagnetic metal, as well as the inverse proximity effect. Moreover, we show how the long-range spin-triplet components can be induced by either uncompensated or magnetic interfaces with magnetic misalignment relative to the AFM Néel vector.

Theory: To study SC-AFM bilayers, we employ the quasiclassical Keldysh formalism derived in [33]. It is valid under the assumption that the Fermi wavelength is short compared to the coherence length and the mean free path, and the chemical potential, μ , is much larger than all other energy scales in the system, except possibly the exchange energy between localized spins and conducting electrons, J . Note that $|J/\mu| < 1$, since $|\mu| = \sqrt{J^2 + t^2}$, where t is the hopping parameter evaluated at the Fermi surface. We also assume the dirty limit, meaning that the system is diffusive, and that there is no electromagnetic vector potential. In this case, the quasiclassical Green's function \check{g} solves [33]

$$i\nabla \cdot \check{\mathbf{j}} + \left[\tau_z(\varepsilon + i\delta) + \hat{\Delta} + \frac{iJ^2}{2\tau_{\text{imp}}\mu^2} \sigma_z \tau_z \check{g} \sigma_z \tau_z, \check{g} \right] = 0. \quad (1)$$

Here, $\check{\mathbf{j}}$ is the matrix current, τ_z and σ_z are Pauli matrices in Nambu- and spin-space, respectively, ε is energy, δ is the Dynes parameter, τ_{imp} is the elastic impurity scattering time and $\hat{\Delta} = \Delta i\tau_y$, under the assumption that the gap parameter Δ is real. The spin-quantization axis is chosen to be parallel

to the Néel vector, which is assumed homogeneous within the AFM. We let the system be large in the directions parallel to the interface, such that the problem becomes an effective 1D problem.

The quasiclassical Green's function can be written

$$\check{g} = \begin{pmatrix} \hat{g}^R & \hat{g}^K \\ 0 & \hat{g}^A \end{pmatrix}, \quad (2)$$

where \hat{g}^R , \hat{g}^A and \hat{g}^K are the retarded, advanced and Keldysh Green's functions, respectively. In thermal equilibrium, which is assumed here, it is sufficient to solve for \hat{g}^R , since $\hat{g}^A = -\tau_z(\hat{g}^R)^\dagger\tau_z$ and $\hat{g}^K = (\hat{g}^R - \hat{g}^A)\tanh(\beta\varepsilon/2)$.

Equation (1) is similar to the Usadel equation for normal metals [34] but is modified by the antiferromagnetic order in two important ways. First, the expression for the matrix current is now

$$\check{j} = -D\check{g}\nabla\check{g} - \check{g}\left[\frac{J^2}{2\mu^2}\sigma_z\tau_z\check{g}\sigma_z\tau_z, \check{j}\right], \quad (3)$$

where D is the diffusion constant. The second way AFMs differ from normal metals is through the term proportional to $\sigma_z\tau_z\check{g}\sigma_z\tau_z$ in Eq. (1). This is exactly the way magnetic impurities enter the Usadel equation for normal metals [35]. Hence, the antiferromagnetic order gives rise to effective magnetic impurities with scattering time equal to $\tau_{\text{imp}}\mu^2/J^2$.

The presence of τ_{imp}^{-1} in the equations requires some special care, as discussed in detail in Ref. [33]. Since the impurity scattering rate, τ_{imp}^{-1} , is small in the dirty limit, one should project onto only the long-ranged components of \check{g} when $J^2/\mu^2 \approx 1$. This is possible because some components become negligible in this limit of very strong exchange coupling. Here, we consider smaller values of J^2/μ^2 . Consequently, the effective magnetic scattering rate $J^2/(\mu^2\tau_{\text{imp}})$ is not necessarily large, and we must keep all components of \check{g} .

To model SC-AFM bilayers, we set $J = 0$ in the SC and $\Delta = 0$ in the AFM. The dimensionless quantity J/μ is non-zero in the AFM, while the gap parameter in the SC is determined through the self-consistency equation [36],

$$\Delta = \frac{1}{4\text{acosh}(\omega_D/\Delta_0)} \int_0^{\omega_D} d\varepsilon \text{Tr}[(\tau_x - i\tau_y)\hat{g}^K], \quad (4)$$

where symmetries of the Green's function were used to write Δ as an integral over only positive energies, ω_D is a cutoff energy and Δ_0 is a material-specific parameter defining the gap parameter in the bulk. We set $\omega_D = 30\Delta_0$.

The two materials must be connected through a boundary condition, which is also derived in [33]. We consider both compensated and uncompensated interfaces. Let the interface be located at $x = 0$, and let $\check{g}_{SC} = \check{g}(0^-)$ and $\check{g}_{AF} = \check{g}(0^+)$ be the quasiclassical Green's functions on the superconducting and antiferromagnetic sides of the interface, respectively. We similarly let \check{j}_{SC} and \check{j}_{AF} be the matrix current on the SC and AFM sides, respectively. The general boundary condition for the matrix current going out of material $\alpha \in \{SC, AF\}$ and into material $\beta \in \{SC, AF\}$ is [33]

$$\mathbf{e}_n \cdot \check{j}_\alpha = [\hat{T}_{\alpha\beta}\check{g}_\beta\hat{T}_{\beta\alpha} + i\hat{R}_\alpha, \check{g}_\alpha]. \quad (5)$$

where \mathbf{e}_n is the outward-pointing normal vector, $\hat{T}_{\alpha\beta}$ is the tunneling matrix and \hat{R}_α is the reflection matrix. For the case of a compensated interface, we assume that tunneling and reflection are independent of spin and sublattice. In this case $\hat{T}_{\alpha\beta} = \hat{T}_{\beta\alpha}^* = t$ and \hat{R}_α are scalars.

In the case of an uncompensated interface, we assume that tunneling can only occur between the SC and the A-sublattice in the AFM. In this case, we find from Ref. [33] that the tunneling matrix becomes

$$T_{SC,AF} = T_{AF,SC}^\dagger = \frac{t}{2} \left[\sqrt{1+J/\mu} + \sqrt{1-J/\mu} + \left(\sqrt{1+J/\mu} - \sqrt{1-J/\mu} \right) \tau_z \mathbf{m} \cdot \boldsymbol{\sigma} \right]. \quad (6)$$

Here we have allowed for a possible misalignment between the magnetization direction in the AFM and the magnetization direction at the interface through the unit vector \mathbf{m} . When the system is uncompensated, there should in general also be spin-dependent reflection. For simplicity, we set the reflection matrix equal at both sides of the interface and equal to $\hat{R}_{SC} = \hat{R}_{AF} = r\tau_z\mathbf{m} \cdot \boldsymbol{\sigma}$. Note that instead of an uncompensated interface, one can instead use a thin ferromagnetic (F) layer. For instance, one could consider an SC/F/I/AFM structure, where the insulator (I) is used to reduce the exchange bias effect. In this case, \mathbf{m} would be the magnetization direction of the ferromagnet.

We solve Eqs. (1) and (3)–(5) numerically using the Riccati-parametrization [37, 38] and a collocation method [33], and determine the matrix current by fixed-point iterations of Eq. (3). For simplicity, we set the diffusion constant to be equal in both materials. We denote by L_{AF} and L_{SC} the lengths of the AFM and SC, respectively, and $\xi = \sqrt{D/\Delta_0}$ is the diffusive coherence length. To find the critical temperature, we use the algorithm described in Ref. [39].

Critical temperature: We plot the critical temperature as a function of AFM length for various values of J/μ in Fig. 1 for the case of a compensated interface. As J/μ is increased, the critical temperature is reduced substantially, which is consistent with experiments [28–30]. While T_C decays slowly, reaching only around one-third of the bulk value in the SC/NM bilayers ($J/\mu = 0$), T_C is reduced all the way to 0 in the SC/AFM bilayers. The AFM length needed to make T_C vanish reduces with increasing J/μ . This can be understood from the effective magnetic impurities in the AFM, which has a scattering rate proportional to J^2/μ^2 . It has long been known that even a small amount of magnetic impurities can strongly reduce the superconducting transition temperature [40–42]. The magnetic impurities give rise to spin-flip scatterings which break the spin-singlet Cooper pairs, thereby lowering the transition temperature.

Note that the maximal suppression of T_C depends on the length of the superconductor and the magnitude of the tunneling amplitude. When the superconductor is long compared to the coherence length, T_C will be non-zero no matter how much the gap is suppressed near the interface. Therefore, while one can observe total T_C suppression for short superconductors, like in Ref. [29], one should expect only a partial suppression, like in Refs. [28, 30], when the superconductor is long or the

tunneling amplitude is small. In the case of partial suppression, one should expect the minimal value to be reached when the length of the antiferromagnet reaches approximately the penetration depth of spin-singlet correlations, determined by τ_{imp} and J/μ .

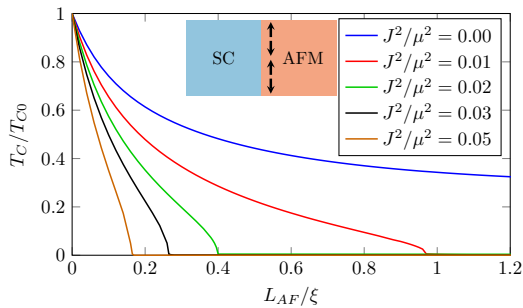


FIG. 1: Critical temperature T_C as a function of AFM length L_{AF} normalized by the coherence length $\xi = \sqrt{D/\Delta_0}$. T_{C0} is the bulk critical temperature. The inset shows a sketch of an SC/AFM bilayer with a compensated interface. The length of the superconductor is $L_{SC} = \xi$, the impurity scattering rate is $1/\tau_{\text{imp}} = 100\Delta_0$, the Dynes parameter is $\delta = 0.001\Delta_0$ and the tunneling amplitude is $t = 3\sqrt{\Delta_0\xi}$.

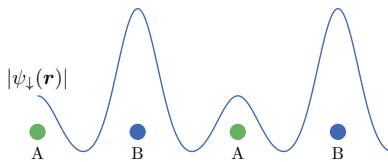


FIG. 2: Exaggerated sketch of the spatial distribution of the conduction electron state with spin down. The overlap is larger with the B-sublattice than with the A-sublattice. As a result, the conduction band electrons with spin-down will be affected more strongly by non-magnetic impurities on the B-sublattice than by non-magnetic impurities on the A-sublattice.

To understand the origin of the effective magnetic impurities, consider the spatial distributions of the two degenerate spin-states of the antiferromagnetic conduction band. The spin-down state is sketched in Fig. 2. The spin-down (spin-up) state has larger amplitude on sublattice B (A) compared to sublattice A. As a result, non-magnetic impurities on sublattice B (A) act like superpositions of non-magnetic impurities and impurities with magnetization in the $-z(+z)$ -direction on the conduction band electrons. Therefore, electrons in the conduction band experience an effective magnetic impurity potential giving rise to spin-flip scattering described by the term proportional to $iJ^2/2\tau_{\text{imp}}\mu^2$ in Eq. (1). The spin orientations of these impurities are locked along the direction of the Néel vector. This gives rise to the possibility of long-ranged triplet correlations, as is shown in the following.

Proximity effect: To study how the proximity effect is

affected by the antiferromagnetic order, we consider the anomalous Green's function, $\text{Tr}[(\tau_x - i\tau_y)\hat{g}^R] = f_0 + \mathbf{f} \cdot \boldsymbol{\sigma}$. Here, f_0 describes the conventional spin-singlet superconducting correlations while $\mathbf{f} = (f_x, f_y, f_z)$ describes the spin-triplet correlations. Note that since we are working with diffusive systems, the spin-singlet and spin-triplet correlations are also even and odd in frequency, respectively.

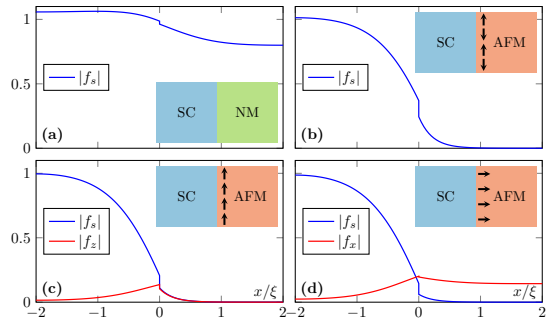


FIG. 3: The non-zero components of the anomalous Green's function $f_0 + f_x\sigma_x + f_z\sigma_z$ evaluated at energy $\varepsilon = D/L_{AF}^2$ for various bilayer cases illustrated by the insets. The SC/AFM interface is at $x = 0$ and the Néel vector points in the z -direction. (a) SC/NM ($J/\mu = 0$), (b) SC/AFM with compensated interface, (c) SC/AFM with uncompensated interface aligned in the z -direction, (d) SC/AFM with uncompensated interface aligned in the x -direction. (a)-(d) have Dynes parameter $\delta = 0.001\Delta_0$, tunneling amplitude $t = 2\sqrt{\Delta_0\xi}$, temperature $T = 0.05T_{C0}$, SC length $L_{SC} = 2\xi$ and AFM length $L_{AF} = 2\xi$. (b)-(d) have $J^2/\mu^2 = 0.1$, $1/\tau_{\text{imp}} = 100\Delta_0$. (c)-(d) have $r = \Delta_0\xi$.

Figure 3 shows the anomalous Green's function for various SC/AFM structures evaluated at $\varepsilon = D/L_{AF}^2$. There is a large singlet component in the SC as expected. In Fig. 3(a), the neighboring material is a normal metal, meaning that $J/\mu = 0$, and therefore the proximity induced f_0 penetrates deeply without significant decay. On the other hand, in Fig. 3(b), the neighboring material has antiferromagnetic ordering with $J^2/\mu^2 = 0.1$ and $J^2/\mu^2\tau_{\text{imp}} = 10\Delta_0$. In this case, the spin-singlet f_0 induced through the compensated interface decays over a much shorter length scale because of the effective magnetic impurities discussed above. Additionally, f_0 is also more suppressed on the SC side, as expected from the T_C results.

With an uncompensated interface, as shown in Fig. 3(c)-(d), spin-triplet correlations, \mathbf{f} , are also induced at the interface. These correlations are aligned parallel to the magnetization direction of the interface. When the correlations are parallel to the Néel-vector of the antiferromagnet, as in Fig. 3(c), they are affected by the magnetic impurities in the same way as the spin-singlet correlations, and therefore decay over the same length-scale. However, when \mathbf{f} is orthogonal to the Néel vector, as in Fig. 3(d), the spin-triplet correlations become long-ranged, decaying over a length scale that is the same as for a normal metal.

Thus, one can distinguish between short-ranged triplets and

long-ranged triplets in diffusive AFMs, just as in FMs. The reason why spin-singlet correlations and $\mathbf{f} \parallel \mathbf{h}$ are short-ranged in FMs with spin-splitting field \mathbf{h} is because \mathbf{h} induces an energy-difference between the electrons in the Cooper pairs, causing decoherence. On the other hand, the spins of the two electrons in $\mathbf{f} \perp \mathbf{h}$ are both parallel to \mathbf{h} , such that they have the same wavelength as they propagate into the FM. In diffusive antiferromagnets with Néel vector \mathbf{n} , the reason for the decoherence is non-magnetic impurities, but the effect is similar. Spin-singlet f_0 and spin-triplet $\mathbf{f} \parallel \mathbf{n}$ are short-ranged while $\mathbf{f} \perp \mathbf{n}$ are long-ranged.

In order to compute the decay length associated with long-ranged and short-ranged correlations, we linearize the retarded component of Eq. (1) in the AFM. We let $\hat{g}^R = \tau_z + i\tau_y f$. To first order in f , we get from Eq. (3) that $\hat{j}^R = -D\tau_x \nabla f / (1 + J^2/\mu^2)$. Inserting this into Eq. (1), we get to first order in f that

$$\frac{D\nabla^2 f}{1 + J^2/\mu^2} = -\left(2i\varepsilon - 2\delta - \frac{J^2}{\tau_{\text{imp}}\mu^2}\right) f + \frac{J^2}{\tau_{\text{imp}}\mu^2} \sigma_z f \sigma_z. \quad (7)$$

Thus, if $\lim_{x \rightarrow \infty} f(x) = 0$ and $f(0) = a_0 + \mathbf{a} \cdot \boldsymbol{\sigma}$ for some constants a_0 , and $\mathbf{a} = (a_x, a_y, a_z)$, then $f = (a_0 + a_z \sigma_z) e^{ik_{\perp}x} + (a_x \sigma_x + a_y \sigma_y) e^{ik_{\perp}x}$, where $k_{\perp} = \sqrt{2(1 + J^2/\mu^2)(i\varepsilon - \delta)}/D$ and $k_{\parallel} = k_{\perp} \sqrt{(i\varepsilon - \delta - \tau_{\text{imp}}^{-1} J^2/\mu^2)/(i\varepsilon - \delta)}$, such that the imaginary parts of k_{\parallel} and k_{\perp} are positive.

To find the decay lengths, we must take the imaginary parts of k_{\parallel} and k_{\perp} . When $\varepsilon \gg \delta$, the long-ranged correlations decay over a length scale equal to $\lambda_{\perp} = 1/\text{Im}(k_{\perp}) = \sqrt{D}/[(1 + J^2/\mu^2)\varepsilon]$. This is on the same order as in a normal metal, $\lambda_{\text{NM}} = \sqrt{D/\varepsilon}$. On the other hand, if $J^2/\mu^2 \tau_{\text{imp}} \gg \varepsilon$, the short-ranged correlations decay over a length scale equal to $\lambda_{\parallel} = \mu l_{\text{mfp}}/[J\sqrt{6(1 + J^2/\mu^2)}]$, which can be compared to the decay length for short-ranged correlations in ferromagnets [18], $\lambda_{\text{FM}} = \sqrt{D}/h$, where h is the spin-splitting energy. Here, $l_{\text{mfp}} = v_F \tau_{\text{imp}}$ is the mean free path, where v_F is the Fermi velocity.

Local density of states: In Fig. 4 we show the normalized density of states, $N/N_0 = \text{Re}(\hat{g}_{11}^R + \hat{g}_{22}^R)/2$, as a function of energy at various positions inside the antiferromagnet with the same parameters as in Fig. 3, except that $J^2/\mu^2 = 0.01$ in Fig. 4(b)-(d). The local density of states in the SC/NM bilayer is shown in Fig. 4(a), and one can see a minigap in the spectrum as expected [43]. However, no minigap is present in the SC/AFM bilayers. This is because the effective magnetic impurities act similarly to inelastic scattering for the spin-singlet correlations, leading to a much weaker suppression in the density of states, and a more smeared-out spectrum. This is true also very close to the interface, as can be seen in Fig. 4(b). As one moves away from the interface as $x = 0$, the spectrum in the Fig. 4(b) rapidly becomes flatter. This is in contrast to the spectrum in the SC/NM system, which retains the minigap also away from the interface. The flatness of the spectrum away from the interface can be understood from the exponential decay coming from the effective magnetic impurities.

Figure 4(c) and Fig. 4(d) shows the local density of states for SC/AFM bilayers with short-ranged and long-ranged triplets respectively. Both show a pronounced peak in the density of

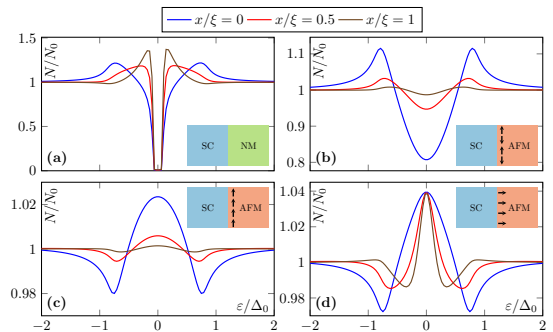


FIG. 4: The local density of states, N , normalized by the normal state density of states N_0 , at different positions inside the antiferromagnet. The parameters are the same as in Fig. 3, except that $J^2/\mu^2 = 0.01$ in (b)-(d).

states at zero energy, similar to ferromagnetic systems with spin-triplet superconductivity [44]. Close to the interface, the spectrum in Fig. 4(c) is more smeared out than the spectrum in Fig. 4(d), probably because the effective magnetic impurities act on the short-ranged spin-triplet correlations in a similar way as they do on the spin-singlet correlations. However, the biggest difference can be observed when going away from the interface. While the spectrum in Fig. 4(c) becomes flatter, as expected from the exponential decay of the superconducting correlations, the spectrum in Fig. 4(d) transforms in the opposite way. The zero-energy peak becomes sharper as the distance to the interface increases.

Conclusion: We have theoretically studied diffusive SC/AFM bilayers with both compensated and uncompensated interfaces. We find a strong suppression of the critical temperature, consistent with experiments [28–30]. This suppression can be explained in terms of effective magnetic impurities. Non-magnetic impurities interact with conduction electrons in the AFM in a similar way as magnetic impurities in NMs. Thus, we predict that cleaner AFMs will suppress superconductivity to a smaller degree, giving rise to higher critical temperatures. The impurities in AFMs not only suppress spin-singlet superconductivity, and thereby T_C , but they also suppress spin-triplet correlations that are oriented parallel to the Néel vector. As a result, spin-singlet correlations and spin-triplet correlations with parallel orientation are short-ranged, decaying exponentially over a length scale determined by the mean free path and the exchange energy between localized spins and conducting electrons. In contrast, spin-triplet correlations with orientation orthogonal to the Néel vector are long-ranged. They can penetrate as far as in normal metals. Such long-range triplets can be induced by misaligned uncompensated interfaces, or by more complicated heterostructures.

Acknowledgments

This work was supported by the Research Council of Norway through grant 323766, and its Centres of Excellence fund-

ing scheme grant 262633 “*QuSpin*”. J.L. also acknowledges computational resources provided by Sigma2 - the National Infrastructure for High-Performance Computing and Data Storage in Norway from project no. NN9577K.

-
- [1] V. Baltz, A. Manchon, M. Tsai, T. Moriyama, T. Ono, and Y. Tserkovnyak, *Rev. Mod. Phys.* **90**, 015005 (2018).
- [2] J. Linder and J. W. A. Robinson, *Nat. Phys.* **11**, 307 (2015).
- [3] F. Parhizgar and A. M. Black-Schaffer, *Phys. Rev. B* **104**, 054507 (2021).
- [4] P. Wadley, B. Howells, J. Železný, C. Andrews, V. Hills, R. P. Campion, V. Novák, K. Olejník, F. Maccherozzi, S. S. Dhesi, S. Y. Martin, T. Wagner, J. Wunderlich, F. Freimuth, Y. Mokrousov, J. Kuneš, J. S. Chauhan, M. J. Grzybowski, A. W. Rushforth, K. W. Edmonds, B. L. Gallagher, and T. Jungwirth, *Science* **351**, 587 (2016).
- [5] P. Vaidya, S. A. Morley, J. van Tol, Y. Liu, R. Cheng, A. Brataas, D. Lederman, and E. del Barco, *Science* **368**, 160 (2020).
- [6] X. Wu, T. Schwemmer, T. Müller, A. Consiglio, G. Sangiovanni, D. Di Sante, Y. Iqbal, W. Hanke, A. P. Schnyder, M. M. Denner, M. H. Fischer, T. Neupert, and R. Thomale, *Phys. Rev. Lett.* **127**, 177001 (2021).
- [7] L. Ma, K. Wang, Y. Xie, X. Yang, Y. Wang, M. Zhou, H. Liu, X. Yu, Y. Zhao, H. Wang, G. Liu, and Y. Ma, *Phys. Rev. Lett.* **128**, 167001 (2022).
- [8] Y.-Z. Chou, F. Wu, J. D. Sau, and S. Das Sarma, *Phys. Rev. Lett.* **127**, 187001 (2021).
- [9] Y. Pan, C. Le, B. He, S. J. Watzman, M. Yao, J. Gooth, J. P. Heremans, Y. Sun, and C. Felser, *Nat. Mater.* **21**, 203 (2022).
- [10] P. A. Lee, N. Nagaosa, and X.-G. Wen, *Rev. Mod. Phys.* **78**, 17 (2006).
- [11] F. D. M. Haldane, *Phys. Rev. Lett.* **50**, 1153 (1983).
- [12] G. Sala, M. B. Stone, B. K. Rai, A. F. May, P. Laurell, V. O. Garlea, N. P. Butch, M. D. Lumsden, G. Ehlers, G. Pokharel, A. Podlesnyak, D. Mandrus, D. S. Parker, S. Okamoto, G. B. Halász, and A. D. Christianson, *Nat. Commun.* **12**, 171 (2021).
- [13] J. Linder and A. V. Balatsky, *Rev. Mod. Phys.* **91**, 045005 (2019).
- [14] K. Fossheim and A. Sudbø, *Superconductivity: physics and applications* (John Wiley & Sons, 2004).
- [15] J. Jin, G. Sheng, Y. Bi, Y. Song, X. Liu, X. Chen, Q. Li, Z. Deng, W. Zhang, J. Zheng, T. Coombs, B. Shen, J. Zhu, Y. Zhao, J. Wang, B. Xiang, Y. Tang, L. Ren, Y. Xu, J. Shi, M. R. Islam, Y. Guo, and J. Zhu, *IEEE Trans. Appl. Supercond.* **31**, 1 (2021).
- [16] A. Pimenov, A. Shuvaev, A. Loidl, F. Schrettle, A. A. Mukhin, V. D. Travkin, V. Y. Ivanov, and A. M. Balbashov, *Phys. Rev. Lett.* **102**, 107203 (2009).
- [17] S. Baierl, J. H. Mentink, M. Hohenleutner, L. Braun, T.-M. Do, C. Lange, A. Sell, M. Fiebig, G. Woltersdorf, T. Kampfrath, and R. Huber, *Phys. Rev. Lett.* **117**, 197201 (2016).
- [18] F. S. Bergeret, A. F. Volkov, and K. B. Efetov, *Rev. Mod. Phys.* **77**, 1321 (2005).
- [19] M. H. bener, D. Tikhonov, I. A. Garifullin, K. Westerholt, and H. Zabel, *Journal of Physics: Condens Matter* **14**, 8687 (2002).
- [20] B. M. Andersen, I. V. Bobkova, P. J. Hirschfeld, and Y. S. Barash, *Phys. Rev. B* **72**, 184510 (2005).
- [21] A. Zaitsev, G. A. Ovsyannikov, K. Y. Constantinian, Y. V. Kisil'skiĭ, A. V. Shadrin, I. V. Borisenko, and P. V. Komissinskiy, *J. Exp. Theor. Phys.* **110**, 336 (2010).
- [22] A. Moor, A. F. Volkov, and K. B. Efetov, *Phys. Rev. B* **85**, 014523 (2012).
- [23] A. Kamra, A. Rezaei, and W. Belzig, *Phys. Rev. Lett.* **121**, 247702 (2018).
- [24] L. G. Johnsen, S. H. Jacobsen, and J. Linder, *Phys. Rev. B* **103**, L060505 (2021).
- [25] M. F. Jakobsen, K. B. Naess, P. Dutta, A. Brataas, and A. Qaiumzadeh, *Phys. Rev. B* **102**, 140504(R) (2020).
- [26] S. S. Luntama, P. Törmä, and J. L. Lado, *Phys. Rev. Research* **3**, L012021 (2021).
- [27] X. Zhou, M. Lan, Y. Ye, Y. Feng, X. Zhai, L. Gong, H. Wang, J. Zhao, and Y. Xu, *EPL* **125**, 37001 (2019).
- [28] B. L. Wu, Y. M. Yang, Z. B. Guo, Y. H. Wu, and J. J. Qiu, *Appl. Phys. Lett.* **103**, 152602 (2013).
- [29] M. Hübener, D. Tikhonov, I. A. Garifullin, K. Westerholt, and H. Zabel, *J. Phys.: Condens. Matter* **14**, 8687 (2002).
- [30] C. Bell, E. J. Tarte, G. Burnell, C. W. Leung, D.-J. Kang, and M. G. Blamire, *Phys. Rev. B* **68**, 144517 (2003).
- [31] N. R. Werthamer, *Phys. Rev.* **132**, 2440 (1963).
- [32] G. A. Bobkov, I. V. Bobkova, A. M. Bobkov, and A. Kamra, *Phys. Rev. B* **106**, 144512 (2022).
- [33] E. H. Fyhn, A. Brataas, A. Qaiumzadeh, and J. Linder, *Phys. Rev. B* **107**, 174503 (2023).
- [34] K. D. Usadel, *Phys. Rev. Lett.* **25**, 507 (1970).
- [35] T. Yokoyama, Y. Tanaka, A. A. Golubov, J. Inoue, and Y. Asano, *Phys. Rev. B* **71**, 094506 (2005).
- [36] S. H. Jacobsen, J. A. Ouassou, and J. Linder, *Phys. Rev. B* **92**, 024510 (2015).
- [37] M. Eschrig, *Phys. Rev. B* **61**, 9061 (2000).
- [38] A. Konstandin, J. Kopu, and M. Eschrig, *Phys. Rev. B* **72**, 140501(R) (2005).
- [39] J. A. Ouassou, A. D. Bernardo, J. W. A. Robinson, and J. Linder, *Sci. Rep.* **6**, 29312 (2016).
- [40] A. A. Abrikosov and L. P. Gor'kov, *Zhur. Eksptl'. i Teoret. Fiz.* **39**, 1781 (1960).
- [41] J. J. Hauser, H. C. Theuerer, and N. R. Werthamer, *Phys. Rev.* **142**, 118 (1966).
- [42] M. Jarrell, *Phys. Rev. Lett.* **61**, 2612 (1988).
- [43] J. C. Hammer, J. C. Cuevas, F. S. Bergeret, and W. Belzig, *Phys. Rev. B* **76**, 064514 (2007).
- [44] J. A. Ouassou, A. Pal, M. Blamire, M. Eschrig, and J. Linder, *Sci. Rep.* **7**, 1932 (2017).

ISBN 978-82-326-7176-2 (printed ver.)
ISBN 978-82-326-7175-5 (electronic ver.)
ISSN 1503-8181 (printed ver.)
ISSN 2703-8084 (online ver.)



NTNU

Norwegian University of
Science and Technology